

# Study of background and transmission properties of the KATRIN spectrometers

Zur Erlangung des akademischen Grades eines  
DOKTORS DER NATURWISSENSCHAFTEN  
von der Fakultät für Physik  
des Karlsruher Instituts für Technologie  
genehmigte  
DISSERTATION

von

**Diplom Physikerin Nancy Wandkowsky**

aus Halle an der Saale

Erstgutachter:

Prof. Dr. G. Drexlin

Institut für Experimentelle Kernphysik, KIT

Zweitgutachter:

Prof. Dr. W. de Boer

Institut für Experimentelle Kernphysik, KIT

Tag der mündlichen Prüfung: 19. Juli 2013



Hiermit versichere ich, dass ich die vorliegende Dissertationsschrift selbständig und nur unter Verwendung der angegebenen Quellen und Hilfsmittel verfasst habe.

Karlsruhe, 11. Juni 2013

---

# Abstract

Neutrinos are the most abundant massive particles in the Universe. Therefore, their properties, and especially their non-vanishing mass, are important parameters in the fields of particle physics and cosmology. So far, there exists only a lower limit of  $0.04 \text{ eV}/c^2$  on the effective mass of the electron anti-neutrino  $m_{\bar{\nu}_e}$  from neutrino oscillations, and an upper limit of  $2 \text{ eV}/c^2$ , provided by direct neutrino mass experiments.

The next generation large-scale tritium  $\beta$ -decay experiment KATRIN (Karlsruhe Tritium Neutrino experiment) is designed to determine  $m_{\bar{\nu}_e}$  with a sensitivity of  $200 \text{ meV}/c^2$  (90% C.L.). This is achieved by a precise scan of the electron energy spectrum close to its endpoint at 18.6 keV. As only a fraction of  $10^{-13}$  of all signal electrons is found in the region-of-interest, a well-understood high-resolution analyzing spectrometer and an ultra-low background rate of less than  $10^{-2}$  counts per second are required to either determine the neutrino mass (if it is larger than  $200 \text{ meV}/c^2$ ) or to improve the upper limit by one order of magnitude compared to predecessor experiments.

The focus of this thesis is on the detailed description and optimization of background and transmission properties of the KATRIN spectrometers. For this purpose, a variety of physics models, describing different processes within electrostatic spectrometers, have been implemented into the KATRIN simulation software KASSIOPEIA. The new features allowed a detailed study of experimental observations with the help of large-scale Monte-Carlo simulations.

An external package (KTRAP) has been developed in the course of this thesis with the aim to optimize the electromagnetic configuration of the main spectrometer. For this purpose, KTRAP especially makes use of the field calculation packages within KASSIOPEIA. An automated procedure was developed to determine optimal current setups for the large volume air coil system, surrounding the main spectrometer, which was designed to fine-tune the magnetic flux tube guiding the signal electrons.

The electron energy scan with an electrostatic spectrometer of the MAC-E filter type requires a detailed understanding of its transmission properties. These are determined by an interplay of the magnetic field, which collimates the signal electron momenta, and the electrostatic potential, responsible for filtering of electrons according to their longitudinal kinetic energy. The precise knowledge of the analyzing magnetic field strength and electrostatic potential is a key requirement for a successful neutrino mass determination. These parameters have to be determined within the main spectrometer commissioning measurements, using an angular-resolved, quasi-monoenergetic electron gun as electron

---

source. This thesis focuses on the development of corresponding measurement and analysis strategies and validates them by application to Monte-Carlo-generated data.

The second main focus of this work is the investigation of possible background-generating mechanisms and their suppression within electrostatic spectrometers of the MAC-E filter type. The dominant background components within the KATRIN main spectrometer are expected to stem from cosmic muon-induced secondary electrons and radon-induced stored electrons.

For the purpose of studying the production and transport mechanisms of low-energy  $\mu$ -induced electrons within the main spectrometer, an external muon detector system was built-up and commissioned. By a combination of various test measurements, using different electromagnetic configurations determined with KASSIOPEIA, this background component can be investigated in detail. Corresponding measurement strategies are outlined and simulations are used to demonstrate the conditions for electron transport from the main spectrometer surface to the detector.

A previously underestimated background contribution are nuclear decays in the main spectrometer. Within test measurements at the pre-spectrometer, radon  $\alpha$ -decays in the spectrometer volume were identified as a major source of background. A single nuclear decay, which produces a high-energy electron stored within the magnetic mirror of the spectrometer, can lead to an enhanced background rate over several hours due to the staged process of background creation via ionization of residual gas molecules. A detailed physics model was developed in the course of this thesis, describing the various electron emission processes, such as conversion, shake-off, relaxation, and shell reorganization, accompanying the initial  $\alpha$ -decay. The model is validated by independent measurements as well as dedicated measurements with the KATRIN pre-spectrometer. The resulting agreement allows to use this model to predict the background rates expected at the much larger main spectrometer. It is shown that, without appropriate counter measures, this background rate would exceed the KATRIN design limit by more than a factor 5, thereby reducing the statistical neutrino mass sensitivity  $m_\nu^{\text{stat}}$ . Moreover, the non-Poissonian nature of this type of background further reduces  $m_\nu^{\text{stat}}$ .

Consequently, in a last step, two active background reduction methods, the *electric dipole method* and the *magnetic pulse method*, have been investigated with regard to their removal efficiency for stored electrons of different energies. It is demonstrated that a very good vacuum on the order of  $10^{-11}$  mbar is required in order to make these methods actually applicable. It is only under these circumstances that the time between two successive ionizing events, and hence two background events at the detector, is large enough so that the frequency of application of the active background reduction methods does not significantly reduce the neutrino mass measurement statistics.

The investigations of this thesis are of utmost importance for the upcoming commissioning measurements with the KATRIN main spectrometer. If no new background sources will arise, the models developed within this work are expected to be sufficient to describe the coming observations.

# Zusammenfassung

Neutrinos sind die mit Abstand häufigsten massiven Teilchen in unserem Universum. Daher sind ihre Eigenschaften, und insbesondere ihre nicht-verschwindende Masse, wichtige Parameter in den Bereichen der Teilchenphysik und Kosmologie. Bis heute konnte die Neutrinomasse lediglich auf einen kleinen Bereich eingegrenzt werden. Ein unteres Limit von  $0.04 \text{ eV}/c^2$  lässt sich dabei aus den beobachteten Eigenschaften der Neutrinooszillationen ableiten, während eine obere Schranke von  $2 \text{ eV}/c^2$  mit Hilfe von Experimenten zur direkten Bestimmung der Neutrinomasse gesetzt wurde.

Das sich im Aufbau befindliche Karlsruhe Tritium Neutrino Experiment (KATRIN) nutzt den  $\beta$ -Zerfall von molekularem Tritium, um die effektive Masse des Elektron-Antineutrinos mit einer bisher unerreichbaren Präzision von  $200 \text{ meV}/c^2$  (90% C.L.) zu bestimmen. Dabei wird das Energiespektrum der Elektronen in einem Bereich nahe des Endpunkts von  $18,6 \text{ keV}$  sehr genau vermessen. Da sich jedoch nur ein Bruchteil von  $10^{-13}$  aller Elektronen in diesem interessanten Energiebereich befindet, benötigt man ein gut verstandenes hochauflösendes Spektrometer, welches die Elektronen analysiert und dabei gleichzeitig eine Untergrundrate von weniger als  $10^{-2}$  Ereignissen pro Sekunde aufweist, um die Designsensitivität zu erreichen.

Der Fokus der vorliegenden Arbeit liegt auf der detaillierten Beschreibung und Optimierung der Untergrund- und Transmissionseigenschaften der KATRIN Spektrometer. Zu diesem Zweck wurden verschiedene Modelle entwickelt, welche die physikalischen Vorgänge in einem elektrostatischen Spektrometer beschreiben, und in die bestehende KATRIN Simulationssoftware KASSIOPEIA integriert. Dadurch wurde es möglich, die experimentellen Beobachtungen im Detail zu verstehen, z.B. mit Hilfe von großangelegten Monte-Carlo Simulationen.

Ein externes Programmpaket namens KTRAP wurde entwickelt mit dem Ziel, die elektromagnetische Konfiguration des Hauptspektrometers zu verbessern. Dazu macht KTRAP vor allem von den in KASSIOPEIA existierenden Feldberechnungsmethoden Gebrauch. Eine automatisierte Routine ermöglicht die Bestimmung von optimierten Stromkonfigurationen für das große externe Luftspulensystem, welches das Hauptspektrometer umgibt. Dieses wurde konzipiert zur Feinformung des magnetischen Flusschlauchs, welcher die Signalelektronen von der Quelle zum Detektor transportiert.

Die Vermessung der Signalelektronenenergien mit Hilfe eines elektrostatischen Spektrometers des MAC-E Filter Typs setzt ein detailliertes Verständnis seiner Transmissionseigenschaften voraus. Diese erschließen sich komplett aus dem Zusammenspiel

---

von magnetischem Feld, welches die Signalelektronen bezüglich ihrer Impulsrichtung parallelisiert, und elektrostatischem Potential, welches die longitudinale kinetische Energie der Elektronen analysiert. Dabei sind das Analysiermagnetfeld und -potential Schlüsselparameter für eine erfolgreiche Messung der Neutrinomasse. Sie sollen mit Hilfe von Testmessungen bestimmt werden, wobei eine winkelselektive, quasi-monoenergetische Elektronenkanone als Quelle benutzt wird. In der vorliegenden Arbeit wurden entsprechende Mess- und Analysestrategien entwickelt und durch Anwendung auf Monte-Carlo-generierte Daten getestet.

Das zweite Hauptaugenmerk dieser Arbeit liegt auf der Untersuchung möglicher Untergrundprozesse in einem elektrostatischen Spektrometer und der Studie etwaiger Untergrundreduktionsmethoden. Es wird erwartet, dass die dominanten Untergrundbeiträge durch Myon-induzierte niederenergetische Sekundärelektronen und durch radon-induzierte hochenergetische gespeicherte Elektronen entstehen.

Um die zugrundeliegenden Produktions- und Transportmechanismen der  $\mu$ -induzierten Elektronen zu untersuchen wurde ein externes Myon-Detektorsystem aufgebaut und in Betrieb genommen. Durch eine Kombination verschiedener Testmessungen bei unterschiedlichen elektromagnetischen Konfigurationen, welche mit Hilfe von KASSIOPEIA bestimmt wurden, lässt sich diese Untergrundkomponente im Detail verstehen. Entsprechende Messstrategien wurden im Rahmen dieser Arbeit untersucht und von Simulationen begleitet. Diese untersuchen unter welchen Bedingungen Elektronen tatsächlich von der Spektrometeroberfläche in das sensitive Volumen transportiert werden können.

Einen bisher unterschätzten Untergrundbeitrag liefern nukleare Zerfälle innerhalb des Spektrometervolumens. Testmessungen mit dem KATRIN Vorspektrometer offenbarten Radon- $\alpha$ -Zerfälle als die dominante Untergrundquelle. Ein einzelner Zerfall kann zu einer Erhöhung der Untergrundrate über einen Zeitraum von bis zu mehreren Stunden führen. Diese Erhöhung wird verursacht durch die Entstehung eines hochenergetischen Elektrons, welches im magnetischen Spiegel des Spektrometers gefangen ist und dort durch Ionisation von Restgasmolekülen Sekundärelektronen erzeugt. Im Rahmen dieser Arbeit wurde ein detailliertes Modell entwickelt, welches die verschiedenen physikalischen Prozesse beschreibt, die im Rahmen eines  $\alpha$ -Zerfalls zur Emission von Elektronen führen können. Das Modell wurde sowohl mit Hilfe von unabhängigen Messungen als auch durch speziell darauf ausgelegte Messungen am Vorspektrometer verifiziert. Anschließend wurde das Modell auf das Hauptspektrometer angewendet, um den zu erwartenden Untergrund zu bestimmen. Es konnte gezeigt werden, dass die Untergrundrate ohne geeignete Gegenmaßnahmen das KATRIN Designlimit um mehr als einen Faktor 5 überschreiten und somit die statistische Neutrinomassensensitivität signifikant verschlechtern würde. Im Speziellen führt die Tatsache, dass die Untergrundrate keiner Poisson-Verteilung folgt, zu einer weiteren drastischen Reduktion der Sensitivität.

Dementsprechend wurden im letzte Schritt zwei Methoden zur aktiven Untergrundbeseitigung hinsichtlich ihrer Effizienz untersucht: der elektrische Dipol und der Magnetpuls. Es konnte gezeigt werden, dass ein sehr gutes Vakuum in der Größenordnung von  $10^{-11}$  mbar benötigt wird, damit diese aktiven Methoden überhaupt eingesetzt werden können. Nur unter diesen Umständen ist die Zeit zwischen zwei aufeinanderfolgenden

Ionisationen (und damit zwischen zwei Untergrundereignissen am Detektor) lang genug, so dass die Häufigkeit der Anwendung der aktiven Untergrundbeseitigungsmethoden die eigentliche Messzeit und damit die Statistik nicht signifikant reduziert.

Die Untersuchungen, die im Rahmen dieser Arbeit durchgeführt wurden, sind von größter Wichtigkeit für die bevorstehenden Testmessungen mit dem KATRIN Hauptspektrometer. Falls keine neuen Untergrundquellen entdeckt werden, sollten mit den Modellen, die in dieser Arbeit entwickelt und getestet wurden, voraussichtlich alle Beobachtungen am Hauptspektrometer erklärt werden können.

---

# Contents

<b>Abstract</b>	<b>i</b>
<b>Zusammenfassung</b>	<b>iii</b>
<b>1 Neutrino physics</b>	<b>1</b>
1.1 The discovery of the neutrino . . . . .	2
1.2 Neutrinos in the Standard Model . . . . .	4
1.3 Neutrino oscillations . . . . .	5
1.3.1 The solar neutrino problem . . . . .	6
1.3.2 Theoretical description of neutrino oscillations . . . . .	7
1.3.3 Oscillation parameters . . . . .	10
1.4 Neutrino mass . . . . .	12
1.4.1 Masses in the Standard Model Lagrangian . . . . .	13
1.4.2 Neutrino mass generating mechanisms . . . . .	14
1.5 Determination of the neutrino mass . . . . .	16
1.5.1 Cosmology . . . . .	17
1.5.2 Neutrinoless double $\beta$ -decay . . . . .	21
1.5.3 Single $\beta$ -decay . . . . .	23
<b>2 The KATRIN experiment</b>	<b>27</b>
2.1 Experimental overview . . . . .	27
2.1.1 Tritium source . . . . .	29
2.1.2 Rear section . . . . .	30
2.1.3 Transport section . . . . .	31
2.1.4 Spectrometer section . . . . .	32
2.1.5 Focal plane detector . . . . .	36
2.2 Measurement principle . . . . .	37
2.2.1 MAC-E filter . . . . .	37
2.2.2 Transmission and response function . . . . .	39
2.3 Sensitivity of the KATRIN experiment . . . . .	42

2.3.1	Statistical uncertainty . . . . .	42
2.3.2	Systematic uncertainty . . . . .	43
2.3.3	KATRIN sensitivity . . . . .	45
2.4	Background processes in a MAC-E filter . . . . .	46
2.4.1	Background sources . . . . .	46
2.4.2	Background reduction . . . . .	48
<b>3</b>	<b>Simulation software</b>	<b>51</b>
3.1	Objectives of the simulation software . . . . .	51
3.2	The KASSIOPEIA package . . . . .	52
3.2.1	Particle generation . . . . .	53
3.2.2	Particle tracking . . . . .	54
3.2.3	Secondary processes . . . . .	58
3.3	Field calculation methods . . . . .	60
3.3.1	Magnetic field calculation . . . . .	60
3.3.2	Electric field calculation . . . . .	64
3.4	External packages using Kasper . . . . .	66
3.4.1	LFCS optimization . . . . .	67
3.4.2	Transmission function analysis . . . . .	68
<b>4</b>	<b>Electromagnetic optimization of the main spectrometer</b>	<b>71</b>
4.1	Electromagnetic design requirements . . . . .	71
4.2	The transmission condition . . . . .	74
4.2.1	Derivation of the transmission function . . . . .	74
4.2.2	Satisfying the transmission condition . . . . .	78
4.3	The KATRIN large volume air coil system . . . . .	80
4.3.1	Earth magnetic field compensation . . . . .	80
4.3.2	Low field correction . . . . .	80
4.4	Automated optimization of the LFCS currents . . . . .	83
4.5	Results . . . . .	87
4.5.1	Nominal field strength . . . . .	88
4.5.2	Increased magnetic field strength . . . . .	96
4.5.3	Conclusion . . . . .	98
<b>5</b>	<b>Study of the main spectrometer transmission properties</b>	<b>99</b>
5.1	Overview of transmission function measurements at KATRIN . . . . .	99
5.2	Parameters influencing the transmission function . . . . .	102
5.2.1	Spectrometer properties . . . . .	102
5.2.2	Source properties . . . . .	105
5.3	Measurement and analysis strategy . . . . .	110
5.3.1	Source energy distribution . . . . .	110
5.3.2	Source angular distribution . . . . .	120
5.3.3	Transmission function depending on starting energy and angular distribution . . . . .	132

5.3.4	Determination of the spectrometer properties . . . . .	136
5.4	Systematic effects and Conclusions . . . . .	137
<b>6</b>	<b>Muon-induced background</b>	<b>139</b>
6.1	Background mechanism . . . . .	140
6.2	Background suppression . . . . .	143
6.2.1	Magnetic shielding . . . . .	143
6.2.2	Electrostatic shielding . . . . .	143
6.3	The KATRIN muon detector system . . . . .	144
6.3.1	Assembly of the muon detector system . . . . .	145
6.3.2	Commissioning measurements . . . . .	152
6.4	Simulations on muon-induced background . . . . .	154
6.5	Measurement strategy . . . . .	159
6.5.1	Measurements with axially symmetric magnetic fields . . . . .	160
6.5.2	Measurements with asymmetric magnetic fields . . . . .	162
6.5.3	Measurements with non-axially symmetric magnetic fields . . . . .	164
6.5.4	Measurements without magnetic fields . . . . .	164
6.6	Impact on the neutrino mass sensitivity . . . . .	165
<b>7</b>	<b>Radon-induced background</b>	<b>167</b>
7.1	Background due to stored electrons in MAC-E filters . . . . .	167
7.2	Electron emission accompanying radon $\alpha$ -decay . . . . .	169
7.2.1	Internal conversion . . . . .	171
7.2.2	Inner shell shake-off . . . . .	172
7.2.3	Relaxation following internal conversion and shake-off processes . . . . .	173
7.2.4	Atomic shell reorganization . . . . .	175
7.3	The radon event generator . . . . .	176
7.3.1	Implementation of the physical processes . . . . .	176
7.3.2	Generator output . . . . .	178
7.3.3	Initial tests of the model . . . . .	180
7.4	Validation of the background model . . . . .	183
7.4.1	Overview of the pre-spectrometer radon measurements . . . . .	186
7.4.2	Spatial distribution of radon decays . . . . .	188
7.4.3	Time structure of radon events . . . . .	190
7.4.4	Rate of single events . . . . .	197
7.4.5	Determination of radon activities . . . . .	197
7.4.6	Summary . . . . .	203
7.5	Impact of radon-induced background on the KATRIN sensitivity . . . . .	203
7.5.1	Implications for the main spectrometer . . . . .	204
7.5.2	Implications for the neutrino mass sensitivity . . . . .	207
7.6	Conclusions . . . . .	209

<b>8</b>	<b>Active removal of stored electrons</b>	<b>211</b>
8.1	Electron storage within the main spectrometer . . . . .	212
8.2	The electric dipole method . . . . .	214
8.2.1	Principle of electron removal by an electric dipole . . . . .	214
8.2.2	Investigation of the removal efficiency . . . . .	216
8.3	The magnetic pulse method . . . . .	220
8.3.1	Principle of electron removal by a magnetic pulse . . . . .	220
8.3.2	Investigation of the removal efficiency . . . . .	225
8.4	Prospects of background reduction at the main spectrometer . . . . .	226
8.4.1	Electron storage times . . . . .	226
8.4.2	Pulsing frequency . . . . .	235
8.4.3	Summary . . . . .	238
<b>9</b>	<b>Conclusion</b>	<b>241</b>
	<b>Appendix</b>	<b>245</b>
.1	Implications of the short-circuited wire electrodes . . . . .	245
.1.1	Transmission condition with electric shorts . . . . .	247
.1.2	Fulfilling the transmission condition with electric shorts . . . . .	249
.2	Background measurements at low retarding voltages . . . . .	249
.2.1	Measurement objectives . . . . .	250
.2.2	Background due to stored electrons . . . . .	252
.2.3	Background due to secondary electron emission . . . . .	254
.3	Main spectrometer electromagnetic field setups . . . . .	255
.4	Adiabatic behavior of electron motion . . . . .	256
.4.1	What is adiabaticity? . . . . .	257
.4.2	How is adiabaticity related to chaos? . . . . .	261
.4.3	How large is the effect at the KATRIN spectrometers? . . . . .	264
	<b>List of Figures</b>	<b>267</b>
	<b>List of Tables</b>	<b>271</b>
	<b>References</b>	<b>274</b>

# Neutrino physics

*“Neutrino physics is largely an art of learning  
a great deal by observing nothing.”*

Haim Harari, 1988

The last decades have been exciting times with many crucial breakthroughs for neutrino physics. For a long time, the unraveling of the elusive nature of the neutrino was a most difficult task for neutrino physics experiments, similar to the proverbial search for a needle in a haystack. Therefore, it comes as no surprise that it took nearly 30 years until the first detection of a neutrino.

One of the most important findings in neutrino physics has been the discovery of neutrino oscillations, which requires neutrinos to be massive. With the help of a large number of experiments, the parameter space of neutrino oscillations has been investigated and constrained. Most importantly, massive neutrinos present the first hint for physics beyond the Standard Model, and thus can contribute to deepening our understanding of the origin and nature of mass. However, oscillation experiments are unable to determine the absolute neutrino mass scale. Therefore, additional experimental approaches are required to determine this parameter, which is of importance for particle physics and cosmology.

Cosmological observations show the fingerprint of neutrinos in the evolution of large-scale structures in the Universe, and give rather stringent bounds on the sum of the neutrino mass, however, with the downside of a strong model-dependence and the  $\Lambda$ CDM paradigm.

The observation of neutrinoless double beta decay would reveal the Majorana nature of neutrinos as well as the equivalent mass  $m_{\beta\beta}$ . Again, a strong dependence of the value of  $m_{\beta\beta}$  on model parameters such as Majorana phases or decay modes exists.

The only 'model-independent' approach is provided by electron spectroscopy of single  $\beta$ -decays, where the most stringent upper limits of 2 eV have been set at Mainz and Troitsk [1, 2]. The KATRIN experiment is designed to improve this sensitivity by one order of magnitude down to 0.2 eV.

This section is targeted to put the KATRIN experiment in the context of neutrino physics, starting with a historical outline in section 1.1. Neutrinos play a special role in the Standard Model of particle physics, as outlined in section 1.2, especially with regard to the discovery of neutrino oscillations, which is discussed in section 1.3. The theoretical mass generation mechanisms for neutrino masses are summarized in section 1.4. Finally, the experimental determination of the absolute neutrino mass scale is the focus of section 1.5.

## 1.1 The discovery of the neutrino

Until the first reliable results of studies of radioactive nuclei were available in the early years of the 20<sup>th</sup> century, neutrinos were not known to exist. Their footprints, however, were observed when studying nuclear decays, strongly puzzling physicists at that time. Three types of radioactivity were under investigation:  $\alpha$ -,  $\beta$ - and  $\gamma$ -decay. It was found that the emitted  $\alpha$ - as well as the  $\gamma$ -spectrum showed discrete lines. Consequently, it came as a surprise when in 1914 James Chadwick [3] discovered that the spectrum of radium  $\beta$ -decay electrons was indeed of continuous nature, as shown in figure 1.1. This behavior could not be explained by the then model of a two-body- $\beta$ -decay, so that Niels Bohr went so far as to question the law of conservation of energy. An alternative way out of this dilemma was proposed by Wolfgang Pauli in his famous letter to his colleagues at a conference in Tübingen [5]. He postulated the existence of an electrically neutral spin 1/2 particle with very low mass, which would be emitted alongside with the  $\beta$ -particle. Within the resulting three-body-decay, the additional particle, which he initially called *neutron*, would share the decay energy with the electron. Although most physicists were rather skeptical to his approach, it was Enrico Fermi, who, after the discovery of the neutron by Chadwick in 1932 [6], formulated a theory of nuclear  $\beta$ -decay [7]. According to Fermi, the reaction must be written as three-body decay

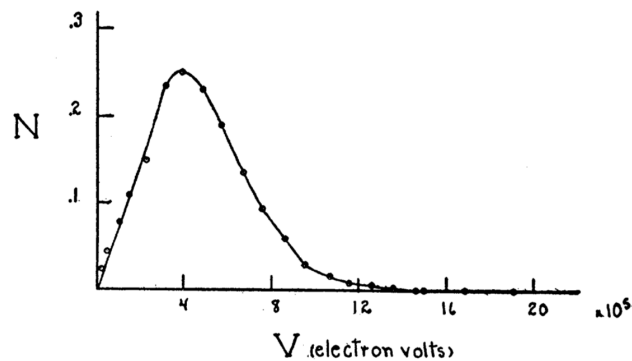
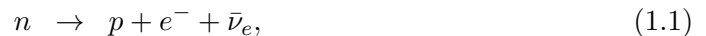


**Figure 1.1:** Continuous energy spectrum of radium  $\beta$ -decay. Figure taken from [4].

where  $\bar{\nu}_e$  was identified to be identical to Pauli's postulated particle, which Fermi re-named to *neutrino*. His initial theory of a point-like contact interaction of four particles is extended and refined by today's *theory of weak interaction*. When first deriving the cross section for the process  $\nu n \rightarrow e^- p$  (or  $\bar{\nu} p \rightarrow e^+ n$ ), Bethe and Peierls in 1934 [8] obtained values as small as  $\sigma < 10^{-44}$  cm<sup>2</sup>. It is this small cross section which prevented a direct detection of the 'ghost particle' until much later in 1956.

The final proof of their existence followed from a series of 'Poltergeist' experiments, headed by Fred Reines and Clyde Cowan [9, 10]<sup>1</sup>. Their experiment made use of the inverse  $\beta$ -decay reaction

$$\bar{\nu}_e + p \rightarrow e^+ + n \quad (1.2)$$

in water, where the electron anti-neutrinos  $\bar{\nu}_e$  were provided in large quantities ( $10^{12} - 10^{13}$  per cm<sup>2</sup> and s) by the Savannah River reactor. The emitted positron in eq. (1.2) quickly annihilates with an electron in the water into two 511 keV photons, which can then be detected with photomultiplier tubes. Despite this characteristic signal, previous experiments within the Poltergeist series suffered from large background rates. A break-through was achieved by adding cadmium-chloride to the water. In this case, the neutron, which was produced in the inverse  $\beta$ -decay reaction, scatters off the water molecules in the detector, thereby slowing down until being captured by a cadmium nucleus. The resulting excited nucleus Cd\* returns to its ground state via the emission of a high-energy photon. The corresponding delayed coincidence signal of this photon with the two 511 keV photons emitted a few microseconds earlier allowed the experiment to distinguish a  $\nu$ -induced signal event from accidental background events. With only a handful of events observed, the Savannah River team derived a cross section of  $\sigma = 6.3 \cdot 10^{-44}$  cm<sup>2</sup> [9]. In 1995, 40 years after the actual discovery and 21 years after Cowan passed away, Reines was finally awarded the Nobel Prize for the groundbreaking discovery.

In 1962, Ledermann, Steinberger and Schwartz found evidence for a second neutrino type, the muon-neutrino  $\nu_\mu$  [11]<sup>2</sup>. Their experiment at the Brookhaven AGS<sup>3</sup> demonstrated that  $\mu$ -neutrinos, produced primarily from pion decay  $\pi^\pm \rightarrow \mu^\pm(\nu/\bar{\nu})$  only created  $\mu$ -mesons but no electrons when interacting with the detector material. From this fact they concluded that their neutrinos must indeed differ from those produced in  $\beta$ -decay, which got rewarded with the Nobel prize in 1988 (well before Reines).

The picture was completed in 2000 when the DONUT experiment at Fermilab finally detected the third type of neutrino, the  $\tau$ -neutrino  $\nu_\tau$  [12]. Its existence was already postulated in 1975, when the  $\tau$ -lepton and hence, a third generation of leptonic particles was discovered. The experiment made use of a beam of protons interacting in a tungsten beam dump, thereby creating a particle shower containing  $D_S$ -mesons, which decay into  $\tau$ -leptons and finally  $\nu_\tau$ . An arrangement of stainless steel sheets interleaved with emulsion plates served as target material for the  $\tau$ -neutrinos. Upon creating a  $\tau$ -lepton

<sup>1</sup>It was Bruno Pontecorvo, who proposed this type of experiments and urged Reines and Cowan to perform them.

<sup>2</sup>Again, the method employed was first proposed by Bruno Pontecorvo in 1959.

<sup>3</sup>AGS: Alternating Gradient Synchrotron

**Table 1.1:** Overview of the leptons and their anti-particles in the Standard Model.

Generation			Electric charge	Lepton number	Interaction
1	2	3			
$e^-$	$\mu^-$	$\tau^-$	-1	+1	weak, electromagnetic
$\nu_e$	$\nu_\mu$	$\nu_\tau$	0	+1	weak
$e^+$	$\mu^+$	$\tau^+$	+1	-1	weak, electromagnetic
$\bar{\nu}_e$	$\bar{\nu}_\mu$	$\bar{\nu}_\tau$	0	-1	weak

(most likely in the steel), the typical signature of a “kink“ in the particle track was observed due to the ‘invisibility’ of the neutrino and the conservation of momentum.

Indirect evidence for the existence of three types of neutrino flavors was already given earlier in 1989 by the ALEPH experiment at LEP, CERN [13, 14]. When comparing the experimentally observed  $Z^0$  boson decay width with theoretical expectations, their findings were best described for the case of  $N_\nu = 3.01 \pm 0.15(\text{exp}) \pm 0.05(\text{theo})^4$  light (active) neutrinos. Note that there is the possibility for the existence of additional sterile neutrinos, which do not participate in the weak interaction. These so far hypothetical particles may be revealed via their contribution to the phenomenon of neutrino mixing [16].

## 1.2 Neutrinos in the Standard Model

The Standard Model of particle physics groups the 6 fundamental leptons (and their corresponding anti-leptons), into 3 generations or families, as listed in table 1.1. While the light particles of the first generation are stable, the more massive muonic and tauonic leptons decay into their lighter flavor types. Each generation forms a weak isospin doublet, and hence transforms under the weak isospin  $SU(2)$  gauge symmetry. Together with the weak hypercharge  $U(1)$  symmetry, it forms the electroweak gauge group  $SU(2) \times U(1)^5$ , also known as Glashow-Weinberg-Salam Standard Model [17–19]. Through the Higgs mechanism [20, 21], three out of the four generators of this group mix with the  $W^\pm$  and  $Z$  bosons, rendering them massive, while the remaining degree of freedom is found in the form of the Higgs boson, which was finally discovered at the LHC in 2012 [22, 23]. The massive  $W^\pm$  and  $Z$  bosons mediate the weak interaction, which is the sole gauge interaction accessible for neutrinos. Weak interactions are distinct due to the fact that they break parity-symmetry as well as CP-symmetry. As a result, a fundamental Left-Right-asymmetry arises. Accordingly, the helicity operator

$$h = \frac{\vec{\sigma} \cdot \vec{p}}{|\vec{p}|}, \quad (1.3)$$

---

<sup>4</sup>More recent analyses gave similar results:  $N_\nu = 2.9841 \pm 0.0083$  [15].

<sup>5</sup>Upon adding the  $SU(3)$  symmetry, which acts on the gluon field, the Standard Model gauge group  $SU(3) \times SU(2) \times U(1)$  is completed.

where  $\vec{\sigma}$  denotes the spin and  $\vec{p}$  the momentum of the particle under consideration, is of key relevance for neutrinos and weak interactions. In 1958, Goldhaber measured the helicity of the neutrino to be negative (or left-handed) [24]. From this one can conclude that neutrinos display a definite helicity and travel at the speed of light. Hence, they have to be massless, or a reference frame would exist for which the momentum changes direction, thus reversing the neutrino's helicity.

In addition to left-handed neutrinos  $\nu_L$ , also right-handed anti-neutrinos  $\bar{\nu}_R$  participate in weak interactions. The fact that the charge conjugation operator  $C$  transforms a particle into its anti-particle reveals that the right-handed anti-neutrino  $\bar{\nu}_R$  is not the anti-particle of the left-handed neutrino  $\nu_L$ :  $(\nu_L)^C \neq \bar{\nu}_R$ , as charge conjugation does not affect handedness. However, these states are linked via the CP-operation:  $(\nu_L)^{CP} = \bar{\nu}_R$ , which can be interpreted in two different ways:

1. The neutrino is its own anti-particle, with  $(\nu_L)^C = \nu_L$  and  $(\bar{\nu}_R)^C = \bar{\nu}_R$ . It was Ettore Majorana who first showed that a massive particle can also be represented by a two-component spinor (as is the case for massless particles), so this type of particles is called *Majorana particles*.
2. There could indeed exist four independent states out of which the states  $(\nu_L)^C$  and  $(\bar{\nu}_R)^C$  have not yet been observed in nature. Due to the description by a four-component Dirac spinor, this type of particles is known as *Dirac particles*.

The Majorana spinor is not invariant under U(1) and will hence not conserve lepton number  $L$ . This opens the opportunity to determine the CP nature of the neutrino by observing neutrinoless double beta decay<sup>6</sup>. However, this decay process can only occur for massive neutrinos (see section 1.5.2), a prerequisite established by the discovery of neutrino oscillations. As mixing of massive neutrinos is not contained within the Standard Model, these effects can be seen as messengers for new physics beyond the Standard Model.

### 1.3 Neutrino oscillations

During the last two decades, the initial hints for a non-zero neutrino mass, and hence physics beyond the Standard Model, have been consolidated by the observation of neutrino oscillations. The striking evidence for  $m_\nu \neq 0$  has far reaching consequences for (astro-)particle physics. In this section, the crucial observations, which have led to the discovery of this phenomenon, will be discussed (section 1.3.1), which is followed by an overview of the theoretical description of this interference phenomenon (section 1.3.2). Finally, the most important experimental results, which have allowed to fully explore the oscillation parameter space, will be summarized (section 1.3.3).

---

<sup>6</sup>The Majorana nature does not show in experiments relying on the kinematics of the decay only, such as the KATRIN experiment.

### 1.3.1 The solar neutrino problem

Since the mid-1960's physicists were puzzled by the so called 'solar neutrino problem'. The Sun is a well-known intense source of neutrinos being created in huge numbers by the ongoing nuclear fusion processes. Figure 1.2 shows the energy spectrum of neutrinos from the dominant pp chain and the sub-dominant CNO cycle. When R. Davis Jr and J. N. Bahcall measured and calculated the flux of neutrinos from the Sun in the Homestake experiment [26, 27], they noticed a deficit of neutrino interactions in comparison to expectations from Standard Solar Model (SSM) calculations [28]. The now famous Davis experiment used a chlorine-based detector where about 800 neutrino events were collected in a measurement period of about 25 years. These pioneering results were later confirmed by other experiments such as GALLEX [29], GNO [30], SAGE [31] (gallium-based), KamiokaNDE [32] and SNO<sup>7</sup> [33] (water-based). Initially, these discrepancies were often attributed to uncertainties in the SSM. At the same time, however, V. Gribov and B. Pontecorvo proposed an alternative mechanism [34]: neutrino oscillations where neutrinos change their flavor as they travel from the Sun to the Earth. The details of this phenomenon will be discussed in section 1.3.2.

In 2001, the issue of the solar neutrino problem was finally resolved by the SNO experiment [35]. In contrast to previous experiments, SNO was able to measure the (bolometric) flux of all neutrino types  $\nu_{e,\mu,\tau}$  in addition to measuring the flavor-type  $\nu_e$ .

<sup>7</sup>GALLEX: GALLium-EXperiment; GNO: Gallium Neutrino Observatory; SAGE: Soviet-American Gallium Experiment; KamiokaNDE: Kamioka Nucleon Decay Experiment; SNO: Sudbury Neutrino Observatory.

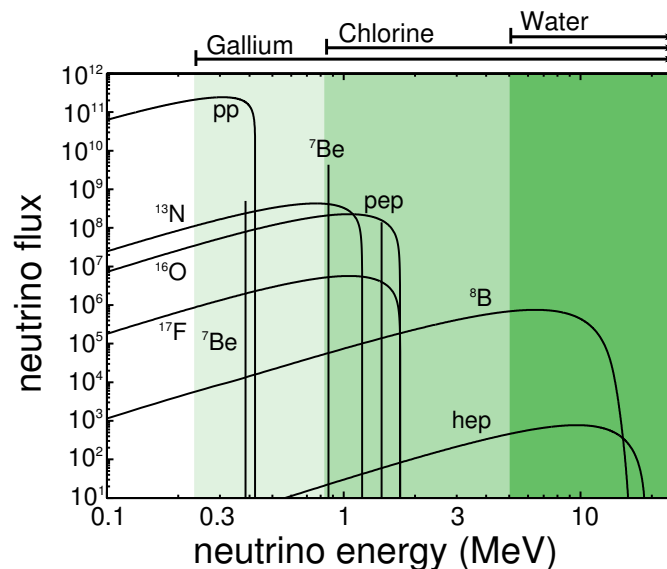


**Figure 1.2:** Solar neutrino flux for the different nuclear fusion processes. The sensitivity region of an experiment depends on the employed target material. Figure adapted from [25].

The following reactions were observed in the heavy water (D<sub>2</sub>O) target [33, 36]:

$$\begin{aligned} \text{elastic scattering (ES): } & \nu_x + e^- \rightarrow \nu_x + e^- \quad (x = e, \mu, \tau), \\ \text{charged current (CC): } & \nu_e + D \rightarrow p + p + e^-, \\ \text{neutral current (NC): } & \nu_x + D \rightarrow n + p + \nu_x. \end{aligned} \tag{1.4}$$

While all neutrino flavors can participate in NC reactions, the neutrino energies (see figure 1.2) are too low to produce  $\mu^-$  and  $\tau^-$  in CC reactions. Hence, the ratio of NC/CC reactions can be used as an indicator for the amount of  $\nu_e$  in the total flux. The electron neutrino rate was observed to be about 1/3 of the total neutrino flux, while the NC rate was in very good agreement with the SSM expectation, giving clear evidence for neutrino flavor transformation. The longstanding solar neutrino problem was finally resolved [37].

### 1.3.2 Theoretical description of neutrino oscillations

When Pontecorvo *et al.* first investigated the concept of neutrino oscillations as a possible solution for the solar neutrino problem, there was no known mechanism inherent to the Standard Model that would allow for this phenomenon. With the extension of massive neutrinos, however, the flavor changing property can be explained. The core of the matter lies in the fact that neutrinos have two fundamental sets of states:

- the *flavor eigenstate*, denoted as  $|\nu_\alpha\rangle$ , where  $\alpha = e, \mu, \tau$ , which has well-defined weak interactions, and
- the *mass eigenstate*, denoted as  $|\nu_i\rangle$ , where  $i = 1, 2, 3$ , which has well-defined mass.

The flavor eigenstates have to be considered when investigating neutrino interactions, while neutrino propagation requires a treatment in terms of the mass eigenstates. The effect of mixing causes each mass state to be a mixture of different flavor states (and vice versa), as described by the following unitary transformation:

$$|\nu_\alpha\rangle = \sum_i U_{\alpha i}^* |\nu_i\rangle, \quad |\nu_i\rangle = \sum_\alpha U_{\alpha i} |\nu_\alpha\rangle. \tag{1.5}$$

The unitary matrix  $U_{\alpha i}$ , also called PMNS matrix<sup>8</sup>, can be parameterized as follows:

$$U = \begin{pmatrix} 1 & 0 & 0 \\ 0 & c_{23} & s_{23} \\ 0 & -s_{23} & c_{23} \end{pmatrix} \begin{pmatrix} c_{13} & 0 & s_{13}e^{-i\delta_D} \\ 0 & 1 & 0 \\ -s_{13}e^{-i\delta_D} & 0 & c_{13} \end{pmatrix} \begin{pmatrix} c_{12} & s_{12} & 0 \\ -s_{12} & c_{12} & 0 \\ 0 & 0 & 1 \end{pmatrix} \begin{pmatrix} e^{i\delta_{M1}} & 0 & 0 \\ 0 & e^{i\delta_{M2}} & 0 \\ 0 & 0 & 1 \end{pmatrix},$$

where  $s_{ij} = \sin \theta_{ij}$  and  $c_{ij} = \cos \theta_{ij}$ . This matrix contains as free parameters the three mixing angles  $\theta_{ij}$ , which describe the contribution of the mass eigenstates to a certain flavor eigenstate (and vice versa), and up to three complex phases. If neutrinos are Dirac

<sup>8</sup>PMNS matrix, named after **M**aki, **N**akagawa, and **S**akata, who introduced it [38], and **P**ontecorvo, who created the theoretical foundation for neutrino oscillations [39].

fermions, only the Dirac phase  $\delta_D$  is physical and can cause CP-violation in the lepton sector [40]. In case of Majorana-type neutrinos, the Majorana neutrino fields cannot "absorb" any phases, which adds the two Majorana CP-phases  $\delta_{M_{1,2}}$ . The matrix  $U$ , as given above, describes the case of three active neutrino flavors. When sterile neutrinos are added, however, these states also participate in the neutrino mixing process. In this case, for each additional sterile neutrino, the matrix  $U$  is extended by one mixing angle  $\theta$  and one CP-phase  $\delta$  [41].

The essential parameter with regard to the observation of neutrino oscillations is the oscillation probability  $P$ , which will be derived in the following [41]. The neutrino mass states  $|\nu_i\rangle$  are eigenstates of the Hamiltonian  $H$ :

$$H |\nu_i\rangle = E_i |\nu_i\rangle, \quad (1.6)$$

with energy eigenvalues

$$E_i = \sqrt{\vec{p}^2 + m_i^2}. \quad (1.7)$$

Following the Schrödinger equation

$$i \frac{d}{dt} |\nu_i(t)\rangle = H |\nu_i(t)\rangle, \quad (1.8)$$

the neutrino states can be treated as plane waves evolving in time:

$$|\nu_i(t)\rangle = e^{-iE_i t} |\nu_i(0)\rangle. \quad (1.9)$$

A neutrino, which was created with a definite flavor  $\alpha$  at time  $t = 0$ , is described by the flavor state  $|\nu_\alpha(t)\rangle$ , with the following time evolution:

$$|\nu_\alpha(t)\rangle = \sum_i U_{\alpha i}^* e^{-iE_i t} |\nu_i\rangle. \quad (1.10)$$

Substituting eq. (1.5) into the above relation yields

$$|\nu_\alpha(t)\rangle = \sum_{\beta=e,\mu,\tau} \left( \sum_i U_{\alpha i}^* e^{-iE_i t} U_{\beta i} \right) |\nu_\beta\rangle. \quad (1.11)$$

Hence, the initial pure flavor state  $|\nu_\alpha(t=0)\rangle$  becomes a superposition of different flavor states  $|\nu_\beta\rangle$  at times  $t > 0$ . The coefficient of  $|\nu_\beta\rangle$

$$A_{\nu_\alpha \rightarrow \nu_\beta}(t) = \langle \nu_\beta | \nu_\alpha(t) \rangle = \sum_i U_{\alpha i}^* U_{\beta i} e^{-iE_i t} \quad (1.12)$$

is the transition amplitude as a function of time, which finally gives the transition probability

$$P_{\nu_\alpha \rightarrow \nu_\beta}(t) = |A_{\nu_\alpha \rightarrow \nu_\beta}(t)|^2 = \sum_{i,j} U_{\alpha i}^* U_{\beta i} U_{\alpha j} U_{\beta j}^* e^{-i(E_i - E_j)t}. \quad (1.13)$$

For ultrarelativistic neutrinos, relation (1.7) can be approximated by

$$E_i \approx E + \frac{m_i^2}{2E} \rightarrow E_i - E_j \approx \frac{\Delta m_{ij}^2}{2E}, \quad (1.14)$$

where  $\Delta m_{ij}^2 = m_i^2 - m_j^2$  is the squared mass difference and  $E = |\vec{p}|$  the neutrino energy (neglecting the mass). Consequently, the transition probability (1.13) can be approximated by

$$P_{\nu_\alpha \rightarrow \nu_\beta}(t) = \sum_{i,j} U_{\alpha i}^* U_{\beta i} U_{\alpha j} U_{\beta j}^* \exp\left(-i \frac{\Delta m_{ij}^2 t}{2E}\right). \quad (1.15)$$

Considering the fact that neutrino oscillation experiments cannot measure the propagation time  $t$ , eq. (1.15) has to be rewritten to

$$P_{\nu_\alpha \rightarrow \nu_\beta}(L, E) = \sum_{i,j} U_{\alpha i}^* U_{\beta i} U_{\alpha j} U_{\beta j}^* \exp\left(-i \frac{\Delta m_{ij}^2 L}{2E}\right), \quad (1.16)$$

using the approximation  $t = L$ , with  $L$  being the distance between the neutrino source and the detector, which is valid due to the fact that neutrinos travel almost at the speed of light. Figure 1.3 visualizes this relation in the generic two-flavor case. The neutrino is initially created in the flavor state  $\nu_\alpha = \nu_\mu$ . The probability waves of the mass states  $|\nu_i\rangle$  travel at different speeds, eventually obtaining a phase relation at a certain value of  $L/E$ , equivalent to a different flavor state  $\nu_\alpha = \nu_e$ . In this case, eq. (1.16) can be rewritten to

$$P_{\nu_\alpha \rightarrow \nu_\beta}(L, E) = \sin^2 2\theta_{ij} \sin^2\left(\frac{\Delta m_{ij}^2 L}{4E}\right), \quad (1.17)$$

which gives the so called oscillation length

$$L_{\text{osc}} = \frac{4\pi E}{\Delta m_{ij}^2}. \quad (1.18)$$

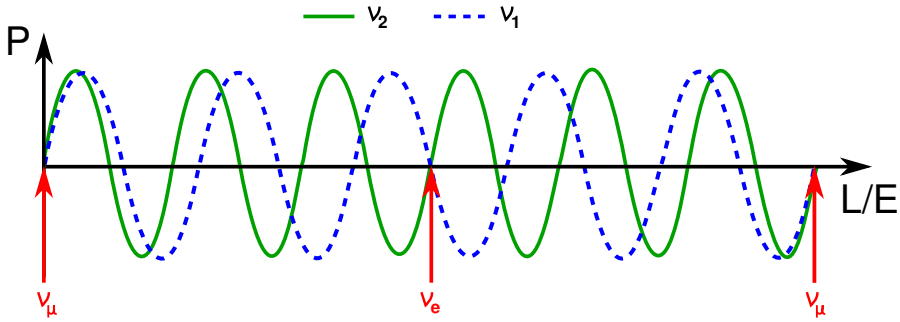


**Figure 1.3:** Illustration of neutrino oscillations in the two-flavor case. The probability waves of the mass states  $|\nu_i\rangle$  travel at different speeds, eventually becoming completely out of phase at a certain value of  $L/E$ , where they appear as a different flavor state  $\nu_\alpha = \nu_e$ . It should be noted that the neutrino wave packet is still coherent. Figure adapted from [42].

The transition probability is very small for values  $L \ll L_{\text{osc}}$ , so that no oscillation can actually be observed, while it oscillates very fast in case of  $L \gg L_{\text{osc}}$ , so that only the average transition probability is observable.

The above discussions consider neutrino propagation in vacuum only. In case of solar neutrinos, the flavor transformation is modified by the so called MSW effect<sup>9</sup> [43, 44], where the coherent forward elastic scattering with the particles in the medium (electrons and nucleons) results in a resonant transformation of  $\nu_e$  into  $\nu_{\mu,\tau}$ .

It was already mentioned above that the presence of sterile neutrinos would contribute to the neutrino mixing process. As sterile  $\nu$ 's do not participate in weak interactions, they cannot be detected directly. Consequently, they manifest themselves only in the mixing processes such as the disappearance of active neutrinos.

### 1.3.3 Oscillation parameters

The phenomenon of neutrino oscillations has been investigated by using many different neutrino sources, covering a wide range of neutrino energies, and using different detector technologies. This diversity is required in order to measure the individual oscillation parameters: the mixing angles  $\theta_{12}$ ,  $\theta_{23}$  and  $\theta_{13}$  and the squared mass differences  $\Delta m_{21}^2$  and  $\Delta m_{31}^2$  ( $\Delta m_{32}^2$ ). Following the above discussion, the large number of current neutrino oscillation experiments can be classified into two generic types:

- **Appearance experiments:** In this type of experiment, the transition from an initial to a previously not produced neutrino flavor type is measured. The sensitivity to small mixing angles requires that the new flavor to be searched for in the detector can unequivocally be attributed to flavor changes.
- **Disappearance experiments:** Here, the survival probability of the initial neutrino flavor is measured. The expected number of events has to be known precisely, requiring typically a two-detector concept. The presence of statistical fluctuations typically prohibits a measurement of very small mixing angles.

It was shown above that the sensitivity to a certain value of  $\Delta m_{ij}^2$  is maximal if  $L/E \approx 1/\Delta m_{ij}^2$ , while for  $L/E \gg 1/\Delta m_{ij}^2$ , only  $\sin^2 2\theta_{ij}$  and the limits for  $\Delta m_{ij}^2$  can be assessed.

In the following, an overview of the current status in the determination of the oscillation parameters will be given by adopting a classification according to the source of the neutrinos: solar, atmospheric, accelerator and reactor neutrinos.

- **Solar neutrinos:** The case of oscillation of solar neutrinos was already discussed above as a solution for the solar neutrino problem. With a source-detector distance of 1 AU and neutrino energies in the MeV-range, solar neutrino experiments are sensitive to very small mass differences  $\Delta m_{21}^2$  and small mixing angles  $\theta_{12}$ . A combined analysis of the different phases of the SNO experiment revealed the following values [45]:

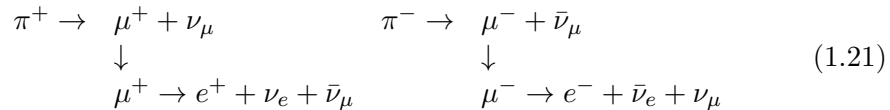
$$\theta_{12} = 34.4_{-1.2}^{+1.3} \text{ (90\% C.L.)}, \quad (1.19)$$

---

<sup>9</sup>Mikheyev-Smirnov-Wolfenstein effect

$$\Delta m_{21}^2 = \Delta m_{\text{sol}}^2 = 7.59_{-0.21}^{+0.19} \cdot 10^{-5} \text{ eV}^2 \text{ (90\% C.L.)}. \quad (1.20)$$

- **Atmospheric neutrinos:** The Earth's atmosphere is permanently being bombarded by energetic particles from outer space (mainly protons). Upon interacting with the molecules in the atmosphere, pions and muons are created. The decay sequence



results in a fixed ratio  $\nu_\mu : \nu_e$  of 2 : 1 over a large energy range. The Super-Kamiokande experiment, originally designed to search for proton decay, was the first to investigate atmospheric neutrinos [46]. Since the Earth is transparent for atmospheric neutrinos with energies  $< 1$  TeV, the Cherenkov technique allowed to investigate the rate of neutrinos coming from different zenith angles and hence different ratios  $L/E^{10}$ . While the expected number of down-going muon-neutrinos was observed, a deficit was found for up-going ones, traveling through the Earth. As the detected rate of electron neutrinos matched expectations, the results were interpreted as oscillations of  $\nu_\mu \rightarrow \nu_\tau$ . The present results on the atmospheric neutrino oscillation parameters are [47]:

$$0.407 \leq \sin^2 \theta_{23} \leq 0.583 \text{ (90\% C.L.)}, \quad (1.22)$$

$$1.9 \cdot 10^{-3} < \Delta m_{32}^2 = \Delta m_{\text{atm}}^2 < 2.6 \cdot 10^{-3} \text{ eV}^2 \text{ (90\% C.L.)}. \quad (1.23)$$

- **Accelerator neutrinos:** The parameter range of oscillation of atmospheric neutrinos can also be studied with artificial sources such as particle accelerators. The main advantage here is that the neutrino energy can be tuned to achieve the highest sensitivity (i.e.  $L/E = 1/\Delta m_{32}$ ). The first experiment of this type was the K2K experiment (KEK to Kamioka), which ran from 1999 to 2004 [48]. A beam of muon neutrinos from the proton synchrotron at the KEK facility was directed towards the Super-Kamiokande detector at a distance of about 250 km. In the  $\nu_\mu \rightarrow \nu_\tau$  oscillation channel, a mass splitting in the range of

$$1.9 \cdot 10^{-3} < \Delta m_{\text{atm}}^2 < 3.5 \cdot 10^{-3} \text{ eV}^2 \text{ (90\% C.L.)} \quad (1.24)$$

at  $\sin^2(2\theta_{23}) = 1$  was obtained. The successor experiment, T2K [49] (Tokai to Kamioka), which uses the J-PARC facility to produce the  $\nu_\mu$  beam, is designed to observe the rare  $\nu_\mu \rightarrow \nu_e$  oscillation and hence to determine the generic 3- $\nu$ -mixing angle  $\theta_{13}$ .

---

<sup>10</sup>The Cherenkov detection technique using 50 kt of water surrounded by photomultipliers allows to determine the direction of the incoming neutrino in the GeV range via reconstruction of the Cherenkov light cone.

- **Reactor neutrinos:** Present reactor neutrino experiments utilize the large flux of electron anti-neutrinos produced by nuclear power plants to study the disappearance of  $\bar{\nu}_e$  at 1-2 km distance, which is governed by the mixing angle  $\theta_{13}$ . Generally, a two-detector design is chosen, where one detector is placed very close to the reactor, at distances  $\mathcal{O}(100)$  m, to measure the total neutrino flux, while the far detector is situated at a distance of  $\mathcal{O}(1)$  km, where the oscillation maximum is expected to occur. For a long time, the last mixing angle  $\theta_{13}$  was constrained by the CHOOZ experiment, putting an upper limit on the  $\bar{\nu}_e \rightarrow \bar{\nu}_e$  disappearance [50]:

$$\sin^2(2\theta_{13}) < 0.2. \quad (1.25)$$

First hints for  $\theta_{13} \neq 0$  were provided by T2K [49], MINOS [51] and Double Chooz [52]. In 2012, several experiments released their compelling data, revealing consistent and rather large values of  $\theta_{13}$ :

$$\text{Daya Bay [53]: } \sin^2(2\theta_{13}) = 0.089 \pm 0.010(\text{stat.}) \pm 0.005(\text{syst.}) \quad (1.26)$$

$$\text{RENO [54]: } \sin^2(2\theta_{13}) = 0.113 \pm 0.013(\text{stat.}) \pm 0.019(\text{syst.}) \quad (1.27)$$

$$\text{Double Chooz [55]: } \sin^2(2\theta_{13}) = 0.109 \pm 0.030(\text{stat.}) \pm 0.025(\text{syst.}) \quad (1.28)$$

$$\rightarrow |U_{e3}| = \sin \theta_{13} \approx 0.15, \quad \theta_{13} \approx 9^\circ. \quad (1.29)$$

It was shown above that the neutrino oscillation parameters are measured with great precision. Figure 1.4 summarizes these findings in a neutrino mass hierarchy diagram. The flavor content of each neutrino mass state is determined by the mixing angles  $\theta_{ij}$ . Oscillation experiments can only determine differences of the squared masses with the sign of  $\Delta m_{32}^2$  ( $\Delta m_{31}^2$ ) presently being unknown. Therefore, two hierarchical scenarios are possible: normal and inverted hierarchy. Additionally, the value of the lightest neutrino mass state cannot be assessed by oscillation experiments, which prohibits a determination of the effective mass of the flavor states. If this state is rather heavy with a mass  $\mathcal{O}(0.1)$  eV, the three mass states become quasi-degenerate, i.e. the mass splittings are negligible. Although neutrino oscillations cannot determine the absolute neutrino mass scale, they can set a lower limit for the heaviest mass state, approximately given by  $\sqrt{|\Delta m_{\text{atm}}^2|} = 0.048$  eV.

## 1.4 Neutrino mass

Within the Standard Model, neutrinos are described as massless particles in contrast to neutrino oscillation results, which have shown that  $m_\nu > 0$ . The smallness of the neutrino mass compared to charged-fermion masses and the large mixing angles pose challenges to theoretical models aiming at explaining mass generating mechanisms [57]. A large variety of possible mechanisms is currently being discussed, so further experimental data are required in order to constrain theoretical models and to identify the mechanism realized in nature. This section gives an introduction to the theoretical mass generating mechanisms, focusing especially on those relevant for the case of neutrinos.

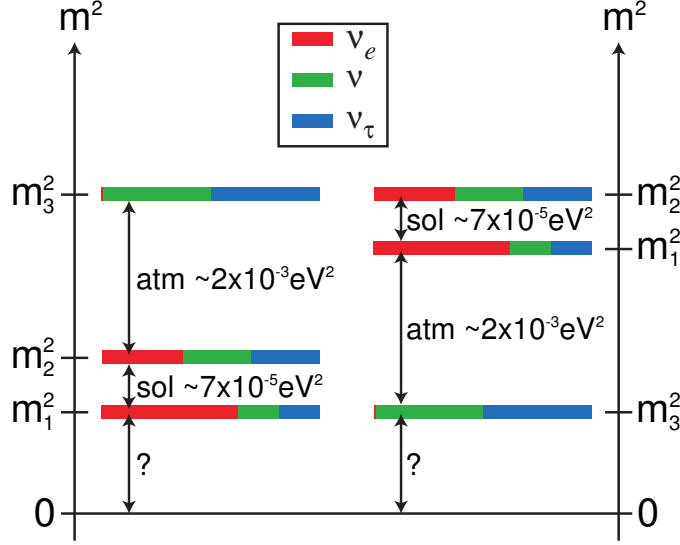


**Figure 1.4:** Neutrino mass hierarchy and flavor content of mass eigenstates. The flavor content is determined by the mixing angles  $\theta_{ij}$ . Oscillation experiments can only determine the squared mass differences, where the sign of  $\Delta m_{32}^2$  ( $\Delta m_{31}^2$ ) is not known. Therefore, two hierarchical scenarios are possible: normal hierarchy (left) and inverted hierarchy (right). Additionally, the value of the lightest neutrino mass state cannot be assessed by oscillation experiments, which prevents a determination of the effective mass of the flavor states. Figure adapted from [56].

#### 1.4.1 Masses in the Standard Model Lagrangian

In Lagrangian mechanics, Hamilton's principle [58] states that the evolution of a system between two states  $q_1 = q(t_1)$  and  $q_2 = q(t_2)$ , with  $q$  being the generalized coordinates, is a stationary point of the action functional

$$S = \int_{t_1}^{t_2} \mathcal{L}(t, q(t), \dot{q}(t)) dt, \quad (1.30)$$

where  $\mathcal{L}(t, q(t), \dot{q}(t))$  is the Lagrangian of the system. In general, it is a function of the kinetic energy  $T$  and potential energy  $V$  of the particle:  $\mathcal{L} = T - V$ . The equation of motion of the system can then be obtained from the Euler-Lagrange equation:

$$\frac{\partial \mathcal{L}}{\partial q} - \frac{d}{dt} \left( \frac{\partial \mathcal{L}}{\partial \dot{q}} \right) = 0. \quad (1.31)$$

When going from this classical description to the case of Quantum Field Theory [59], which describes the elementary particles as fields with spatial and temporal dependence  $\phi_\mu(\vec{q}, t)$ , the above equation has to be reformulated to a relativistic treatment of space and time:

$$\frac{\partial \mathcal{L}}{\partial(\partial_\mu \phi)} = \frac{\partial \mathcal{L}}{\partial \phi}. \quad (1.32)$$

For spin-1/2 fermions, described by Dirac fields  $\psi = \psi_L + \psi_R$ <sup>11</sup>, the equation of motion is given by the Dirac equation

$$(i\gamma^\mu \partial_\mu - m)\psi = 0, \quad (1.33)$$

where  $\gamma^\mu$  are the gamma matrices and  $m$  represents the particle mass. The corresponding Lagrangian is then determined to

$$\mathcal{L}_D = \bar{\psi}(i\gamma^\mu \partial_\mu - m)\psi. \quad (1.34)$$

Application of the right-handed projection operator  $(1 + \gamma^5)/2$  to the Dirac equation (1.33) yields

$$i\gamma^\mu \partial_\mu \psi_L - m\psi_R = 0. \quad (1.35)$$

The left-handed and right-handed fermion fields,  $\psi_L$  and  $\psi_R$ , are coupled via the mass term  $m$ .

The question is now how the mass term  $m\bar{\psi}\psi$  arises in (1.34). In the Standard Model, all particles are initially assumed to be massless<sup>12</sup> [60]. The non-zero masses are generated through the Higgs mechanism [21, 61], where the fermion fields  $\psi_L$  and  $\psi_R$  couple to the vacuum expectation value  $v$  of the scalar Higgs field  $\phi_0$ , consisting of a complex doublet  $\phi_0 = \frac{1}{\sqrt{2}} \begin{pmatrix} 0 \\ v \end{pmatrix}$ . Considering now the leptons of the first generation  $\psi_L = \begin{pmatrix} \nu_e \\ e^- \end{pmatrix}_L$  and  $\psi_R = e_R$ , this so called Yukawa-coupling can be integrated into the Lagrange density:

$$i\gamma^\mu \partial_\mu \begin{pmatrix} \nu_e \\ e^- \end{pmatrix}_L = g_e \frac{1}{\sqrt{2}} \begin{pmatrix} 0 \\ v \end{pmatrix} e_R, \quad (1.36)$$

where  $g_e$  is the Yukawa coupling constant. By comparison to eq. (1.35), one finds the following lepton masses:

$$m_e = \frac{g_e v}{\sqrt{2}}, \quad m_\nu = 0. \quad (1.37)$$

All fermions in the Standard Model obtain their mass accordingly. Obviously, the fact that there are no 'right-handed' neutrinos leads to massless neutrinos in the Standard Model.

### 1.4.2 Neutrino mass generating mechanisms

The mechanism to generate neutrino masses is coupled to the intrinsic CP properties of neutrinos [41]. If neutrinos are Dirac fermions, their masses may arise similarly as for the charged fermions (*Dirac mass*), albeit with different Yukawa coupling. In case of Majorana fermions, however, the mass generating mechanism could be quite different (*Majorana mass*).

---

<sup>11</sup>The indices  $L$  and  $R$  denote the handedness of the particle, which defines its chirality state.

<sup>12</sup>This follows from the requirement of gauge invariance, with gauge bosons being described by field equations for massless particles.

### Dirac mass

The most simple extension of the Standard Model would be the addition of a right-handed neutrino field  $\nu_R$ , which only shows up to give neutrinos mass, but is of sterile nature concerning the weak interaction [62]. A Yukawa coupling term for the neutrino would be added to eq. (1.36), with coupling strength  $g_\nu$ . An issue here is the extreme fine-tuning of  $g_\nu \sim 10^{-13}$ , which is required to accommodate the smallness of the neutrino mass.

### Majorana mass

While charged fermions can only obtain Dirac-type masses, neutral fermions, such as the neutrino, could also feature a so called Majorana mass term. It was shown above that Dirac masses require left-handed as well as right-handed chiral states. E. Majorana managed to construct a mass term using only the left-handed states [63] by splitting the Dirac Lagrangian (1.34) into its chiral components. This reveals two Dirac equations

$$i\gamma^\mu \partial_\mu \psi_{L/R} = m\psi_{R/L}, \quad (1.38)$$

coupled by the mass term. As a consequence, massless particles can be described by a single chiral field, which has two independent components (two-component spinor or Weyl spinor) [64]. At first, one would expect that a four-component spinor is required to describe a massive particle. Majorana found that by defining the right-handed field as  $\psi_R = C\bar{\psi}_L^T$ , where  $C$  is the charge conjugation matrix and  $T$  denotes the transpose, the Majorana field becomes  $\psi = \psi_L + \psi_L^C$ , where the fields  $\psi_L$  and  $\psi_R$  are not independent. Furthermore, this implies that the neutrino is its own anti-particle. With this field it is possible to add a Majorana mass term to the Lagrangian:

$$\mathcal{L}_L^M = -\frac{1}{2}m_L\bar{\nu}_L^C\nu_L. \quad (1.39)$$

The Dirac and Majorana descriptions only differ in case of massive neutrinos, as otherwise the right-handed chiral component does not come into play.

### Dirac-Majorana mass term

It was shown above that, if only the left-handed chiral field  $\nu_L$  exists, the Lagrangian contains only the Majorana mass term (1.39). In case of an additional field  $\nu_R$ , also a Dirac term

$$\mathcal{L}^D = -m_D\bar{\nu}\nu, \quad \nu = \nu_L + \nu_R, \quad (1.40)$$

and a right-handed Majorana term

$$\mathcal{L}_R^M = -\frac{1}{2}m_R\bar{\nu}_R^C\nu_R \quad (1.41)$$

exist. Therefore, the most general Lagrangian contains the Dirac-Majorana mass term

$$\mathcal{L}^{D+M} = \mathcal{L}^D + \mathcal{L}_L^M + \mathcal{L}_R^M. \quad (1.42)$$

With the useful definition of the column matrix of left-handed chiral fields

$$N_L = \begin{pmatrix} \nu_L \\ \nu_R^C \end{pmatrix}, \quad (1.43)$$

the Dirac-Majorana mass term can be written as

$$\mathcal{L}^{D+M} = -\frac{1}{2} N_L^T M N_L, \quad (1.44)$$

with the symmetric matrix

$$M = \begin{pmatrix} m_L & m_D \\ m_D & m_R \end{pmatrix}. \quad (1.45)$$

In this case, the chiral fields  $\nu_L$  and  $\nu_R$  do not have a definite mass. The matrix  $M$  has to be diagonalized in order to find the field of massive neutrinos.

### See-Saw mechanism

An interesting case is found for  $m_L = 0$  and  $m_D \ll m_R$ . Diagonalizing (1.45) yields the massive neutrino fields:

$$m_1 \approx \frac{m_D^2}{m_R}, \quad m_2 \approx m_R. \quad (1.46)$$

In this case, the mass  $m_2$  is very heavy, while  $m_1$  is very light, which would naturally solve the problem of the smallness of the neutrino mass. The mixing angle, given by  $\tan 2\theta = 2m_D/m_R$ , is very small, which implies that  $\nu_1$  is composed mainly of the active chiral field  $\nu_L$ , while  $\nu_2$  consists mainly of the sterile  $\nu_R$ .

In addition to this so called See-Saw type I mechanism [65, 66], a type II mechanism exists [67], which assumes that  $m_L > 0$ , leading to an additional term in equ. (1.46).

Furthermore, it is possible to introduce neutrino masses in the Lagrangian via approaches involving radiative corrections [68], Higgs-triplets [69, 70], supersymmetry [71, 72] or extra dimensions [73].

## 1.5 Determination of the neutrino mass

A primary goal of experimental neutrino physics is to determine the neutrino mass scale. As previously shown, neutrino oscillation experiments can only reveal the mass splittings  $\Delta m^2$ . Therefore, additional methods are required, which will be discussed in this section. These can be sub-divided into the groups of direct and indirect methods. While direct methods rely purely on the kinematics of the decay process, indirect methods are based on model assumptions, which can even incorporate certain neutrino properties. In one approach, the cosmological studies, one focuses on the imprint of neutrino masses on the evolution of large-scale structures in the Universe (section 1.5.1). A second indirect approach is the search for the neutrinoless double  $\beta$ -decay (section 1.5.2). Finally, as a direct method, the single  $\beta$ -decay approach, which the KATRIN experiment relies on, is discussed (section 1.5.3). It should be emphasized that all approaches measure different effective neutrino mass parameters.

### 1.5.1 Cosmology

The  $\Lambda$ CDM cosmological model describes the development of the Universe from a hot Big Bang to its present state dominated by dark energy ( $\Lambda$ ) and dark matter (CDM) [74]. At a very early stage, the Universe was filled with a hot quark-gluon plasma, which, upon expansion, quickly cooled down to temperatures where deuterium nuclei could form. This led to a decoupling of photons when their energy was insufficient for further photo-disintegration of deuterium nuclei. While free-streaming through the expanding Universe, these photons further cooled-down. The resulting Cosmic Microwave Background (CMB) was discovered in 1965 [75], displaying an effective temperature of  $\sim 2.7$  K [76].

The 'freeze-out' of radiation is a fundamental mechanism, which also occurred for other particles or interactions, such as the weak interaction. Cosmic neutrinos were kept in thermal equilibrium with the rest of the plasma until their weak interaction rate  $\Gamma_\nu \approx \langle \sigma_\nu n_\nu \rangle$ , governed by the interaction cross section  $\sigma_\nu$  and the neutrino number density  $n_\nu$ , fell below the expansion rate  $H$  of the Universe. In the case of neutrinos, to first order, the decoupling took place at a temperature  $T_{\text{dec}} \approx 1$  MeV [77]. Correspondingly, a cosmic neutrino background (C $\nu$ B) is expected, which consists of relic neutrinos as thermal left-overs from the Big Bang. Although the C $\nu$ B has not been observed yet, the agreement of the observed and calculated primordial abundances of light elements gives indirect evidence for its existence.

In order to understand the influence of relic neutrinos on structure formation of the Universe, the evolution of the C $\nu$ B itself after decoupling has to be investigated. The expansion of the Universe is described by the Friedmann-Robertson-Walker metric [78]:

$$ds^2 = dt^2 + a(t)^2 \delta_{ij} dx^i dx^j, \quad (1.47)$$

where  $a(t)$  denotes the scale factor, normalized to the current value  $a(t_0) = 1$ , which is related to the redshift  $z$ :  $a(t) = 1/(1+z)$ . According to General Relativity, a homogeneous, isotropic, and flat (i.e.  $k = 0$ ) Universe can be described by the 1. Friedmann equation [79] (derived from the 00 component of Einstein's field equations [80]):

$$\left(\frac{\dot{a}}{a}\right)^2 = H^2 = \frac{8\pi G}{3} \rho = H_0^2 \frac{\rho}{\rho_c}, \quad (1.48)$$

which relates the Hubble parameter  $H$ , with its current value  $H_0 = (67.3 \pm 1.2)$  km/s Mpc, to the total energy density  $\rho$  [81]. The critical density today  $\rho_c = 1.88 \cdot 10^{-29} h^2 \text{ g cm}^{-3}$  entails a spatially flat Universe, where  $h = H_0/(100 \text{ km s}^{-1} \text{ Mpc}^{-1})$  is the dimensionless Hubble parameter. The different contributions to the total energy density

$$\rho_{\text{tot}} = \rho_\gamma + \rho_{\text{cdm}} + \rho_{\text{b}} + \rho_\nu + \rho_\Lambda, \quad (1.49)$$

are shown in figure 1.5 in terms of the density fractions  $\Omega_i = \rho_i/\rho_c$ . The contribution of neutrinos to  $\rho_{\text{tot}}$  depends on their number density  $n_\nu = (3/11)n_\gamma = 339/\text{cm}^3$  and their

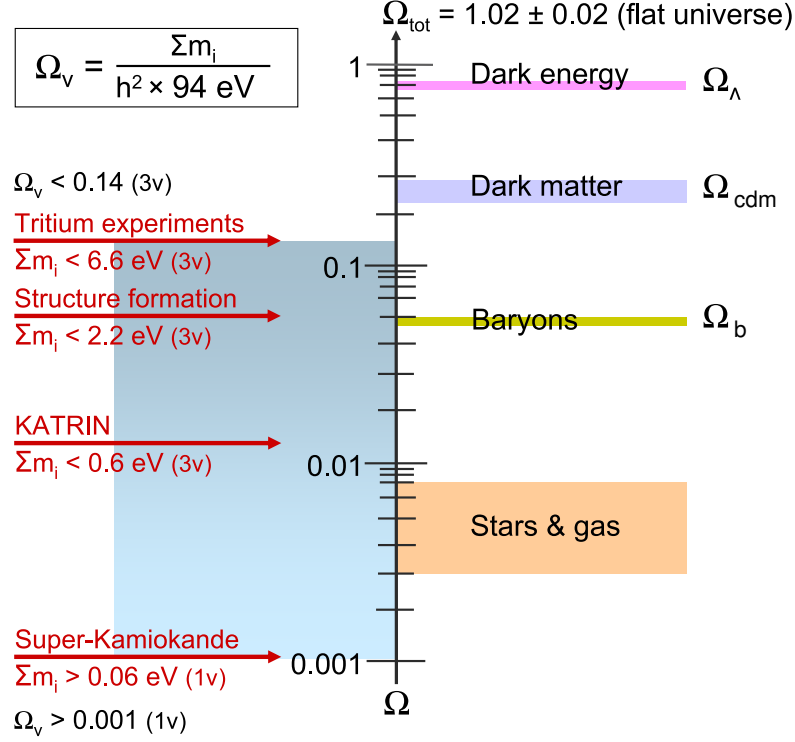


**Figure 1.5:** Contribution of neutrinos to the total energy density of the Universe, as a function of their mass. The experimental bounds on  $\sum m_i$  limit the minimal and maximal contribution of  $\Omega_\nu$  to  $\Omega_{\text{tot}}$ . Figure according to [82].

mass  $m_\nu = \sum_i m_i$ , which includes all masses of neutrino states which are non-relativistic today [77]:

$$\Omega_\nu = \frac{\rho_\nu}{\rho_c^0} = \frac{\sum_i m_i}{93.14 h^2 \text{ eV}}. \quad (1.50)$$

A rather model-independent upper bound on the neutrino mass can be derived from the observation of a flat Universe with  $\Omega_{\text{tot}} = 1$  in combination with a total matter contribution  $\Omega_{\text{m}} \approx 0.3$ :

$$\sum_i m_i \leq 15 \text{ eV}. \quad (1.51)$$

More stringent bounds are found when calculating the influence of massive neutrinos on the large-scale structures of the Universe.

Figure 1.6 visualizes the relative contributions of the energy densities of (1.49) as a function of the scale factor or, equivalently, temperature. The different phases of radiation, matter and dark energy domination are clearly visible. The important point here is that relativistic neutrinos contribute to the radiation density at early times, while they behave like pressure-less matter after becoming non-relativistic. In the non-relativistic limit, the neutrino contribution is dominated by their mass, as indicated for three exemplary neutrino masses in figure 1.6.

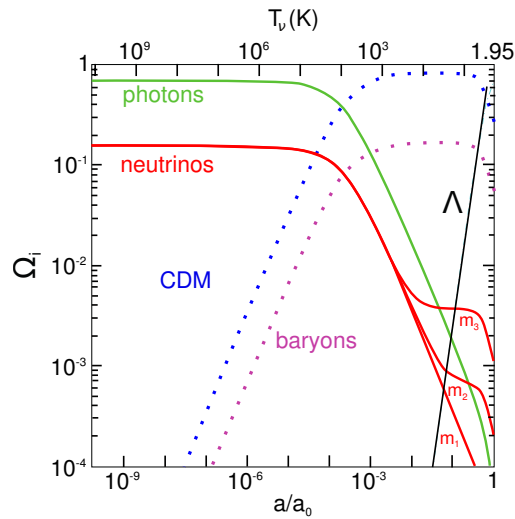


**Figure 1.6:** Evolution of the energy densities in the Universe as a function of the scale factor  $a$  or temperature  $T$ . The different areas of radiation, matter and dark energy domination are clearly visible. Model parameters:  $h = 0.7$ ,  $\Omega_\lambda = 0.7$ ,  $\Omega_b = 0.05$ ,  $\Omega_{\text{cdm}} = 1 - \Omega_\lambda - \Omega_b - \Omega_\nu$ . The three assumed neutrino masses are:  $m_1 = 0$ ,  $m_2 = 0.009$  eV, and  $m_3 = 0.05$  eV. Figure adapted from [77].

Measurements of matter density fluctuations at large scales have been carried out by a variety of experiments such as the Sloan Digital Sky Survey [83]. Different experimental techniques are sensitive to specific scales, allowing to map the so called matter power spectrum over different wave numbers, as displayed in figure 1.7 (a). Here, the strength of matter fluctuations  $P$  is shown as a function of their scale given by the wavelength  $\lambda$  (or wavenumber  $k = 1/\lambda$ ).

Two distinct slopes can be identified, with a turning point at a certain wavenumber, which approximately corresponds to the time of matter-radiation equality [85]. In the radiation dominated phase (smaller wavenumbers), the Jeans length<sup>13</sup> is of the order of the Hubble radius. Radiation fluctuations (including neutrinos) on smaller scales oscillate as sound waves such that their time-averaged density contrast vanishes. In this regime, the effect of neutrino free-streaming can be neglected, which is confirmed by figure 1.7 (b), where the influence of different neutrino masses on the matter power spectrum is shown.

At larger wavenumbers, the Universe becomes  $\Lambda$ -dominated and gravitational potential wells decay due to the expansion of the Universe. This effect results in a continuous decrease of power in the spectrum of figure 1.7 (a). Additionally, non-relativistic neutrinos affect the power spectrum at these small scales. In this context, it is useful to investigate the free-streaming length  $\lambda_{\text{FS}}$  of non-relativistic neutrinos, which corresponds to the distance that neutrinos can travel before slowing down to non-relativistic veloci-

<sup>13</sup>The Jeans length denotes the critical scale where gravitational attraction and radiation pressure are balanced.

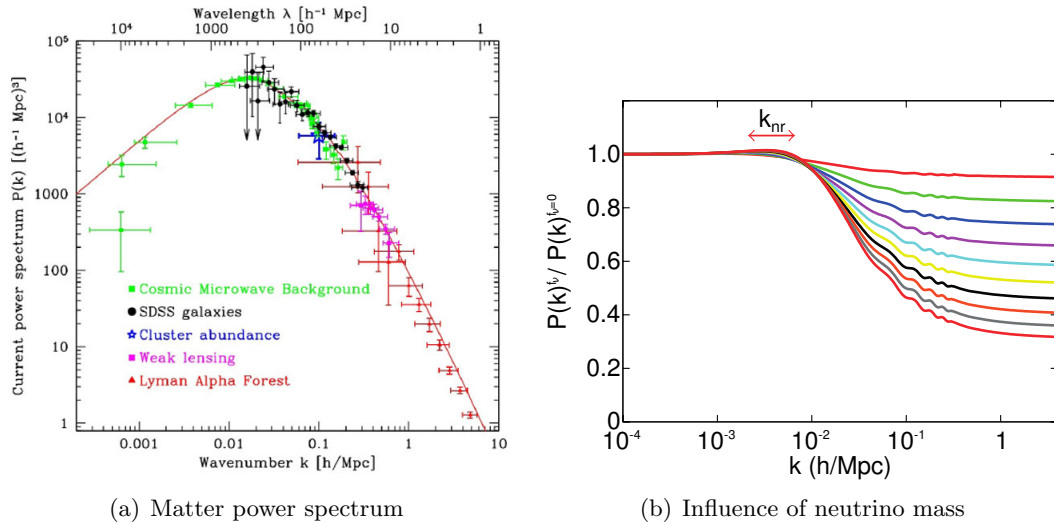


**Figure 1.7:** (a) Matter power spectrum  $P(k)$ : Strength of matter fluctuations as a function of their scale. Small scales are damped by neutrino free-streaming, while large scales remain unaffected. Figure from [84]. (b) Influence of different neutrino masses on the matter power spectrum  $P(k)$ . Shown is the ratio of  $P(k)$  for massive neutrinos with density fraction  $f_\nu = \Omega_\nu/\Omega_m$  to that of massless neutrinos. The curves correspond to  $f_\nu = 0.01, 0.02, \dots, 0.1$  (from top to bottom). The parameter  $k_{nr}$  denotes the transition from the relativistic to the non-relativistic regime. Figure according to [77].

ties:

$$\lambda_{FS}(t) = 8 \frac{1+z}{\sqrt{\Omega_\Lambda + \Omega_m(1+z)^3}} \left( \frac{1 \text{ eV}}{m_\nu} \right) h^{-1} \text{ Mpc}. \quad (1.52)$$

As a consequence of free-streaming, small-scale density fluctuations are effectively washed out as neutrinos cannot be confined in regions smaller than  $\lambda_{FS}$  [85]. Figure 1.7 (b) underlines the distinct influence of different neutrino masses on the matter power spectrum. Shown here is the ratio of  $P(k)$  in the case of massive neutrinos  $P(k)^{f_\nu}$  to the case of massless neutrinos  $P(k)^{f_\nu=0}$  for different neutrino density fractions  $f_\nu = \Omega_\nu/\Omega_m$ .

As a result, observations of the large-scale structure of the Universe can in principle reveal the sum of neutrino masses, where an exemplary bound comes from a combined analysis of SDSS, CMB, supernova and BAO<sup>14</sup> data [86]:

$$f_\nu < 0.049 \rightarrow \sum m_i < 0.51 \text{ eV} \quad (95\% \text{ C.L.}). \quad (1.53)$$

The fact that the obtained neutrino mass bounds vary significantly, depending on the underlying data sample, shows the model-dependence of a determination of the neutrino mass with the help of cosmological observations [87]. This effect is caused by a parameter degeneracy where different parameter combinations can mimic the similar effect of  $m_\nu$  on the measured observable.

<sup>14</sup>Baryonic Acoustic Oscillations

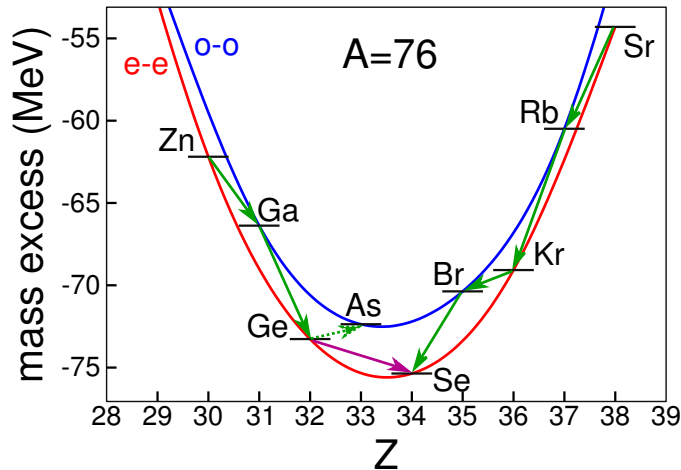


**Figure 1.8:** Energies of the  $A=76$  isobars. The single  $\beta$ -decay between  $^{76}\text{Ge}$  and  $^{76}\text{As}$  (dotted green arrow) is energetically forbidden, leaving double  $\beta$ -decay between  $^{76}\text{Ge}$  and  $^{76}\text{Se}$  (purple arrow) as the only decay channel. Figure according to [88].

### 1.5.2 Neutrinoless double $\beta$ -decay

The process of double  $\beta$ -decay is a second order weak (nuclear) process, and takes place when the single  $\beta$ -decay of a nucleus is energetically forbidden. This process thus occurs between two  $Z$ -even  $N$ -even isobars, where  $N$  denotes the number of neutrons and  $Z$  the number of protons or the atomic number, as shown in figure 1.8. The pairing interaction shifts the binding energy of the even-even nuclei with respect to the odd-odd nuclei, resulting in two distinct mass parabolas. In case of  $^{76}\text{Ge}$ , the single  $\beta$ -decay to  $^{76}\text{As}$  is energetically forbidden, leaving double  $\beta$ -decay to  $^{76}\text{Se}$  as the only decay channel:



This two-neutrino decay mode (abbreviated  $2\nu\beta\beta$ -decay) was originally proposed by M. Goeppert-Mayer in 1935 [89] and requires no extension of Standard Model particle physics. Being a second-order weak process, the decay rate is very low with exceedingly long half-lives in the range  $10^{19} - 10^{21}$  years. The first laboratory detection was hence only achieved in 1987 for the isotope  $^{82}\text{Se}$  [90]. Since then,  $2\nu\beta\beta$ -decay has been observed for an additional 11 isotopes.

An alternative process, where the nucleus decays without the emission of neutrinos ( $0\nu\beta\beta$ -decay), has been proposed in 1937 by G. Racah [91] and in 1939 by W. Furry [92], after E. Majorana had theoretically shown that neutrinos could be their own antiparticles [63]. In this hypothetical process, massive Majorana-type neutrinos are exchanged<sup>15</sup> as virtual particles between two neutrons, as shown in figure 1.9 (left). Such a process

<sup>15</sup>The transition is not necessarily due to the exchange of Majorana neutrinos. Other mechanisms such as the exchange of right-handed W-bosons or Kaluza-Klein excitations could also contribute. A disentanglement of these mechanisms could be possible via an analysis of the angular correlations of the emitted electrons or by studying the decay to the excited  $0^+$  states [93].

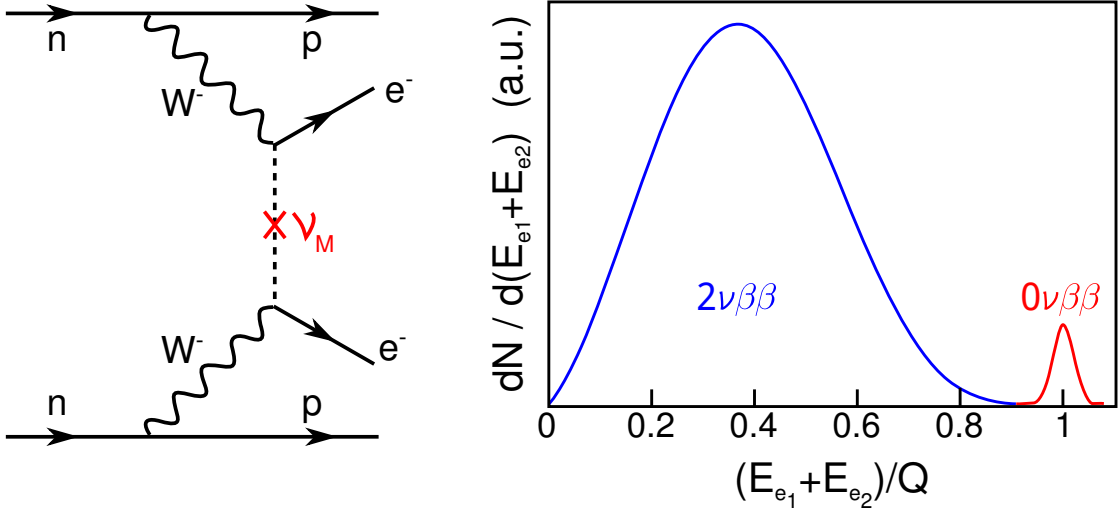


**Figure 1.9:** Left: Feynman graph of the  $0\nu\beta\beta$ -decay. Two neutrons decay simultaneously into two protons and two electrons via exchange of a virtual Majorana neutrino  $\nu_M$ . Right: Sum energy spectrum of  $2\nu\beta\beta$ -decay and  $0\nu\beta\beta$ -decay. If neutrinos are emitted, they carry part of the decay energy  $Q$ , leading to a continuous  $2\nu\beta\beta$  energy spectrum. Without the emission of neutrinos, the summed electron energy is found at the  $Q$ -value.

is violating lepton number conservation by two units and hence is indicating for physics beyond the Standard Model. The observation of a  $0\nu\beta\beta$ -decay would imply that neutrinos are massive particles [94, 95]. During the  $\beta$ -decay of a neutron, an antineutrino with a right-handed chirality (positive helicity) is emitted. For the inverse  $\beta$ -decay of the second neutron, it has to be absorbed as a neutrino with left-handed chirality (negative helicity) [96]. While for massless particles, chirality is identical to helicity, in case of massive neutrinos, these properties have to be distinguished. The weak interaction is related to the conserved Lorentz parameter chirality which, in turn, is related to the  $\gamma^5$  matrix in Dirac spinor space. Helicity, however, is related to physical space and hence, it is frame dependent, i.e. the observer can find a reference frame for which the neutrino appears to move backwards resulting in a reversed helicity.

Due to the virtual character of the exchanged massive Majorana neutrino, the  $0\nu\beta\beta$  experiments measure an effective Majorana mass  $\langle m_{\beta\beta} \rangle$ . This mass is formed by the coherent sum of the neutrino mass eigenstates  $m_i$ :

$$\langle m_{\beta\beta} \rangle = \left| \sum_{i=1}^3 U_{ei}^2 m_i \right| = \left| \sum_{i=1}^3 |U_{ei}|^2 m_i e^{i\delta_{M_i}} \right|. \quad (1.55)$$

The CP-violating Majorana phases  $\delta_{M_i}$  can lead to cancellations so that  $\langle m_{\beta\beta} \rangle < m_i$ .

In  $0\nu\beta\beta$  searches the half-life  $T_{1/2}^{0\nu\beta\beta}$  of the decay is the observable, which is related

to  $m_{\beta\beta}$  by [97]

$$\left(T_{1/2}^{0\nu\beta\beta}\right)^{-1} = G^{0\nu\beta\beta}(Q_{\beta\beta}, Z) \cdot \left| M_{\text{GT}}^{0\nu\beta\beta} - \left(\frac{g_V}{g_A}\right)^2 M_{\text{F}}^{0\nu\beta\beta} \right|^2 \cdot \frac{\langle m_{\beta\beta} \rangle^2}{m_e^2}, \quad (1.56)$$

where  $G^{0\nu\beta\beta}$  denotes the phase space factor, which depends on the endpoint  $Q_{\beta\beta}$  of the decay and on the atomic number  $Z$ , and  $M_{\text{GT}/\text{F}}$  are the Gamov-Teller and Fermi nuclear matrix elements. The largest theoretical uncertainties (up to factors of 2-3) arise from the calculations of the matrix elements. Therefore, an observation of the  $0\nu\beta\beta$ -decay process in different isotopes would be advantageous to narrow the parameter space of  $\langle m_{\beta\beta} \rangle$ .

In  $0\nu\beta\beta$  searches, the  $\beta\beta$ -active material is either surrounded by an external detector or intrinsically acts as detector. After elimination of background events, the  $0\nu\beta\beta$  signature would look similar to figure 1.9 (right): the continuous  $2\nu\beta\beta$ -decay spectrum is separated from a peak at the endpoint of the spectrum. Note that the relative heights of the two spectra are not realistic, as  $0\nu\beta\beta$ -decay is strongly suppressed compared to  $2\nu\beta\beta$ -decay.

The Heidelberg-Moskow experiment has studied the decay of enriched germanium (see decay process (1.54)) in a well-shielded underground setup. In 2002, a subgroup of the Heidelberg-Moskow collaboration claimed to have found evidence for a Majorana neutrino mass  $\langle m_{\beta\beta} \rangle \approx 0.4$  eV [98]. This result is heavily disputed among the community [99]. Therefore, several experiments such as GERDA [100, 101], CUORE [102–104] and EXO [105, 106], are being performed to confirm or disprove this result.

### 1.5.3 Single $\beta$ -decay

The only 'model-independent' method to determine the neutrino mass is based on the investigation of the kinematics of weak decays, as the experimental method relies on momentum and energy conservation only. A measurement of the  $\beta$ -decay electrons allows a determination of the effective mass of the electron anti-neutrino  $m_{\bar{\nu}_e}$ , which is the incoherent sum of the mass eigenstates  $m_{\nu_i}$  [107]:

$$m_{\bar{\nu}_e}^2 = \sum_i |U_{ei}^2| m_{\nu_i}^2. \quad (1.57)$$

In contrast to  $0\nu\beta\beta$ -decay, no CP-phases enter the mass term.

In a nuclear  $\beta^-$ -decay process, the weak interaction converts a neutron into a proton while emitting an electron and an electron-antineutrino:

$$n \rightarrow p + e^- + \bar{\nu}_e, \quad (1.58)$$

as shown in figure 1.10 (left). The released energy is distributed between the three decay products. The mass of the remaining nucleus can, in a first order approximation, be treated as infinitely large in comparison to the mass of the electron and the neutrino. Therefore, the decay energy is split only between the electron and the neutrino where

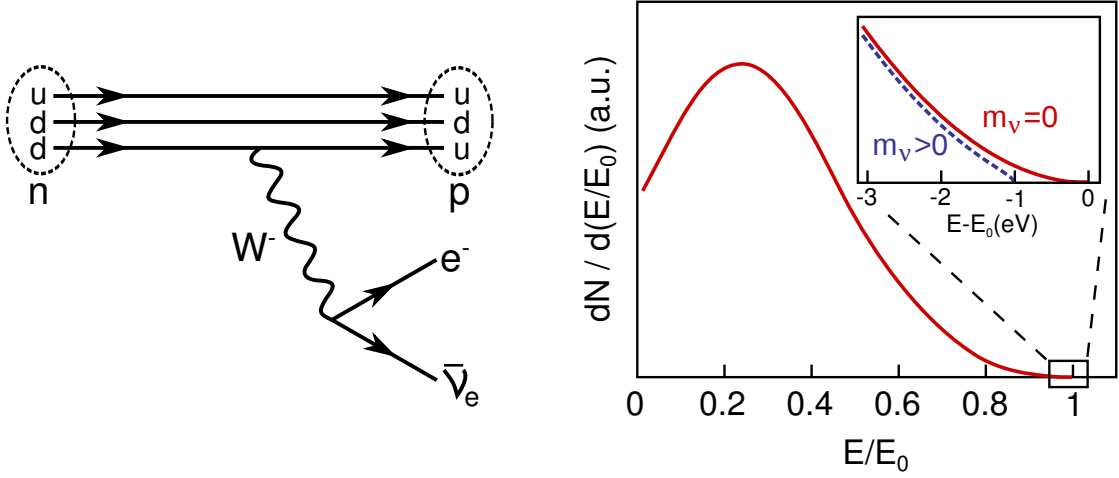


**Figure 1.10:** Left: Feynman graph of the single  $\beta$ -decay. A neutrons decays into a proton, an electron and an electron anti-neutrino. Right: Energy spectrum of the  $\beta$ -decay electrons. A non-vanishing neutrino mass manifests itself close to the spectral endpoint  $E_0$ . Figure according to [108].

the neutrino takes away the energy  $E_\nu = \sqrt{m_\nu^2 c^4 + p_\nu^2 c^2}$ . The maximum kinetic energy of the electron is thud reduced by the finite rest mass of the neutrino, as indicated in figure 1.10 (right). As the neutrino mass enters the kinematic considerations through the above relativistic invariant, an energy uncertainty directly translates into a neutrino mass uncertainty [109]:

$$\delta m_\nu = \frac{E_\nu}{m_\nu} \delta E_\nu = \gamma \delta E_\nu. \quad (1.59)$$

This implies that the more relativistic the neutrino becomes ( $p_\nu \gg m_\nu$ ), the harder it is to assess its rest mass. The neutrino mass  $m_{\bar{\nu}_e}$  can thus be determined by a measurement of the (relative) shape of the  $\beta$ -spectrum in the region close to the endpoint  $E_0$ , where the neutrino momentum vanishes.

The energy distribution of the decay electrons can be calculated with the help of Fermi's Golden Rule [7]

$$T = \frac{d^2 N}{dt dE} = \frac{2\pi}{\hbar} |\mathcal{M}|^2 \rho(E). \quad (1.60)$$

The transition rate  $T$  depends on the strength of the coupling between the initial and final state of the system and on the number of possible transitions, which is given by the density of the final states  $\rho(E)$ . A transition will proceed more rapidly if the coupling, determined by the matrix element  $\mathcal{M}$ , between the initial and final state is larger. This leads to the following relation [110]:

$$\frac{dN}{dE} = R(Z, E) \cdot (E_0 - E) \cdot \sqrt{(E_0 - E)^2 - m_{\bar{\nu}_e}^2 c^4} \cdot \Theta(E_0 - E - m_{\bar{\nu}_e} c^2), \quad (1.61)$$

where

$$R(Z, E) = \frac{G_F^2}{2\pi^3 \hbar^7} \cdot \cos^2(\theta_C) \cdot |\mathcal{M}|^2 \cdot F(Z, E) \cdot p \cdot (E + m_e c^2) \quad (1.62)$$

contains several kinematic parameters and fundamental constants, namely

$G_F$ : Fermi coupling constant	$\Theta_C$ : Cabibbo angle
$M$ : transition matrix element	$F$ : Fermi function
$p$ : electron momentum	$m_e$ : electron mass
$E_0$ : endpoint energy of $\beta$ -spectrum	$E$ : electron kinetic energy.

The step function  $\Theta(E_0 - E - m_{\bar{\nu}_e}c^2)$  ensures energy conservation, so that a neutrino can only be produced if the available energy is larger than its rest mass.

Both  $\mathcal{M}$  and  $F(Z, E)$  are independent of  $m_{\bar{\nu}_e}$ . Therefore, the influence of  $m_{\bar{\nu}_e}$  on the spectrum results mainly from the phase space factor  $(E_0 - E) \cdot [(E_0 - E)^2 - m_{\bar{\nu}_e}^2 c^4]^{1/2}$ . In principle, the neutrino mass could be determined just by looking at the difference between the measured endpoint energy and the expected endpoint  $E_0$  which can be seen in figure 1.10. However, both values can not be measured with a sufficiently high precision. Therefore, the influence of the neutrino mass on the shape of the spectrum in the narrow region up to a few eV below the endpoint has to be measured. In this region, neutrinos are non-relativistic ( $p_\nu \approx m_\nu$ ) and their momentum-energy relation can be probed.

### Experiments using cryo-bolometers

An interesting approach for the investigation of the kinematics of  $\beta$ -decays is the use of cryogenic microcalorimeters (cryo-bolometers) [111], similar to those used in some  $0\nu\beta\beta$ -decay experiments [103]. The advantage of this method is the fact that the whole decay energy is deposited in the detector, including excitations of the daughter atoms.

A suitable candidate is the isotope  $^{179}\text{Re}$ , which has the lowest known endpoint energy of  $Q = 2.67$  keV [112], ensuring that a large fraction of the  $\beta$ -electrons carries useful information on the spectrum. On the other hand, due to its exceedingly long half-life of  $T_{1/2} = 4.3 \cdot 10^{10}$  y, large amounts of Rhenium are required to obtain a source with a sufficiently high activity. In order to avoid pile-up effects, only very small detector units can be used, resulting in designs with large arrays comprising thousands of single modules.

The first experiments of this type were the MANU experiment in Genova and the MIBETA experiment in Milano [113]. Both used an array of several thermal microcalorimeters serving as source and detector at the same time, where the temperature rise after a  $\beta$ -decay of  $^{187}\text{Re}$  was read out by thermistors. The MIBETA collaboration published an upper limit on the neutrino mass of

$$m_{\bar{\nu}_e} < 15 \text{ eV (90\%C.L.)}. \quad (1.63)$$

The successor experiment MARE<sup>16</sup> [114, 115] aims to improve this sensitivity down to the sub-eV range. A first set of 72 channels has been deployed and is currently taking data [116].

<sup>16</sup>Microcalorimeter Arrays for a Rhenium Experiment

Another isotope under investigation is  $^{163}\text{Ho}$ , which decays via electron capture, with a very low  $Q$ -value in the range of 2.2-2.8 keV and a comparably low half life  $\mathcal{O}(10^3)$  y. Unfortunately, the current uncertainty in the determination of  $E_0$  directly translates into an uncertainty on the neutrino mass sensitivity [117]. The MARE collaboration as well as the ECHO<sup>17</sup> collaboration are investigating the potential of  $^{163}\text{Ho}$  as a suitable candidate to measure neutrino masses in the sub-eV range [118, 119].

### Experiments using tritium

The almost ideal characteristics of tritium as a  $\beta$ -emitter



have resulted in a long series of experiments using tritium-based sources [120]. The advantages of using tritium are based on several important facts:

- **Low endpoint energy:**  $E_0 \approx 18600$  eV. The fraction of  $\beta$ -decay electrons in the endpoint region scales as  $1/E_0^3$ . Hence, in case of a small  $Q$  value of the source material the count rate close to the endpoint is relatively large. Also, as  $\Gamma \propto E_0^5$ , it is advantageous to use  $\beta$ -emitters at rather large  $E_0$ .
- **Short half life:**  $t_{1/2} = 12.3$  a. This unique property of tritium ensures a large decay rate per unit volume of source material.
- **Super-allowed process,** transition between mirror nuclei: No corrections from the matrix element  $\mathcal{M}$  have to be taken into account. The matrix element is energy independent and has a rather large value.
- **Electronic structure:** Due to the low nuclear charge of tritium ( $Z = 1$ ), the electronic structure of the atomic shell is rather simple and can be computed with high precision, which reduces the systematic uncertainties.
- **Inelastic scattering:** As tritium is a low  $Z$  nucleus, the fraction of decay electrons undergoing inelastic scattering off the molecules in the source, which entails a loss of kinetic energy, is relatively small.

Tritium  $\beta$ -decay experiments have been performed for more than half a century, with the most sensitive results coming from the Mainz [1] and Troitsk [2] experiments:

$$\text{Mainz: } m(\bar{\nu}_e) \leq 2.3 \text{ eV (95\% CL.); Troitsk : } m(\bar{\nu}_e) \leq 2.05 \text{ eV (95\% CL.).} \quad (1.65)$$

Both experiments were based on the then new principle of an electrostatic spectrometer, which the KATRIN experiment [82] is going to push to its technological limits. A detailed insight into this part of the experiment will be given in the next chapter.

---

<sup>17</sup>Electron Capture  $^{163}\text{Holmium}$  experiment

# The KATRIN experiment

The **K**arlsruhe **T**ritium **N**eutrino (KATRIN) experiment [82] is targeted to determine the “effective mass of the electron anti-neutrino”  $m_{\bar{\nu}_e}$  with a sensitivity of 200 meV (90% C.L.). To achieve this goal, KATRIN will investigate the kinematics of tritium  $\beta$ -decay with unprecedented precision close to the  $\beta$ -decay endpoint  $E_0 \approx 18.6$  keV. It is only in this narrow region of neutrino emission with almost vanishing neutrino momenta that one can gain access to  $m_{\bar{\nu}_e}$ .

The experimental setup will be described in section 2.1, while section 2.2 will focus on the measurement principle, the MAC-E filter. The discovery potential of KATRIN will be discussed in section 2.3. Finally, an overview of the different background processes within electrostatic spectrometers, which have been investigated within this thesis, will be given in section 2.4.

## 2.1 Experimental overview

A high-precision measurement of the integral  $\beta$ -spectrum requires a high-luminosity  $\beta$ -source with well-understood systematics, a variable high-precision filter with well-defined transmission characteristics for electron energies close to the endpoint and a position sensitive detector to count them. Previous experiments at Mainz [1, 121] and Troitsk [122, 123] were built according to this concept. As shown in figure 2.1, the 70 m long KATRIN experimental setup substantially upscales these experiments. This extended size is necessary to reach the design sensitivity of 200 meV/ $c^2$  compared to  $\sim 2$  eV/ $c^2$  of the predecessor experiments, as key experimental parameters have to be improved by two orders of magnitude (as  $m_{\bar{\nu}_e}^2$  is the observable). The stringent benchmark parameters, which have to be met for the individual components of KATRIN, will be detailed below.

## 2.1. Experimental overview

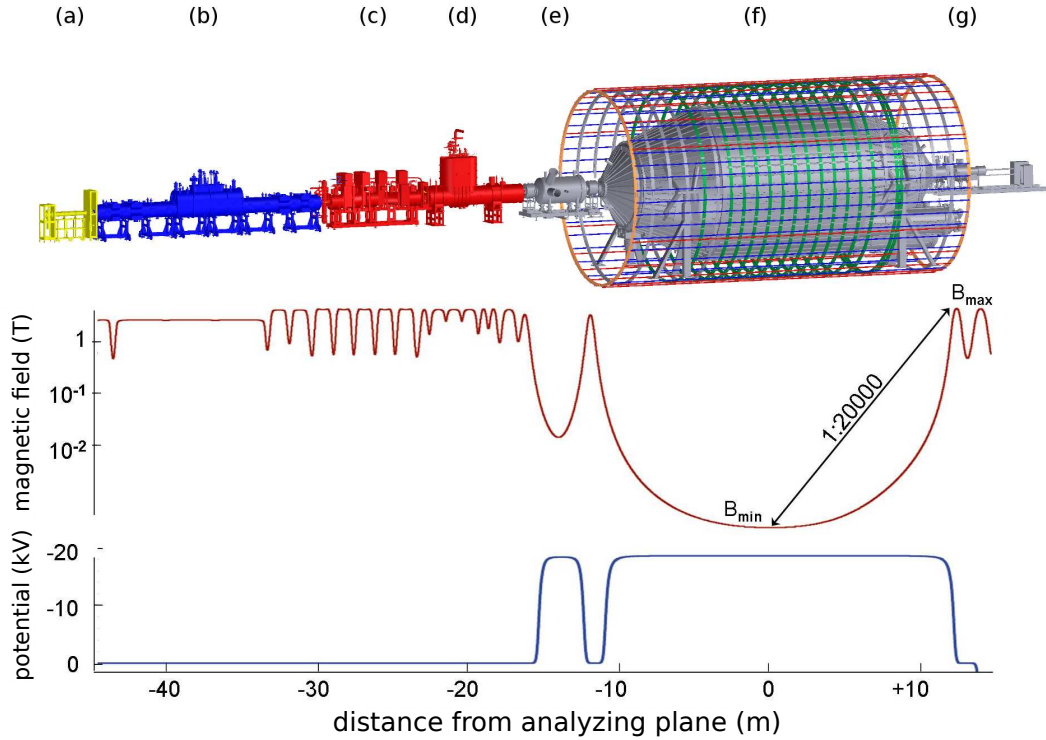


**Figure 2.1:** The 70 m long KATRIN experimental setup. (a) Rear section for source monitoring (section 2.1.2); (b) windowless gaseous tritium source WGTS (section 2.1.1); (c) differential and (d) cryogenic pumping section to remove tritium (section 2.1.3); (e) pre-spectrometer for pre-filtering of low-energy electrons (section 2.1.4); (f) main spectrometer for high-resolution  $\beta$ -spectroscopy (section 2.1.4); (g) detector to count the number of transmitted electrons (section 2.1.5). The lower part of the figure shows the magnetic field and electrostatic potential throughout the complete system.

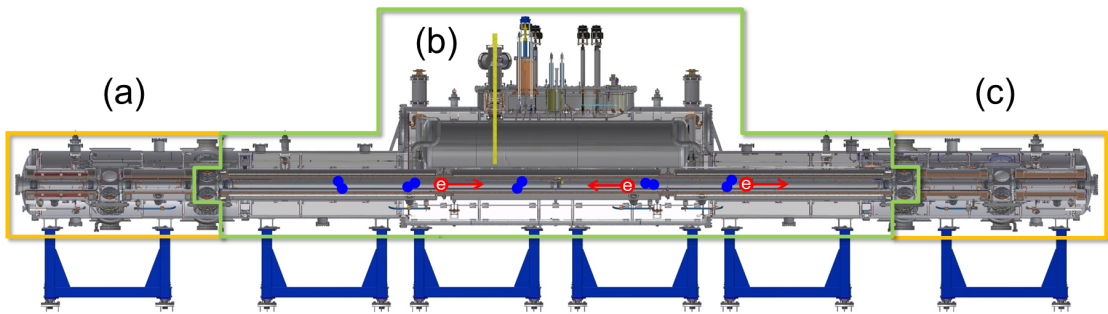


**Figure 2.2:** CAD drawing of the windowless gaseous tritium source (WGTS). Tritium molecules (blue) are injected in the middle of the 11 m long beam tube (b). When decaying, electrons (red) are released and guided by magnetic field lines to both ends (a) and (c) of the tube, where tritium is pumped out by turbo molecular pumps.

### 2.1.1 Tritium source

The windowless gaseous tritium source (WGTS) [124] is a high-luminosity ( $> 10^{11}$  Bq)  $\beta$ -decay source contained in a large and complex cryostat consisting of three functional modules (see figure 2.2). In the center unit (length  $l = 10$  m, diameter  $d = 90$  mm) of the WGTS, tritium is injected at the middle so that a fraction of  $\sim 10^{-9}$  of the  $\beta$ -active molecules will decay while diffusing to both ends of the stainless steel beam tube. There, two 3 m long units (DPS1-F, DPS1-R) will pump out tritium by means of two pump-ports housing large turbo molecular pumps (TMP). This tritium will be re-injected, thus forming a closed tritium cycle (inner loop) [125]. These units hence act as first differential pumping systems at the front and rear ends of the WGTS, reducing the tritium flow by 2 orders of magnitude. The gas injection pressure  $p_{\text{in}}$  allows to adjust the source column density  $\rho d$ . As this parameter governs the source luminosity, fluctuations thereof represent the main systematic uncertainty of the WGTS system, requiring a stabilization at the  $10^{-3}$  level. For an inlet pressure  $p_{\text{in}} = 3.4 \cdot 10^{-3}$  mbar and a source tube temperature  $T = 27$  K, one obtains the reference value for the column density:

$$\rho d = 5 \cdot 10^{17} \text{ cm}^{-2}. \quad (2.1)$$

The following physics processes all lead to systematic effects in the neutrino mass measurement and, hence, the corresponding key operation parameters need to be controlled precisely:

- The effect of the Doppler shift, resulting from the thermal and bulk motion of the molecules, will smear out the decay electron energy. This effect is minimized by cooling the gas down to 27 K, the lowest temperature regime before tritium molecules start to form clusters.
- Potential plasma effects would result in a non-uniform charge-up of the source which in turn would influence the decay electron energy. This distortion is reduced by injecting low-energy electrons from the rear section to obtain a quasi-neutrality of the plasma (section 2.1.2).
- A maximal fluctuation of the source temperature of  $\Delta t < 30$  mK is required to stabilize the column density at the  $10^{-3}$  level. This challenging demand will be met by a novel two-phase neon beam tube cooling system, which has already successfully been tested [126, 127].
- A reliable and fast ( $\mathcal{O}(60$  s)) determination of the isotopic composition of the high-purity tritium source (isotopic purity of  $\epsilon_{\text{T}} > 95\%$ ) requires in-line and near time monitoring by a dedicated Laser Raman system LARA [108].
- As the vibrational and rotational states of the  ${}^3\text{HeT}^*$  daughter molecule as well as electronic excitations (*final state distribution*) influence the decay electron energy, the molecular excitation has to be modeled with high precision [128, 129].

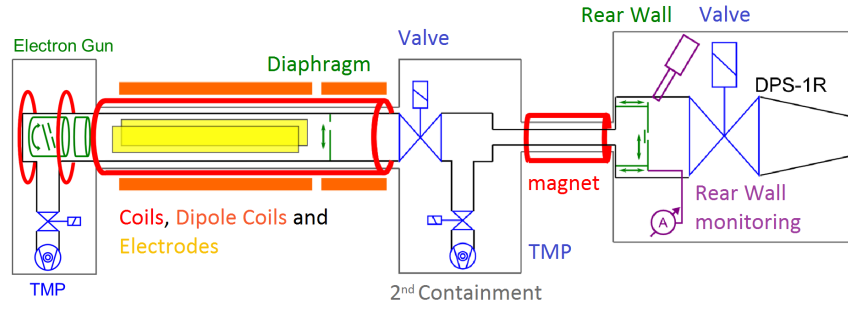


**Figure 2.3:** Schematic drawing of the rear section. The rear wall is responsible for monitoring the tritium activity and controlling the source potential. An electron gun is used to determine the source column density and to measure the KATRIN response function. The WGTS will be connected via a valve to the rear section. Figure adapted from [130].

After the extensive tests with the WGTS demonstrator test setup have been successfully completed [124], the system is currently being assembled to the final WGTS cryostat until spring 2015 by an industrial partner.

The decay electrons are guided within the  $191 \text{ Tcm}^2$  transported flux tube to both ends of the WGTS by a system of superconducting solenoids with 3.6 T field strength, which surround the central beam tube. Thus, one half of the decay electrons will be guided to the spectrometer part, where the energy analysis takes place. The other half will be transported to the rear section.

### 2.1.2 Rear section

As pointed out above, the continuous near-time and in-line monitoring of the source parameters is a key requirement to reach the KATRIN design sensitivity [124]. A key component in this context is the rear system (see figure 2.3) consisting of active and passive control and monitoring systems. The rear wall<sup>1</sup> will monitor the tritium activity via Beta-Induced X-ray Spectroscopy BIXS [131] and also control the source plasma potential. In addition, a high-intensity electron gun will be used for repeated measurements of the source column density. Furthermore, it will be used to measure the KATRIN response function to determine the inelastic scattering characteristics of the signal electrons in the source (more details can be found in section 2.2.2). As electrons from the electron gun are guided through a central small hole in the rear wall, magnetic dipoles at the first superconducting magnet of the WGTS will be used to shift the electron beam across the beam tube, allowing a 2-dimensional coverage of the entire flux tube to map potential fluctuations of the column density.

<sup>1</sup>One design is a gold-plated silicon wafer with a TiN adhesion layer.

### 2.1.3 Transport section

On the opposite (front) side of the WGTS, the transport section guides electrons to the spectrometer section. It consists of two functional units, the differential pumping section (DPS2-F) and the cryogenic pumping section (CPS). In combination with the DPS1-F, these tritium retention systems reduce the tritium flow rate by 14 orders of magnitude thus preventing tritium migration to the spectrometer section. A tritium partial pressure below  $10^{-20}$  mbar in the main spectrometer is required in order to keep the background [132, 133] by tritium below the design limit (more details in sections 2.1.4 and 7). Concurrently, signal electrons have to be guided adiabatically through the transport section without distorting effects by the tritium retention process.

#### Differential pumping section (DPS)

The first retention method for tritium is based on differential pumping by TMPs (see figure 2.4). Following the initial stages of differential pumping in the DPS1-F, the DPS section is based on the same principle. The 5 beam tubes, situated inside the warm bores of superconducting solenoids with field strengths of up to 5.5 T, are tilted against each other, thus preventing a direct line-of-sight for the tritium molecules to avoid the molecular beaming effect [134]. A TMP with large pumping speed is housed at each main pump port (4 in total), reducing the total tritium content by another 5 orders of magnitude.

A first version of the DPS2-F system, using a single cryostat design with a pumping scheme, which is almost identical to the one discussed above, was tested at KIT and achieved a tritium retention factor of  $> 2.5 \cdot 10^4$  [133, 135]. This is a promising result for the upcoming commissioning of the final system in 2014.

An important beam tube instrumentation unit of the DPS2-F system is the FT-ICR (Fourier Transform-Ion Cyclotron Resonance) diagnostic tool [136, 137] to determine

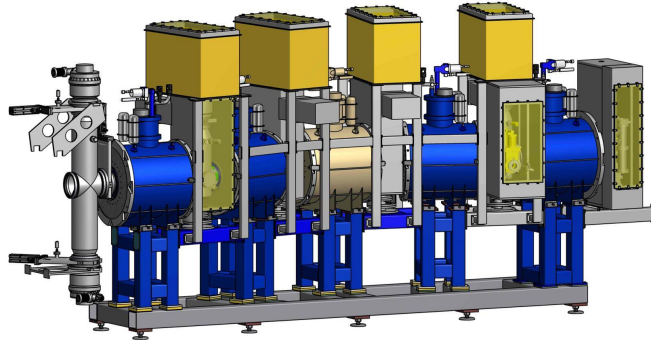


**Figure 2.4:** Differential pumping section. A total of 5 superconducting solenoids with field strengths up to 5.5 T adiabatically guide the signal electrons through two  $20^\circ$  chicanes while tritium is pumped out by 4 main TMPs, one at each of the pump ports between two adjacent beam tubes.

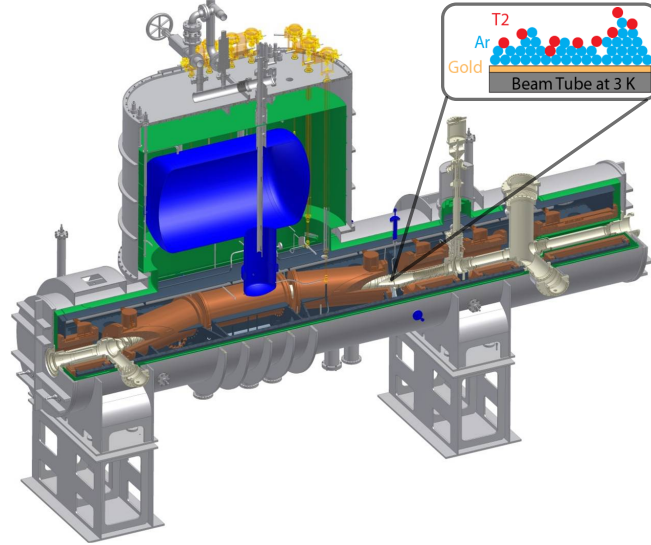


**Figure 2.5:** Cryogenic pumping section. While electrons are guided through two chicanes by a total of 7 superconducting solenoids with a field strength of up to 5.5 T, tritium molecules will hit the cold beam tube surface and remain there. The trapping probability is enhanced by a coverage with argon frost due to the increased surface.

the ion content from the WGTS. Furthermore, ions can actively be removed by a system of electrostatic dipole electrodes, also integrated into the DPS beam tube [138–140]. This device is necessary because ions are not affected by differential or cryogenic pumping as the magnetic field guides them through the chicanes directly towards the spectrometer, where they would dominate the background.

### **Cryogenic pumping section (CPS)**

Further tritium reduction by more than 7 orders of magnitude will be achieved by the CPS [141], which is schematically shown in figure 2.5. The working principle of this unit is based on cryo-sorption of the tritium molecules on the ultra-cold surface of parts of the CPS beam tube. The trapping efficiency is enhanced by covering the surface with argon frost. As in the case of the DPS, the dangerous molecular beaming effect of tritium is hindered by tilting the beam tubes [142]. When the surface is saturated to 1% with tritium, it has to be reconditioned, which occurs approximately every 3 months. Again a system of 7 superconducting solenoids adiabatically guides the signal electrons to the spectrometer section.

#### **2.1.4 Spectrometer section**

There are two electrostatic retarding spectrometers used in the main KATRIN beam line: the pre-spectrometer and the large main spectrometer. A third spectrometer, the monitor spectrometer, will be used in a separate beam line. The latter plays an essential

role as a monitoring device for fluctuations of the high voltage (HV) which is applied to the main spectrometer. The working principle of all spectrometers is based on the MAC-E filter, which will be explained in detail in section 2.2.1. The different purposes of each system will be illustrated below.

### Pre-spectrometer

The pre-spectrometer setup (see figure 2.6) is the first spectrometer encountered by the  $\beta$ -decay electrons. It is located adjacent to the cryogenic pumping section and represents the first essentially tritium-free component in the beam line. Signal electrons are guided through the pre-spectrometer by a magnetic field produced by two superconducting solenoids with a field strength of up to 4.5 T. The pre-spectrometer offers the option to operate as pre-filter, where low-energy signal electrons carrying no information on the neutrino mass are rejected by a potential barrier adjustable from 0 up to -18.3 kV. The optimal pre-filter potential setting has to be determined within future test measurements targeted to minimize the spectrometer background rate [143]. If operated at the maximum retarding potential of -18.3 kV, the electron flux into the main spectrometer would be reduced by 7 orders of magnitude.

Until 2011, the pre-spectrometer was used as a stand-alone test facility to investigate electron transport and relevant background production mechanisms in electrostatic spectrometers [144–149]. Important parts of this work were performed in the framework of these extensive pre-spectrometer measurements.

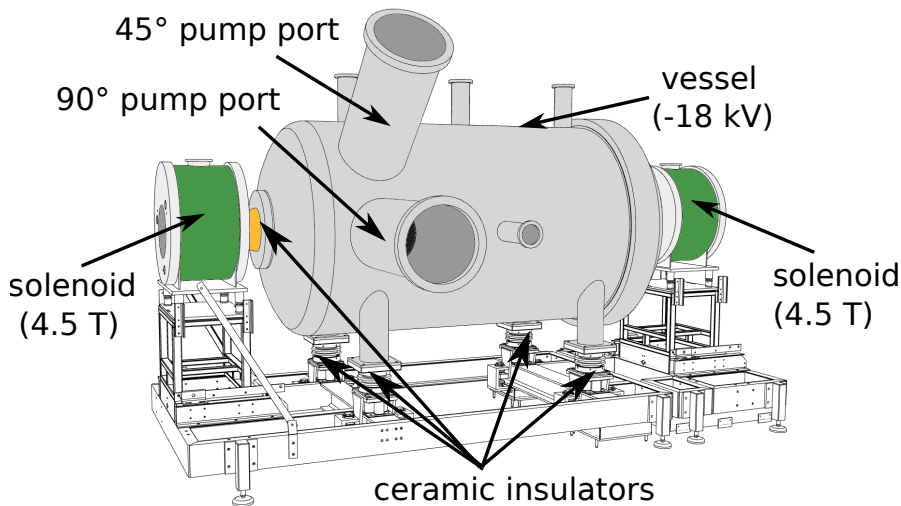


**Figure 2.6:** Pre-spectrometer setup (length 3.4 m, inner diameter 1.7 m, volume 8.5 m<sup>3</sup>). Two superconducting solenoids produce a magnetic guiding field for the signal electrons. The low-energy part of the  $\beta$ -spectrum, which carries no information on the neutrino mass, is filtered out by the electrostatic retarding potential  $U \in [-18.3 \text{ kV}, 0]$ .

### **Main spectrometer**

Electrons which pass the potential barrier of the pre-spectrometer will enter the much larger main spectrometer (length 23.6 m, diameter 10 m, volume 1250 m<sup>3</sup>). There, high-precision energy-filtering takes place which typically will allow only the highest energetic electrons to be transmitted to the detector. The most important contribution to the magnetic guiding field is, on the one hand, created by 4 superconducting solenoids: the two pre-spectrometer solenoids (PS1 and PS2) at the entrance, and a pinch (PCH) and detector (DET) magnet at the exit. On the other hand, a second field shaping element is provided by a large volume air coil system [150, 151], which will be detailed in section 4.3. The pre-spectrometer as well as the main spectrometer are based on a novel concept where the vessel itself is elevated to the retarding high voltage. On the inside, a nearly massless wire electrode system [152–156] is installed to fine-tune the electrostatic field (see section 5) and to further reduce background from the 690 m<sup>2</sup> vessel surface (see section 6). An ultra high vacuum (UHV) of 10<sup>-11</sup> mbar or better is required in order to reduce the probability for ionizing collisions of signal electrons with the residual gas inside the main spectrometer volume. Clearly, signal electrons should not lose even small amounts of kinetic energy due to inelastic scattering while being transmitted through the spectrometer as this would directly influence the measured  $\beta$ -spectrum. Moreover, the time intervals between ionizing collisions of stored electrons has to be maximized so that active background suppression methods can be applied (see sections 7 and 8). To achieve such a low pressure regime inside this very large volume, two different pumping systems are employed [157]: active pumping of non-getterable gas species (such as noble gases) by a system of six cascaded TMPs (Leybold MAG-W-2800), and passive pumping by a very large non-evaporable getter (NEG, SAES St707) pump [158, 159]. While the TMPs have a pumping speed of 10<sup>4</sup>  $\ell$ /s for H<sub>2</sub> and also pump other gas species (albeit at slightly reduced efficiency), the NEG pump is much more powerful with a capacity of 10<sup>6</sup>  $\ell$ /s mainly targeted at H<sub>2</sub>, keeping the partial pressure from outgassing at a small level. A picture of the main spectrometer surrounded by the large volume air coil system is shown in figure 2.7.

### **Monitor spectrometer**

In parallel to the 70 m long main beam line, a second shorter ( $\sim$ 4.5 m) beam line for monitoring purposes forms an integral part of the KATRIN setup. It consists of a solid-state krypton source [160, 161] which emits mono-energetic K-32 conversion electrons into the monitor spectrometer (the former Mainz spectrometer), to be detected by a silicon based PIN-diode array. The central aspect here is the fact that the spectrometer will be fed with the same retarding high voltage as the main spectrometer and thus provides an online-monitoring of the HV stability by continuously recording the 17.8 keV <sup>83m</sup>Kr (K-32) line position [162]. To minimize disturbing magnetic stray fields from one beam line towards the other, the two systems are assembled in two separate buildings located at a distance of about 20 m. Installation of this unit at the KIT site and commissioning took place in 2010-2012 [163, 164]. A picture of the installed system can



**Figure 2.7:** Photograph of the main spectrometer, surrounded by the large volume air coil system (photo: KIT).



**Figure 2.8:** Monitor spectrometer, installed at the KIT site. Two solenoids and 4 air coils (3 visible, 4<sup>th</sup> hidden by the middle one) produce the magnetic guiding field.

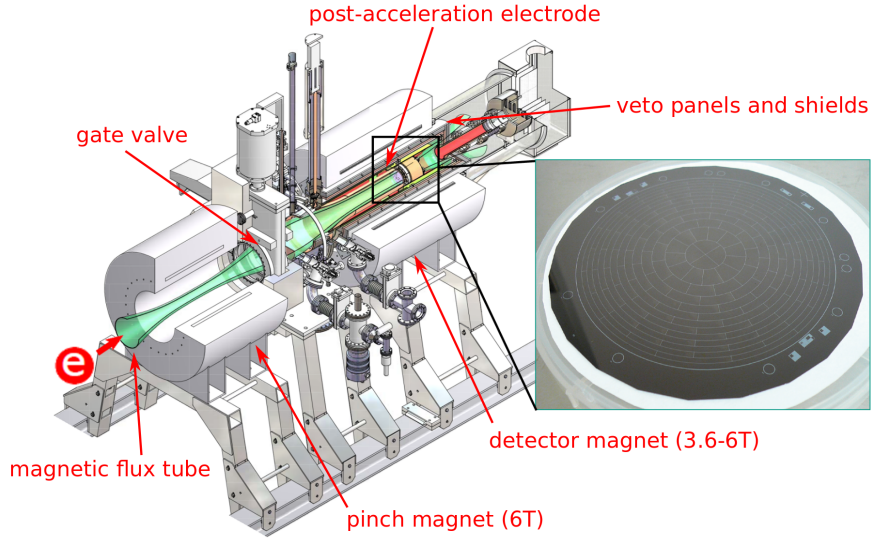


**Figure 2.9:** Focal plane detector system. The silicon PIN-diode detector is located inside the warm bore of the detector magnet, passively and actively shielded from cosmic and  $\gamma$  radiation. The pinch magnet delivers the strongest magnet field in the whole KATRIN setup. A post-acceleration electrode can increase electron energies by up to 10 keV into a region of lower background. The main spectrometer and detector systems can be decoupled by closing the gate valve.

be found in figure 2.8.

### 2.1.5 Focal plane detector

The typically rather small number of electrons, which is transmitted through the main spectrometer, is counted by the focal plane detector (FPD) [165]. The detector is a segmented silicon PIN-diode array with 148 pixels<sup>2</sup>, which is located inside the warm bore of the detector magnet (see figure 2.9). As the expected signal rate is very low ( $10^{-2}$  cps), challenging demands are put on the detection efficiency and the intrinsic detector background rate. A low background of currently<sup>3</sup>  $10^{-3}$  cps/keV has been achieved by careful selection and screening of materials with low intrinsic radioactivity and a combination of passive (lead and copper) and active (muon veto) shielding. Furthermore, a post-acceleration electrode is installed, which can increase the energies of signal electrons by up to 10 keV into a region of lower background. The moderate energy resolution of  $\sim 1.4$  keV for X-rays and  $\sim 1.6$  keV for electrons (both FWHM) is sufficient to discriminate signal electrons from the continuum Compton background. Two calibration sources are integrated into the setup, an  $^{241}\text{Am}$   $\gamma$ -source (using the 60 keV line) and a

<sup>2</sup>146 pixels are working during the on-going commissioning phase, exceeding the design requirement of 141 working pixels.

<sup>3</sup>The notion *per keV* accommodates the fact that the detector has a limited energy resolution, i.e. the signal rate has to be integrated over the energy region-of-interest.

UV-illuminated titanium disc for electrons with kinetic energies of up to 25 keV.

## 2.2 Measurement principle

To determine the absolute neutrino mass scale in the sub-eV region, the electron energy spectrum of tritium  $\beta$ -decay has to be measured close to its endpoint  $E_0$  with extremely high precision. Electrostatic spectrometers, which were pioneered in [1, 123] and currently are refined for high-precision  $\beta$ -spectroscopy, utilize the MAC-E filter principle, which will be detailed in section 2.2.1. The properties of this spectrometer type are typically described by the transmission function (spectrometer only) or response function (spectrometer and tritium source), which is the focus of section 2.2.2.

### 2.2.1 MAC-E filter

The high neutrino mass sensitivity of KATRIN can only be reached by combining a spectrometer with large angular acceptance, low background and high energy resolution with a stable, ultra-luminous tritium source. The energy analysis at the main spectrometer (as well as at the pre- and monitor spectrometer) is based on the MAC-E filter<sup>4</sup> principle, which was first proposed in [166] and further refined in [167, 168]. The main features of a MAC-E filter are illustrated in figure 2.10.

In this setup, superconducting magnets at both ends of the spectrometer create a magnetic guiding field for the signal electrons, which enter from the source side with an acceptance angle of up to  $2\pi$ . Due to the Lorentz force the incoming electrons perform a gyration around the magnetic field lines, so that their kinetic energy is composed of a longitudinal component  $E_{\parallel}$  and a transversal component  $E_{\perp}$  (with respect to the field line direction):

$$E_{\text{kin}} = E_{\parallel} + E_{\perp}. \quad (2.2)$$

The spectrometer vessel and the inner electrode system are elevated on a negative potential (typically close to the endpoint of tritium  $\beta$ -decay at -18.6 kV). Due to the ground potential at the entrance and exit of the spectrometer, an electric field is created with direction parallel to the magnetic field lines. Therefore, electrons are only filtered according to their longitudinal energy  $E_{\parallel}$ . However, as signal electrons are isotropically emitted during  $\beta$ -decay in the source, their transversal energy fraction can be significant. Without appropriate measures, most electrons would not pass the potential barrier despite having sufficient total kinetic energies. The solution is to significantly reduce the magnetic field strength from the value  $B_s$  at the source to a value  $B_{\text{min}}$  at the point of maximal electrostatic potential. As the main spectrometer was designed to transport electrons adiabatically, the first adiabatic invariant

$$\gamma\mu = \frac{\gamma + 1}{2} \cdot \frac{E_{\perp}}{B} \quad (2.3)$$

---

<sup>4</sup>Magnetic Adiabatic Collimation combined with an Electrostatic filter

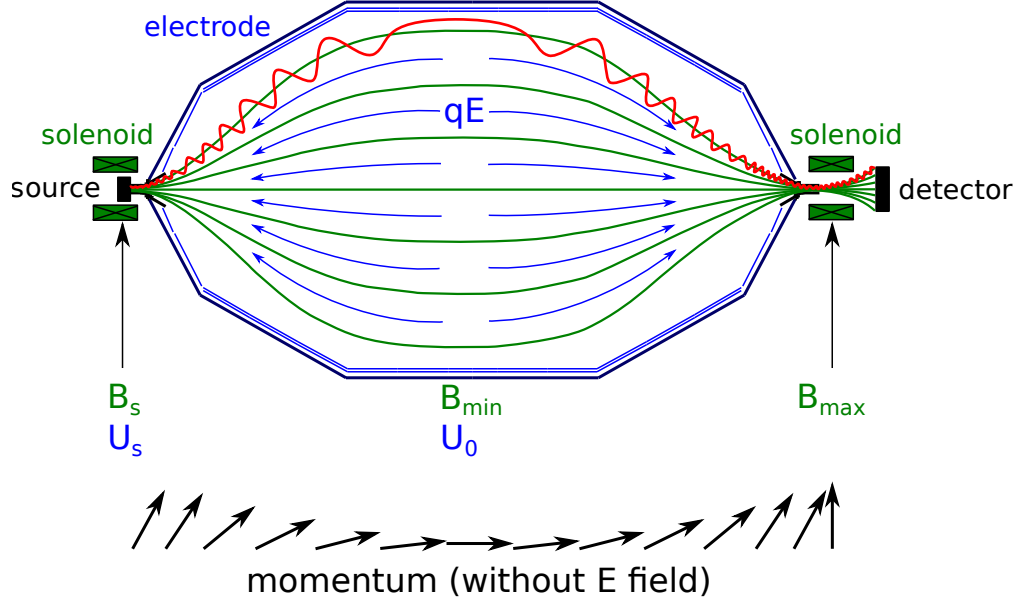


**Figure 2.10:** MAC-E filter principle. Superconducting magnets (green) produce a guiding field, where the magnetic gradient transforms the electron’s (red) transversal momentum into longitudinal momentum (lower part). The electric field (blue) acts on the longitudinal energy  $E_{\parallel}$  only, filtering out those electrons with  $E_{\parallel} < |qU_0|$ .

is approximately constant. Here,  $\gamma$  is the relativistic Lorentz factor and  $\mu$  the orbital magnetic moment of the electron. Following this relation, a reduction of the magnetic field results in an appropriate reduction of the transversal energy component. Due to the conservation of total energy, the longitudinal energy increases likewise. It is important that this transformation is performed in a well-defined way, adjusted to the variation of the electrostatic potential. This important aspect will be investigated in more detail in section 4.2. If the longitudinal energy component of an electron is positive at all times along its trajectory, it will be transmitted to the detector, otherwise it will be reflected back to the source where it is absorbed.

Evidently, the transformation  $E_{\perp} \rightarrow E_{\parallel}$  cannot be perfect (due to  $B_{\min} > 0$ ), so that a certain energy portion (the remaining component  $E_{\perp}$ ) remains “invisible” in the filtering process of the spectrometer and hence defines its energy resolution:

$$\frac{\Delta E}{E} = \frac{B_{\min}}{B_{\max}}. \quad (2.4)$$

For the main spectrometer reference values and an isotropic distribution of signal electrons, the maximal unaccounted energy portion at the  $\beta$ -endpoint energy of 18.6 keV is

$$\Delta E = 18600 \text{ eV} \cdot \frac{3 \cdot 10^{-4} \text{ T}}{6 \text{ T}} = 0.93 \text{ eV}. \quad (2.5)$$

In addition to the process of electrostatic reflection by the potential barrier, also the magnetic field can reflect electrons with large starting polar angles<sup>5</sup>. When traveling towards an increasing magnetic field, the transversal momentum component is increased until full conversion is reached which initiates the subsequent reflection. This is known as *magnetic mirror effect* [169]. KATRIN makes use of this effect to reject those electrons which were emitted with large polar angles in the source. This is advantageous as a large polar angle entails an increased path length inside the source tube, which in turn enhances the probability for scattering off tritium molecules and also maximizes synchrotron losses. Accordingly, these electron trajectories are less favorable for high-precision  $\beta$ -spectroscopy and would contribute significantly to the systematic uncertainty budget. With a source magnetic field strength  $B_s = 3.6$  T and a maximum magnetic field  $B_{\max} = 6$  T, the maximum accepted starting angle can be calculated:

$$\sin \theta_{\max} = \sqrt{\frac{B_s}{B_{\max}}} \rightarrow \theta_{\max} = 50.77^\circ. \quad (2.6)$$

Note that this consideration is only valid in the absence of an electrostatic potential at the positions of source and maximum magnetic field (see section 7.1 for the case with electrostatic potential).

### 2.2.2 Transmission and response function

The selectivity of the spectrometer with regard to kinematic parameters of signal electrons is conveniently described by the *transmission function*  $T$ . When discussing the characteristics of the entire beam line, where source-related effects have to be taken into account, the relevant quantity is the *response function*  $f_{\text{res}}$ .

#### Transmission function

The probability for an electron to be transmitted through a spectrometer depends on its starting kinetic energy and starting polar angle. For a fixed retarding potential  $U_0$ , electrons with rather large starting angles need a specific amount of surplus energy ( $E_{\text{start}} - qU_0$ ,  $q$  being the electron charge) to pass the potential barrier due to the non-perfect transformation  $E_{\perp} \rightarrow E_{\parallel}$ . Fig. 2.11 shows the fraction of transmitted electrons as a function of their surplus energy for an isotropic  $\beta$ -source. Evidently, the transmission probability increases with increasing surplus energy, as electrons with consecutively larger polar angles are being transmitted. For a specific electron energy it reaches unity. For isotropic signal electrons (as shown in figure 2.11), the transmission function can be described analytically by:

$$T(E, qU_0) = \begin{cases} 0 & E - qU_0 < 0 \\ \frac{1 - \sqrt{1 - \frac{E - qU_0}{E} \cdot \frac{B_s}{B_a}}}{1 - \sqrt{1 - \frac{\Delta E}{E} \cdot \frac{B_s}{B_a}}} & 0 \leq E - qU_0 \leq \Delta E \\ 1 & E - qU_0 > \Delta E \end{cases}, \quad (2.7)$$

<sup>5</sup>The polar angle is defined as the angle between the direction of the magnetic field and the momentum.

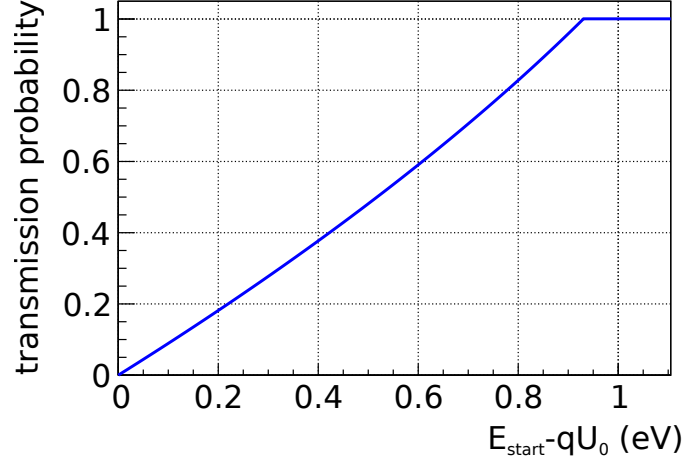


**Figure 2.11:** Normalized transmission function for the main spectrometer reference values:  $B_{\text{min}} = 3 \cdot 10^{-4}$  T,  $B_{\text{max}} = 6$  T,  $U_0 = -18600$  V. For increasing surplus energies  $E_{\text{start}} - qU_0$  consequently larger starting angles are transmitted.

where  $B_s$  denotes the magnetic field at the source position and  $B_a$  the magnetic field at the analyzing point. For a given angular distribution of electrons leaving the source, which approximately is of isotropic nature, the width of the transmission function (corresponding to the energy resolution (2.5) of the spectrometer) and its shape are determined by the relative magnetic field strengths  $B_s/B_a$ . A general derivation of eq. (2.7) can be found in section 4.2.1. It is of major importance for  $\beta$ -spectroscopy that this function has no tails towards lower or higher energies (as usually encountered in detectors such as cryo-bolometers) and only depends on the magnetic field ratios in the experimental setup. However, (2.7) can be distorted by various effects, which will be investigated in section 5 and Appendix .1.

### Response function

The transmission function  $T$  only describes the spectroscopic features of KATRIN in the ideal case where electrons do not lose any amount of energy along their trajectory from the starting point in the source to the analyzing point. However, there is a non-negligible probability for electrons to scatter off tritium molecules in the WGTS due to the rather large column density  $\rho d$  there. The corresponding energy loss is characterized by the normalized energy loss function

$$f(\Delta E) = \frac{1}{\sigma_{\text{tot}}} \cdot \frac{d\sigma}{d\Delta E}, \quad (2.8)$$

where  $\Delta E$  is the electron energy loss and  $\sigma_{\text{tot}}$  the total scattering cross section. Actually, the energy loss function  $d\sigma/d\Delta E$  also depends on the scattering angle. However, for the energy losses relevant for the later neutrino mass analysis ( $\leq 30$  eV), the angular change can be neglected ( $\sim 1^\circ$ ). The response function is obtained by convoluting

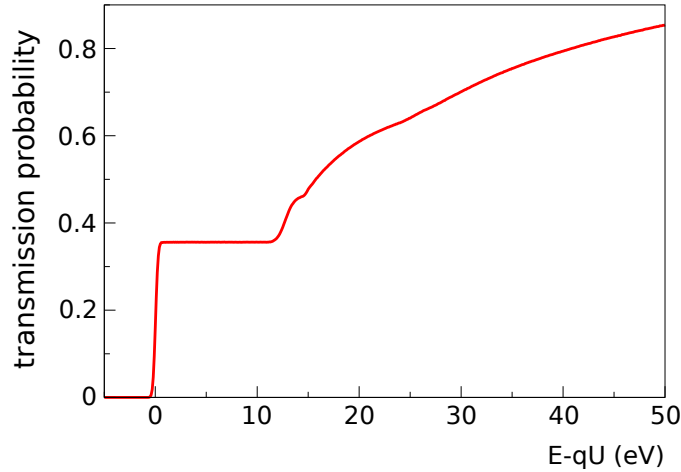


**Figure 2.12:** KATRIN response function for isotropically emitted electrons with fixed energy  $E$  as a function of the surplus energy  $E - qU$  ( $B_s = 3.6$  T,  $B_{\min} = 3 \cdot 10^{-4}$  T, column density  $\rho d = 3 \cdot 10^{17}$  cm $^{-2}$ ). The figure is adapted from [170].

the transmission function  $T$  with the energy loss distribution. When multiple,  $i$ -fold scattering is taken into account (with scattering probability  $P_i$ ), this translates into:

$$\begin{aligned}
 f_{\text{res}}(E, qU) = & T(E, qU) \otimes P_0 & + \\
 & T(E, qU) \otimes P_1 \cdot f(\Delta E) & + \\
 & T(E, qU) \otimes P_2 \cdot [f(\Delta E) \otimes f(\Delta E)] & + \\
 & \dots &
 \end{aligned} \tag{2.9}$$

An example for such a response function ( $B_s = 3.6$  T,  $B_{\min} = 3 \cdot 10^{-4}$  T, column density  $\rho d = 3 \cdot 10^{17}$  cm $^{-2}$ ) is shown in figure 2.12. Between 0 and  $\sim 10$  eV, the shape of the response function is similar to the transmission function because inelastic scattering events imply a minimal energy loss of 10 eV. However, deviations of the spectral shape occur due to changes of the polar angles [171]. The overall fraction of these so called “no loss” electrons is however only  $\sim 0.4$  for typical values of  $\rho d$ . As the retarding potential is decreased (i.e. when moving towards larger values of  $E - qU$ ), the number of transmitted electrons increases because those electrons which have experienced inelastic scatterings and lost kinetic energy are now able to pass the reduced potential barrier of the spectrometer.

The description of the energy loss distribution from literature is not sufficient to compile the response function. Therefore, it has to be determined in a special pre-measurement before the  $T_2$  scanning procedure starts. Here, the fact that the response function strongly depends on the source column density is utilized. The response function has to be determined over the entire cross section of the tritium source. Consequently, radial scanning is required to accommodate larger inhomogeneities of  $\rho d$  in the WGTS as well as radial dependencies of the magnetic field and the electrostatic potential in the spectrometer. Additionally, azimuthal scanning is needed because of  $\rho d$  variations arising

from the beam tube cooling principle [129] and possible distortions due to the magnetic chicanes in the transport section which break the axial symmetry of the experiment.

## 2.3 Sensitivity of the KATRIN experiment

The energy distribution of transmitted signal electrons at the detector is described by a convolution of the response function  $f_{\text{res}}$  with the differential energy spectrum  $dN_{\beta}/dE$ , which describes the number of decays per second, per nucleus and per energy bin. From this an integral spectrum is obtained when measuring at different retarding potentials  $U$ . The number of counts at each retarding potential can be calculated according to

$$N_{\text{theo}}(qU, E_0, m_{\nu}^2) = N_{\text{tot}} \cdot t_U \int_0^{E_0} \frac{dN_{\beta}}{dE}(E_0, m_{\nu}^2) \cdot f_{\text{res}}(E, qU) dE, \quad (2.10)$$

with  $N_{\text{tot}}$  being the total number of tritium nuclei in the source and  $t_U$  denoting the measuring time at a certain potential  $U$ . When additionally taking into account background events  $N_{\text{b}}$ , which are assumed to be Poisson-distributed at a constant and energy-independent rate, eq. (2.10) has to be extended:

$$N_{\text{theo}}(qU, R_{\text{s}}, R_{\text{b}}, E_0, m_{\nu}^2) = R_{\text{s}} \cdot N_{\text{s}}(qU, E_0, m_{\nu}^2) + R_{\text{b}} \cdot N_{\text{b}}, \quad (2.11)$$

where  $R_{\text{s}}$  and  $R_{\text{b}}$  are the relative contributions of signal and background rate. The free parameters  $R_{\text{s}}$ ,  $R_{\text{b}}$ ,  $E_0$  and  $m_{\nu}^2$  can be obtained by minimizing the difference between measured and theoretical count rates at the individual potentials:

$$\chi^2(R_{\text{s}}, R_{\text{b}}, E_0, m_{\nu}^2) = \sum_i \left( \frac{N_{\text{meas}}(qU_i) - N_{\text{theo}}(qU_i, R_{\text{s}}, R_{\text{b}}, E_0, m_{\nu}^2)}{\sigma_{\text{theo}}(U_i)} \right)^2, \quad (2.12)$$

where  $\sigma_{\text{theo}}(U) = \sqrt{N_{\text{s}} + N_{\text{b}}}$  is the theoretically expected statistical fluctuation of the count rate.

### 2.3.1 Statistical uncertainty

The statistical uncertainty of a long-term tritium scanning run can be obtained by simulating KATRIN-like spectra, which incorporate physical processes within the experimental setup as precisely as possible. The minimization (2.12) has to be repeated many times, using simulated spectra  $N_{\text{sim}}$  instead of measured spectra  $N_{\text{meas}}$ , where  $N_{\text{sim}}$  follows a Gaussian distribution  $\sigma_{\text{theo}}(U) = \sqrt{N_{\text{s}} + N_{\text{b}}}$ . The width of the resulting distribution of  $m_{\nu}$  corresponds to the statistical uncertainty.

The reference value of the statistical uncertainty is  $\sigma_{\text{stat}} = 0.018 \text{ eV}^2/c^4$ , which is approximately of the same size as the expected overall systematic uncertainty (see below)<sup>6</sup>. In order to achieve this sensitivity, a measurement time of three “full-beam” years is

---

<sup>6</sup>Natural units will be used for the remainder of this work, i.e.  $c = 1$ .

required. Taking into account regular calibration and maintenance phases, the total runtime will amount to about 5 calendar years.

It is important to notice that the background rate has a strong influence on the statistical uncertainty. A minimization of the statistical uncertainty requires an optimization of the scanning procedure, i.e. it has to be determined how much measurement time ideally has to be spent at each individual retarding potential. A measurement close to the endpoint obviously has the highest sensitivity to the neutrino mass. However, if the background is large, this region could be hidden due to the large fluctuations in the number of background events which is superimposed on the number of signal events. Consequently, measurements further away from the endpoint are required. Due to the decreasing neutrino mass sensitivity further away from  $E_0$ , longer measurement times at each retarding potential are needed in order to reach the same statistical uncertainty [129].

The situation is considerably aggravated if the background is not constant, but shows an energy or time dependence. In case of a constant background rate and an optimized measurement time distribution, the statistical uncertainty scales as  $N_b^{1/6}$ . For any non-Poisson distributed background rate this dependence becomes less favorable. An initial consideration of the impact of non-Poissonian background can be found in [132, 146] and in a more defined context in section 7.5.

### 2.3.2 Systematic uncertainty

Unaccounted systematic effects can significantly limit the experimental sensitivity of KATRIN. These could arise from limitations in the precision and trueness of the theoretical description of the  $\beta$ -spectrum (such as the final state distribution) as well as from KATRIN specific experimental parameters (such as the knowledge of  $\rho d$  or the retarding potential  $U_0$ ). In general, no single systematic effect should exceed a limit of  $\Delta m_\nu^2 = 7.5 \cdot 10^{-3} \text{ eV}^2$  to constrain the total systematic uncertainty budget.

#### Molecular tritium $\beta$ -spectrum

The generic tritium  $\beta$ -spectrum of eq. (1.61) does not include final state effects for the daughter molecule ( $^3\text{HeT}$ )<sup>+</sup> such as:

- *molecular recoil*: The finite mass of the T<sub>2</sub> molecule implies a recoil energy  $E_{\text{rec}} \approx 1.7 \text{ eV}$ , which is almost independent of the energy of the emitted electron within the narrow region-of-interest  $[E_0 - 30 \text{ eV}, E_0 + 5 \text{ eV}]$ . This effect can be accounted for with high precision in the spectrum analysis.
- *final state distribution*: As the electron actually initially recoils from a single tritium atom, the overall recoil energy of  $\sim 3.4 \text{ eV}$  is split: about half of this value, 1.7 eV, is used for the recoiling motion of the tritium molecule, while the remaining energy is converted into rotational-vibrational (rovib) motion of the daughter molecule. Actually, many different rovib states can be excited, forming a distribution of final states with a mean at 1.7 eV and a width of  $\sim 0.4 \text{ eV}$ . Further into the

electron  $\beta$ -spectrum ( $>20$  eV below the endpoint), also electronic excitation of the daughter ion has to be taken into account. The complete final state distribution can be calculated very precisely [172, 173] and therefore is taken into account in the analysis [128, 129, 174]. Furthermore, radiative corrections from real and virtual photons are rather small, but are taken into account for a most precise description of the spectral shape [129].

To account for the individual final states of the daughter molecules of energy  $V_j$ , eq. (1.61) has to be rewritten into a sum of  $\beta$ -spectra with endpoint energies  $\epsilon_j = E_0 - V_j$ , weighted with their probability  $W_j$ :

$$\frac{dN}{dE} = C \cdot F(Z, E) \cdot p(E + m_e c^2) \cdot \sum_j W_j \cdot (\epsilon_j - E) \cdot \sqrt{(\epsilon_j - E)^2 - m_\nu^2} \cdot \Theta(\epsilon_j - E - m_\nu). \quad (2.13)$$

When all above mentioned effects are included in the spectral analysis, their contribution to the systematical uncertainty of  $\Delta m_\nu^2 < 6 \cdot 10^{-3} \text{ eV}^2$  is below the required limit.

### Experimental parameters

The complexity of the KATRIN experimental setup implies a variety of key experimental parameters, which have to be known very precisely. They can be determined either by simulations, thereby making use of detailed models, or by dedicated test measurements. The precision and trueness associated with these parameters is directly linked to systematic uncertainties. In the following, a short overview of the important experimental parameters, influencing the KATRIN response function  $f_{\text{res}}(E, qU)$ , will be given.

First, an accurate knowledge of the scattering probabilities  $P_i$  of electrons off hydrogen isotopologues is required to describe the response function. These parameters are influenced by the source column density  $\rho d$  and the electron path length in the source. The former depends on various parameters such as the source temperature, the gas injection rate and the pump-out rate at the WGTS tube ends. It has to be measured regularly to keep the systematic effect below the allowed limit. The envisaged procedures would result in a contribution to the systematic uncertainty of  $\Delta m_\nu^2 < 1.5 \cdot 10^{-3} \text{ eV}^2$ . The electron path length in the source depends on the starting polar angle, where the maximal accepted starting angle is set by the ratio of the magnetic field strength in the WGTS compared to the maximal magnetic field strength at the pinch magnet. Consequently, any changes of the source magnetic field (or the pinch field) will lead to variations in the average electron track length. However, as the magnetic field is supposedly stable on the  $10^{-4}$  level within a period of 3 months, this effect can be neglected.

Inelastic scattering of signal electrons off tritium molecules results in a significant number of electron-ion pairs ( $\sim 10^6 \text{ cm}^{-3}$ ). Accordingly, a space charge potential could build up locally, resulting in small-scale variations of the source potential or time-dependent variations of the potential difference between the position of electron creation and analysis by the MAC-E filter, which shifts the position of the transmission function. If the potential variations can be constrained to a level of about 10 mV, this would lead to a systematic shift  $\Delta m_\nu^2 = 2 \cdot 10^{-4} \text{ eV}^2$ , which is well below the required limit.

The process of elastic  $e^-$ -T<sub>2</sub> scattering results in very small energy losses ( $\langle E_{\text{loss}} \rangle = 16$  meV) and small angular changes ( $\langle \Delta\theta \rangle = 3^\circ$ ) of the signal electrons. The influence of this effect on the response function can largely be neglected. Even if this effect would be completely unaccounted, the resulting systematic uncertainty is  $\Delta m_\nu^2 = 0.005$  eV<sup>2</sup>, which is well below the design limit.

Another source for systematic uncertainties is the Doppler effect, caused by the thermal and bulk motion of the tritium molecules. The electron energies are shifted by typical values  $\Delta E = 100$  meV for the WGTS reference temperature of 27 K. The precise Doppler shifts can be computed for a given thermal velocity distribution of the molecules, bulk gas flow and molecular composition [128].

Finally, a variation of the absolute value of the retarding high voltage of the main spectrometer results in a shift of the position of the transmission function. The corresponding change of the absolute energy scale has a systematic effect on  $m_\nu$ . A maximal systematic uncertainty of  $\Delta m_\nu^2 = 7.5 \cdot 10^{-3}$  eV<sup>2</sup> implies a maximal Gaussian variation of the high voltage of 60 mV, corresponding to a relative stabilization of the HV scale of 3 ppm at  $U_0 = -20000$  V.

### 2.3.3 KATRIN sensitivity

None of the individual sources for systematic uncertainties, which were considered above, is expected to exceed the design limit of  $\Delta m_\nu^2 = 7.5 \cdot 10^{-3}$  eV<sup>2</sup>. When adding all systematic uncertainties (a complete list can be found in [82]) quadratically<sup>7</sup> a total systematic uncertainty budget of  $\sigma_{\text{sys,tot}} \approx 0.01$  eV<sup>2</sup> results. Therefore, a conservative limit of

$$\sigma_{\text{sys,tot}} \leq 0.017 \text{ eV}^2 \quad (2.14)$$

seems achievable.

The measurement time of KATRIN was chosen in a way that the statistical uncertainty is of the same size as the systematic uncertainty:

$$\sigma_{\text{stat,tot}} \leq 0.018 \text{ eV}^2. \quad (2.15)$$

Adding the statistical and systematic uncertainties quadratically yields the total error budget

$$\sigma_{\text{tot}} \approx 0.025 \text{ eV}^2. \quad (2.16)$$

After three full-beam years the resulting neutrino mass sensitivity is

$$m_{\bar{\nu}_e} = 200 \text{ meV} \quad (90\% \text{C.L.}). \quad (2.17)$$

A neutrino mass  $m_{\bar{\nu}_e} = 350$  meV could accordingly be observed with a significance of  $5\sigma$ . This unprecedented level of precision in  $\beta$ -spectroscopy also allows to search for light sterile neutrinos [175], right-handed currents [176] or violations of Lorentz invariance [177, 178].

<sup>7</sup>The systematic effects are uncorrelated.

## 2.4 Background processes in a MAC-E filter

As outlined above, the background rate and characteristics strongly influence the neutrino mass sensitivity. There are various sources of background in a spectrometer of the MAC-E filter type, which will be reviewed in section 2.4.1. In the course of this work, a detailed background model was developed, which was used to show that the resulting background would exceed the design limit if no appropriate counter measures are taken [132, 146]. Section 2.4.2 will then give a short overview of the different methods to reduce background in a MAC-E filter.

### 2.4.1 Background sources

There are three main sources of background which previously have been identified in electrostatic spectrometers: Penning traps, magnetically stored particles and cosmic ray-induced emission of secondary electrons from surfaces. The latter two cases have been investigated in detail in the course of this work.

#### Penning traps

A Penning trap is created by an interplay of a magnetic and an electrostatic field, as shown in figure 2.13 (left). In this type of trap, electrons are locally confined in axial direction by potential wells, as well as in radial direction by the magnetic field enforcing a cyclotron motion of the electron. Depending on the depth<sup>8</sup> of the trap, a single stored electron, with kinetic energy below the depth of the trap, can produce many background events over a large volume via messenger particles (ions or photons). A detailed description of the background mechanism can be found in [146, 180]. Very small volumes on the order of  $\text{cm}^3$  suffice to produce background rates in the range of  $10^3$  cps.

In this context it is important to note that a large volume Penning trap is created between the pre-spectrometer and the main spectrometer in case both of them are operated at a large negative potential. In this configuration, electrons created near the ground

<sup>8</sup>The 'depth' denotes the maximal potential difference within the trap.

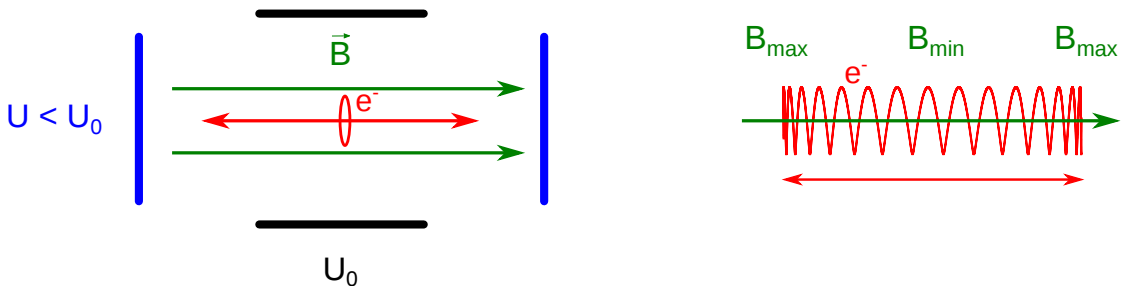


**Figure 2.13:** The electromagnetic configuration of a MAC-E filter can give rise to particle traps. Left: Penning trap created by a combination of electric and magnetic fields. Right: Magnetic mirror trap due to a magnetic field gradient. The figure is adapted from [179].

electrodes close to the position of the second pre-spectrometer solenoid can get trapped, so that they can undergo inelastic scattering interactions on the residual gas molecules. The positive ions from these ionizing collisions are able to leave the trap towards the main spectrometer where they can further ionize residual gas. It is those tertiary electrons which actually do contribute to the background. Inside the trap, the number of trapped electrons increases in an avalanche-like manner, keeping the trap filled. This trap can be avoided by operating the pre-spectrometer at (or close to) ground potential. Corresponding simulations have shown that this configuration without pre-filtering does not have a negative influence on the signal electron propagation [181] and that the background due to a  $10^7$ -fold increase of the number of signal electrons entering the main spectrometer is much smaller than the background produced by the large-volume Penning trap [146].

### Magnetically stored particles

A second Penning-type background source is formed by magnetically stored particles. If charged particles are created in the volume of a spectrometer, they can get trapped due to the *magnetic mirror effect* [169]. When flying towards the increasing magnetic field at the entrance and exit region of the spectrometer, the longitudinal momentum of an electron will be transformed into transversal momentum (see figure 2.13 right). If its longitudinal momentum vanishes, the electron is reflected back into the spectrometer. There are several sources known to create electrons in the spectrometer volume:

- *Radon decay*: The radon isotopes  $^{219}\text{Rn}$ ,  $^{220}\text{Rn}$ , and  $^{222}\text{Rn}$  are neutral noble gas atoms which can propagate with thermal velocities in the spectrometer and which can emit electrons when undergoing nuclear  $\alpha$ -decay. The NEG material, which is used for pumping the spectrometers, and other structural materials are potential sources for radon emanation. A detailed investigation of this important background component is performed in section 7 and in [145, 146].
- *Tritium decay*: The tritium gas flow out of the gaseous source is suppressed by 14 orders of magnitude by the tritium retention systems. The remaining tritium (largely in the form of HT molecules) which enters the main spectrometer will predominantly be pumped out by the non-evaporable getter (NEG) pump. However, a small fraction will  $\beta$ -decay and release electrons with energies up to 18.6 keV. This background component was investigated initially in [146] and also needs to be taken into account in refined form for the final considerations in section 7.5.
- *Positive ions*: As outlined above, there are known sources for positive ions in a MAC-E filter. When these ions scatter off residual gas molecules, electrons can be produced via ionization, which then contribute to the background.

### Electron emission from surfaces

The huge surfaces of the main spectrometer vessel ( $690\text{ m}^2$ ) and its inner electrode system ( $460\text{ m}^2$ ) are potential areas of electron emission and thus of relevance for background

investigations. Two processes can lead to the emission of electrons on these surfaces:

- *secondary emission*: Cosmic muons, high-energy  $\gamma$ 's from natural radioactivity (both created outside of the spectrometer) or  $\gamma$ 's from near-surface radioactivity (inside the spectrometer) can interact with the stainless steel of the spectrometer vessel and create secondary electrons. If the interaction occurs close to the inner surface, these secondary electrons have a large probability to enter the spectrometer volume.
- *field emission*: Remaining sharp edges at the inner electrode system or surface irregularities at the spectrometer vessel after electro-polishing are capable to create high electric field strengths within a narrow region. This in turn can lead to the process of field emission, where electrons leave the metal surface via the tunnel effect.

In both cases, these electrons are created at the surface of the main spectrometer and thus do not contribute to the spectrometer background *ab initio*, as the 191 Tcm<sup>2</sup> magnetic flux tube which is transported to the detector keeps a certain geometrical distance to the spectrometer surface and inner wires. There are two effects which suppress a possible radial motion of electrons into the sensitive volume, namely *magnetic shielding*, which is the dominant effect, and *electrostatic shielding*, which adds to the former effect (for details, see section 6.1). Even the combined magnetostatic and electrostatic shielding is not perfect, as there are known disturbances to these shielding mechanisms [182], which enable a radial electron drift. The background production mechanism and a possible resulting contribution to the overall main spectrometer background is investigated in detail in section 6.

### 2.4.2 Background reduction

Although there is a variety of background sources present within a MAC-E filter, their contribution to the overall background can be largely suppressed by appropriate countermeasures.

- *Small volume Penning traps*: Careful design considerations of the electromagnetic layout of the main spectrometer can avoid the occurrence of harmful Penning traps. The corresponding design of electrode and magnet components was carried out taking into account all the experiences from the pre-spectrometer test experiments as well as from the former Mainz experiment [146, 183]. Therefore, it can be expected that Penning traps are minimized to a level so that they are of no major concern for the background.
- *Large volume Penning trap between spectrometers*: This trap can be completely avoided when operating the pre-spectrometer at zero retarding potential. However, if the operation at a certain potential would be required for specific test measurements, such as to measure tritium migration from the CPS in an in-situ way [184], a so called wire scanner can be put into operation. It consists of a metal wire

which frequently is swept through the trap volume, collecting the stored electrons and hence emptying the trap [185].

- *Electrons from surfaces:* As already mentioned, the inherent magnetic shielding of a MAC-E filter and the sub-dominant additional electric shielding are vital elements to suppress this background component by several orders of magnitude.
- *Stored electrons:* A previously disregarded background component was identified in the framework of recent experiments at the pre-spectrometer [145, 146]. It results from stored electrons following nuclear  $\alpha$ - and  $\beta$ -decays in the spectrometer volume. The inherent background suppression by electric and magnetic shielding is not effective in this case as the decay processes of neutral atoms or molecules create electrons directly within the flux tube. Therefore, additional passive and active background reduction techniques are required. A passive background reduction suppressing radon emanation from the NEG material has been achieved by the installation of LN<sub>2</sub> cooled baffles in front of the getter pumps of the pre-spectrometer, which are the major radon source [149]. Radon emanation from structural materials cannot be suppressed by this method but the pumping speed for the noble gas Rn could be increased. However, source-related tritium is unaffected by this method. For these reasons, three active background reduction techniques are under investigation: the electric dipole method, which was already used at previous experiments and whose efficiency for the main spectrometer was investigated within this work (see section. 8.2); the magnetic pulse method, which was first proposed in [186] and investigated in more detail in [180] and in this work (see section 8.3); and finally the electron cyclotron resonance, a novel method proposed and investigated in [146].

When employing both active as well as passive methods the main spectrometer background is expected to be suppressed below the required limit of  $10^{-2}$  cps.



## Simulation software

An experiment as versatile and demanding as the KATRIN experiment requires a simulation software which describes its very details most precisely. The measurement principle of high-resolution  $\beta$ -spectroscopy via a MAC-E filter requires an extremely precise calculation of the electromagnetic fields influencing the electron motion within the whole setup. Appropriate stand-alone program packages were originally developed by F. Glück. These were combined in the powerful simulation software KASSIOPEIA [187], with notable contributions, among many, by D. Furse [188] and S. Mertens [146]. KASSIOPEIA has been integrated with other simulation and analysis tools within the global KATRIN simulation and analysis framework KASPER [189]. The various applications which KASPER and especially KASSIOPEIA can be used for are motivated in section 3.1. Section 3.2 describes the most important parts of KASSIOPEIA, focusing especially on the additions which have been made within this work. The development of appropriate field calculation methods for KATRIN has been a major effort, which will be addressed in section 3.3. Finally, section 3.4 will give an overview of the optimization and analysis tools using KASPER, which have been developed in the course of this thesis.

### 3.1 Objectives of the simulation software

The KASPER program package allows to investigate a variety of key experimental parameters. In the following, an overview of the objectives, which are of importance for this thesis, will be given.

**Electromagnetic optimization:** An essential prerequisite for a successful neutrino mass determination is a carefully selected electromagnetic setup, which ensures a precise analysis of the electron energy. Several important and also challenging design criteria, such as the transmission condition (discussed in section 4), have to be fulfilled. The electromagnetic design, especially of the main spectrometer, can be optimized using the various electric and magnetic field calculation methods, which are integrated into KASSIOPEIA and KEMFIELD [190, 191].

**Transmission investigations:** As discussed in section 2.2.2, the probability for transmission of an electron strongly depends on its starting energy and angular distribution. Furthermore, the electric and magnetic fields at the starting position and at the analyzing point have to be known precisely in order to determine the transmission function (2.7). These parameters have to be derived through a combination of test measurements and field calculations, as discussed in detail in section 5. In addition, electrons moving through the KATRIN experimental setup can experience a variety of secondary energy-loss effects, such as synchrotron radiation or scattering. As their impact on the transmission function cannot be neglected, Monte-Carlo simulations allow to study in detail the influences of the individual as well as the combined effects. Only by these means the necessary detail of understanding of the transmission properties of the KATRIN experiment can be achieved.

**Background investigations:** Due to the extremely low signal count rates close to the tritium endpoint, a comparably low background rate is a key requirement for a successful neutrino mass determination. Previous MAC-E filter setups revealed a variety of background sources, which are described in section 2.4.1. A detailed understanding of the background production mechanisms is essential in order to reach the design limit of  $< 10^{-2}$  cps. Monte-Carlo simulations using various background models, which were implemented into the simulation software, are an adequate tool to gain the required comprehension. Of equal importance is the ability to develop and improve appropriate background reduction techniques with the help of simulations. The corresponding background sources and mechanisms are described in sections 6 and 7, while active background reduction techniques are investigated in section 8.

**Statistical and systematic analysis:** The overall goal of the investigations carried out within this thesis is to contribute to a full characterization of the properties of the electromagnetic spectrometers and to a better understanding and active suppression of background processes therein. This is of vital importance for the future neutrino mass measurements and to make sure that KATRIN will reach or even exceed its design sensitivity of  $0.2 \text{ eV}/c^2$ . Taken together with other works which have been focused on implementing a detailed tritium source model [128, 129, 174], the current thesis has been instrumental to reach the current state-of-the-art, where the simulation of actual neutrino mass measurements is possible. In this context, the fitting routines within KASPER allow a detailed determination of the influences of the various systematic effects on the integrated tritium  $\beta$ -spectrum and thus the neutrino mass sensitivity of KATRIN. In line with this, extensive sensitivity studies concerning the transmission properties of the main spectrometer are carried out in section 5.4, while the influence of various background contributions is discussed in sections 6.6 and 7.5.

## 3.2 The Kassiopeia package

A detailed description of the structure and functional design of the KASSIOPEIA package is given in [146]. The focus of this work is related to implement physical modules to KASSIOPEIA, including the generation and tracking of particles (sections 3.2.1 and 3.2.2).

For these reasons, the principles of particle tracking in electromagnetic fields is discussed. Furthermore, secondary processes such as scattering and synchrotron emission are investigated in section 3.2.3).

### 3.2.1 Particle generation

The code package Kassiopeia Particle Generator (KPaGe) [174] is responsible to generate the initial state of a particle, which is completely described by the following 8 parameters: position, energy, direction, time. Instead of choosing energy and direction, also the parameters of momentum could be used. However, the default set of energy and direction appears to be more appropriate for discussing particle motion in a MAC-E filter. KPaGe is managed in a modular way, i.e. a stand-alone *creator* exists for each of these properties. The user can combine arbitrary creators to accommodate best the specific problem to be tackled. The following list summarizes the different *creators* which are essential for this work:

- Position creators:
  - *Fix*: A fixed starting position can be chosen, which is mostly used for testing purposes.
  - *Disk*: In this case, a homogeneous distribution on a disk allows to start electrons at a well-defined  $z$ -position over the entire flux tube, or parts thereof (e.g. in the entrance magnet PS1 of the spectrometer). This allows to focus on specific parts of the experiment, so that electrons do not have to be tracked from the source through the source and transport section, which saves computation time.
  - *Surface*: Also, a homogeneous distribution can be achieved on any surface, which is defined in the geometry formats inherent to KASSIOPEIA. This creator allows to investigate secondary electron motion starting from the spectrometer vessel surface.
  - *Volume*: A homogeneous starting point distribution within any volume defined in the geometry formats inherent to KASSIOPEIA can be chosen, which e.g. allows to investigate stored electron motion.
  
- Direction creators:
  - *Fix*: In this case, a fixed starting angle is set, which is mostly used for testing purposes.
  - *Gauss*: Here, a gaussian angular distribution is diced as an approximation for the emission characteristics of an angular resolved electron gun.
  - *Isotropic*: An isotropic angular distribution is appropriate for electrons created in nuclear decays (tritium, radon, krypton).

- *Surface*: The angular distribution for particles starting from a surface (isotropic around surface normal vector) has to be combined with the above-defined position creator *surface*.
- Energy creators:
  - *Fix*: A fixed starting energy is useful for testing and adiabaticity studies.
  - *Equal*: Equally distributed energies between a user-defined lower and upper boundary are used to investigate energy-dependent storage probabilities within MAC-E filters.
  - *Gauss*: A gaussian energy distribution can serve as an approximation for the emission characteristics of a quasi-mono-energetic electron gun.
  - *Tritium, Krypton, Radon*: Here, electron energies are diced according to specific decay spectra. In the case of tritium, the spectrum is continuous while a line spectrum is used in the case of Krypton; Radon is a special case because it has a continuous as well as a discrete component (more details in section 7.2).

The starting time is typically chosen to be zero for any event. Nevertheless, an arbitrary starting time distribution can be added during the analysis of the simulation output. Consequently, the same simulation results can be adjusted to various start time distributions, which saves a lot of computation time since the same Monte-Carlo data can be re-used for different analyses. The majority of the above described creators have been developed in the course of this thesis, owing to the variety of problems investigated here.

### 3.2.2 Particle tracking

Once the initial states of particles have been created with the help of KPaGe, their path through the experimental setup, along a magnetic field line through regions of different electrostatic and magnetostatic fields, has to be calculated. In doing so, the particle tracking routine propagates the particles in small steps using either the *exact calculation method* or the *adiabatic approximation method*, as illustrated in figure 3.1.

**Exact calculation method:** The motion of a particle with charge  $q$  in electric and magnetic fields,  $\vec{E}$  and  $\vec{B}$ , is fully described by the classical Lorentz equation

$$\vec{F}_L = q(\vec{E} + \vec{v} \times \vec{B}), \quad (3.1)$$

with  $\vec{F}_L$  being the Lorentz force and  $v$  the velocity of the particle. The method most frequently applied to solve this equation is based on an 8<sup>th</sup> order Runge-Kutta algorithm (RK8) [192]. However, in our case further methods have been implemented:

- Embedded Runge-Kutta [193–195]: Here, solvers of different orders are combined ( $4^{th}/5^{th}$ ,  $5^{th}/6^{th}$ ,  $6^{th}/8^{th}$ ,  $7^{th}/8^{th}$ ) which enables an internal error estimation and step size control,

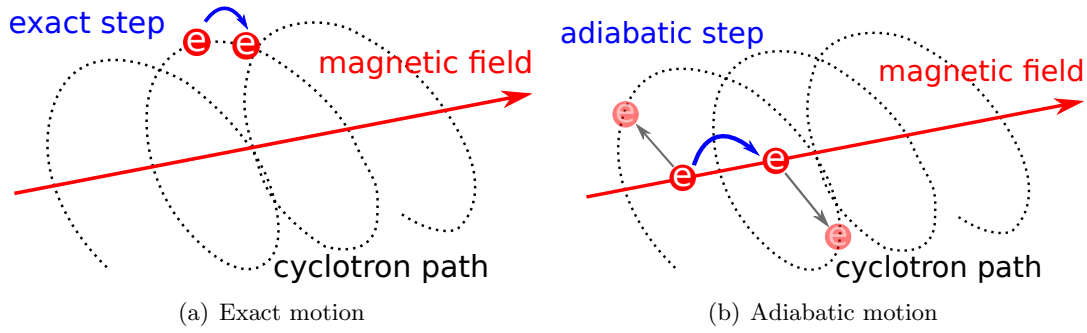


**Figure 3.1:** Illustration of the two generic particle tracking methods. (a) Exact particle motion, achieved by solving the Lorentz equation. (b) A fully adiabatic particle motion requires the propagation of the guiding center along the magnetic field line only, including the possibility to add gyration.

- Predictor-Corrector [196, 197]: By making use of the Adams-Bashforth-Moulton scheme, the first step to be carried out is the predictor (Adams-Bashforth part), which uses the information of the previous steps to determine a first guess for the following step. Within the corrector step (Adams-Moulton part), the initial guess is improved and the difference between predicted and corrected values can be used as an internal error estimation and step size control.

As the RK8 algorithm can only solve first order ordinary differential equations (ODE), eq. (3.1) has to be reformulated to

$$\begin{aligned}\dot{\vec{x}} &= \vec{v}, \\ \dot{\vec{p}} &= \vec{F}_L,\end{aligned}\tag{3.2}$$

where  $\vec{v}$  and  $\vec{p}$  are connected by the relativistic momentum equation

$$\vec{p} = \frac{m_0 \vec{v}}{\sqrt{1 - v^2/c^2}}.\tag{3.3}$$

**Adiabatic approximation method:** The adiabatic motion of a charged particle can be decoupled into two orthogonal terms:

- a motion along a magnetic field line, due to the longitudinal velocity component  $v_{||}$ , and
- a cyclotron motion around the guiding center on the magnetic field line, due to the transversal velocity component  $v_{\perp}$ .

The guiding center is defined by the coordinates  $\vec{x}_{GC}$  on the corresponding field line, with the unit vector  $\hat{B}$  pointing in the direction of the field line. Within the adiabatic

approximation method, only the longitudinal guiding center motion has to be calculated. The following equations are solved using the ODE solvers described above:

$$\begin{aligned}\dot{\vec{x}}_{\text{GC}} &= \hat{B} \cdot v_{\parallel}, \\ \dot{p}_{\parallel} &= -\frac{\mu}{\gamma} \left( \nabla |\vec{B}| \right) + q\vec{E} \cdot \hat{B},\end{aligned}\tag{3.4}$$

with  $\mu$  being the orbital magnetic moment, which is a constant within the adiabatic approximation. If requested, the cyclotron motion can be calculated separately by the magnetic field strength at the particle position. This gyration is then added to the guiding center motion (see figure 3.1). Furthermore, there is the possibility to enable the  $\vec{E} \times \vec{B}$  (eq. 6.2) and  $\nabla \vec{B} \times \vec{B}$  (eq. 6.3) drift components, which result in an azimuthal and/or radial particle motion in case that the field directions of  $\vec{E}$  and  $\vec{B}$  are not parallel or if the particle moves within a non-uniform magnetic field. When adding cyclotron and drift motion, the resulting particle trajectory is equivalent to the result of the *exact calculation method*.

The distinct advantage of the *adiabatic approximation method* is the fact that large step sizes can be used while sustaining the same accuracy. However, as will be outlined in section 4, the motion of electrons in the KATRIN experimental setup is not necessarily adiabatic in specific field configurations. This in turn renders the adiabatic approximation invalid for such cases.

**Step size controls:** The accuracy in calculating the particle motion strongly depends on the step size. In this context, each step requires 13 evaluations of the electric and magnetic fields, which is the most time-consuming part of the calculation. Accordingly, a compromise between accuracy and speed has to be found.

The accuracy of a step is generally defined by the degree to which the conservation of total energy is maintained numerically. As this issue is of major concern and interest for KATRIN, various step size options have been implemented in KASSIOPEIA:

- *fix*: A fixed step size is mostly used for testing purposes.
- *energy*: Here, lower and upper bounds for the degree of conservation of total energy can be defined.
- *cyclotron*: In regions with steep gradients of the magnetic field of the KATRIN setup, a step size control according to the size of the cyclotron period  $T$

$$T = \frac{2\pi}{\omega} = 2\pi \cdot \frac{\gamma m_0}{qB}\tag{3.5}$$

is most useful. By choosing the number of steps in which one cyclotron period should be divided into, this method automatically adjusts the step size along the particle's path.

- *scattering*: If electron scattering off residual gas (section 3.2.3) is activated, this step size control can be used to ensure that the scattering probability within one step is less than unity.
- *synchrotron*: If emission of synchrotron radiation (section 3.2.3) is activated, this step size control can be used to restrict the maximum synchrotron energy loss per step to a preset value.
- *numerical*: Within this step size control, the numerical error on the position and longitudinal momentum of the particle is used to restrict the step size.

It is also possible to activate several step size controls simultaneously. In this case, the smallest suggested step size is applied to the calculation. After a single step was carried out, the step control unit checks if any of the user-defined accuracy limits was exceeded. If this was the case, the step is repeated with a smaller step size.

**Track terminators:** A particle trajectory calculation should be terminated if one or any combination of the following implemented track terminator conditions set in:

- *max path length*: A track is terminated after a pre-defined maximal path length. This terminator is mostly used for testing purposes.
- *max elapsed time*: Here, a track is stopped after a pre-defined time-of-flight, which is especially useful for investigations where long particle storage times are expected.
- *z position*: This terminates when a track propagates beyond a pre-defined  $z_{\min}/z_{\max}$  limit.
- *geometry hit/field validation*: A track is ended when reaching too close (i.e. distance smaller than the pre-defined limit) to any user-defined geometry (e.g. vessel surface). This is of interest mostly for storage investigations.
- *instant death*: This terminates a track which enters a pre-defined region. This option has been implemented to describe particle absorption by mechanical barriers (e.g. wire scanner [180], static pin [198]).
- *magnetron*: A track is terminated after performing  $n$  full magnetron motions, where  $n$  has to be defined by the user. This terminator is used for investigations concerning active removal of stored particles by the electric dipole method or the magnetic pulse method (section 8.2).
- *min energy*: Here, a trajectory is stopped if the energy of the tracked particle falls below a pre-defined limit. This terminator is especially useful for investigation of stored electrons whose kinetic energy fell below the ionization threshold, as further cool down proceeds very slowly. Hence, this option allows to save much computation time.

- *trapped*: A track is terminated after  $n$  axial turns, where  $n$  has to be defined by the user. It is mostly used to determine particle storage probabilities with minimal computational effort.
- *drift ratio*: This option terminates a track if the ratio of azimuthal to radial drift velocity ( $v_{\text{azi}}/v_{\text{radi}}$ ) is larger than the pre-defined limit. This allows to investigate particle motion from the vessel surface into the flux tube as the probability for radial particle motion decreases with increasing  $v_{\text{azi}}/v_{\text{radi}}$  (for details see section 6).

#### 3.2.3 Secondary processes

The motion of a particle is influenced not only by the field values along the particle trajectory, but also by secondary processes such as synchrotron radiation or scattering off residual gas molecules. Both these processes can substantially change the properties of the particle, so that they have to be taken into account.

**Scattering:** The scattering routines, which are implemented into KASSIOPEIA, describe the elastic, excitation and ionization processes accompanying the interaction of electrons with  $H_2$  molecules, which is the dominant gas species within the KATRIN main spectrometer. The corresponding cross sections [199–203], energy loss values [204, 205] and scattering angles allow to precisely investigate the impact of  $H_2$  as dominant gas species on the electron tracks. However, scattering cross sections and energy losses vary significantly for different gas species. Correspondingly, primary electrons with identical start parameters will experience different storage times and thus generate different numbers of secondary electrons. Initial mass spectrometry measurements [145] showed that the residual gas inside the pre-spectrometer mainly consists of hydrogen with smaller contributions from water and nitrogen, while argon was used within specific test measurements to increase the pressure to a desired value. When studying electron cooling by scattering off residual gas, the ionization process is the dominant energy loss mechanism. It contributes to  $> 80\%$  of the total energy loss for electrons above 1 keV when scattering off hydrogen takes place. Hence, molecule-specific ionization cross sections and energy losses are used within the simulation (water, nitrogen [206], argon [207]). In the case of elastic or excitation processes, energy losses are computed using molecular hydrogen input data, which is a sufficient approximation. To reflect an actual measurement in the simulation, arbitrary residual gas compositions consisting of hydrogen, water, nitrogen or argon can be defined via specific configuration files. The fact that electron cooling strongly depends on the residual gas pressure and composition has been used to gain insight into background processes by comparing corresponding measurements and simulations (see section 7).

When investigating storage conditions in the main spectrometer, electron cool-down to extremely low energies of 1 eV has to be followed by the simulations, as this value corresponds to the trapping threshold. Therefore, low-energy interactions such as rotational and vibrational excitations of residual gas molecules become important. The corresponding calculation routines have been adapted from the original code of F. Glück to fit into

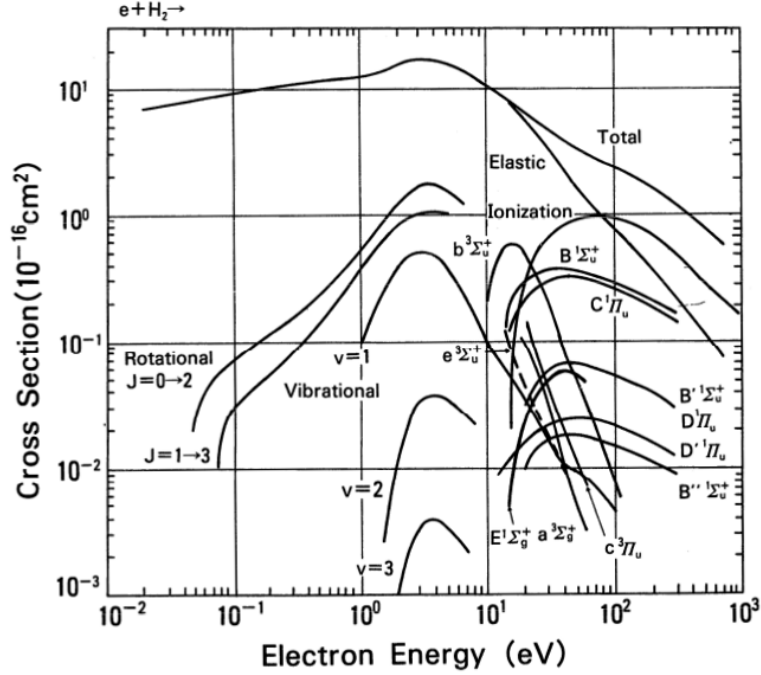


**Figure 3.2:** Overview of electron-hydrogen scattering cross sections. Figure taken from [199].

the KASSIOPEIA framework. Additionally, if electrons cool down to thermal energies (which happens in specific electromagnetic configurations, see appendix .2), they can even gain energy when interacting with the molecules which are themselves in thermal equilibrium. The kinetic energy of molecules follows a Maxwell-Boltzmann distribution (at 300 K), so that a center-of-mass interaction calculation has to be carried out to determine if the electron has gained or lost energy within the interaction.

Within this thesis, the scattering routine (originally developed by F. Glück) has been implemented into KASSIOPEIA and extended to accommodate additional gas species and low-energy scattering interactions. Fig. 3.2 gives a detailed overview of the processes involved in electron-hydrogen scattering and their cross-sections over an energy range from 10 meV to 1 keV.

**Synchrotron radiation:** Another secondary energy loss mechanism implemented into KASSIOPEIA is the *synchrotron* radiation process. Due to their cyclotron motion, electrons continuously emit synchrotron radiation. In the non-relativistic limit, the energy loss per unit time interval  $\Delta t$  (in SI units) by this radiative process is given by

$$\frac{\Delta E_{\perp}}{\Delta t} = \frac{4}{3} \frac{e^4}{m_e^3 c} \cdot B^2 \cdot E_{\perp} \approx 0.4 \cdot B^2 \cdot E_{\perp}, \quad (3.6)$$

where  $B$  denotes the magnetic field,  $c$  the velocity of light, and  $e$  and  $m_e$  the electron charge and mass. To good approximation only the transversal kinetic energy component

$E_{\perp}$  is affected by this process. In KASSIOPEIA, synchrotron energy losses within a Runge-Kutta step are determined by using the average magnetic field during the step. From eq. (3.6) follows that the cooling effect due to synchrotron radiation is most efficient for large transversal kinetic energies and large magnetic fields. At the same time, the scattering cross section decreases steeply for increasing electron kinetic energies (see figure 3.2), so that synchrotron losses dominate at higher energies (tens of keV).

## 3.3 Field calculation methods

A detailed understanding of the motion of charged particles in electromagnetic fields calls for dedicated fast and precise field calculation tools. The KASSIOPEIA program package offers a variety of corresponding methods for magnetic (section 3.3.1) and electric (section 3.3.2) fields. Furthermore, the KEMFIELD package [191], which is also part of the KASPER framework, offers the possibility to perform fully 3-dimensional calculations of the main spectrometer.

### 3.3.1 Magnetic field calculation

The sources for magnetic fields in the KATRIN experiment can be divided into two categories:

- Axially symmetric sources: These comprise the superconducting coils and the LFCS coils of the KATRIN setup.
- Non-axially symmetric sources: Major contributions are magnetic materials, the earth magnetic field and the EMCS coils.

The magnetic field which is generated by an electric current  $I$  running through a line segment  $d\vec{s}$  which points in the direction of conventional current can be calculated according to the Biot-Savart law [208]:

$$d\vec{B} = -\frac{\mu_0}{4\pi} \cdot \frac{I\vec{r} \times d\vec{s}}{r^3}, \quad (3.7)$$

where  $\mu_0$  is the magnetic permeability constant and  $d\vec{B}$  is the net magnetic field, induced by  $I$  running through  $d\vec{s}$ . Here,  $\vec{r} = r\hat{r}$  is the full displacement vector from the wire element to the point at which the field is being computed.

**Axially symmetric magnetic field calculation:** The geometry of a coil or solenoid (see figure 3.3) is completely defined by the coordinates of the central points  $p_{1,2}$  at the coil ends and the inner and outer coil radii  $r_{i1,2}$ ,  $r_{o1,2}$ . For this kind of geometry, two field calculation methods are available, *elliptic integrals* and *zonal harmonics expansion*:

- **Elliptic integrals:** For a thin coil, the Biot-Savart law (3.7) can be expressed by

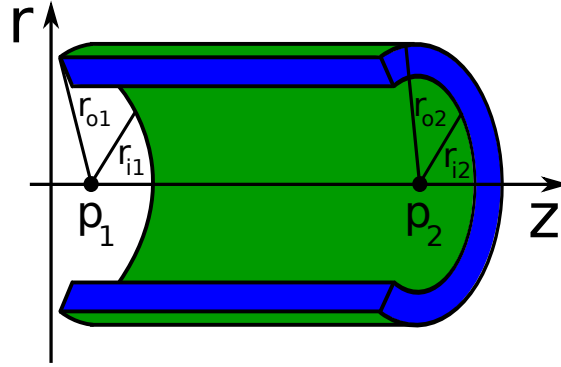


**Figure 3.3:** Cross section of a coil, which is fully described by the coordinates of the central points  $p_{1,2}$  at the coil ends and the inner and outer coil radii  $r_{i1,2}$ ,  $r_{o1,2}$ .

the complete elliptic integrals of the first (I) and second (II) kind:

$$\begin{aligned} (I) \quad K(k) &= \int_0^{\varphi} \frac{d\theta}{\sqrt{1-k^2 \sin^2 \theta}}, \\ (II) \quad E(k) &= \int_0^{\varphi} \sqrt{1-k^2 \sin^2 \theta} d\theta. \end{aligned} \quad (3.8)$$

The notion 'complete' implies  $\varphi = \pi/2$ , with  $\varphi$  being the 'amplitude'. The parameter  $k$  is the 'elliptic modulus', i.e. the eccentricity and  $\theta$  denotes the azimuthal angle (see figure 3.4).

For a thick coil, a two-dimensional numerical integration of (3.7) along the axial ( $z$ ) and radial ( $r$ ) coil dimensions is needed. This additional step largely increases the required computation time. Therefore, also the complete elliptic integral of the third (III) kind is used:

$$(III) \quad \Pi(n, k) = \int_0^{\pi/2} \frac{d\theta}{(1-n^2 \sin^2 \theta) \sqrt{1-k^2 \sin^2 \theta}}, \quad (3.9)$$

with the 'characteristic'  $n$ . The problem is now reduced to a one-dimensional integration in radial direction. Actually, the axial and radial magnetic field components for an infinitesimally thin solenoid can be calculated analytically via:

$$B_z = \hat{B}_z(Z_{max}) - \hat{B}_z(Z_{min}), \quad B_r = \hat{B}_r(Z_{max}) - \hat{B}_r(Z_{min}), \quad (3.10)$$

with

$$\hat{B}_z(Z) = -\frac{\mu_0 \lambda}{\pi} \cdot \frac{(z-Z)R}{(R+r)S} \left[ K(k) + \frac{R-r}{2R} (\Pi(n, k) - K(k)) \right], \quad (3.11)$$

$$\hat{B}_r(Z) = -\frac{\mu_0 \lambda}{\pi} \cdot \frac{R}{S} \left[ 2 \frac{E(k) - K(k)}{k^2} + K(k) \right], \quad (3.12)$$

$$S = \sqrt{(r+R)^2 + (z-Z)^2}, \quad k = 2\frac{\sqrt{Rr}}{S}, \quad n = 2\frac{\sqrt{Rr}}{R+r}, \quad (3.13)$$

and

$\lambda = dI/dz$ :	linear current density,
$z$ :	axial position of the field point to be calculated,
$r$ :	radial position of the field point to be calculated,
$Z$ :	$Z \in [Z_{min}, Z_{max}]$ , i.e. axial thickness of the coil,
$R$ :	$R \in [R_{min}, R_{max}]$ , i.e. radial thickness of the coil.

Performing an additional integration over the radial extension of the solenoid yields the total vector potential and magnetic field generated by the coil. Carlson's method [209] was chosen to solve above elliptic integrals.

Field points close to the  $z$ -axis have to be handled with care in order to avoid singularities and numerical cancellations. The advantage of the elliptic integral method is the possibility to calculate the magnetic field at any position, even inside the coil windings. In return, the computation time is large. For fast trajectory calculations, a better-suited method should be used, the *zonal harmonics expansion*.

- **Zonal harmonics expansion:** It is a special property of an axially symmetric coil system that the magnetic field at an arbitrary off-axis point  $p(z, r)$ , located not too far from the axis, can be expressed in terms of the Legendre polynomial expansion and its derivatives at a source point  $z_0$ , which lies on the symmetry axis.

If the distance  $\rho$  between  $p$  and any of the  $z_0$  is smaller than the distance  $\rho_{cen}$  between  $z_0$  and its closest coil (see figure 3.4 (a)), the magnetic field can be calculated by the central expansion:

$$\begin{aligned} B_z &= \sum_{n=0}^{\infty} B_n^{cen} \cdot \left(\frac{\rho}{\rho_{cen}}\right)^n \cdot P_n(u), \\ B_r &= -s \cdot \sum_{n=1}^{\infty} \frac{B_n^{cen}}{n+1} \cdot \left(\frac{\rho}{\rho_{cen}}\right)^n \cdot P'_n(u), \end{aligned} \quad (3.14)$$

where  $\rho_{cen} = \sqrt{(z-z_0)^2 + r^2}$  and  $s = \sin \theta = \sqrt{1-u^2} = r/\rho$ .  $B_0^{cen}$  denotes the magnetic field at  $z_0$  and the parameters  $B_n^{cen}$  ( $n \geq 1$ ) are proportional to its  $n$ 'th derivative. The latter are also called *central source coefficients* and depend on the particular coil properties such as geometry and current. The zonal harmonics  $\rho^n P_n(u)$  (of order  $n$ ) are a general solution of the Laplace equation for an axially symmetric system in vacuum, where  $P'_n(u)$  denotes the first derivatives. The central expansion will only converge within the convergence circles (colored region in figure 3.4 (a)). The convergence region increases for decreasing source point spacings. However, the computation time increases with the number of source points. A compromise between these parameters has to be found (which KASIOPEIA does automatically). The expansion converges faster for smaller ratios  $\rho/\rho_{cen}$  (i.e. smaller distance between  $p$  and  $z_0$ ). Therefore, the program automatically searches for the closest source point. The source points for a certain magnetic

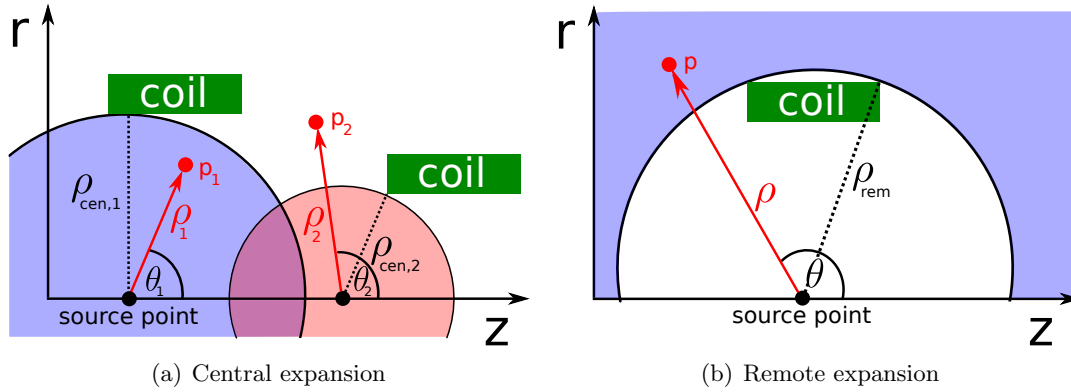


**Figure 3.4:** (a) Central and (b) remote Legendre polynomial expansion. Magnetic fields can only be evaluated in the convergence region (colored area), i.e. for  $p_2$  the expansion does not converge.

field configuration have to be calculated once prior to a field evaluation and are stored to a file for repeated usage.

For points outside of the central convergence region, there exists the remote Legendre polynomial expansion (figure 3.4 (b)). The magnetic field components can be calculated as follows:

$$\begin{aligned} B_z &= \sum_{n=2}^{\infty} B_n^{\text{rem}} \cdot \left(\frac{\rho_{\text{rem}}}{\rho}\right)^{n+1} \cdot P_n(u), \\ B_r &= -s \cdot \sum_{n=2}^{\infty} \frac{B_n^{\text{rem}}}{n} \cdot \left(\frac{\rho_{\text{rem}}}{\rho}\right)^{n+1} \cdot P_n'(u), \end{aligned} \quad (3.15)$$

where  $\rho_{\text{rem}}$  is the maximum distance between the source point  $z_0$  and the source.  $B_n^{\text{rem}}$  ( $n \geq 2$ ) are the *remote source coefficients* and  $\rho^{-(n+1)}P_n(u)$  denotes the zonal harmonics of the remote expansion. As for the central expansion, the series converges fast if the convergence ratio  $\rho_{\text{rem}}/\rho$  is small (i.e. the distance between  $p$  and  $z_0$  is large, as opposed to the central convergence case).

This method is much faster than the calculation with elliptic integrals. However, there are regions close to or inside a coil where neither the central nor the remote expansion converge. In such regions, the program automatically switches to the elliptic integral method [210, 211].

**Non-axially symmetric magnetic field calculation:** In reality, there are magnetic field sources present in the KATRIN experiment which do not show an axial symmetry. Their presence has major implications for the background as shown in section 6. To include these fields, two methods to perform fully three-dimensional field calculations are available:

- **Integrated Biot-Savart:** A coil of arbitrary shape can be approximated as a collection of line segments. The magnetic field  $\vec{B}_i$  of a single line segment  $d\vec{s}_i$  can

be calculated by integrating the Biot-Savart law (3.7) along  $d\vec{s}$ . The magnetic field produced by several line segments can be determined using the superposition principle:

$$\mathbf{B}_{\text{tot}} = \sum_{i=1}^N \mathbf{B}_i. \quad (3.16)$$

The accuracy of the calculation increases with smaller line segments (i.e. better discretization), however, then the computation time suffers.

- **Magnetic dipoles:** Magnetic materials such as the steel bars serving as concrete reinforcements within the KATRIN experimental hall will contribute to the magnetic stray fields. These elements are longitudinally magnetized rods, which can be approximated as magnetic dipoles with a magnetic charge  $Q$  at each end. The magnetic field at a point  $\mathbf{p}$ , produced by a single rod, can thus be calculated using Coulomb's law:

$$\mathbf{B}_i(\mathbf{p}) = -Q \cdot \frac{\mu_0}{4\pi} \cdot \left( \frac{\mathbf{r}_a}{|\mathbf{r}_a|^3} + \frac{\mathbf{r}_b}{|\mathbf{r}_b|^3} \right), \quad (3.17)$$

with  $Q = |\mathbf{M}| \cdot \pi r^2$ ,  $\mathbf{M}$  being the magnetization and  $r$  the radius of the rod,  $a$  and  $b$  denoting its two ends. The total field can again be obtained by a superposition of the individual field contributions. However, the situation is complicated by the fact that the real dipole distribution is not known. Therefore, this distribution has to be modeled from a huge set of magnetic field measurements carried out in the experimental hall [182].

A collection of various magnetic field calculation codes and the corresponding documentation can be found in [212].

#### 3.3.2 Electric field calculation

When computing the electric field and potential produced by an electrode over the spectrometer volume, the exact charge distribution within the electrode has to be determined. This parameter strongly depends on the geometry of the electrode and its surrounding. There exist various methods for electric field computation: the finite difference method (FDM) [213], the finite element method (FEM) [214] and the boundary element method (BEM) [215]. Given the huge volume of the KATRIN main spectrometer, where a good knowledge of the electric field is most important, BEM is the preferred method as it is more efficient for problems with a small surface-to-volume ratio.

**Boundary Element Method:** BEM relies on a discretization of the boundary surface into  $N$  sub-elements  $S_j$  [216]. The complete geometry  $S$  can thus be written as:

$$S = \sum_{j=1}^N S_j. \quad (3.18)$$

Evidently, a discretization into smaller sub-elements increases the accuracy of the results at the expense of decreasing the calculation speed.

The first step is a determination of the charge densities  $\sigma_j$ , which are approximated as constant values within an individual sub-element. The electric potential  $U_i$ , which is applied to electrode  $i$ , and the  $\sigma_j$  of the electrode sub-elements are related by:

$$U_i(\mathbf{r}) = \sum_{j=1}^N C_{ij} \sigma_j, \quad (3.19)$$

where  $C_{ij} = C_j(\mathbf{r}_i)$  are the Coulomb-matrix-elements. They account for the fact that the individual electrodes influence each other. An individual Coulomb integral number  $C_{ij}$  corresponds to the potential in the middle of the electrode element  $i$  due to the sub-element  $j$  with unit charge density. They can be calculated by:

$$C_j(\mathbf{r}_i) = \frac{1}{4\pi\epsilon_0} \int_{S_j} \frac{1}{|\mathbf{r}_i - \mathbf{r}_S|} d^2\mathbf{r}_S. \quad (3.20)$$

The charge densities are then obtained by solving the linear algebraic equation system (3.19) by either the Gauss-Jordan-algorithm, or the Lower-Upper (LU) method [209]. The resulting charge densities and the geometrical and potential parameters of the independent sub-elements are then stored in a data file.

BEM calculations usually result in a calculation with fully populated matrices. Therefore, the required memory and computational time grows as  $N^2$ . Thus there is a limit to the number of sub-elements  $N$ . Accordingly, iterative methods, such as the Robin Hood algorithm [217], are applied to circumvent this problem.

In close analogy to the case of magnetic fields, both axially symmetric as well as non-axially symmetric electrodes are present at KATRIN.

**Axially symmetric electric field calculation:** As for the magnetic field calculation, the electric potential can be calculated either by using elliptic integrals or the zonal harmonics expansion. Again, the latter method is faster but it is also constrained to regions where the series is convergent.

For the elliptic integral method, the electric potential at a point  $(z, r)$ , due to the full electrodes, is a superposition of the potentials from thin charged rings, obtained by discretization:

$$\Phi(z, r) = \sum_{j=1}^N \frac{Q_j}{2\pi^2\epsilon_0} \frac{K(k_j)}{S_j}, \quad (3.21)$$

where the parameters  $S_j$  and  $k_j$  are defined according to eq. (3.13). The rings have the axial coordinate  $Z_j$ , the radius  $R_j$  and the total charge  $Q_j$ . Here,  $K(k_j)$  denotes the first complete elliptic integral calculated in the Chebyshev approximation [218].

The electric potential due to a wire (approximated as line segments with endpoints  $P_a$  and  $P_b$ ) can be calculated by:

$$\Phi = \frac{\lambda}{4\pi\epsilon_0} \ln \left( \frac{D_a + D_b + L}{D_a + D_b - L} \right), \quad (3.22)$$

where  $L$  is the length of the line segment,  $D_a$  and  $D_b$  are the distances of its endpoints from the field point  $(z, r)$  and  $\lambda = Q/L$  is the linear charge density of the segment with total charge  $Q$ . The total potential at the field point  $(z, r)$  is again a superposition of all line segments.

The following equations for the potential and the electric field components apply for the central Legendre polynomial expansion:

$$\begin{aligned}\Phi(z, r) &= \sum_{n=0}^{\infty} \phi_n^{\text{cen}}(z_0) \left(\frac{\rho}{\rho_{\text{cen}}}\right)^n P_n(u), \\ E_z(z, r) &= -\frac{1}{\rho_{\text{cen}}} \sum_{n=0}^{\infty} \phi_{n+1}^{\text{cen}}(z_0)(n+1) \left(\frac{\rho}{\rho_{\text{cen}}}\right)^n P_n(u), \\ E_r(z, r) &= \frac{s}{\rho_{\text{cen}}} \sum_{n=0}^{\infty} \phi_{n+1}^{\text{cen}}(z_0) \left(\frac{\rho}{\rho_{\text{cen}}}\right)^n P_n'(u),\end{aligned}\tag{3.23}$$

where  $s = r/\rho = \sin\theta$  is defined analogous to the magnetic field calculation. Accordingly,  $\phi_n^{\text{cen}}$  are the central source coefficients,  $P_n(u)$  the Legendre polynomials and  $\rho$  the distance from the field point  $(z, r)$  to the source point  $z_0$ .

The same advantages and disadvantages as in the case of the calculation of the magnetic fields by Legendre polynomial expansion also apply for the electric field calculation.

For more detailed information, see [211] and [219].

**Non-axially symmetric electric field calculation:** The inner surface of the KATRIN main spectrometer is covered with an electrode system with complex geometry. Specifically, the corresponding potential-carrying elements (wire modules, holding structures) are no longer axially symmetric. When moving close to these structures, the electric fields and potentials have to be calculated in a fully three-dimensional fashion requiring a discretization of the complete geometry, where wires are approximated as line segments, while other surfaces are meshed from triangles and rectangles. For each of the obtained sub-elements, the charge density has to be determined in the same way as for the axially symmetric calculation. However, the number of sub-elements is much larger now ( $\mathcal{O}(10^6)$  instead of  $\mathcal{O}(10^3)$ ), necessitating the usage of the Robin Hood algorithm. The calculation of electric field and potential values cannot utilize the fast zonal harmonics expansion anymore. Instead, Coulomb integration of all the individual sub-elements has to be carried out, which results in large computation times. On a CPU, the evaluation of a single field points takes about three seconds, while the usage of GPUs results in a speed-up by a factor  $\sim 10$ .

The KEMFIELD program package, developed by T.J. Corona [190, 191, 220] (based on the original work of F. Glück [210, 219, 221]), was optimized to cope with the computation of huge geometries with  $\mathcal{O}(10^6)$  sub-elements, utilizing the Robin Hood algorithm and GPU computing for maximum accuracy and speed.

### 3.4 External packages using Kasper

The distinct advantage of the KASPER package stems from its modularity, allowing an easy usage as a library for external program packages. This section will introduce

KTRAP (KATRIN Transmission Analysis Package), an external program package which makes use of the features of KASPER. At present, KTRAP consists of the two main modules *LFCS optimization* (section 3.4.1) and *Transmission function analysis* (section 3.4.2), which will be detailed below.

### 3.4.1 LFCS optimization

A neutrino mass sensitivity of 200 meV can only be achieved with optimized and well known transmission and background properties of the main spectrometer. Both are defined by the electric and magnetic field configuration. While careful optimizations of the electric field have been carried out in [183], this work focuses on the details of the magnetic field configuration. The stringent requirements on the magnetic guiding field are given in section 4.1. In order to meet these requirements, the free parameters which influence the field configuration have to be optimized, namely the currents running through the LFCS coils (see section 4.3).

A program to automatically determine these currents, accommodating various user-defined requirements, has been developed in close collaboration with F. Glück [151, 222], T. Platon and N. Stallkamp [223, 224].

In this section, only the general structure of the program will be presented. Details about the physics goals and the various results will be given later in section 4.4.

The work flow of the program consists of three steps: *Initialization*, *Specification*, and *Optimization*.

- **Initialization:** At first, the user has to define in a configuration file which electrode and magnet geometry as well as field calculation method should be used for the optimization. Subsequently, the program initializes all of these methods with the required parameters. Various other parameters are also read in and stored for later use before the *Specification* step is called.
- **Specification:** Within this step, the *Optimization* is being prepared. This involves: *a)* setting of the starting conditions for the coil currents (user defined and/or random values), *b)* definition of restrictions for the available current range (defined by the LFCS hardware), *c)* initialization of the function to be minimized with the starting conditions, and *d)* setting termination conditions for the minimization routine (maximal number of iterations, accuracy requirement). Finally, the minimization routine is called, which performs the actual *Optimization*.
- **Optimization:** Here, the objective function is minimized, using a user-defined routine. To do so, several minimizers are available within KASPER: ROOT's Minuit2 algorithm [225], Markov-Chain-Monte-Carlo techniques [189, 226] and the simplex method [227]. The latter method was used to obtain the results of this thesis. The optimized current values are returned from the minimizer and stored to a file for later use.

The *Initialization* step requires the XML feature of KASPER (*Common* package) to easily access user-specified input files. All field calculations utilize either the field classes

within KASSIOPEIA or within KEMFIELD, which both are part of KASPER. For the optimization, the minimization routines from the fit package of KASPER are consulted.

### 3.4.2 Transmission function analysis

The importance of the transmission function for KATRIN was pointed out already. It is a complex function of the source properties (energy and angular emission characteristics) and the spectrometer properties (electric and magnetic fields), which will be shown in detail in section 5. Further, the importance to simulate the transmission function in detail will be pointed out. The corresponding purpose of this analysis tool is threefold:

- Investigation of various distorting influences on the transmission function: As important information for high-precision  $\beta$ -spectroscopy will be extracted from a transmission function measurement, the impact of possible distorting influences has to be studied in close detail.
- Development of a measurement strategy: The transmission function is influenced by an ensemble of parameters at the same time. As these partly have very similar footprints, a strategy has to be developed to disentangle these parameters.
- Development of an analysis strategy: The transmission function measurements are applicable to various rather different problems (see section 5.1), each of them requiring different approaches to the analysis of measurement or simulation results.

In the following, the general principles and functionalities of the so-far implemented programs will be presented shortly. More detailed considerations can be found in section 4 and 5.

**TransmissionProperties:** This program allows the user to check the transmission properties of a certain electromagnetic field setup. It computes relevant particle and field properties along magnetic field lines. Corresponding figures are created automatically, providing visualization to the user with regard to the transmission properties of the setup under investigation.

**AnalyzingPointSearch:** Again, the transmission properties along magnetic field lines are calculated. An additional step is performed, namely the search for the points in space where the signal electron's energy is actually analyzed. This knowledge is indispensable for a determination of the transmission function itself. Accordingly, appropriate figures are created again automatically.

**PerPixelTransmission:** Any non-negligible electric and magnetic field inhomogeneities will lead to variations of the transmission function for different field lines. However, as the analysis tool will make use of transmission functions averaged over an ensemble of field lines ending at a single detector pixel, this module determines the average transmission function (for a user defined pixel) for a given electromagnetic configuration.

**CreateTransmissionFile:** In order to be able to compare measured and simulated transmission function results, a common data format is required. This program, devel-

oped in [16], translates a given input format into this common format to be used by subsequent analysis tools, such as the *TransmissionFitter*.

**TransmissionFitter:** A transmission function is composed of a series of measurement or simulation points. Within this tool, the individual points are evaluated and combined to form a complete transmission function. Various parameters can be extracted from the obtained function, either by fitting or by differentiation.

All of these individual tools utilize the XML feature of KASPER to allow a configuration by the user. The field line calculator inherent to KASSIOPEIA is required for a determination of the transmission properties, which additionally requires access to the various field calculation methods of KASSIOPEIA and KEMFIELD.

KTRAP is still under development and will obtain a variety of new features shortly [16].



# Electromagnetic optimization of the main spectrometer

The key task of the main spectrometer resides in the analysis of tritium decay electron energies with unprecedented precision. A neutrino mass sensitivity of 0.2 eV can only be achieved with optimized and well-known transmission and background properties of the main spectrometer. Both issues strongly depend on the actual electromagnetic field configuration implemented. Careful optimization of the electrostatic field has been carried out in [154, 183]. This work focuses on the details of the magnetic field configuration. At first, the electromagnetic design criteria, which have to be fulfilled, are defined (section 4.1). Special emphasize is put on the transmission condition which allows a general derivation of the transmission function (section 4.2). The specific focus of this work is related to an optimization of the working parameters of a large volume air coil system, which allows to fine-tune the magnetic field in the main spectrometer (section 4.3). It turned out that this optimization is best achieved by an automated procedure (section 4.4). This offers a high degree of versatility in the field optimization as various investigations to be performed at the main spectrometer each ask for specific magnetic field configurations. The details of some exemplary field configurations, which were used to perform a variety of simulations in the framework of this thesis, will be presented (section 4.5).

## 4.1 Electromagnetic design requirements

To optimize the background and transmission properties of the main spectrometer, the magnetic field has to meet certain design criteria [151, 228, 229], which will be detailed in this section.

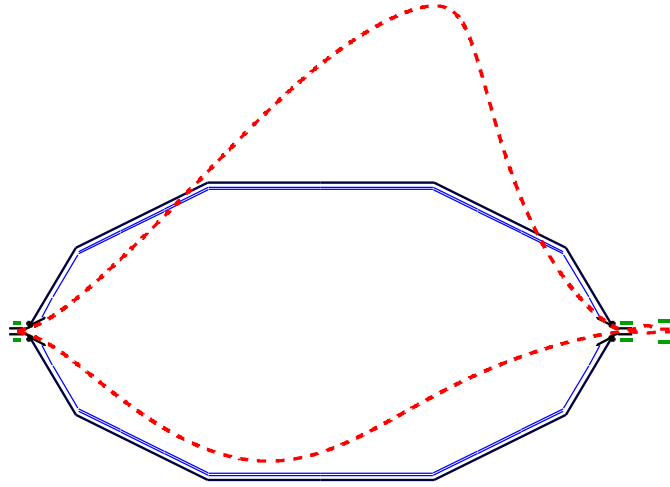


**Figure 4.1:** The  $191 \text{ Tcm}^2$  flux tube (dashed line) produced by superconducting solenoids only is strongly distorted by the earth magnetic field. Also, the magnetic field strength in the central spectrometer volume is too low to constrain the flux tube to the spectrometer.

### Magnetic guidance

An essential design cornerstone is that all signal electrons within the  $191 \text{ Tcm}^2$  flux tube are transported through the main spectrometer. Otherwise, the neutrino mass measurement statistics would be reduced, while at the same time the background rate would be increased. The latter effect is caused by field lines which would directly connect large parts of the vessel wall with the detector, thereby providing magnetic guiding conditions for  $\mu^-$  or  $\gamma$ -induced secondary electrons. Therefore, it has to be ensured that the flux tube does not touch any beam line elements.

Figure 4.1 shows the flux tube as produced by the superconducting solenoids as well as the earth magnetic field ( $B_{\text{EMF}} = 5 \cdot 10^{-5} \text{ T}$ ), which strongly distorts the flux tube in the low magnetic field region ( $B_{\text{sol}} = 1 \cdot 10^{-4} \text{ T}$ ) in the central part of the spectrometer. Consequently, the flux tube does not fit into the main spectrometer, and, hence, additional field shaping elements are needed in order to fulfill the magnetic guidance requirement.

### Transmission condition

As pointed out in section 2.2.2, a precise knowledge of the transmission function is an essential pre-requisite for a successful neutrino mass determination. In order to compute the transmission function, the magnetic field and electrostatic potential at the analyzing point have to be known. Here, the analyzing point is defined as the point in space where a signal electron would be reflected if its longitudinal kinetic energy does not allow to overcome the potential barrier. This point generally depends on the electron starting polar angle, which implies a complicated procedure to determine the

transmission function. Therefore, the first transmission condition is applied:

1. *The analyzing point should be independent of the starting polar angle.* (4.1)

The above considerations are restricted to a specific magnetic field line. In general, the transmission function analysis is clearly simplified if the axial coordinates of the analyzing points do not show a radial dependence.

Therefore, the second transmission condition is employed:

2. *The analyzing points of the individual field lines should reside within a common plane, the so called **analyzing plane**, located in the center of the main spectrometer ( $z = 0$  m).* (4.2)

A detailed understanding of the transmission condition is required for a determination of the main spectrometer transmission properties. Therefore, section 4.2 will be focused on all required details concerning the transmission condition.

### Radial homogeneity

Even in case that both transmission conditions are fulfilled, the magnetic field will vary between the analyzing points of individual field lines due to the inherent radial magnetic field inhomogeneity. Although the detector offers a good spatial resolution (central bulls-eye surrounded by 12 rings), the radial distance  $\Delta r$  in the spectrometer center covered by a single pixel is quite large ( $\Delta r = 0.66$  m for the bulls-eye,  $\Delta r = 0.18$  m for the outermost ring). Over this distance, the field change can only be calculated. As the magnetic field inhomogeneity generally increases towards larger radii, the detector ring radii decrease to compensate this effect (as well as the similar inhomogeneity of the electrostatic potential). Inhomogeneities of the magnetic field will lead to a broader transmission function, which would directly influence the neutrino mass sensitivity (see section 5).

### Magnetic shielding

The fact that electrons generally move along magnetic field lines and not perpendicular to them leads to an intrinsic shielding effect against background electrons created outside of the sensitive flux tube volume. It was experimentally shown at the pre-spectrometer [148, 179] and at the Mainz spectrometer [230, 231] that a larger magnetic field increases the magnetic shielding efficiency. This effect can be explained by the stronger Lorentz force on electrons which normally move parallel to magnetic field lines but not orthogonal to them. However, small field disturbances can lead to a perpendicular motion, which results in a drift of background electrons into the sensitive spectrometer volume. In this context, a larger magnetic field has two advantages: The relative influence of the disturbances is reduced and the flux tube has a larger distance to surfaces where background electrons are emitted from. However, when doing so, the transmission function will suffer from broadening, which in turn will decrease the energy resolution and hence will slightly reduce the signal rate. The magnetic shielding properties will be further investigated in section 6.

### Adiabaticity

Signal electrons require an adiabatic guidance through the main spectrometer, i.e. their motion has to be completely reversible. If the magnetic field strength changes too fast or if the field strength is too low, signal electrons could undergo an uncontrolled angular change, which does not satisfy the adiabatic condition (*adiabaticity*). As the electron polar angle directly influences the transmission condition, also the transmission function is affected. However, due to the extended size of the main spectrometer with a length of 23 m, the magnetic field can be tailored to change rather slowly, ensuring an adiabatic electron transport. Nevertheless, for the case of stored high-energy electrons, non-adiabatic effects become more pronounced. Details thereof are outlined in section .4.

## 4.2 The transmission condition

Within this section, the importance of obeying the transmission condition will be highlighted by a general derivation of the transmission function (section 4.2.1). There exist two generic electromagnetic configurations to fulfill the transmission condition. Each requires a careful optimization of the operation values of the field shaping elements surrounding the KATRIN main spectrometer (section 4.2.2).

### 4.2.1 Derivation of the transmission function

In order to compute the transmission function, the precise location of the actual analyzing points has to be known. For the following discussion, the analyzing point  $\mathbf{P}_a$  is defined as the point along a magnetic field line where the longitudinal energy of an electron with a definite starting angle reaches its minimal value, while the index  $s$  will denote the starting point of the electrons.

#### Definition of the transmission energy

The kinetic energy  $E_p$  of an electron at an arbitrary point  $p$  along its trajectory is determined by the starting conditions through energy conservation:

$$E_{\text{tot}} = E_s + qU_s = E_p + qU_p, \quad (4.3)$$

where  $U$  is the electrostatic potential and  $q$  the signed electron charge. The kinetic energy  $E_{p/s}$  is composed of a longitudinal component  $E_{p/s,\parallel}$  and a transversal component  $E_{p/s,\perp}$  relative to the magnetic field direction:

$$E_s = E_{s,\parallel} + E_{s,\perp}, \quad E_p = E_{p,\parallel} + E_{p,\perp}. \quad (4.4)$$

Due to the energy-momentum relation  $E \propto p^2$ , the starting transversal component can be expressed as:

$$E_{s,\perp} = E_s \sin^2(\theta_s), \quad (4.5)$$

where  $\theta_s$  is the polar starting angle of the electron. According to eq. (2.3), the transversal components  $E_{p,\perp}$  and  $E_{s,\perp}$  are related by

$$\frac{\gamma_p + 1}{2} \cdot \frac{E_{p,\perp}}{B_p} = \frac{\gamma_s + 1}{2} \cdot \frac{E_{s,\perp}}{B_s}. \quad (4.6)$$

Combining eq. (4.4), (4.5) and (4.6) with eq. (4.3) yields the adiabatic longitudinal energy at any point along a certain magnetic field line (i.e. on a certain electron path):

$$E_{p,\parallel} = E_s - E_s \cdot \sin^2(\theta_s) \cdot \frac{B_p \cdot (\gamma_s + 1)}{B_s \cdot (\gamma_p + 1)} - q(U_p - U_s). \quad (4.7)$$

The analyzing point  $\mathbf{P}_a$  corresponds to the point  $p$ , where eq. (4.7) reaches its minimal value. An electron needs a certain minimal starting energy to pass the point  $\mathbf{P}_a$ , the so called *transmission energy*  $E_{tr}$ . For  $E_s = E_{tr}$ , the longitudinal energy  $E_{p,\parallel}$  vanishes at the analyzing point  $\mathbf{P}_a$ . From eq. (4.7) follows a concise expression for the transmission energy:

$$E_{tr} = \frac{q(U_{P_a} - U_s)}{1 - \frac{B_{P_a} \cdot (\gamma_s + 1)}{B_s \cdot (\gamma_{P_a} + 1)} \cdot \sin^2(\theta_s)}. \quad (4.8)$$

### Dependence of the transmission energy

Figure 4.2 (b) shows the dependence of the transmission energy on the starting polar angle for different field lines within the 191 Tcm<sup>2</sup> flux tube (1: 0 Tcm<sup>2</sup>, 2: 12 Tcm<sup>2</sup>, 3: 48 Tcm<sup>2</sup>, 4: 108 Tcm<sup>2</sup>, 5: 191 Tcm<sup>2</sup>). For this calculation it was assumed that the transmission condition is fulfilled, i.e.  $U_{P_a} = U(z = 0)$  and  $B_{P_a} = B(z = 0)$ .

The shape of  $E_{tr}(\theta_s)$  is determined by the denominator of eq. (4.8) and thus depends on two parameters: the starting polar angle  $\theta_s$  and the magnetic field ratio  $B_{P_a}/B_s$ .

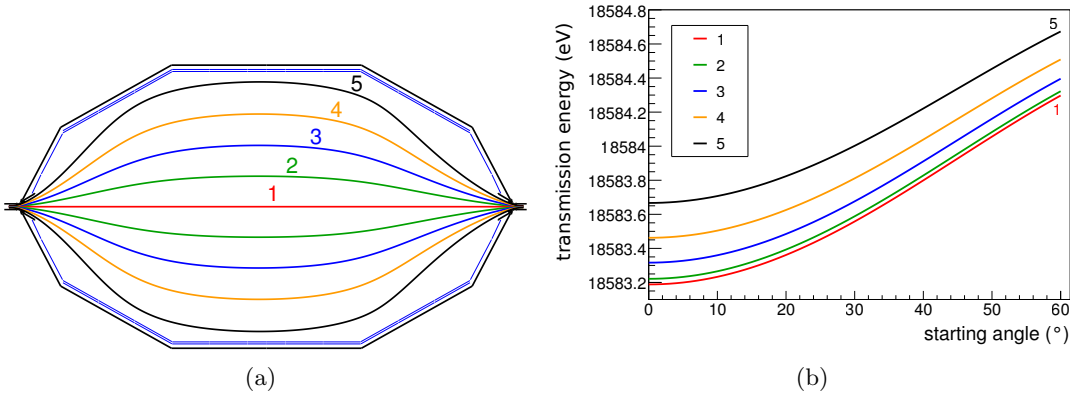


**Figure 4.2:** Dependence of the transmission energy for selected field lines. (a) Location of the selected field lines within the 191 Tcm<sup>2</sup> flux tube. (b) Transmission energy as a function of the starting polar angle for the individual field lines shown in (a). The standard potential configuration of table 4 was used for this calculation.

In the actual KATRIN setup, electrons are created at the source within a magnetic field  $B_s$ , which is smaller than the maximal magnetic field  $B_{\max} = 6$  T at the pinch magnet. In the case of figure 4.2 a value of  $B_s = 4.5$  T was assumed. For this case, polar angles up to  $\theta_{s,\max} = 60^\circ$  will be transmitted (higher angles are reflected by the magnetic mirror effect). The difference between  $E_{\text{tr}}(\theta_{s,\min} = 0^\circ)$  and  $E_{\text{tr}}(\theta_{s,\max} = 60^\circ)$  corresponds to the width of the transmission function. For starting polar angles  $\theta_s < 60^\circ$ , and a starting energy above the transmission energy ( $E_s > E_{\text{tr}}$ ), the electron is transmitted to the detector, while for  $\theta_s > 60^\circ$  or  $E_s < E_{\text{tr}}$  the electron is reflected back to its source.

The offset between the individual field lines results from the radial inhomogeneity of the electrostatic potential  $U_{\text{Pa}(r)}$  which appears in the numerator of eq. (4.8).

### Transmission function for an isotropic source

The knowledge of the transmission energy is crucial in order to compute the transmission function. We recall that this is the transmission probability for an electron with a fixed starting energy:  $T(E_s)$ . A fixed starting energy implies a maximal polar angle for an electron to be transmitted:  $\theta_{\max}(E_s)$  (neglecting magnetic mirror reflection), so that all electrons with angles  $\theta_s < \theta_{\max}$  are transmitted (assuming the transmission condition is fulfilled). The electrons which are emitted from the source typically display a well-defined angular distribution  $\omega(\theta, \varphi)$ , where  $\varphi \in [0, 2\pi]$  is the azimuthal angle around a magnetic field line.

In case of an isotropic source, where scattering effects within the source can be neglected, the parameter  $u = \cos \theta$  is equally distributed:

$$\int_0^1 du = 1. \quad (4.9)$$

The angular distribution  $\omega(\theta, \varphi)$  is defined as:

$$du = -\omega(\theta, \varphi)d\theta d\varphi \rightarrow \omega(\theta, \varphi) = \sin(\theta). \quad (4.10)$$

Transformation of the integral boundaries ( $0 \rightarrow \pi$  and  $1 \rightarrow 0$ ) yields the integral over the whole phase space:

$$\omega_{\text{tot}} = \int_0^{2\pi} \int_0^\pi \sin(\theta)d\theta d\varphi = 4\pi. \quad (4.11)$$

However, only half of the phase space, i.e.  $\omega_{\text{tot}}/2 = 2\pi$ , is emitted towards the spectrometer. Therefore, the transmission probability for a fixed starting energy  $E_s$  is given by the fraction  $d\omega/(\omega_{\text{tot}}/2)$  between minimal and maximal starting polar angle ( $\theta_{\min}(E_s) = 0^\circ$  and  $\theta_{\max}(E_s)$ ):

$$\begin{aligned} T(E_s) &= \frac{1}{\omega_{\text{tot}}/2} \cdot \int 1 \cdot d\omega(\theta, \varphi) \\ &\stackrel{(4.11)}{=} \frac{1}{2\pi} \int_0^{2\pi} \int_{\theta_{\min}}^{\theta_{\max}} \sin \theta d\theta d\varphi \\ &= \int_0^{\theta_{\max}(E_s)} \sin \theta d\theta \\ &= 1 - \cos[\theta_{\max}(E_s)]. \end{aligned} \quad (4.12)$$

The functional relation  $\theta_{\max}(E_s)$  can be obtained by inverting eq. (4.8):

$$\theta_{\max}(E_s) = \arcsin \sqrt{\left(1 - \frac{q(U_{P_a} - U_s)}{E_s}\right) \cdot \frac{B_s}{B_{P_a}}}. \quad (4.13)$$

Here, the validity of the approximation  $\gamma_s \approx \gamma_{P_a}$  was used to simplify the equation. With the relation  $\cos[\arcsin(\sqrt{x})] = \sqrt{1-x}$ , the transmission probability is obtained when combining eq. (4.13) with eq. (4.12):

$$T(E_s, q\Delta U) = \begin{cases} 0 & \text{for } E_s < q\Delta U \\ 1 - \sqrt{\left(1 - \frac{q\Delta U}{E_s}\right) \cdot \frac{B_s}{B_{P_a}}} & \text{for } q\Delta U < E_s < q\Delta U + \Delta E \\ 1 & \text{for } E_s > q\Delta U + \Delta E \end{cases}, \quad (4.14)$$

where  $\Delta U = U_{P_a} - U_s$  and  $\Delta E = E_s \cdot \frac{B_{P_a}}{B_{\max}}$  is the spectrometer energy resolution (2.4). The transmission function (4.14) does not take into account possible modifications due to the magnetic mirror effect, which occurs if the source magnetic field  $B_s$  is lower than the maximal magnetic field  $B_{\max}$ . Incorporating this additional condition, given by eq. (2.6), yields the complete (normalized) transmission function

$$T(E_s, q\Delta U) = \begin{cases} 0 & \text{for } E_s < q\Delta U \\ \frac{1 - \sqrt{\left(1 - \frac{q\Delta U}{E_s}\right) \cdot \frac{B_s}{B_{P_a}}}}{1 - \sqrt{1 - \frac{B_s}{B_{\max}}}} & \text{for } q\Delta U < E_s < q\Delta U + \Delta E \\ 1 & \text{for } E_s > q\Delta U + \Delta E \end{cases}, \quad (4.15)$$

which is equivalent to eq. (2.7).

Note that this result is a simplification, because the analyzing point can depend on the starting polar angle, i.e.  $B_{P_a} \rightarrow B_{P_a(\theta_s)}$  and  $U_{P_a} \rightarrow U_{P_a(\theta_s)}$ . In this case, the inversion (4.13) yields a much more complicated relation. Therefore, fulfilling the first transmission condition (4.1) is a necessary requirement to be able to determine the transmission function.

Furthermore, field lines cannot be analyzed individually, i.e. a possible radial ( $r$ ) and azimuthal ( $\phi$ ) dependence<sup>1</sup> has to be taken into account:  $E_{\text{tr}} \rightarrow E_{\text{tr}}(\theta_s, r, \phi)$ ,  $B_{P_a(\theta_s)} \rightarrow B_{P_a(\theta_s, r, \phi)}$  and  $U_{P_a(\theta_s)} \rightarrow U_{P_a(\theta_s, r, \phi)}$ .

The azimuthal dependence of  $P_a$  can be avoided if the magnetic field and electrostatic potential are axially symmetric, which is the case for regions sufficiently far away from the magnetic and electric field sources.

A radial dependence of  $P_a$  is circumvented if the second transmission condition (4.2) is fulfilled. However, the potential and magnetic field display an intrinsic radial dependence, which can be calculated though.

---

<sup>1</sup>Here, a spatial azimuthal dependence within the spectrometer coordinate system  $(x, y, z)$  is considered, with  $z$  pointing from the source to the detector. The coordinates of a point  $p$  within the main spectrometer are given by  $(-r \cdot \sin \phi, r \cdot \cos \phi, z)$ .

In summary, there are three possible scenarios:

- *Case 1*: Ideally, the first and second transmission condition are fulfilled. Then, the transmission function is determined by a minimal set of parameters ( $B_s$ ,  $U_s$ ,  $B_{P_a}$ ,  $U_{P_a}$ , and  $B_{\max}$ ).
- *Case 2*: If the second transmission condition is not fulfilled, the axial position of the analyzing points shows a radial and/or azimuthal dependence. In this case, the transmission function has to be determined by integration over  $r$  and/or  $\phi$ .
- *Case 3*: In the worst case scenario, the analyzing points also depend on the starting polar angle, i.e. the first transmission condition is not fulfilled. As a result, the derivation of the transmission function would require a very complicated procedure.

### 4.2.2 Satisfying the transmission condition

The fulfillment of the transmission condition(s) depends on the subtle interplay between magnetic field and electrostatic potential within the main spectrometer. In general, three generic field configurations can occur, which will be detailed in the following.

#### I. Inhomogeneous electrostatic potential

If the electrostatic potential is rather inhomogeneous, the third (electric) term of eq. (4.7) is dominant. Consequently, the minimum of the longitudinal energy is located at the position where the electrostatic potential has its maximal negative value, as indicated in figure 4.3 (a). However, in this configuration it has to be ensured that the longitudinal energy does not drop below zero before the mirror plane, i.e. the magnetic field should not decrease too slowly in the beginning as the third (magnetic) term counteracts the second (electric) term.

#### II. Homogeneous electrostatic potential and global magnetic field minimum

The inner electrode system is designed to create a very homogeneous electrostatic potential over a large region symmetric to the main spectrometer mid-plane (see figure 4.3 (b)). This is of advantage as a good axial homogeneity implies a good radial homogeneity, also, which is necessary to precisely determine the transmission function for an individual detector pixel covering a distinct radial range of the flux tube.

For a starting angle  $\theta_s = 0^\circ$ , the minimum of the longitudinal energy coincides with the negative maximum of the electrostatic potential, which is located at the  $z_{\text{mirror}} = 0$  m mirror plane. Here, the magnetic term in eq. (4.7) vanishes, i.e.  $E_{\parallel}$  is determined by the electrostatic potential only. For higher starting angles, the magnetic term increases, thereby decreasing the longitudinal energy when moving away from the global magnetic field minimum at  $z_{\text{mirror}}$ . If the electrostatic potential is very homogeneous, it cannot supply the electron with enough longitudinal acceleration to counteract the effect of the magnetic field. Consequently, the minimum of  $E_{\parallel}$  for different starting angles could

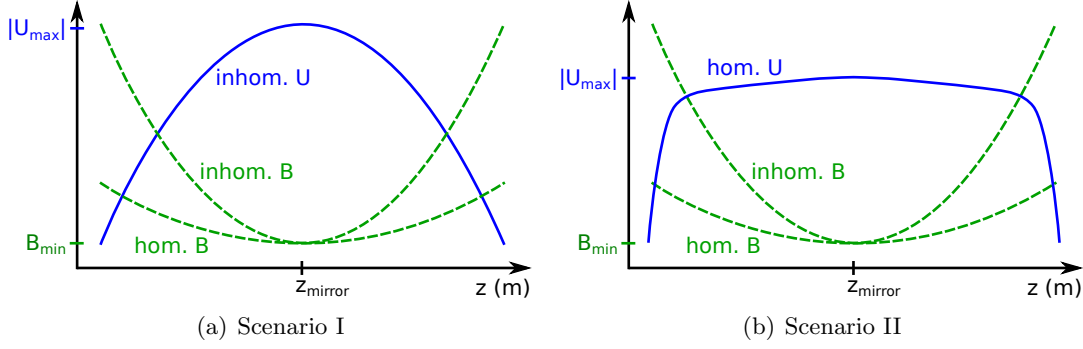


**Figure 4.3:** The transmission condition can be fulfilled by implementing a global magnetic field minimum (green, dashed curves). (a) An inhomogeneous electrostatic potential (blue, solid curve) automatically satisfies the transmission condition, independently of the homogeneity of the magnetic field. (b) The homogeneous electrostatic potential at KATRIN requires a homogeneous magnetic field to satisfy the transmission condition.

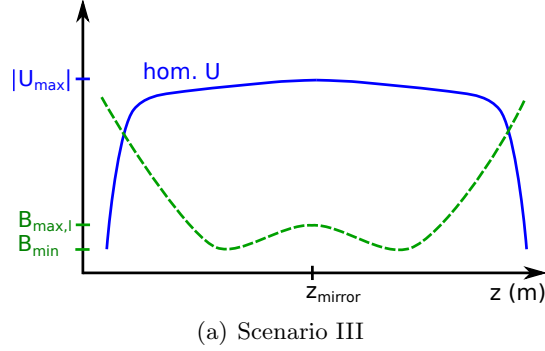


**Figure 4.4:** Here, the transmission condition is fulfilled in a configuration with a local magnetic field maximum. The local magnetic field maximum at  $z_{\text{mirror}}$  ensures compliance with the transmission condition because the position of the longitudinal energy minimum is determined by the position of the negative maximum of the electrostatic potential.

be located at a significant distance from  $z_{\text{mirror}}$ , thus violating the first transmission condition (4.1). Therefore, a homogeneous magnetic field is required around  $z_{\text{mirror}}$ . In addition, the fast increase of the electrostatic potential at the entrance and exit region requires a correspondingly steep drop of the magnetic field in this region. Otherwise  $E_{\parallel}$  could drop below zero, resulting in an early retardation of the electron.

### III. Homogeneous electrostatic potential and local magnetic field maximum

A third possible field configuration features a local magnetic field maximum at  $z_{\text{mirror}}$  and two local minima at a certain distance from  $z_{\text{mirror}}$  (see figure 4.4). When moving away from  $z_{\text{mirror}}$ , the longitudinal energy is ensured to increase as the electric and magnetic terms in eq. (4.7) act together until the local magnetic field minima are reached. Beyond

these points, the magnetic term decreases  $E_{||}$ , however, the increasingly inhomogeneous electrostatic potential is able to compensate this effect.

### 4.3 The KATRIN large volume air coil system

The stray fields of the superconducting solenoids of the source and transport section as well as the detector side do not generate a magnetic stray field in the inner parts of the main spectrometer which fulfills the design requirements defined in the previous section. Therefore, an additional field forming element, the large volume air coil system is an essential design feature of the electromagnetic layout of the spectrometer section. It consists of two independent sub-systems, the earth magnetic field compensation system EMCS (section 4.3.1) and the low field correction system LFCS (section 4.3.2).

#### 4.3.1 Earth magnetic field compensation

As shown in figure 4.1, the low magnetic field region in the main spectrometer is distorted due to the earth magnetic field ( $B_x = 5 \cdot 10^{-6}$  T,  $B_y = -43.6 \cdot 10^{-6}$  T,  $B_z = 20.6 \cdot 10^{-6}$  T [232–234], with  $B_z$  pointing along the beam axis towards the detector). The most distinct distortion is caused by the large vertical earth magnetic field component  $B_y$ , which is non-negligible if compared to the magnetic stray field strength of  $B_{\text{sol}} \approx 230 \cdot 10^{-6}$  T generated by the solenoids. Therefore, a coil system for compensation of the earth magnetic field is required. The almost due north-south alignment of the KATRIN beam line makes it advantageous to compensate  $B_x$  and  $B_y$  separately, while leaving the  $B_z$  component uncompensated (for explanation see section 4.3.2). In principle, Helmholtz-type coil systems [235–237] as well as spherical cosine coil systems [238, 239] are known to produce very homogeneous magnetic fields. While the first solution would require a coil dimension larger than the size of the KATRIN building, the second would require a geometrical coil shape which is not compatible with the cylindrical geometry of the main spectrometer. Alternatively, a modified cosine coil system is realized, using loops on a cylindrical surface surrounding the main spectrometer. The individual loops are distributed according to a  $\cos(\theta)$ -current density distribution. An individual compensation of the horizontal and vertical earth magnetic field components is achieved by employing two independent systems of this kind [240–242]. If not explicitly stated otherwise, all simulations in the remainder of this work assume a perfectly compensated earth magnetic field. More information on technical details of the EMCS can be found in [150]. The resulting flux tube, compensated in the  $B_x$  and  $B_y$  components, is shown in figure 4.5. Obviously, the full flux of electrons is still not transmitted in the central low field region. Hence, a second air coil system is required, the low field correction system LFCS.

#### 4.3.2 Low field correction

The LFCS comprises 14 large coils (diameter 12.6 m), which are arranged coaxially with the main spectrometer vessel and the superconducting solenoids. Each coil is powered

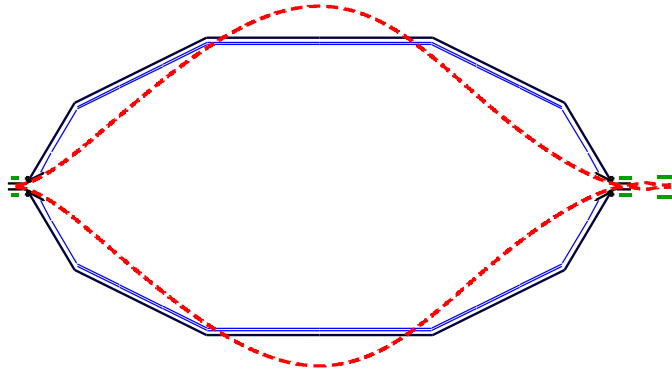


**Figure 4.5:** 191 Tcm<sup>2</sup> flux tube produced by superconducting solenoids with compensated  $B_x$  and  $B_y$  earth magnetic field components.

separately, which allows to individually adjust its field contribution. The corresponding coil properties and maximal applicable currents are listed in table 4.1. The possibility to tune the individual LFCS currents is essential to fulfill the magnetic design requirements. By increasing the central magnetic field strength to a minimal value of  $\sim 3 \cdot 10^{-4}$  T, the full flux tube is contained within the spectrometer and inner electrode geometry. In case of an exceedingly large background rate, an increased magnetic field strength would result in an improved magnetic shielding efficiency, however, at the cost of a reduced energy resolution. To study these interplays of background rate and energy resolution, the LFCS was designed to create a maximal magnetic field strength of  $\sim 12 \cdot 10^{-4}$  T at maximal current capacity, including solenoid stray fields.

In addition, the LFCS is a versatile design element to shape the magnetic field in a way that the transmission condition is satisfied. Firstly, without LFCS there is a magnetic field asymmetry with respect to the  $z = 0$  m mirror plane. This asymmetry is caused by the significantly larger magnetic moments of the detector side solenoids compared to the source side solenoids, which results in correspondingly larger stray fields coming from the detector side. In this case, when considering the highly homogeneous electrostatic potential in the center of the main spectrometer, the transmission condition could be violated, as outlined in section 4.2.2. With the LFCS, however, a compensation of this asymmetry is possible. For this purpose, the LFCS coil 14 (displayed in figure 4.6) is operated with a current direction opposite to all other coils. A full compensation requires a rather large number of current loops, which is not bearable by a single mechanical support structure. Hence, LFCS 14 was laid out as a double coil system, the so called *counter coil*.

Evidently, the currents of the individual LFCS loops have to be optimized in order to best fulfill the transmission condition. The flexibility of the LFCS is employed to maximum advantage if the magnetic field contribution of the LFCS is large. Accordingly, the overall magnetic field direction along the 70 m long KATRIN beam line (and along the main spectrometer) is chosen opposite to the earth magnetic field component  $B_z$ . Thus, the stray field of the superconducting solenoids is reduced by  $B_z$ , increasing the relative

### 4.3. The KATRIN large volume air coil system

**Table 4.1:** Overview of LFCS parameters.  $z_c$  is the axial position of the coil center,  $N_{\text{turns}}$  denotes the number of loops per coil and  $I_{\text{max}}$  the maximal applicable current (both current directions are possible). The *counter coil* (14) is a double coil powered by the same supply. All coils have an inner radius of 6.3 m, a radial thickness of 1.4 cm (single layer) to 2 cm (double layer) and an axial length of 19 cm.

coil index	$z_c$ (m)	$N_{\text{turns}}$	$I_{\text{max}}$ (A)
1	-6.79	14	100
2	-4.94	14	100
3	-4.04	8	125
4	-3.14	8	125
5	-2.24	8	125
6	-1.34	8	125
7	-0.44	8	125
8	0.46	8	125
9	1.35	8	125
10	2.26	8	125
11	3.16	8	125
12	4.06	14	100
13	4.95	14	100
14	6.60 and 6.90	14+14	70

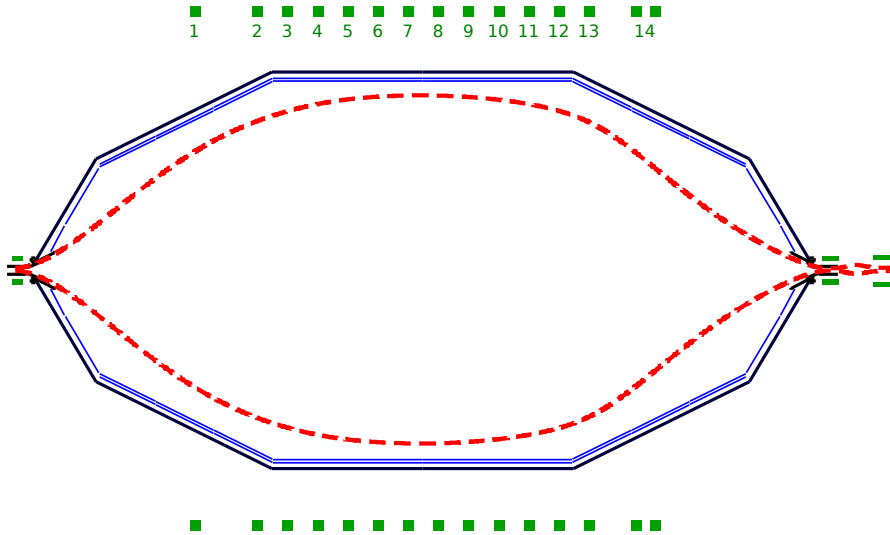


**Figure 4.6:** 191 Tcm<sup>2</sup> flux tube produced by superconducting solenoids and optimized LFCS (indicated by green boxes 1-14) currents, with compensated  $B_x$  and  $B_y$  earth magnetic field components.

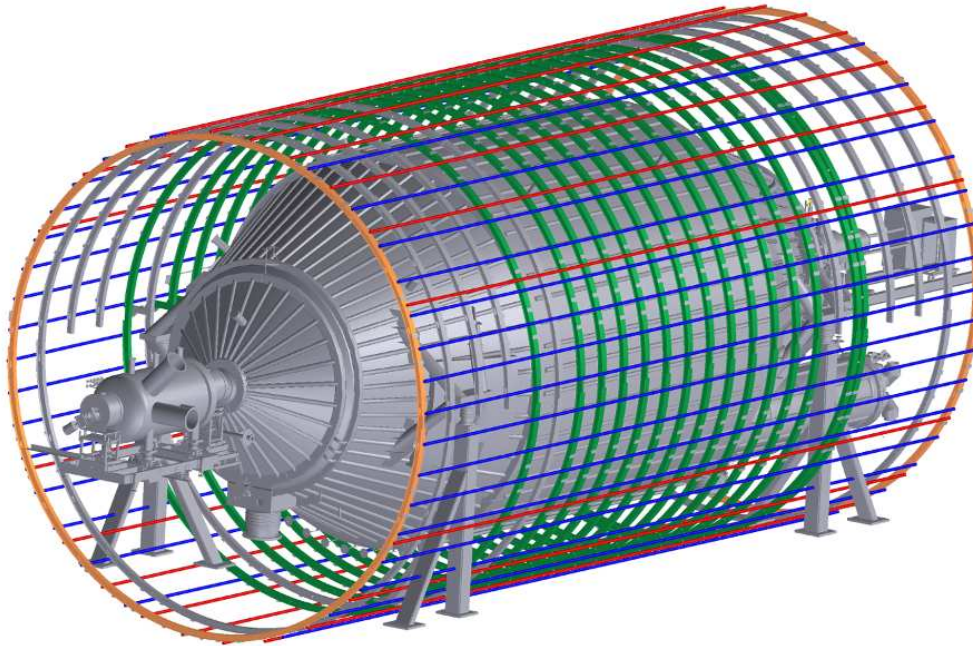


**Figure 4.7:** The main spectrometer surrounded by the large volume air coil system. The LFCS consists of the 14 green current loops. The blue and red straight segments belong to the vertical and horizontal EMCS current loops. They are connected via circular segments along the orange end rings.

influence of the LFCS.

Figure 4.6 shows the resulting flux tube for an optimized LFCS setup and compensated earth magnetic field, while figure 4.7 pictures the two sub-systems EMCS and LFCS of the large volume air coil system surrounding the main spectrometer.

The procedure, which is employed to optimize the LFCS currents according to the various needs of the experimentalists performing measurements with the main spectrometer, will be presented in the next section.

#### 4.4 Automated optimization of the LFCS currents

With the help of the LFCS, the magnetic field strength as well as its shape inside the main spectrometer can be adjusted in a highly versatile way in order to fulfill the magnetic design requirements. However, the parameter space is quite large when considering an ensemble of 14 individual coils, even when taking into account the current limits according to table 4.1. Therefore, an optimization by hand is no longer practical and does not necessarily yield the most suitable results. Instead, a mathematical optimization routine was developed, which automatically adjusts the coil currents to the user-defined requirements.

## Overview

In general, when addressing a mathematical (numerical) optimization [243–245], in a first step one has to formulate the actual problem. This task involves to define the design variables (free parameters) and the objective function (goal) which has to be optimized, usually with some external constraints on the design variables. More advanced problems generally comprise several goals and requirements to be fulfilled simultaneously, resulting in a multi-objective optimization problem. In our case, the design variables correspond to the 14 LFCS currents, while the goals are specified by the actual requirements on the magnetic field setup, such as perfect transmission characteristics or a specific minimal magnetic field strength. In the second step, the objective function has to be minimized by applying an appropriate minimization technique to find the optimal values of the design variables.

## The objective function

A convenient way to formulate the optimization problem is to introduce a composite objective function  $F$  as the weighted sum of the individual objectives  $O_k$ :

$$F = \sum_{k=1}^N \omega_k O_k. \quad (4.16)$$

The weights  $\omega_k$  are required to accommodate the relative importance and different scalings of the objectives. Following this, summands with large contributions to  $F$  are most strongly influenced by the subsequent minimization routine. In the case considered here, the requirements on the magnetic field are best described by the following objectives [151, 222, 223]:

1. *Magnetic field strength:* The user has to pre-define a magnetic field value  $B_{\text{input}}$  to be achieved in the main spectrometer center. The objective  $O_1$  is then realized by defining the squared deviation of the value  $B_0 = B(z = 0, r = 0)$  from  $B_{\text{input}}$ , where  $B_0$  has to be calculated from the 14 LFCS currents:

$$O_1 = (B_0 - B_{\text{input}})^2.$$

Thereby,  $B_{\text{input}}$ , as the sum of solenoid stray field and LFCS field contributions, is constrained to values smaller than 1.2 mT due to the existing LFCS current limitations.

2. *Mirror symmetry around  $z = 0$  m:* A second objective in the field layout (typically for tritium scanning or electron gun measurements) is to satisfy the transmission condition. In this case, the LFCS has to compensate the asymmetry induced by the stray fields of the solenoids. In this regard it is advantageous to recall that symmetry is characterized by magnetic field lines which are approximately perpendicular to the  $z = 0$  m mirror plane, so that the radial magnetic field component  $B_r$  vanishes. It is important that all field lines are affected by this

optimization. Therefore, an ensemble of  $n = 10$  points at  $z = 0$  and different radii  $r_p = 0.43p$  ( $p = 1, \dots, n$ ) is chosen (the maximal flux tube radius at  $z = 0$  m is about 4.3 m). At each point, the radial magnetic field component  $B_r(p)$  is computed. The largest value of these ten test points is chosen for the second objective:

$$O_2 = |B_r^{\max}|.$$

A perfect mirror symmetry can only be achieved in a limited region around the central plane of the main spectrometer due to the fact that when moving closer to the solenoids the LFCS field cannot compete any longer with the increasing magnetic stray field of the superconducting solenoids. However, this is of no concern because the transmission condition is most easily violated close to the center which can then be counteracted by the LFCS.

3. *Extremum values at  $z = 0$  m:* A third objective is given by the fact that for axially symmetric fields the radial magnetic field component on the axis ( $r = 0$ ) is always zero. Therefore, an additional condition which aids in fulfilling the transmission condition was employed. The previously discussed magnetic field setups with one global magnetic field minimum or a local maximum (section 4.2.2) feature an extremal point at the mirror plane. To check for an extremal point, the axial gradient field component  $\partial_z B$  is computed at different radii  $r_p = 0.43p$  with  $p = 0, \dots, 11$  (note that  $p$  starts at zero now as compared to the previous condition). The third objective is then defined as the maximal value  $|\partial_z B(p)|$ :

$$O_3 = |\partial_z B^{\max}|.$$

In our case, a numerical differentiation technique was used to obtain  $\partial_z B(p) \approx \frac{B(z=\epsilon, r=r_p) - B(z=-\epsilon, r=r_p)}{2\epsilon}$  with  $\epsilon = 0.1$  mm.

4. *Radial homogeneity:* Finally, as a fourth objective, a homogeneous magnetic field is required to be able to reliably calculate the transmission function for an individual detector pixel, even when considering that each pixel is extended in radial direction. Within this objective, the magnetic field strength at different radii  $r_p = 0.43p$  ( $p = 1, \dots, 10$ ) is computed and compared to the user-defined value  $B_{\text{input}}$  (see first objective). The resulting deviations are used to quantify as fourth objective the radial homogeneity:

$$O_4 = \sum_{p=1}^{10} (B(z = 0, r = r_p) - B_{\text{input}})^2.$$

The composite objective function is then formed by the weighted sum of the individual objectives. The weight factors have to be chosen according to the required importance of the objective, taking into account their different scalings. In general, the following weight factors of  $\omega_1 = 1$ ,  $\omega_2 = \omega_3 = 10$ , and  $\omega_4 = 1$  are recommended.

### Optimization

In the next step, the objective function (4.16) has to be minimized in order to obtain the optimized current values  $I_j$  ( $j = 1, \dots, 14$ ) for the 14 LFCS coils. A minimization usually requires a rather large number of iterations, which in turn necessitates a large number of magnetic field evaluations (the most time-consuming part of the optimization). However, the points where the magnetic field values have to be computed are fixed and hence are independent of the optimization. The total magnetic field at a specific point within the main spectrometer can be obtained as a superposition of the magnetic field contributions  $b_j$  of the individual coils. As the contributions  $b_j$  scale linearly with the applied currents  $I_j$ , it is sufficient to compute them once at each point with a current of 1 A. During the optimization, the total field is then obtained by the linear superposition

$$B = B_{\text{fix}} + \sum_{j=1}^{14} b_j I_j, \quad (4.17)$$

where  $B_{\text{fix}}$  denotes the contributions of the superconducting coils and of the horizontal earth magnetic field.

According to table 4.1, the LFCS currents cannot exceed certain limits for technical restrictions. These constraints also have to be taken into account for the optimization:  $I_{\text{min}} = -100$  A,  $I_{\text{max}} = 0$  A for LFCS 1-13 and  $I_{\text{min}} = 0$  A,  $I_{\text{max}} = 70$  A for LFCS 14. To do so, the following variable transformation was introduced

$$I_j = \frac{1}{2} \cdot I_{\text{min},j} + (I_{\text{max},j} - I_{\text{min},j}) \cdot (1 + \cos(x_j)). \quad (4.18)$$

By making use of the variable  $x_j$  for the optimization instead of the parameters  $I_j$  the constrained optimization is transformed into an unconstrained optimization, which can be achieved much easier.

The actual minimization is carried out by utilizing the Nelder-Mead downhill simplex method [209, 227], which has the great advantage that only the evaluation of functions is required, and not of their derivatives. It is based on the notion of a simplex, i.e. a geometrical figure with  $n+1$  points (vertices) in the  $n$ -dimensional design variable (LFCS currents) space. The simplex is initially created near the starting conditions and changed via various transformations (reflection, expansion, inner/outer contraction) during the minimization. Thereby the average function value at the simplex vertices continually decreases until the simplex arrives at a local (or global) minimum of  $F$ .

The result of this minimization strongly depends on the initial conditions, i.e. the chosen starting currents  $I_j$ , because of the huge number of potential local minima in the 14-dimensional variable space. Two approaches were contemplated to determine reasonable starting conditions:

- *optimization-by-eye*: Within this approach, the currents were changed by hand and the results (flux tube size, symmetry, transmission condition) were checked by eye, using appropriate visualizations (see section 4.5). After a few iterations of varying the currents it is possible to find a setup which approximately fulfills the design criteria.

- *Monte Carlo*: To perform a completely automated optimization, randomly chosen starting values could be used. With this method, it is also possible to map out a large fraction of the parameter space, with results corresponding to the several existing local minima. However, it is still necessary to check the quality of the results by eye.

While the *optimization-by-eye* method has the disadvantage that it requires the user to spend a certain time (usually  $\sim 30$  minutes per setup) to obtain the starting values, the results of the *Monte Carlo* method often feature large jumps in the currents of neighboring coils, implying unnecessary large currents for some coils. However, an additional fifth objective (e.g. total electric power of the coils) could prevent these jumps. The results presented in the next section were obtained with the automated optimization routine, presented here, utilizing starting conditions which were determined with the *optimization-by-eye* method.

## 4.5 Results

The optimization routine, which was explained in the previous section, was used to determine a variety of different magnetic field configurations. This section will show selected results, including setups at nominal magnetic field ( $\sim 3.5 \cdot 10^{-4}$  T) featuring a global magnetic field minimum or a local maximum at the  $z = 0$  m mirror plane (section 4.5.1), and a setup with an increased field strength of  $\sim 6 \cdot 10^{-4}$  T (section 4.5.2). All configurations were determined using contributions from all superconducting magnets of the source and transport section, see table 4.2.

**Table 4.2:** Overview of the magnetic contribution from the earth magnetic field as well as the superconducting coils of the KATRIN setup (WGTS, DPS, CPS, pre-spectrometer 1&2, pinch and detector magnet). The parameter  $z_c$  denotes the central axial position of the individual coil systems,  $B_c$  the magnetic field strength at this position and  $B_0$  the resulting contribution to the magnetic field strength in the center of the main spectrometer ( $z = r = 0$  m).

component	$z_c$ (m)	$B_c$ (T)	$B_0$ ( $10^{-4}$ T)
earth field	-	-	20.0
WGTS	-38.87	3.6	-9.7
DPS	-27.25	5.0	-16.3
CPS	-20.58	5.6	-38.2
PS1	-16.46	4.5	-18.5
PS2	-12.10	4.5	-46.5
PCH	12.18	6.0	-65.2
DET	13.78	3.6	-48.4

### 4.5.1 Nominal field strength

As outlined earlier, a small magnetic field strength in the center of the KATRIN main spectrometer in general results in a good energy resolution. At the same time, the field setup has to fulfill the key electromagnetic design requirements. The smallest magnetic field strength fulfilling all criteria hence is about  $3.5 \cdot 10^{-4}$  T. Table 4.3 shows the optimized currents for two configurations for this nominal field strength, one featuring a global magnetic field minimum at the  $z = 0$  m mirror plane and the other with a local maximum at  $z = 0$ .

In both cases the current of coil 14 is opposite to all other superconducting and LFCS coils. In this way LFCS 14 can compensate the magnetic field asymmetry which is induced by the larger stray fields of the pinch and detector coils. Figure 4.8 (a) shows the on-axis magnetic field strength around the  $z = 0$  plane for superconducting coils only (sc) and for LFCS coils in addition (sc+LFCS). Clearly, the symmetry is improved close to the  $z = 0$  mirror plane by the LFCS field contribution, as can be seen from the ratio  $B(+z)/B(-z)$  in figure 4.8 (b). Further away from  $z = 0$ , the relative contribution of the LFCS field is too small to significantly reduce the asymmetry.

Figure 4.9 shows the field lines of the  $191 \text{ Tcm}^2$  flux tube within the main spectrometer vessel for the two configurations at nominal field strength. In figure 4.9 (a) a setup with a global magnetic field minimum in the  $z = 0$  plane for all field lines is shown, while setup (b) features, on outer field lines, a local magnetic field maximum at  $z = 0$  and two local magnetic field minima further away from the mirror plane. In both cases, the flux tube fits well into the main spectrometer vessel with a safety distance of about 0.3-0.4 m to the inner wire electrode. Close to the  $z = 0$  m plane, the field lines show a very good symmetry, implying that the compensation by the LFCS is successful. Towards the detector side magnets, the flux tube has a smaller diameter compared to the source side due to the larger solenoid stray field.

The magnetic field strength along the corresponding field lines is shown in figure 4.10. Colors were chosen according to figure 4.9. The inlet shows a zoom into the region close to  $z = 0$ , where the difference between the two setups is most distinctive. The magnetic field strength on the outer field lines is dominated by the LFCS contribution, while for inner field lines the superconducting coils dominate. As solenoids intrinsically produce a magnetic field featuring a local minimum close to  $z = 0$ , local magnetic field maxima can only be achieved on outer field lines.

Such local maxima on outer field lines are of distinct advantage when considering the transmission condition. As figure 4.11 shows, the inner electrodes create local minima in the electrostatic potential amplitude between two module rings<sup>2</sup> because the more positive potential of the vessel is less shielded. Correspondingly, the potential is maximal in the middle of a ring, and the longitudinal energy  $E_{||}$  is reduced to a minimum value. Hence, at these places, a violation of the transmission condition could occur if the magnetic field is not adjusted properly. A visualization of the behavior of  $E_{||}$  can be found in figure 4.12. The longitudinal energy was computed for an electron starting in

---

<sup>2</sup>A wire electrode module ring spans about 1.8 m in axial direction.

**Table 4.3:** Overview of optimized LFCS current settings. For coil parameters, see table 4.1. Two setups with nominal magnetic field strength of  $\sim 3.5 \cdot 10^{-4}$  T are shown, one featuring a global magnetic field minimum (Setup 1) at  $z = 0$  and the other with two local magnetic field minima further away from  $z = 0$  (Setup 2). The third setup was computed for an increased central field value of  $\sim 6 \cdot 10^{-4}$  T with a local magnetic field maximum (Setup 3).

coil index	$I_{\text{Setup1}}$ (A)	$I_{\text{Setup2}}$ (A)	$I_{\text{Setup3}}$ (A)
1	-11.2	-0.5	-99.2
2	-15.3	0.0	-4.0
3	-7.9	-4.8	-18.3
4	-13.4	-7.1	-40.3
5	-12.2	-6.6	-5.4
6	-24.2	-19.4	-92.1
7	-17.1	-57.2	-46.0
8	-20.3	-51.2	-86.4
9	-18.5	-22.7	-57.0
10	-23.1	-12.5	-17.5
11	-21.9	-7.7	-30.4
12	-18.1	-16.8	-69.6
13	-13.3	-15.9	-1.0
14	27.3	42.1	8.5

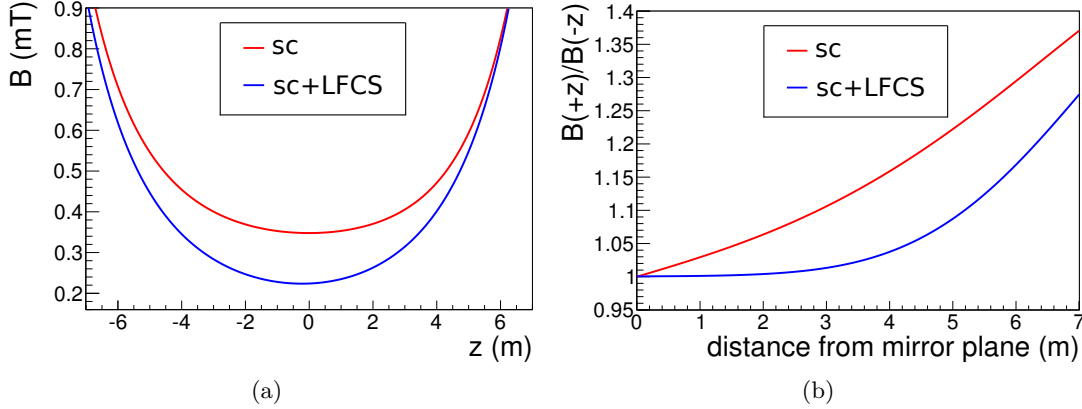
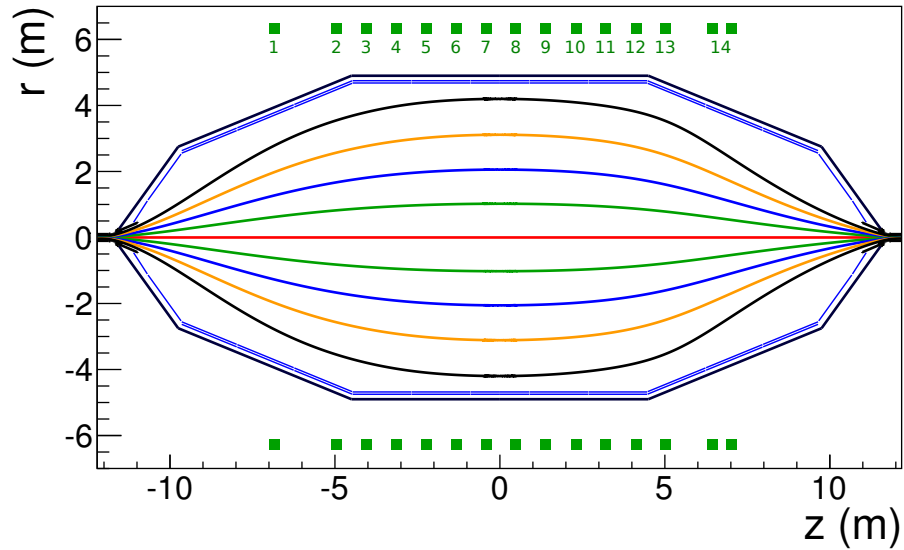
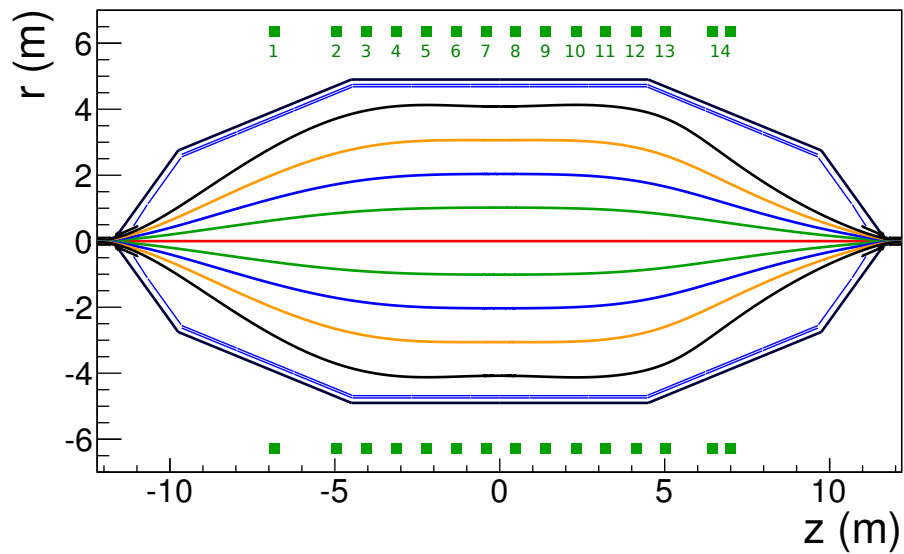


**Figure 4.8:** Magnetic field asymmetry in the main spectrometer. (a) On-axis magnetic field strength for superconducting coils only (sc) and for LFCS coils in addition (sc+LFCS). (b) The field ratio  $B(+z)/B(-z)$  is displayed for both cases shown in (a). Clearly, the symmetry is improved close to  $z = 0$  by the LFCS coils.

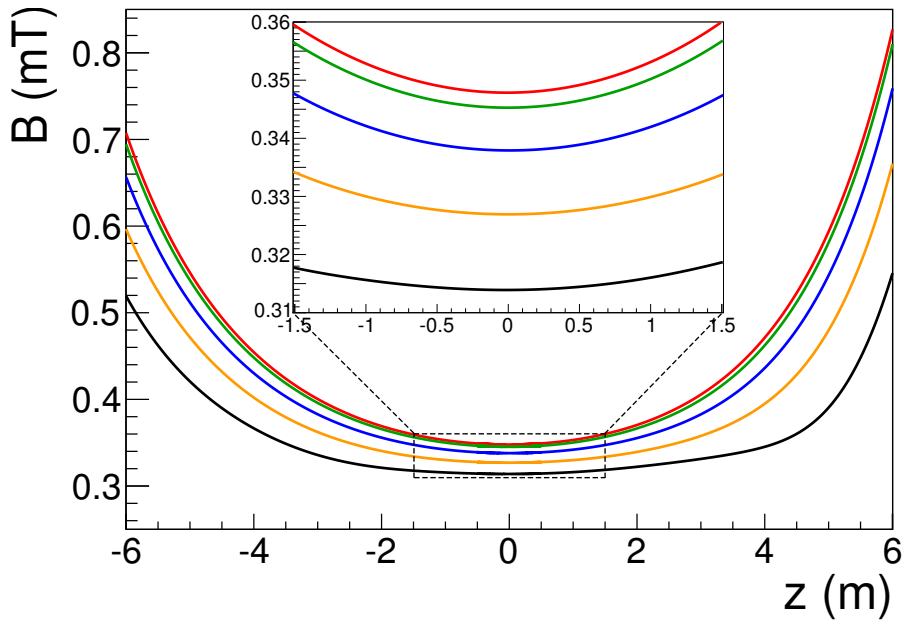


(a) Global magnetic field minimum solution

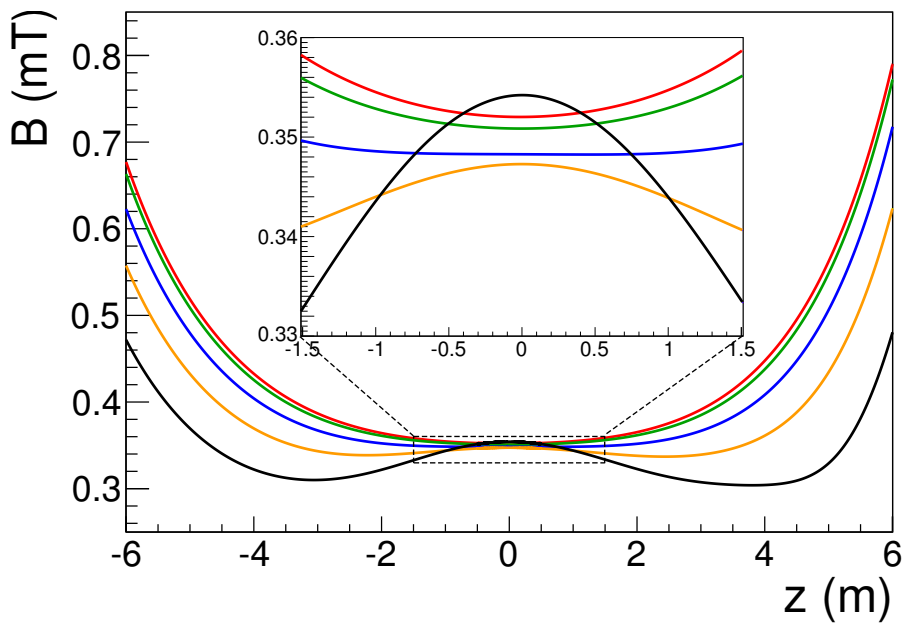


(b) Local magnetic field maximum solution

**Figure 4.9:** Magnetic field lines of the 191 Tcm<sup>2</sup> flux tube. (a) Configuration with a global magnetic field minimum at  $z = 0$ . (b) Configuration with a local maximum at  $z = 0$  m and two local minima at  $z \approx 3$  m for the outer field lines. The LFCS coil cross sections are not to scale but increased for better visibility.

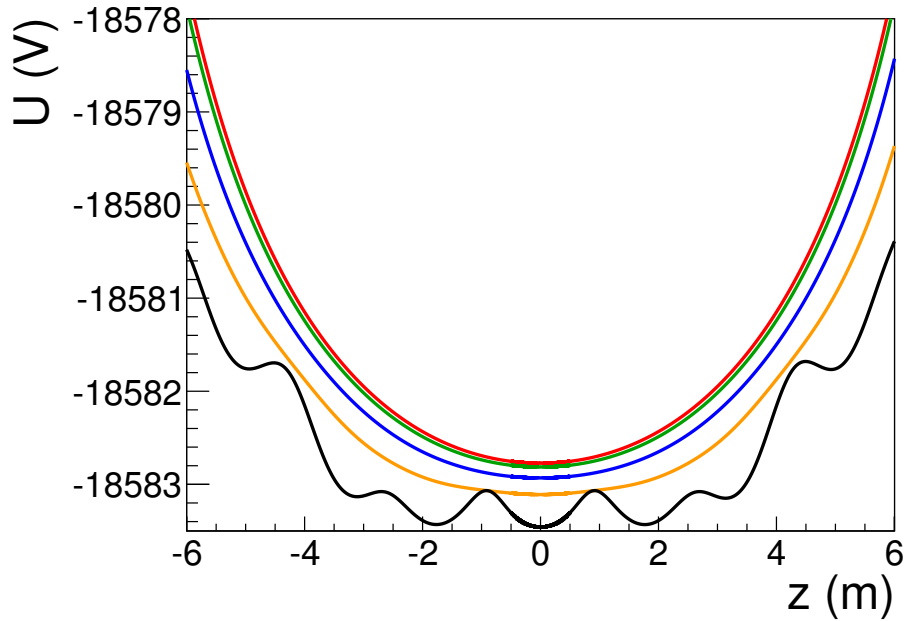


(a) Global magnetic field minimum solution

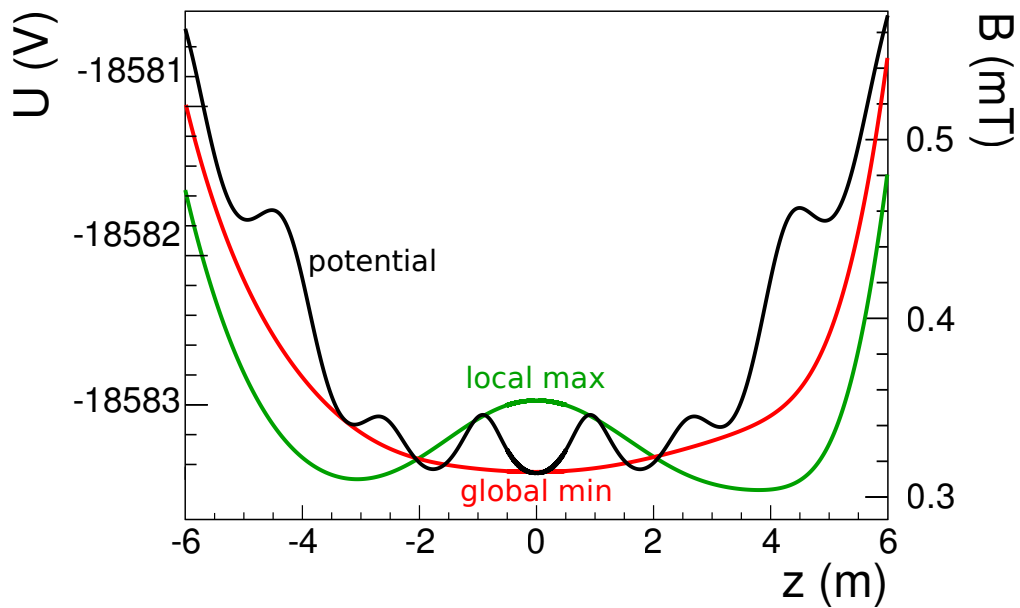


(b) Local magnetic field maximum solution

**Figure 4.10:** Magnetic field strength along the field lines shown in figure 4.9. (a) Configuration with a global magnetic field minimum at  $z = 0$  for all field lines. (b) Configuration with a local magnetic field maximum at  $z = 0$  for outer field lines. The inlets show a zoom into the region [ $z = -1.5$  m,  $z = 1.5$  m].

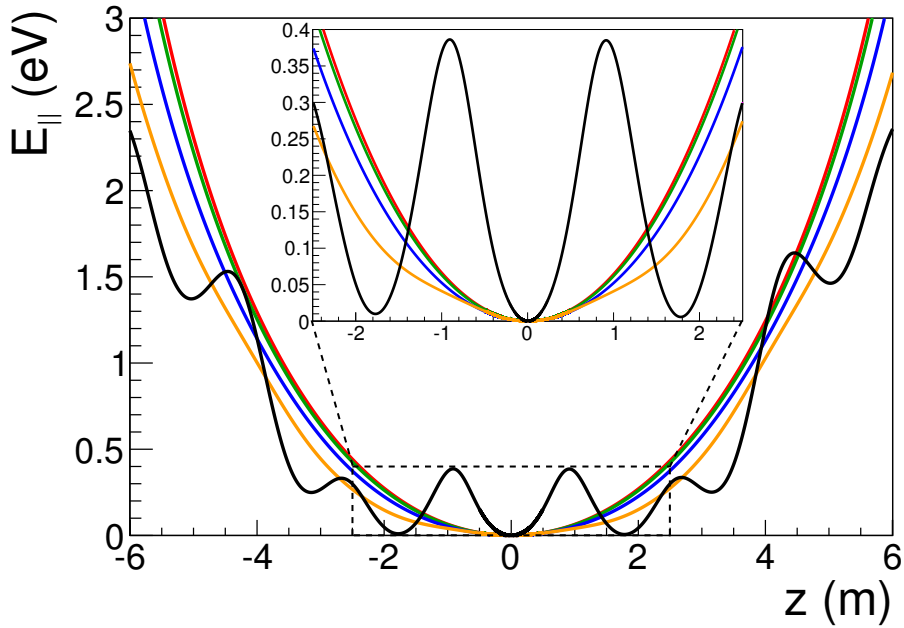


(a) Electrostatic potential

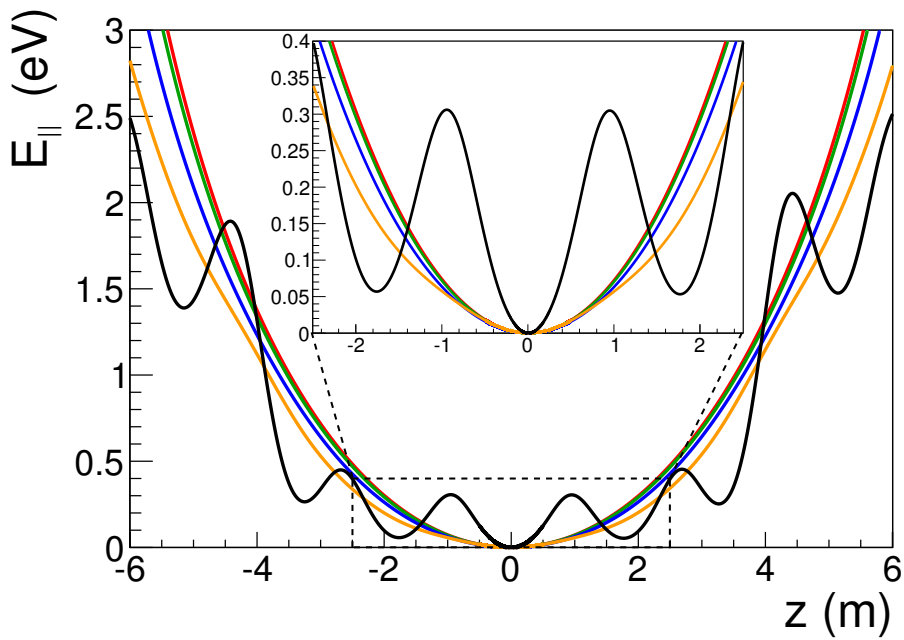


(b) Interplay between potential and magnetic field

**Figure 4.11:** Electrostatic potential in the main spectrometer and interplay with magnetic field. (a) Potential along the field lines shown in figure 4.9. The potential setup can be found in table 4. Local potential maxima occur at positions where the more positive vessel potential is shielded less efficiently due to the gap between two wire module rings. (b) Interplay between electrostatic potential and magnetic field on the outer field line. The local magnetic field maximum solution fulfills the transmission condition more reliably than the global magnetic field minimum solution.



(a) Global magnetic field minimum solution



(b) Local magnetic field maximum solution

**Figure 4.12:** Longitudinal energy along the field lines shown in figure 4.9. The computation was performed for an electron, which starts with the maximal polar angle  $\theta = 51^\circ$  in the source ( $B_s = 3.6$  T). Obviously, the local maximum solution (b) yields a larger safety margin, especially on the outer (black) field line, than the global minimum solution (a).

the source ( $B_s = 3.6$  T) with maximal polar angle  $\theta = 51^\circ$  and with the transmission energy  $E_{\text{tr}}$ , calculated according to eq. (4.8). The highest possible starting angle was chosen because fulfilling the transmission condition, i.e.  $E_{\parallel} > 0$  everywhere but at the  $z = 0$  plane, is most critical for large angles as the magnetic transformation  $E_{\perp} \rightarrow E_{\parallel}$  has to match the axial distribution of the electrostatic potential, which reduces  $E_{\parallel}$ . In both cases, the transmission condition is fulfilled. The local energy minima coincide with the potential maxima of figure 4.11. A zoom into the region  $z \in [-2.5 \text{ m}, 2.5 \text{ m}]$  is shown in the inlays. The transmission condition would be violated if the local minima would result in  $E_{\parallel}$  dropping below zero, which is not the case for both setups. However, the local maximum setup yields a larger safety margin and hence occurs to be more stable with regard to small disturbances. In the case of one global magnetic field minimum, there are three minima of  $E_{\parallel}$  in the central 5 m of the spectrometer. The global minimum occurs, as required at  $z = 0$  m, but the two side-minima of  $E_{\parallel}$  at  $z = \pm 1.8$  m are only separated from the global minimum by  $\sim 10$  mV. For the case of the two minima solution, the two side-minima of  $E_{\parallel}$  remain, however, separated by  $\sim 50$  mV from the global one.

A more detailed evaluation of the quality of the magnetic field setup under investigation can be performed when examining the spatial distribution of the analyzing points (i.e. the coordinates where  $E_{\parallel}$  reaches zero). Figure 4.13 compares the results for the two configurations (global minimum, local maximum). Four representative starting angles are considered, which are equally distributed between  $\theta_{\text{min}} = 0^\circ$  and  $\theta_{\text{max}} = 51^\circ$ . The axial spread of the analyzing points increases with increasing starting polar angle. However, the maximal distance to the  $z = 0$  m mirror plane is  $< 2.5$  mm for both setups. When optimizing the LFCS currents by hand, maximal deviations of  $\sim 20$  cm were obtained. Hence, the mathematical optimization yields an improvement by two orders of magnitude. A decreased axial distribution of the analyzing points can be directly translated into a decreased uncertainty of the analyzing potential and magnetic field. While

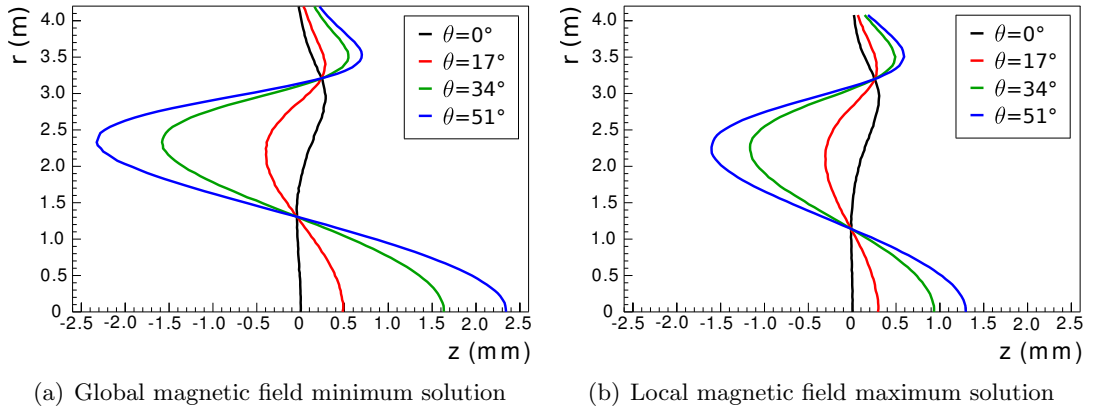


**Figure 4.13:** Spatial coordinates of the analyzing points for different starting polar angles  $\theta$ . A negligible spread of  $< 2.5$  mm in axial direction is observed for both setups. The local maximum solution yields slightly improved results.

a magnetic field setup which was optimized by hand can result in an uncertainty of the analyzing potential of about 20 mV, the mathematical optimization reduces this value by two orders of magnitude. Any further improvement of this analyzing point spread is not meaningful since small magnetic and electric field disturbances will influence the results.

The final parameter to be investigated is the radial homogeneity of the magnetic field in the  $z = 0$  plane, which is shown in figure 4.14. A configuration with a local magnetic field maximum at  $z = 0$  yields a better radial homogeneity than in the case of a global minimum. In principle, this is of advantage when considering the transmission function because the energy resolution decreases for very inhomogeneous magnetic fields. However, the radial segmentation of the detector already reduces this distorting effect to a level below a value where it would impact the neutrino mass analysis.

More importantly, the local maximum solution features an increasing field strength towards larger radii, while the magnetic field decreases for the global minimum solution. As the magnetic field intrinsically acts as dominant shield against low-energy secondary electrons from the vessel surface, shielding is more effective for larger field values close to the vessel. Therefore, an enhanced background suppression is expected for the local maximum setup. As a drawback, the local magnetic field minima inherently act as magnetic mirror traps for electrons which are produced within these minima. According to eq. (2.6), only electrons with polar angles above a certain threshold are trapped, independently of their starting kinetic energy. This threshold depends on the ratio of minimal to maximal magnetic field strength within the trap. As the local magnetic field

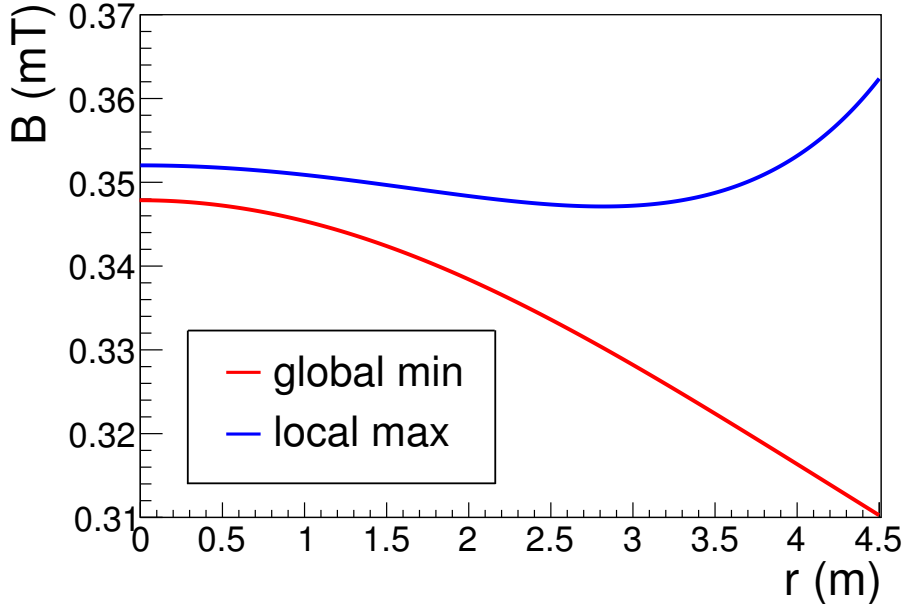


**Figure 4.14:** Radial magnetic field inhomogeneity at  $z = 0$ . The configuration with a local magnetic field maximum at  $z = 0$  shows a better homogeneity, which is advantageous for the transmission function analysis (small variation within a detector pixel).

minimum is very shallow, the corresponding starting polar angle has to be very large in order to result in a trapped electron. Furthermore, the main spectrometer itself is a large magnetic mirror trap. Section 7.1 will show that all electrons with a transversal kinetic energy above a certain trapping threshold are trapped by this large volume trap anyway. Hence, only for electrons with extremely small kinetic energies ( $< 1$  eV), additional trapping could occur within the local magnetic field minima. As the kinetic energy of these electrons is substantially smaller than the ionization threshold of  $\sim 15$  eV, they are of no concern for the background within the KATRIN main spectrometer. The overall performance of the two generic field configurations discussed above will be investigated within the upcoming commissioning measurements.

### 4.5.2 Increased magnetic field strength

During the early commissioning measurements of the spectrometer as well as later of the entire beam line, it could turn out that the standard magnetic field strength of  $3.5 \cdot 10^{-4}$  T is not sufficient to fulfill the transmission condition while at the same time maintaining an ultra-low background rate of  $< 10^{-2}$  cps. In that case, a higher magnetic field strength would be advantageous to meet both of these requirements albeit at the cost of a reduced energy resolution of the spectrometer.

An exemplary value of  $6 \cdot 10^{-4}$  T for the central magnetic field strength was chosen to underline specific differences relative to the setup featuring the nominal field values. Figure 4.15 shows the field lines of the standard 191 Tcm<sup>2</sup> flux tube. The increased central field strength reduces the diameter of the flux tube in the main spectrometer center. Correspondingly, the distance to the vessel surface, where secondary electrons are created, is increased which strongly suppresses electron motion into the sensitive volume. Furthermore, the axial symmetry of the flux tube is improved as the EMCS provides a better earth magnetic field compensation in the central region of the main spectrometer. In general, a higher magnetic field provides a larger magnetic shielding efficiency because the relative influence of any disturbing magnetic field is reduced.

The magnetic field strength along the field lines is shown in figure 4.16. As the majority of the field strength is provided by the LFCS coils, a setup with a local magnetic field maximum on the outer field lines is achieved automatically in most cases when running the mathematical optimization. Correspondingly, a very good radial homogeneity of the magnetic field is achieved.

At large distances to the inner electrodes, the influence of the single wires and holding structures is negligible. Consequently, the absolute value of the electrostatic potential along the field lines increases very smoothly towards the main spectrometer center, as shown in figure 4.17 (left). This behavior is reflected directly in the distribution of the longitudinal energy, see figure 4.17 (right). A particularly attractive behavior of such a setting is the fact that no local side-minima of  $E_{\parallel}$  are observed, i.e. fulfilling the transmission condition is greatly simplified with such a setup. A central magnetic field strength of  $4 \cdot 10^{-4}$  T is sufficient to get rid of the local minima of  $E_{\parallel}$ .

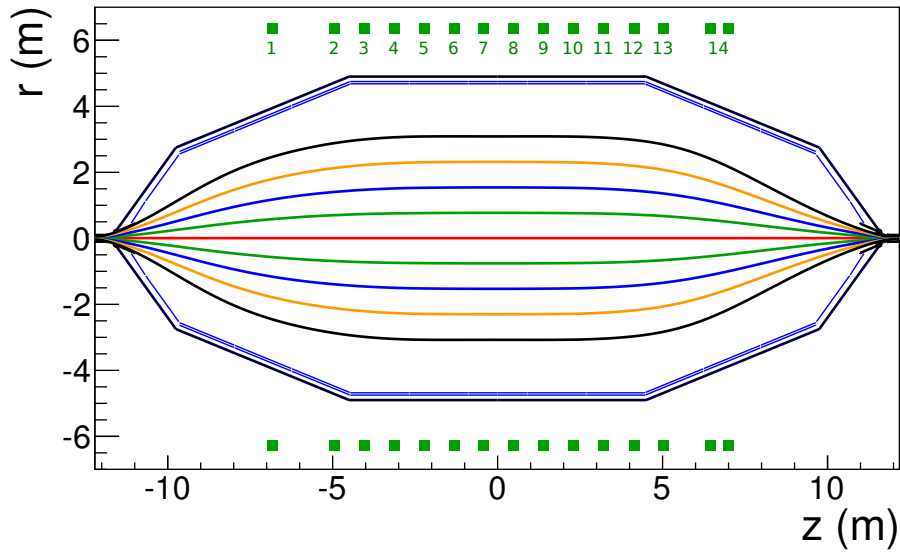


Figure 4.15: Field lines in the main spectrometer vessel for a  $6 \cdot 10^{-4}$  T setup.

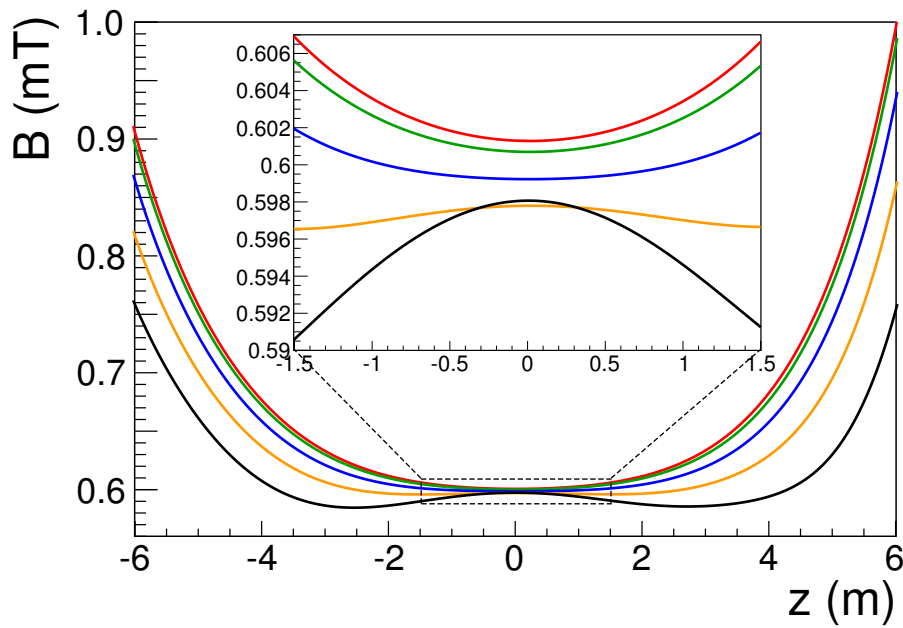
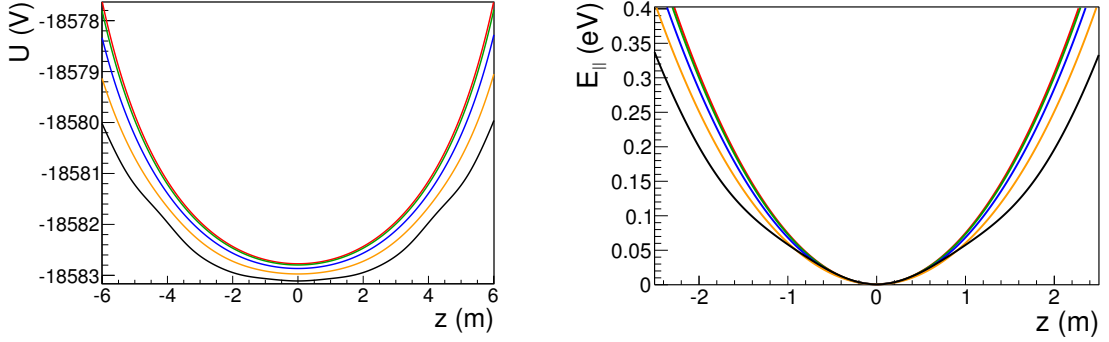


Figure 4.16: Magnetic field strength along the field lines shown in figure 4.15.



**Figure 4.17:** Electrostatic potential (left) and longitudinal kinetic energy (right) along the field lines shown in figure 4.15.

### 4.5.3 Conclusion

In addition to these generic examples of LFCS current settings, several other configurations have been calculated. Especially during the upcoming main spectrometer commissioning measurements, not all superconducting coils of the full KATRIN setup will be available. With the mathematical optimization presented above, a determination of suitable magnetic field setups is possible on a time-scale of minutes. Therefore, new setups, depending on the magnetic field sources which are available for a certain measurement, can be computed quickly. In this context, XML-based input files enable the user to easily configure the routine to accommodate the requirements on the sought-after setup.

Three different magnetic field setups were presented. For the standard magnetic field strength of  $\sim 3.5 \cdot 10^{-4}$  T in the center of the main spectrometer, either a setup featuring a global magnetic field minimum at the  $z = 0$  m plane or a setup with two local minima further away from  $z = 0$  is available. The setup with two local minima is advantageous with regard to the transmission properties, but will create tiny magnetic mirror traps for sub-eV electrons. If neither of these setups achieves sufficiently good transmission and/or background properties, an alternative setup with an increased magnetic field strength in the main spectrometer center can be employed. Here, a configuration with a central field strength of  $\sim 6 \cdot 10^{-4}$  T was presented, but any field strength up to a maximal value of  $\sim 10 \cdot 10^{-4}$  T can be implemented with the LFCS.

# Study of the main spectrometer transmission properties

As outlined earlier, the transmission function for electrons in the main spectrometer has to be known with a precision of 1% to obtain the reference neutrino mass sensitivity of 200 meV. This is challenging, both on the hardware side (quasi-monoenergetic electron emitter) as well as on the theoretical side where detailed field calculation and particle trajectory programs such as KASSIOPEIA are required. Beginning with an overview of the importance of transmission measurements in section 5.1, it will then be discussed how the transmission function depends on the source and spectrometer properties. It is essential that their effects have to be understood and disentangled from each other. Section 5.2 will thus show which experimental parameters are important and demonstrate their manifestations. Within section 5.3, a measurement and analysis strategy will be proposed which allows to reliably determine the different parameters independently from each other. Finally, section 5.4 will summarize the various systematic effects which influence the transmission function.

## 5.1 Overview of transmission function measurements at KATRIN

Transmission function measurements at KATRIN will be based on an angular resolved electron gun (e-gun) [183, 246] as a source for quasi-mono-energetic ( $\sim 0.2$  eV spread) electrons. The core features of such an electron emitter, a small angular and energy spread, will allow to investigate and characterize the main spectrometer as a MAC-E filter in great detail.

### **Integrity of the wire electrode system**

An initial check to be performed during the commissioning measurement phase as well as before regular neutrino runs is an integrity test of the inner electrode system. It has to be assured that e.g. no wires are broken or hanging down. As the influence of the inner electrode system on the electrostatic potential in the main spectrometer volume is most significant close to the wires, the measurements will focus on electron trajectories at large radii. To do so, the central magnetic field can be decreased, if necessary, so that the outermost field lines, ending at the outer detector pixels, reach close to the wires. Alternatively, the earth magnetic field compensation system can be used to shift the flux tube in an arbitrary radial direction. A large number of measurement points is required in order to scan the whole azimuthal circumference of about 30 m with a precision of a few mm to cm.

In this context it is important to recall that a single detector pixel has an azimuthal coverage of about  $30^\circ$ , while a single electrode module only spans about  $18^\circ$ . Any inhomogeneity, which is induced by the wires themselves or by the support structures, will influence the overall transmission function of a pixel. Therefore, measurements with sub-pixel resolution would be useful to investigate such small scale effects. However, their feasibility depends on the actual size of the electron beam, which is required to be smaller than a detector pixel. Furthermore, effects at pixel boundaries, such as charge sharing between pixels, have to be measured and taken into account.

### **Optimization and determination of the transmission properties**

As outlined in section 4, the main spectrometer transmission properties are very sensitive to the electromagnetic field setup. Although simulations can provide test setups with theoretically optimal transmission properties, the input parameters, such as the electrode geometry, are approximative in their nature and perturbing effects are either neglected or modeled with limited precision. Therefore, the properties of a specific electromagnetic layout have to be tested within dedicated measurements. When a configuration is found which fulfills the transmission condition while at the same time keeping the background level sufficiently low, a detailed determination of the transmission function for the full flux tube has to be performed. However, during the initial main spectrometer commissioning, not all components in the KATRIN beam line, which contribute to the overall magnetic field configuration, will be operational. The commissioning schedule of KATRIN, with the subsequent putting into operation of the DPS and CPS, and finally the WGTS, allows to study their impact on the spectrometer transmission. Once the final configuration is implemented, a full-scale study of both transmission as well as response function will be initiated, utilizing an e-gun placed within the rear section (see section 2.1.2). However, to study inhomogeneities within a pixel, measurements with sub-pixel resolution would be required, so that these effects have to be determined with the help of simulations.

### Validation of the simulation software

The simulation tools, which are included in the KASPER package (see section 3), allow to precisely calculate the electromagnetic fields within the volume of the main spectrometer. However, the simulation results strongly depend on the accuracy of geometrical input data. The inner electrode system was installed with a positioning precision on the order of mm to cm (compared to a vessel diameter of 10 m). Detailed position measurements of each module were performed. The subsequent initial bake-out procedure<sup>1</sup> in early 2013 (as well as further bake-out procedures later on) could result in slight changes of the wire module positions. As the final positions cannot be measured anymore since the vessel is closed, the software geometry has to be validated with the help of measurements. To do so, data taken during the optimization of the transmission properties of the main spectrometer will be compared to equivalent simulations. Any possible deviation needs to be compensated by either an appropriate change of the input parameters or by an implementation of so far unaccounted for disturbing effects, e.g. additional magnetic field sources such as magnetic materials in the surrounding building.

As pointed out above, the transmission measurements alone will not be able to cover the full parameter space. Therefore, it is of vital importance to be able to simulate the full electromagnetic setup.

### Investigation of electron adiabatic behavior

The MAC-E filter principle is based on an adiabatic transport of electrons through the main spectrometer. In case of violation of adiabaticity, the adiabatic invariant is no longer a constant, i.e. the collimating process does not obey eq. (2.3) anymore. The degree of adiabaticity strongly depends on the initial conditions of an electron (e.g. its starting energy and angle). Consequently, when enlarging this parameter space, the transmission function can be modified by much more complex relations. It is useful to recall that the main spectrometer was designed to provide adiabatic guiding particularly for electrons with rather low surplus energies (several tens of eV). When using high surplus energies of several keV, though, a non-adiabatic electron motion can result. This is of particular importance in the context of background due to stored high-energy electrons (see section 7 and Appendix .4). Furthermore, as the KATRIN experimental setup could be used to study the existence of keV sterile neutrinos, an adiabatic transport of electrons with up to 18 keV surplus energy would be required. Due to the well-defined starting conditions of electrons from an e-gun, any non-adiabatic behavior can be studied by a comparison of dedicated measurement and simulation results.

### Time-of-flight studies

The purpose of time-of-flight (ToF) studies is twofold [247]. Firstly, they can be used as a diagnostic tool for the main spectrometer properties not only in the analyzing plane but

---

<sup>1</sup>Bake-out refers to a measure to improve the vacuum conditions of the main spectrometer by heating the vessel up to 300°C to remove water and other impurities from the inner surface.

along the whole electron trajectory. Within these measurements, electrons with energies of several eV above the transmission threshold will be created in a pulsed mode of the e-gun. Short pulses with a typical time scale of  $\mathcal{O}(20 \text{ ns})$ , together with a good timing resolution of the detector of  $\mathcal{O}(50 \text{ ns})$ , will allow to precisely determine the electron's time-of-flight, which is expected to be  $\mathcal{O}(\mu\text{s})$ . As the time-of-flight is an integral over the entire electron path, measurements at different electromagnetic setups yield information on the deceleration and acceleration pattern.

A second application is the determination of tritium  $\beta$ -decay electron energies by a MAC-E filter operated in ToF mode. The time-of-flight  $t_F$  of an electron on a certain field line within a particular electromagnetic configuration is defined solely by its starting energy and angle relative to the field line if the particle motion is adiabatic. Generically, a determination of  $t_F$  requires a start and a stop signal. While the stop signal is given by the detector timing signal, to identify the start time is much more challenging if the source is not intrinsically pulsed like in the case of a UV-based pulsed e-gun. The extended gaseous tritium source of KATRIN could be operated in a pulse-like mode by frequently applying a high voltage with a very steep rise and fall time, typically at the pre-spectrometer. However, the energy resolution as well as the luminosity would be decreased in this mode.

## 5.2 Parameters influencing the transmission function

As outlined above, the transmission function depends on different source as well as spectrometer properties. Their close relation is best discussed by the transmission energy (4.8):

$$E_{\text{tr}} = \frac{q(U_{\text{Pa}} - U_{\text{s}})}{1 - \frac{B_{\text{Pa}} \cdot (\gamma_{\text{s}} + 1)}{B_{\text{s}} \cdot (\gamma_{\text{Pa}} + 1)} \cdot \sin^2(\theta_{\text{s}})}. \quad (5.1)$$

On the one hand, the source determines the starting energy  $E_{\text{s}}$  and polar angular  $\theta_{\text{s}}$ , where it is useful to recall that transmission occurs for energies  $E_{\text{s}} > E_{\text{tr}}$ . On the other hand, the analyzing potential  $U_{\text{Pa}}$  and magnetic field  $B_{\text{Pa}}$  depend on the specific electromagnetic setup of the main spectrometer. In the following, the different influences will be shown qualitatively, pointing out key issues which have to be taken into account in a transmission function measurement.

### 5.2.1 Spectrometer properties

At first, the case of an 'ideal' source is discussed, emitting mono-energetic electrons at one definite polar angle. In this case, the transmission function is given by a step function, as shown in figure 5.1. Following eq. (5.1) the transmission energy for a starting angle  $\theta_{\text{s}} = 0^\circ$  is defined by the electrostatic potential only. Electrons with larger starting angles require a certain surplus energy due to the limited energy resolution of the spectrometer, which results from the imperfect transformation of transversal energy into longitudinal energy  $E_{\perp} \rightarrow E_{\parallel}$ . For a source which is situated in the center of the second pre-spectrometer magnet PS2 ( $B_{\text{s}} = 4.5 \text{ T}$ ), it follows from eq. (2.6) that a starting angle

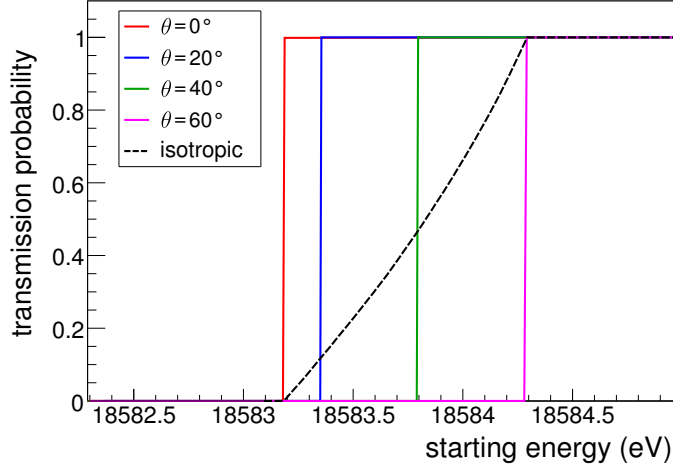


**Figure 5.1:** Transmission function for an ideal angular selective, mono-energetic source (sharp transmission lines occur at  $\theta = 0^\circ - 60^\circ$ ) and an isotropic, mono-energetic source (broad transmission function). For this simulation, a main spectrometer electromagnetic configuration characterized by the following parameters was used:  $U_{P_a} = -18583.19$  V,  $U_s = 0$  V,  $B_{P_a} = 3.5 \cdot 10^{-4}$  T,  $B_s = 4.5$  T,  $B_{\max} = 6$  T.

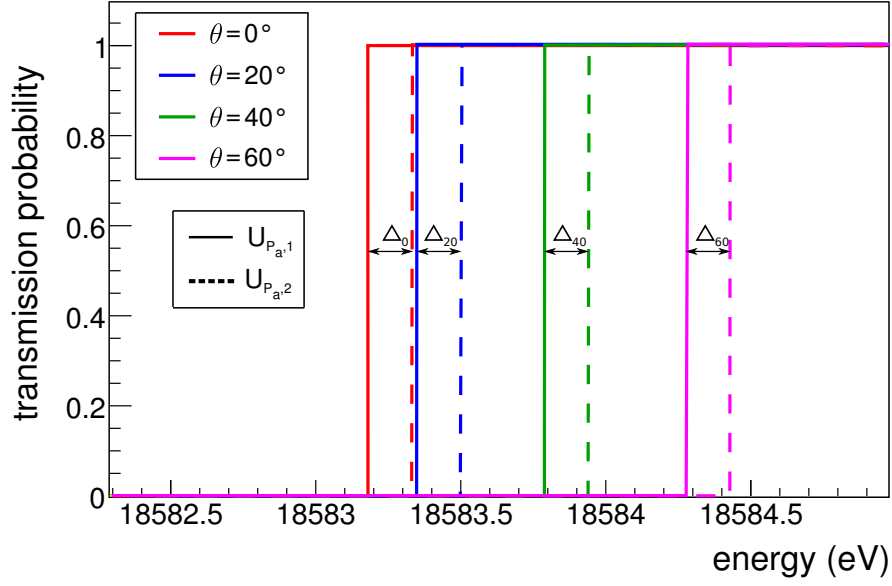
of  $\theta_s = 60^\circ$  corresponds to the maximal angle  $\theta_{\max}$  where electrons are not magnetically reflected by the pinch magnetic field strength  $B_{\max} = B_{\text{pinch}} = 6$  T. The energy difference between the minimal and maximal transmitted starting angle determines the energy resolution, which is  $\sim 1.1$  eV in a configuration with  $B_{P_a} = 3.5 \cdot 10^{-4}$  T. The ideal transmission function of figure 5.1 can be smeared out due to instrumental effects arising from variations or fluctuations of the electrostatic potential or the magnetic field (more details will be given below). Figure 5.2 (a) shows that a shift of the electrostatic potential translates directly into a shift of the transmission line at a specific starting polar angle. For small changes of the electrostatic potential, the effect is approximately independent of the starting polar angle, as can be seen from eq. (5.1)<sup>2</sup>. Consequently, the total transmission width, given by  $E_{\text{tr}}(\theta_{\max}) - E_{\text{tr}}(\theta_{\min})$ , does not change.

The influence of an increased magnetic field strength, as shown in figure 5.2 (b), has a different effect on the transmission lines. While the transmission function for  $\theta_s = 0^\circ$  is not affected by the analyzing magnetic field strength (due to  $\sin(0^\circ) = 0$ ), transmission lines corresponding to larger angles are shifted towards higher transmission energies. An increasing shift is observed towards larger  $\theta_s$ , which results in a broadening of the total transmission width and, hence, a decreased energy resolution.

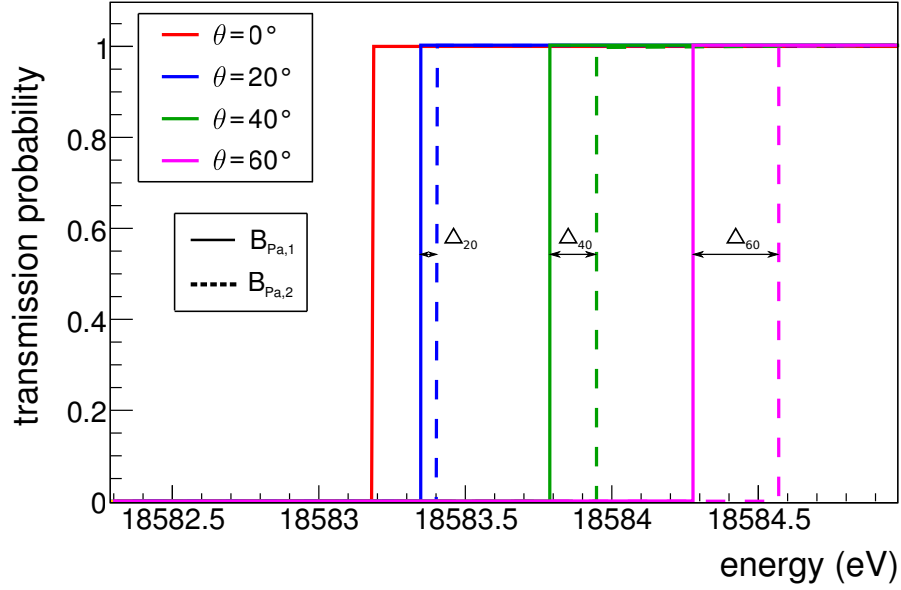
There are various possibilities how the electrostatic potential or the magnetic field in the main spectrometer can be influenced:

- Of major importance are the intrinsic radial inhomogeneities ( $U_{P_a(r)}$ ,  $B_{P_a(r)}$ ), which lead to a broadening of the total transmission width for an individual de-

<sup>2</sup>Note that this only holds within an interval where the electron's relativistic Lorentz factor is approximately constant.



(a) Influence of the electrostatic potential



(b) Influence of the magnetic field

**Figure 5.2:** Transmission function for an ideal angular selective, mono-energetic source as influenced by the electromagnetic setup of the main spectrometer. (a) Influence of a shift of the electrostatic potential. All transmission lines are shifted equally by  $q\Delta U = q(U_{P_{a,2}} - U_{P_{a,1}}) = 150$  meV. (b) Influence of an increased magnetic field strength ( $B_{P_{a,1}} = 3.5 \cdot 10^{-4}$  T,  $B_{P_{a,2}} = 4.5 \cdot 10^{-4}$  T). Due to the  $\sin^2(\theta_s)$  dependence of eq. (5.1), electrons with larger starting polar angles experience an increased shift of their transmission energy  $E_{tr}$ , which results in a larger total transmission width  $E_{tr}(\theta_{max}) - E_{tr}(\theta_{min})$ .

tector pixel.

- Remnant fields from magnetic materials of the experimental hall or remaining non-compensated contributions of the earth magnetic field can contribute to  $B_{P_a}$ . In a worst case scenario this could lead to a violation of the transmission condition ( $B_{P_a(r,\theta_s)}$ ). Furthermore, possible deviations from axial symmetry can result in transmission properties, which depend on the azimuthal angle ( $B_{P_a(r,\theta_s,\phi)}$ ).
- Non-aligned solenoids or LFCS coils with a specific tilt relative to the beam line will have similar effects as a remaining earth magnetic field contribution.
- Changes in the work function of the spectrometer, caused by surface impurities or venting of the vessel, will modify the actual electrostatic potential.
- The influence of possible HV fluctuations in the electrostatic retarding potential, which could be induced e.g. by the power supplies, depends on the frequency of the distortion. If the potential oscillates with frequencies on the order MHz, the transmission width is effectively broadened. Fluctuations at small frequencies, however, would result in systematic effects because individual scanning points will be influenced differently.
- A radial displacement of electrode modules will modify the resulting electrostatic potential, possibly leading to a violation of the transmission condition ( $U_{P_a(r,\theta_s)}$ ).
- Finally, non-axially symmetric potential contributions, e.g. from the large pump ports [248], possibly entail azimuthally dependent transmission properties ( $U_{P_a(r,\theta_s,\phi)}$ ).

The ideal case, where the sources for the electrostatic potential and the magnetic field are well-defined, stable and known precisely, will only be an approximation to the realistic case, where modifications arise from several or all of the above-mentioned effects. In view of this, the optimization of the transmission properties to fulfill the transmission condition is essential for a reliable determination of the main spectrometer transmission function. Furthermore, it has to be noted that the above considerations assume an ideal (mono-energetic, angular selective) source. The influence of realistic source parameters will be shown in the next section.

### 5.2.2 Source properties

The main spectrometer transmission properties will be optimized using an angular-selective, quasi-mono-energetic electron gun. Both the starting angle as well as the starting energy will be subject to an intrinsic spread, though. The e-gun setup [183] is based on a rotatable plate capacitor, as schematically shown in figure 5.3. Electrons are emitted from the illuminated back plate and are accelerated by the potential difference between the two plates  $U_f - U_b$ . They will pass through the hole in the front plate and are then released towards the spectrometer.

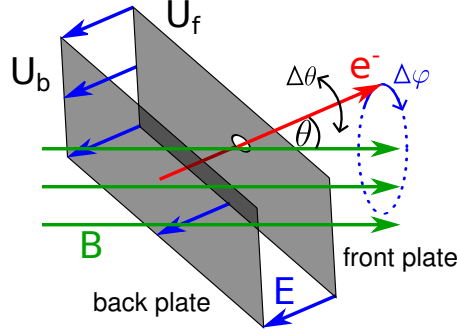


**Figure 5.3:** Illustration of the e-gun principle. Electrons are created in a plate capacitor and are accelerated by the potential difference  $U_f - U_b$  between the front and the back plate. The plates can be rotated with regard to the magnetic field, thereby defining the starting polar angle  $\theta$ . The finite size of the hole in the front plate results in an angular spread of the emitted electrons.

### Angular emission characteristics

The electron angular spread is caused by the aperture (the finite size of the hole) [246], and increases for larger polar angles. Within this work, a Gaussian angular spread  $\sigma_\theta \sim 1^\circ - 5^\circ$  around the actual e-gun polar angle  $\theta_{\text{egun}}$  (varying between  $0^\circ$  and  $60^\circ$ ) is assumed. The azimuthal angle  $\varphi$  is also affected by the aperture. However, in case of perfect axial symmetry, the azimuthal angle does not influence the transmission function. As deviations from this symmetry are expected to be rather small in the final KATRIN setup (see [182]), they are neglected in the following. A detailed investigation of the angular emission profile of the e-gun, using simulations of the exact setup, is carried out in [183, 246].

### Energy emission characteristics

The cathode is illuminated either by a UV-laser or by a UV-LED. The kinetic energy  $E_{\text{kin}}$  of the released electrons is determined by the photon energy  $h\nu$  in combination with the work function  $E_B$  of the cathode material [249]:

$$E_{\text{kin}} = h\nu - E_B, \quad (5.2)$$

where  $h\nu$  is determined by the photon line width and  $E_B$  by the Fermi distribution (thermal energy  $k_B T$  of the electron gas in the metal) as well as local effects such as patch fields. Consequently, both components are non-uniform, adding up to an overall distribution of electron starting energies. For the simulations within this work, a Gaussian energy distribution around an expectation value  $\langle E \rangle$  with standard deviation  $\sigma_E = 0.2$  eV is assumed. The electrons, which are emitted from the cathode surface, are accelerated by the e-gun potential  $U_{\text{egun}}$ , resulting in a total starting energy  $E_s = qU_{\text{egun}} + E_{\text{kin}}$ , where  $E_{\text{kin}}$  incorporates the initial energy spread.

For the following investigations, a common axial position has to be defined, which the angular and energy emission profiles are referred to. It the local coordinates of

the e-gun would be used, all following considerations would be changed if the e-gun would be placed at a different position in the solenoid stray field. The axial position is, hence, best fixed to a point where the electron production and acceleration are fully completed but the main spectrometer electromagnetic field configuration does not have a significant influence yet. Therefore, the center of the second pre-spectrometer solenoid PS2, which is closest to the main spectrometer, is a good choice. On the one hand, the influence of the main spectrometer electrostatic potential is reduced such that the remaining potential at the electron starting position  $U_s$  is on the order of a few mV only. On the other hand, the magnetic field is very homogeneous in radial direction and very strong ( $B_{PS2} = 4.5$  T), so that disturbing effects there have a negligible influence. The corresponding angles (as well as their intrinsic spread) at the location of the e-gun can be calculated once the position of the e-gun is defined [183].

### Influences on transmission lines

Fig. 5.4 shows the corresponding transmission behavior for electrons with small Gaussian spreads in energy and angle. For the top figure, a Gaussian energy distribution with  $\sigma_E = 0.2$  eV was assumed. The dashed lines correspond to the ideal case of monoenergetic electrons with  $E_s = qU_{\text{egun}}$ . It has to be recalled that full transmission occurs for  $E_s > E_{\text{tr}}$ . As the longitudinal component  $E_{s,\parallel}$  decreases for increasing starting polar angles, ever larger surplus energies  $E_s - qU_{P_a}$  are needed for transmission. Evidently, a Gaussian energy spread of the e-gun results in transmission lines that are equally broadened, independently of the actual starting polar angle. Also, the energy shift between individual starting angles is not affected.

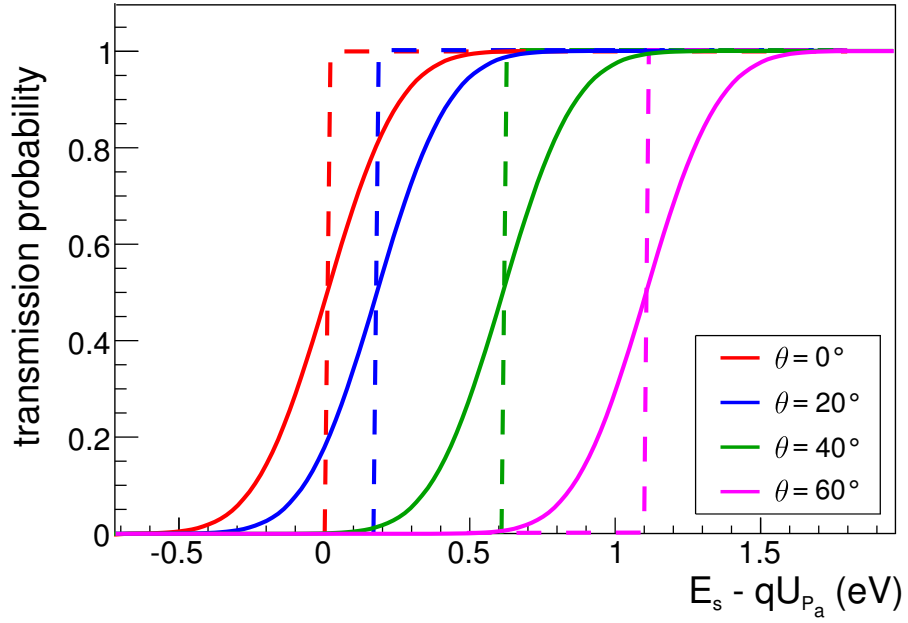
In the bottom figure the influence of an angular spread is displayed. As the angular spread of electrons at the position of PS2 increases for larger starting polar angles, the following polar angles with  $\pm 1\sigma$  distributions are assumed for the simulations:

$$\theta_s = 0^\circ \pm 1^\circ, \theta_s = 20^\circ \pm 2^\circ, \theta_s = 40^\circ \pm 3^\circ, \theta_s = 60^\circ \pm 5^\circ.$$

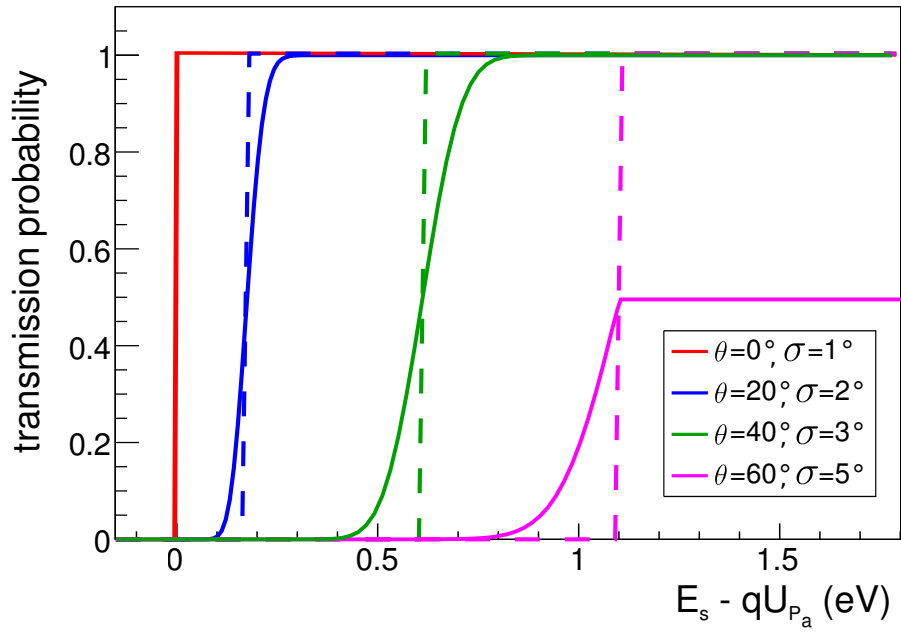
For small polar starting angles, the influence of the correspondingly small angular spread is rather negligible, while the effect increases towards larger angles. At the maximal angle  $\theta = 60^\circ$ , full transmission cannot be achieved anymore due to magnetic reflection at the pinch magnet, causing electrons with angles above  $60^\circ$  not to be transmitted.

As the e-gun is characterized by an angular as well as an energy spread, the combined effect has to be considered, which is shown in figure 5.5 for an exemplary e-gun angle  $\theta_{\text{egun}} = 40^\circ$ . Both distributions lead to a broadening of the transmission line. With the parameters of this simulation, the effect of the energy distribution is clearly dominant. However, the angular spread cannot be neglected and becomes more important towards larger angles.

Table 5.1 summarizes the most important conclusions about the effects of the spectrometer and the source properties on the transmission lines of an angular resolved source.



(a) Influence of the source energy distribution



(b) Influence of the source angular distribution

**Figure 5.4:** Transmission function as influenced by the source energy or angular distribution. (a) Gaussian energy distribution with  $\sigma_E = 0.2$  eV. (b) In case of a Gaussian angular distribution,  $\sigma_\theta$  depends on the polar angle, so that the shapes of the transmission functions differ.

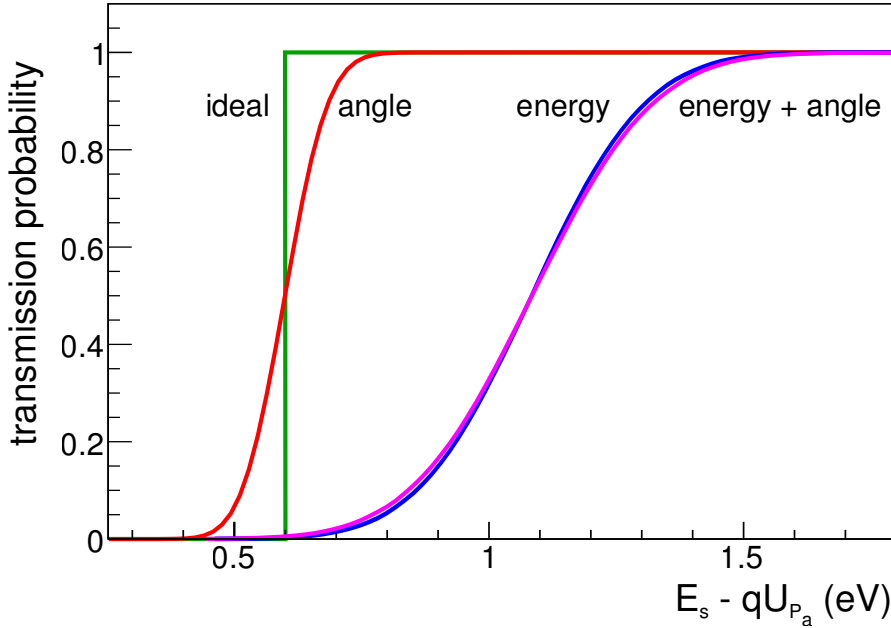


**Figure 5.5:** Transmission function as influenced by the source angular and energy distribution. The transmission line for an e-gun angle  $\theta_{\text{egun}} = 40^\circ$  is shown exemplary, with  $\sigma_E = 0.2$  eV and  $\sigma_\theta = 3^\circ$ . The effect of the intrinsic energy spread of the e-gun clearly dominates in the parameter range adopted here.

**Table 5.1:** Influences of the spectrometer and source properties on the transmission characteristics. The different parameters and their corresponding effects on the transmission lines of an angular resolved source are given.

parameter	effect
analyzing potential $U_{P_a}$	A shift $\Delta U_{P_a}$ leads to a shift $q\Delta U_{P_a}$ of the minimal required starting energy $E_s$ , independently of $\theta_s$ .
analyzing magnetic field $B_{P_a}$	A larger $B_{P_a}$ requires larger $E_s$ such that $E_s > E_{\text{tr}}$ . The shift of $E_s$ increases for larger $\theta_s$ due to $E_{s,\parallel} = E_s \cdot \cos \theta_s$ . $\theta_s = 0^\circ$ is not affected.
source energy $E_s$	An energy distribution $F(E_s)$ broadens the individual transmission lines, independently of $\theta_s$ .
source angle $\theta_s$	An angular distribution $\omega(\theta_s)$ broadens the individual transmission lines. The width of $\omega(\theta_s)$ is expected to increase for larger $\theta_s$ .

## 5.3 Measurement and analysis strategy

The transmission function (TF) in the standard definition according to (2.7) determines the transmission probability for a fixed starting energy, depending on an isotropic angular emission. However, due to the inability to produce a source which emits mono-energetic electrons, this *theoretical transmission function* cannot be measured directly. Nevertheless, it can be calculated analytically if the spectrometer properties (analyzing potential and magnetic field,  $U_{P_a}$  and  $B_{P_a}$ , and maximal magnetic field  $B_{\max}$ ) are known. Therefore, these parameters have to be determined within a dedicated pre-measurement, which is the focus of this section. For these measurements, the angular-resolved, quasi-mono-energetic e-gun will be used as a source. These special source properties necessitate a generalization of the theoretical TF (2.7) to incorporate arbitrary angular as well as energy distributions. The resulting *practical transmission function* is influenced by the source properties as well as the spectrometer properties. Their effects have to be decoupled by a suitable sequence of measurements. The general strategy is thereby as follows:

1. Determination of the source energy distribution (section 5.3.1).
2. Determination of the source angular distribution (section 5.3.2, considering an angular spread only, and section 5.3.3, considering an energy as well as an angular spread).
3. Determination of the spectrometer properties (section 5.3.4).

Hereby, the source properties are ideally determined independently of the details of the spectrometer properties. A well-characterized source, in turn, allows a full determination of the main spectrometer transmission characteristics. However, it will become clear that a complete disentanglement is not possible, so that various cross-checks are required to fully characterize the e-gun as well as the spectrometer. For each of the above steps, different measurement strategies are proposed and the corresponding analysis procedure is demonstrated for simulated data.

### 5.3.1 Source energy distribution

The angular resolved e-gun allows measurements at starting polar angles  $\theta_s = 0^\circ$ . This has two advantages: Firstly, the angular spread of the source is expected to be very small ( $\sim 1^\circ$ ), which results in a negligible broadening of the transmission line. Secondly, the transmission energy (5.1) is independent of the actual magnetic field configuration<sup>3</sup>:  $E_{\text{tr}} = q(U_{P_a} - U_s)$ .

The analyzing potential  $U_{P_a}$  follows from the potential  $U_0$ , which is actually applied to the spectrometer and its inner electrode system. As has been outlined earlier, the absolute value of  $U_{P_a}$  is non-uniform and decreases towards smaller radii  $r$ . For this

---

<sup>3</sup>This fact only holds for magnetic field configurations which ensure adiabatic guidance of signal electrons.

reason, the following investigations are restricted to the central field line at  $r = 0$  m, which corresponds to the symmetry axis. However, the strategies suggested here can be applied to other radial positions  $r$  and spatial azimuthal angles  $\phi^4$ .

Correspondingly,  $U_s$  denotes the potential at the starting position of the electron. In case of e-gun measurements, this value is influenced by the spectrometer potential. This effect has to be considered even in a configuration where the beam line elements close to the spectrometer are at ground potential, such as the position of the second pre-spectrometer solenoid PS2. Moreover, effects directly related to the e-gun, such as the work function or possible patch fields on the cathode surface, have to be considered and need to be propagated from the real starting position at the e-gun to the effective starting position at PS2, which is considered here. The important bottom line here is that any measurement is only sensitive to the difference  $U_{P_a} - U_s$ .

Following the above arguments, the transmission function  $T(E_s)$  at a polar starting angle  $\theta_s = 0^\circ$  is described by a step function, which depends on the starting energy  $E_s$  of the electron only. Electrons with energies  $E_s \geq qU_{P_a}$  are transmitted to the detector, whereas those with  $E_s < qU_{P_a}$  are reflected back to the source.

There are two approaches to measure the energy-dependent transmission function. In both cases it is assumed that the spectrometer and electron gun are elevated to the same potential, so that HV fluctuations cancel out. The small voltages, which have to be applied during first order scanning should thus not imply large fluctuations beyond the meV scale.

- *Variation of the spectrometer potential  $U_0$ :* In this case, the e-gun is kept at a fixed potential  $U_{\text{egun}}$ . As given in section 5.2.2, the electron energy  $E_s = qU_{\text{egun}} + E_{\text{kin}}$  is characterized by an initial spread, with  $E_{\text{kin}}$  following a Gaussian distribution  $F(E_{\text{kin}})$  around the expectation value  $\langle E \rangle$  with variance  $\sigma_E$ :

$$F(E_{\text{kin}}) = C_0 \cdot \exp\left(-\frac{(E_{\text{kin}} - \langle E \rangle)^2}{2\sigma_E^2}\right), \quad (5.3)$$

where  $C_0$  is a normalization constant such that  $\int_{-\infty}^{\infty} F(E_{\text{kin}})dE_{\text{kin}} = 1$ . As the e-gun potential  $U_{\text{egun}}$  simply yields a constant offset for the expectation value of the Gaussian energy distribution, the final electron energy distribution is correspondingly given by

$$F(E_s) = C_0 \cdot \exp\left(-\frac{[E_s - (\langle E \rangle + qU_{\text{egun}})]^2}{2\sigma_E^2}\right). \quad (5.4)$$

Figure 5.6 visualizes the above relation for a fixed e-gun potential  $U_{\text{egun}}$ , resulting in a Gaussian distribution of electron starting energies. If  $qU_{P_a}$  is very close to  $E_s$ , only those parts of the Gaussian distribution with  $E_s > qU_{P_a}$  are transmitted, which is illustrated by the shaded areas for two different analyzing potentials  $U_{P_a,1}$

<sup>4</sup>Note that  $\phi$  denotes the azimuthal position in the  $x - y$ - (analyzing) plane and is different from  $\varphi$ , which describes the azimuthal angular emission of the electron source.

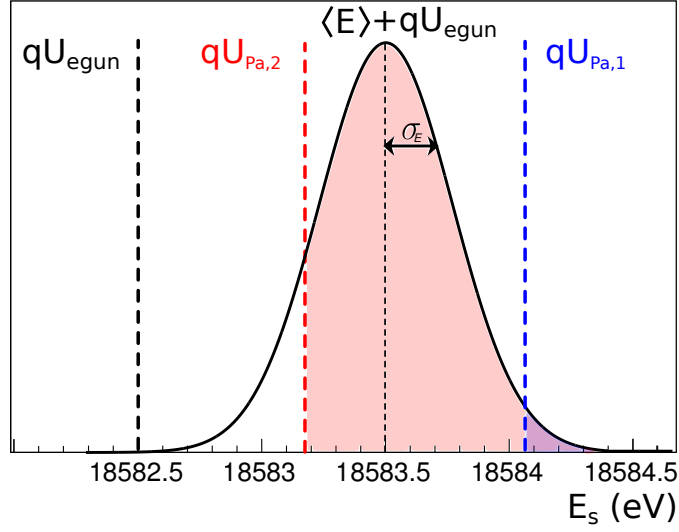


**Figure 5.6:** Effect of a source energy distribution on the transmission probability for a measurement at zero starting polar angle, using a variable analyzing potential  $U_{\text{Pa}}$ . Here, an energy spectrum  $E_s$  of electrons from an e-gun following a Gaussian distribution around  $\langle E \rangle + qU_{\text{egun}}$  is assumed. If  $qU_{\text{Pa}}$  is close to this value, only a fraction (shaded area) of the total number of emitted electrons fulfills the transmission condition  $E_s > qU_{\text{Pa}}$ . This is visualized for two values  $U_{\text{Pa},1}$  and  $U_{\text{Pa},2}$ .

and  $U_{\text{Pa},2}$ . A larger spectrometer potential  $U_0$  increases the analyzing potential  $U_{\text{Pa}}$  and hence decreases the fraction of transmitted electrons. The transmission probability as function of  $U_0$  is thus defined as

$$T(U_0) = \int_{qU_{\text{Pa}}}^{\infty} F(E_s) dE_s. \quad (5.5)$$

- *Variation of the e-gun potential  $U_{\text{egun}}$ :* An equivalent transmission function is obtained if the spectrometer potential  $U_0$  is fixed and the e-gun potential  $U_{\text{egun}}$  is variable. Using the variable transformation  $\epsilon = E_s - (\langle E \rangle + qU_{\text{egun}})$  yields the analogous energy distribution

$$\hat{F}(\epsilon) = \hat{C}_0 \cdot \exp\left(-\frac{\epsilon^2}{2\sigma_E^2}\right), \quad (5.6)$$

and finally the transmission probability for a specific e-gun potential

$$\hat{T}(U_{\text{egun}}) = \int_{qU_{\text{Pa}} - (\langle E \rangle + qU_{\text{egun}})}^{\infty} \hat{F}(\epsilon) d\epsilon. \quad (5.7)$$

Figure 5.7 illustrates this situation. In case of a variable e-gun potential the number

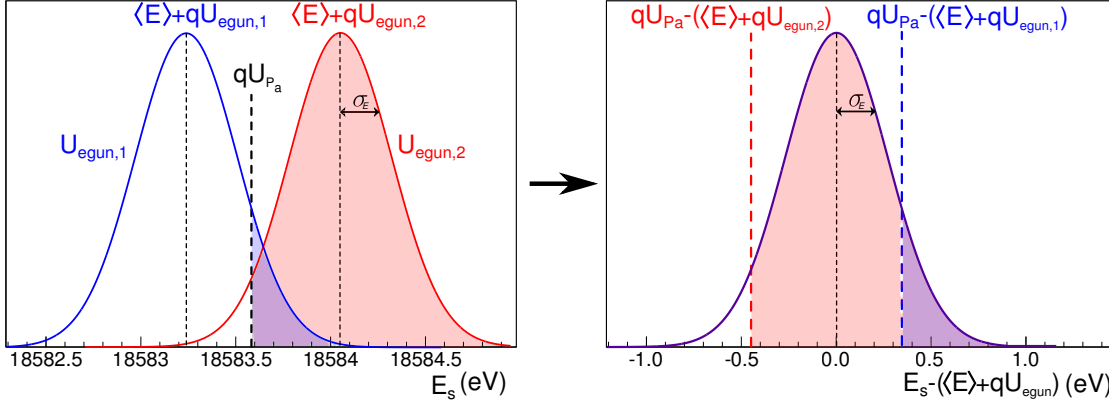


**Figure 5.7:** Effect of a source energy distribution on the transmission probability for a measurement with variable e-gun potential. With a variable transformation  $E_s \rightarrow \epsilon = E_s - (\langle E \rangle + qU_{\text{egun}})$ , this case is equivalent to the case of variable spectrometer potential.

of transmitted electrons increases as the e-gun potential increases from  $U_{\text{egun},1}$  to  $U_{\text{egun},2}$ , as indicated by the shaded area in figure 5.7 (left). With a variable transformation  $E_s \rightarrow \epsilon = E_s - (\langle E \rangle + qU_{\text{egun}})$ , this case is analogous to the case of variable spectrometer potential.

For the remainder of this chapter, the case of variable e-gun potential is adopted to outline measurement and analysis strategies.

The first goal is a determination of the starting energy distribution of the e-gun electrons. The corresponding measurement and analysis procedures comprise the following steps:

1. Measurement of  $T^{\text{meas}}(U_{\text{egun}})$ .
2. Determination of the energy distribution  $\hat{F}(\epsilon)$ .
3. Determination of the analytical transmission function  $T^{\text{theo}}(U_{\text{egun}})$ .
4. Determination of  $U_{\text{Pa}}$ .
5. Comparison of  $T^{\text{meas}}(U_{\text{egun}})$  and  $T^{\text{theo}}(U_{\text{egun}})$ .

Each step will be explained in detail in the following.

### 1. Measurement of $T^{\text{meas}}(U_{\text{egun}})$

At first, an actual spectrometer potential  $U_0$  has to be chosen, from which the approximate analyzing potential  $U_{\text{Pa}}$  can be calculated. Here, a potential setup according to table 4 was chosen with the e-gun placed such that it releases electrons along the central beam axis with a polar starting angle  $\theta_s = 0^\circ$ .

Secondly, the range of e-gun potentials has to be narrowed down to cover the entire transmission curve from zero to full transmission. Assuming an approximate energy spread

$\sigma_E \approx 0.2$  eV, the total width of the transmission function is expected to be  $\sim 1.5$  eV (see figure 5.4). Therefore, varying  $U_{\text{egun}}$  in step sizes of 0.5 V around the calculated value of  $U_{\text{Pa}}$  suffices for a first rough transmission scan. In the case simulated here, the e-gun potential is varied between  $U_{\text{egun,min}} = -18581$  V and  $U_{\text{egun,max}} = -18583$  V. For this set of parameters, a Monte-Carlo simulation was used to determine the transmission function. A step size of  $\Delta U_{\text{egun}} = 100$  mV was adopted up to the onset of transmission, and  $\Delta U_{\text{egun}} = 40$  mV from then on until full transmission. The underlying electron starting energy distribution was based on a Gaussian distribution around the expectation value  $qU_{\text{egun}} + \langle E \rangle$  with  $\langle E \rangle = 1$  eV and a variance  $\sigma_E = 0.2$  eV. Evidently, in case of a real measurement, it is this distribution which has to be determined experimentally. In the KASSIOPEIA simulation performed here, a total of  $N_{\text{tot}} = 100,000$  electrons was simulated for each e-gun potential. Figure 5.8 shows the simulation results. The statistical error for the individual points can be determined according to a binomial distribution [250]  $\sigma_{\text{stat}}^2 = N_{\text{tot}} \cdot p_{\text{tr}} \cdot (1 - p_{\text{tr}})$ , where  $p_{\text{tr}}$  is the transmission probability. The error bars are on the order of  $10^{-3}$  and hence not visible.

In the following, these Monte-Carlo-generated data are used to test an analysis strategy to extract the energy distribution  $\hat{F}(\epsilon)$ , which in case of e-gun measurements is not known a priori. The only parameters used for this analysis chain hence are the applied spectrometer potential  $U_0$ , the e-gun potential  $U_{\text{egun}}$  and the e-gun angle  $\theta_{\text{egun}}$ .

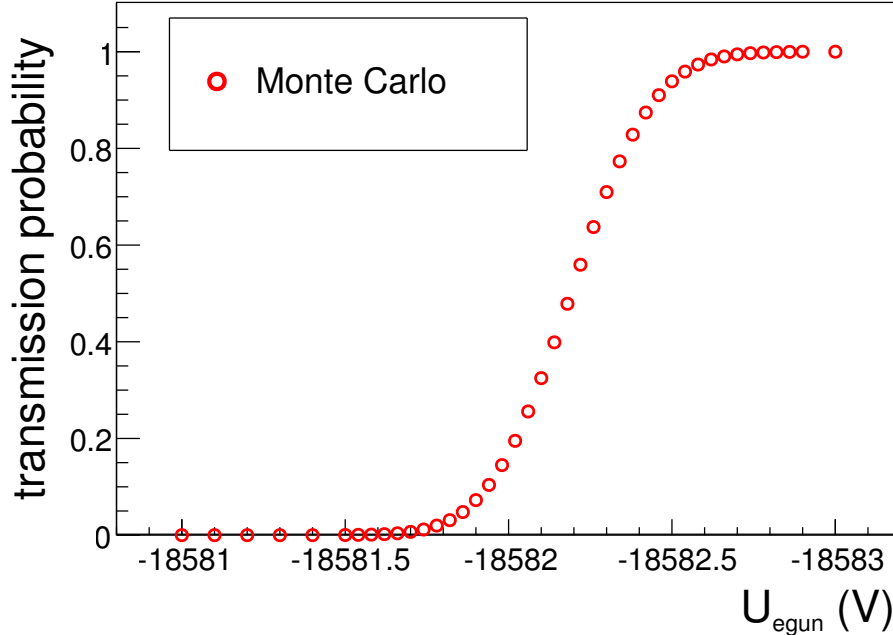


**Figure 5.8:** Transmission function as determined with a Monte-Carlo simulation (100,000 electrons per step, step size of 40 mV, Gaussian energy distribution  $\sigma_E = 0.2$  eV around  $qU_{\text{egun}} + \langle E \rangle$ ).

## 2. Determination of the energy distribution $\hat{F}(\epsilon)$

To determine the source energy distribution (5.6), a differentiation of the transmission probability (5.7) with respect to  $U_{\text{egun}}$  has to be carried out:

$$\hat{F}(\epsilon) = \left. \frac{\partial \hat{T}(U_{\text{egun}})}{\partial U_{\text{egun}}} \right|_{U_{\text{egun},i}}. \quad (5.8)$$

When using Lagrange's formula for the differentiation, one obtains [251, 252]:

$$\hat{F}(\epsilon_2) = a_1 \cdot T(U_{\text{egun},1}) + a_2 \cdot T(U_{\text{egun},2}) + a_3 \cdot T(U_{\text{egun},3}) \quad (5.9)$$

with

$$\begin{aligned} a_1 &= \frac{U_2 - U_3}{(U_1 - U_2) \cdot (U_1 - U_3)}, \\ a_2 &= \frac{2 \cdot U_2 - U_1 - U_3}{(U_2 - U_1) \cdot (U_2 - U_3)}, \\ a_3 &= \frac{U_2 - U_1}{(U_3 - U_1) \cdot (U_3 - U_2)}, \end{aligned} \quad (5.10)$$

where  $U_{\text{egun},i}$  was replaced by  $U_i$ . Figure 5.9 illustrates the differentiation routine. For the first and last element of  $\hat{F}(\epsilon)$ , which each have only one neighboring point  $U_n$ ,

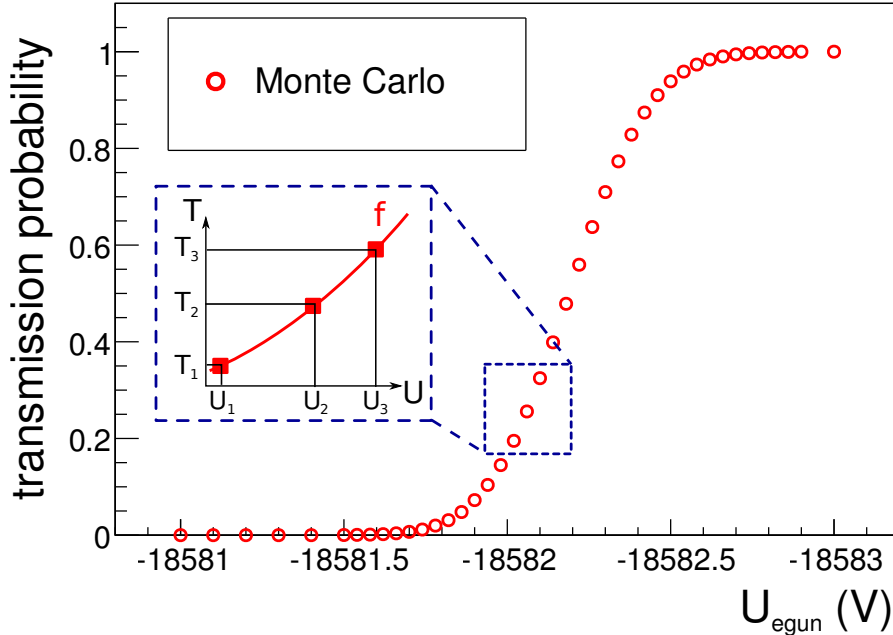


**Figure 5.9:** Illustration of the numerical differentiation of a measured transmission function via Lagrange's formula (5.9).

Taylor's theorem is applied:

$$\begin{aligned}\hat{F}(\epsilon_{\text{first}}) &= \frac{T(U_n) - T(U_{\text{first}})}{U_n - U_{\text{first}}}, \\ \hat{F}(\epsilon_{\text{last}}) &= \frac{T(U_{\text{last}}) - T(U_n)}{U_{\text{last}} - U_n}.\end{aligned}\tag{5.11}$$

Carrying out the differentiation as described above yields a source energy distribution as shown in figure 5.10. A Gaussian fit to the resulting distribution yields an energy spread  $\sigma_E = 0.2002 \pm 0.0004$  eV, which is in excellent agreement with the input of 0.2 eV. However, for realistic measurement conditions, the intrinsic energy distribution cannot necessarily be described by an analytical function. Therefore, it is better to use the calculated binned energy distribution of figure 5.10 for the upcoming steps.

### 3. Determination of the analytical TF $T^{\text{theo}}(U_{\text{egun}})$

The source energy distribution, which was determined above, can now be used to analytically calculate the transmission probability as a function of the e-gun potential. These results can finally be compared to actual measurements (step 5) to validate  $\hat{F}(\epsilon)$ . In order to calculate the integral (5.7), the lower and upper integration limits,  $\epsilon_{\text{min}}$  and  $\epsilon_{\text{max}}$ , have to be determined.

As an infinite upper limit is not feasible for numerical integration, a finite energy width

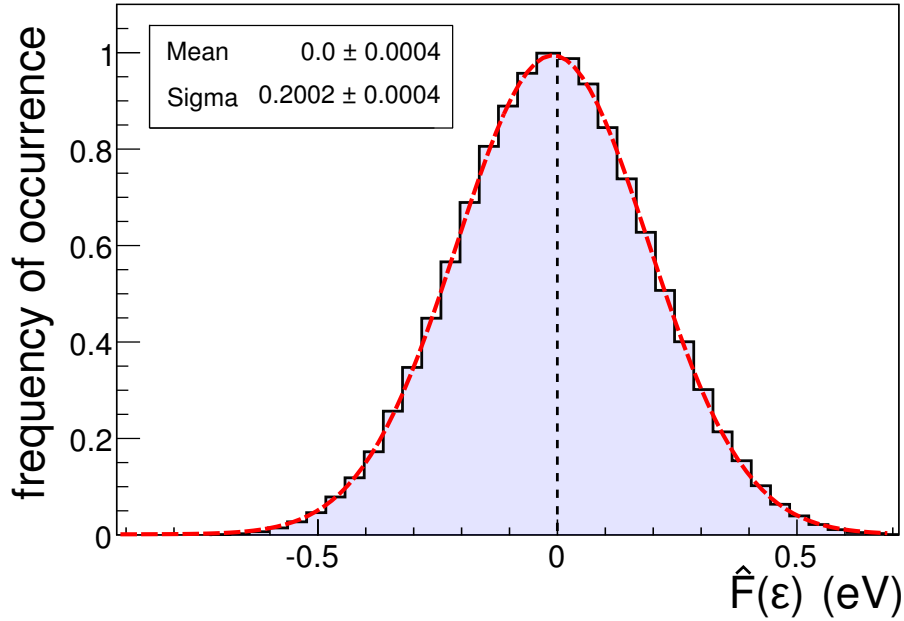


**Figure 5.10:** Calculated source energy distribution from numerical differentiation of the Monte-Carlo data of figure 5.8. A Gaussian fit to the differentiated distribution yields  $\sigma_E = 0.2002 \pm 0.0004$  eV, in good agreement with the input value of 0.2 eV. In case that the source energy distribution is non-analytical, binned data as shown here will be used.

has to be defined for which the error is still acceptable. In the following investigations, the distributions are integrated within their  $5\sigma$  boundaries, such that  $\epsilon_{\max} = 1$  eV.

The lower integration limit depends on the actual e-gun potential according to  $\epsilon_{\min} = qU_{P_a} - (\langle E \rangle + qU_{\text{egun}})$ . Here, the problem is that  $U_{P_a}$  and  $\langle E \rangle$  are not known. Although the shift  $\langle E \rangle$  is induced by the source, the only measurable variable is  $U_{\text{egun}}$ . Consequently, the transmission probability can only be determined as a function of the reduced 'effective' analyzing potential  $U_{P_a}^{\text{eff}} = U_{P_a} - \langle E \rangle / q$ . The intermediate step then is to determine  $T(\epsilon)$  by integration of  $\hat{F}(\epsilon)$ . In doing so, the same step size of 40 meV is chosen between  $\epsilon_{\min}$  and  $\epsilon_{\max}$  as for the simulated data. In order to perform a general integration of the extracted binned energy distribution, intermediate values of  $\epsilon$  and their corresponding probabilities have to be calculated. This computation is done using a cubic interpolation between the existing values in the histogram. The numerical integration is carried out using the Gaussian quadrature rule.

Figure 5.11 shows the integration result  $T(\epsilon)$ . From figure 5.7 follows that the transmission probability has to increase for decreasing  $\epsilon$ . In order to obtain the desired transmission function  $T(U_{\text{egun}})$ , the relation  $\epsilon = qU_{P_a}^{\text{eff}} - qU_{\text{egun}}$  can be used. Here, the effective analyzing potential  $U_{P_a}^{\text{eff}}$  is a free parameter, as discussed above.

Figure 5.12 (analytical w/o fit) shows  $T(U_{\text{egun}})$  for an initial guess of  $U_{P_a}^{\text{eff}} = -18583$  V. For comparison, also the Monte-Carlo data are shown. Obviously, the two transmission functions do not match together. However, their shape, which is determined by the energy distribution, looks rather similar. Therefore, the next step is a determination of the actual value of  $U_{P_a}^{\text{eff}}$ .

#### 4. Determination of $U_{P_a}^{\text{eff}}$

To determine the effective analyzing potential  $U_{P_a}^{\text{eff}}$ , a fitting routine is applied with  $U_{P_a}^{\text{eff}}$  as free parameter. A  $\chi^2$  fit is performed according to

$$\chi^2(U_{P_a}^{\text{eff}}) = \sum_{i=1}^n \frac{N_{\text{tr},i}^{\text{MC}} - N_{\text{tr},i}^{\text{ana}}}{\sigma_i^2}, \quad (5.12)$$

where  $i$  denotes the different simulated steps of  $U_{\text{egun}} = U_{P_a}^{\text{eff}} - \epsilon$ ,  $N_{\text{tr},i}^{\text{MC}}$  and  $N_{\text{tr},i}^{\text{ana}}$  is the number of transmitted electrons at a particular potential for the Monte-Carlo simulation and the analytical calculation, respectively. Furthermore,  $\sigma_i^2 = N_{\text{tot},i} \cdot p_{\text{tr},i}^{\text{ana}} \cdot (1 - p_{\text{tr},i}^{\text{ana}})$ , where  $N_{\text{tot}}$  is the total number of simulated electrons and  $p_{\text{tr}}^{\text{ana}}$  the transmission probability as determined via integration of (5.7). An effective potential  $U_{P_a}^{\text{eff}} = -18583.2$  V was determined. The resulting analytical transmission function is shown in figure 5.12 (analytical with fit). As the underlying points correspond to the initial Monte-Carlo points, the real effective potential can be calculated. Its value  $U_{P_a}^{\text{eff,MC}} = -18583.19$  V agrees with the fitted value on the meV-level.

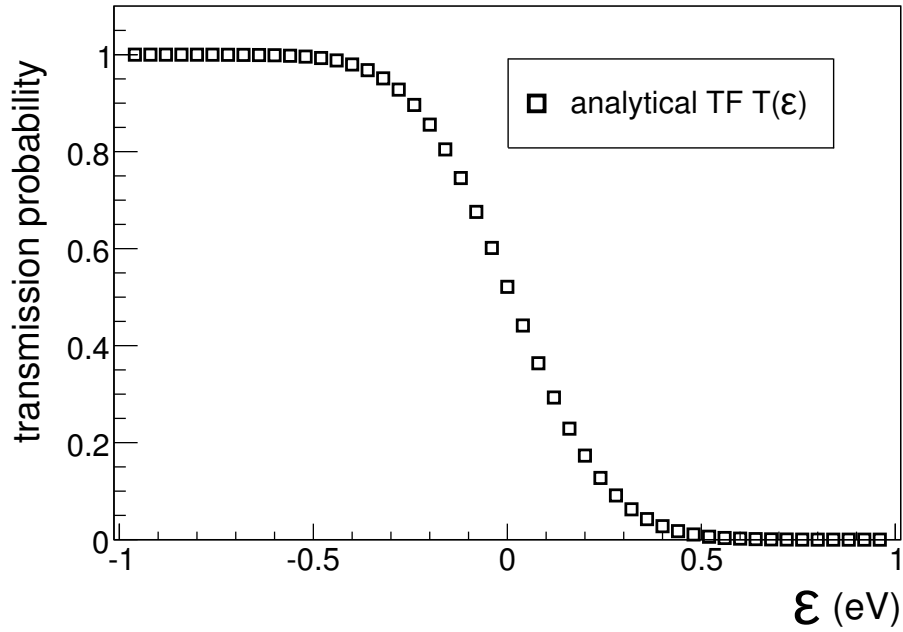


**Figure 5.11:** Intermediate step of a determination of the analytical transmission function  $T(\epsilon)$ . The source energy distribution of figure 5.10 was used to calculate the integral (5.7) after substituting  $\epsilon$  for  $U_{\text{egun}}$ .

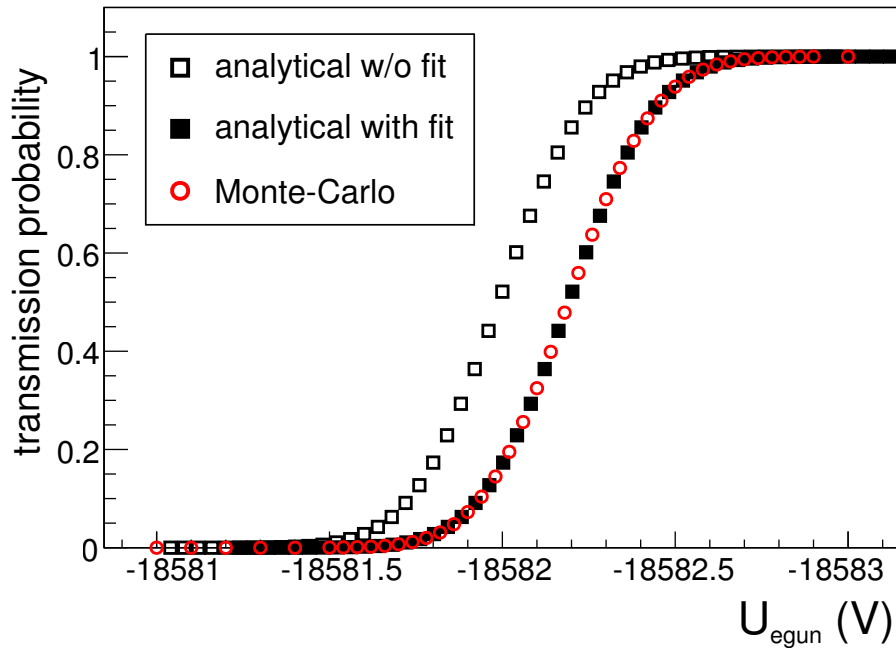


**Figure 5.12:** Analytical TF  $T(U_{\text{egun}})$ . Additionally, the Monte-Carlo data are shown. Monte-Carlo without fit: Analytical TF for  $U_{\text{Pa}}^{\text{eff}} = -18583$  V. Monte-Carlo with fit: Resulting analytical TF after determination of  $U_{\text{Pa}}^{\text{eff}} = -18583.2$  V by a fit.

### 5. Comparison of $T^{\text{meas}}(U_{\text{egun}})$ and $T^{\text{theo}}(U_{\text{egun}})$

Although figure 5.12 (right) already indicates a rather good agreement between the simulated and the analytical transmission functions, a more detailed comparison is performed in figure 5.13. The figure displays the ratio between the transmission probability as determined with the Monte-Carlo simulation and the probability as calculated analytically. Two Monte-Carlo simulations are shown, one featuring just a Gaussian energy spread and another one with an additional Gaussian angular spread with  $\sigma_\theta = 1^\circ$ . No significant additional deviation is induced by the angular emission profile. Therefore, it can be neglected within this kind of measurement. In both cases, larger deviations occur at low e-gun potentials, where the number of transmitted electrons is rather small. To counteract this behavior, a measurement procedure with roughly identical statistical errors can be envisioned. For major parts of the transmission function (beyond  $T(U_{\text{egun}}) > 0.1$ ), an agreement on the level of  $\sim 1\%$  is achieved which corresponds to the required precision following from simulations of the neutrino mass sensitivity of KATRIN [253].

Although the angular spread of the e-gun has no significant influence on the result of the measurement, the rather limited spread of the input parameters which were used could be too optimistic. If this is the case, a second measurement could be conducted where the spectrometer retarding potential is reduced by 2 orders of magnitude, which improves the energy resolution to about 0.01 eV. Consequently, the influence of the polar starting angle is as well suppressed by two orders of magnitude. Evidently, the e-gun potential has to be decreased likewise. The potential setup can be found in table 5. Again, a measurement with zero starting polar angle is performed. The source parameters for the Monte-Carlo simulation were chosen to  $U_{\text{egun}} \in [-184.1 \text{ V}, -185.75 \text{ V}]$ ,  $\sigma_E = 0.2 \text{ eV}$ ,  $\theta_{\text{egun}} = 0^\circ$ , and  $\sigma_\theta = 1^\circ$ . Performing the same procedure as outlined above yields a

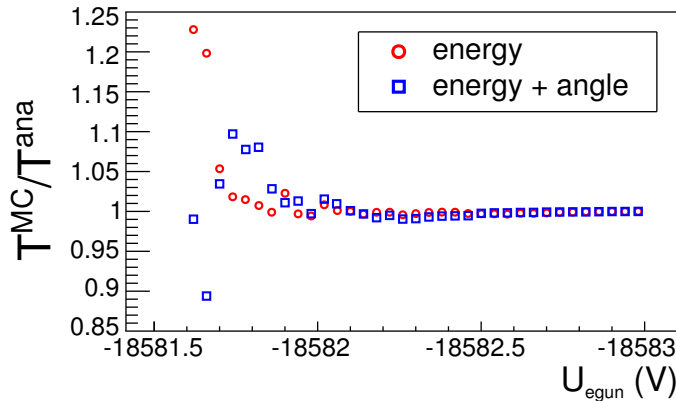


**Figure 5.13:** Deviation of Monte-Carlo and analytical results. The quotient of the transmission probability as determined via Monte Carlo simulation and via analytical calculation is shown. In the region of low count rates also the agreement between Monte-Carlo and analytical results suffers. The Monte-Carlo results are shown for a Gaussian energy distribution only (circles) and for an additional Gaussian angular distribution with  $\sigma_\theta = 1^\circ$  (squares). The results agree within the statistical fluctuations, therefore, the angular spread can be neglected.

Gaussian spread of  $\sigma_E = 0.2013 \pm 0.0004$  eV, which agrees with the input value on the required 1% level. The results of both measurements should agree as the accelerating e-gun potential should not influence the electron energy distribution. However, possible fluctuations of the spectrometer retarding potential could affect the measurement. A lower retarding potential is supposedly more stable. Therefore, smaller fluctuations are expected within this second type of measurement.

### 5.3.2 Source angular distribution

When determining the source angular distribution, a non-negligible issue is the fact that all measurements are sensitive to the magnetic field values at particular points of the main spectrometer. Therefore, appropriate methods have to be found to reduce these influences as much as possible. In the following, two measurements to address these issues will be discussed:

- a) Measurement at varying pinch magnetic field strength.
- b) Measurement at increased analyzing magnetic field strength.

Both measurement procedures require a re-formulation of the transmission probability to take into account the angular dependence. For simplification, a mono-energetic source is assumed at first in this section. The case of combined angular and energy distributions is detailed in section 5.3.3.

#### a) Measurement at varying pinch magnetic field strength

The method of varying the pinch magnetic field strength relies on the magnetic mirror effect for electrons with a starting polar angle exceeding the limit of

$$\theta_{\max} = \arcsin \left( \sqrt{\frac{B_s}{B_{\max}}} \right), \quad (5.13)$$

with  $B_s = 4.5$  T being the fixed magnetic field strength in the center of the second pre-spectrometer solenoid PS2, which is again treated as the electron starting position. The maximal magnetic field strength  $B_{\max}$  is generally found in the center of the pinch magnet. For the method investigated here, the magnetic field values  $B_{\max} = B_{\text{pinch}}$  have to be varied between 4.5 T and 6 T. Consequently, the previously unexplored angular interval between  $60^\circ$  and  $90^\circ$  can be tested with this method. It is important to notice that the angular spread depends on the actual value of the starting polar angle. Hence, the angular range below  $60^\circ$ , which is used for standard transmission function measurements, cannot directly be tested by this method. Nevertheless, there are prospects to determine the angular distribution by detailed simulations of the e-gun setup, including the full acceleration mechanism [183]. The validity of these simulations can then be checked by comparing Monte-Carlo results to the particular type of measurement proposed here. These investigations would create added value due to the fact that a

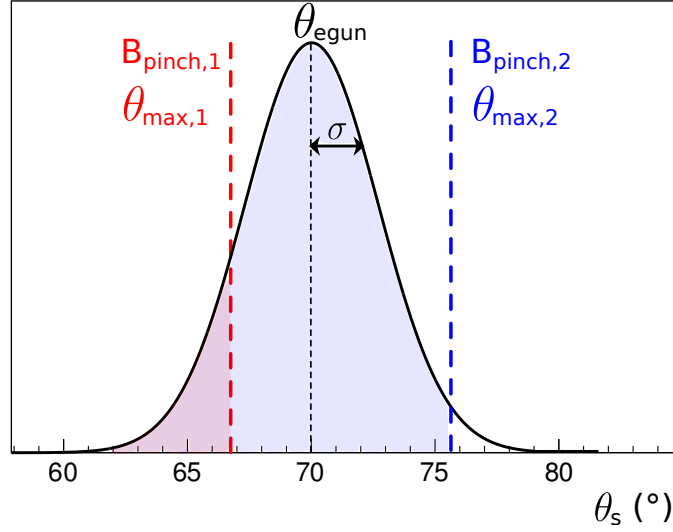


**Figure 5.14:** Illustration of a measurement at a large polar angle ( $70^\circ$ ) and spread ( $\sigma = 3^\circ$ ). When decreasing the pinch magnetic field strength from  $B_{\text{pinch},1}$  to  $B_{\text{pinch},2}$ , the maximal transmitted starting polar angle is increased from  $\theta_{\text{max},1}$  to  $\theta_{\text{max},2}$ . This results in an increased number of transmitted electrons.

thorough understanding at large polar angles would result in a more reliable calculation of angular distributions at smaller polar angles.

Figure 5.14 illustrates the underlying principle of this method. If the e-gun is adjusted to create electrons with starting polar angles  $\theta_s > 60^\circ$  for measurements with maximal pinch magnetic field  $B_{\text{pinch}} = 6 \text{ T}$ , all electrons are magnetically reflected, independently of their starting kinetic energy. Following eq. (5.13), a decrease of the pinch field from  $B_{\text{pinch},1}$  to  $B_{\text{pinch},2}$  results in a larger maximal transmitted starting polar angle, i.e. an increase from  $\theta_{\text{max},1}$  to  $\theta_{\text{max},2}$ . This method has the clear advantage that it is completely independent of the (a priori unknown) starting energy distribution of the source due to the specific mechanism of magnetic reflection. However, the starting magnetic field and the magnetic field at the point of reflection have to be known rather precisely. In this case, the transmission function depends neither on the e-gun potential  $U_{\text{egun}}$  nor on the spectrometer potential  $U_0$  as long as large enough values are chosen for  $U_{\text{egun}}$  such that all electrons are transmitted over the potential barrier. Accordingly, a definition of the transmission function as a function of the pinch magnetic field strength is found:

$$T(B_{\text{pinch}}) = \int_{\theta_{\text{min}}}^{\theta_{\text{max}}(B_{\text{pinch}})} \omega(\theta) d\theta, \quad (5.14)$$

where  $\omega(\theta)$  is the source angular distribution. The measurement and analysis procedures to determine the angular distribution by this method can be divided into the following steps:

1. Measurement of  $T^{\text{meas}}(B_{\text{pinch}})$ .

2. Determination of the angular distribution  $\omega(\theta)$ .
3. Determination of the analytical transmission function  $T^{\text{theo}}(B_{\text{pinch}})$ .
4. Comparison of  $T^{\text{theo}}(B_{\text{pinch}})$  and  $T^{\text{meas}}(B_{\text{pinch}})$ .

Again, Monte-Carlo data are used to demonstrate the single steps in the measurement and analysis procedure.

**1. Measurement of  $T^{\text{meas}}(B_{\text{pinch}})$ :**

As this method should only rely on magnetic reflection, electron starting energies above the transmission energy have to be used. The setup investigated here features an analyzing potential  $U_{P_a} = -18582.19$  V, so a fixed e-gun potential  $U_{\text{egun}} = -18590$  V is chosen. For this range of parameters, the pinch magnetic field strength has to be varied from  $B_{\text{pinch}} = B_s$  (no magnetic reflection) to  $B_{\text{pinch}} = B_{\text{max}}$  (maximal magnetic reflection). Thereby, a constant step size of  $\Delta B_{\text{pinch}} = 0.05$  T is chosen initially<sup>5</sup>. Figure 5.15 (red data points) shows the resulting transmission probability as a function of the magnetic field strength at the pinch magnet.

**2. Determination of the angular distribution  $\omega(\theta)$ :**

From this functional behavior the source angular distribution can be determined by differentiation:

$$\omega(\theta_{\text{egun}}) = \left. \frac{\partial T(B_{\text{pinch}})}{\partial B_{\text{pinch}}} \right|_{B_{\text{pinch},i}}. \quad (5.15)$$

Again, Lagrange's formula (5.9) is used to calculate the derivatives by replacing the parameter  $U_{\text{egun}}$  for  $B_{\text{pinch}}$ , which results in an angular distribution as shown in figure 5.16.

Obviously, the step size chosen initially is not suited to determine the source angular distribution at large polar angles. This systematic effect is caused by the non-linear relation (5.13) between  $\theta_{\text{max}}$  and  $B_{\text{max}}$ . Ideally, constant step sizes between the individual angle values are chosen, which requires an adjustment of  $B_{\text{pinch}}$  according to eq. (5.13). However, an improvement can also be achieved if smaller, equally spaced steps are chosen for small values of  $B_{\text{pinch}}$  where the region of large polar angles is scanned. The corresponding Monte-Carlo data and the retrieved angular distribution are shown in blue in figures 5.15 and 5.16. As figure 5.16 shows, the agreement between the derived angular distribution and the Gaussian input distribution is improved significantly when using smaller step sizes. Therefore, the improved stepping data are considered for the following calculations. However, the angular region below  $60^\circ$  cannot be accessed by this measurement unless the magnetic field ratio  $B_{\text{pinch}}/B_s$  could be increased further. Finally, electrons emitted with starting polar angles  $\theta_s > 90^\circ$  do not travel towards the detector and can hence not be investigated either.

**3. Determination of the analytical transmission function  $T^{\text{theo}}(B_{\text{pinch}})$ :**

The angular distribution of figure 5.16 is again used to calculate the analytical transmission function  $T^{\text{theo}}(B_{\text{pinch}})$  by integrating (5.14). The lower limit  $\theta_{\text{min}}$  is fixed to

---

<sup>5</sup>It has to be noted that a strong decrease of the value  $B_{\text{pinch}} < 5$  T will result in a flux tube at the detector-facing ground electrode of the spectrometer that starts to touch the inner electrode surface. As one is only interested in on-axis electron trajectories, these distorting effects at large radii do not have to be investigated further.

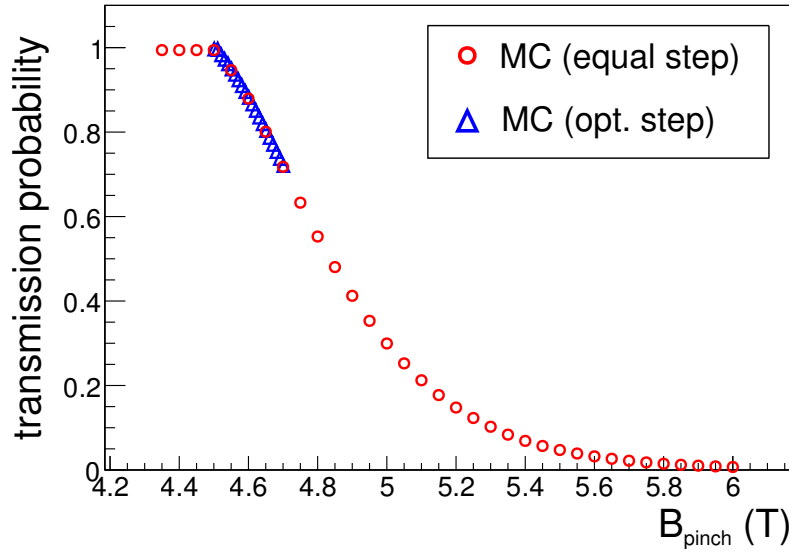


**Figure 5.15:** Transmission values as a function of the pinch magnetic field strength. Here, Monte-Carlo simulations with constant step size of  $\Delta B_{\text{pinch}} = 0.05$  T throughout the whole sequence (red circles) and a simulation using smaller step sizes of  $\Delta B_{\text{pinch}} = 0.01$  T at small magnetic fields (blue triangles) are shown.

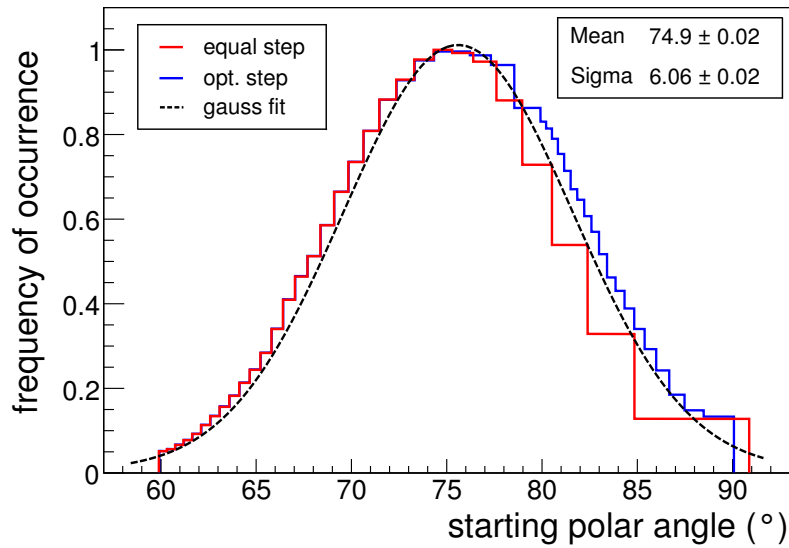


**Figure 5.16:** Angular distribution as determined by differentiation of the Monte-Carlo data of figure 5.15. Obviously, the case where additional steps at small values of the pinch magnetic field strength are implemented, yields a better agreement with the input Gaussian distribution. The Gaussian fit was performed for the results of the simulation with optimized step sizes. Fitting the two shoulders separately gives the following fit parameters. Left:  $\langle \theta \rangle = (74.6 \pm 0.08)^\circ$ ,  $\sigma = (5.9 \pm 0.04)^\circ$ , right:  $\langle \theta \rangle = (74.78 \pm 0.27)^\circ$ ,  $\sigma = (6.13 \pm 0.14)^\circ$ .

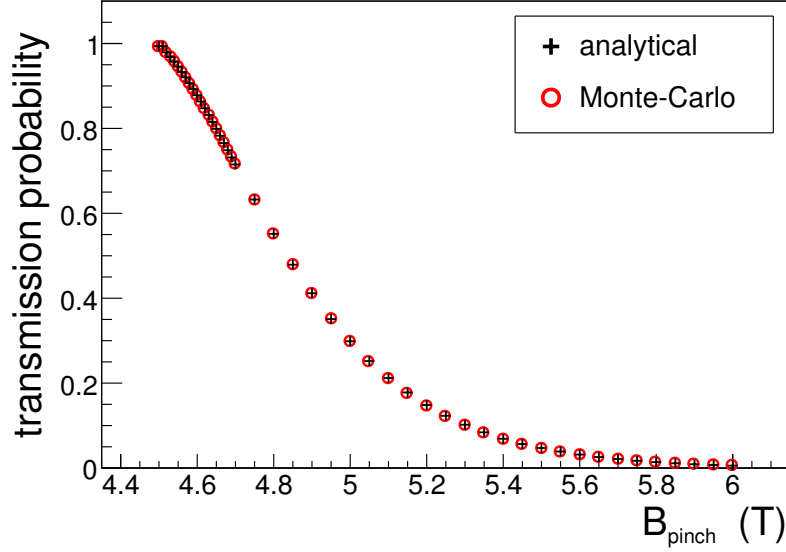


**Figure 5.17:** Analytical transmission function as determined from the source angular distribution of figure 5.16, using the optimized step size distribution. The Monte-Carlo data are shown for comparison.

the smallest value within the calculated angular distribution, while the upper limit  $\theta_{\max}$  depends on the pinch magnetic field strength according to eq. (5.13). Carrying out the integration yields a transmission function as shown in figure 5.17.

#### 4. Comparison of $T^{\text{meas}}(B_{\text{pinch}})$ and $T^{\text{theo}}(B_{\text{pinch}})$ :

For comparison, figure 5.17 also shows the underlying Monte-Carlo data. Obviously, the two transmission functions show a very good agreement. However, it has to be considered that the results strongly depend on the magnetic field values  $B_{\text{pinch}}$  and  $B_s$ . For the analysis, which was shown above, the values  $B_{\text{pinch,max}}^{\text{ana}} = 6$  T and  $B_s^{\text{ana}} = 4.5$  T were chosen, while the exact values within the Monte-Carlo simulation were  $B_{\text{pinch,max}}^{\text{MC}} = 6.035$  T and  $B_s^{\text{MC}} = 4.507$  T, which deviate by less than 1%. This assumption, though, could be a too optimistic case given realistic measurement conditions.

#### b) Measurement at increased analyzing magnetic field strength

A second set of measurements can be employed to determine the source angular distribution. The standard energy-dependent transmission function incorporates an angular dependence if a starting polar angle  $\theta_s > 0^\circ$  is chosen. Therefore, such a measurement (now at first for the ideal case of mono-energetic electrons) can be used to unfold the angular distribution with the help of an appropriate analysis. In section 4.2.1, the transmission function for mono-energetic electrons with starting energy  $E_s$  was derived:

$$T(E_s) = \int_{\varphi_{\min}}^{\varphi_{\max}} \int_{\theta_{\min}}^{\theta_{\max}(E_s)} \omega(\theta, \varphi) d\theta d\varphi, \quad (5.16)$$

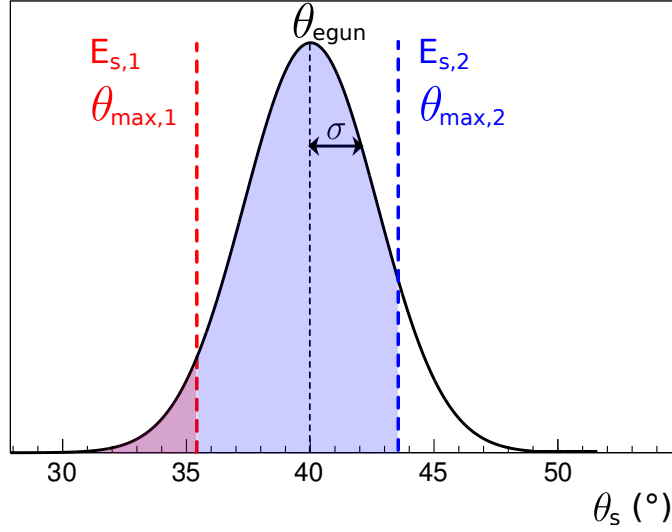


**Figure 5.18:** Illustration of the dependence of the transmission probability on the source angular distribution. Increasing the electron starting energy from  $E_{s,1}$  to  $E_{s,2}$  also increases the maximal transmitted starting polar angle  $\theta_{\max}$ , which results in a larger number of transmitted electrons.

where  $\omega(\theta, \varphi)$  represents the source angular distribution. The azimuthal part ( $\varphi$ ) of the angular distribution does not influence the transmission probability as long as it is independent of the polar part ( $\theta$ ). Therefore, it can be absorbed in the normalization constant of the angular distribution. Figure 5.18 visualizes the relation between  $\theta_{\max}$  and  $E_s$ . For a fixed starting polar angle  $\theta_s$ , an electron is transmitted if its starting kinetic energy  $E_s$  exceeds the transmission energy  $E_{tr}$  (5.1). Electrons with smaller starting angles are also transmitted. Hence, for a given angular distribution, all electrons with angles equal to or below  $\theta_s(E_{tr})$  can pass the spectrometer potential barrier. When increasing the starting kinetic energy from  $E_{s,1}$  to  $E_{s,2}$ , the maximal transmitted polar angle  $\theta_{\max}(E_s)$  increases as well and hence the overall transmission probability. The relation  $\theta_{\max}(E_s)$  can thereby be obtained by inverting (5.1):

$$\theta_{\max}(E_s) = \arcsin \sqrt{\left(\frac{E_s - qU_{Pa}}{E_s}\right) \cdot \frac{(\gamma_{Pa} + 1) \cdot B_s}{(\gamma_s + 1) \cdot B_{Pa}}}. \quad (5.17)$$

An exemplary Gaussian angular distribution is chosen for the following investigations:

$$\omega(\theta) = C_0 \cdot \exp\left(-\frac{(\theta - \theta_{\text{egun}})^2}{2\sigma_\theta^2}\right) \quad (5.18)$$

where  $C_0$  is a normalization constant such that  $\int_{-\infty}^{\infty} d\omega = 1$ . From eq. (5.17) follows that  $\theta_{\max}(E_s)$  depends on the spectrometer properties  $U_{Pa}$ ,  $B_{Pa}$  and  $B_s$ . The analyzing potential is chosen initially to be the value which was fitted when determining the source energy distribution<sup>6</sup>. It should be recalled that  $B_s$  is the magnetic field in the center of

<sup>6</sup>Also here,  $U_{Pa}$  should actually be the effective analyzing potential  $U_{Pa}^{\text{eff}}$ .

the pre-spectrometer solenoid, where the field strength can be calculated rather precisely, so a value of 4.5 T can be used. The largest uncertainty is thus associated with the analyzing magnetic field strength  $B_{P_a}$ . In the standard magnetic field setup with  $B_{P_a} \sim 3.5 \cdot 10^{-4}$  T, even small disturbances will impede a reliable calculation of the exact value. Therefore, the idea for this measurement is to increase  $B_{P_a}$  to a value of  $\sim 1 \cdot 10^{-3}$  T. This change can be implemented by increasing the currents of the LFCS coils. As the geometry of these coils is known rather precisely (the positioning precision is of the order of cm for a coil with dimension of 10 m), their field contribution can be calculated to a good accuracy (a  $10^{-3}$  agreement with measured values has been reached in [182]). A further advantage of a larger central field strength results from an increased sensitivity to the source angular distribution. This follows from the fact that the transmission function is significantly broadened due to the reduced spectrometer energy resolution. As an added bonus, the transmission condition can be fulfilled more reliably at larger central magnetic field values. The measurement and analysis strategies thus involve the following steps:

1. Measurement of  $T^{\text{meas}}(E_s)$  at increased magnetic field: for a fixed e-gun angle  $\theta_{\text{egun}} > 0^\circ$  the parameters  $U_{\text{egun}}$  or  $U_0$  are varied.
2. Determination of the angular distribution  $\omega(\theta_{\text{egun}})$ : The function  $T^{\text{meas}}(E_s)$  is differentiated with respect to  $E_s$ .
3. Determination of the analytical TF  $T^{\text{theo}}(E_s)$ : Calculation of the integral (5.16).
4. Measurement of  $T^{\text{meas}}(E_s)$  at the standard magnetic field.
5. Determination of the free parameters  $B_{P_a}$  and  $U_{P_a}$ .

As done previously, each step will be explained in detail in the following.

### 1. Measurement of $T^{\text{meas}}(E_s)$ at increased magnetic field

First, an appropriate magnetic field setup has to be specified. In this work, an analyzing field strength of  $B_{P_a} = 1 \cdot 10^{-3}$  T was chosen and the LFCS optimizer, which was described in section 4.4, was used to determine the LFCS current values. Table 2 shows the results of the optimization procedure. As usual, Monte-Carlo-generated data are used as replacement for measured data. The e-gun is adjusted to an exemplary starting polar angle  $\theta_{\text{egun}} = 40^\circ$ , releasing electrons along the central beam axis. The corresponding transmission function can be measured either by a variation of the e-gun potential  $U_{\text{egun}}$  or of the spectrometer potential  $U_0$ . Here, again the case of variable  $U_{\text{egun}}$  is chosen. Note that up to now, a fixed e-gun potential is supposed to yield a fixed electron starting energy  $E_s = qU_{\text{egun}}$ . To scan the region-of-interest, the interval where the e-gun potential has to be varied is determined to ensure that the number of transmitted electrons rises from zero to full transmission. This first rough scan can be carried out with large potential step sizes of 0.1-0.2 V. In this case, the necessary scan range was identified to lie between  $U_{\text{egun},\text{min}} = -18584.1$  V and  $U_{\text{egun},\text{max}} = -18585.9$  V.

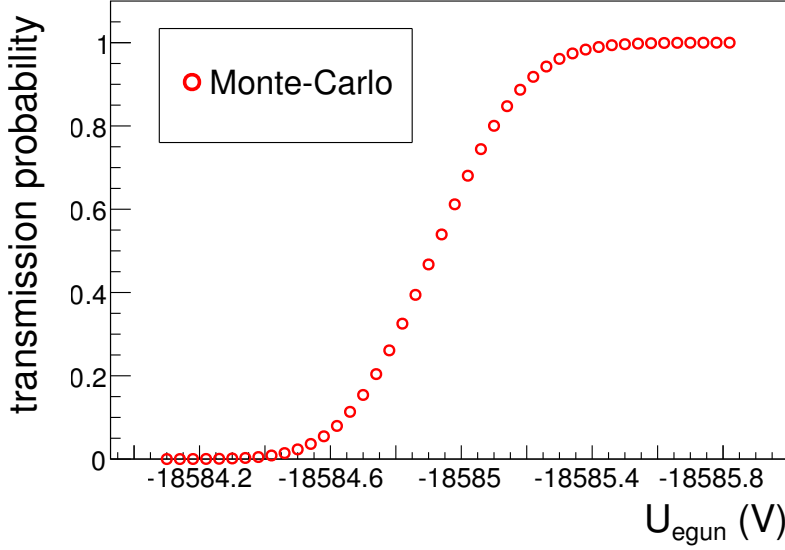


**Figure 5.19:** Transmission function as determined with a Monte-Carlo simulation (100,000 electrons per step, step size of 40 mV, Gaussian angular distribution with expectation value  $\theta_{\text{egun}} = 40^\circ$  and variance  $\sigma_\theta = 3^\circ$ ).

A step size of  $\Delta U_{\text{egun}} = 40$  mV was chosen within this interval with  $N_{\text{tot}} = 100,000$  electrons, which were simulated per step. Figure 5.19 shows the simulation results. The small error bars ( $10^{-3}$  relative error) are also indicated. Known parameters within this measurement are the applied e-gun potential  $U_{\text{egun}}$  and the e-gun angle  $\theta_{\text{egun}}$ . Furthermore, the effective analyzing potential  $U_{\text{P}_a}^{\text{eff}} = -18583.2$  V is taken from the previous source energy distribution determination. For the starting magnetic field strength, the calculated value  $B_s = 4.5$  T is taken as input. The effect of a variation of the input values will also be discussed.

## 2. Determination of the angular distribution

The angular distribution of the source (5.18) can be determined by a differentiation of the transmission probability (5.16) with respect to  $E_s$ :

$$\omega(\theta_{\text{egun}}) = \left. \frac{\partial T(E_s)}{\partial E_s} \right|_{E_{s,i}}. \quad (5.19)$$

Again, Lagrange's formula (5.9) is used again to perform this task. The resulting angular distribution is shown in figure 5.20. The above-mentioned "standard" input values were used to obtain this distribution. A Gaussian fit to the results yields an expectation value  $\langle \theta \rangle = 39.73^\circ$  and a standard deviation  $\sigma_\theta = 3.013^\circ$ , in good agreement with the input values  $\langle \theta^{\text{input}} \rangle = 40^\circ$  and  $\sigma_\theta^{\text{input}} = 3^\circ$ . As these standard parameters do not necessarily represent reality, the effect of a variation of these input parameters should be investigated. Table 5.2 gives an overview of the influence of a variation of single input

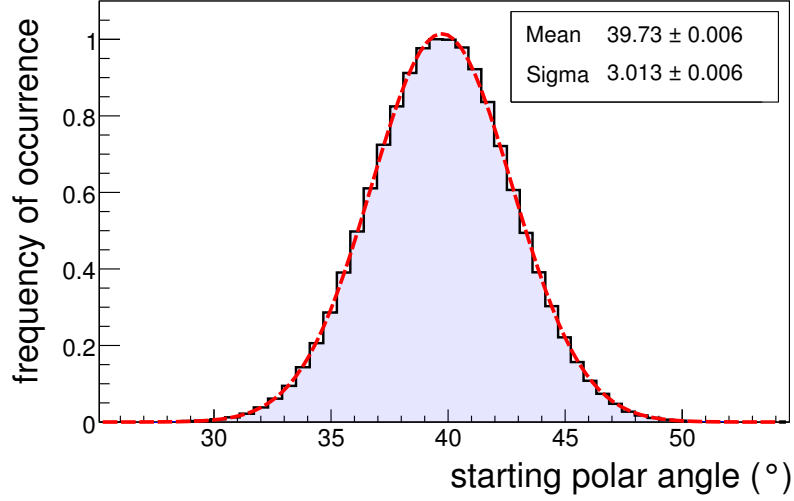


**Figure 5.20:** Source angular distribution as determined by differentiation of the measured TF of figure 5.19. Input values:  $U_{P_a}^{\text{eff}} = -18583.2$  V,  $B_s = 4.5$  T,  $B_{P_a} = 1 \cdot 10^{-3}$  T.

**Table 5.2:** Overview of the influence of the chosen input parameters on the calculated angular distribution. The standard setup ( $U_{P_a}^{\text{eff}} = -18583.2$  V,  $B_s = 4.5$  T,  $B_{P_a} = 1 \cdot 10^{-3}$  T) is compared to a variation of the individual parameters  $U_{P_a}^{\text{eff}}$ ,  $B_s$  and  $B_{P_a}$ , as well as a combination of these.

varied parameter	$\langle \theta \rangle$ (°)	$\sigma_\theta$ (°)
standard setup	39.73	3.013
$U_{P_a}^{\text{eff}} = -18583.3$ V	38.34	3.044
$B_s = 4.45$ T	39.47	2.985
$B_{P_a} = 1.05 \cdot 10^{-3}$ T	38.60	2.893
combination	37.02	2.901

parameters as well as a combination of all of them on the fit result. The assumed amplitudes of the variations are an upper limit for what is expected in reality. Additionally, the individual effects are correlated, as an increase or decrease of  $B_s$  and  $B_{P_a}$  by the same relative amount does not change the results at all. As the real angular distribution will not be a perfect Gaussian distribution, the binned data set is used for the further analysis procedure.

### 3. Determination of the analytical TF $T^{\text{theo}}(E_s)$

The angular distribution of the source, which was previously determined via differentiation, is now used to calculate the transmission probability depending on the electron start energy  $E_s = qU_{\text{egun}}$ . A calculation of the integral (5.16) requires a determination of the lower and upper integration limits,  $\theta_{\text{min}}$  and  $\theta_{\text{max}}$ . Here,  $\theta_{\text{min}}$  is fixed to some value where the angular distribution of figure 5.20 has dropped to a negligible value, e.g.  $\theta_{\text{min}} = 20^\circ$ . The upper integration limit depends on the actual starting energy  $E_s$

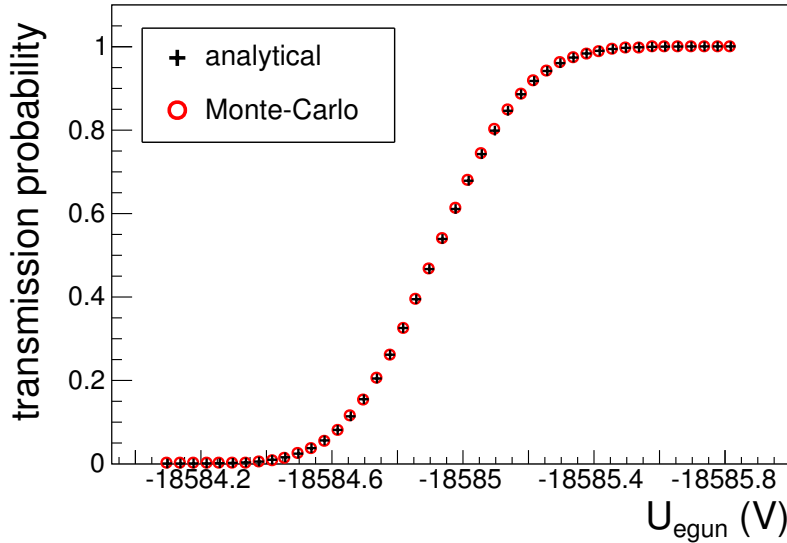


**Figure 5.21:** Calculated analytical transmission function for  $B_{p_a} = 1 \cdot 10^{-3}$  T. For comparison, also the Monte-Carlo data are shown. The source angular distribution of figure 5.20 was used along with the “standard setup” input values of table 5.2.

and can be calculated according to eq. (5.17). Figure 5.21 shows the resulting analytical transmission function. The source angular distribution according to the histogram of figure 5.20 was used to determine the transmission probability for the same energy values  $E_s = qU_{\text{egun}}$  as were used for the Monte-Carlo simulation. The upper integration limit  $\theta_{\text{max}}(E_s)$  was calculated with the same input values which were used to obtain the angular distribution of figure 5.20 (labeled as “standard input” in table 5.2). Additionally, the underlying Monte-Carlo data is shown. Apparently, the two transmission functions agree very well. A more quantitative comparison is shown in figure 5.22, where the ratio between the transmission probability from the Monte-Carlo simulation and the probability as calculated analytically is displayed.

Two different analytical calculations are shown. For the “standard setup” data, steps 2 and 3 were carried out using the “standard input” of table 5.2. Additionally, a calculation using the “combination” setup is displayed. As in the case for the determination of the energy distribution, large deviations occur at low e-gun potentials, where the count rate is also low. However, the two analyses agree within these statistical fluctuations. Therefore, it can be concluded that the determination of the source angular distribution via this method is not oversensitive to small deviations of the chosen analysis parameters.

#### 4. Measurement of $T^{\text{meas}}(E_s)$ at the standard magnetic field

The next step to approve the validity of the previously determined source angular distribution is a measurement of the transmission function at standard spectrometer conditions. Therefore, the magnetic field is reduced back to  $\sim 3.5 \cdot 10^{-4}$  T, using the

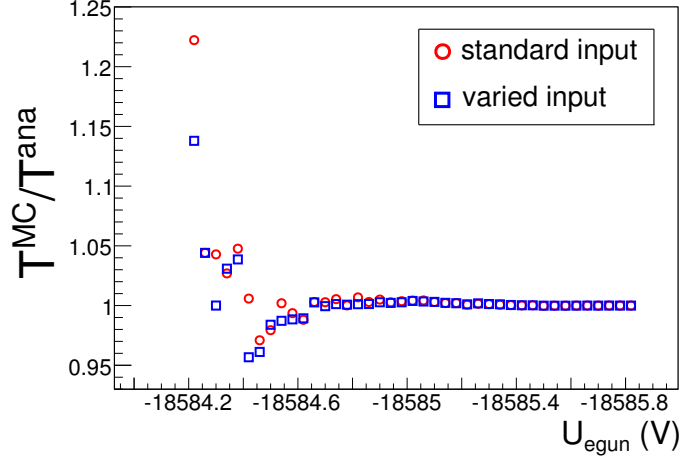


**Figure 5.22:** Comparison of the transmission function as determined with a Monte-Carlo simulation and with an analytical calculation. Two calculations are shown, one using the “standard input” of table 5.2 and one using the “combination” setup where all three parameters have been altered.

1 *minimum* LFCS setup of table 1. With a magnetic field, which is reduced by a factor of 3, also the width of the transmission function is expected to be decreased from  $\sim 1.5$  eV ( $B_{P_a} = 1 \cdot 10^{-3}$  T) to a value of  $\sim 0.5$  eV ( $B_{P_a} = 3.5 \cdot 10^{-4}$  T). To be able to map the transmission function sufficiently well, a smaller step size of 20 mV is chosen for the e-gun potential within this Monte-Carlo simulation (note again that it is assumed that fluctuations of this value are negligible due to the elevation of both spectrometer and e-gun to the same potential). The results are shown in figure 5.23. In order to calculate the corresponding analytical transmission function, the angular distribution is used, which was determined within the measurement at increased magnetic field strength. Carrying out the integration (5.16) with an input central field strength  $B_{P_a} = 3.5 \cdot 10^{-4}$  T yields a transmission function as displayed in figure 5.24 (squares). For comparison, also the Monte-Carlo data are shown. Obviously, the two transmission functions show large deviations, which are caused by incorrectly assumed values for the analyzing magnetic field and electrostatic potential.

## 5. Determination of the free parameters $B_{P_a}$ and $U_{P_a}$

As pointed out above, the analytical transmission function can only be determined correctly, if the analyzing magnetic field  $B_{P_a}$  and electrostatic potential  $U_{P_a}$  are known. They can be determined if the above analyses steps 2-4 are performed within a  $\chi^2$  fit according to (5.12). Carrying out such a fit yields  $B_{P_a} = 3.48 \cdot 10^{-4}$  T and  $U_{P_a} = -18583.19$  V, which agrees well with the input values  $B_{P_a}^{\text{input}} = 3.475 \cdot 10^{-4}$  T and  $U_{P_a}^{\text{input}} = -18583.19$  V. The resulting transmission function is also shown in figure 5.24 (crosses). Obviously, an improved agreement is achieved by the fitting procedure.

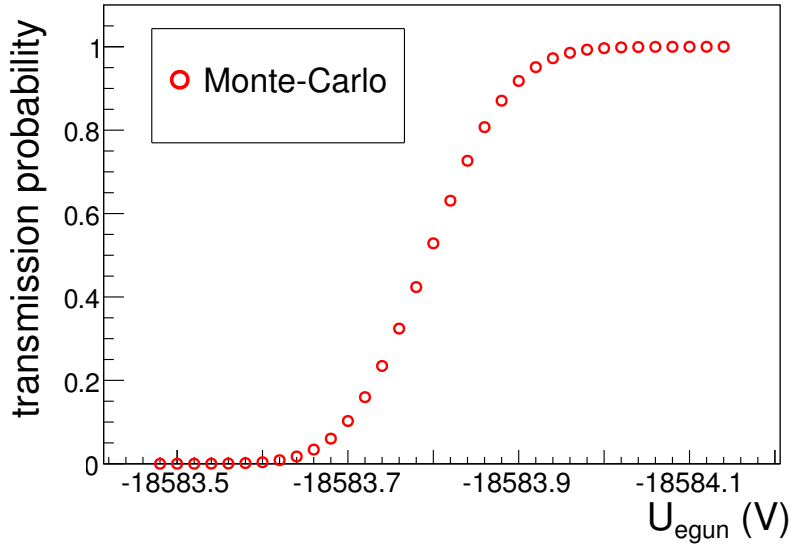


**Figure 5.23:** Transmission function for an analyzing magnetic field strength  $B_{P_a} = 3.5 \cdot 10^{-4}$  T as determined with a Monte-Carlo simulation.

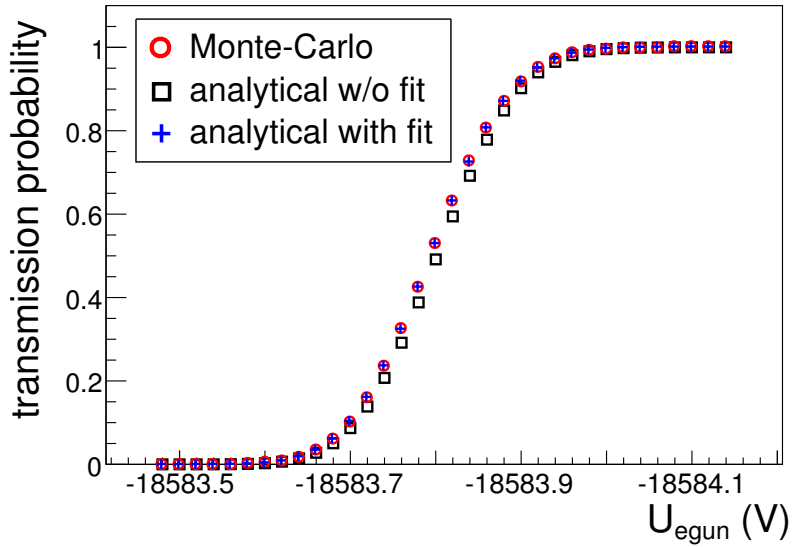


**Figure 5.24:** Analytical transmission function as calculated from the source angular distribution of figure 5.20 for the standard analyzing magnetic field strength. The Monte-Carlo data are shown for comparison. Squares: Analysis with assumed “standard setup”  $U_{P_a} = -18583.2$  V,  $B_{P_a} = 3.5 \cdot 10^{-4}$  T and  $B_s = 4.5$  T. Crosses: Analysis with  $U_{P_a}$  and  $B_{P_a}$  as free parameters, which are determined by fitting  $T^{\text{theo}}$  to  $T^{\text{meas}}$ .

### 5.3.3 Transmission function depending on starting energy and angular distribution

The above considerations to determine the angular distribution of the source have neglected the fact that the electrons are not strictly mono-energetic but display an intrinsic energy distribution. In reality, however, these effects have to be combined into a single two-dimensional transmission function  $T_{\text{tot}}(U_{\text{egun}}, \theta_{\text{egun}})$ . A visualization of the combined effect of a source energy and angular distribution on the transmission probability can be found in figure 5.25. Within the figure, fixed values for the spectrometer potential  $U_0$ , the e-gun potential  $U_{\text{egun}}$  and the e-gun angle  $\theta_{\text{egun}}$  are assumed, i.e. a single measurement point is considered for which the transmission probability has to be determined. The minimal starting angle  $\theta_{\text{min}}$  determines the minimal required starting energy  $\epsilon_{\text{min}}(U_{\text{egun}}, \theta_{\text{min}})$  for which transmission is actually possible. For all energies  $\epsilon_i > \epsilon_{\text{min}}$ , the transmission probability  $T(\theta_{\text{max}}(\epsilon_i))$  can be determined by an integration of the source angular distribution  $\omega(\theta)$  within the interval from  $\theta_{\text{min}}$  to  $\theta_{\text{max}}(\epsilon_i)$ . In order to obtain the total transmission probability  $T(U_{\text{egun}}, \theta_{\text{egun}})$ , the probabilities  $T(\theta_{\text{max}}(\epsilon_i))$  have to be weighted by their probability within the energy distribution  $\hat{F}(\epsilon)$  and added up.

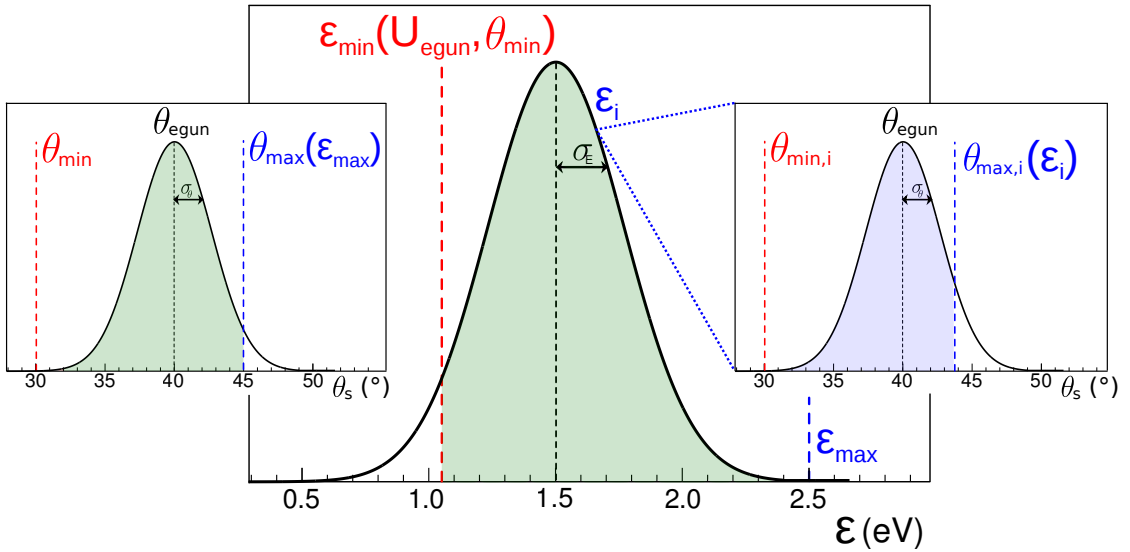


**Figure 5.25:** Illustration of the transmission probability depending on the source energy and angular distribution. For a particular e-gun potential  $U_{\text{egun}}$ , the minimal starting angle  $\theta_{\text{min}}$  determines the minimal starting energy  $\epsilon_{\text{min}}(U_{\text{egun}}, \theta_{\text{min}})$  required for transmission. Correspondingly, the maximal starting energy  $\epsilon_{\text{max}}$  restricts the transmitted electrons to angles below  $\theta_{\text{max}}(\epsilon_{\text{max}})$ . The total transmission probability can be obtained by integration over the angular distribution between  $\theta_{\text{min}}$  and  $\theta_{\text{max}}(\epsilon_i)$  for all  $\epsilon_i > \epsilon_{\text{min}}(U_{\text{egun}}, \theta_{\text{min}})$ .

This procedure is expressed by the following integral:

$$\begin{aligned}
 T(U_{\text{egun}}, \theta_{\text{egun}}) &= \int_{\epsilon_{\min}(U_{\text{egun}}, \theta_{\min})}^{\epsilon_{\max}} T(\theta_{\max}(\epsilon_i)) \cdot \hat{F}(\epsilon_i) d\epsilon \\
 &= \int_{\epsilon_{\min}(U_{\text{egun}}, \theta_{\min})}^{\epsilon_{\max}} \left( \int_{\theta_{\min}}^{\theta_{\max}(\epsilon_i)} \omega(\theta) d\theta \right) \cdot \hat{F}(\epsilon_i) d\epsilon
 \end{aligned} \tag{5.20}$$

If the energy and angular distribution are known, this integral allows to calculate the transmission probability, taking into account the full source effects. However, as pointed out in the previous section, this relation at first has to be used to determine the source angular distribution.

Unfortunately, the two integrals are not independent from each other, but form a so called Fredholm integral equation [254]. Such integral equations often do not have an analytical solution and consequently must be solved numerically. The first step here is a discretization of the unknown function. In our case, the angular distribution  $\omega(\theta)$  is divided into  $n$  steps with equal step size  $\Delta\theta$  between  $\theta_{\min}$  and  $\theta_{\max}$ . Secondly, the the integral (5.20) has to be rewritten to

$$\begin{aligned}
 T(U_{\text{egun}}) &= \int_{\theta_{\min}}^{\theta_{\max}} \omega(\theta) \left( \int_{\epsilon_{\min}(U, \theta)}^{\epsilon_{\max}} \hat{F}(\epsilon) d\epsilon \right) d\theta \\
 &= \int_{\theta_{\min}}^{\theta_{\max}} \omega(\theta) g(U, \theta) d\theta,
 \end{aligned} \tag{5.21}$$

and must be replaced by a quadrature rule:

$$T_j = \Delta\theta \cdot \sum_{i=1}^n \omega_i \cdot g(U_j, \theta_i), \tag{5.22}$$

where  $i$  denotes the discretized values of  $\theta$  and  $j$  denotes the measurement points at different e-gun potentials  $U_{\text{egun},j}$ . This system of linear equations can be solved if the coefficients  $c_{ji} = \Delta\theta \cdot g(U_j, \theta_i)$  are known. These can be calculated by integrating the source energy distribution from the variable lower limit  $\epsilon_{\min}(U_j, \theta_i)$  to the fixed upper limit  $\epsilon_{\max}$ . Ideally, the system of linear equations (5.22) would be solved by using an iterative solver such as the LU decomposition method [209]. However, this method is only applicable if the solution vector, corresponding to the transmission probabilities  $T_j$ , and the coefficient matrix  $c_{ji}$  match very well such that the system is actually solvable. In reality, though,  $T_j$  is influenced by statistical and systematic effects, and the coefficients  $c_{ji}$  depend on the underlying model of e.g. the source energy distribution. Therefore, direct solvers are not suitable in the majority of cases. Instead, a determination of the angular distribution is achieved by a  $\chi^2$ -fit analogously to (5.12). The theoretical transmission rate is calculated via (5.22), leaving the  $\omega_i$  as free parameters. Thereby, for the initial discretization of the angular distribution  $\omega(\theta)$  into  $n$  intervals between  $\theta_{\min}$  and  $\theta_{\max}$ ,  $n$  has to be smaller or equal to the number of measurement points. For the fit to work reliably, an initial guess for  $\theta_{\min}$ ,  $\theta_{\max}$  and  $\omega_i$  has to be used. These starting values

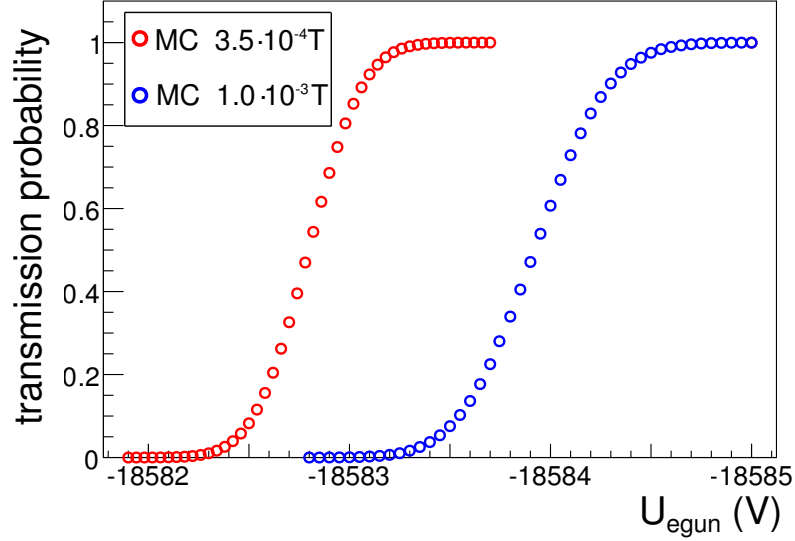


**Figure 5.26:** Monte-Carlo simulation of transmission functions for two different central field values  $B_{P_a} = 3.5 \cdot 10^{-4}$  T and  $B_{P_a} = 1 \cdot 10^{-3}$  T taking into account the energy as well as angular distribution of the source.

should ideally be based on measurements with the pinch method and simulations.

In principle, this method can also be applied to the previous investigations (determination of the energy and angular distribution of the source by the pinch method). However, larger errors are expected due to the discretization.

The measurement procedure is analogously to that of section 5.3.2 b), which is based on Monte-Carlo data as shown in figure 5.26. The measurement strategy involves a measurement at the standard central magnetic field  $B_{P_a} = 3.5 \cdot 10^{-4}$  T, and at an increased field strength of  $B_{P_a} = 1 \cdot 10^{-3}$  T, which are both shown in the form of Monte-Carlo data. Obviously, the transmission function is broader for higher central magnetic field values. Furthermore, in this case larger e-gun potentials are required as the transformation  $E_{\perp} \rightarrow E_{\parallel}$  is less efficient at higher  $B_{P_a}$ . When applying the above described method to the simulation with an increased analyzing field strength, an angular distribution as displayed in figure 5.27 is obtained. The data for an increased central magnetic field strength is used in this first step for the same reasons which were already explained in section 5.3.2. Comparing these results to the case without source energy distribution, see figure 5.20, it can be seen that the angular distribution shows larger deviations from the Gaussian distribution which was used as an input. Although the fit still yields good agreement between calculated values and input values ( $\theta_{\text{egun}}^{\text{fit}} = 40.01^{\circ}$  and  $\theta_{\text{egun}}^{\text{input}} = 40^{\circ}$ ,  $\sigma_{\theta}^{\text{fit}} = 2.978^{\circ}$  and  $\sigma_{\theta}^{\text{input}} = 3^{\circ}$ ), the binned data has to be used for the following calculation of the analytical transmission function. Calculating the transmission probabilities for the individual e-gun potentials according to (5.22) gives an analytical transmission function as shown in figure 5.28. For comparison, also the Monte-Carlo data are shown. Very good agreement on the  $10^{-3} - 10^{-2}$  level is achieved at large e-gun potentials and

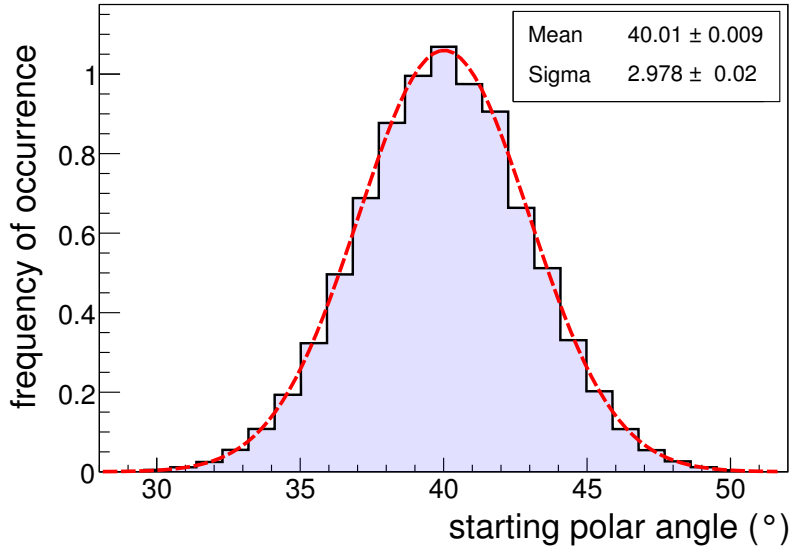


**Figure 5.27:** Source angular distribution as determined from the MC data of figure 5.19, taking into account the full source effects of energy and angular distribution. A Gaussian fit to the resulting distribution shows good agreement with the input values  $\theta_{\text{egun}} = 40^\circ$  and  $\sigma_\theta = 3^\circ$ .

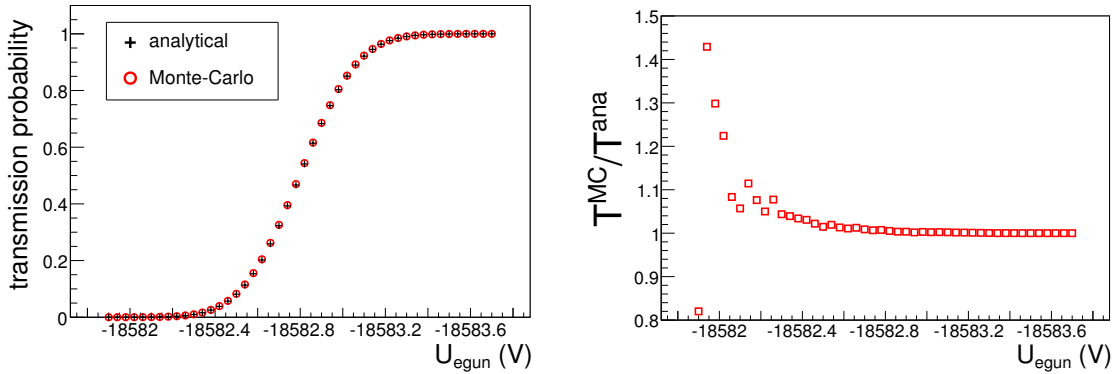


**Figure 5.28:** Transmission function with full source effects. The analytical TF was determined by calculating (5.22) using the angular distribution of figure 5.27. Comparing the analytical results to the Monte-Carlo data yields good agreement except for the statistical limitations at low count rates.

correspondingly large count rates. The large fluctuations at very low count rates result from the statistical limitations in this region. However, in the intermediate region, the deviation between Monte-Carlo and analytical results only slowly approaches the desired sub-percent level. This behavior is attributed to the complex relation between the angular and energy emission characteristics of the source and the transmission function. An imprecision in the determination of the source properties obviously directly influences the precision with which the measured data can be reproduced.

#### 5.3.4 Determination of the spectrometer properties

In the previous sections it was shown that the transmission probability as a general rule depends on the spectrometer properties, which complicates an independent determination of the source properties (and vice versa). However, it was also demonstrated that an agreement between analytical and measured transmission functions can be achieved when leaving the spectrometer properties as free parameters within a  $\chi^2$ -fit.

To begin with, it was shown that the effective analyzing potential  $U_{P_a}^{\text{eff}} = U_{P_a} + \langle E \rangle / q$ , which incorporates effects from the source, can be determined when measuring the source energy distribution. However, it is the analyzing potential  $U_{P_a}$  which is the actual quantity to be measured. As pointed out, the source energy spread is caused by the finite UV-photon energy width used for illumination in combination with the cathode work function. Independently of the shape of the actual distribution, electrons with vanishing starting energies are expected when the photon energy exactly matches the work function. For these electrons, at the very low end of the tail, the kinetic energy is completely determined by the e-gun potential. As this can be set very precisely, the determination of the analyzing potential comes down to a determination of the specific e-gun potential for which transmission just starts. However, the number of electrons, which are released at such low energies is very small. Therefore, low count rates are expected even in case of high e-gun emission rates. Consequently, the spectrometer and detector background has to be lower than the actual count rate there for this method to work.

For all of the above simulations, a standard potential setup with inner electrode potentials which are more negative than the vessel potential was used. Such a setup is required in order to reduce the background below an acceptable limit ( $< 10^{-2}$  cps). However, due to the large count rates ( $> 10^3$  cps) which are ideally used for standard transmission function measurements, an increase of the background rate even by two orders of magnitude would be negligible. Therefore, measurements could be conducted where the inner electrode is elevated to the same potential as the main spectrometer vessel. Such a setup has the distinct advantage that the electrostatic potential can be calculated rather precisely. When the source energy distribution is determined under such conditions, the relation between the e-gun potential  $U_{\text{egun}}$  and the actual electron starting energy  $E_s$  would be revealed. With this additional information, the real analyzing potential  $U_{P_a}$  can be determined for the standard potential setup.

Secondly, the analyzing magnetic field  $B_{P_a}$  has to be determined. It was shown, that a true and precise value of  $B_{P_a}$  can be obtained by performing the analysis procedure based on an increased central field strength within a fitting routine, leaving the

analyzing magnetic field as a free parameter. However, this method is only reliable if other influences on the transmission function can be neglected. Otherwise, the fitting procedure could try to compensate these effects by adjusting  $B_{Pa}$  to obtain a better agreement between analytical calculation and Monte-Carlo or measured data.

## 5.4 Systematic effects and Conclusions

The results, which were shown for the above measurement and analysis procedure, were obtained by assuming idealized measurement conditions. Evidently, systematic effects will arise from the non-ideal conditions of an actual measurement:

- The magnetic field setup was assumed to fulfill the transmission condition, which may not be guaranteed within the initial measurements.
- Disturbing magnetostatic effects, such as localized stray fields from magnetic materials, an imperfect compensation of the earth magnetic field or tilted coils have not been taken into account. These effects influence the experimental magnetic field configuration, resulting in a deviation from simulation input.
- The position of electric field shaping elements could deviate from the nominal position, thereby influencing the electrostatic potential in the volume of the spectrometer.
- If the source properties can only be assessed with limited precision, this would directly translate into imprecisions in the determination of the spectrometer properties.
- The source energy distribution could change with time, e.g. due to a damage of the cathode coating by ion bombardment, which directly influences the transmission function measurements. On top of this, the angular emission characteristics of the e-gun could change with time due to aging.
- As many transmission function measurements are required to fully investigate and characterize the main spectrometer, the electron rates have to be rather large ( $\mathcal{O}(10 - 100\text{kHz})$ ). However, the detector efficiency could decrease at such high rates [255], an effect which is still under investigation. Possible pile-up effects and DAQ or electronics dead-time could result in systematic effects on the transmission function.

Simulations of the KATRIN neutrino mass sensitivity revealed that the required precision in the determination of the transmission function has to be on the level of 1-2%. The measurement and simulation strategies, which were presented within this section have shown that this precision can be reached indeed if disturbing influences can be controlled and minimized. However, should any of the above mentioned effects be larger than expected, this goal might not be met. Therefore, strong and sustained efforts have to be made to suppress these influences below an acceptable limit.



## Muon-induced background

An important background contribution of central relevance to the design of electrostatic spectrometers stems from secondary electrons emitted from the large spectrometer surface. The majority of these electrons is expected to be muon-induced, but also a  $\gamma$ -induced component exists. The background generating mechanism (section 6.1) is identical for both sources and based on a radial drift of electrons due to static distortions of the electromagnetic field. As the KATRIN experiment is built at ground level, a large number of muons ( $10^5/\text{s}$ ) passes through the spectrometer. Due to the high interaction probability with the stainless steel of the vessel, a large number of secondary electrons is expected to be produced. Even if the spectrometer would be completely surrounded by a muon veto with negligible inefficiency, the combination of high veto rate and the long time constants between the primary muon and the eventual background hit at the detector ( $\mathcal{O}(10^{-3})$  s) would inhibit this active veto method, which has been successfully applied to surface-level detectors elsewhere.

Hence, alternative measures to suppress the background from these secondary electrons have to be employed (section 6.2). However, given the high expected initial rate of  $10^5$  electrons/s, the remaining background rate could possibly exceed the KATRIN design limit of  $10^{-2}$  counts per second (cps). Therefore, a muon detector system was built up and commissioned within this work to investigate in detail the muon-induced background component (section 6.3). Corresponding simulations (section 6.4) have revealed unfavorable electromagnetic conditions so that a secondary electron actually can penetrate into the sensitive volume of the main spectrometer. By combining these simulations with dedicated measurements, for which an appropriate strategy is outlined in section 6.5, the necessary understanding of the muon-induced background component can be obtained to suppress it below the design limit of  $10^{-2}$  cps. The necessity of such a low background rate is demonstrated in section 6.6, where the statistical neutrino mass sensitivity is investigated.

## 6.1 Background mechanism

Background investigations at Mainz [231, 256, 257] showed that the dominant part of the background arises from low-energy electrons, which are created at the vessel surface and penetrate into the flux tube. Although a large number of secondary electrons is produced at sea level ( $\sim 100$  per  $\text{m}^2$ ) at the inner surface of a spectrometer, only a small fraction of these can actually reach the sensitive volume of the spectrometer and finally hit the detector, where they contribute to the overall background rate. Initially, two mechanisms were discussed, which could lead to a radial electron motion:

- radial collisional diffusion, and
- radial magnetron motion due to small deviations from axial symmetry.

As shown in [258], analytical calculations suggest that the radial diffusion times average on the order of minutes. However, within test experiments at Mainz, using a pulsed X-ray source, it was shown that the background started to rise immediately after switching on the X-ray tube, thus ruling out radial collisional diffusion as the major responsible effect for the observed background.

In order to be able to investigate the second possible effect, namely the radial magnetron motion, the electron motion within the electromagnetic field configuration of a MAC-E filter has to be discussed in broader terms. Generally, the electron motion is composed of three components:

1. a fast gyration around the so called *guiding center*,
2. a longitudinal motion of the guiding center along the guiding magnetic field line, resulting in axial oscillations for trapped particles and
3. a slower motion perpendicularly to this field line.

All of these motions are governed by the layout of the electromagnetic fields. Of particular interest for the investigations here is the third component, the so called *magnetron drift*. The corresponding drift velocity  $\vec{v}_d$  is composed of two main components:

$$\vec{v}_d = \vec{v}_{E \times B} + \vec{v}_{\nabla B}, \quad (6.1)$$

where the first term is the  $\vec{E} \times \vec{B}$  drift, given by

$$\vec{v}_{E \times B} = \frac{1}{B^2} \vec{E} \times \vec{B}, \quad (6.2)$$

and the second term is the *gradient B drift*:

$$\vec{v}_{\nabla B} = \frac{E_{\perp} + 2E_{\parallel}}{eB^3} \cdot (\nabla \vec{B} \times \vec{B}). \quad (6.3)$$

Here,  $\vec{E}$  and  $\vec{B}$  denote the electric and magnetic fields,  $E_{\perp}$  and  $E_{\parallel}$  the transversal and longitudinal components of the kinetic energy of the electron,  $e$  the unsigned electron charge and  $c$  the velocity of light.

Ideally,  $\vec{E}$  and  $\vec{B}$  are axially symmetric around the central beam axis. In this case,  $\vec{E}$ ,  $\vec{B}$  and  $\nabla B$  are parallel with the z-r plane, as shown in figure 6.1. The components of  $\vec{E}$  and  $\nabla B$ , which are perpendicular to  $\vec{B}$ , cause azimuthal drift velocities  $\vec{v}_{E \times B, \text{azi}}$  and  $\vec{v}_{\nabla B, \text{azi}}$ . Consequently, electrons cannot change their radial position by this kind of motion. If, however, there exist small deviations from axial symmetry, the drift velocities also obtain radial components, as visualized in figure 6.2. Here, the specific case of a non-axially symmetric magnetic field in azimuthal direction  $\vec{B}_{\text{azi}}$  is shown. The same behavior is also observed in case of a non-axially symmetric electric field  $\vec{E}_{\text{azi}}$ <sup>1</sup>.

Such disturbances can result from magnetic structural materials surrounding the main spectrometer. Of major relevance in this context is the steel reinforcement of the concrete foundation of the KATRIN experimental hall, which was identified as a major source for non-axially symmetric magnetic fields. Therefore, stainless steel was used in the direct vicinity of the spectrometer [259]. Nevertheless, smaller magnetic disturbances on the order of  $\mu\text{T}$  were measured in [182].

As the major magnetic field contribution originates from the superconducting solenoids and the LFCS system, geometry effects from tilted or deformed coils could also induce significant non-axially symmetric magnetic fields. It was shown in [146] that the known remaining deformation of the LFCS coils leads to a radial electron drift which is about a factor of three smaller than the one induced by the magnetic materials.

In summary, the presence of non-axially symmetric electric or magnetic field components will result in a magnetron drift with an azimuthal as well as a radial component. The resulting magnetron motion causes electrons to move on a closed surface around the spectrometer axis. Without distorting non-axially symmetric contributions, this surface is symmetric around the axis, i.e. the guiding center retains the same radial coordinate for a fixed axial position. When non-axially symmetric fields are present, the radial coordinate will change, however, in the course of a single magnetron turn. The maximal radial drift distance is then determined by the radial drift velocity  $\vec{v}_{\text{d},r}$  and the time  $t_{\text{mag}}$  spent to complete one magnetron turn. Thereby, the parameter  $t_{\text{mag}}$  is determined by the azimuthal drift velocity  $\vec{v}_{\text{d},\text{azi}}$ . Consequently, the radial drift distance increases for decreasing values of  $\vec{v}_{\text{d},\text{azi}}$ . Section 6.4 will discuss in detail the influences of different electromagnetic field configurations on the probability for radial motion of low-energy electrons ( $<100$  eV).

As the main spectrometer is on sea level, the expected muon flux is rather large ( $\sim 1$  muon/( $\text{cm}^2 \cdot \text{min}$ )). Minimum ionizing muons with energies below 200 GeV easily penetrate the 3.5 cm thick stainless steel vessel where they lose energies on the order of 50 MeV due to ionization (generally  $dE/dx \sim 2$  MeV/( $\text{g} \cdot \text{cm}^2$ )). Secondary electrons, which are created close to the inner spectrometer surface (either directly by the muon or by muon-induced high-energy electrons) can exhibit a range in stainless steel which is sufficient to leave the vessel wall and propagate into the main spectrometer vacuum. For KATRIN, the low-energy part of the electron spectrum is most relevant as only these have a non-negligible probability to penetrate the flux tube. However, standard simulation

<sup>1</sup>This effect can be exploited to remove stored electrons from the main spectrometer volume by application of an electric dipole pulse, as discussed in section 8.2.1.

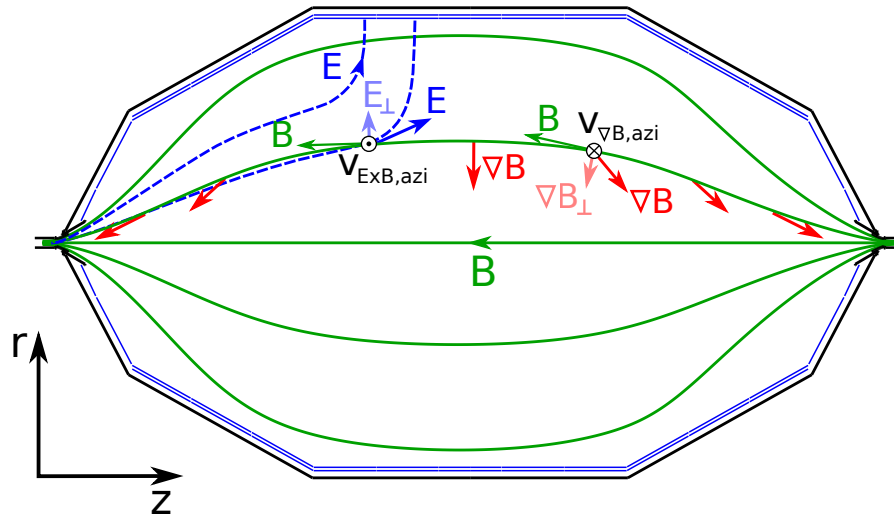


**Figure 6.1:** Illustration of the magnetron drift within axially symmetric electric and magnetic fields. The resulting drift velocities point in azimuthal direction and, hence, cannot change the radial position of the electron.

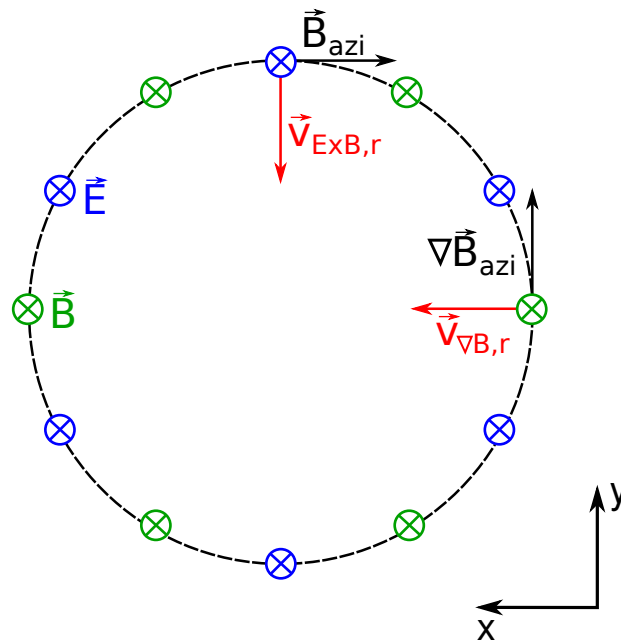


**Figure 6.2:** Illustration of the magnetron drift of electrons in presence of non-axially symmetric electric and magnetic fields. The resulting radial magnetron drift components can cause radial electron motion.

tools such as GEANT4 [260, 261] are not capable to reliably determine electron energy spectra below 1 keV due to the missing experimental data in this low-energy range. This also prevents an implementation of a reliable muon-induced electron energy generator into the KATRIN simulation software KASSIOPEIA so far. Consequently, the expected number of secondary electrons, emitted from the spectrometer surface, cannot easily be calculated. This calls for dedicated measurements with spectrometers of the MAC-E filter type to determine the secondary electron emission rate experimentally. Such measurements have been performed at the Mainz experiment and at the pre-spectrometer [262]. Both investigations revealed a rate of about 140 electrons per  $\text{m}^2$  and second emitted from the inner vessel surface. Correspondingly, the large inner surface of the main spectrometer ( $690 \text{ m}^2$ ) implies an overall electron emission rate as large as  $10^5/\text{s}$ . Comparing this value to the above considerations on the muon hit rate of the spectrometer, each muon should on average produce about 1.5 electrons on the inner vessel surface.

In order to be able to maintain a background rate as low as  $10^{-2}$  cps, only a fraction of  $< 10^{-7}$  of these secondary electrons may enter the flux tube. Accordingly, a highly efficient background suppression is required to fulfill this criterion.

## 6.2 Background suppression

There are two effects, which reduce the  $\mu$ -induced background rate, namely *magnetic* and *electrostatic shielding*.

### 6.2.1 Magnetic shielding

As already discussed above, in case of a perfectly axially symmetric magnetic field, the radial electron motion is prohibited. Due to the Lorentz force, the electrons are constrained to a cyclotron motion around the guiding magnetic field line and are hence reflected back to the surface where they have been emitted from. Only electrons which start with very small polar angles could circumvent this magnetic shielding. However, these electrons are guided along magnetic field lines on trajectories well outside of the sensitive spectrometer volume, as the flux tube has a safety distance of about 30 cm to the spectrometer surface. Based on previous measurements at the Mainz experiment, the magnetic shielding factor at the main spectrometer is expected to be of the order of  $\sim 10^5$ . This is not sufficient for a total shielding factor of  $\sim 10^7$ . Consequently, an additional background suppression method has to be employed.

### 6.2.2 Electrostatic shielding

Figure 6.3 visualizes the principle of electrostatic shielding for the case of to the main spectrometer. There, a double-layer inner electrode system was installed with a distance  $d_1 = 15 \text{ cm}$  and  $d_2 = 22 \text{ cm}$  to the inner vessel surface for the outer and inner layer, respectively. These wire layers are elevated onto a more negative potential ( $\Delta U_1 = -100 \text{ V}$ ,  $\Delta U_2 = -200 \text{ V}$ ) than the spectrometer vessel operated at its potential  $U_0$ . As

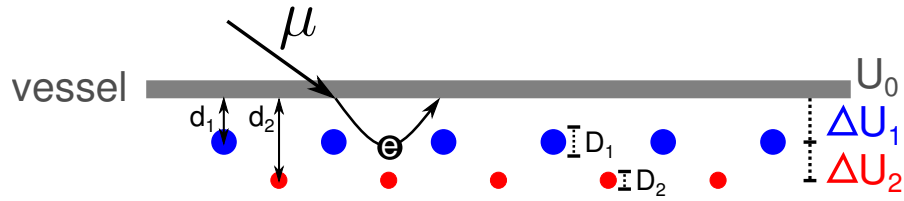


**Figure 6.3:** Electrostatic shielding principle. The more negative potential of the inner wire layers (placed at a distance  $d_1$ ,  $d_2$ ) repels low-energy electrons such that they cannot pass the inner electrode system. A double-layer system reduces the background more efficiently than a single-layer system due to the low mass (wire diameter  $D_2 < D_1$ ) of the inner layer.

a result, low-energy electrons ( $E_{\text{kin}} < q \cdot (U_1 - U_0)$ ) are repelled electrostatically and cannot reach the inner parts of the spectrometer volume. The key to a high background reduction factor is thus a low mass inner electrode system. Hence, a double-layer system, where the wires of the inner layer feature smaller diameters ( $D_2 = 0.2$  mm) than the outer layer ( $D_1 = 0.3$  mm) is more efficient than a single-layer system. A major advantage of such a setup is the fact that the support structure, which is the most massive part of the electrode system, is shielded by the second wire layer. On the basis of test experiments at Mainz [231, 257], a background reduction factor of  $\sim 10^2$  is expected.

Together with the dominant magnetic shielding, a total background reduction factor of  $\sim 10^7$  is expected for the  $\mu$ -induced background component. However, this reduction factor can be missed if magnetic distortions are larger than anticipated or if the inner wire electrode system cannot be operated in the double-layer mode (section 6.4). Both of these possible negative effects can be counteracted by increasing the central magnetic field strength above the nominal value  $B = 3.5 \cdot 10^{-4}$  T. This can be achieved by increasing the LFCS currents up to a maximal field strength  $B = 12 \cdot 10^{-4}$  T.

### 6.3 The KATRIN muon detector system

As pointed out in section 6.1, a thorough ab initio simulation of the  $\mu$ -induced background component is rather difficult, calling for dedicated test measurements to determine the background contribution of this particular source. For this purpose, an external muon detector system has been built [263] and commissioned [264] in the framework of this thesis. A part of the scintillation detectors, which were formerly used as muon veto at the KARMEN experiment<sup>2</sup> [267] have been refurbished and optimized for operation at the KATRIN experiment (section 6.3.1). After installation, commissioning measurements have been performed to determine the muon detection efficiency and the stability of the system (section 6.3.2).

<sup>2</sup>The KARlsruhe-Rutherford-Medium-Energy-Neutrino experiment (1990-2001) [265, 266] has investigated neutrino oscillations and neutrino-nucleus interactions with  $^{12}\text{C}$ ,  $^{13}\text{C}$  and  $^{56}\text{Fe}$  using charged current (CC) and neutral current (NC) reactions. Located at the Rutherford Appleton Laboratory in England, it used the ISIS rapid cycling synchrotron as a neutrino source from the  $\pi^+ - \mu^+$ -decay chain at rest with well-known energy and good time structure.

### 6.3.1 Assembly of the muon detector system

#### The scintillator modules

Figure 6.4 shows a schematic drawing of a scintillator module, which is part of the external muon detector system, comprising 8 modules arranged in 4 towers (see figures 6.7 and 6.8). Each module, made from polyvinyltoluol based organic plastic scintillator (BICRON BC-412), has a length of 3.15 m, a width of 0.65 m and a thickness of 0.05 m. When a muon penetrates through the scintillator material, photons are isotropically produced with an emission spectrum as shown in figure 6.5. In the case of a premium plastic scintillator such as BC-412, about 8500 photons are created per MeV of deposited energy. These photons are detected by four 2-inch photomultipliers (PMT)<sup>3</sup>, which are attached at each side of a module. It was shown in [267] that the photon detection efficiency can be increased if intermediate light guides (dimensions: 6 cm × 10 cm), to which the PMTs are attached, are mounted on the scintillator material. This improvement is due to the minimization of “blind” regions in the vicinity of the PMTs which would occur in case of direct coupling to the scintillator. The following parameters influence the muon-detection efficiency:

- The photon emission spectrum  $\phi_{\text{em}}(\lambda)$  has to match the work function of the bialkali photocathode material, which shows the highest quantum efficiency (26.5%) at a wavelength of 400 nm.
- When propagating through a material with a certain attenuation length  $\Lambda(\lambda)$ , the emission spectrum will be redshifted. This can be calculated by the Lambert-Beer law:

$$\phi_{\text{res}}(\lambda, x) = \phi_{\text{em}}(\lambda) \cdot \exp(-x/\Lambda(\lambda)), \quad (6.4)$$

where  $x$  is the path length of a photon. For BC-412,  $\Lambda(\lambda)$  was measured to about 380 cm at the emission maximum [267], which is larger than the size of a module.

- For the module geometry (see figure 6.4), total internal reflection is highly efficient to guide the photons with minimal losses. The refractive index of the scintillator ( $n_{\text{sc}} \approx 1.58$ ) as compared to that of air ( $n_{\text{air}} \approx 1$ ) prevents photons with incident angles above  $39^\circ$  to leave the scintillator. By additionally wrapping the scintillator material in creased aluminum foil (to minimize the area of direct contact, thereby leaving an air gap), those photons which left the scintillator can be reflected back with a probability of  $\sim 90\%$ . The aluminum foil had to be replaced as it was damaged during the decommissioning works at KARMEN and several subsequent transports.
- At the transition from the scintillating material to the light guide and finally to the PMT, reflection effects have to be minimized. For this purpose, optical bonding cement is used to glue the PMTs to the light guide (and the light guide to the scintillator). By this technique, air is removed from the contact area. Moreover,

---

<sup>3</sup>PMT type: Philip Valvo XP 2262/PA.

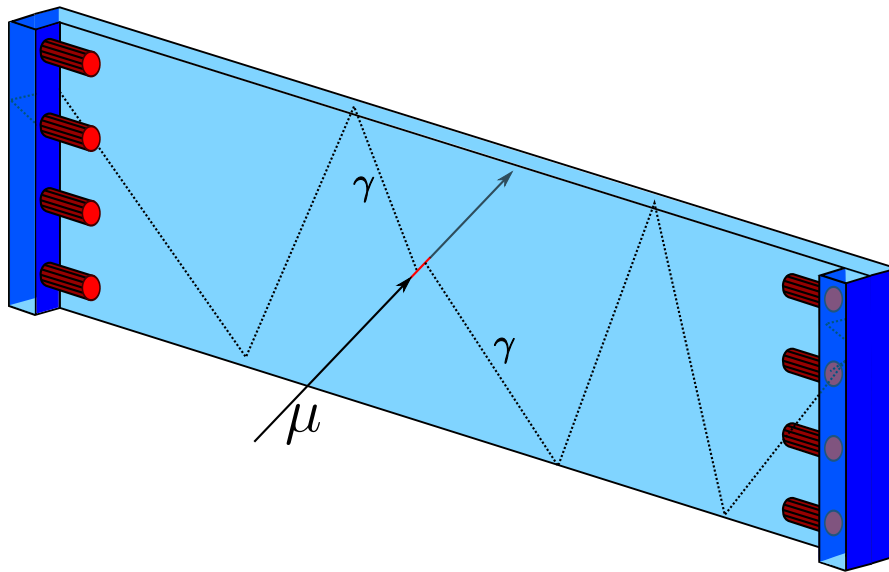


**Figure 6.4:** Schematic drawing of a muon detector module used as external counter. Each module, made from organic plastic scintillator (BICRON BC-412) (light blue), has dimensions  $615 \times 65 \times 5$  cm. Light guides (dimensions:  $6 \text{ cm} \times 10 \text{ cm}$ ) couple the scintillator bars to four 2-inch PMTs at both ends of the module, while high-reflectivity mirrors (dark blue) reduce photon losses.

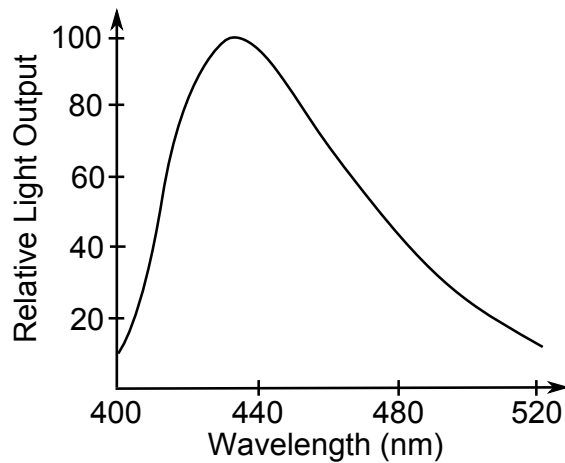


**Figure 6.5:** Emission spectrum of the organic plastic scintillators BICRON BC-412. The PMTs show the highest quantum efficiency at a wavelength of 400 nm. Therefore, the emission spectrum may not be shifted significantly towards higher wavelengths.

the loss effects due to the different refractive indices of the light guide ( $n = 1.58$ ) and the glass window of a PMT ( $n = 1.54$ ) are mitigated when using a material with an intermediate refractive index (here  $n = 1.56$ ). The majority of the PMTs were detached due to the long storage time of the modules and the shaking during transportation and had to be glued to the light guides with the same optical cement as it was used originally. Beforehand, the functionality of each PMT was checked with the help of a small scintillator sample coupled to the PMT within a light tight box.

- At the module ends and between the PMTs, high reflectivity mirrors (95% as compared to the 90% of the aluminum foil) are installed to minimize photon losses.
- The working principle of a PMT requires a specific high-voltage to be applied to the dynodes in order to achieve a sufficient electron multiplication factor  $f$ . In case of a 12 dynode-stage PMT (as used here), a voltage of  $U = -1.5$  kV yields values  $f = 10^6 - 10^7$ .

After re-furbishing of the modules, they were wrapped in light-tight PE foil.

Detailed simulations to optimize the module geometry and operating parameters have been performed in [267].

### Operation in magnetic fields

As the KATRIN main spectrometer is surrounded by a large air coil system (see section 4.3), the objective of maximizing the solid angle between towers on either side of the spectrometer (see figures 6.7 and 6.8) calls to place the muon-detector modules as close as possible to these coils. From this, the PMTs are subject to magnetic fields of up to  $10^{-3}$  T. However, the PMT gain is sensitive to magnetic fields as electrons, which move between the dynodes, are affected by the resulting  $\vec{E} \times \vec{B}$  drift. Consequently, the path of the electron is distorted in a way that it may not hit the next dynode, thereby reducing the multiplication factor  $f$  and hence the detection efficiency. Figure 6.6 shows the measured PMT rate as a function of the nearby air coil current. This test measurement, which was performed before the refurbishment, did employ smaller test scintillator modules, which were utilized within test experiments for the Edelweiss experiment. These modules were made by cutting a large module in half, and using PMTs only on one side. All LFCS coils were ramped simultaneously in 2 A steps, performing 20 min long rate measurements at each current setting. At LFCS currents above 40 A, which corresponds to a field strength of about  $3 \cdot 10^{-4}$  T at the position of the PMT, the rate started to drop significantly. The same behavior was observed largely independent of the orientation of the PMTs with respect to the magnetic field.

To shield the PMTs from the disturbing magnetic field, a common technique is to surround the units by a cylindrical casing made of a nickel-iron alloy (so called *mu-metal*) featuring a high magnetic permeability. These casings have a length  $l = 120$  mm, a diameter  $D = 56$  mm and a thickness  $d = 0.8$  mm. A drawback of this technique of implementing mu-metal casings is the fact that they locally produce a non-axially

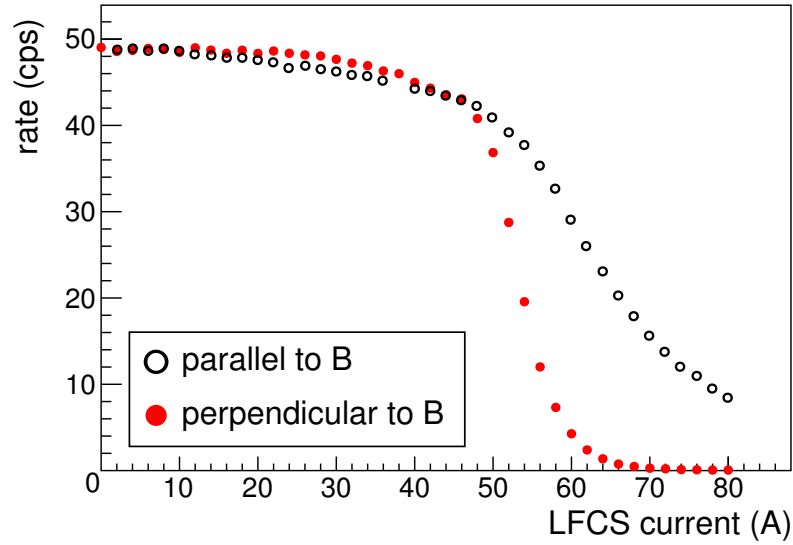


**Figure 6.6:** Break-down of the PMT detection efficiency as a function of the nearby magnetic fields. The maximal LFCS current of 80 A corresponds to an approximate field strength of  $6 \cdot 10^{-4}$  T at the position of the PMTs.

symmetric magnetic field, which could possibly increase the background rate at the main spectrometer. The strength of the magnetic disturbance can be estimated by the following analytical calculation. Assuming that all field lines, which formerly passed through the cross section of the mu-metal, are now within the mu-metal, a corresponding magnetic field strength of  $B_\mu = D/(2 \cdot d) \cdot 3 \cdot 10^{-4}$  T =  $1.05 \cdot 10^{-2}$  T is found. The magnetic moment  $\mu = M \cdot V$  of a cylindrical casing with mu-metal volume  $V = \pi \cdot D \cdot l \cdot d = 1.7 \cdot 10^{-5}$  m<sup>3</sup> and magnetization  $M = B_\mu/\mu_0$  can be used to calculate its contribution to the magnetic field at a certain distance  $r$ :

$$B = \frac{\mu_0}{4\pi} \cdot \frac{\mu}{r^3} = \frac{V \cdot B_\mu}{4\pi \cdot r^3}. \quad (6.5)$$

A total of 64 casings are used within the whole setup. If all casings were clumped up at the minimal distance of  $\sim 3$  m from the flux tube, a disturbing magnetic field strength  $B = 3.4 \cdot 10^{-8}$  T is expected, which is 2 orders of magnitude smaller than the contribution of the magnetic materials within the building and, hence, negligible.

In the original design of the modules, the PMTs were supported by large steel frames, which were replaced by stainless steel frames to further suppress magnetic disturbances.

### The support structure

A total of 8 detector modules was refurbished to survey specific parts of the large surface (690 m<sup>2</sup>) of the main spectrometer. To investigate different parts of the surface, the modules were stacked in towers and mounted on movable support structures. Two different designs were employed:

- a rate-sensitive design and
- a position-sensitive design.

**Rate-sensitive design:** The goal of this setup is to achieve a maximal geometrical coverage of the main spectrometer, hence maximizing the observed rate. Figure 6.7 shows a schematic drawing of the setup. In the following, these modules are labeled as M1 and M2. Within this setup, the entire main spectrometer surface is covered by the detectors if they are placed at the axial position of the analyzing plane. GEANT4 simulations targeted to calculate the expected number of coincident muon hits on the main spectrometer and on the muon detector are currently being performed [264]. When combining this information with the actual number of coincident electron events detected at the FPD, the ejection probability of electrons from the spectrometer surface per muon hit could be determined<sup>4</sup>.

**Position-sensitive design:** A second design, based on a coincidence technique between counters at adjacent vessel sides, is shown in figure 6.8. This design is employed to observe only a small part of the vessel surface. This setup gives a good position resolution for the location of the muon hit on the vessel. The three modules of the tower on the west side (labels M3, M4 and M5) are analyzed for coincidences with the second tower, also comprising three modules, on the east side (labels M6, M7 and M8). Three exemplary cases are shown, illustrating the position sensitivity as compared to the rate-sensitive layout. The east side modules can also be analyzed for internal coincidences, similar to the above rate-sensitive design. Section 6.5 will point out the necessity of both designs for the upcoming commissioning measurements.

## HV supply and data acquisition

The PMTs are supplied with high-voltage by a CAEN SY127 unit [269]. Each set of four PMTs at one side of a module is supplied by the same HV. Hence, the PMTs were matched according to their multiplication factors. The signals of the PMTs at each frontface of a module are passively added and guided by 25 m long 50  $\Omega$  coaxial cables to the data acquisition (DAQ) system. A DAQ electronics system, which was developed at IPE, KIT (version: IPE-4), is used. A detailed description of the electronics can be found in [270]. The DAQ electronics is controlled via the software ORCA<sup>5</sup> [271], which is also used in other experiments such as SNO [272] and MAJORANA [273]. The acquired data is converted into a ROOT tree [274], which can then be analyzed by the KASPER simulation and analysis software. The muon detector DAQ is synchronized to the focal plane detector DAQ via a GPS clock, also developed at IPE. This synchronization is necessary to be able to relate muon hits on the vessel surface (releasing electrons) with actual background events at the focal plane detector.

<sup>4</sup>The ejection probability has been measured in [268] to be about 2%. Measurements at the Mainz spectrometer and at the pre-spectrometer, however, suggest a 100% emission probability per muon hit.

<sup>5</sup>ORCA - Object-oriented Real-time Control and Acquisition

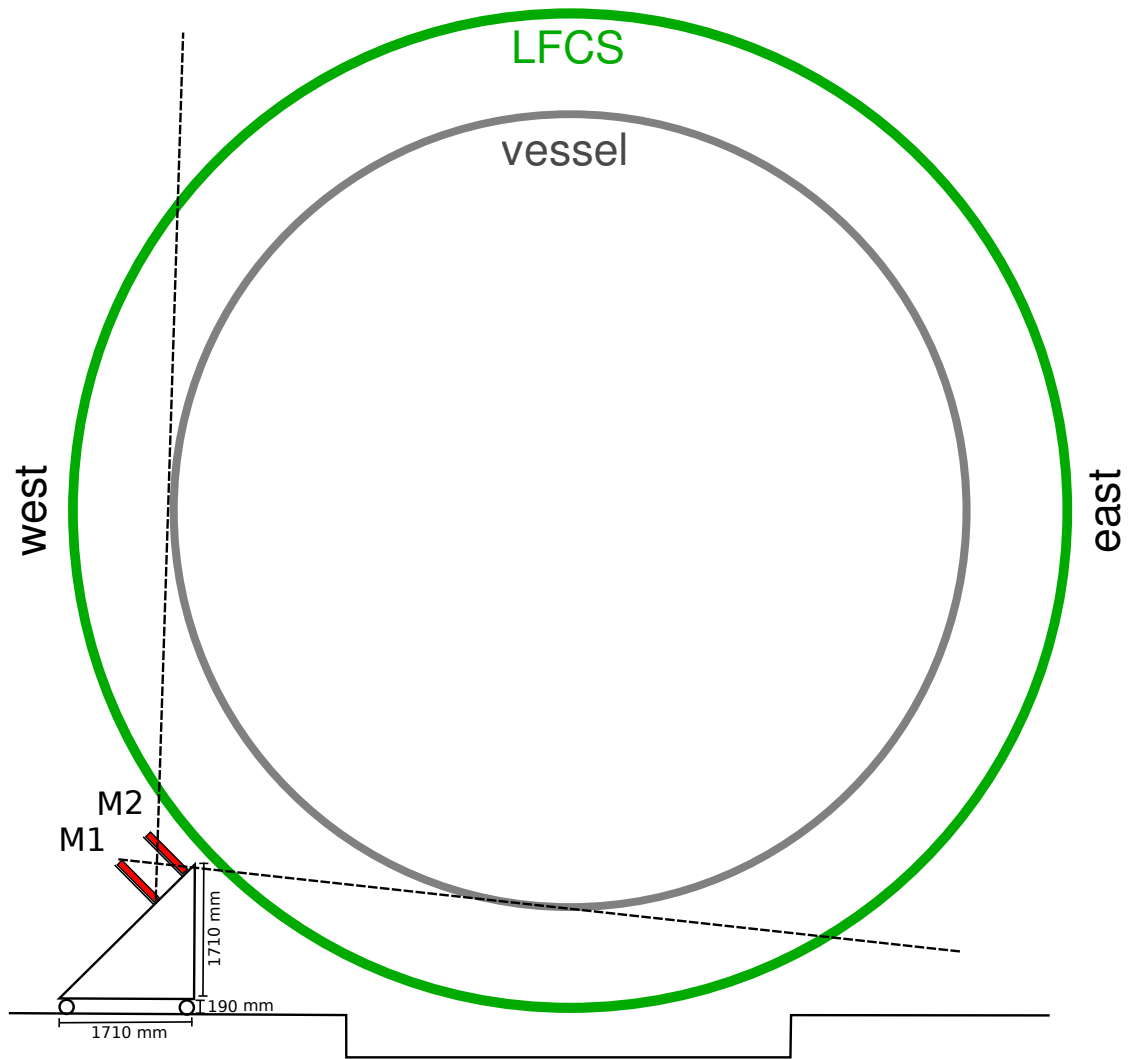


**Figure 6.7:** Schematic drawing of the rate-sensitive detector design. The maximal geometrical coverage is reached with this setup. This rather small unit can be positioned at any axial coordinate along the main spectrometer.

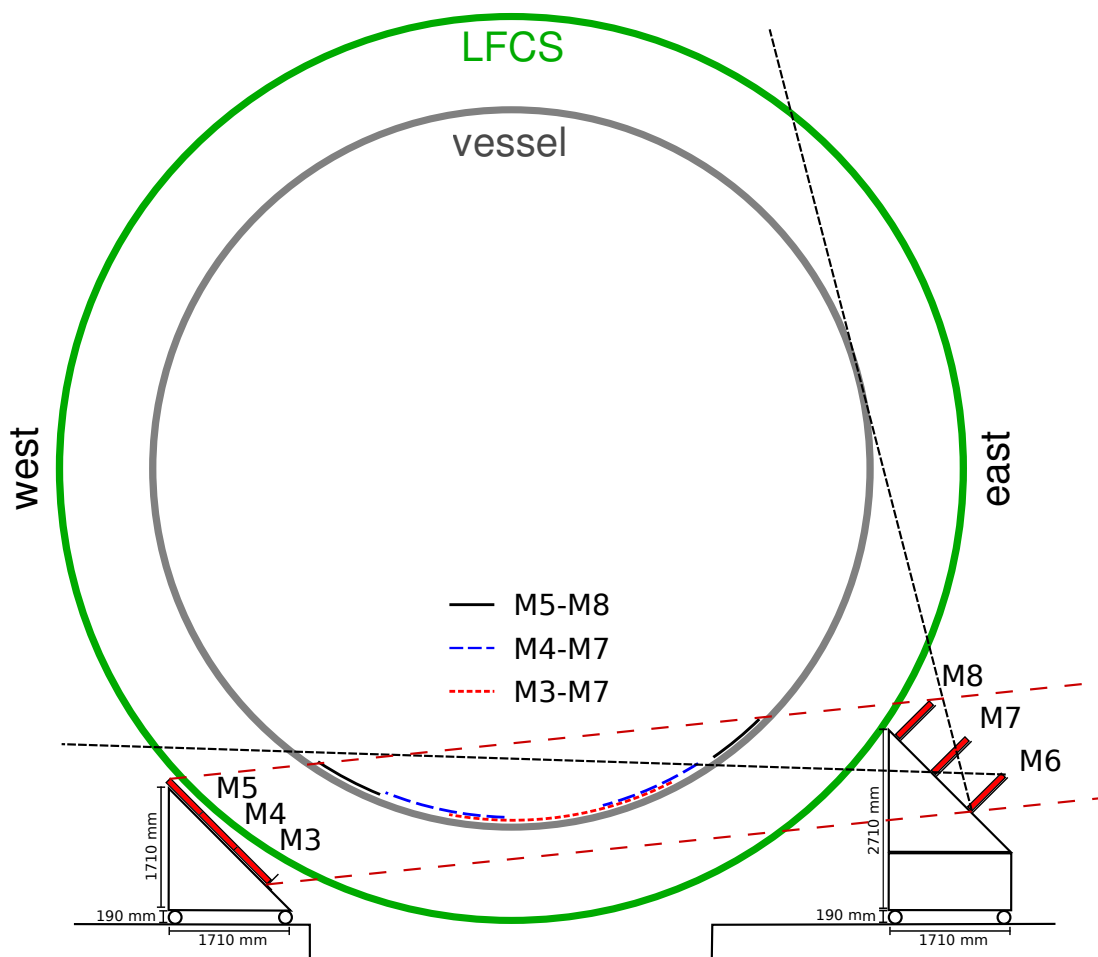


**Figure 6.8:** Schematic drawing of the position-sensitive detector design. Different parts of the spectrometer surface are mapped when analyzing coincidences between different modules. Additionally, M6-M8 can be used as rate-sensitive layout. However, due to the large height of the east module, the axial position can only be varied by about 3 m.

### 6.3.2 Commissioning measurements

During commissioning of the system, the basic functionality and muon detection efficiency had to be shown. To do so, several measurements were performed [264, 275], with the most important ones being presented here shortly:

**Optimization of working parameters:** In a first step, the supply voltages and the DAQ parameters (signal threshold and gain) had to be optimized. A minimal detection threshold had to be applied to cut off the “low-energy” noise from the PMTs. The signal gain was optimized to lift the signal above this threshold while avoiding events spilling over to the so called overflow bin (the DAQ system is limited to 4096 ADC channels). All parameters were chosen such that the Landau spectra of minimum ionizing muons of individual modules match each other, as shown in figure 6.9.

**Magnetic field dependence:** The functionality of the PMTs in the magnetic field of the LFCS was tested. Figure 6.10 shows the observed rate as a function of the air coil current after installation of the magnetic shields. Even at maximal magnetic field strength, a detection efficiency  $\epsilon > 0.9$  is observed. At the usual operating currents of  $< 50$  A, the efficiency loss amounts to less than  $4 \cdot 10^{-3}$ .

**Muon detection efficiency:** A test measurement was performed to determine the muon detection efficiency of an individual module. The modules M6, M7 and M8 were used for this purpose. All muon tracks which give rise to a coincidence of the modules M6 and M8 necessarily have to pass through module M7. The detection efficiency is then determined by the number of events, which was found in all three modules compared to that found in M6 and M8 only. The analysis of 40 individual runs with a length of 30 mins each revealed a detection efficiency of  $\epsilon = 0.936 \pm 0.003$ .

**Fluctuations of the muon rate:** The rate of cosmic ray muons at sea level is subject to small variations due to changing meteorological parameters in the upper atmosphere (pressure level 100-200 mbar) where muon production peaks. To test the size of the effect for the lower level of the KATRIN experimental hall, a long-term measurement (306 h total measurement time) was performed with all modules. The individual modules show typical rates of  $\sim 240$  cps, corresponding to a muon rate<sup>6</sup> of about 1 per  $\text{cm}^2$  and minute, in very good agreement with the expectations. Figure 6.11 shows the fluctuations of the average rate  $\langle r \rangle = 240$  cps as a function of time for module M1. The rate  $r$  was averaged over time bins of 300 s. All modules showed similar fluctuations on time scales of several hours, underlining the meteorological origin of the fluctuations of the muon rate.

More details on the individual measurements can be found in [264].

---

<sup>6</sup>Each module has dimensions  $315 \times 65$  cm and is tilted by  $45^\circ$ , which reduces the effective area. Considering also the detection efficiency  $\epsilon$ , gives a muon rate of 1.06 muons per  $\text{cm}^2$  and minute.

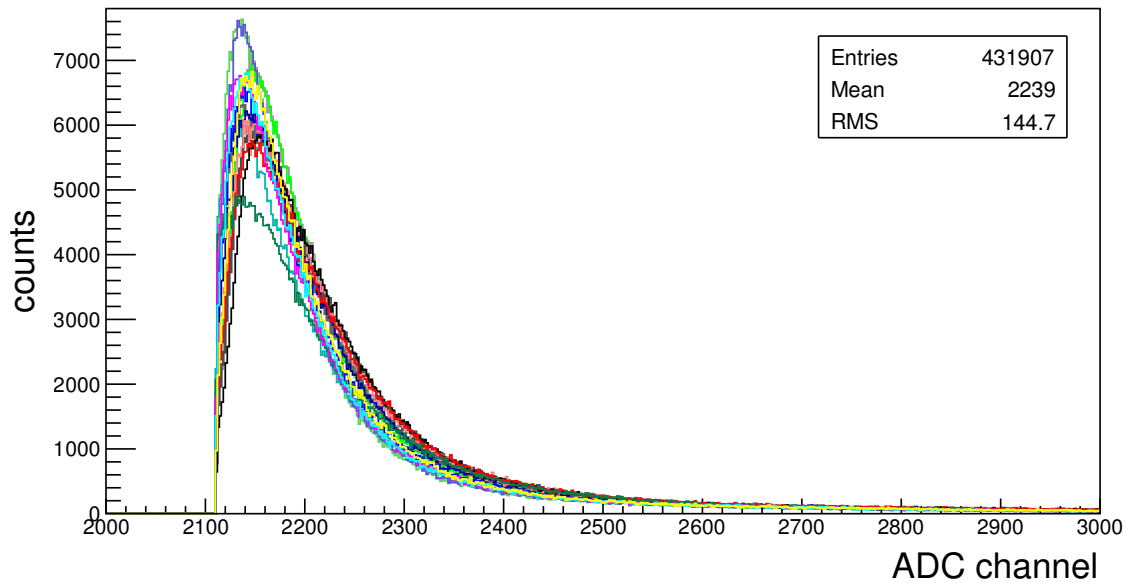


**Figure 6.9:** Landau spectra of each set of PMTs after optimization of the working parameters.

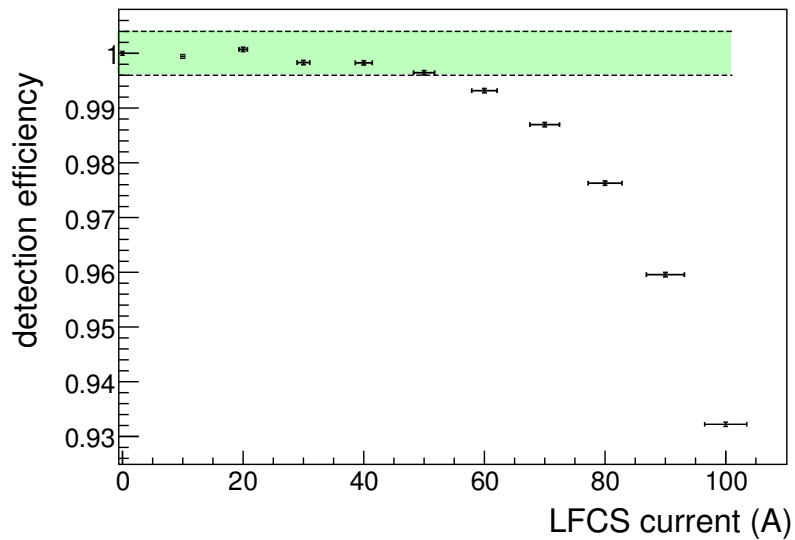


**Figure 6.10:** Detection efficiency in magnetic fields after installation of the mu-metal shielding. The nominal main spectrometer magnetic field setup requires LFCS currents up to about 40 A. For this parameter range, the muon detection efficiency is reduced by less than 0.4% (shaded area).

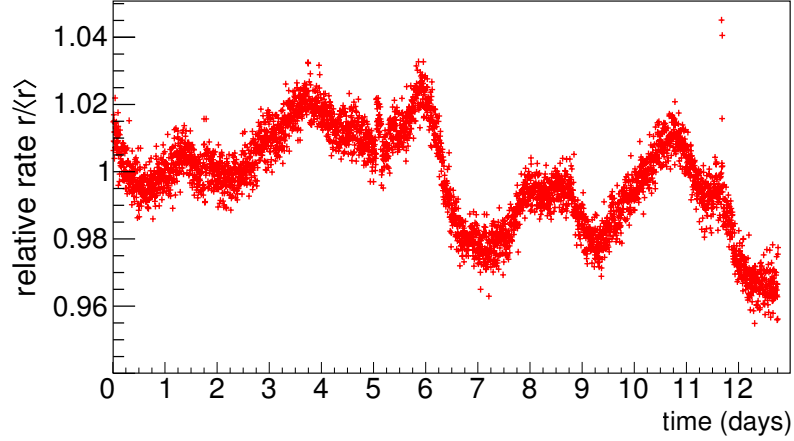


**Figure 6.11:** Fluctuations of the detected muon rate due to changing meteorological parameters. Shown is the deviation of the rate  $r$  (averaged over bins of 300 s) from the average rate  $\langle r \rangle = 240$  cps.

## 6.4 Simulations on muon-induced background

The intrinsic magnetic shielding properties as well as the additional electrostatic shielding by the inner electrode system strongly suppress  $\mu$ -induced background. As mentioned earlier in this chapter, the probability for radial electron motion depends on the starting energy of the electron as well as the electromagnetic configuration. A radial drift is only possible if the radial drift velocity is not much smaller than the azimuthal drift velocity. Following figure 6.1, the azimuthal drift velocities  $\vec{v}_{E \times B, azi}$  and  $\vec{v}_{\nabla B, azi}$  can even cancel each other. For a particular electromagnetic configuration, this cancellation occurs for a critical energy  $E_c$  (note that only the *gradient B drift* is energy-dependent). Electrons with kinetic energies close to  $E_c$  can drift into the flux tube and hence contribute to the background [258, 276, 277]. The majority of  $\mu$ -induced secondary electrons emitted from the inner vessel surface is expected to display a continuous, steeply falling energy spectrum up to about 100 eV. The value  $E_c$  is not universal as it depends slightly on the polar angle of the electron. Considering the two facts that electrons have to be trapped in order to drift into the flux tube and that their starting kinetic energies are rather low, a large polar angle (here  $90^\circ$ ) is assumed in the following.

The following combinations of the electromagnetic setup have been investigated:

1. Double-layer inner electrode (IE) at standard potential with global minimum magnetic field (MF).
2. Double-layer IE at standard potential with local maximum MF.
3. Single-layer IE at standard potential with global minimum MF.
4. Single-layer IE at low potential with global minimum MF.

### 1. Double-layer IE at standard potential with global minimum MF

The electrode potential and LFCS current configurations for this standard setup can be found in tables 4 and 1, respectively. As electrons drift from the surface into the sensitive volume, the outermost field line of the flux tube is considered for these investigations. Figure 6.12 (a) shows the  $E \times B$  and the *gradient B drift* velocities along this field line for an electron with a kinetic energy of 1 eV. In this case,  $v_{E \times B}$  is positive for all axial positions, while  $v_{\nabla B}$  changes its sign at the marked positions. Regions where both velocities point in the same direction are ruled out as possible parameter space for radial electron motion. Figure 6.12 (b) displays the critical kinetic energy  $E_c$ . Electrons with a kinetic energy close to  $E_c$  are most likely to drift into the flux tube. In the central spectrometer part, which comprises the main surface area, values of  $E_c \approx 5$  eV are found. An important parameter to consider in this context is the potential difference  $\Delta U$  between the inner wire layer ( $U_{\text{innerwire}}$ ), which is the main origin of  $\mu$ -induced secondary electrons<sup>7</sup>, and a particular point in space ( $U(\vec{r})$ ) in the volume. The value  $\Delta U = U(\vec{r}) - U_{\text{innerwire}}$  is called *potential penetration*. Figure 6.13 shows  $\Delta U$  along the field line, which was also considered for figure 6.12. In the case of an inner electrode operated in double-layer mode,  $U(\vec{r})$  is more positive (by about 17 V) than  $U_{\text{innerwire}}$  due to the more positive potential of the outer wire layer, which is not shielded completely by the inner wire layer. As a consequence, electrons emitted from the inner wire electrode are accelerated and end up with a minimal kinetic energy  $E_{\text{min}} = 17$  eV. Hence, if

<sup>7</sup>Electrons can also originate from the vessel and the inner electrode support structure, however, they need a certain minimal kinetic energy ( $> 100$  eV) to pass the screening potential of the inner wire layer. The majority of electrons is expected to be created with a kinetic energy  $< 100$  eV.

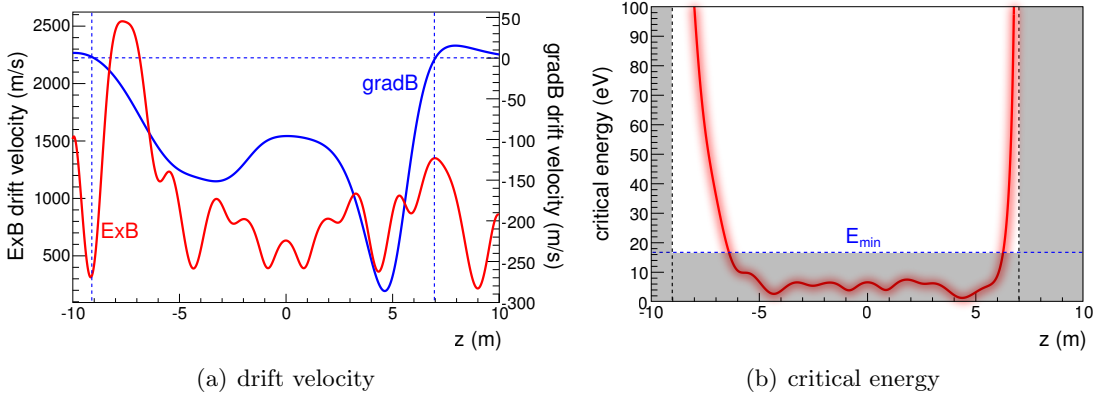


**Figure 6.12:** Drift velocities and critical electron energy for setup 1: double-layer IE at standard potential and global magnetic field minimum. The *gradient B drift* velocity is computed for an electron with a kinetic energy of 1 eV and a polar angle of  $90^\circ$ . The shaded area in (b) indicates the parameter space, where no significant radial electron motion is possible (for explanations see text). The fuzziness of the curve indicates that  $E_c$  is not a sharp limit for radial electron motion, but that this motion becomes more probable for kinetic energies close to  $E_c$ .

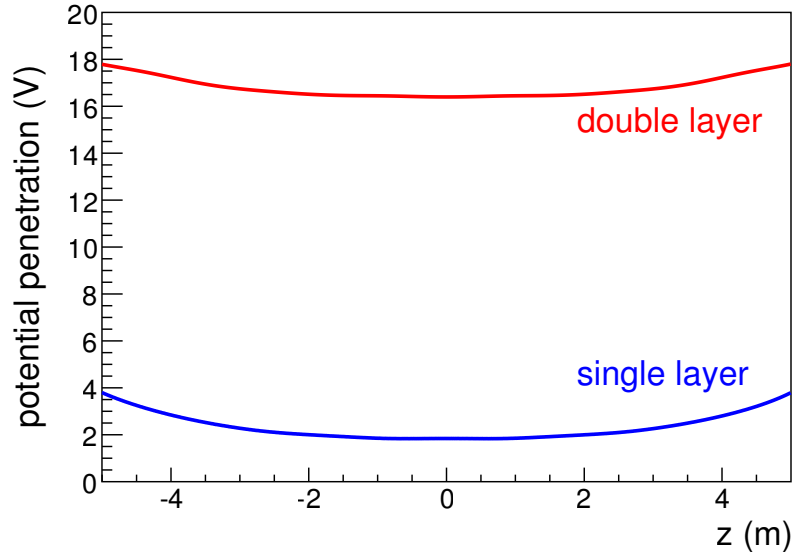


**Figure 6.13:** Potential penetration on the outer field line for double-layer and single-layer mode of the inner electrode. Electrons, which originate from the wire electrodes, are accelerated by this potential difference.

they reach the flux tube boundary, their kinetic energy is well above the critical energy, preventing a significant radial motion further into the flux tube (as indicated by the shaded area in figure 6.12). The remaining parameter space, which favors a radial drift motion (red curve in the non-shaded area of figure 6.12) is rather small. Therefore, good shielding properties are expected for such an electromagnetic setup.

## 2. Double-layer IE at standard potential with local maximum MF

In this case, a magnetic field configuration with a local maximum is chosen according to table 1. The corresponding drift velocities are shown in figure 6.14 (a). The main difference to the previous case is the positive *gradient B drift* velocity close to the analyzing plane. This behavior becomes clear from figure 4.14 in section 4.5.1, which shows the radial homogeneity of the magnetic field  $B$  for the two magnetic field configurations. While  $B$  continuously decreases in the case of a global minimum, the local maximum solution features an increasing magnetic field strength at larger radii around the analyzing plane. Consequently, the parameter space for radial electron motion is further reduced (compared to the global minimum MF solution), which likely leads to an enhanced shielding efficiency.

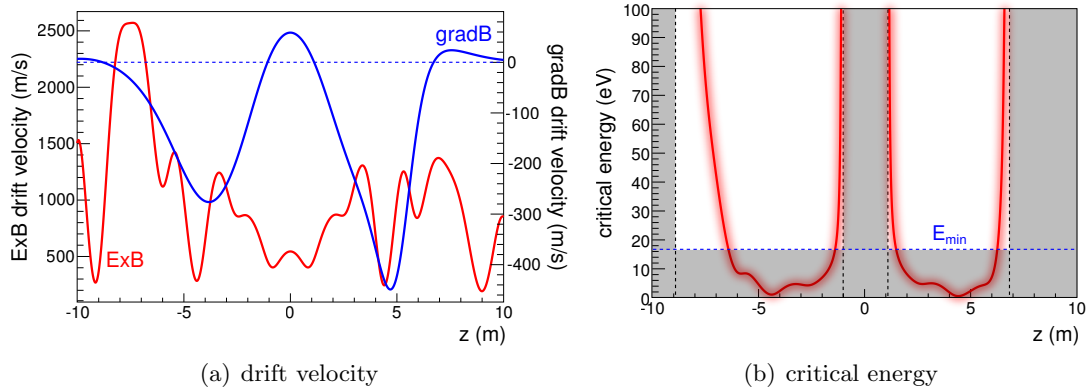


**Figure 6.14:** Drift velocities and critical electron energy for setup 2: double-layer IE at standard potential and local magnetic field maximum. The *gradient B drift* velocity is computed for an electron with a kinetic energy of 1 eV and a polar angle of  $90^\circ$ . The shaded area in (b) indicates the parameter space, where no significant radial electron motion is possible (for explanations see text).

### 3. Single-layer IE at standard potential with global minimum MF

Within the third setup, the inner electrode is operated in single-layer mode where both wire layers are on the same potential<sup>8</sup>. The main difference to the double-layer mode is the resulting potential penetration, which is shown in figure 6.13. With both wire layers on the same potential, the more positive potential of the vessel is shielded very efficiently, resulting in a reduced value of  $\Delta U \approx 2$  V. Although the behavior of the critical energy, shown in figure 6.15 (a), does not significantly change, the minimal electron energy  $E_{\min}$  is now smaller than  $E_c$ , which increases the parameter space favoring a radial electron motion. As a result, a significantly increased background contribution from  $\mu$ -induced secondary electrons is expected due to the more disadvantageous electromagnetic field configuration. Additionally, the outer wire layer and the support structure are no longer shielded by the inner wire layer, which has two effects:

- The area, from which secondary electrons can possibly drift into the flux tube is increased.
- The potential shows an azimuthal dependence due to the geometry of the inner electrodes.

According to [276], the unshielded surface area is increased by about a factor of 10, which likewise will increase the expected background rate. The second effect results in an azimuthal dependence of the radial electric field, which causes the  $E \times B$  drift, as shown in figure 6.15 (b). The wire support structure of each module consists of 4 approximately equally spaced massive C-profiles, which shield the vessel potential more efficiently than

<sup>8</sup>Such a setup was investigated due to the fact that electrical short circuits between the individual wire layers developed during the first bake-out of the main spectrometer after electrode installation.

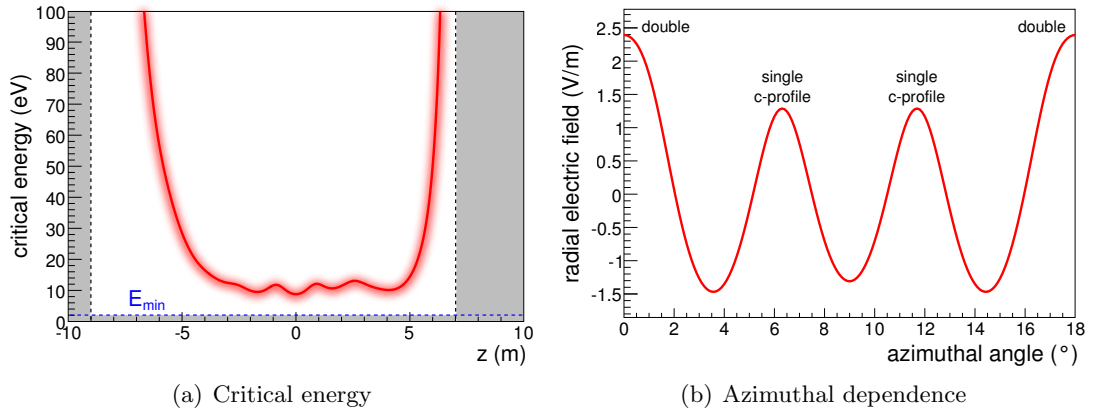


**Figure 6.15:** Setup 3: single-layer mode of the inner electrode with global minimum magnetic field. (a) Drift velocity: The minimal electron kinetic energy is only about 2 eV (see figure 6.13), which significantly increases the parameter space for a radial drift motion. (b) Radial electric field: Additionally, the unshielded wire electrode support structure results in an azimuthal dependence of the radial electric field, which is responsible for the  $E \times B$  drift. Here an azimuthal path at  $z = 0$  m and  $r = 4.3$  m was chosen.

the wires. In general, the electric field points radially outwards as the potential is more positive for smaller radii. Close to the electrode system, however, local electric fields due to the potential differences between regions close to the wires and those close to the C-profiles can change the direction of the electric field. At the boundary between two modules, the occurrence of two abutting C-profiles increases the local electric field strength.

This azimuthal dependence complicates a possible estimation of the total expected background increase as compared to the double-layer mode.

#### 4. Single-layer IE at low potential with global minimum MF

Over the course of the initial test measurements, the main spectrometer vessel will be on ground potential. Consequently, only moderate retarding potentials ( $|U| < 1$  kV) can be applied to the inner electrode system. An electrode potential configuration according to table 6 was chosen to demonstrate the background behavior for such a setup. Figure 6.16 (a) shows the resulting drift velocities. In this setup, the reduced potential entails an improved radial homogeneity of the electric field which decreases the values of  $v_{E \times B}$  by about a factor 5 compared to the case of standard potential. Consequently, also the critical energy is reduced by this factor down to about 2 eV, as shown in figure 6.16 (b). The potential penetration, and hence the minimal electron energy, is identical to the case with standard potential as it only depends on the potential difference between vessel and inner electrode system. According to the figure, the critical energy is found just at the border of the ruled out area. By increasing the inner electrode potential,  $E_{\min}$  is increased, suppressing radial electron motion. This effect enables an

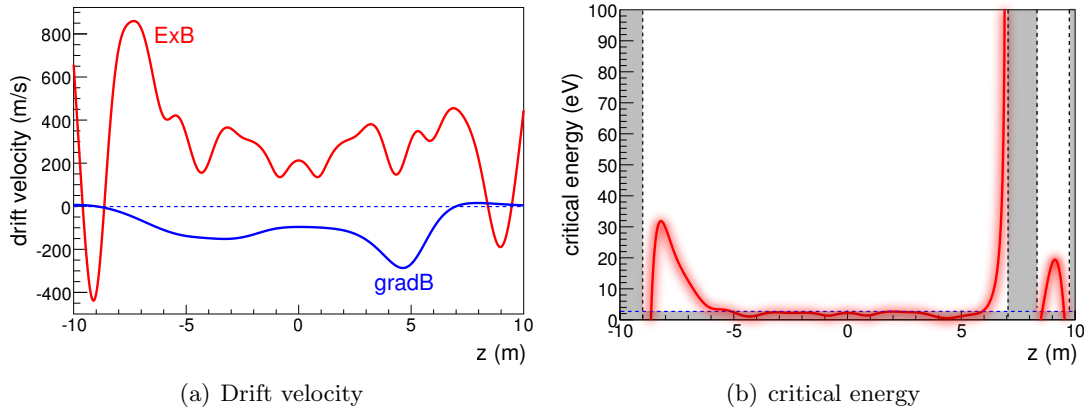


**Figure 6.16:** Drift velocities and critical electron energy for setup 4: single-layer IE at low potential, global minimum MF. The parameter space for radial drift motion is reduced to a minimum. In this case, only a small contribution of  $\mu$ -induced background events to the total observed background rate is expected.

investigation of the background suppression as a function of the inner electrode potential.

Based on investigations in [258, 276, 277], it was shown within this section that the  $\mu$ -induced secondary electron background is expected to strongly depend on the electromagnetic configuration of the main spectrometer. Therefore, a suitable measurement strategy has to be developed to fully investigate this background component and to optimize the electromagnetic configuration to obtain a low background level.

## 6.5 Measurement strategy

A variety of test measurements can be performed to advance our understanding of the  $\mu$ -induced background component. The high versatility of the air coil system allows to perform detailed studies, which can be divided into the four basic classes, using

1. axially symmetric magnetic field configurations,
2. asymmetric magnetic field configurations,
3. non-axially symmetric magnetic field configurations, and
4. vanishing magnetic fields.

It is only by a combination of these types of measurements that the full parameter space can be explored to fully characterize the  $\mu$ -induced background component.

### 6.5.1 Measurements with axially symmetric magnetic fields

#### Confined field lines

The standard magnetic field setup of KATRIN is expected to exhibit a high degree of axially symmetry (with small non-axially symmetric contributions from magnetic materials and non-aligned coil stray fields). Within such a setup, the intrinsic magnetic shielding will prevent low-energy secondary electrons from moving directly from the vessel surface to the detector. Instead, the slow radial magnetron drift velocities will transport the stored electrons into the flux tube. Due to this time delay between a muon hit on the vessel (and muon detector) and the corresponding secondary electron hit on the detector, a correlation between individual muon and background events is rather difficult given the high rate of muons. In this case, the measurements can determine the background rate as a function of the electromagnetic configuration. Though such measurements cannot ascertain that a particular background event was indeed  $\mu$ -induced or rather originated from a nuclear decay event (and subsequent ionizing processes), the radial dependence of the two possible background-generating mechanisms ( $\mu$ -induced and nuclear decay induced) could be used as an indicator for the origin. However, in both cases, the number of background events is expected to increase towards larger radii.

In case of high-energy secondary electrons, the direct correlation between muon detector and focal plane detector events could be restored as such electrons can leave the spectrometer very quickly due to non-adiabatic effects. This behavior was observed in Mainz [257] and can hence also be expected for the main spectrometer (identical central magnetic field strength). For such a measurement, the rate-sensitive detector design is especially useful to maximize the number of coincident events between muon detector and focal plane detector.

#### Unconfined field lines

A more direct access to the  $\mu$ -induced background component is obtained when lowering the magnetic field strength in the main spectrometer center such that field lines from the outer detector pixels connect with the vessel, as shown in figure 6.17. As the magnetic field is still axially symmetric, the background within the pixels of a particular detector ring is expected to increase uniformly. This particular behavior can be used as a measure for the alignment of the detector wafer and magnet system with respect to the main spectrometer. However, this assumption only holds if the electron emission rate is independent from the direction of the muon with regard to the spectrometer surface. Geometrical effects arising from the geometry of the experimental hall, as well as muon-electron correlations can be tested by a combination of the position-sensitive detector design (observing only the bottom part of the spectrometer) and the rate-sensitive design (observing the whole circumference).

By varying the LFCS currents, different parts of the spectrometer surface can be mapped to the detector, as shown for two exemplary configurations S1 and S2 (see table 3). In case of an axially symmetric setup, a ring structure (obtained by rotating the indicated surface part around the spectrometer axis) is monitored by the detector.

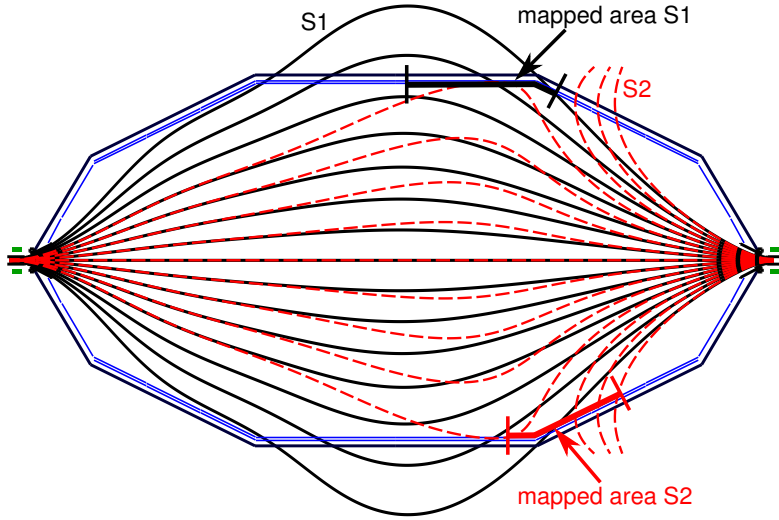


**Figure 6.17:** Field lines for symmetric magnetic field setups. Two different setups S1 and S2 are shown, mapping different parts of the spectrometer surface to the detector.

The movable muon detector system can be placed below the mapped surface area to increase the detection efficiency. In the case of figure 6.17, the mapped area spans  $\sim 4$  m in axial direction and can hence nearly fully be covered by the 3.15 m long muon detector modules. It is important to notice that, although there is a direct connection between the vessel wall and the detector, not all secondary electrons will actually reach the detector. The resulting expected count rate is influenced by the following effects:

- Due to the magnetic mirror effect, all electrons exceeding a maximal transversal starting kinetic energy  $E_{\perp, \max}$  are rejected. Thereby,  $E_{\perp, \max}$  strongly depends on the magnetic field  $B$  and the electrostatic potential  $U$  at the starting position (as will be shown in section 7.1, eq. (7.1)). An increase of either  $B$  or  $|U|$  decreases the number of reflected electrons and, hence, increases the count rate. However, the mapped area is expected to change, which has to be taken into account when comparing different setups.
- Electrons with large starting energies of  $> 1$  keV could experience a non-adiabatic change of their polar starting angle, thereby leaving or entering the loss cone.
- The number of background events is expected to decrease with increasing potential difference between the inner electrode ( $U_{\text{wire}}$ ) and the vessel ( $U_0$ ). A determination of the background rate as a function of  $U_{\text{wire}}$  then yields the electrostatic shielding efficiency.

### Low retarding potential

The entrance and exit regions of the main spectrometer incorporate an in-beam-line valve, which can be used to separate the main spectrometer volume from the adjacent

beam line elements. If the source side valve is closed while the detector side valve is open, the central magnetic field lines directly connect the detector with the source side valve. Consequently, electrons emitted there are directly guided to the 'bull's eye' part of the detector, if no electrostatic potential is applied to the spectrometer (otherwise the low-energy electrons are reflected by the potential barrier) [191]. When increasing the retarding potential, the energy spectrum of the  $\mu$ -induced secondary electrons can be scanned, giving useful information for the modeling of this background component.

### 6.5.2 Measurements with asymmetric magnetic fields

A second set of measurements can be performed by implementing an asymmetric magnetic field setup. Such a setup can be realized by turning off the source-side solenoids PS1 and PS2, as shown in figure 6.18. Within this particular setup, the pinch and detector magnets carry their nominal currents, while all LFCS coils are switched off. In comparison to the symmetric setup, here also the region beyond the analyzing plane can be investigated. The observed area can be tuned by varying the LFCS currents. As in this case the mapped area is rather large, it is useful to investigate the magnetic field and electrostatic potential along the field lines, which is shown in figure 6.19. Evidently, the magnetic field decreases with increasing distance to the pinch and detector magnets. In this case, for electrons starting on field lines connecting to the inner pixels, the starting magnetic field is about an order of magnitude smaller than for those on the outer field lines. Hence, when determining the expected count rate, all non-adiabatic effects and the well known magnetic mirror effect have to be modeled precisely to obtain reliable results. Additionally, when operating the main spectrometer on high voltage, the potential changes along the field line. Evidently, electrons created in a region beyond the analyzing plane will need a certain minimal kinetic energy in order to pass the potential barrier. This effect can again be used to scan the secondary electron energy spectrum.

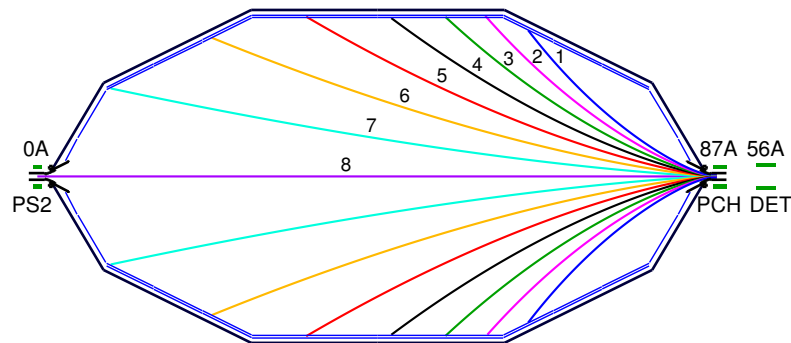
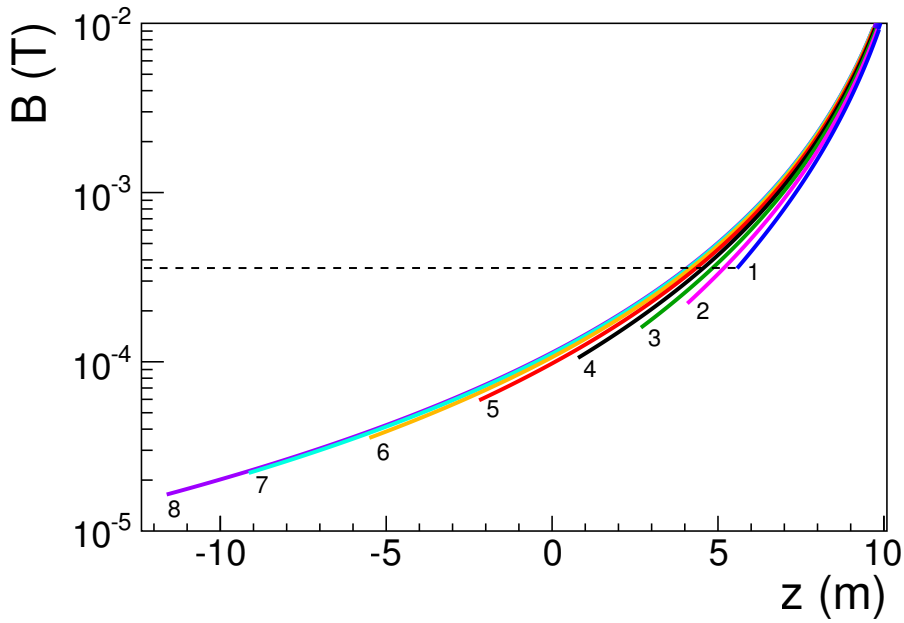
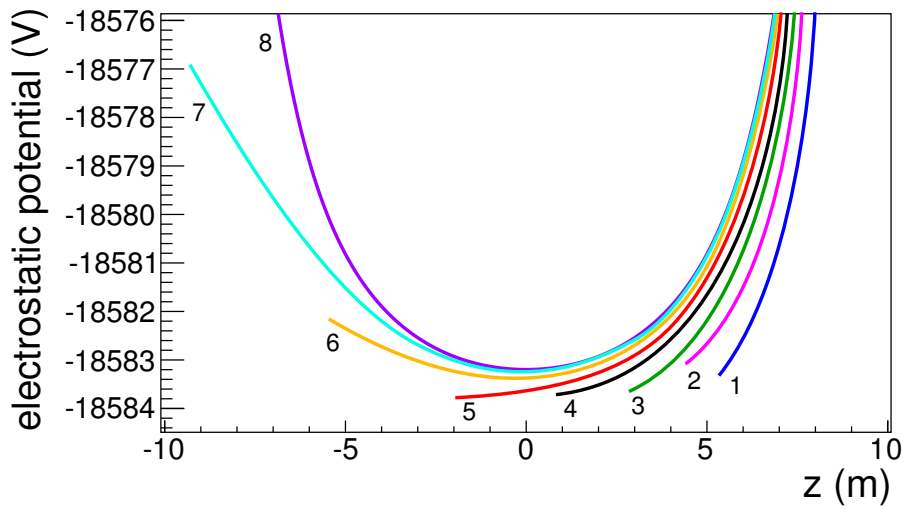


**Figure 6.18:** Field lines for asymmetric magnetic field setup.



(a) Magnetic field



(b) Electrostatic potential

**Figure 6.19:** Magnetic field and electrostatic potential along the field lines of the asymmetric magnetic field setup of figure 6.18. The large variation of the magnetic field strength changes the magnetic reflection properties for electrons on different field lines. The more negative electrostatic potential in the center of the main spectrometer can reflect electrons with very low starting energies and hence reduce the count rate for field lines reaching beyond the analyzing plane.

### 6.5.3 Measurements with non-axially symmetric magnetic fields

Obviously, the inherent non-axially symmetric stray fields of magnetic materials and non-aligned coils should influence all of the above measurements. However, in this context the large count rates, which are expected in the case of field lines touching the vessel surface, should not significantly be influenced by these additional small-scale effects. Nevertheless, it is exactly these small disturbances which could possibly result in background rates exceeding the KATRIN design limit. Therefore, dedicated measurements have to be performed using an artificial non-axially symmetric source to investigate the impact of this distortion on the background rate. This knowledge could be essential in case the  $\mu$ -induced background rate for the reference setup would be too large. This could point to magnetic disturbances, where huge efforts have to be made to compensate them. An artificial non-axially symmetric magnetic field can be produced by the following sources:

- The EMCS coils can shift the flux tube in an arbitrary radial direction without making it touch the vessel.
- An external coil (as utilized for test measurements at the pre-spectrometer [180]) can be placed at axial positions along the main spectrometer, where no effects due to remnant magnetization are expected.
- Tilting of superconducting solenoids.

The strength of these sources should be chosen to be on the same order of magnitude as expected for the magnetic materials. In addition one can measure how the background rate depends on the central field strength in the presence of a known non-axially symmetric magnetic field contribution. This can be used to determine the magnetic shielding factor.

A combination of such an artificial non-axially symmetric magnetic field with an artificial source, such as  $^{60}\text{Co}$ , to produce secondary electrons in a particular region of the main spectrometer surface, would be best suited for a detailed investigation. Again, the background can be tested as a function of the inner electrode potential. More details on test measurements concerning the influences of non-axially symmetric magnetic fields can be found in [182, 184].

### 6.5.4 Measurements without magnetic fields

In the presence of a magnetic field, the electron motion is governed by the direction of the magnetic field lines. In case of a magnetic field-free spectrometer (all solenoids and LFCS coils turned off, EMCS turned on to compensate the earth magnetic field), i.e. in the presence of an electrostatic potential only, electrons move towards the regions of more positive potential. Figure 6.20 shows three exemplary trajectories of electrons, which started from the eastern steep cone. The majority of electrons is expected to be guided to some electrode surface. However, a small fraction will be directed towards the ground electrode at the detector side. According to simulations for the pre-spectrometer,

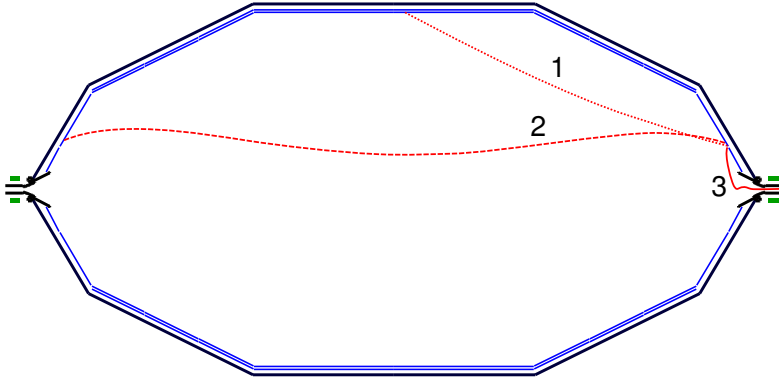


**Figure 6.20:** Electron trajectories for a setup without magnetic field. Electrons, starting from the inner surface, are guided towards regions of more positive electrostatic potential. Most electrons (trajectory 1 and 2) will be re-absorbed by the inner electrode. A small part (trajectory 3) will be guided towards the ground electrode and has the chance to hit the detector.

about 0.2% of all electrons, starting randomly on the inner spectrometer surface, will reach the detector [262]. In case of the main spectrometer, the large distance between the ground electrode, which is the most positive part of the spectrometer, and the detector would prevent most electrons from reaching the detector. However, when applying a post-acceleration voltage (positive polarity), these electrons would not hit the beam tube but instead be accelerated towards the detector. A comparison of simulations for the main spectrometer with actual measurements could reveal the secondary electron emission rate and validate the observations at the pre-spectrometer and at the Mainz spectrometer.

## 6.6 Impact on the neutrino mass sensitivity

Within this section it was shown that  $\mu$ -induced secondary electrons could contribute significantly to the overall main spectrometer background. Especially if the inner electrode system cannot be operated in a double-layer configuration, a background increase by about a factor of 10 is expected if no countermeasures are taken, such as increasing the magnetic field strength. In this context it is important to investigate the effect of an increased background rate on the statistical neutrino mass sensitivity. As the neutrino mass sensitivity is largest in a region close to the endpoint, where the count rate is rather low, an increased background rate could hide the actual signal there. Consequently, measurements further away from the endpoint are required, where the neutrino mass sensitivity due to large neutrino momenta there is reduced. Due to the Poisson nature of the  $\mu$ -induced background component, the statistical uncertainty  $\sigma_{\text{stat}}$  on the observable  $m_{\nu_e}^2$  scales approximately as  $N_b^{1/6}$  [82, 278], where  $N_b$  is the observed number of background events. This behavior is shown explicitly in figure 6.21. The statistical neutrino mass sensitivity for the design background rate of  $10^{-2}$  cps is reduced by about

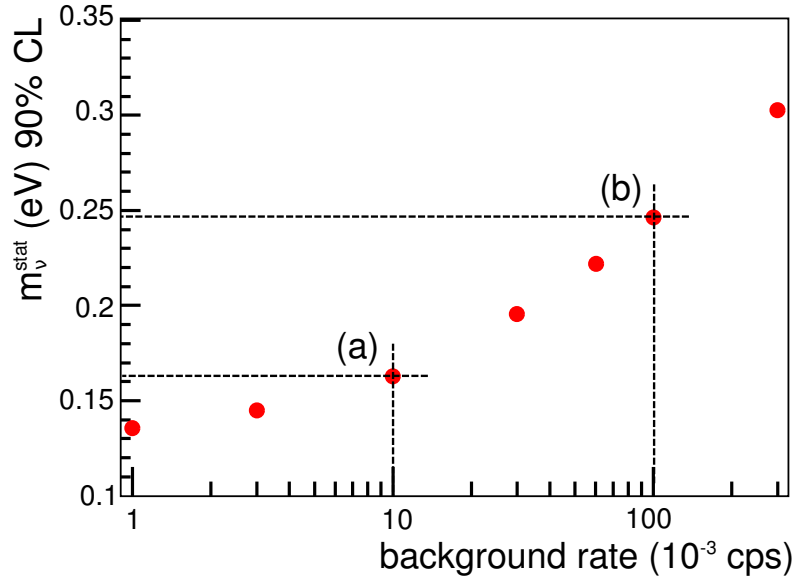


**Figure 6.21:** Statistical neutrino mass sensitivity as a function of the background rate. (a) The design sensitivity is reached for a background rate of  $10^{-2}$  cps. (b) In case the main spectrometer background is dominated by  $\mu$ -induced secondary electrons and the inner electrode system cannot be operated in a double-layer configuration, a background increase by about a factor of 10 is expected, reducing the statistical neutrino mass sensitivity by about a factor of 1.6.

a factor of 1.6 in case of a background increase by a factor of  $10^9$ . This significant influence on the KATRIN sensitivity underlines the importance of a low background within the main spectrometer. Consequently, large efforts are required to minimize disturbing influences of non-axially symmetric magnetic stray fields and to maximize the magnetic and electrostatic shielding against  $\mu$ -induced secondary electrons from the large inner surface of the main spectrometer.

<sup>9</sup>It has to be noted that the measurement time distribution was not optimized for the new background level. An improvement of the neutrino mass sensitivity can be expected after a corresponding adjustment.

## Radon-induced background

In addition to muon- or  $\gamma$ -induced background, a previously underestimated background component [82] resulting from stored electrons in the spectrometer volume was investigated in detail within this work. Previous measurements at the pre-spectrometer [132, 145, 146, 279] have revealed that  $\alpha$ -decays of  $^{219,220}\text{Rn}$  atoms in the spectrometers can produce background rates exceeding the design limit of  $10^{-2}$  counts per second (cps). The correct interpretation of these measurements requires a detailed understanding of the mechanisms of electron storage and subsequent background production in a MAC-E filter (section 7.1). In particular, a detailed background model has been developed which describes the electron emission processes following the  $\alpha$ -decays of the isotopes  $^{219,220}\text{Rn}$  (section 7.2). This model has been implemented into the KATRIN simulation package KASSIOPEIA to investigate the background mechanism from the point of electron creation until its detection, taking into account all experimental details (section 7.3). The model was validated in detail experimentally by making use of precise electron trajectory calculations in a MAC-E filter to describe the initial background investigations reported in [145, 146, 279], as well as the more in-depth studies performed in this work [280, 281] (section 7.4). Finally, the implications of this new background source for the neutrino mass sensitivity of KATRIN have been investigated (section 7.5).

### 7.1 Background due to stored electrons in MAC-E filters

While the magnetic field setup of a MAC-E filter allows for unsurpassed precision in the scanning of the tritium  $\beta$ -decay spectrum close to  $E_0$ , it also acts inherently as a magnetic bottle for electrons created isotropically in the flux tube of the spectrometer (see figure 7.1). The longitudinal energy  $E_{\parallel}$  of such an electron is transformed into transversal energy  $E_{\perp}$  when propagating towards the increasing magnetic field strength at the entrance and exit region of the spectrometer. At the same time, the electron concurrently gains longitudinal energy by the accelerating electric potential. If the transversal energy of the electron is above a certain threshold, the magnetic transformation is dominant and  $E_{\parallel}$  will be converted completely into  $E_{\perp}$ . Consequently, this electron is reflected by

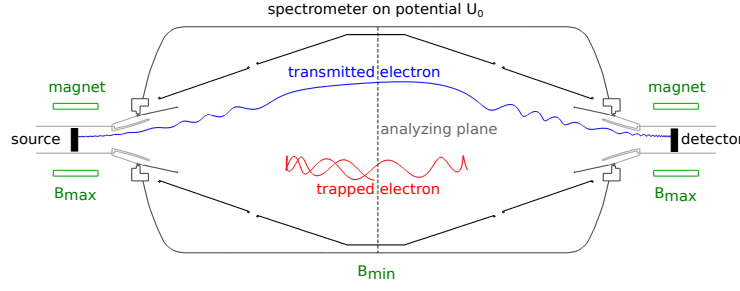


**Figure 7.1:** Electron storage within a MAC-E filter. The magnetic field of the superconducting magnets which increases towards the entrance and exit region of a spectrometer acts as a magnetic mirror for electrons which are generated inside the volume of the spectrometer.

the *magnetic mirror effect* [169], which results in a stable storage condition within the spectrometer volume. An electron, starting at an initial point  $\vec{p}_s$  within the spectrometer, can have a maximal transversal energy  $E_{\perp,\max}$  in order not to be stored, which is given by

$$E_{\perp,\max}(\vec{p}_s) = qU(\vec{p}_s) \cdot \frac{B(\vec{p}_s)}{B_{\max}}, \quad (7.1)$$

where  $U(\vec{p}_s)$  and  $B(\vec{p}_s)$  are the electrostatic potential and magnetic field at the starting position  $\vec{p}_s$  and  $B_{\max}$  is the maximal magnetic field which the electron would experience on its path. From this relation it is obvious that the accelerating electrostatic potential (which increases  $E_{\perp,\max}$ ) counteracts the reflecting magnetic field (which decreases  $E_{\perp,\max}$ ). The maximal starting kinetic energy  $E_{\text{kin},\max}(p)$  hence depends on the starting polar angle  $\theta_s$  and follows from eq. (4.5):

$$E_{\text{kin},\max}(\vec{p}_s) = \frac{E_{\perp,\max}(\vec{p}_s)}{\sin^2(\theta_s)}. \quad (7.2)$$

Consequently, electrons starting with larger polar angles are more likely to be stored.

When trapped, electrons scatter off residual gas species, thereby slowly cooling down until their transversal energy drops below the storage threshold and they can escape the trap. In the course of this process, a large number of low-energy secondary electrons ( $<100$  eV) are produced via ionizing collisions. These secondaries are accelerated by the retarding potential and, when escaping the magnetic bottle, will hit the detector within the energy region-of-interest, thus producing an irreducible background class.

Depending on its initial kinetic energy, a single stored primary electron can produce up to several thousands of secondary electrons which contribute to the background. Owing to the excellent ultra-high vacuum (UHV) conditions of  $p < 10^{-10}$  mbar [157] in the KATRIN spectrometer section, the time between two successive scattering events is on the order of 10 s, resulting in a total primary electron storage time of up to several hours. Due to its non-Poissonian nature, this background source can significantly constrain the neutrino mass sensitivity of KATRIN (see [132] and section 7.5), if no countermeasures are taken (see [282] and section 8).

The main source for stored electrons within the electrostatic spectrometers of KATRIN are nuclear decays in the spectrometer volume. Despite strong efforts to prevent tritium migration from the source to the spectrometers, a non-negligible amount of tritium molecules ( $\sim 10^4 - 10^5$  molecules/s) will flow into the main spectrometer. When undergoing  $\beta$ -decay within this volume, an electron with a kinetic energy of up to 18.6 keV is produced. Within this energy regime, electrons have a large storage probability of  $> 90\%$ . Besides tritium, also radon  $\alpha$ -decays can be accompanied by the emission of one or more electrons. Especially the short-lived isotopes  $^{219}\text{Rn}$  and  $^{220}\text{Rn}$  are of concern for KATRIN. Therefore, a detailed model has been developed in the course of this work, incorporating all relevant processes such as internal conversion, inner shell shake-off, atomic relaxation and shell reorganization, which will be outlined in the next section.

## 7.2 Electron emission accompanying radon $\alpha$ -decay

An essential design feature of high-resolution tritium  $\beta$ -spectroscopy by a MAC-E filter is an excellent UHV in the pressure range  $p \leq 10^{-10}$  mbar, such that background-generating ionization processes of signal electrons during the filter process are minimized. In the case of the KATRIN spectrometers, this is achieved by non-evaporable getter (NEG) strips totaling a length of 3 km in the main spectrometer and 90 m in the pre-spectrometer. As shown in [279], the large surface of the porous NEG strips gives rise to emanation of radon atoms associated with the primordial  $^{232}\text{Th}$ ,  $^{235}\text{U}$  and  $^{238}\text{U}$  decay chains (see figure 7.2). Furthermore, the large stainless steel surface of the spectrometer vessel (main spectrometer: 650 m<sup>2</sup>, pre-spectrometer: 25 m<sup>2</sup>) and auxiliary equipment attached to it also contribute to the radon emanation due to small quantities of radon progenitors contained near the surface.

Due to its long half-life of  $t_{1/2}(^{222}\text{Rn}) = 3.82$  d [283] compared to the pump out time of radon in the KATRIN spectrometers ( $t_{\text{prespec}} \approx 25$  s,  $t_{\text{mainspec}} \approx 360$  s), the isotope  $^{222}\text{Rn}$  is essentially being pumped out of the spectrometer before it decays. Therefore, its background contribution can be neglected. The short-lived isotopes  $^{219}\text{Rn}$  ( $t_{1/2} = 3.96$  s) and  $^{220}\text{Rn}$  ( $t_{1/2} = 55.6$  s), however, will  $\alpha$ -decay uniformly over the entire spectrometer volume ( $V_{\text{prespec}} = 8.5$  m<sup>3</sup>,  $V_{\text{mainspec}} = 1250$  m<sup>3</sup>) to their respective daughter nuclei  $^{215}\text{Po}$  and  $^{216}\text{Po}$  (see figure 7.2). The important aspect for the investigations of this work is the fact that the  $\alpha$ -decays of heavy atoms such as radon are accompanied by the emission of atomic shell electrons from the eV up to the multi-keV scale. The  $\alpha$ -particle as well as X-ray fluorescence photons, however, are of no interest for background studies concerning KATRIN. If the electrons are emitted into the sensitive volume of the spectrometer, they can contribute significantly to the background rate via secondary processes.

There are various atomic processes which can result in the emission of up to 20 electrons in a single  $\alpha$ -decay. A particularly troublesome background process is initiated if the  $\alpha$ -decay populates an excited level of the daughter nucleus, as the process of internal conversion, which is described in section 7.2.1, will result in the emission of

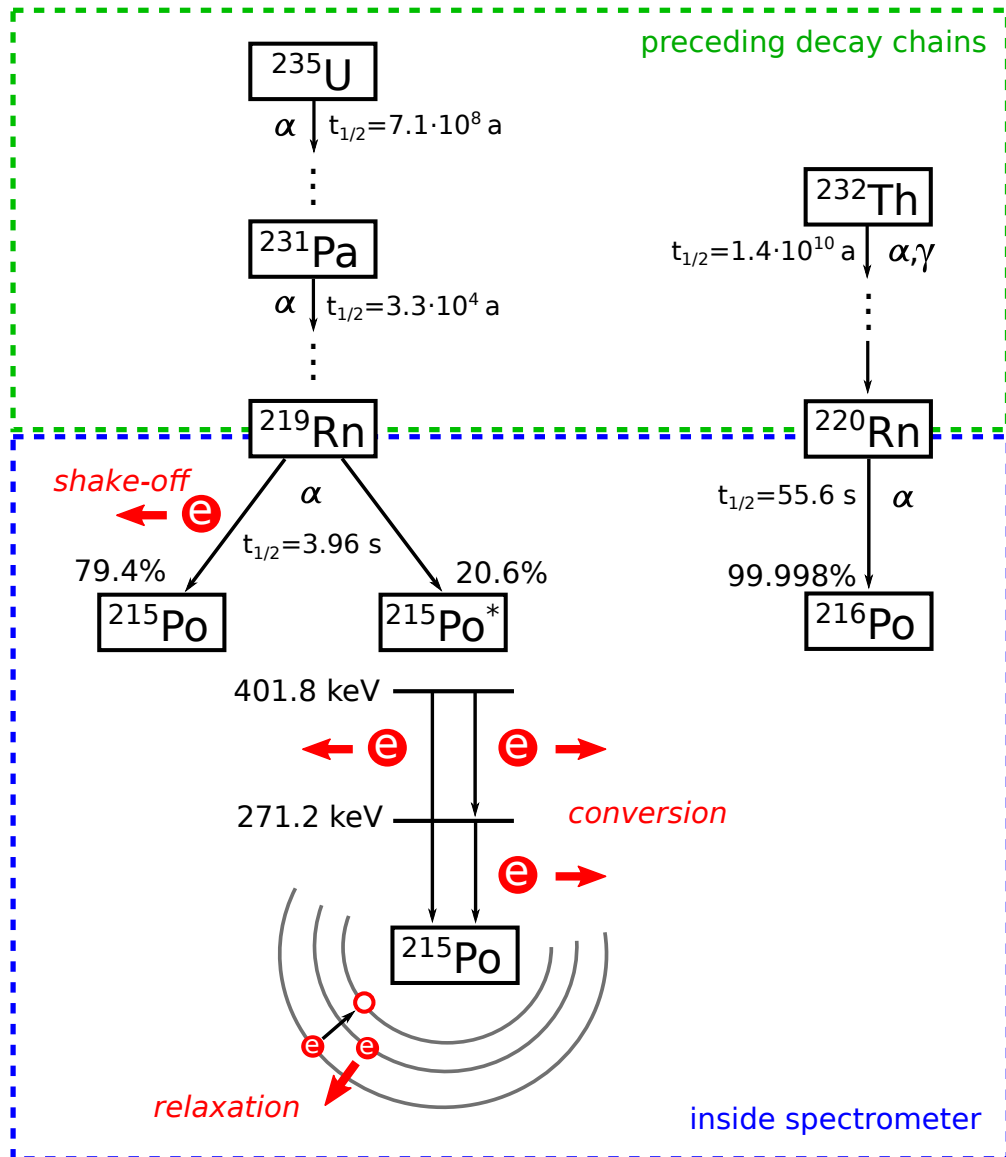


**Figure 7.2:** Top: In the KATRIN spectrometers, non-equilibrium decay chains lead to emanation of the two short-lived radon isotopes  $^{219}\text{Rn}$  and  $^{220}\text{Rn}$ . Bottom: radon  $\alpha$ -decay processes inside the spectrometer and subsequent electron emission processes resulting from shake-off (both isotopes), conversion (mainly  $^{219}\text{Rn}$ ) and shell relaxation (following conversion and shake-off processes).

electrons with energies of up to several hundreds of keV. Also, the emitted  $\alpha$ -particle has a specific probability to interact with electrons of the inner atomic shells, leading to so called shake-off processes, as detailed in section 7.2.2. In both cases vacancies in the inner electron shells are produced. These are successively filled by atomic relaxation processes, which are the focus of section 7.2.3. Finally, the shell reorganization process of outer shell electrons is described in section 7.2.4.

### 7.2.1 Internal conversion

In an internal conversion (IC) process the excited level of the daughter nucleus, which is populated by the  $\alpha$ -decay process, interacts electromagnetically with an inner-shell electron, which thus is emitted from the atom. As the IC process is competing with radiative processes, it is only dominant for heavy nuclei such as polonium ( $Z = 84$ ) due to the probability scaling as  $Z^3$  [284, 285]. In addition, the probability for an IC process decreases for larger transition energies, so it is relevant only for low-lying levels. In the specific case, which is investigated here, IC processes are thus of importance only for  $^{219}\text{Rn} \rightarrow ^{215}\text{Po}^*$  decays, where significant branching ratios lead to the two excited levels ( $7/2^+$ , 271.2 keV) and ( $5/2^+$ , 401.8 keV) shown in figure 7.2. In case of  $^{220}\text{Rn} \rightarrow ^{216}\text{Po}$  decays, the even-even nucleon configuration of the  $^{216}\text{Po}$  daughter creates a paucity of low-lying excited nuclear states, implying that IC processes following  $\alpha$ -decays of  $^{220}\text{Rn}$  are exceedingly rare processes.

In an IC process, an inner-shell electron with binding energy  $E_b$  is emitted into the continuum with a kinetic energy of

$$E_{\text{kin}} = E^* - E_b, \quad (7.3)$$

where  $E^*$  denotes the excitation energy of the nucleus (the small recoil effects are neglected). For the specific case of  $^{215,216}\text{Po}^*$  daughters, conversion electron energies between about 40 keV and 500 keV have been observed and are listed in [286, 287].

The total conversion probability amounts to about 3.3% per  $\alpha$ -decay when integrating over all electron shells in the case of  $^{215}\text{Po}^*$ . The probability is largest for K-shell electrons (2%) as their wave function at the nucleus is larger than for other p or d orbitals. Table 7.1 lists the dominant electron emission probabilities and electron energies for the decay  $^{219}\text{Rn} \rightarrow ^{215}\text{Po}^*$  [286]. Additionally, there is the possibility for consecutive IC processes in case the initial de-excitation process does not result in a ground state configuration of the polonium daughter. For completeness, also the rare IC process of the decay  $^{220}\text{Rn} \rightarrow ^{216}\text{Po}^*$  [287], populating the excited level ( $2^+$ , 549.7 keV), was included into the model, but its contribution of  $\mathcal{O}(10^{-5})$  is negligible for the investigations in [132, 281]. As mentioned above, the emission of a conversion electron leaves a vacancy in the electron shell, leading to subsequent complex atomic shell relaxation processes, which are described in sections 7.2.3 and 7.2.4.

**Table 7.1:** The table gives an overview of the relative probabilities  $P_i$  (per  $\alpha$ -decay) of the dominant IC lines and of the corresponding electron energies  $E_{\text{kin}}$  for  $^{219}\text{Rn}$ , as measured by [286]. The electron energy is given by eq. (7.3) and can thus be attributed to specific excited levels of energy  $E^*$  via the known values of the binding energy  $E_b$  (K: 93.1 keV, L: 16.9 keV, M: 4.1 keV, N: 1 keV). Only electron lines with an emission probability larger than 0.05% are given. In the model of this work, also the possibility of consecutive IC processes within a single  $\alpha$ -decay in case that the 401.8 keV level of  $^{215}\text{Po}^*$  is populated and de-excites to the 271.2 keV level, was implemented.

$E_{\text{kin}}$ (keV)	$P_i$ (%)	shell	$E^*$ (keV)
37.5	0.4	K	130.6
113.7	0.13	L	130.6
178.13	1.27	K	271.2
254.29	0.74	L	271.2
267.08	0.19	M	271.2
270.24	0.064	NP	271.2
308.71	0.233	K	401.8
384.87	0.102	L	401.8

### 7.2.2 Inner shell shake-off

A nuclear  $\alpha$ -decay leads to a perturbation of the atomic shells, as the electrons experience the passage of the outgoing  $\alpha$ -particle through the atomic orbitals, as well as the sudden change  $\Delta Z = Z' - Z = -2$  of the Coulomb potential of the nucleus with initial state  $Z = 86$  for radon and final state  $Z' = 84$  for polonium [288]. The impact of both processes on inner-shell (K, L, M) electrons is different than on outer-shell (N or higher) electrons due to the significantly different orbital velocities. The orbital period of inner-shell electrons in a heavy atom is much larger than the orbital passage time of the  $\alpha$ -particle such that  $v_\alpha/v_e \approx 0.1$ , with  $v_e$  being the electron orbital velocity and  $v_\alpha$  the  $\alpha$ -particle velocity. For outer-shell electrons, this ratio is reversed, i.e.  $v_e/v_\alpha \approx 0.1$ . Accordingly, inner shell electrons will adjust adiabatically to the sudden change of nuclear charge. Outer shell electrons, in contrast, remain 'frozen' in their parent atom ground state ( $6p^6$  for radon) and will only slowly rearrange to the daughter orbitals ( $6p^4$  for polonium), see section 7.2.4.

However, inner shell electrons can exchange energy with the out-going  $\alpha$ -particle via the Coulomb interaction [288–290]. In this case, the  $\alpha$ -particle, which has already gained 99% of its final kinetic energy inside the mean radius of the K-shell, can eject an inner shell electron into the continuum (shake-off) or to an excited level (shake-up). Thereby, the decay energy is shared between the  $\alpha$ -particle and the electron. As only atomic ionization processes are relevant for the investigations of this work, only the shake-off reactions are considered. In this process, the energy, which is transferred to the electron, is in general rather small and typically of the same order of magnitude as the shell binding energy  $E_b$ . Therefore, in the adiabatic transition, the shake-off (SO) process results in a continuous, steeply falling energy spectrum. In this thesis the parameterization of Bang

**Table 7.2:** Shake-off probabilities for electrons from specific inner shells in  $^{210}\text{Po}$ , as measured by [292, 293].

shell	probability
K [292]	$1.6 \cdot 10^{-6}$
LI [293]	$5.1 \cdot 10^{-4}$
LII [293]	$0.6 \cdot 10^{-4}$
LIII [293]	$1.5 \cdot 10^{-4}$
M [293]	$1.8 \cdot 10^{-2}$

and Hansteen [291] is used to determine the emission probability for a SO electron with a certain kinetic energy  $E_{\text{shake}}$ :

$$N(E_{\text{shake}}) = \left( \frac{E_{\text{b}}}{E_{\text{b}} + E_{\text{shake}}} \right)^8. \quad (7.4)$$

The SO probabilities for  $^{210}\text{Po}$  have been measured [292–294] and calculated [289, 295] and are used as a good approximation for the  $^{215,216}\text{Po}$  isotopes which are considered here. The values, which are listed in table 7.2, underline the well-known fact that the ejection probability from shaking strongly increases for higher shells. For the M shell, only the total emission probability is listed. Within the model, however, the 5 sub-shells are considered individually, adapting the corresponding emission probabilities. Since there was no experimental data available, an equal distribution amongst the five individual sub-shells is used as an approximation. The shaking of N-shell electrons and higher orbitals is treated separately (see section 7.2.4).

The effect of shake-off in internal conversion, which is discussed in [288], was not taken into account. This neglect, however, has only a small effect as, e.g., the probability for L shake-off per K conversion is only 0.9%.

### 7.2.3 Relaxation following internal conversion and shake-off processes

An electron, which is emitted via an IC or SO process, will leave a vacancy in an inner shell, as shown schematically in figure 7.3. As a consequence, the electron structure of the atom has to rearrange, thereby releasing binding energy. This can, on the one hand, be in the form of a fluorescence photon (radiative transition), which is of no concern for this work, as X-rays are emitted isotropically from the atom and are absorbed by the spectrometer walls. On the other hand, the relaxation can proceed non-radiatively in the form of an Auger electron, if the electron filling the vacancy originates from a different shell, or a Coster-Kronig electron, in case it is emitted from a sub-shell of the same level [296]. In case of a radiative transition, the initial vacancy is transferred to a higher atomic shell, while for non-radiative transitions the atomic shell is left with two vacancies after the first relaxation step. The relaxation processes then propagate up

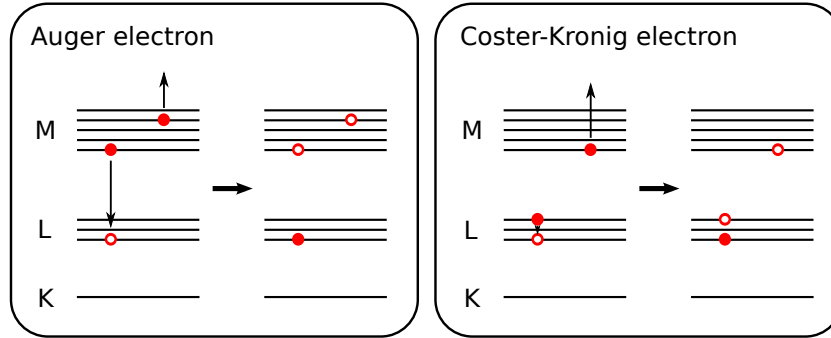


**Figure 7.3:** Sketch of an atomic relaxation process with electron emission. An inner shell vacancy is filled by an electron from an outer shell or a neighboring sub-shell, thereby releasing the corresponding difference in binding energy. This energy can be transferred to another electron, which then is ejected from the atom. Depending on the origin of the electron filling the vacancy, the emitted electrons are called Auger electrons or Coster-Kronig electrons.

to the outermost shell, thereby typically doubling the number of vacancies in each step. Large cascades are observed in heavy atoms such as polonium, when inner-shell vacancies are successively filled by non-radiative transitions (“Auger explosions”). Consequently, highly charged polonium ions are created, which cannot be neutralized when propagating in the spectrometer UHV environment. These ions are eventually neutralized when impinging on the spectrometer vessel surface. This happens in the topmost few nm of the stainless steel surface, resulting in an implantation of a neutral polonium atom close to the surface. The subsequent  $\alpha$ -decay activity of the polonium daughters is of no concern for the background investigations here as the time spent in-flight ( $\mathcal{O}(10^{-6})$  s) is much smaller than their lifetime ( $t_{1/2}({}^{215}\text{Po}) = 1.781$  ms,  $t_{1/2}({}^{216}\text{Po}) = 145$  ms). Electrons, which are eventually emitted during polonium  $\alpha$ -decay in the stainless steel vessel, cannot reach the sensitive volume of the spectrometer due to the excellent magnetic shielding properties, which are also responsible for suppressing the cosmic  $\mu$ -induced background component.

An electron emitted in a non-radiative transition will receive a distinct kinetic energy. In the example of figure 7.3, the Auger electron kinetic energy can, in a first approximation, be determined by

$$E_{\text{kin}} = (E_{\text{b,L1}} - E_{\text{b,M1}}) - E_{\text{b,M4}}, \quad (7.5)$$

where the  $E_{\text{b},i}$  are the binding energies of the involved shells  $i$ . In case of a radiative transition, the photon would have received the energy difference  $E_{\gamma} = E_{\text{b,L1}} - E_{\text{b,M1}}$ . The above approximation neglects two effects [297]:

- A pair of holes in the atomic orbitals retains interaction energy.
- The relaxation of the atomic orbitals results in a lowering of the final state energy, which alters the ionization energies of electron shells containing holes.

The Auger electron energies, which are applied in the model of this work, are indeed corrected for the aforementioned effects, using the intermediate coupling model of [297]. In the case of polonium, relaxation electron energies can reach up to about 93 keV, which approximately corresponds to the K-shell binding energy.

In addition to the above considerations, sudden changes of the atomic potentials occur during vacancy cascade development, which can lead to the emission of further electrons [298]. However, due to their relatively low emission probabilities, this effect is only of minor importance and is neglected within this work. Furthermore, as the number of vacancies in the atomic shells increases, the electron binding energies decrease which can lead to the closure of some Coster-Kronig channels, reducing the average charge state of the daughter atom [298]. In fact, for KATRIN, obtaining an exact multiplicity distribution of emitted electrons (predominantly of exceedingly low energies  $< 100$  eV) is not the primary focus, because the subsequent ionization processes of high-energy IC and inner-shell SO electrons in collisions with residual gas will produce several hundred or even thousand secondary electrons due to their magnetic storage in the spectrometer, enhancing the importance of the high-energy part of the radon energy spectrum as compared to the low-energy part.

#### 7.2.4 Atomic shell reorganization

In the above described processes the atomic shell of the polonium daughter is left in a highly excited state, and the subsequent de-excitation follows a rather complex scheme involving many different pathways within relaxation cascades. However, if the  $\alpha$ -decay process leaves the atomic shell unperturbed, or if the SO process of the  $\alpha$ -particle only involves an outer shell (N or higher) electron, the relaxation processes can be modeled in a much simpler way. The underlying effect is that the outer-shell electron wave function cannot adjust adiabatically to the final state due to the fact that the outer-shell electron velocity is much smaller than the  $\alpha$ -particle velocity. In any case the atomic system will relax to the smaller ( $Z - 2$ ) nuclear charge of the daughter nucleus.

There is a gradual transition of  $\alpha$ -decay processes resulting in a highly excited final state to a configuration where the atomic shell is virtually unperturbed, such that the initial state with the shell configuration of radon ( $6p^6$ ) has to adjust to the ground state shell configuration of polonium ( $6p^4$ ). Within the model of this work, both processes are treated in an identical manner.

The energy scale of these reorganization electrons can be estimated (there are no experimental data) by the following considerations. The change in nuclear charge ( $Z - 2$ ) due to the  $\alpha$ -decay  ${}_{86}\text{Rn} \rightarrow {}_{84}\text{Po}$  results in a change  $\Delta E = 37.7$  keV of the total binding energy of the atomic shell electrons, if the relativistic Hartree-Fock-Slater calculations of [299] are used. The parameter  $\Delta E$  is composed of a sudden energy exchange component  $\Delta E_{\text{sud}}$  and a much slower rearrangement component  $\Delta E_{\text{R}}$  [290]. As the fast inner electrons can adjust adiabatically to the reduction of the (effective) nuclear charge by rearranging to daughter orbitals, almost all of  $\Delta E$  occurs suddenly ( $\Delta E_{\text{sud}}$ ) and has to be supplied by the outgoing  $\alpha$ -particle, which results in an equivalent retardation of its kinetic energy. The remaining small fraction  $\Delta E_{\text{R}}$  (typically of the order of  $0.01 \cdot \Delta E$ )

is retained by the atom as temporary excitation energy for the much slower shell rearrangement in the outer shells. Here, a scenario is employed where the average outer shell atomic rearrangement energy  $\overline{\Delta E_{R,outer}}$  ( $6p^6 \rightarrow 6p^4$ ) of about 250 eV [290] is shared statistically by two electrons from the outermost shells. If their kinetic energy is larger than the polonium ionization energy for P-shell electrons (1-9 eV), they are emitted into the continuum, which results in a flat energy spectrum of low-energy “shell reorganization” electrons.

As the probability for inner shell SO (see table 7.2) and IC (see table 7.1) is rather small, the above described atomic shell reorganization (SR) is the most frequent electron emission process accompanying  $\alpha$ -decay. If, however, the electron shell in the final state is found in an excited state, caused either by IC or by inner shell SO, the full atomic relaxation is calculated as described in detail in the next section.

## 7.3 The radon event generator

To study the event topologies of electrons from the  $\alpha$ -decay of  $^{219,220}\text{Rn}$  atoms, and to estimate background rates and characteristics due to their subsequent trapping, a detailed code for particle trajectory calculations in the complex electromagnetic field configuration of the KATRIN spectrometer is required. This challenging task is met by the KATRIN simulation package KASSIOPEIA, which allows to track electrons over long periods of time with machine precision. For the purpose of this work a Monte Carlo event generator to describe electron emission following  $^{219,220}\text{Rn}$   $\alpha$ -decay was developed based on the above-mentioned physical processes. Section 7.3.1 will outline the implementation into KASSIOPEIA. The generator output will be shown in section 7.3.2 and an initial test of the model will be performed in section 7.3.3.

### 7.3.1 Implementation of the physical processes

The detailed physical model for signal events and background processes is implemented into the KASSIOPEIA package via MC-based event generators. For the investigations of this work, a radon background generator was developed to describe the processes accompanying the initial radon  $\alpha$ -decay, such as internal conversion (IC), shake-off (SO), relaxation (RX) and shell reorganization (SR) which are detailed in the previous section. Figure 7.4 shows a flowchart of the radon event generator.

The simulation can be configured by the user to study the impact of different processes on the background. The following choices are available (options in brackets):

- activate/deactivate individual physical processes (SO, IC, SR, RX)
- enforce physical processes (SO, IC)
- select radon isotope (219, 220)

During initialization, all data files, which are required for the computation of the various physical processes for a specific isotope, are read in. Enforcing SO and IC processes can

be useful as they are rather rare processes with a probability of only up to a few %. If this option is enabled, it is assured that the according processes are executed within every generated event by scaling up the emission probabilities of the individual shells until their sum totals 100%.

The first physical process to be carried out (if activated by the user) is the SO process, as it is directly caused by the passage of the  $\alpha$ -particle through the atomic shell. At first, a random number is generated by the ROOT TRandom3 routine, which is based on the Mersenne Twistor algorithm [300]. The SO subroutine then uses the generated random number to initiate an SO process with the corresponding probabilities for the individual (sub-)shells. Consequently, this can in some rare cases result in the emission of multiple SO electrons [288]. For the determination of the SO electron energy the acceptance-rejection method [301] is applied to eq. (7.4).

In case of one or more SO electrons being emitted, the RX process will be executed (if activated by the user). Within the generator routine, which is implemented into KASSIOPEIA, the Monte Carlo technique [302] is employed to simulate the highly complex pathways of an initial single vacancy, where a large number of intermediate electron shell configurations is being involved. In a first step, the fluorescence yield  $\omega_i$  and the Auger

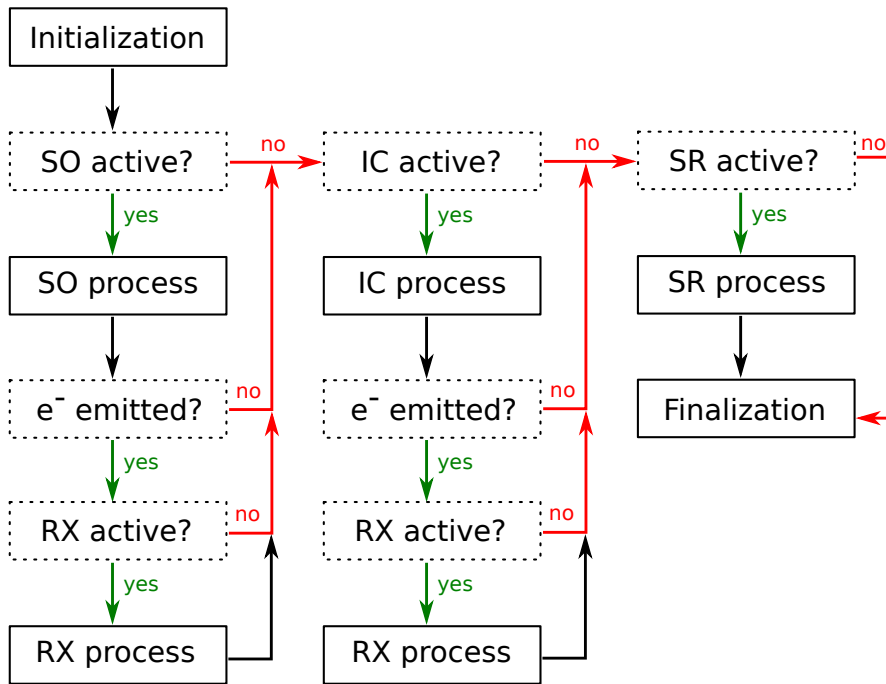


**Figure 7.4:** Event generator flowchart: After initialization of the generator, the different physical processes (SO: shake-off, IC: internal conversion, RX: relaxation, SR: shell reorganization), represented as solid boxes, are processed according to the model, which is described in more detail in the main text. The user has the possibility to configure the generator, e.g. turn on or off certain processes to study specific aspects. Corresponding decision points are given in dashed boxes.

yield  $\alpha_i$  of the shell  $i$  which is under investigation are used to determine the transition type. For K- and L-shell vacancies the data of [303], and for M- and N-shell vacancies those of [304, 305] is used. If a radiative transition is diced, the vacancy is simply transferred to a higher shell, where the new vacancy is determined from the available final states according to their relative probabilities. Non-radiative transitions up to and including the M-shell result in two vacancies, while several vacancies can be created by N-shell vacancy de-excitation due to super-Coster-Kronig transitions, i.e. all transitions happen within the N-shell. The described process is repeated until all vacancies reach the outer O- or P-shells or until no further de-excitations are energetically possible. As small modifications of the energies of electron shells due to the actual relaxation process are not taken into account, the de-excitations result in discrete energy lines.

After the RX process was completed, or if, initially, the SO process was deactivated, the IC process is performed (if activated by the user). This specific ordering is justified by the fact that shell relaxation processes are completed on a much faster time scale ( $10^{-15}$  s) [306] than internal conversion processes ( $10^{-12}$  s) [307]. Similar to the SO subroutine, a random number is used to initiate an IC process with the correct probability. Because the excited nucleus can decay into an intermediate energy state instead of the ground state, this has to be taken into account by allowing consecutive IC processes (so called double conversion [290]). The interrelated energy levels are marked as such in the input file, which allows for reliable bookkeeping of the involved states. The IC electron energy depends solely on the decaying nuclear state and the binding energy of the emitted electron, resulting in discrete IC lines.

The final process to be carried out is the SR process. At first, the SR subroutine checks if any SO or IC processes occurred previously. If this is the case, the SR process is skipped because the Po daughter has already relaxed via the above mentioned processes. Otherwise, an unperturbed shell is assumed, which results in the excitation of two electrons, statistically sharing the shell reorganization energy of  $\Delta\bar{E}_R = 250$  eV. These electrons are actually only emitted from the atom if their energy exceeds the outer shell binding energy of about 1 eV (first ionization) or 9 eV (second ionization). Consequently, the shell binding energy has to be deducted from the shell reorganization energy in order to obtain the actual kinetic energy of the emitted electrons.

In the final step of the event generation, all electrons, which were generated by a single  $\alpha$ -decay, are passed to the particle tracking part of the KASSIOPEIA simulation software. Thereby, the electrons are labeled according to their originating process, which enables the user to distinguish them within the analysis of the simulation data.

### 7.3.2 Generator output

Figure 7.5 shows the energy spectra and energy-dependent emission probabilities as obtained with the event generator, which is described above. The discrete IC and relaxation lines, as well as the steeply falling power law dependence of the SO spectrum can be clearly identified. The flat energy spectrum dominating the low-energy part originates from the implemented model of SR electrons in case of negligible atomic shell perturbation ( $6p^6 \rightarrow 6p^4$ ), as the two electrons statistically share an energy of 230-250 eV. The

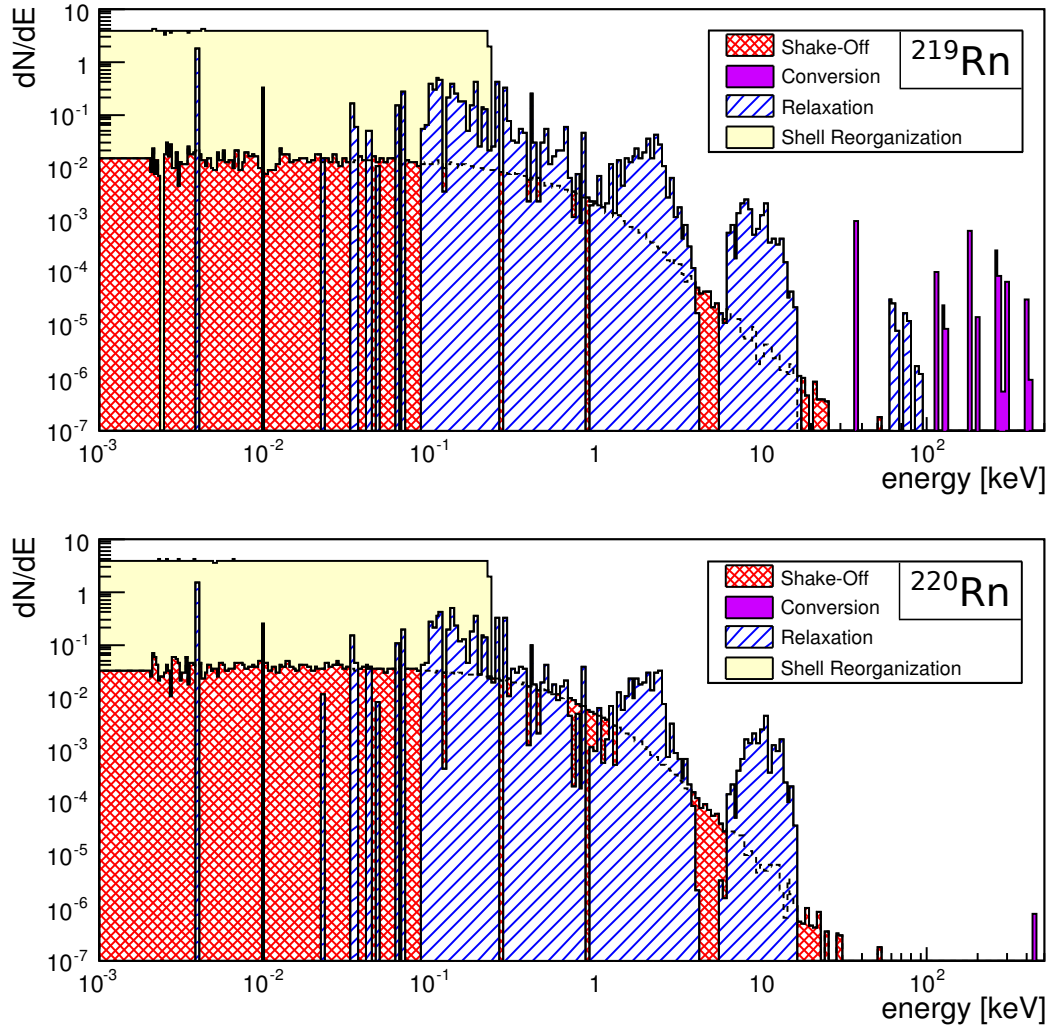


**Figure 7.5:** Output of the radon event generator: energy spectra of IC, inner-shell SO, relaxation and SR electrons for the case of  $^{219}\text{Rn} \rightarrow ^{215}\text{Po}$  (top) and  $^{220}\text{Rn} \rightarrow ^{216}\text{Po}$  (bottom)  $\alpha$ -decay. SR electrons, which originate from unperturbed atomic shell relaxation, are distinguished from K-, L- and M-shell SO electrons. The electron energy axis is subdivided into 250 intervals between 1 eV and 500 keV with logarithmically increasing bin size.

modeling of inner-shell SO and SR processes of the two polonium isotopes  $^{215,216}\text{Po}$  is treated identically due to their similar atomic shell configuration. As the SO probability is negligible for the inner K-shell ( $\mathcal{O}(10^{-6})$ ), the low-energy part of the relaxation spectrum mainly results from L-shell (or higher) SO, and hence reaches up to about 17 keV (L-shell binding energy). As stated above, the IC process is of importance only in the decay  $^{219}\text{Rn} \rightarrow ^{215}\text{Po}^*$ . In this case, there is a high probability for vacancies in the inner K-shell, leading to the high-energy part (up to about 90 keV) of the relaxation spectrum.

The total probability for electron emission by a specific process can be obtained by integrating over the whole energy spectrum. The corresponding results are summarized in table 7.3.

### 7.3.3 Initial tests of the model

Due to the complex nature of the response of the atomic shells during and after the emission of an  $\alpha$ -particle, it is of vital importance to compare the present model with independent measurements. Generic parameters for comparison are:

(i) the final charge state of the daughter atom, because it is highly sensitive to a correct description of processes such as atomic relaxation after generation of an inner-shell vacancy, and

(ii) the electron energy spectrum in the multi-keV range, which can be estimated from the number of secondary electrons produced in the electrostatic spectrometer [281].

Figure 7.6 shows the distribution of polonium charge states following  $^{219}\text{Rn}$  and  $^{220}\text{Rn}$  decays as obtained with the generator of this work, in comparison to the independent measurement reported in [294]. Overall, there is good agreement between measured and simulated frequencies of occurrence of different  $^{216}\text{Po}$  charge states, which underlines the basic validity of the model's description of inner-shell shake-off and subsequent atomic relaxation processes.

As can be seen in figure 7.6, the majority of  $\alpha$ -decays results in the emission of two low-energy SR electrons. When comparing the experimental data of [294] with the results of the Monte-Carlo generator it has to be noted that the detection of neutral

**Table 7.3:** Electron emission probabilities  $P$  per decay, depending on the emission process, based on the  $^{219}\text{Rn}$  and  $^{220}\text{Rn}$  event generators of this work.  $P > 1$  implies that more than one electron can be emitted per decay.

process	P ( $^{219}\text{Rn}$ )	P ( $^{220}\text{Rn}$ )
inner-shell SO	$2.08 \cdot 10^{-2}$	$2.15 \cdot 10^{-2}$
IC	$3.31 \cdot 10^{-2}$	$5.0 \cdot 10^{-5}$
relaxation	$2.29 \cdot 10^{-1}$	$6.81 \cdot 10^{-2}$
SR	1.89	1.96

daughter states, as outlined in [294], was rather challenging. The discrepancy for a neutral charge final state is thus ascribed to experimental difficulties in assessing the efficiency in detecting neutral atoms after  $\alpha$ -decay.

The significant difference between the two simulated isotopes in electron multiplicities, and correspondingly in the charge distribution of the daughter ion, is due to IC processes in the case of  $^{219}\text{Rn} \rightarrow ^{215}\text{Po}^*$ . As they are emitted from inner shells, highly charged final states result from complex relaxation cascades. Such events are also found in the case of  $^{220}\text{Rn}$   $\alpha$ -decay but with a much smaller probability. Given the rather complex nature of the atomic relaxation processes in heavy atoms and the approximations, which are used within the model, the observed agreement in the case of  $^{220}\text{Rn}$  is of particular importance for the further investigations. In particular, this allows to put a high degree of confidence into the modeling of the more complex decay sequence  $^{219}\text{Rn} \rightarrow ^{215}\text{Po}^*$  (there are no experimental data for this process due to the short lifetime of  $^{219}\text{Rn}$ ).

The second important parameter which is of key importance to validate the model is the energy spectrum of the emitted electrons in the multi-keV range. In an electrostatic

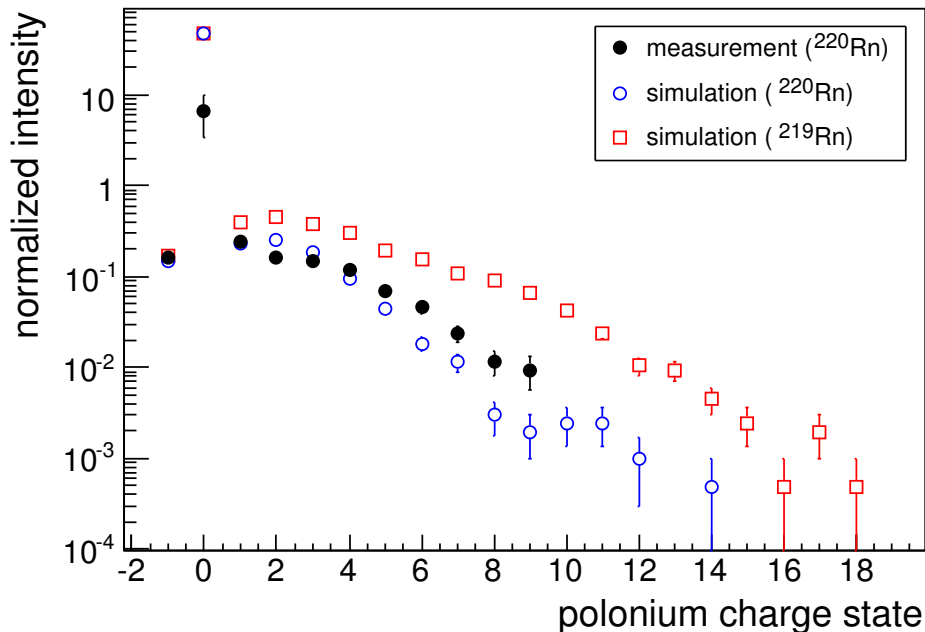


**Figure 7.6:** Charge states of  $^{216}\text{Po}$  (daughter of  $^{220}\text{Rn}$ ) and  $^{215}\text{Po}$  (daughter of  $^{219}\text{Rn}$ ), as obtained with the generator which was implemented into KASSIOPEIA within this work. The simulation is compared to an independent measurement of the  $^{216}\text{Po}$  charge state [294]. The values obtained with the  $^{220}\text{Rn}$  generator were normalized to the overall rate of non-zero charge states as the experimental precision for the detection of neutral daughter atoms was rather limited in [294]. For the  $^{219}\text{Rn}$  results, the same normalization constant was used to emphasize the difference between the two isotopes.

spectrometer of the MAC-E filter type, this parameter cannot be measured directly, as electrons are trapped over long periods of time [132, 145, 146, 279, 281]. However, an indirect method to assess the energy of stored multi-keV electrons is to make use of their subsequent cooling via ionization of residual gas and to count the number of produced secondary electrons in a detector. A single radon  $\alpha$ -decay can lead to a large number of detector hits  $N_{\text{det}}$ . Up to 1500 hits corresponding to a single event were observed at the KATRIN pre-spectrometer. Thereby, on average about 95% of all detector hits are caused by the secondary electrons, while primary electrons only contribute with about 5% to the total background rate. There is a good correlation between primary electron energy, shown in figure 7.5, and  $N_{\text{det}}$ , which is, however, not strictly linear due to competing energy losses by synchrotron radiation and due to non-adiabatic effects at higher energies. Figure 7.7 displays the number of detector hits following single radon  $\alpha$ -decays in the KATRIN pre-spectrometer in an experimental configuration where ionizing collisions with residual gas (Ar at  $p = 2 \cdot 10^{-9}$  mbar) were maximized at the expense of synchrotron losses. The measured spectrum is compared to corresponding Monte-Carlo simulations with the radon generator of this work. There is good agreement between the experimental data and the MC simulation, taking into account the limited number of radon  $\alpha$ -decays (127 events) accumulated over a measuring period of about 500 hours. The simulation reproduces the main features of the measured distribution: a large number of Rn-events with rather few detector counts, caused by the low-energy plateau of the shake-off events, and a steep decrease (tail of the shake-off spectrum)

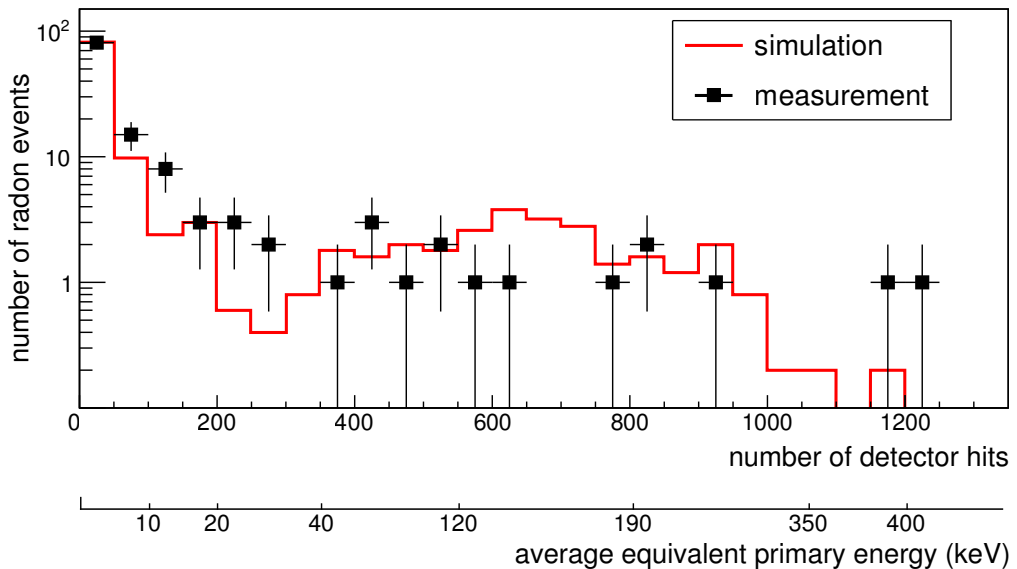


**Figure 7.7:** Comparison of measured and simulated numbers of detector hits produced by individual radon  $\alpha$ -decay events within the KATRIN pre-spectrometer. An equivalent energy scale can be reconstructed when using average energy losses due to scattering and synchrotron radiation [281]. The non-linearity of the energy scale results from the decreasing scattering cross section for higher energies in combination with linearly increasing synchrotron losses.

towards a flat plateau of very few events featuring a large number of detector hits, caused by conversion electrons.

A thorough understanding of radon-induced background is crucial for a successful neutrino mass determination with the KATRIN experiment. Therefore, further detailed background studies comparing measurements and simulations with different experimental conditions were carried out in [281] and are presented in the next section.

## 7.4 Validation of the background model

Initial measurements with the KATRIN pre-spectrometer in a test set-up configuration revealed  $\alpha$ -decays of  $^{219,220}\text{Rn}$  atoms in the volume of an electrostatic spectrometer as a significant source of background. Section 7.4.1 will give an overview of the specific pre-spectrometer measurements, which were used to validate the background model of this work. Figure 7.8 shows an exemplary background measurement over a time period of 50 hours. Within these measurements, constant background rates close to the intrinsic detector background of  $(6.3 \pm 0.2) \cdot 10^{-3}$  cps were observed most of the time. However, specific time intervals of up to two hours duration showed significantly enhanced background rates of up to  $250 \cdot 10^{-3}$  cps. These distinct intervals occurred about 7 times per day, each caused by a single nuclear  $\alpha$ -decay of a specific radon isotope.

There are various potential sources of radon emanation to take into account. Firstly, the stainless steel vessel of the pre-spectrometer, shown in figure 7.1, with its diameter of 1.7 m and length of 3.3 m features a large electropolished inner surface of 25 m<sup>2</sup>, including weld seams, which act as a potential source of radon emanation [308]. In addition, several auxiliary devices such as vacuum gauges and glass windows as well as

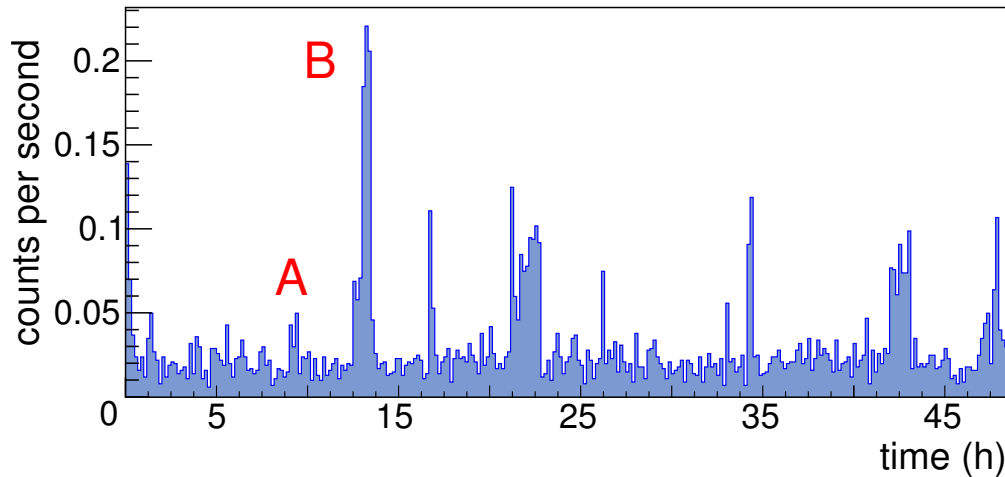


**Figure 7.8:** A typical pre-spectrometer background measurement over a time of about 50 hours with typically low count rates close to the intrinsic detector background of  $(6.3 \pm 0.2) \cdot 10^{-3}$  cps. However, intervals of elevated rate featuring different numbers of events (event A: 20 counts, event B: 848 counts) are observed about 7 times a day.

an inner electrode system can also emanate radon atoms as a result of their primordial abundance of  $^{232}\text{Th}$ ,  $^{235}\text{U}$  and  $^{238}\text{U}$ . A major source of  $^{219}\text{Rn}$  emanation was identified to be the non-evaporable getter (NEG) material [159] (consisting of strips with a total length of 90 m), used as an efficient pump for hydrogen. Details on the different sources of radon emanation can be found in [279].

While the  $\alpha$ -particle itself and the fluorescence X-rays of atomic relaxation processes do not contribute to the background in MAC-E filters, energetic electrons, which are emitted during the nuclear  $\alpha$ -decay [280], have a large probability to be stored inside the pre-spectrometer. Thus, they will lose their kinetic energy via secondary processes such as scattering or synchrotron radiation. Assuming that electrons cool down exclusively via scattering off molecular hydrogen, the average energy lost per produced secondary electron is  $\omega \approx 33$  eV. This value was determined with the scattering routines implemented in KASSIOPEIA and is in good agreement with the value of  $\omega \approx 37$  eV, which was calculated in [309].

For primary multi-keV electrons trapped within the pre-spectrometer flux tube, the number of secondary electrons is influenced by several effects:

- For the pre-spectrometer field configuration detailed in figure 7.1, only electrons with a kinetic energy above about  $E_{\perp}^{\text{min}} = 60$  eV are stored magnetically. Consequently, when a high-energy (keV) electron cools down it will not transform its entire kinetic energy into secondary electrons. Furthermore, the low-energy secondary electrons have a small storage probability and, hence, only a small number of tertiary electrons is created.
- Electrons experience non-negligible radiative energy losses due to the emission of synchrotron radiation. According to eq. (3.6), the synchrotron losses increase linearly for larger electron transversal energies, and increase  $\propto B^2$ , thus occurring predominantly in the high B-field region close to the entrance and exit of the pre-spectrometer.
- For electrons with a starting kinetic energy of more than 100 keV, the trapping probability is affected by non-adiabatic effects, resulting from the specific electromagnetic field configuration of the pre-spectrometer. Non-adiabaticity is induced if the magnetic field changes significantly within one gyration, such that the transformation of  $E_{\perp}$  into  $E_{\parallel}$  and vice versa is no longer proportional to the change of the magnetic field. Consequently, the polar angle of the electron will change randomly, eventually hitting a value below the trapping threshold.
- Additionally, electrons with very high kinetic energies have large cyclotron radii which can cause electrons to hit the spectrometer vessel, thus prematurely terminating the background-generating process.

To study background-generating processes and non-adiabatic effects, large-scale Monte-Carlo simulations, using the KASSIOPEIA package, were carried out on the TESLA cluster at KIT [280]. Within a first set of simulations, the radon event generator, which

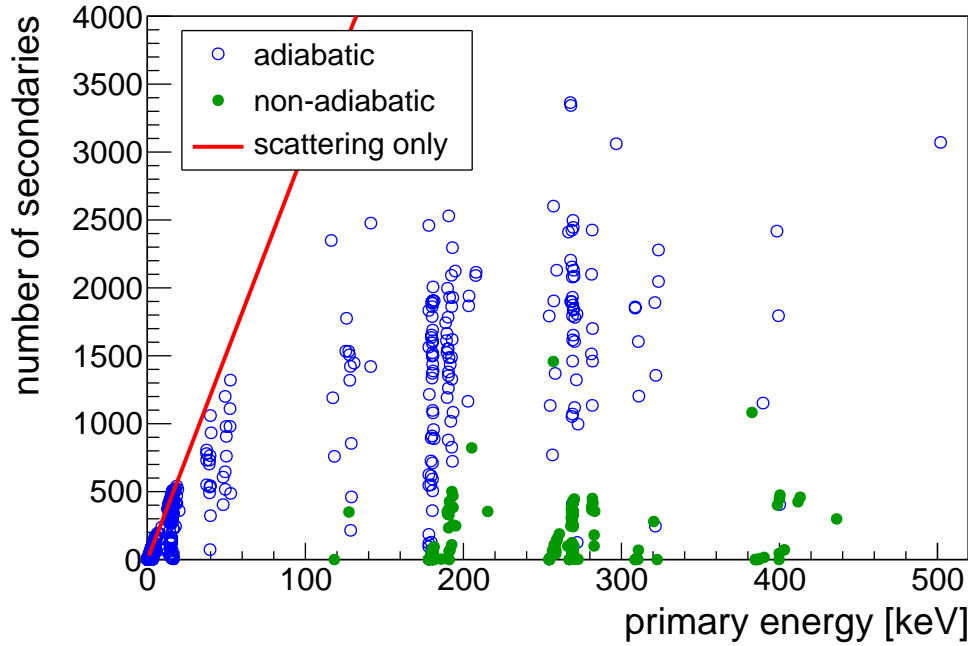


**Figure 7.9:** Number of produced secondary electrons as a function of the starting kinetic energy of the primary electron. In this case the  $^{219}\text{Rn}$  event generator was used and electrons were tracked in the pre-spectrometer. The red line corresponds to an average energy loss of  $\omega = 33$  eV per ionization. The actual number of secondary electrons remains below this limiting curve because the primary electron also loses energy due to synchrotron radiation. The sub-class of non-adiabatic events is marked as full circles, populating the area where a high-energy primary only generates several hundred secondaries.

was described above, was used to start a total of 10000 electrons with energies of up to 500 keV for subsequent tracking in the pre-spectrometer under standard operating conditions ( $p = 10^{-10}$  mbar,  $B_{\text{max}} = 4.5$  T,  $B_{\text{min}} = 15.6$  mT,  $U_0 \approx -18400$  V). Figure 7.9 shows the resulting number of electrons produced via ionization processes as a function of the primary electron energy. From the figure it is evident that primary electrons of several hundred keV, originating from the internal conversion process, can produce up to 3500 secondary electrons. Furthermore, the number of secondaries, which is generally produced by high-energy primaries, is smaller than what is expected from an average energy loss of  $\omega = 33$  eV. This reduction is mainly due to the rather large synchrotron energy losses in the pre-spectrometer field geometry. In addition, electrons released from the spectrometer magnetic bottle due to non-adiabatic effects contribute to this behavior.

When transferring these numbers into background rates it is important to note that only a fraction of the produced secondary electrons will actually reach the detector. Firstly, for symmetry reasons, only half of the electrons will escape towards the detector side of the pre-spectrometer. Secondly, the electrostatic field configuration of this setup

contains a shallow Penning trap in the center of the pre-spectrometer with a depth of up to 12 V in the sensitive volume. As a result, low-energy secondary electrons are stored within this trap with a probability of about 60 %. Despite these background-reducing factors, radon-induced events can still induce enhanced background rates, where up to 1500 detector hits were observed over time periods of up to 2 hours ( $N_{\text{bg}} \approx 280 \cdot 10^{-3}$  cps). Due to the broad energy spectrum of primary electrons emitted during radon  $\alpha$ -decay, the number of secondaries which is generated subsequent to a single decay varies by 3 orders of magnitude.

In the following a detailed experimental validation of the radon event generator [280] and the corresponding Monte Carlo simulations described above will be performed. The experimental information is based on specific measurements with the pre-spectrometer, described in [145], motivated to give complementary high-precision information on background characteristics and mechanisms. Firstly, an overview of the different measurements, which were performed at the pre-spectrometer, will be given (section 7.4.1). Secondly, the specific event topology of trapped electrons in the form of ring structures at the detector will be discussed, which gives access to the spatial distribution of radon decays inside the spectrometer (section 7.4.2). Additionally, the specific time-structure of the measured ring events can be investigated and compared to simulated data (section 7.4.3). A further important background characteristic is the rate of single events where Monte Carlo simulations can be compared to measurements (section 7.4.4). Finally the Monte Carlo results are used to determine the radon activities in the pre-spectrometer setup, which then are compared to the independent values derived in [279] (section 7.4.5).

##### 7.4.1 Overview of the pre-spectrometer radon measurements

In order to further validate the model of radon-induced background, which was developed within this thesis, more reliably, three different pre-spectrometer background measurements have been investigated in detail. In the following, an overview of the measurement strategy will be given and the corresponding experimental results will be presented.

As outlined above, the storage time of an electron strongly depends on the residual gas pressure inside the spectrometer. Therefore, two measurements at different pressures were performed. A first measurement at the standard pre-spectrometer operating pressure of  $p_{\text{LPG}} = 10^{-10}$  mbar with the residual gas composed mainly of hydrogen, water and nitrogen was followed by a second measurement at a higher pressure of  $p_{\text{HPG}} = 2 \cdot 10^{-9}$  mbar, which was achieved by injecting argon gas into the spectrometer<sup>1</sup>. In both measurements, the vacuum system consisted of the NEG pump (emanating  $^{219}\text{Rn}$ ) and one turbo molecular pump (TMP) for non-getterable gas species. In the following, these configurations are labeled LPG (low pressure with getter) and HPG (high pressure with getter), respectively. In order to definitely confirm the getter material as a major source for  $^{219}\text{Rn}$ , the NEG pump was removed for a third measurement. A

---

<sup>1</sup>Note that a background contribution of the radioactive isotope  $^{39}\text{Ar}$  can be neglected due to the low natural abundance of  $10^{-15}$  and the large half-life of 239 a, yielding a decay constant  $\lambda \approx 1.7 \cdot 10^{-10}/\text{s}$ .

**Table 7.4:** Pumping speeds and decay probabilities inside the pre-spectrometer for  $^{219}\text{Rn}$  ( $t_{1/2} = 3.96$  s [283]),  $^{220}\text{Rn}$  ( $t_{1/2} = 55.6$  s [283]) and  $^{222}\text{Rn}$  ( $t_{1/2} = 3.82$  d [283]), depending on the number of active TMPs [279]. The total pre-spectrometer volume amounts to  $V = 8.5$  m<sup>3</sup>.

# TMPs	speed ( $\ell/\text{s}$ )	$^{219}\text{Rn}$	$^{220}\text{Rn}$	$^{222}\text{Rn}$
1	194	0.885	0.353	$9.2 \cdot 10^{-5}$
2	402	0.787	0.208	$4.4 \cdot 10^{-5}$

**Table 7.5:** Overview of UHV measurement conditions and resulting radon-induced background rates. For the three different measurement conditions (low-pressure (LPG) and high-pressure (HPG) with getter installed, and high-pressure without getter (HP)) the events were categorized into three different classes according to the number of radon-induced counts (cts) at the detector: CI (10-50 cts), CII (51-500 cts), CIII (>500 cts). Event rates and contributions to the total spectrometer background  $r_{\text{bg}}$  are shown for the individual classes.

measurement	LPG	HPG	HP
getter	yes	yes	no
# TMPs	1	1	2
pressure (mbar)	$1 \cdot 10^{-10}$	$2 \cdot 10^{-9}$	$1 \cdot 10^{-9}$
gas composition	$H_2, H_2O, N_2$	$Ar$	$H_2, H_2O, N_2$
events/day (CI)	$4.2 \pm 1.4$	$5.5 \pm 1.2$	$2.0 \pm 0.6$
$r_{\text{bg}}(\text{CI})$ ( $10^{-3}$ cps)	$0.85 \pm 0.1$	$1.1 \pm 0.1$	$0.49 \pm 0.03$
events/day (CII)	$1.7 \pm 0.9$	$0.8 \pm 0.5$	$0.24 \pm 0.24$
$r_{\text{bg}}(\text{CII})$ ( $10^{-3}$ cps)	$3.6 \pm 0.15$	$1.6 \pm 0.1$	$0.17 \pm 0.02$
events/day (CIII)	$1.0 \pm 0.7$	$0.8 \pm 0.5$	$0.31 \pm 0.28$
$r_{\text{bg}}(\text{CIII})$ ( $10^{-3}$ cps)	$8.1 \pm 0.2$	$10.1 \pm 0.2$	$1.38 \pm 0.05$

second TMP then had to be activated to compensate for the loss in pumping power. As these modifications resulted in a relatively high pressure value of  $p_{\text{HP}} = 10^{-9}$  mbar, this measurement is labeled HP (high pressure - without getter). Of particular importance for the investigations is the fact that the number of active TMPs influences the pump-out time for gases, and thus the decay probability of the different radon isotopes, as shown in table 7.4. In all cases, the decay of  $^{222}\text{Rn}$  can be neglected.

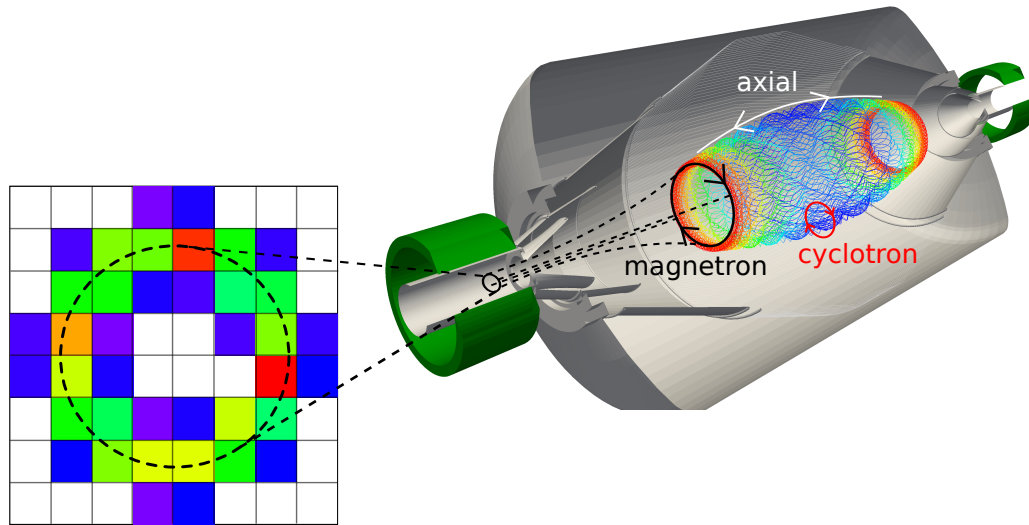
The intervals with elevated background rate caused by a single radon decay were (in close analogy to [279]) categorized into three different event classes, depending on the number of counts (cts) at the detector: CI (10-50 cts), CII (51-500 cts) and CIII (>500 cts). According to Monte-Carlo simulations, CI and CII events originate from radon decays which produce shake-off electrons or electrons from the low-energy part of the conversion line spectrum. However, only the high-energy electrons of the IC process can produce CIII-type events. These conversion electrons originate practically only from the decay of  $^{219}\text{Rn}$ , with the NEG pump identified as a major source of this isotope. However, even after the complete de-installation of the NEG pump (measurement HP), the distinct CIII signature of  $^{219}\text{Rn}$  events was still observed, though at a greatly reduced rate. Consequently, a background model was implemented where three different sources contribute to the total radon activity inside the spectrometer:  $^{219}\text{Rn}$  from the getter ( $^{219}\text{Rn}_G$ ), and  $^{219}\text{Rn}$  as well as  $^{220}\text{Rn}$  from the spectrometer bulk material and auxiliary equipment attached to it ( $^{219}\text{Rn}_B, ^{220}\text{Rn}_B$ ). As  $\gamma$ -spectroscopy measurements at MPI Heidelberg, performed in collaboration with H. Simgen, showed no traces of the  $^{220}\text{Rn}$  progenitor  $^{228}\text{Ac}$  within the investigated sample of the getter material, it was not considered as a possible source for these investigations.

Table 7.5 gives a summary of the measurement conditions in the three configurations, which have been used as input for the Monte-Carlo simulations. Furthermore, the observed occurrence of CI-III events and their contributions to the total spectrometer background are given. These values will be compared to those derived via simulations (section 7.4.5).

#### 7.4.2 Spatial distribution of radon decays

Apart from generating elevated levels of background over extended periods of time, the event topology of radon-induced background is an important tool to characterize the background-generating mechanism.

The emanation of electrically neutral radon atoms from the above discussed sources will result in a uniform decay probability over the entire spectrometer volume (with no visible effect of magnetic shielding as expected in the case of charged particles). In the following, it will be shown that this expectation can be tested by the specific topology of background events, which results from the rather complex motion of stored electrons in a magnetic bottle. Due to the excellent radial mapping characteristics of a MAC-E filter (see figure 7.10), radon-induced background at the 8x8 silicon pixel detector will form a generic ring pattern [145, 146]. This radon-induced event topology can be understood by first principles of particle motion, as well as by more detailed simulations of electron trajectories in the pre-spectrometer set-up. The electron motion is composed of



**Figure 7.10:** Simulated trajectory of a single trapped electron with start energy  $E = 1000$  eV. The electron motion consists of a very fast cyclotron motion around the magnetic field line, a fast axial motion and a slower magnetron motion around the beam axis. Secondary electrons generated by the primary electron along its path are therefore seen as rings on the pixel detector. One can identify the main hit region (green to red colors, corresponding to a large number of hits) and a surrounding fuzzy region (blue, only a few hits) due to the cyclotron motion of the primary electron. The same signature was found within the measurements, where figure 7.11 shows some example events.

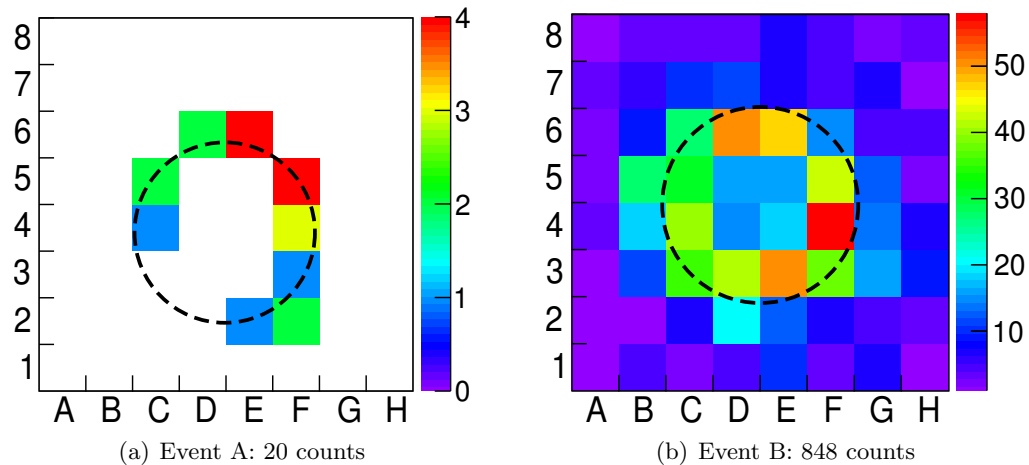


**Figure 7.11:** Detector signature of typical radon-induced background events. Shown are the events A and B of figure 7.8. Event A, featuring 20 counts, is categorized as CI event, while event B belongs to CIII with 848 counts.

a very rapid cyclotron motion around the guiding magnetic field line, an axial motion of intermediate velocity between the points of reflection due to the magnetic mirror, and a slower magnetron motion around the beam axis. The magnetron motion is caused by the  $\vec{E} \times \vec{B}$  and the  $\vec{\nabla}|\vec{B}| \times \vec{B}$  drift, which result from the inhomogeneities of the electric ( $\vec{E}$ ) and magnetic ( $\vec{B}$ ) field configurations inside the spectrometer. Secondary electrons, originating from ionizing collisions of the stored primary electron with residual gas molecules, thus monitor this motion. As a low-energy secondary electron (in the energy range from 12-60 eV) is generally not trapped, it flags the radius of the slow magnetron motion of the stored high-energy primary by following the magnetic field lines when escaping the magnetic mirror trap. Consequently, the magnetron drift of trapped electrons in combination with the well-defined imaging characteristics of a MAC-E filter produce a characteristic ring structure at the detector. The example in figure 7.10 shows the image of such a trapped electron, characterized by a main hit region (green to red pixels, multiple hits per pixel) which can easily be identified from the surrounding rather fuzzy region (blue pixels, single hits per pixel) due to the overlaying faster cyclotron motion of the primary electron, which smears out the sharp magnetron ring. This unique feature of ring-structures allows to make use of a ring-fitting algorithm to unambiguously identify radon-induced background events [145]. Figure 7.11 shows two exemplary measured ring events of (a) CI-type and (b) CIII-type, with their corresponding ring fits. Obviously, the characteristic features, which are expected from theory, are observed in the experiment.

The ring radius fit determines the radial position  $r$  (relative to the central axis) of the primary  $\alpha$ -decay which has generated the primary electron. For a homogeneous distribution of  $\alpha$ -decays inside the spectrometer volume, the number of rings  $N(r)$  in a fixed interval  $[r, r + dr]$  is expected to increase linearly with the radius (see figure 7.12). When comparing measured and simulated spatial ring distributions, the good agreement visible in figure 7.12 implies that  $\alpha$ -decays indeed occur with uniform probability over the entire flux tube, as expected for neutral atoms emanating into the UHV region. The smaller number of ring structures with radii  $r_{\text{fit}} > 20$  mm is a result of the limited dimensions of the Si-PIN diode array (length= 40 mm), which does not cover the entire flux tube (see figure 7.10). Nevertheless, events which produce a significant amount of detector hits in the corner pixels with  $r_{\text{fit}} > 20$  mm can still be identified, albeit with a reduced geometrical efficiency. From figure 7.12 it appears that the simulated ring events are shifted towards larger radii than the measurement. This effect could be caused by the imprecise knowledge of the exact detector position. As the detector is placed close to the center of the pre-spectrometer solenoid ( $z_{\text{sol}} = 2.15$  m,  $z_{\text{det}} = 2.3$  m), a small deviation of 5 cm shifts the observed ring radii by 2 mm, which would explain the deviation between measured and simulated data.

### 7.4.3 Time structure of radon events

Another important characteristic of Rn-induced background is the intrinsic time structure within a period of elevated rate. Figure 7.13 shows the typical time structure of detector hits, resulting from a single (or several) stored high-energy electron(s). Obviously,

a long plateau is followed by a steep rate increase towards the end of the event. This structure can be understood when considering that the time between two detector hits, which belong to the same radon decay event, is mainly determined by the time between two successive ionizing collisions. From figure 3.2 follows that the ionization cross section increases with decreasing kinetic energy. Taking into account the fact that the

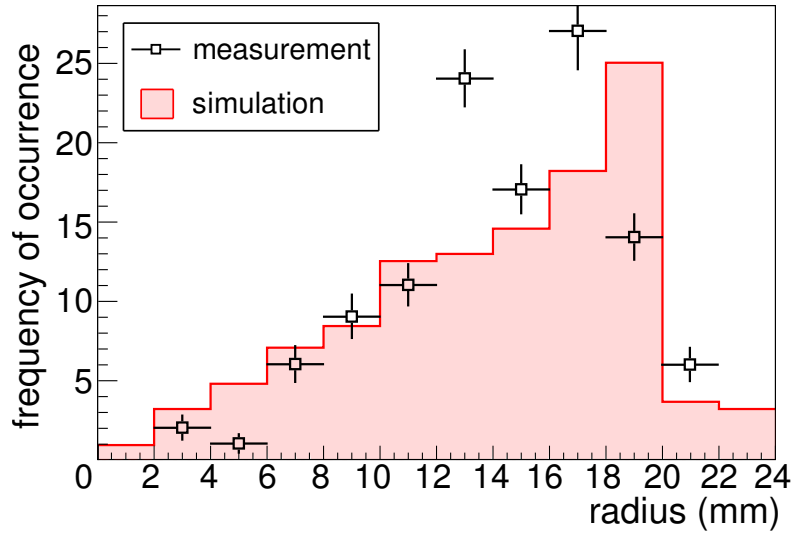


**Figure 7.12:** Distribution of fitted ring radii  $r_{\text{fit}}$  as determined via measurement and Monte-Carlo simulation, and normalized to the total measured event rate. The measured data was adopted from [279]. The good agreement verifies the assumption of a uniform distribution of radon decays inside the spectrometer volume.

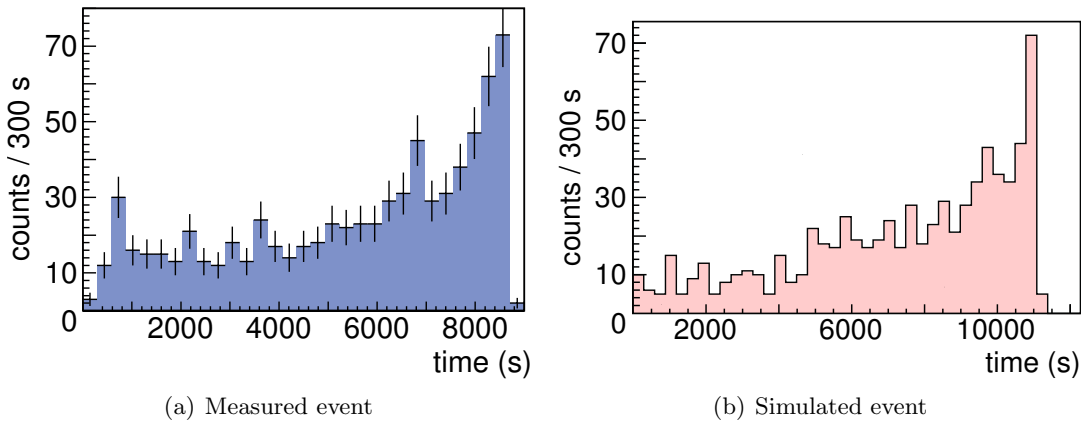


**Figure 7.13:** Time structure of a period of elevated rate, likely caused by a single stored high-energy electron. In the measurement (a) as well as in the simulation (b), the time structure shows a long plateau followed by an increase in rate towards the end of the event. This characteristic development is caused by the increasing scattering cross section as the stored primary electron cools down.

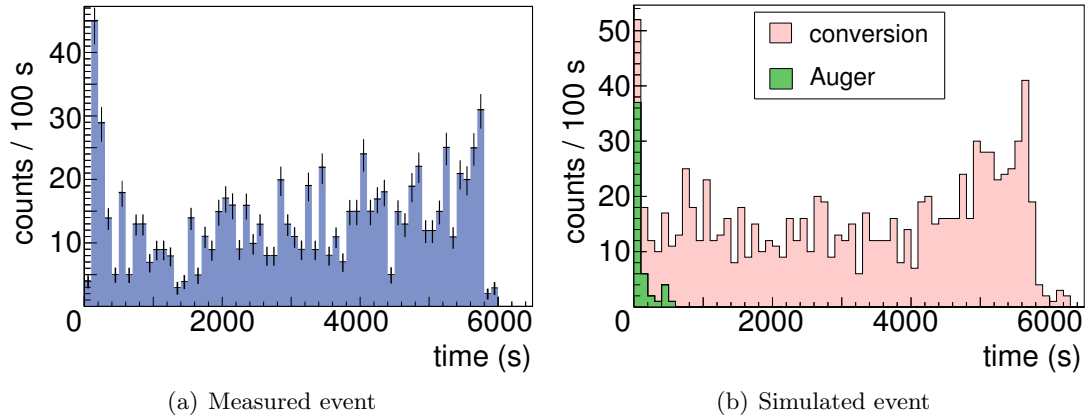


**Figure 7.14:** The time structure of a (a) measured and (b) simulated event with specific electron emission characteristics feature both an increased rate at the very beginning and at the very end of the  $^{219}\text{Rn}$ -event. In case of the simulation, the time spectrum of the detector hits is colored according to the process by which their parent electron was created. The initial high rate is caused by a low-energy Auger electron ( $E = 2$  keV) which is emitted together with the high-energy conversion electron ( $E = 178$  keV). Finally, the rather large fluctuations of the experimental rate have to be noted, which may be due to the impact of the Penning trap in the center of the spectrometer.

low-energy secondary electrons are not stored within the pre-spectrometer, successive detector events will occur on faster time scales as the electron cools down. This pattern is well reproduced by the corresponding Monte-Carlo simulations with KASSIOPEIA: an initial plateau followed by a steep increase right up to the end of particle storage.

In some cases, events were observed featuring equivalent high rates right at the beginning as well as at the end of the event. An example of this pattern is shown in figure 7.14 (a). The corresponding simulations (b) for a specific  $^{219}\text{Rn}$   $\alpha$ -decay reproduce this kind of behavior. As the simulation allows to trace back the origin of each electron which reaches the detector, the increased rate at the beginning can be attributed to a low-energy ( $\mathcal{O}(0.1-10)$  keV) Auger electron, which is emitted together with the vacancy producing high-energy ( $\mathcal{O}(100)$  keV) electron.

A key parameter in the discussion of background characteristics is the time difference between two successive detector events. Figure 7.15 shows these interarrival times  $\Delta_{\text{exp}}T$  for all events, which were observed within the LPG and the HPG measurement, respectively, and for the corresponding simulation. The experimental distributions of  $\Delta_{\text{exp}}T$  show (quasi-)exponential distributions with two characteristic slope parameters  $\tau_1$  and  $\tau_2$ , which are linearly dependent on the residual gas pressure. The overall exponential behavior points to underlying purely stochastic processes, where rate parameters  $\lambda = 1/\tau$  characterize the Poisson nature of the arrival times of background events. This implies that the background production is almost “memoryless“, where the actual number of background hits during a Rn-spike event is almost independent of the arrivals occurring before. However, this generic Poisson feature is only approximated here (due

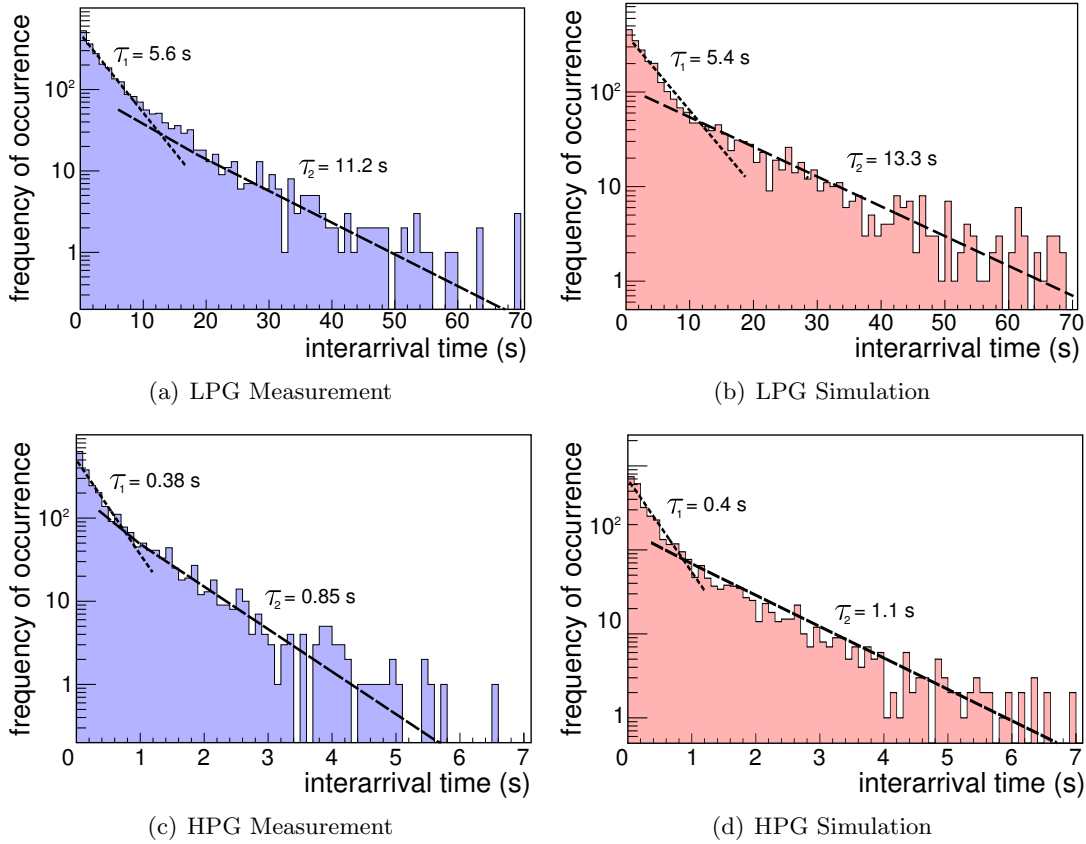


**Figure 7.15:** Time difference between successive detector hits for the LPG (a and b) and HPG (c and d) scenarios. These interarrival times show two characteristic slopes, which can be attributed to low-energy ( $< 10$  keV) and high-energy ( $> 10$  keV) stored electrons, featuring different scattering cross sections.

to the energy dependence of the elastic and inelastic cross sections, see below), implying a time dependence of the parameter  $\lambda = \lambda(t)$ . Table 7.6 gives an overview of the slopes and rate parameters for the two investigated scenarios LPG and HPG. The parameters of the measurement and the Monte-Carlo simulation results are in good agreement.

In order to understand the observation of two distinct slopes, it has to be investigated which parameters influence the time  $\Delta_{\text{exp}}T$ . To first order, the average time between two ionizing events  $dT_{\text{ion}}$  governs the overall time distribution. A second effect arises from the fact that only a fraction of the secondary electrons will actually impinge on the detector, resulting in an increased value  $\Delta_{\text{exp}}T > dT_{\text{ion}}$ .

The time  $dT_{\text{ion}}$  depends in particular on the kinetic energy of the stored electron. When discussing the stochastic nature of ionization processes, it is useful to recall that a stored high-energy electron will perform rather fast axial oscillations in the pre-spectrometer ( $\sim 10^6$  per second), which has two major effects:

**Table 7.6:** Slope and rate parameters for the time difference investigations of figure 7.15.

scenario	$\tau_1$ (s)	$\lambda_1$ (1/s)	$\tau_2$ (s)	$\lambda_2$ (1/s)
LPG (meas)	$5.6 \pm 0.19$	$0.178 \pm 0.006$	$11.2 \pm 1.26$	$0.089 \pm 0.01$
LPG (simu)	$5.4 \pm 0.20$	$0.185 \pm 0.007$	$13.3 \pm 0.89$	$0.075 \pm 0.005$
HPG (meas)	$0.38 \pm 0.02$	$2.63 \pm 0.13$	$0.85 \pm 0.05$	$1.18 \pm 0.07$
HPG (simu)	$0.4 \pm 0.02$	$2.5 \pm 0.1$	$1.1 \pm 0.06$	$0.91 \pm 0.05$

- Over each axial cycle the electron experiences significant changes of its kinetic energy due to the non-uniform axial electrostatic field, where the lowest kinetic energies will be reached in the center of the pre-spectrometer, while the maximum kinetic energy is attained at the magnetic mirror point, where the electrostatic potential is lowest. As a result, for each axial cycle this oscillation rapidly modifies the electrons' ionization cross section  $\sigma_{\text{ion}}(E)$  (see figure 8.15). For an exemplary electron with a kinetic energy of 10 keV, the energy gain by the electrostatic potential is on average about 5 keV, which reduces the ionization cross section by about a factor of 1.5 when moving away from the center of the spectrometer. In terms of ionization probability per unit time this is, however, counter acted by the fact that electrons experience longer path lengths in higher magnetic fields due to the increased cyclotron path. The above 10 keV electron, which starts under an angle of  $45^\circ$  in the spectrometer center spends about 70% of its path in a region further away than 1 m from the analyzing plane. As the axial oscillation is much faster than the typical time scale of an ionization process, this translates into an average time  $dT_{\text{ion}}$  if one integrates over one or several axial oscillation cycles so that a uniform ionization probability can be defined on time scales larger than  $10^{-5}$  s but still small with regard to the interarrival times  $\Delta_{\text{exp}}T$  (these are typically  $> 10^{-1}$  s).
- The synchrotron energy losses ( $\Delta E \propto E_{\perp} \cdot B^2$ ) strongly depend on the axial position in the pre-spectrometer as the magnetic field strength  $B$  as well as the transversal energy of the electron  $E_{\perp}$  increases further away from the analyzing plane. Generally, larger kinetic energies entail larger synchrotron losses, while scattering losses are minimized due to the decreased scattering cross sections.

Due to the repeated energy losses by ionizing collisions, as well as the continuous energy loss due to the emission of synchrotron radiation, the energy of the stored electron constantly decreases, thus increasing its ionization cross section  $\sigma_{\text{ion}}(E)$  up to the maximum of  $10^{-16}$  cm<sup>2</sup> at 60-100 eV, where the storage condition no longer holds. As a result, the observed interarrival times  $\Delta_{\text{exp}}T$  will be a superposition of different exponential slopes, reflecting the on-going cooling of the primary stored electron and its increase of ionization probability.

The slope  $\tau_2$  is about a factor of two larger than  $\tau_1$ , for both measurement scenarios. In principle, one would expect a larger factor ( $\sim 3 - 10$ , see below) between the two empirical slope factors, reflecting the variation of  $\sigma_{\text{ion}}(E)$  over the entire range of trapping energies. This apparent discrepancy can be understood in terms of the relative energy losses due to scattering processes and synchrotron emission. The range of interarrival times, governed by  $\tau_2$ , should correspond to the initial parts of a Rn-background period, where a high-energy electron with small  $\sigma_{\text{ion}} \ll 10^{-16} \text{ cm}^2$  is stored. At this point it is useful to perform a back-of-the-envelope calculation for the average time  $dT_{\text{ion}}$  between two ionizing collisions of the primary high-energy stored electron from a Rn  $\alpha$ -decay for the LPG measurements at  $10^{-10}$  mbar (note however, that this discussion is largely independent of the number primary multi-keV stored particles generated by the decay process). For this pressure one obtains a corresponding number density  $n = 2.4 \cdot 10^{12} / \text{m}^3$  (eq. (8.5)). For an electron kinetic energy in the range of 10 keV (100 keV), where  $\sigma_{\text{ion}} \approx 5 \cdot 10^{-18} \text{ cm}^2$  ( $5 \cdot 10^{-19} \text{ cm}^2$ ), one obtains with eq. (8.6) a rough estimate for the average time between two ionizing collisions of electron scattering off  $\text{H}_2$ :  $dT_{2,\text{LPG}} \approx 11 \text{ s}$  (35 s). The fact that about 60% of all secondaries is stored in the large volume Penning trap and only 50% of the remaining electrons is actually released towards the detector side yields an expected interarrival time of about  $\Delta_{2,\text{LPG}}T \approx 36 \text{ s}$  (117 s). This discrepancy is somewhat reduced when considering that 60% of the residual gas is  $\text{H}_2\text{O}$  with its 4 times larger cross section relative to  $\text{H}_2$ . Accordingly, one expects  $\Delta_{2,\text{LPG}}T \approx 15 \text{ s}$  (49 s). This is still about a factor 3-10 (depending on the kinetic energy) larger than observed which indicates that a second effect reduces  $\tau_2$ .

Several effects can cause such a behavior. One important process is the emission of synchrotron radiation which dominates the overall energy loss in case of the pre-spectrometer. As synchrotron losses compete with ionizing collisions (see section 7.4.4), and enhance  $\sigma_{\text{ion}}$  of the (lower energy) electrons, their net effect is to shorten  $\tau_2$  (this is supported by Monte-Carlo simulations, where synchrotron losses have been inhibited, leading to a longer  $\tau_{2,\text{MC}}$  which is not compatible with the measurements). Another effect could stem from the Penning trap in the center of the pre-spectrometer, where the low-energy secondaries can be trapped. Depending on the polar angle of the primary electron, its axial path can extend beyond the central Penning trap region, thus creating secondaries outside of the trap.

It is important to underline that the Monte-Carlo simulation, which take into account both processes reproduce the experimental slope parameter  $\tau_2$  with very good precision.

The slope parameter  $\tau_1$  thus corresponds to low-energy stored particles. Again, a calculation of the average time between two ionizations can be performed. In this second case, where the electron kinetic energy is in the range of 100 eV, and where  $\sigma_{\text{ion}}$  is maximal, one obtains with eq. (8.6) a corresponding estimate for the average time between two ionizing collisions  $dT_{1,\text{LPG}}(\text{H}_2) \approx 6.5 \text{ s}$  in case of electron scattering off  $\text{H}_2$ . Applying the gas composition corrections and the geometrical corrections yields a value of  $\Delta_{1,\text{LPG}}T \approx 9 \text{ s}$ . This value is still larger than the experimental value, even for the case of a maximum ionizing electron. Possible causes are uncertainties in the scattering cross sections (see deviations in figure 8.15) or in the actual residual gas

composition. A more detailed investigation of these effects is beyond the scope of this thesis. However, a cross check can be performed when comparing the LPG and the HPG scenarios. In the HPG case, the residual gas pressure was artificially increased by about a factor of 20 using argon, which has about a factor of 2 higher cross sections than H<sub>2</sub>. The above obtained value  $dT_{1,\text{LPG}}(\text{H}_2) \approx 6.5$  s is thus reduced by a factor of 40, which gives  $dT_{1,\text{HPG}} \approx 0.16$  s and finally  $\Delta_{1,\text{HPG}}T \approx 0.27$  s<sup>2</sup>. The fact that the results are consistent with each other and the excellent agreement of the experimental data with the corresponding Monte-Carlo data based on KASSIOPEIA underlines that the electron cooling processes in electrostatic spectrometers are extremely well understood. This in turn will allow to use the interarrival times of detector hits at the FPD to serve as an in-situ measurement of the residual pressure in the main spectrometer, even down to very low pressure regimes of 10<sup>-12</sup> mbar, where conventional pressure gauges reach the limit of their range<sup>3</sup>. The exact knowledge of the residual pressure in the main spectrometer is of crucial importance with regard to two issues:

- This allows to calculate the background rate of low-energy electrons produced by the full flux of tritium  $\beta$ -decay electrons during the scanning process in the entrance region of the main spectrometer (in the proposed electromagnetic layout where the pre-spectrometer will be operated at a very low retarding potential), and
- as the interarrival times depend on and vary with the residual pressure the knowledge of the latter is crucial to evaluate the impact of active background suppression methods. This aspect will be discussed in more detail in section 8.4.

An additional effect has to be considered when discussing interarrival times: the time of an ionizing collision and the arrival time of the low-energy electron generated during the interaction can differ due to storage effects for low-energy electrons. In case of the pre-spectrometer, these effects at very low energy only play a minor role and can be neglected (typically, secondary electrons are not stored in the pre-spectrometer). At the larger main spectrometer, however, the importance of storage of low-energy electrons is strongly increased. For completeness, the effect of the subsequent storage of the low-energy electrons on the interarrival times  $\Delta T_{\text{exp}}$  will be discussed briefly. In this case, angular changes of the stored electron due to the elastic scattering processes will contribute to its escape probability from the spectrometer. Consequently, a time distribution similar to consecutive radioactive decays is expected with

$$N_{\text{hit}}(t) = \frac{\lambda_{\text{ion}}}{\lambda_{\text{elas}} - \lambda_{\text{ion}}} \cdot [\exp(-\lambda_{\text{ion}} \cdot t) - \exp(-\lambda_{\text{elas}} \cdot t)]. \quad (7.6)$$

This implies that the interarrival times will be governed either by the average time of

---

<sup>2</sup>Note that the cross sections of argon, which was the main gas contribution in the HPG measurement, are only a factor of 2 larger than for H<sub>2</sub>.

<sup>3</sup>This investigation can be performed in dedicated measurements with an electron gun operated at a fixed frequency and high surplus energies (for different radii and polar angles), as the exponential slope of interarrival times of stored electrons from inelastic scatterings can easily be separated from the flat background created by electrons undergoing no interaction.

an ionizing collision (characterized by  $\lambda_{\text{ion}}$ ) or by the average time it takes to break the storage condition for the low-energy electron (characterized by  $\lambda_{\text{elas}}$ ).

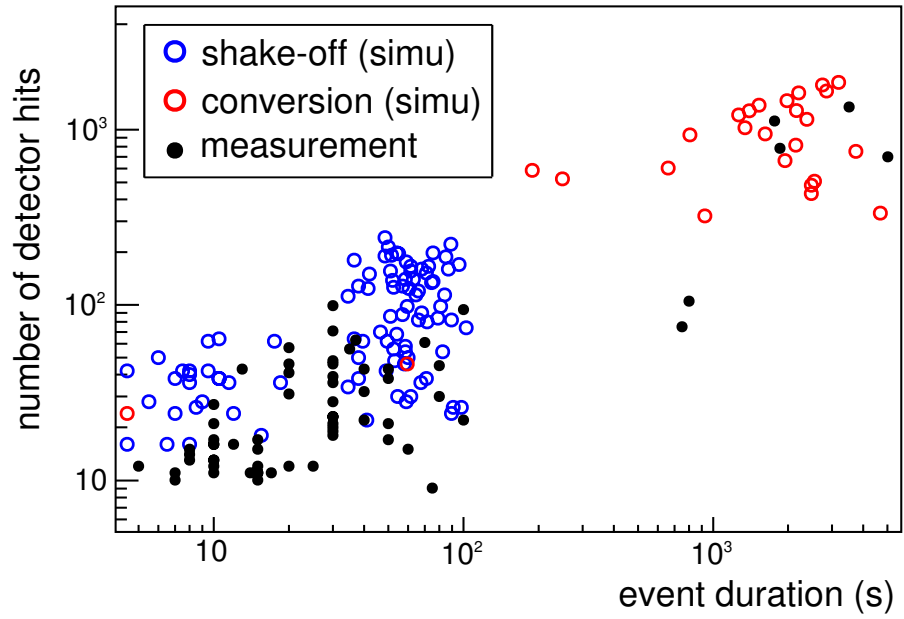
#### 7.4.4 Rate of single events

The above discussions have shown that the observed spatial and interarrival time distributions of the detector hits within single radon  $\alpha$ -decay spike events can be reproduced with simulations incorporating the electron emission model of this work. An additional important quantity for comparison is the correlation of the number of produced secondaries  $N_{\text{sec}}$  and the total event duration  $t_{\text{ev}}$ . As these parameters are influenced by the specific model of electron production as well as the ability to precisely simulate the electron trajectories within the complex KATRIN geometries, an agreement with measured data would ultimately validate the model of radon-induced background processes within a MAC-E filter. To do so, the two measurements at different pressures (measurements HPG and LPG) were investigated. Figure 7.16 compares the results of measurements and corresponding simulations.

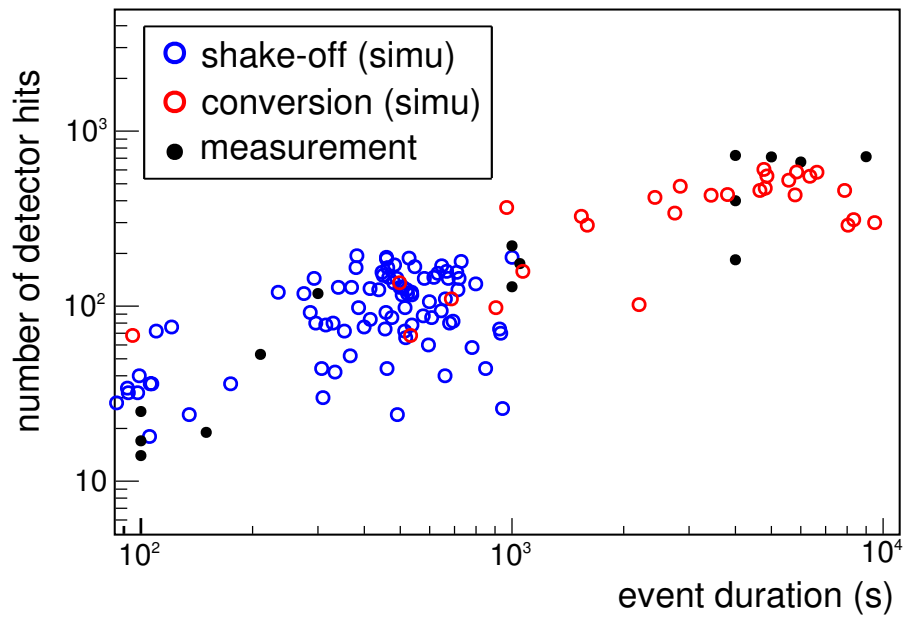
The storage time of a primary electron and the number of secondary electrons it produces strongly depend on the starting kinetic energy of the primary electron and on the residual gas pressure  $p$  in the spectrometer volume. The number  $N_{\text{sec}}$  will increase for higher pressure levels as scattering energy losses increase at the expense of synchrotron energy losses. By the same token, the storage time decreases because successive scattering events will happen faster. Accordingly, for the HPG measurement, the electron energy losses are dominated by scattering processes (see figure 7.16 (a)). Interestingly, both measurement and simulation show two separate, distinct regions with regard to the event duration ( $t_{\text{ev}} \leq 10^2$  s,  $t_{\text{ev}} > 10^2$  s). The simulation, which can distinguish between conversion and shake-off events, reveals that this characteristic is due to differing primary electron emission processes. While the majority of the shake-off electrons has less than 20 keV kinetic energy, conversion electrons typically are found above 100 keV. For this pressure regime, the parameter  $t_{\text{ev}}$  allows to distinguish conversion electrons ( $t_{\text{ev}} > 10^2$  s) from inner shell shake-off processes ( $t_{\text{ev}} \leq 10^2$  s). On the other hand, at low pressures in the LPG measurement (figure 7.16 (b)), synchrotron energy losses tend to smear out this difference. While shake-off electrons at low energies are barely affected by synchrotron losses, these losses are dominant in the case of conversion electrons. Consequently, the gap between the two emission classes closes. The impact of increased losses due to synchrotron radiation at excellent UHV conditions is further confirmed by the fact that the overall number of secondary electrons is reduced by a factor of 1.5 for the LPG measurement.

#### 7.4.5 Determination of radon activities

Following the above considerations, the cooling time of a single electron can vary between a few seconds for very low energies at high pressures, and a few hours for the highest energies at low pressures. In case of the pre-spectrometer background measurements the radon activity in general was low enough so that the average time between two events



(a) HPG setup ( $p = 2 \cdot 10^{-9}$  mbar)



(b) LPG setup ( $p = 1 \cdot 10^{-10}$  mbar)

**Figure 7.16:** Number of detector hits as a function of the event duration for the HPG measurement (a) and the LPG measurement (b). The simulations (open circles) nicely reproduce the features of the measurements (full circles), which is described in more detail in the main text.

was larger than the typical event duration. Therefore, individual  $\alpha$ -decays can be clearly discriminated, which allows for their counting.

The excellent agreement between Monte Carlo simulations and experimental data, as well as the different vacuum conditions of the three measurements (LPG, HPG and HP), which influence shake-off and conversion electrons differently, can now be used to determine the  $\alpha$ -decay activities of the two isotopes ( $^{219}\text{Rn}$  or  $^{220}\text{Rn}$ ), as well as their origin (getter, bulk) yielding the three observables<sup>4</sup>  $^{219}\text{Rn}_\text{B}$ ,  $^{219}\text{Rn}_\text{G}$  and  $^{220}\text{Rn}_\text{B}$ . To discriminate between  $^{219}\text{Rn}$  and  $^{220}\text{Rn}$  induced events, the simulated decay probabilities for CI-III events were used to fit the experimental data of table 7.5. Finally the more detailed results of this work are compared to the earlier results in [279], which were based on measurements only.

Table 7.7 summarizes the simulated probabilities of CI-CIII events following  $^{219}\text{Rn}$  and  $^{220}\text{Rn}$  decays for the three experimental configurations. The key experimental parameters pressure and gas composition are identical to table 7.5. Furthermore, the average number of detector hits per event  $\langle N_{\text{det}} \rangle$  is shown, which is required to determine the actual background contribution.

The event rates  $r_i$  for the individual classes  $C_i$ , with  $i = I, II, III$ , are determined from the activities of the three different radon sources  $A(^{219}\text{Rn}_\text{B})$ ,  $A(^{219}\text{Rn}_\text{G})$  and  $A(^{220}\text{Rn}_\text{B})$ , the corresponding probabilities  $P_i$  for the occurrence of an event of class  $C_i$  and the decay probability  $\epsilon$ :

$$r_i = \sum_{k=^{219}\text{Rn}_\text{B}, ^{219}\text{Rn}_\text{G}, ^{220}\text{Rn}_\text{B}} \epsilon(k) \cdot A(k) \cdot P_i(k). \quad (7.7)$$

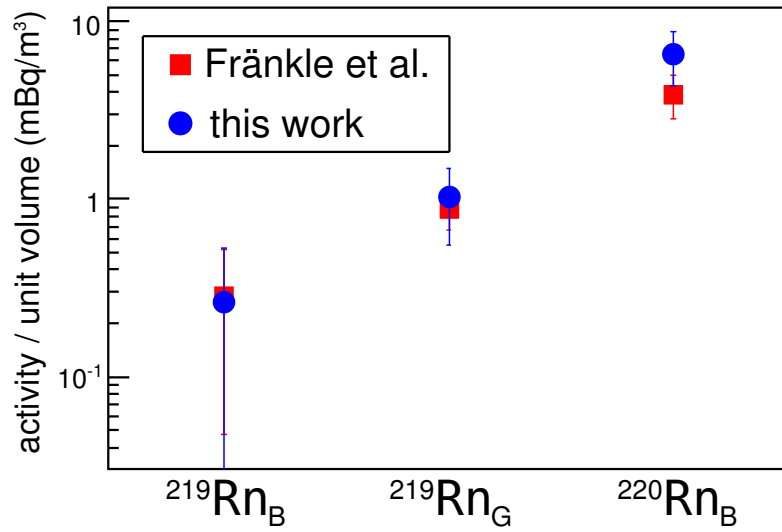
The probabilities  $P_i(k)$  are taken from table 7.7 and the decay probabilities  $\epsilon(k)$  from table 7.4. The only free parameters remaining are thus the radon activities  $A(k)$ , which can be determined by a three-parameter  $\chi^2$ -fit of the simulated event rates  $r_i$  to the measured rates of table 7.5. Figure 7.17 shows the fit results for the radon activities per unit volume in the pre-spectrometer (total volume:  $8.5 \text{ m}^3$ ). The obtained values are compared to the activities which were observed in the measurements of Fränkle et al. [279]. The simulated activities in general are somewhat larger than the measured ones, which can be explained by two facts. First, the effects of non-adiabaticity were not considered in [279]. Furthermore, the extensive simulations have revealed that some CI events are not imaged as rings on the detector, and, consequently, could not be attributed to radon-induced background within the analysis of [279].

Table 7.8 gives the emanation rates of  $^{219,220}\text{Rn}_\text{B}$  into the KATRIN pre-spectrometer stainless steel vessel per unit volume. The values are compared to the independent measurement of the  $^{222}\text{Rn}$  emanation for the empty and fully equipped GERDA cryostat, as reported in [310, 311]. When comparing these values, one has to bear in mind that the isotopes  $^{219,220}\text{Rn}$  originate from the  $^{235}\text{U}$  and  $^{232}\text{Th}$  decay chains, while  $^{222}\text{Rn}$  is part of the  $^{238}\text{U}$  decay chain. Unfortunately, the measurement technique applied in [310] does not allow detection of the short-lived  $^{219,220}\text{Rn}$  isotopes. As the authors of [310]

<sup>4</sup>Note that investigations of Rn-activities have revealed that the NEG material contains negligible amounts of  $^{220}\text{Rn}$  so that the parameter  $^{220}\text{Rn}_\text{G} = 0$  in this work.

**Table 7.7:** Overview of simulation results, comprising 10000 electrons for each configuration and radon isotope. The probability  $P$  for the occurrence of CI-III events per decay and the average number of detector hits  $\langle N_{\text{det}} \rangle$  per event are shown.

measurement	LPG		HPG		HP	
radon type	$^{219}\text{Rn}$	$^{220}\text{Rn}$	$^{219}\text{Rn}$	$^{220}\text{Rn}$	$^{219}\text{Rn}$	$^{220}\text{Rn}$
$P$ ( $10^{-3}$ ) (CI)	8	5.8	9.2	5	6.8	5.7
$\langle N_{\text{det}} \rangle$ /event (CI)	22.8	19	24.3	21.9	25.3	21.4
$P$ ( $10^{-3}$ ) (CII)	3.9	2.1	3.3	0.8	3.3	0.8
$\langle N_{\text{det}} \rangle$ /event (CII)	130.3	71.6	123.2	58.6	134.4	51.3
$P$ ( $10^{-3}$ ) (CIII)	4.2	0	2.7	0	5.3	0
$\langle N_{\text{det}} \rangle$ /event (CIII)	677.9	0	932.7	0	1033.8	0



**Figure 7.17:** Total activity of  $^{219}\text{Rn}_B$  (bulk material of the spectrometer vessel),  $^{219}\text{Rn}_G$  (getter material) and  $^{220}\text{Rn}_B$  inside the pre-spectrometer. The values have been determined by a three-parameter fit of simulated to measured event rates. The simulation results of this work (circles) are compared to values derived from measurements of Fränkle et al. [279] (squares).

**Table 7.8:** Comparison of radon emanation rates normalized to a unit volume in the KATRIN and GERDA stainless steel vessels. The simulated  $^{219,220}\text{Rn}_B$  concentrations for the fully equipped KATRIN pre-spectrometer stainless steel vessel ( $V = 8.5 \text{ m}^3$ ,  $A = 25 \text{ m}^2$ ) are compared to the  $^{222}\text{Rn}$  concentrations in case of an empty and a fully equipped GERDA cryostat [310, 311] ( $V = 65 \text{ m}^3$ ,  $A = 70 \text{ m}^2$ ).

	concentration (mBq/m <sup>3</sup> )
$^{219}\text{Rn}$ [this work]	$0.26 \pm 0.26$
$^{220}\text{Rn}$ [this work]	$6.53 \pm 2.18$
$^{222}\text{Rn}$ [310] (empty)	$0.22 \pm 0.03$
$^{222}\text{Rn}$ [311] (fully equipped)	$0.85 \pm 0.06$

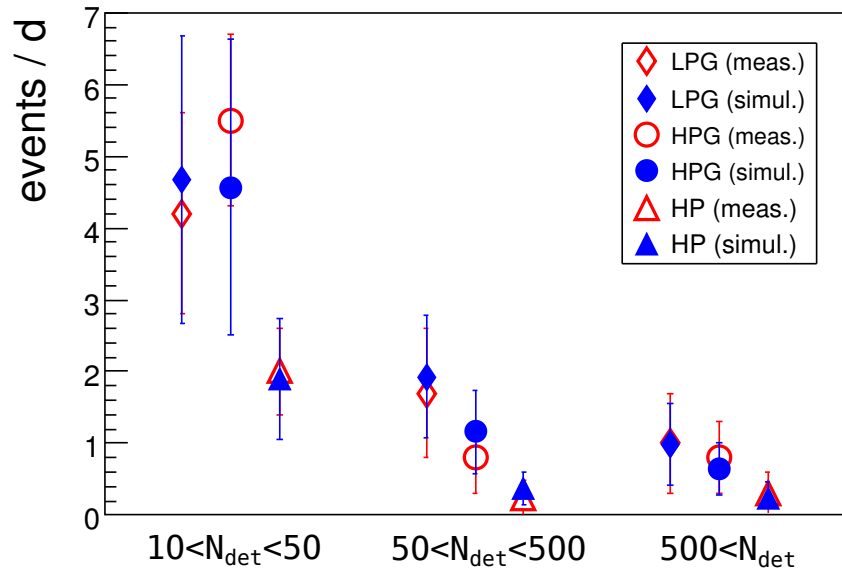
have pointed out, stainless steel vessels in general show much larger radon emanation rates than pure stainless steel plates, which can be attributed to welding procedures in the vessel manufacture. Furthermore, any auxiliary equipment attached to the vessel will significantly increase the radon emanation rate, an effect both observed in KATRIN and GERDA for different isotopes.

Figure 7.18 compares the event rates determined according to eq.(7.7) to those derived within the measurements of this work. The values are in good agreement within their error margins (propagated from the errors on the activities).

In figure 7.19, the background contributions of the individual classes are shown. These values are determined by multiplying the calculated event rates with the simulated average number of detector hits per event ( $\langle N_{\text{hit,MC}} \rangle$ ) of each class for the different radon isotopes.

After subtracting the contributions of CI-III events from the total measured background rate, a background component of about  $3 \cdot 10^{-3}$  cps remains. A fraction of this background results from radon decays which produce less than 10 detector hits, or are not detected as ring events by the analysis software (in the following labeled C0 events). These are mainly  $\alpha$ -decay events where only two low-energy shell reorganization electrons are emitted [280], which have a low probability of being magnetically stored in the pre-spectrometer. The simulations reveal that these radon decays produce on average 0.2 detector hits. Table 7.9 summarizes the C0 contributions to the background rate for the three measurements considered. The fact that all simulated rates contribute significantly, but do not exceed the remaining measured single hit background rate is another important validation of the background model, showing that radon-induced processes also contribute to the measured C0 class. As outlined previously, a model was employed where the shell reorganization energy retained by the atom is statistically distributed between two electrons. In view of the simplicity of this model and the subtlety of non-trapping or trapping of low-energy electrons within the pre-spectrometer<sup>5</sup>, the agreement between simulation and experiment within a factor of 2 is a strong indication for a back-

<sup>5</sup>The electrons are produced with energies close to the trapping threshold of 60 eV.



**Figure 7.18:** Event rates for the individual classes and measurements, determined according to eq.(7.7). The simulations (full symbols, blue) are in good agreement with the measurement results (open symbols, red).

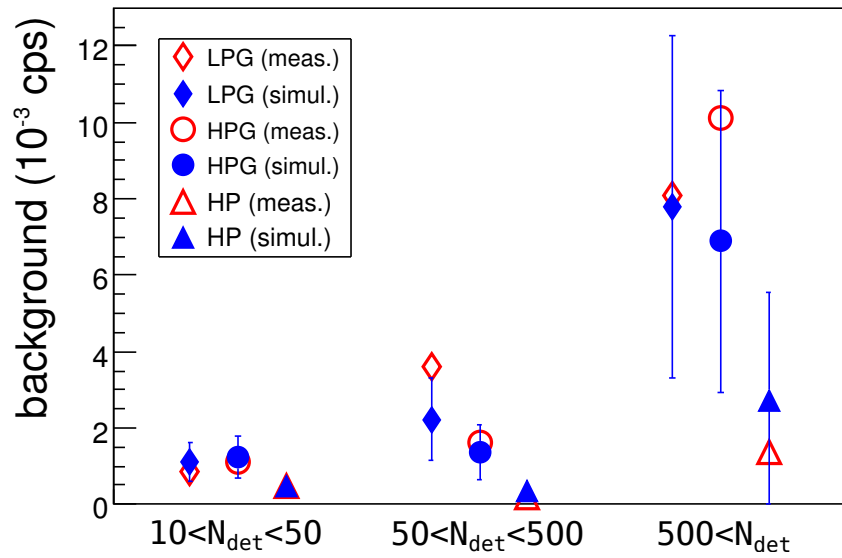


**Figure 7.19:** Background contribution from the individual classes. The simulations (full symbols, blue) are in agreement with the measurement results (open symbols, red).

**Table 7.9:** Simulated and measured background rate ( $r_{\text{C0, simu}}$ ,  $r_{\text{C0, meas}}$ ) due to C0 single hit events.

measurement	$r_{\text{C0, simu}}$ ( $10^{-3}$ cps)	$r_{\text{C0, meas}}$ ( $10^{-3}$ cps)
LPG	$1.6 \pm 0.03_{\text{stat}}$	$3.2 \pm 0.3$
HPG	$1.4 \pm 0.03_{\text{stat}}$	$3.4 \pm 0.3$
HP	$0.8 \pm 0.02_{\text{stat}}$	$2.0 \pm 0.3$

ground model, where the entire C0 background class originates from shell reorganization following  $^{219,220}\text{Rn}$  decays in the spectrometer. Within the upcoming main spectrometer measurements, a larger sensitivity to the low-energy part of the energy spectrum can be expected (due to the decreased trapping threshold of 1 eV), thus allowing a final test of the developed model.

#### 7.4.6 Summary

Within this section, the model of radon-induced background within MAC-E filters was validated by comparison to independent measurements and dedicated pre-spectrometer measurements. It was shown that the model successfully reproduces a variety of experimental observables such as polonium charge multiplicities, as well as spatial and temporal event distribution in background measurements with the pre-spectrometer. The relative contribution of the two isotopes  $^{219}\text{Rn}$  and  $^{220}\text{Rn}$  has been determined in a novel method by varying the pressure in the UHV recipient. In addition, by removing the NEG strips from the pre-spectrometer pump port, the radon emanation rate of the vessel surface and other auxiliary equipment was determined. As a result, the radon-induced background in the KATRIN pre-spectrometer has been fully characterized.

These findings are of major importance for the KATRIN measurements with the main spectrometer. In [132, 146], the background model of this work was extrapolated to the different electromagnetic layout at the large main spectrometer, taking into account the much larger NEG pump in operation there. The initial findings there have been refined within this work and the results thereof are presented in the next section.

## 7.5 Impact of radon-induced background on the KATRIN sensitivity

The detailed model of radon-induced background processes within MAC-E filters, which was developed and validated by dedicated measurements with the pre-spectrometer within this thesis, can be used to extrapolate the background rate expected for the final KATRIN setup. Initial simulations have been performed in [132, 146] and the impact of radon-induced background on the KATRIN sensitivity has been studied. Within

this thesis, the initial model has been refined, giving a more realistic prospect of the implications for the main spectrometer background (section 7.5.1) and finally the KATRIN neutrino mass sensitivity (section 7.5.2).

### 7.5.1 Implications for the main spectrometer

The main spectrometer employs the same UHV technique as the pre-spectrometer and thus is likely to be affected by a non-negligible Rn-background. As in the case of the pre-spectrometer, a NEG pump will be used to achieve a pressure level of  $p = 10^{-11}$  mbar. However, to achieve a sufficient pumping speed, NEG strips with a total length of 3 km have to be employed as compared to the 90 m, which have been installed at the pre-spectrometer. Consequently, the expected number of radon atoms emanating into the main spectrometer volume is much larger than in the case of the pre-spectrometer.

In addition to radon, also tritiated molecules from the WGTS could contribute to the main spectrometer background rate. Despite a huge tritium retention factor of  $10^{14}$ , non-negligible amounts of tritiated molecules ( $\approx 3 \cdot 10^3$ /s) can enter the main spectrometer. A small number will decay there before being pumped out, releasing  $\beta$ -decay electrons with a continuous spectrum up to  $E_0 = 18.6$  keV. Additionally, low-energy shake-off electrons ( $< 100$  eV) are emitted with a probability of 15% per  $\beta$ -decay [312]. The contribution of these shake-off electrons has been neglected previously [132, 146], but was added in the course of this work.

In order to be able to extrapolate from the pre-spectrometer (PS) findings to the main spectrometer (MS), the storage behavior of electrons with energies between 1 eV and several hundreds of keV has to be investigated first. The relevant differences between the PS and the MS include the vessel dimensions (PS:  $l = 3.3$  m,  $d = 1.7$  m; MS:  $l = 23$  m,  $d = 10$  m) and the central magnetic field strength ( $B_{\min}^{\text{PS}} = 15.6$  mT,  $B_{\min}^{\text{MS}} = 0.35$  mT). Figure 7.20 shows the trapping probability in the two spectrometers for electrons, which were started homogeneously and isotropically in the spectrometer volume with discrete kinetic energies (both spectrometers are on identical retarding potential of -18.6 keV).

For the PS, low-energy electrons of up to about 12 eV have a large storage probability due to a Penning trap in the spectrometer volume, featuring a depth of up to 12 V [145]. It is important to notice that these electrons cannot escape the electrostatic trap in axial direction and hence do not contribute to the background rate observed at the detector.

The trapping probability decreases for increasing kinetic energies, as all electrons with longitudinal kinetic energies  $> 12$  eV will escape this trap. However, for energies exceeding 60 eV, magnetic storage sets in, as discussed earlier in this section. At very high energies ( $> 100$  keV), the cyclotron radius starts to exceed the diameter of the pre-spectrometer. Furthermore, non-adiabatic changes of the polar angle of the stored electrons can break the storage condition.

In case of the MS, electrostatic storage is not observed as no volume Penning trap is expected to exist within this electromagnetic configuration [191]. Consequently, electrons at the lowest energies below the magnetic storage threshold of 1 eV are not stored. Due to the lower analyzing magnetic field strength of 0.35 mT (PS: 15.6 mT), and consequently

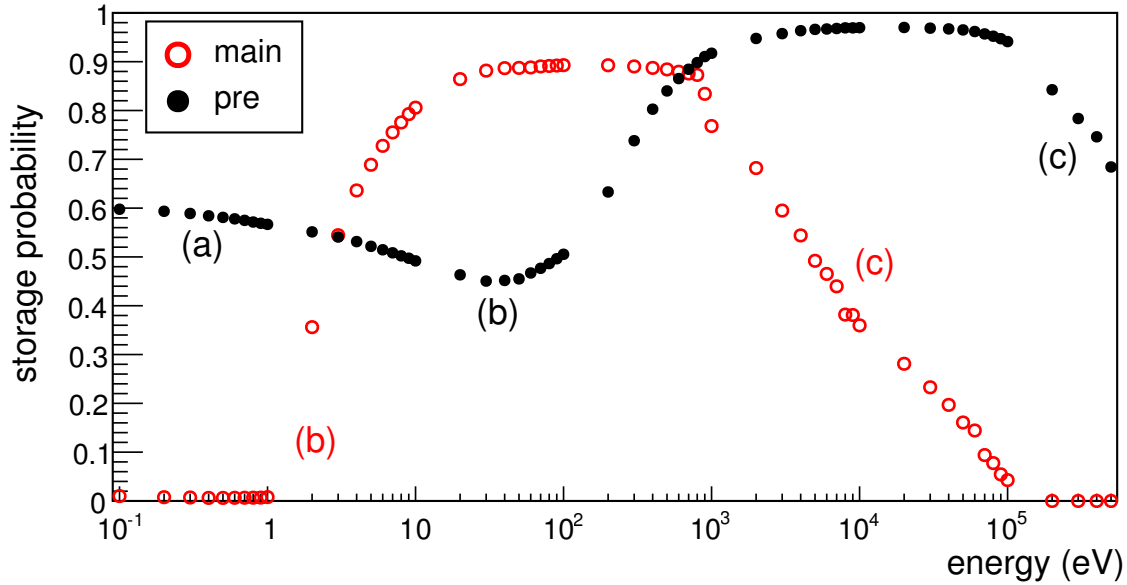


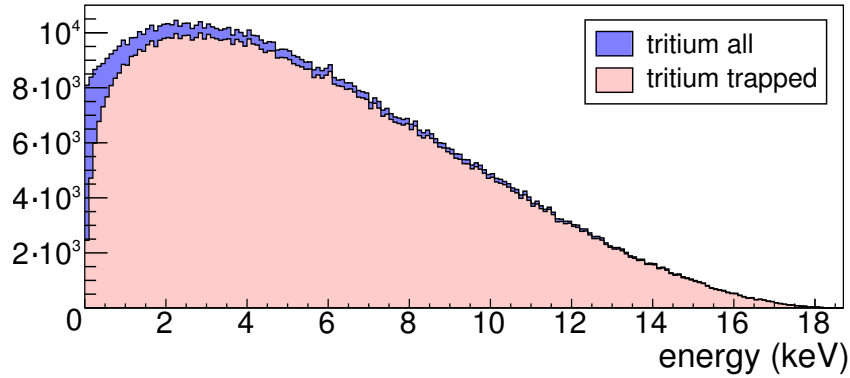
**Figure 7.20:** Storage probability in the pre- and main spectrometer. Pre-spectrometer: (a) electrostatic storage due to an up to 12 V deep Penning trap in the volume, (b) storage threshold of 60 eV, (c) cyclotron and adiabaticity cut-off. Main spectrometer: an electrostatic trap does not exist here, (b) storage threshold of 1 eV, (c) cyclotron and adiabaticity cut-off.

larger cyclotron radii, than in the PS case, electrons with larger kinetic energies are more likely to hit the vessel, reducing the overall trapping probability. Additionally, non-adiabatic effects are observed for electrons with energies above 1 keV (PS: 100 keV). It should be noted here that a larger value of the analyzing magnetic field (say to a value of 0.5-0.6 mT, as has been discussed in this thesis) will change this trapping behavior. It is evident that this value crucially influences the observed background rates.

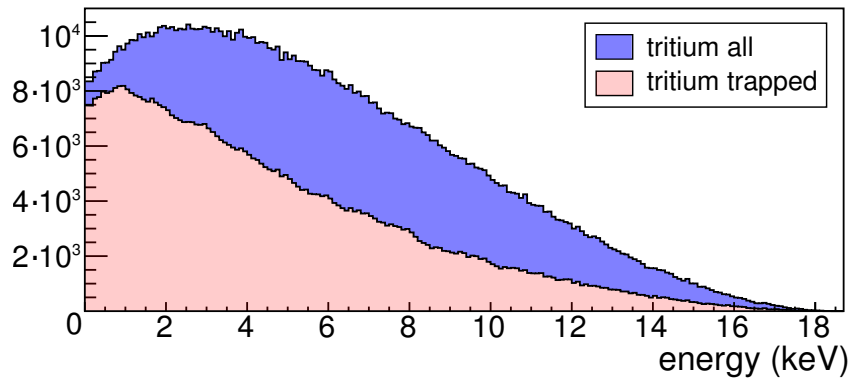
Following these generic considerations, the storage behavior of electrons created within the nuclear decays of tritium and radon can be investigated by high statistics Monte-Carlo simulations, with electrons starting within the spectrometer volumes according to the tritium and radon energy spectra.

Figure 7.21 shows the simulation results for the case of tritium. The energy spectrum of all electrons started (identical for the PS and the MS) is compared to the distribution of stored electrons. In the PS case, the storage probability decreases with decreasing kinetic energies (down to 12 eV), which is caused by the large magnetic storage threshold. The MS, in contrast, stores mainly low-energy electrons (i.e. with small surplus energy above the potential) as visible from the large suppressed high-energy tail of the tritium  $\beta$ -spectrum. The shake-off electrons ( $E_{\text{kin}} < 100$  eV), which are not shown in the figure, have storage probabilities of  $p_{\text{sto}}(\text{PS}) = 0.47$  and  $p_{\text{sto}}(\text{MS}) = 0.89$ .

The equivalent storage pattern of electrons from radon decays is shown in figure 7.22. The PS stores all radon-induced electrons with energies above 1 keV, while the majority of low-energy shell-reorganization electrons ( $< 100$  eV) is not stored. A different behavior



(a) pre-spectrometer

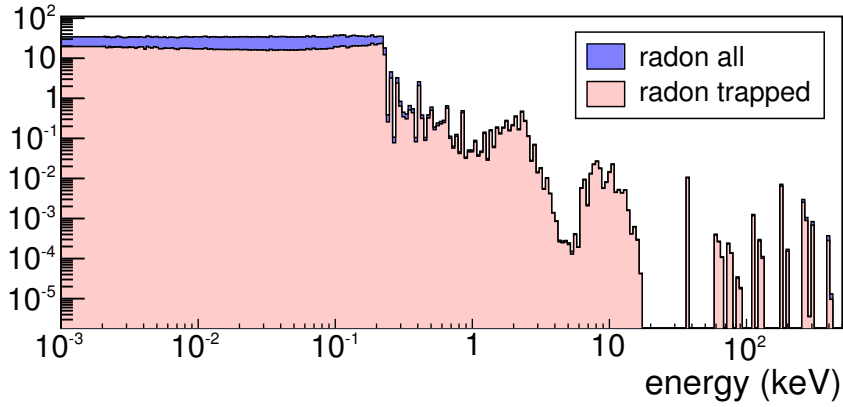


(b) main spectrometer

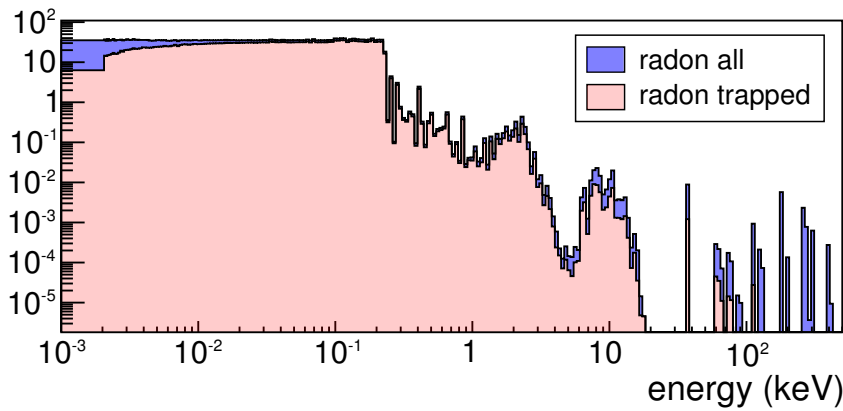
**Figure 7.21:** Tritium storage behavior in the (a) pre- and (b) main spectrometer. The shake-off electrons, which are not shown, have the following storage probabilities:  $p_{\text{sto}}(\text{PS}) = 0.47$  and  $p_{\text{sto}}(\text{MS}) = 0.89$ .

is observed in case of the MS. Here, the high-energy conversion electrons ( $> 50$  keV) are barely stored. Although electrons of intermediate energies ( $< 10$  keV) are stored, the majority of background events is expected from the low-energy shell reorganization electrons due to their vast number.

It can be concluded that the pre-spectrometer is most sensitive to the high-energy part of the electron spectrum so that the primary energy can be estimated from the observed number of detector hits. At very low energies ( $< 200$  eV), though, electrons are not trapped and, hence, do not convert their full kinetic energy into secondary electrons, resulting in a loss of information on their energy spectrum. In case of the main spectrometer, the high-energy part of the spectrum ( $> 50$  keV) will not contribute significantly to the background for the reference analyzing field strength of 0.35 mT. However, an increased sensitivity to the low-energy part can be expected. Hence, the details of the description of the shell reorganization electrons can be investigated within the commissioning measurements.



(a) pre-spectrometer



(b) main spectrometer

**Figure 7.22:** Radon storage behavior in the (a) pre- and (b) main spectrometer.

The above described Monte-Carlo simulations can now be used to investigate the implications of this type of background for the neutrino mass sensitivity.

### 7.5.2 Implications for the neutrino mass sensitivity

It was shown in section 2.3 that the background rate significantly influences the neutrino mass sensitivity. In the standard case of a Poisson-distributed background, the statistical uncertainty  $\sigma_{\text{stat}}$  on the observable  $m_{\nu_e}^2$  scales approximately as  $N_b^{1/6}$  [82, 278], where  $N_b$  is the observed number of background events. However, in the case of nuclear decays, a different distribution of the background events is observed. At the pre-spectrometer, intervals of elevated rate were observed, which were caused by a single nuclear event. In between such events, a smaller background rate with a rate drop-off of more than two orders of magnitude was found. This time-dependence of the background requires a different treatment of the background than in the case of Poisson-distributed events. Therefore, a detailed model describing the background as a function of time over the full

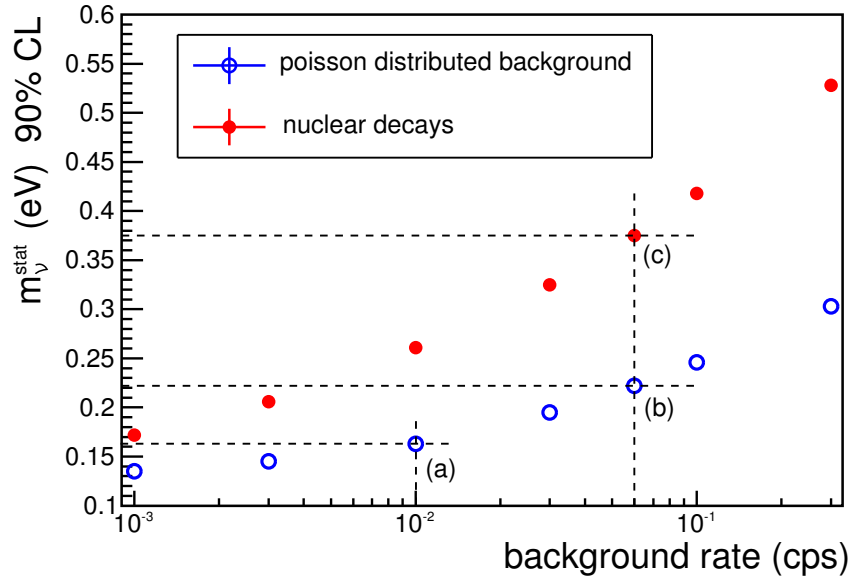


**Figure 7.23:** Neutrino mass sensitivity as a function of the background rate.

three years measurement time of KATRIN was implemented in [146]. Here, the results of a refined calculation based on Monte-Carlo simulations will be given. The statistical sensitivity  $m_\nu^{\text{stat}}$  is determined by fitting the theoretical integral  $\beta$ -spectrum (2.11) to  $10^4$  simulated KATRIN measurements. Figure 7.23 shows  $m_\nu^{\text{stat}}$  as a function of the background rate in the case of Poisson-distributed background as well as in the case of background due to nuclear decays. For each KATRIN measurement, the simulated background events were randomly distributed over the measurement time. The number of primary nuclear decay processes to be inserted evidently depends on their (a priori) unknown actual rate. Detailed calculations concerning the expected number of nuclear decay processes within the main spectrometer volume for the actual layout of the vacuum system have been carried out in [132, 146]. An optimized scenario, using the maximum amount of getter material (3 km) to suppress tritium-induced background and LN-cooled baffles to suppress radon-induced background has been adopted here. The average expected background rate for this scenario is  $r_{\text{bg}} = 6 \cdot 10^{-2}$  cps, exceeding the design limit of  $r_{\text{bg}} = 1 \cdot 10^{-2}$  cps. As figure 7.23 shows, for the case of a Poisson-distributed background, the (statistical) neutrino mass sensitivity is reduced from 0.16 eV to 0.22 eV by an increased background rate. However, if non-Poissonian background with additional temporal fluctuations of  $r_{\text{bg}}$  is included, a significant deterioration of the sensitivity of 0.37 eV is observed. Within the previous investigations in [146], a value of  $m_\nu^{\text{stat}} = 0.28$  eV was obtained. The difference results from the fact that the time specific distribution of background events within a single interval of elevated rate were assumed to be flat in [146]. As figures 7.13 and 7.14 show, this assumption does not hold, resulting in even larger fluctuations than anticipated in [146]. Correspondingly, the statistical neutrino mass sensitivity would be further reduced if no active countermeasures would

be taken.

## 7.6 Conclusions

In the course of this work a comprehensive and detailed model of electron emission processes following the  $\alpha$ -decays of the two radon isotopes  $^{219}\text{Rn}$  and  $^{220}\text{Rn}$  was developed. These investigations were motivated by the earlier observations, reported in [279], of periods with significantly enhanced background rates at the KATRIN pre-spectrometer measurements.

The background model incorporates various processes such as internal conversion, shake-off and relaxation of the atomic shells during or after the  $\alpha$ -emission. The resulting electron energies cover a wide range between a few eV up to several hundred keV, and involve highly charged polonium daughter ions. The model successfully reproduces polonium charge multiplicities as well as electron energies in the multi-keV range, which were experimentally observed within independent measurements. Further experimental validation of the complete physics model was performed by a comparison to the background behavior observed within dedicated background measurements at the pre-spectrometer. For this purpose, a radon event generator has been developed in the course of this work and was used as an input for extensive Monte Carlo simulations with the KASSIOPEIA simulation package. The validity of the background model and corresponding Monte Carlo simulations has been confirmed by a comparison with key experimental observables. As a result, the radon-induced background has been fully characterized.

With the help of the developed model, the background rates to be expected at the much larger main spectrometer have been extrapolated. The different electromagnetic configurations of the pre- and the main spectrometer (size and magnetic field strength) result in different storage conditions for high-energy as well as low-energy electrons. While the observed pre-spectrometer background rate is dominated by secondary electrons following very high-energy primaries (10-100 keV), the low-energy part of the spectrum ( $< 10$  keV) is expected to cause a majority of background events at the main spectrometer. These findings are of major importance for the development of active background reduction methods, as will be discussed in section 8. It was shown that, without such counter measures, the particular non-Poissonian nature of background due to nuclear decay processes will significantly reduce the neutrino mass sensitivity of KATRIN.



## Active removal of stored electrons

Besides  $\mu$ -induced secondary electron emission, stored high-energy electrons from nuclear decay processes in the active flux tube of the spectrometer are expected to contribute substantially to the total background rate of the KATRIN experiment. As discussed in section 7, an increased background rate in combination with the non-Poissonian nature of this type of background would significantly reduce the neutrino mass sensitivity of KATRIN. Therefore, counter measures have to be taken to eliminate stored electrons before they are released from the magnetic mirror trap towards the detector. The successful development and implementation of such counter measures requires a detailed understanding of the storage behavior of electrons in the KATRIN main spectrometer (section 8.1). Several methods are under investigation to reduce this type of background to an acceptable limit. These techniques can be divided into the two groups of *passive* and *active methods*. Passive methods prevent migration of unstable atoms to the sensitive flux tube and thus the creation of stored electrons in the volume *ab initio*. An important asset in these activities is the installation of liquid nitrogen cooled baffles in front of the large getter pumps [149]. The rationale here is that radon atoms, which originate from the getter pumps and which are a potential source for stored high-energy electrons, will be cryo-trapped onto the cold baffle surface long enough to decay there.

Within this thesis, the focus is on the investigation of active methods for electron removal. Three active methods are considered for KATRIN: electron cyclotron resonance (ECR), the electric dipole method and the magnetic pulse method. While the ECR method has been investigated theoretically as well as experimentally in [146, 282], detailed simulations concerning the electric dipole (section 8.2) and the magnetic pulse (section 8.3) have been carried out in this work. The magnetic pulse method has been successfully tested to remove stored electrons from the monitor spectrometer [313] as well as from the Penning trap between the pre-spectrometer and the main spectrometer [180]. The prospected background reduction factor for the main spectrometer can be estimated for the known background components, such as nuclear decays (section 8.4).

## 8.1 Electron storage within the main spectrometer

The detailed understanding of the storage behavior of electrons in the energy range from the eV-scale up to several hundreds of keV is a necessary requirement for the optimization of background suppression. Only by investigating the motion of single stored electrons and by performing large-scale Monte-Carlo studies covering the full parameter-space, appropriate background reduction methods can be developed.

By selecting a test particle, the working principles of the active background reduction methods can be illustrated. Figure 8.1 shows an electron starting in the analyzing plane of the main spectrometer at a radial position of 3.5 m with a kinetic energy of 1 keV. As can be expected from figure 7.20, this electron is magnetically trapped, and performs a magnetron motion governed by the actual electrostatic and magnetic fields. A full magnetron turn is shown in the figure. If all fields are stationary, such an electron will contribute to the background via secondary electrons, which are created via ionization of residual gas molecules. Therefore, the prime objective of any active background reduction method is the fast removal of these primary electrons from the main spectrometer volume, well before ionizing events actually occur. Secondary electrons in the few-eV range are stored themselves, thus they can also be removed by active background reduction methods, as will be discussed in section 8.4. To do so, electrons either have to be guided radially onto the vessel wall, where they are absorbed, or axially to the source or the detector side.

Additionally, extensive Monte-Carlo simulations have been performed, where electrons of discrete energies between a few eV and 300 keV were started homogeneously distributed within the main spectrometer volume. An isotropic starting angular distribution was chosen to reflect the emission characteristics of nuclear decays. In all cases,

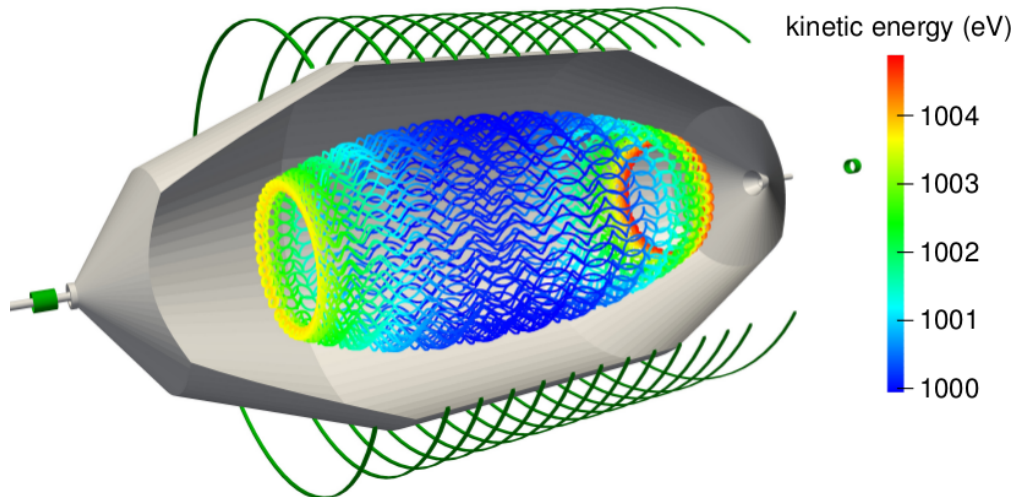


**Figure 8.1:** 3-dimensional view of an electron, which is trapped within the KATRIN main spectrometer. The electron was started in the center of the spectrometer at a radius of 3.5 m with a kinetic energy of 1 keV. A full magnetron turn is shown.

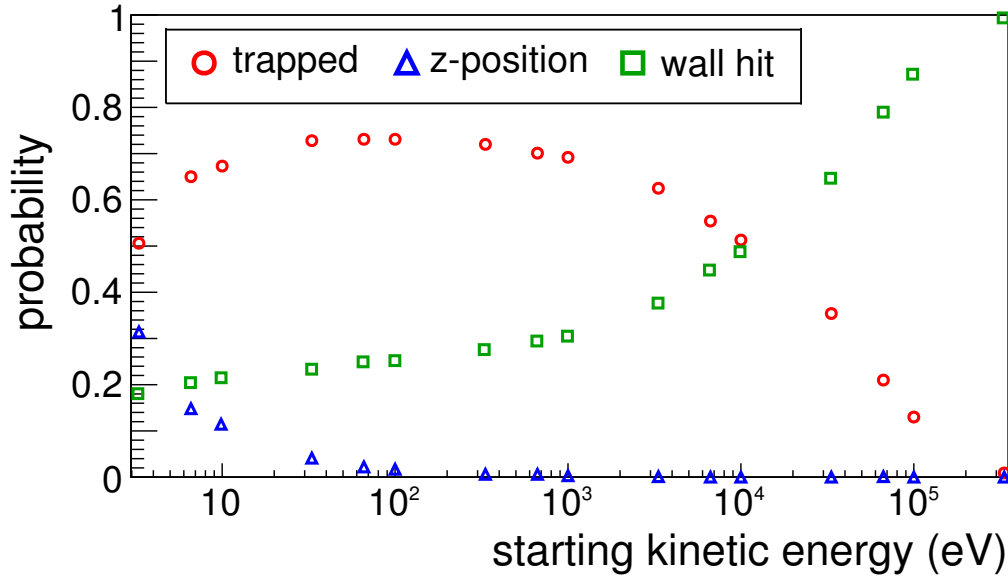


**Figure 8.2:** Monte-Carlo simulation results for exit conditions of electrons, which were started in a homogeneous distribution within the main spectrometer operated at 0.35 mT central field strength. An ensemble of discrete energies between 3 eV and 300 keV was investigated to obtain the probability for a specific exit condition (trapped, z-position, wall hit).

a central field strength of 0.35 mT was adopted (for higher B-field values, the results presented here have to be adapted). For each starting kinetic energy, an ensemble of 1000 electrons was tracked until one of the following exit conditions set in:

- The electron changed its direction of motion twice (trapped).
- The electron left the spectrometer towards either the source or the detector side (z-position).
- The electron hit the main spectrometer vessel (wall hit).

Figure 8.2 shows the simulation results, showing the likelihood of the above mentioned exit conditions. Electrons with starting kinetic energies between  $\sim 10$  eV and  $\sim 1$  keV are most likely to be trapped. At low energies up to  $\sim 100$  eV, electrons can leave the spectrometer in axial direction as there is a non-negligible probability that their transversal starting kinetic energy is smaller than  $\sim 1$  eV, which is the trapping threshold due to the energy resolution of the main spectrometer, as discussed in section 7.1. Beyond a value of  $\sim 100$  eV, the storage probability continually decreases as electrons start hitting the spectrometer wall due to their increasing cyclotron radius  $r = m_e v_{\perp} / eB$  ( $m_e$  and  $e$  being the electron mass and charge,  $v_{\perp}$  the transversal electron velocity and  $B$  the magnetic field strength). At energies beyond  $\sim 100$  keV, the cyclotron radius exceeds the diameter of the main spectrometer, preventing any electrons from being trapped. Note that for this simulation, electrons were only tracked for very short periods of time ( $\mathcal{O}(\mu\text{s})$ ) with few axial oscillations such that non-adiabatic electron motion did not come

into effect. If this effect is considered, the storage probability for electrons with kinetic energies of  $> 1$  keV is further suppressed (see Appendix .4).

## 8.2 The electric dipole method

The viability of a static electric dipole as a means to reduce background within a MAC-E filter has been proven already in the predecessor experiment at Mainz [231, 257, 314]. Within this thesis, the prospects to apply this technique to the main spectrometer have been investigated. In order to interpret the simulation results, the principles of electron removal by a static electric dipole has to be understood (section 8.2.1). Monte-Carlo simulations are an appropriate tool to investigate the removal efficiency for various electron energies and dipole field strengths at the KATRIN main spectrometer (section 8.2.2).

### 8.2.1 Principle of electron removal by an electric dipole

The electric dipole method relies on the impact of an additional electric field  $\vec{E}$ , acting on the trajectories of stored electrons. This dipole field can only be applied during short 'off-beam' measurements as it would strongly disturb the filtering process. This type of electric field can be produced by the inner wire electrode system. As indicated in figure 8.3 (a), the system consists of two half shells, which can be operated at different potentials.

The potential difference  $\Delta U$  between the dipole shells must not exceed 1 kV as

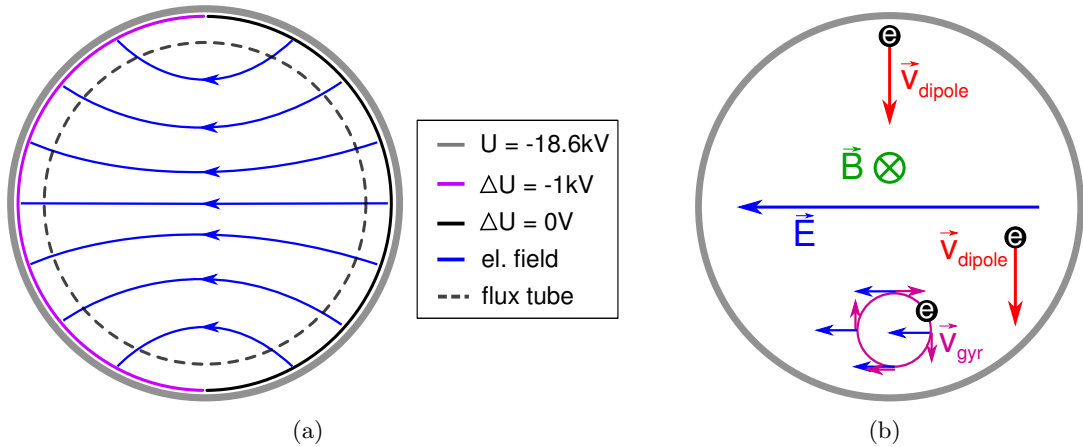


**Figure 8.3:** Visualization of the working principle of the electric dipole method. (a) When put on different potentials, the half shells of the inner electrode system produce an electrostatic field in the main spectrometer volume. The maximal potential difference of 1 kV results in an electric field strength of about 100 V/m for major parts of the flux tube. (b) The electrostatic field of the left figure, in combination with the magnetic guiding field, causes a drift velocity in a particular direction, independently of the actual electron position. Due to the gyrating electron motion, the electron does not gain any net energy when moving within the dipole field.

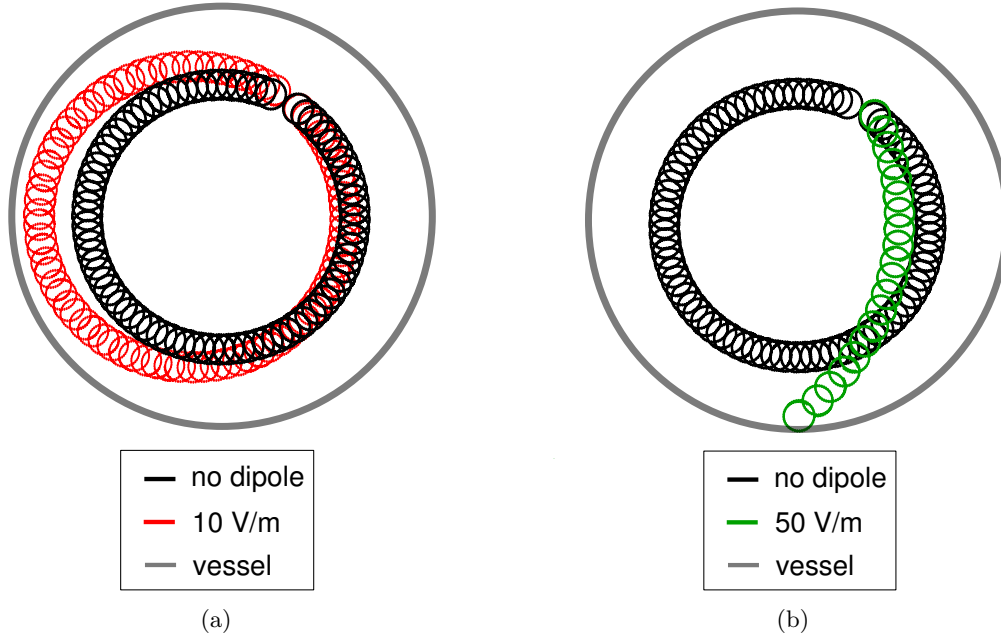


**Figure 8.4:** Illustration of the effect of different dipole strengths on the trajectory of a 1 keV stored electron. (a) A weak electric field of 10 V/m distorts the electron trajectory and destroys the axial symmetry of the electron trajectory. Nevertheless, the electron is still stored. (b) An electric field strength of 50 V/m is sufficient to drift the stored electron onto the spectrometer wall, where it is absorbed.

geometrically they reach very close to each other on the top and bottom of the spectrometer. Additionally, the inner electrode potential should always be chosen to be equal to or more negative than the vessel potential. Otherwise, the large number of  $\mu$ -induced secondary electrons ( $\sim 10^5$  cps), which is produced on the inner vessel surface, would be accelerated towards the sensitive volume of the main spectrometer, the flux tube. Due to the large main spectrometer diameter of  $\sim 10$  m, a resulting rather moderate electric field strength of  $\sim 100$  V/m is found for major parts of the flux tube volume. In combination with the magnetic guiding field, this electric field results in an  $\vec{E} \times \vec{B}$  drift, see eq. (6.2), of electrons within the main spectrometer volume, in addition to the inherent magnetron drift velocity, see eq. (6.1), and as illustrated in figure 8.3 (b). Due to the electron gyration around the magnetic field lines, no net kinetic energy is gained by an electron moving within the electrostatic dipole field. For a homogeneous electric field, as it is found for major parts of the flux tube volume, the dipole induced drift velocity  $\vec{v}_{\text{dipole}}$  points in the same direction, independently of the particular point in space of the electron. Such a drift distorts the electron trajectory within a full magnetron turn, which was formerly symmetric around the central beam axis, as shown in figure 8.4. The 1 keV test electron visualized in figure 8.1 (here, the black trajectory without additional electric field) is compared to a simulation using two different electric

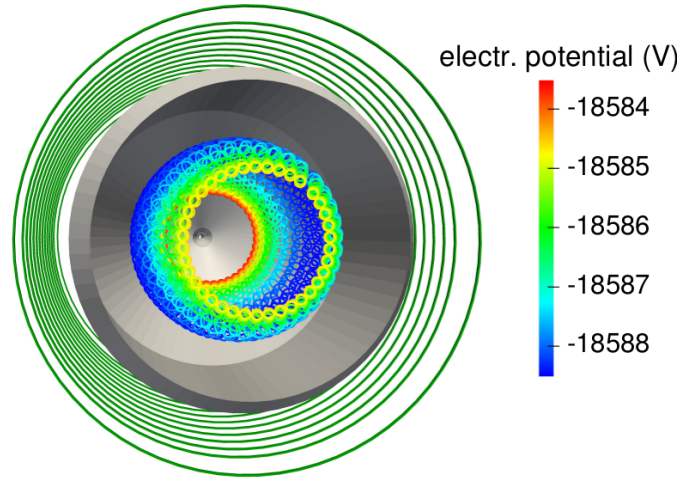
field strengths of 10 V/m and 50 V/m. The weak electric field strength of 10 V/m is not sufficient to remove the electron from the spectrometer volume. Although a distortion of the magnetron motion is observed, the electron trajectory is still confined within the main spectrometer. This is caused by the fact that the drift velocity  $\vec{v}_{\text{dipole}}$  only points radially outwards within half of the spectrometer volume. There, the electron is moved towards larger radii. At the same time, the azimuthal drift velocity increases in an effort to compensate the dipole drift. If the electron has passed this volume without reaching a metal surface, where it could be absorbed, the previous distortion is reversed such that the electron ends up at its starting radius after a full magnetron turn. As figure 8.4 (b) shows, a moderate increase of the electric field strength to a value of 50 V/m is sufficient to remove the stored electron from the sensitive spectrometer volume.

The visualization tools, which are incorporated into the KASSIOPEIA program package, can be used to display important aspects of electron motion within KATRIN. An example is given in figure 8.5, which shows a 3-dimensional view of the electron trajectory in (a) the undisturbed case and (b) in the case of an electric field of 50 V/m. The main spectrometer vessel and the surrounding air coil system are displayed. The electron trajectory is colored according to the value of the electrostatic potential at each particular point. In the undisturbed case, the good axial symmetry of the electrostatic potential is visible. When subject to a radial drift, the electron in this particular case moves towards larger radii, where the electrostatic potential is more negative, up to the maximal value of -18.6 kV, which is applied to the inner wire electrode. As any particle property and/or the present electromagnetic fields can be used for display, this tool allows a detailed visualization of electron motions within a MAC-E filter.

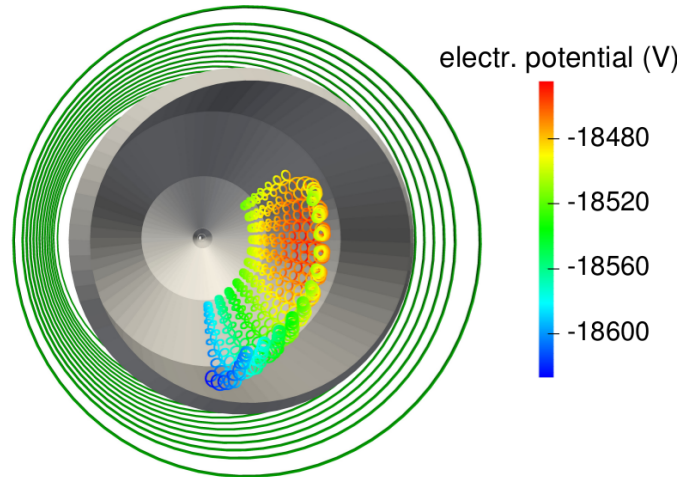
### 8.2.2 Investigation of the removal efficiency

The discussion above have shown that the efficiency of electron removal strongly depends on the strength of the applied electric dipole. Additionally, the kinetic energy of the electron plays an important role. At the main spectrometer, the maximal dipole strength is limited to a potential difference of 1 kV between the two dipole halves. As the resulting electric field is rather homogeneous in the major volume of the main spectrometer with its diameter of 10 m, an approximation as a spatially constant electric field with a dipole strength of up to 100 V/m was used for the Monte-Carlo simulations. To compare the efficiency of the dipole technique, the electron parameters for this simulation were identical to the Monte-Carlo without an electric dipole (see figure 8.2). Two field values were chosen, in the one case 50 V/m, and in the other case 100 V/m.

Figure 8.6 shows the simulation results. Here, only the trapping probability is shown, as this is the relevant quantity of interest when applying an electric dipole. Obviously, for both values of the electric dipole field, electrons with energies below 500 eV can be removed with a probability close to unity. The stronger dipole field also efficiently removes electrons with up to 1 keV. For higher energy electrons, though, the removal efficiency is drastically reduced. This rather abrupt loss of removal above a specific energy is caused by the fact that the electric dipole has to remove the electron within one magnetron turn, as shown in figure 8.4. A particular dipole strength results in a definite



(a) without electric dipole field



(b) with electric dipole field of 50 V/m

**Figure 8.5:** 3-dimensional illustration of the effect of an electric dipole field on the motion of a stored electron. (a) Undisturbed electron trajectory, colored according to the electrostatic potential value at the particle position. (b) The electron of the left figure is subject to an electric field (50 V/m) and drifts towards the inner electrode surface, where the electrostatic potential is more negative than in the center of the main spectrometer.

velocity with which a stored electron is drifted towards a spatially constant direction. The total radial drift distance, which can be achieved, then depends on the time spent within one magnetron turn. Following eq. (6.3), the  $\text{grad}\vec{B}$ -drift velocity increases approximately as  $E_{\text{kin}}$ , so that higher energy electrons also perform a faster magnetron motion and, hence, cannot drift to the same extent as low-energy electrons with their very slow magnetron drift velocities. Additionally, as mentioned before, the azimuthal magnetron drift velocity increases approximately linearly with the radius, which com-

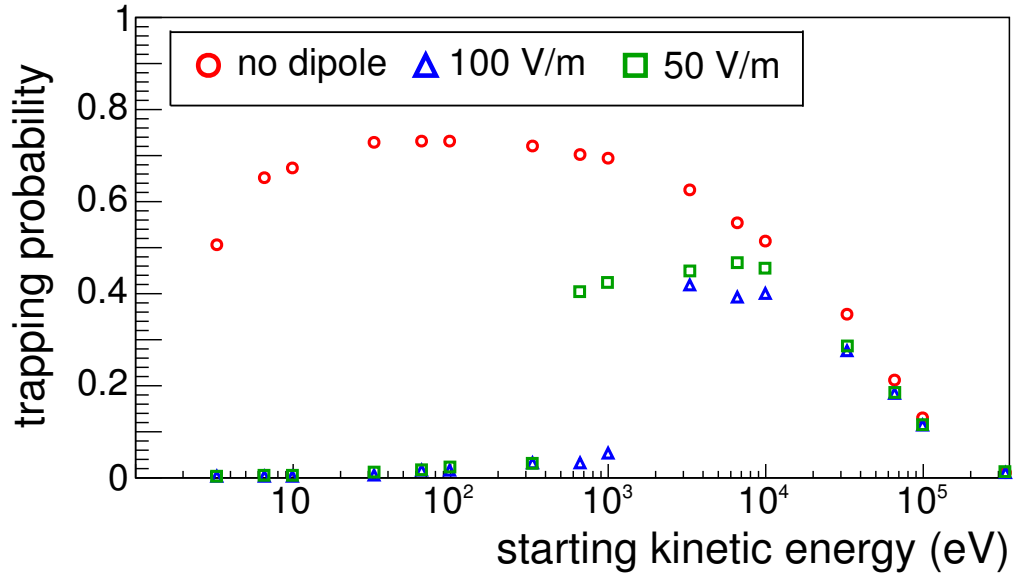


**Figure 8.6:** Monte-Carlo simulation results for the investigation of the removal efficiency of the electric dipole method. The trapping probability without an electric dipole applied is compared to that for the case of two different dipole field strengths of 50 V/m and 100 V/m, respectively.

**Table 8.1:** Path length and duration of an electron trajectory within a full magnetron turn as a function of the electron kinetic energy  $E$  and the radial position  $r$  in the center of the spectrometer.

	E=10 eV		E=100 eV		E=1 keV	
	path (m)	time (ms)	path (m)	time (ms)	path (m)	time (ms)
$r = 1$ m	$7.36 \cdot 10^4$	33.3	$5.97 \cdot 10^3$	1.00	$1.71 \cdot 10^3$	$9.1 \cdot 10^{-2}$
$r = 2$ m	$7.13 \cdot 10^4$	32.7	$5.93 \cdot 10^3$	0.99	$1.74 \cdot 10^3$	$9.3 \cdot 10^{-2}$
$r = 3$ m	$7.06 \cdot 10^4$	33.0	$5.78 \cdot 10^3$	0.97	$1.72 \cdot 10^3$	$9.2 \cdot 10^{-2}$
$r = 4$ m	$5.10 \cdot 10^4$	24.9	$5.51 \cdot 10^3$	0.93	$1.66 \cdot 10^3$	$8.8 \cdot 10^{-2}$

pensates for the advantage of having electrons move on outer radii. Consequently, the cut-off approximately happens as soon as the drift distance is reduced below the average distance of the electrons to the vessel wall. Table 8.1 shows the path length and duration of an electron performing a full magnetron turn as a function of the electron energy and radial starting position in the main spectrometer center. The numbers clearly underline the above mentioned effects of a strong dependence on the electron energy and a increased azimuthal velocity for larger radial electron positions.

The behavior, which was discussed above, is analog to the case of background creation via radial motion of  $\mu^-$ - or  $\gamma$ -induced secondary electrons from the vessel surface

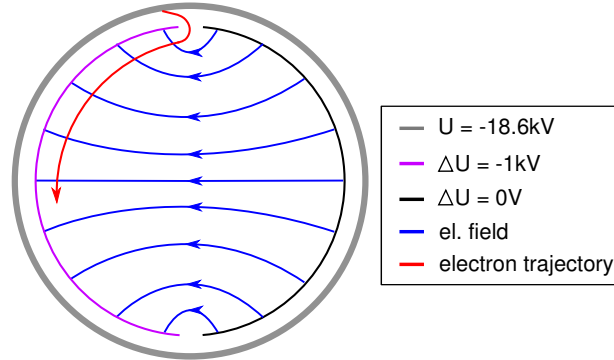


**Figure 8.7:** Possible mechanism for background production by application of an electric dipole.  $\mu$ -induced secondary electrons move perpendicularly to the electric field lines. Consequently, electrons could enter the main spectrometer volume through the gaps between the dipole halves.

(section 6). There, a small disturbance of the electromagnetic field configuration, which is caused e.g. by magnetic materials, can lead to a radial drift of electrons if the azimuthal magnetron drift component is rather small. Although only a small fraction of electrons will comply with this criterion (i.e. those within the right energy regime), the large number of produced secondary electrons ( $\sim 10^5/\text{s}$ ) results in a non-negligible amount of electrons reaching the sensitive spectrometer volume. In the case of background removal, the electric dipole is used as an artificial disturbance to ideally remove all electrons from the volume. To compensate for the fact that the azimuthal magnetron drift component increases with increasing kinetic energies, larger dipole field strengths have to be applied. Consequently, it can be concluded that the electric dipole method is able to efficiently remove low-energy stored electrons ( $< 1 \text{ keV}$ ) from the main spectrometer volume.

Moreover, the fact that the efficiency of the electric dipole method is very sensitive to the kinetic energy of the stored electrons can be used to determine their energy spectrum. Performing background measurements at different dipole field strengths between  $0 \text{ V/m}$  and  $100 \text{ V/m}$  and comparing the results with corresponding simulations will yield an integrated spectrum.

A potential drawback of the dipole method is the fact that electrons originating from specific parts of the main spectrometer vessel could be drifted into the sensitive flux tube volume. Figure 8.7 illustrates the trajectory of a muon-induced secondary electron from the wall in the presence of an electric dipole field  $\vec{E}$ . As electrons move perpendicular to  $\vec{E}$  (due to the  $E \times B$ -drift), they can only enter the main spectrometer volume through the rather small gap ( $\mathcal{O}(\text{cm})$ ) between the two dipole halves. A calculation of the actual expected number of background events is complicated due to the complex inner electrode structure, which has to be simulated in great detail for such an investigation. However, particle tracking within fully 3-dimensional geometries is very time consuming, making Monte-Carlo studies rather impracticable. However, an experimental study of this effect is possible if a radioactive source<sup>1</sup> or an X-ray tube is placed outside of the spectrometer,

<sup>1</sup>A source, e.g. made of  $^{60}\text{Co}$ , featuring very high-energy gammas is required in order to be able to

as it was shown at the Mainz experiment [257] and at the pre-spectrometer [148]. If the source is placed close to the gap between the dipole halves an increased background is expected for a particular direction of the electric dipole field, whereas measurements with a reversed field direction should yield lower background rates. The background increase can be investigated as a function of the dipole field strength for different positions of the radioactive source.

## 8.3 The magnetic pulse method

Besides the electrostatic potential, also a non-static magnetic field can be used to get rid of stored electrons. The magnetic pulse method, which was first proposed in [186], is based on the reduction of the magnetic field in large parts of the main spectrometer volume within a short pulse (section 8.3.1). In close analogy to the electric dipole case, extensive Monte-Carlo studies were performed to investigate the efficiency of removal for the magnetic pulse method (section 8.3.2).

### 8.3.1 Principle of electron removal by a magnetic pulse

The nulling of the magnetic field within the main spectrometer, which is required for this method, is achieved by a corresponding change of the LFCS currents. There are two accompanying effects which can lead to the removal of stored electrons from the volume:

1. **Magnetic field reduction:** The reduction of the magnetic field has several advantages concerning electron removal. Firstly, the field lines, which guide the stored electrons, are moved outwards closer to the main spectrometer vessel wall, as shown in figure 8.8. The weaker the magnetic field becomes, the more field lines are connected to the wall, which immediately breaks the storage condition for electrons moving along these field lines. If the magnetic field can be reversed, the magnetic bottle will be emptied completely. However, at the same time the direct connection of field lines to the vessel wall will allow  $\mu$ -induced secondary electrons to move from the wall into the spectrometer volume. Consequently, when the magnetic field strength is increased back to its nominal value, such electrons could be “soaked” into the main spectrometer. Therefore, the required magnetic field reduction should be as small as possible to suppress this effect.

A second beneficial effect is the increase of the cyclotron radius of trapped electrons when the magnetic field values decrease, as illustrated in figure 8.10 (a) and figure 8.12 (a). For finite magnetic field values, when the guiding magnetic field line has not yet reached the vessel, the gyrating electron can already be absorbed when the cyclotron motion makes up for the missing radial distance.

Thirdly, lower magnetic field values will enhance the onset of non-adiabatic motion of stored high-energy electrons. As the electron trajectory becomes unstable, the storage condition can be broken (for details see section .4).

---

penetrate the several cm thick main spectrometer vessel wall.

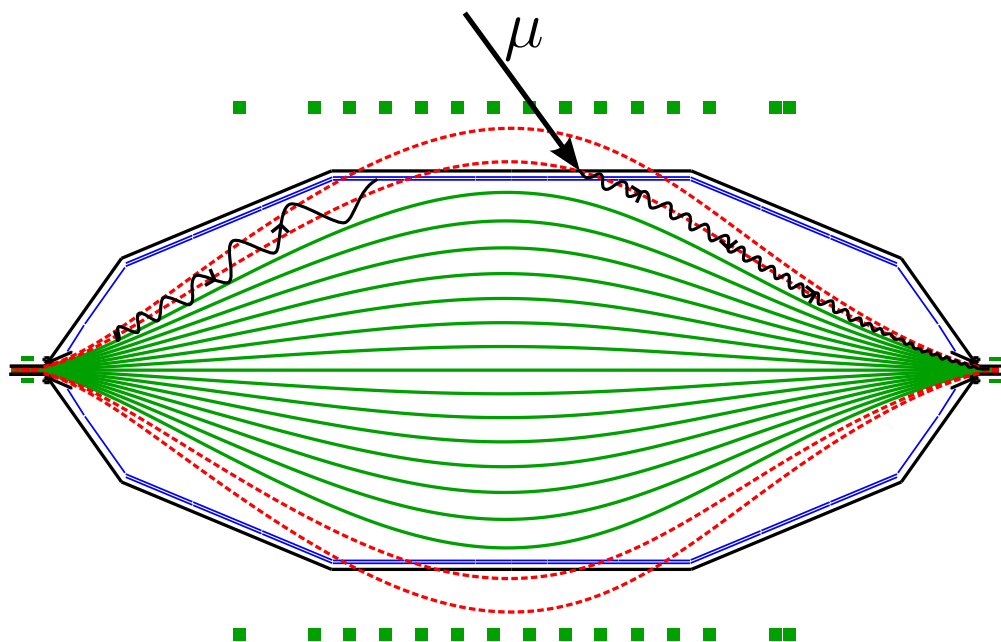


**Figure 8.8:** The effect of the magnetic field reduction in the magnetic pulse method will increase the  $191\text{ Tcm}^2$  flux tube radius such that stored electrons on outer field lines are absorbed at the vessel wall. At the same time, however,  $\mu$ -induced secondary electrons can enter the flux tube, possibly leading to a counterbalancing increase of the background rate.

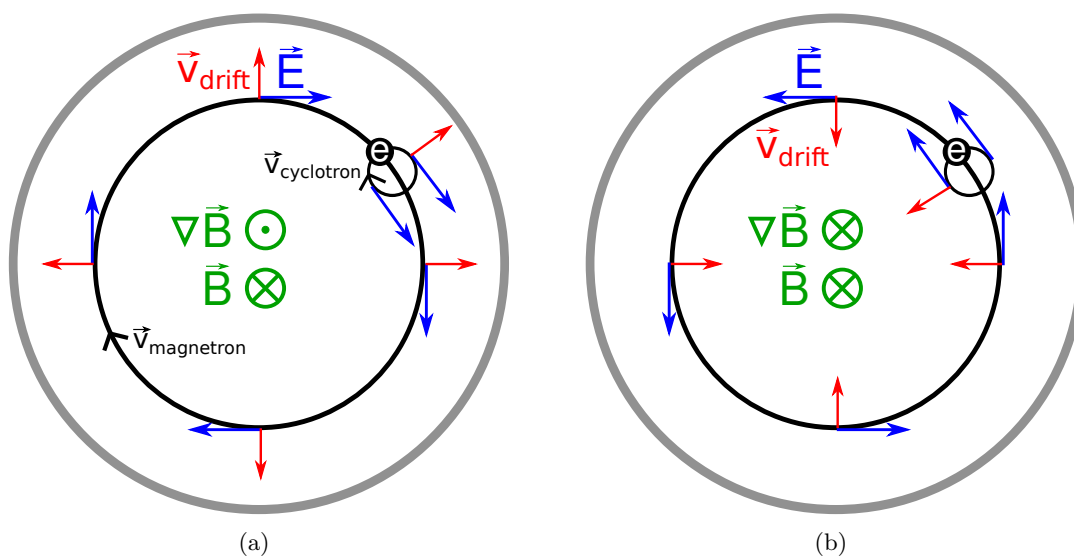


**Figure 8.9:** Illustration of the effect of an electric field, which is induced by a time-dependent magnetic field. (a) A decreasing magnetic field leads to a drift velocity, which points radially outwards in all points of space. (b) An increasing magnetic field leads to an electron motion which is directed radially inwards.

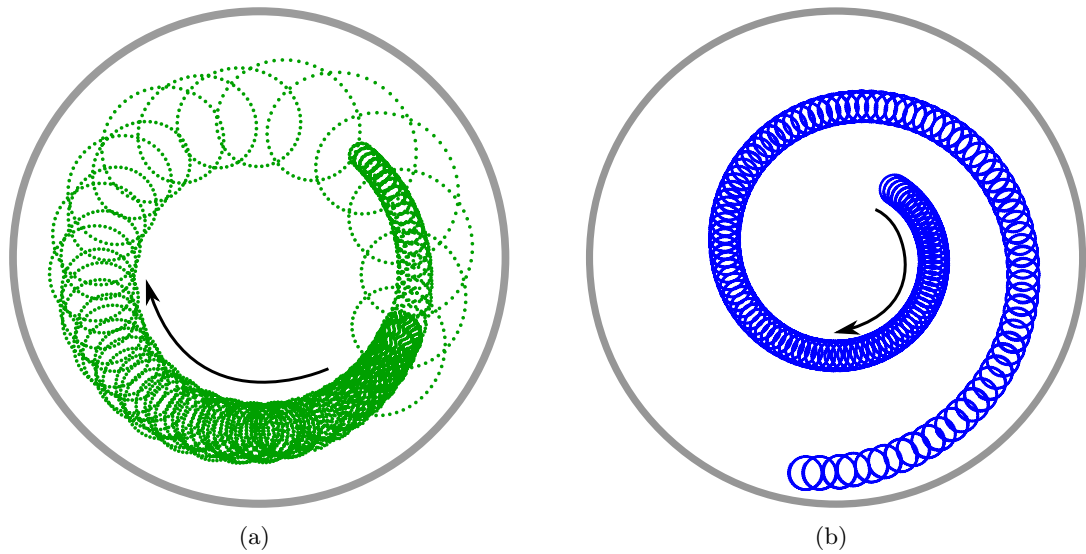


**Figure 8.10:** Illustration of the two effects, which the magnetic pulse method relies on. (a) Reducing the magnetic field increases the cyclotron radius and moves the guiding field line towards the wall (compare to figure 8.8). (b) The time-dependent magnetic field induces an electric vortex field. Consequently, an  $\vec{E} \times \vec{B}$  drift velocity is induced which points radially outwards for a decreasing magnetic field and radially inwards for an increasing magnetic field. The effect of figure (a) was omitted for illustratory purposes.

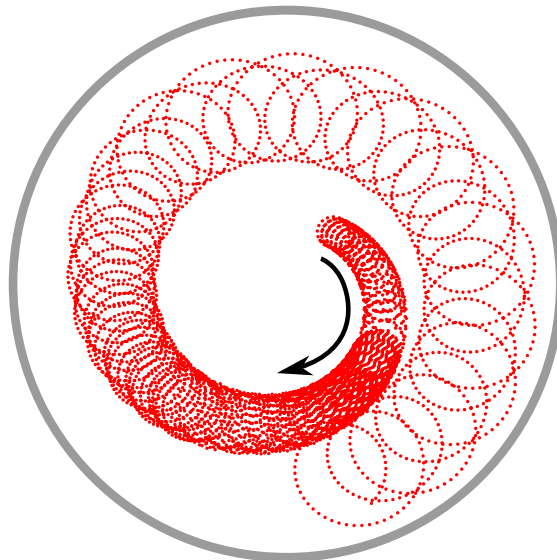
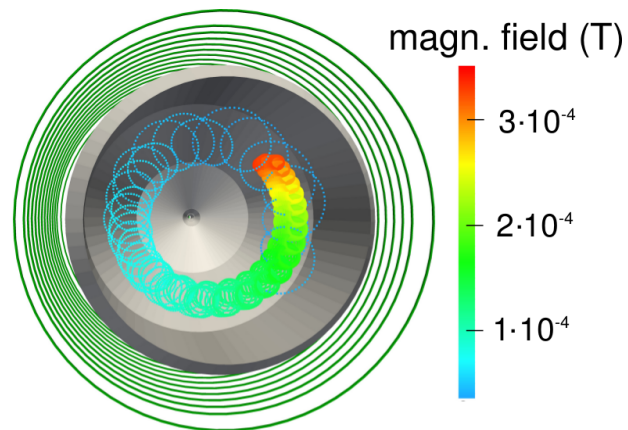
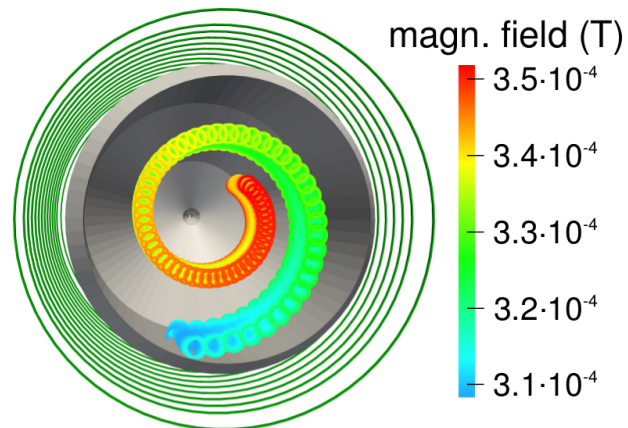


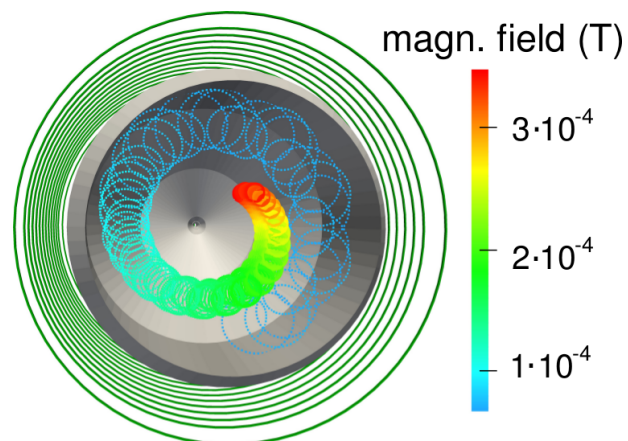
**Figure 8.11:** The magnetic pulse principle. In combination, the two effects of figure 8.10 lead to an electron trajectory as shown here. Evidently, both effects act in favor of a removal of the stored electron.



(a) Reduced magnetic field only



(b) Induced electric field only



(c) Combined effect

**Figure 8.12:** 3-dimensional illustration of the effect of a magnetic pulse on the motion of a stored electron. (a) The increasing cyclotron radius, which results from a decreasing magnetic field, is shown. (b) An electric vortex field alone leads to a radial electron drift. (c) In total, a time-dependent magnetic field leads to an effective electron drift towards the main spectrometer vessel wall, where it can be absorbed.

2. **Electric field induction:** The time-dependent magnetic field induces an electric vortex field according to Faraday's law of induction

$$\text{rot}\vec{E} = -\frac{\partial\vec{B}}{\partial t} \rightarrow \vec{E} = -\frac{r}{2}\frac{\partial\vec{B}}{\partial t}, \quad (8.1)$$

where  $r$  corresponds to the radial distance of the electron to the beam axis. The corresponding effect of such an electric field on the electron motion is illustrated in figure 8.9 and in figure 8.10 (b). A decreasing magnetic field  $\partial\vec{B}/\partial t < 0$  results in a drift velocity  $\vec{v}_{\text{drift}}$ , which points radially outwards in all points in space. Correspondingly, an increasing magnetic field  $\partial\vec{B}/\partial t > 0$  leads to an electron motion into the flux tube.

In combination, both of these effects lead to a motion of stored electrons towards the main spectrometer vessel wall in case of a decreasing magnetic field and in the opposite direction for an increasing magnetic field, as shown in figures 8.11 and 8.12 (c). Thereby, the minimal duration of a pulse is determined by

- the minimal required time for the LFCS power supplies to switch the current.
- the time-constant of the penetration of a magnetic field change through the stainless steel vessel.

While the first condition depends on the actual switching method, the second one defines an absolute lower limit for the pulse duration. Inside the stainless steel vessel, the response to the magnetic field change is delayed by the time-constant  $\tau = L/R$ , where  $L$  is the inductance of the vessel and  $R$  its ohmic resistance. Treating the main spectrometer as a long coil with  $N = 1$  winding, the inductance can be calculated by

$$L = \frac{\mu_0\mu_r N^2 A}{l}, \quad (8.2)$$

where  $\mu_0$  and  $\mu_r$  are the magnetic constant and permeability, respectively,  $A = \pi(D/2)^2$  is the cross-sectional area of the vessel with diameter  $D = 10$  m, and  $l$  is its length. The ohmic resistance of the main spectrometer can be approximated via

$$R = \rho \frac{l'}{A'} = \rho \frac{\pi D}{l \cdot d}, \quad (8.3)$$

with  $\rho$  being the electrical resistivity of the stainless steel vessel and  $d = 0.032$  m its thickness. The main spectrometer is manufactured from stainless steel type 1.4429 (316LN), which has a relative permeability  $\mu_r \approx 1$  H/m and a resistivity  $\rho = 0.75 \cdot 10^{-6}$   $\Omega\text{m}$ . A time-constant  $\tau = L/R = 0.134$  s is calculated from the above approximations. Considering the fact that this calculation is just an approximation, which neglects e.g. the massive LFCS support structure, the minimal required time for a complete pulse is expected to be on the order of 0.5 s.

### 8.3.2 Investigation of the removal efficiency

Within the standard main spectrometer field layout with an analyzing magnetic field strength  $B_{P_a} \approx 3.5 \cdot 10^{-4}$  T, it is possible to completely revert the magnetic field in the main spectrometer volume, connecting all central field lines to the vessel wall. Consequently, the magnetic bottle is emptied completely [313]. However, when restoring the measurement conditions, major parts of the vessel surface are connected to the volume via field lines, possibly leading to a motion of  $\mu$ -induced low-energy secondary electrons into the flux tube volume.

The removal efficiency was thus investigated for the novel idea of not completely nullifying the field but only reducing the magnetic field strength. Again, the same ensemble of stored electrons, which was already considered for the investigation of the electric dipole method, was used to determine the removal efficiency of the magnetic pulse method. Figure 8.13 shows the simulation results. The three different cases of a magnetic field reduction by  $\Delta B = 1 \cdot 10^{-4}$  T,  $2 \cdot 10^{-4}$  T, and  $3 \cdot 10^{-4}$  T considered here show that, as expected, a larger magnetic field reduction  $\Delta B$  increases the removal efficiency. In contrast to the electric dipole method, the magnetic pulse method is efficient also in removing high-energy electrons, resulting from the effects discussed above.

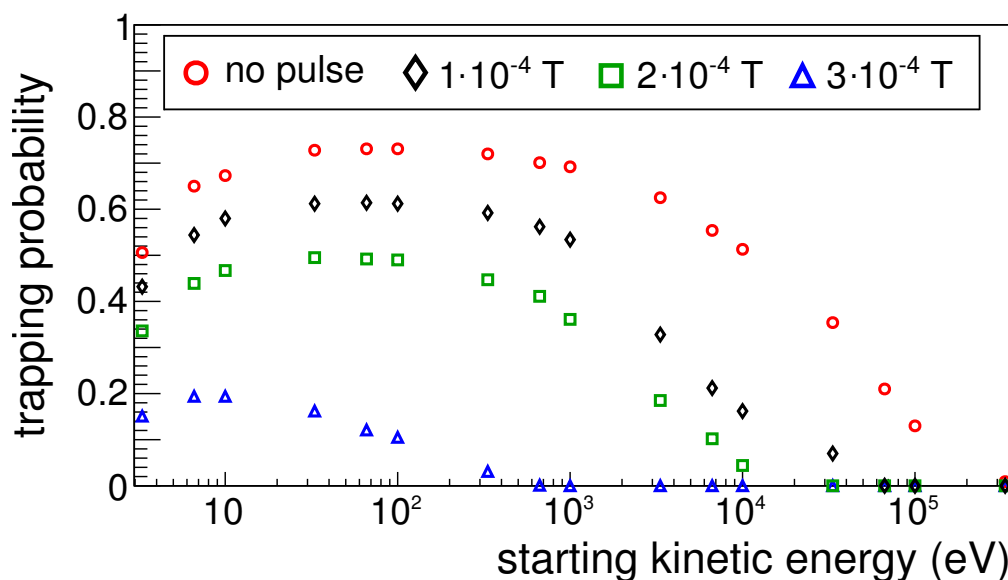


**Figure 8.13:** Monte-Carlo simulation results for the investigation of the removal efficiency of the magnetic pulse method. The trapping probability without a magnetic pulse is compared to three different pulse strengths of  $\Delta B = 1 \cdot 10^{-4}$  T,  $2 \cdot 10^{-4}$  T, and  $3 \cdot 10^{-4}$  T.

## 8.4 Prospects of background reduction at the main spectrometer

In the previous sections it could be demonstrated by simulations that the application of an electric dipole or a magnetic pulse are appropriate means to remove stored electrons from the main spectrometer volume. While the electric dipole method is most efficient in removing electrons with kinetic energies below 1 keV, the magnetic pulse method also clears electrons with energies above 1 keV from the sensitive volume. Consequently, by combining the two methods, a complete clearance of the main spectrometer volume could be feasible. The disadvantage of the two methods has been pointed out, which is the possibility for electron motion from the main spectrometer vessel surface into the sensitive flux tube volume. Consequently, the previously stored electrons are replaced by  $\mu$ -induced low-energy secondary electrons. Within the magnetic pulse method, a major part of the surface is affected, while for the electric dipole method, only the small gaps between the wire electrode dipole halves act as possible background sources. Therefore, the following sequence is proposed:

- At first, a magnetic pulse should be applied, which removes the stored high-energy electrons. By doing so, the number of stored low-energy electrons could be increased considerably when restoring the nominal magnetic field strength.
- Subsequently, an electric dipole pulse is used to remove all stored low-energy electrons, including those which were added by the previous magnetic pulse. The number of stored electrons, which could be induced by the electric dipole is expected to be rather small.

The total background reduction factor which can be expected for the main spectrometer by the combination of the two methods will depend on the following parameters, which have to be investigated:

1. The storage time of the primary as well as the secondary electrons (section 8.4.1).
2. The frequency of application of the active removal methods (section 8.4.2).

### 8.4.1 Electron storage times

Stored high-energy electrons will continuously produce secondary low-energy electrons which eventually hit the FPD and produce irreducible background there. The primary goal of an active background reduction method<sup>2</sup> is thus the removal of the primary electrons before they can cool-down via the creation of secondary electrons. However, if the secondaries are stored themselves, the pulses could also act on those low-energy electrons. Thereby, the storage time  $t_{\text{sto}}$  has to be investigated as a function of the starting kinetic energy of the electron and of the vacuum conditions within the main spectrometer.

---

<sup>2</sup>Within the remainder of this section, the active background reduction methods will be referred to as *pulses*.

The parameter  $t_{\text{sto}}$  is on the one hand defined by the average time between two succeeding scattering events ( $t_{\text{scat}}$ ) and on the other hand by the average number of scatterings ( $N_{\text{scat}}$ ), which is required until the electron can escape the spectrometer magnetic mirror trap. In the following, these parameters are derived analytically and compared to the Monte-Carlo results for stored electrons produced within the nuclear decays of radon and tritium in the main spectrometer.

### Analytical derivation of $t_{\text{scat}}$

The scattering probability  $P$  is given by

$$P = s \cdot \sigma \cdot n, \quad (8.4)$$

where  $s$  is the path length of the electron,  $\sigma$  is the scattering cross section and  $n$  is the number of scattering targets per unit volume. The number density  $n$  can be calculated according to the ideal gas law

$$n = \frac{p}{kT}. \quad (8.5)$$

For a main spectrometer pressure of  $p = 10^{-11}$  mbar and at room temperature  $T = 300$  K, the number density is  $n = 2.4 \cdot 10^{11}/\text{m}^3$ .

Using the total scattering cross section  $\sigma_{\text{tot}} = 1.1 \cdot 10^{-15} \text{ cm}^2$  ( $6.4 \cdot 10^{-18} \text{ cm}^2$ ) as determined by KASSIOPEIA for an electron with a kinetic energy  $E_{\text{kin}} = 10 \text{ eV}$  (10 keV), a mean free path of  $s = 1/(\sigma_{\text{tot}} \cdot n) = 3.8 \cdot 10^7 \text{ m}$  ( $6.5 \cdot 10^9 \text{ m}$ ) between two successive scattering events follows from eq. (8.4). The corresponding time between two scattering events is calculated to

$$t_{\text{scat}} = \sqrt{\frac{m_e s^2}{2E_{\text{kin}}}} \approx 21 \text{ s} \quad (110 \text{ s}). \quad (8.6)$$

Figure 8.14 shows the parameter  $t_{\text{scat}}$  as a function of the kinetic energy of the stored electrons for three different main spectrometer vacuum scenarios ( $p = 10^{-9}$  mbar,  $10^{-10}$  mbar,  $10^{-11}$  mbar). As  $t_{\text{scat}}$  scales linearly with the pressure, the three curves are parallel to each other, separated by one order of magnitude each. The shape of the individual curves can be understood when considering the total scattering cross section as a function of the kinetic energy of the electron, which is shown in figure 8.15. The initial decrease of  $t_{\text{scat}}$  with increasing energy (up to  $\sim 5 \text{ eV}$ ) results from the increasing elastic scattering cross section, which dominates the low-energy part of the spectrum. Towards higher energies, the total scattering cross section shows an approximately linear dependence on the electron energy, which is reflected in the correspondingly linear increase of  $t_{\text{scat}}$ . The apparent discontinuities of the curves result from the different calculation methods, which have been used to determine the scattering cross sections in different parts of the energy spectrum.

### Derivation of $N_{\text{scat}}$

The typical number of scattering events  $N_{\text{scat}}$  required for an electron to eventually escape the magnetic mirror trap depends on the electromagnetic configuration of the

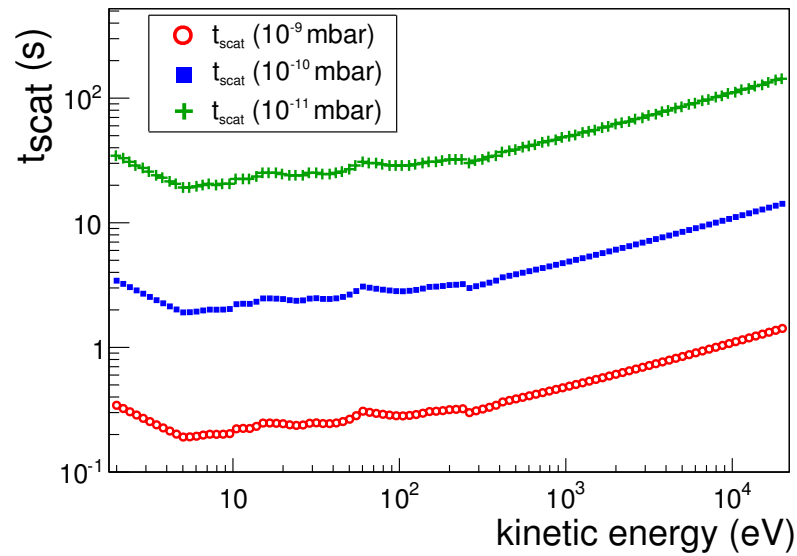


**Figure 8.14:** Calculated mean time period between two successive scattering events ( $t_{\text{scat}}$ ) as a function of the kinetic energy of the electron for different vacuum conditions within the main spectrometer.

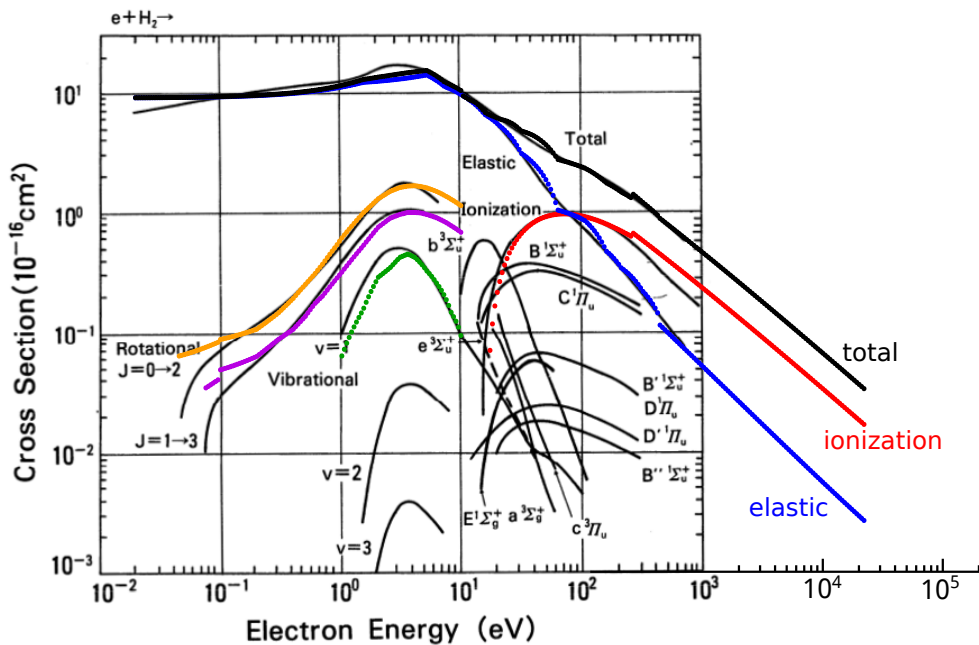


**Figure 8.15:** The scattering cross section implemented within KASSIOPEIA is compared to literature data [199]. For clarity, only the dominant contributions to the total scattering cross section are shown for the case of KASSIOPEIA. However, the remaining processes are also included into the simulation software. The energy scale of the original plot has been extended to accommodate all energies, which are relevant for the KATRIN main spectrometer.

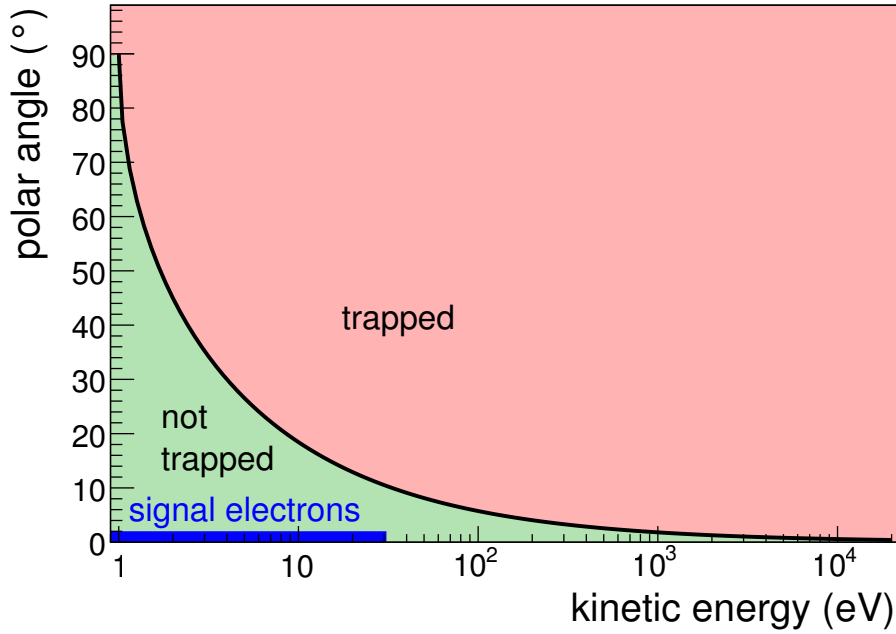


**Figure 8.16:** Visualization of the trapping (red) and escape (green) domains as a function of the electron kinetic energy and polar angle. Additionally, the parameter space occupied by the signal electrons is shown.

main spectrometer. For the reference field layout, only electrons with a transversal kinetic energy  $E_{\perp} < E_{\perp,\max} = 1$  eV are not stored in general. Following

$$E_{\perp} = E_{\text{kin}} \cdot \sin^2 \theta, \quad (8.7)$$

the escape and the trapping probability, related by  $P_{\text{esc}} = 1 - P_{\text{trap}}$ , depend on the kinetic energy  $E_{\text{kin}}$  and the polar angle  $\theta$  of the electron. Figure 8.16 visualizes the above relation and shows that the parameter space contributing to  $P_{\text{trap}}$  is much larger than that for  $P_{\text{esc}}$  (note the logarithmic energy axis). The exact values of  $P_{\text{trap}}$  and  $P_{\text{esc}}$  depend on the particular angular and energy distribution. Assuming an isotropic angular distribution of electrons<sup>3</sup>, the probability  $P_{\text{esc}}$  can be calculated by

$$P_{\text{esc}} = 1 - \cos(\theta_{\max}) = 1 - \cos\left(\arcsin\sqrt{\frac{E_{\perp,\max}}{E_{\text{kin}}}}\right) \quad (8.8)$$

$$= 1 - \sqrt{1 - \frac{E_{\perp,\max}}{E_{\text{kin}}}} = 1 - \sqrt{1 - \frac{E_{\perp,\max}}{E_{\perp}} \cdot \sin^2 \theta}. \quad (8.9)$$

For an electron with an energy of 500 eV,  $P_{\text{esc}}$  is already smaller than 0.1%. For energies  $E_{\text{kin}} \gg E_{\perp,\max}$ , a Taylor expansion can be used to approximate the square root

<sup>3</sup>Note that signal electrons from tritium  $\beta$ -decay have an angle  $\ll 10^\circ$  (MAC-E filter principle) and energies  $E < 30$  eV (scanning regime).

in eq. (8.9), which yields a linear dependence of the escape probability on the kinetic energy.

Following these considerations, there are two effects, which can lead to an escape of a stored electron from the main spectrometer magnetic mirror trap:

1. The escape probability increases for decreasing kinetic energies of the stored electron.
2. The escape probability increases for decreasing polar angles of the stored electron.

**1. Energy loss:** During cool-down, electrons lose energy mainly via ionization and electronic excitation until they reach the energy thresholds of  $\sim 15$  eV and  $\sim 10$  eV, respectively. For lower kinetic energies, these processes can no longer occur energetically (see figure 8.17). Further cool-down proceeds via elastic scattering and rotational or vibrational excitation with energy losses in the sub-eV range. If all electrons with a certain starting kinetic energy would have to cool-down below 1 eV in order to leave the magnetic mirror trap, then the required number of scattering events  $N_{\text{scat}}$  would be given by figure 8.18 (red triangles). Due to the small energy losses within elastic events,  $N_{\text{scat}}$  varies by less than an order of magnitude over an energy range of 4 orders of magnitude. Only for electrons with starting energies just above the electronic excitation threshold, smaller values of  $N_{\text{scat}}$  are observed as electrons can 'skip over' major parts of the elastic regime within one excitation.

**2. Angular change:** When scattering off residual gas molecules, the stored electrons will experience a change of their polar angle, as shown in figure 8.19 for three representative electron energies. As expected, electrons with higher kinetic energies are most likely to be forward scattered, while low-energy electrons experience a more

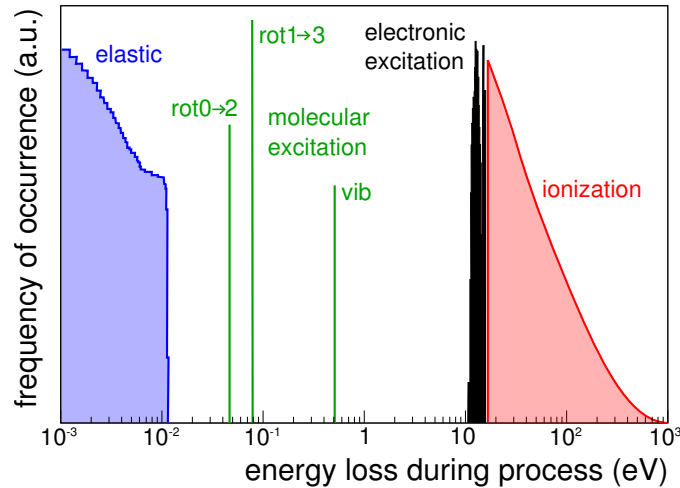


**Figure 8.17:** Energy loss of 1000 electrons with a starting kinetic energy of 10 keV due to different scattering processes on  $\text{H}_2$ . The KASSIOPEIA scattering routine was used without actually tracking the electrons (i.e. no synchrotron losses or non-adiabatic effects).

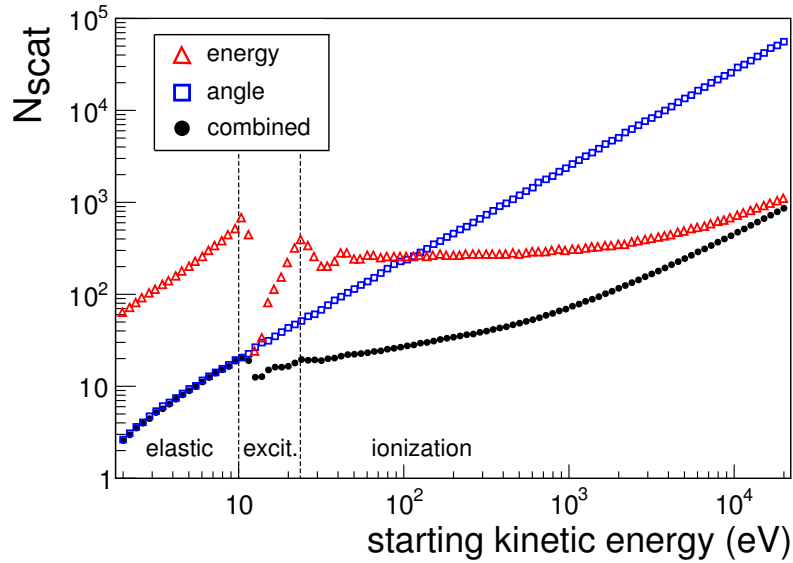


**Figure 8.18:** Required number of scattering events  $N_{\text{scat}}$  for an electron to escape the magnetic mirror trap in case (a)  $E_{\perp} < 1$  eV has to be reached via energy loss only (red triangles), (b) via an angular change only (blue squares), or (c) via a combination of both (black circles), which reflects reality.

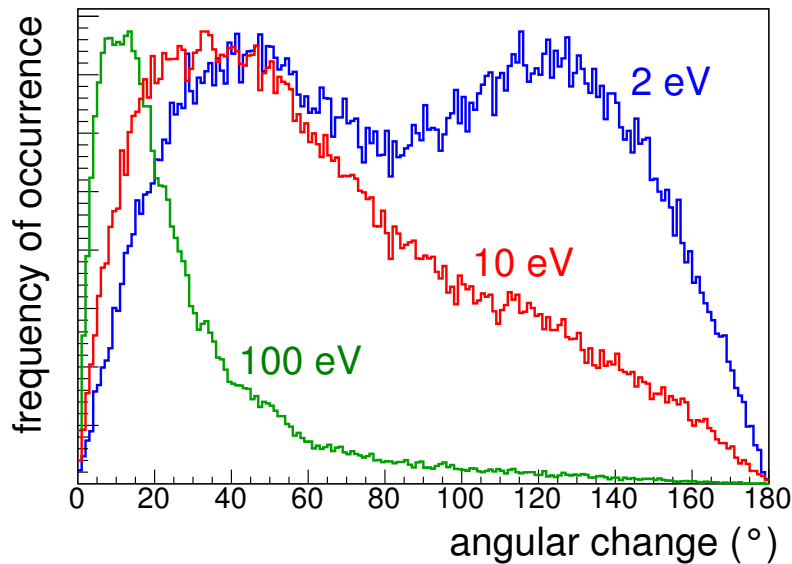


**Figure 8.19:** Change of the polar angle of the primary electron when undergoing scattering events for three different kinetic energies of 2 eV, 10 eV, and 100 eV.

isotropic angular change. Figure 8.18 (blue squares) shows the required number of scattering events if the electron could only leave the magnetic mirror trap by hitting a polar angle below the trapping threshold angle  $\theta_{\max}$ , which is defined by eq. (8.8). An approximately linear dependence of  $N_{\text{scat}}$  on the starting kinetic energy is observed, as expected from eq. (8.9). For kinetic energies within the elastic regime  $E < 10$  eV, electrons have a high probability to end up in the loss cone<sup>4</sup> after a scattering event. Consequently, in this regime,  $N_{\text{scat}}$  is much smaller than in the above discussed case of energy loss only. Beyond  $\sim 100$  eV, however,  $N_{\text{scat}}$  increases linearly in the case of an angular change only due to the decreasing loss cone.

**Combined energy and angular change:** The two effects, which were discussed above, have to be considered simultaneously, as scattering events influence the energy as well as the polar angle of the electron. The third curve of figure 8.18, labeled as *combined*, shows the combined case. A comparison shows that, in the low-energy regime, where elastic scattering dominates,  $N_{\text{scat}}$  is mainly defined by the probability that the electron undergoes an appropriate angular change below the trapping threshold  $E_{\perp} = E_{\text{kin}} \cdot \sin^2 \theta < 1$  eV. This behavior is illustrated in figure 8.16, demonstrating that the region below 10 eV dominates the parameter space of  $P_{\text{esc}}$ . For higher kinetic energies, the energy loss mechanism due to inelastic scattering becomes more important. Considering the fact that both effects can lead to an escape of the stored electron, the *combined* curve of elastic and inelastic scattering in figure 8.18 will evidently stay below the (theoretical) curves for the individual mechanisms.

### Electron storage times

When the two parameters  $N_{\text{scat}}$  and  $t_{\text{scat}}$  are known as a function of the electron kinetic energy, the average electron storage time  $\langle t_s \rangle$  can be determined. Figure 8.20 shows the result of the analytical calculation. Again, three different vacuum scenarios are considered. The most important fact at this point is that the storage time varies by three orders of magnitude within the energy regime of  $1 - 10^4$  eV. This huge factor has to be considered when discussing stored electrons within the main spectrometer.

These analytic calculations only approximate the actual storage times, as the trapping threshold  $E_{\perp, \max}$  will depend on the actual electron position and trajectory due to the variation of the magnetic field in axial as well as radial direction. Consequently, the above calculated storage times are upper limits as the value  $E_{\perp, \max} = 1$  eV corresponds to the central (lowest) magnetic field strength, so that  $E_{\perp, \max}$  is larger for electrons propagating further away from the central plane of the spectrometer. Furthermore, the onset of non-adiabatic effects at higher kinetic energies will further reduce the average storage times of high-energy electrons (these effects were not considered within the analytical calculations).

A more realistic description of electron storage can be obtained by Monte-Carlo simulations. Primary electrons from radon (see figure 7.22) and tritium (see figure 7.21)

---

<sup>4</sup>The loss cone is defined by the maximal polar angle  $\theta_{\max} = \arcsin(\sqrt{E_{\perp, \max}/E_{\text{kin}}})$  for which an electron is not magnetically stored. The value  $\theta_{\max}$  increases from  $\theta_{\max}(E_{\text{kin}} = 10 \text{ eV}) = 18^\circ$  up to  $\theta_{\max}(E_{\text{kin}} = 1 \text{ eV}) = 90^\circ$ .

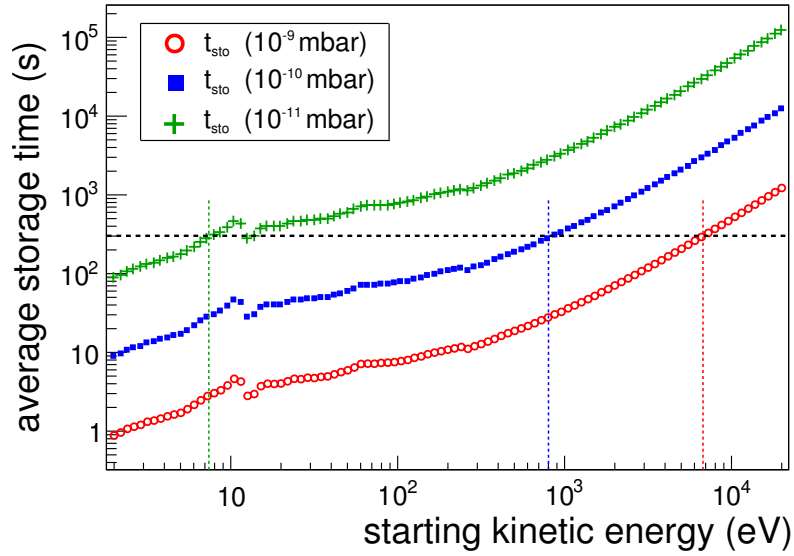


**Figure 8.20:** Analytically calculated storage times of electrons as a function of the starting kinetic energy for three different main spectrometer vacuum conditions. The figure underlines the importance of obtaining excellent UHV conditions in the spectrometer, ideally below  $10^{-11}$  mbar. In this case, only low-energy electrons  $< 10$  eV are stored over time periods shorter than 300 s, which is a typical repetition time scale of short active background removal periods.

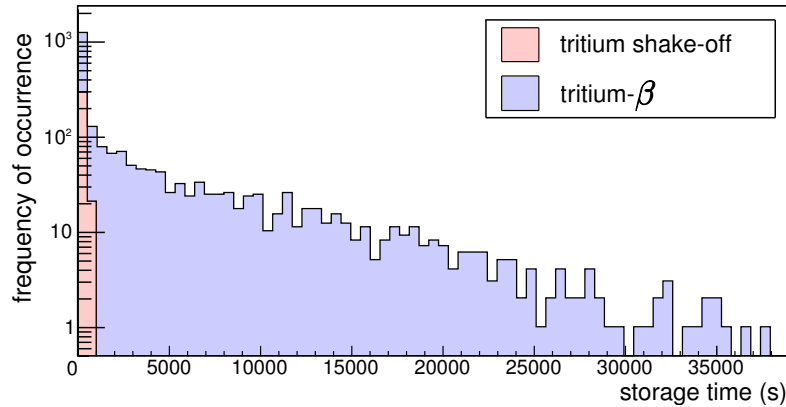


**Figure 8.21:** Storage times of tritium  $\beta$ -decay electrons. The large number of electrons, which escapes within the first 1000 s, corresponds to low-energy shake-off electrons, which have an overall emission probability of 15% for each tritium  $\beta$ -decay. A pressure of  $p = 10^{-11}$  mbar was assumed for this simulation.

decays were started homogeneously distributed within the main spectrometer volume. Figures 8.21 and 8.22 show the resulting storage times of the primary electrons for tritium and radon, respectively, for a main spectrometer pressure of  $p = 10^{-11}$  mbar (note the different time scales of both plots). As the storage time scales linearly with the pressure, the corresponding values can be obtained by re-scaling the storage time

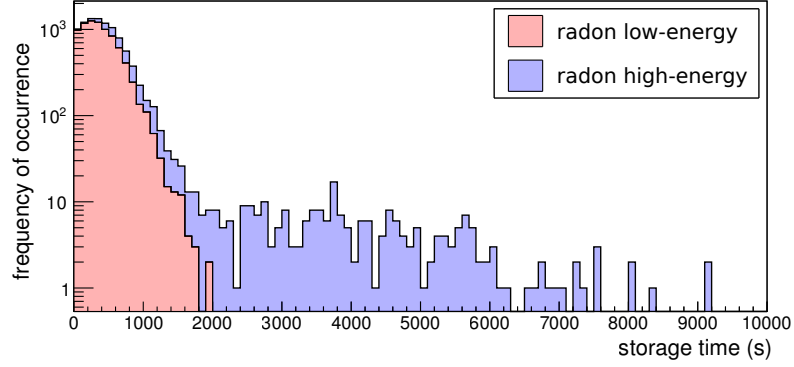


**Figure 8.22:** Storage times of electrons accompanying radon  $\alpha$ -decays of the isotope  $^{219}\text{Rn}$ . The low-energy part comprises mainly shell reorganization from figure 7.5 with a kinetic energy below 200 eV. Their storage time is comparable to the one of low-energy secondary electrons from ionizing collisions of keV-range electrons. The high-energy part of the spectrum ( $E_{\text{kin}} > 200$  eV) displays much longer storage times. A pressure of  $p = 10^{-11}$  mbar was assumed for this simulation.

**Table 8.2:** Average storage times  $t_{\text{sto}}$  for the low-energy and high-energy part of the  $^{219}\text{Rn}$  and tritium  $\beta$ -decay energy spectrum as well as for some representative secondary electron kinetic energies. The values as determined with a Monte-Carlo simulation are compared to the analytical calculations, assuming a pressure of  $p = 10^{-11}$  mbar.

energy (eV)	$t_{\text{sto}}^{\text{MC}}$ (s)	$t_{\text{sto}}^{\text{ana}}$ (s)
radon $E < 200$ eV	409	608
radon $E > 200$ eV	1470	3002
tritium shake-off	219	430
tritium- $\beta$	4413	9080
3	95	125
6	135	215
10	211	421
30	275	474
60	341	713
100	419	764

axis. Each simulation shows that the low-energy components (tritium: shake-off, radon: shell reorganization and low-energy shake-off) feature much smaller storage times than the high-energy components (tritium:  $\beta$ -decay electrons, radon: conversion and Auger). Furthermore, by comparing the two nuclear decay processes, it becomes obvious that the relative amount of high-energy events is larger in the case of tritium  $\beta$ -decay, resulting in longer average storage times, as summarized in table 8.2.

During their time period of magnetic storage, primary electrons will produce low-

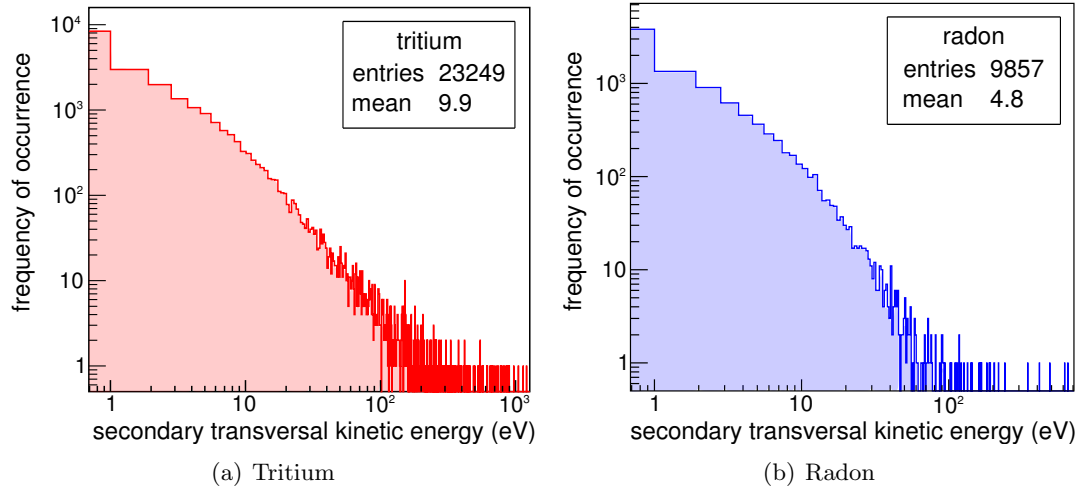


**Figure 8.23:** Secondary electron transversal kinetic energies as determined with a Monte-Carlo simulation of (a) radon- and (b) tritium-induced primary electrons. The first bin includes all events with  $E_{\perp} < 1$  eV.

energy secondaries, whose energy spectrum is shown in figure 8.23 for (a) the case of tritium and (b) radon decays. Due to the on average higher primary kinetic energies of tritium, the secondary electrons from these decays will have on average larger kinetic energies. In both cases, the majority of electrons has transversal kinetic energies below 100 eV. Table 8.2 lists the storage times for some representative secondary electron kinetic energies. The values were determined via a Monte-Carlo simulation of electrons with discrete starting kinetic energies. Secondary electrons with transversal kinetic energies of less than 1 eV are generally not stored within the main spectrometer and can hence not be tackled by an active background reduction method. From figure 8.23 follows that about 38% (41%) of all secondary electrons following a primary tritium  $\beta$ -decay (radon  $\alpha$ -decay) will directly be released from the magnetic mirror.

Comparing the storage times as determined with the Monte-Carlo simulation with those calculated analytically shows that the analytical values in general are about a factor 2 smaller. This is caused by the fact that the storage threshold of  $E_{\perp, \max} = 1$  eV only holds in the central part of the spectrometer. In the domain of higher magnetic field strengths further away from the analyzing plane, the storage threshold is larger, reducing the average storage time for electrons in the more detailed Monte-Carlo calculations.

#### 8.4.2 Pulsing frequency

An efficient removal of stored electrons by means of an active background reduction method requires the repetition of pulses on time scales much shorter than the average electron storage times. As the above investigations have shown, radon as well as tritium decays generate both high-energy primary and low-energy electrons (either as primary or via secondary ionization), with storage times varying by three orders of magnitude.

Low-energy secondaries in particular are dangerous, as they either leave the spectrometer directly ( $\sim 40\%$ ) or are stored for only short times (order of minutes for the ideal case of  $p = 10^{-11}$  mbar).

As outlined, both the creation of low-energy secondaries by ionizing collisions, as well as the eventual release via elastic scattering are stochastic processes. The achievable background reduction factor  $f_{\text{red}}$  by application of an active background reduction method hence strongly depends on the frequency of application of the pulses. Evidently, the pulse repetition rate should not be too high to retain a high 'beam-on'/'beam-off' ratio (duty cycle). From the Monte-Carlo data,  $f_{\text{red}}$  can be obtained by determining the number of detector hits without pulse ( $N_{\text{det}}$ ) and with pulse ( $N_{\text{det,pulse}}$ ):

$$f_{\text{red}} = \frac{N_{\text{det}} - N_{\text{det,pulse}}}{N_{\text{det,pulse}}}. \quad (8.10)$$

Assuming pulses occur at regular intervals, with  $\Delta t_{\text{pulse}}$  denoting the time between two pulses, each simulated event can be analyzed separately, using a random number to determine the time  $t_{\text{pulse}} \in [0, \Delta t_{\text{pulse}}]$  of the pulse within this particular event. When assuming that a pulse removes all stored electrons,  $N_{\text{det}}$  is reduced by the number of

- secondary electrons, which were created after  $t_{\text{pulse}}$ .
- primary and secondary electrons, which were still stored at the time  $t_{\text{pulse}}$ .

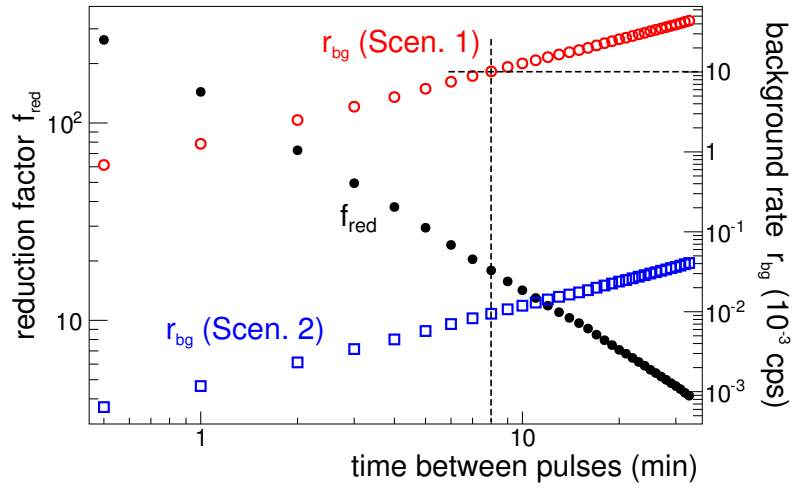
Figure 8.24 shows the simulation results as a function of  $\Delta t_{\text{pulse}}$ . The tritium and radon background components are treated separately. This separation is useful, as the required pulsing frequency strongly depends on the electron storage times, which are quite different for the two nuclear decay processes (compare figure 8.21 and 8.22). A larger reduction factor is observed in the case of tritium due to the longer storage times. For an exemplary value of  $\Delta t_{\text{pulse}} = 5$  min, a reduction factor of  $f_{\text{red}} = 30$  is observed for tritium, while the radon background is reduced by only a moderate factor of  $f_{\text{red}} = 2$ .

In order to assess the impact of these reduction factors on the actual background rates, the rates of tritium and radon nuclear decays have to be estimated. Two exemplary scenarios were chosen from various scenarios investigated in [132]:

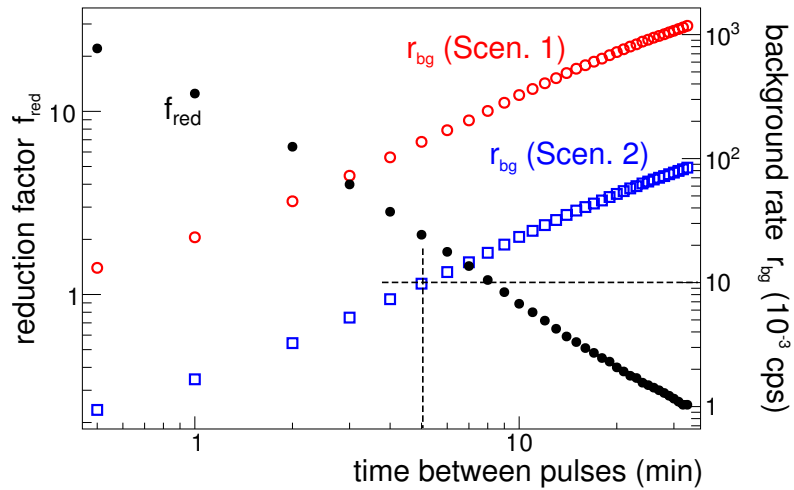
- Scenario 1: Within this scenario, no NEG pump or baffles are installed. Consequently, a larger tritium activity of  $A_{\text{tri}}^{\text{sce1}} = 21.9$  mBq is expected. Furthermore, the radon emanation into the main spectrometer vessel is not suppressed, yielding a total radon activity of  $A_{\text{rad}}^{\text{sce1}} = 95.1$  mBq.
- Scenario 2: Here, the maximal amount of getter (3 km) is installed to suppress the tritium activity down to  $A_{\text{tri}}^{\text{sce2}} = 0.02$  mBq. Additionally, the baffle is installed and operated as cryotrap reducing the radon contribution from the NEG as well as from the main spectrometer vessel down to  $A_{\text{rad}}^{\text{sce2}} = 6.8$  mBq.

The individual background contributions of tritium and radon can then be computed for the two scenarios via:

$$r_{\text{bg}} = A_{\text{tri/rad}}^{\text{sce1/2}} \cdot \langle N_{\text{det,tri/rad}} \rangle, \quad (8.11)$$



(a) Tritium



(b) Radon

**Figure 8.24:** Background reduction for (a) tritium- and (b) radon-induced background rates as a function of the pulsing frequency. Two different background scenarios are shown. Scenario 1: without getter and baffle, Scenario 2: with getter and baffle (see text).

**Table 8.3:** Background rates  $r_{\text{bg}}$  produced by tritium and radon decays, calculated from the average number of detector hits per decay  $\langle N_{\text{det}} \rangle$  for two scenarios with different activities  $A^{\text{sce}1/2}$ .

parameter	tritium	radon
$\langle N_{\text{det}} \rangle$	8.4	3.1
$A^{\text{sce}1}$ (mBq)	21.9	95.1
$r_{\text{bg}}^{\text{sce}1}$ ( $10^{-3}$ cps)	183	290
$A^{\text{sce}2}$ (mBq)	0.02	6.8
$r_{\text{bg}}^{\text{sce}2}$ ( $10^{-3}$ cps)	0.17	20.8

where  $\langle N_{\text{det,tri/rad}} \rangle$  is the average number of detector hits per tritium/radon decay event as determined with the Monte-Carlo simulations. Table 8.3 gives the resulting background rates for the scenarios investigated. The obtained values can be used to calculate the actual expected background rate as a function of the pulsing frequency. The results are shown in figure 8.24 and can be summarized as follows:

- Tritium: The background contribution of tritium is negligible within scenario 2, even without the application of a pulse. In case of scenario 1, however, pulses as frequently as every 7 minutes are required to suppress the background below the design limit of  $10^{-2}$  cps. However, as tritium-decay is not the only background-generating process, even more frequent applications are required.
- Radon: In the case of radon-induced background, the large radon activity within scenario 1 would require the application of pulses on a time scale  $< 1$  min. As this would result in a significant loss of measurement time, the installation of the LN-cooled baffles is an essential requirement (scenario 2). Considering the fact that radon from the main spectrometer vessel also freezes to the baffles, a background suppression below  $10^{-2}$  cps is possible in the case of scenario 2 for  $\Delta t_{\text{pulse}} < 5$  min.

These results highlight the importance of

- the installation of the NEG pump to suppress tritium-induced background.
- the installation of the baffle to suppress radon-induced background.
- an UHV on the order of  $p = 10^{-11}$  mbar, as storage times decrease linearly for increasing  $p$ .

### 8.4.3 Summary

Within this section, it was shown that active background reduction methods are essential to reach the design background level of  $10^{-2}$  cps. Apart from this, also an excellent UHV

in the range of  $p < 10^{-11}$  mbar is required to optimize the impact of active background reduction methods. As the average time between two successive scattering events is inversely proportional to the pressure, an increase of the residual pressure by one order of magnitude to a value of  $10^{-10}$  mbar would call for pulses with a repetition rate of  $3 \cdot 10^{-2}$  Hz, which would be an order of magnitude larger than suggested within this section. Applying these pulses very often would also reduce the effective neutrino mass measurement time as no neutrino mass data can be taken during the pulse and until the main spectrometer high voltage (electric dipole) and magnetic field (magnetic pulse) have stabilized again.

It turned out that the low-energy part of the energy spectrum of stored electrons plays a significant role when investigating active background reduction methods, as these electrons feature very short storage times. Especially in case of radon  $\alpha$ -decays a large number of low-energy electrons is produced. The pre-spectrometer measurements, which were used to validate the radon model (section 7), have not offered analysis of this low-energy part due to the large trapping threshold there of about 60 eV. The upcoming main spectrometer measurements will therefore chart new territory of low-energy electrons below 60 eV. It will be of crucial importance to understand the energy spectrum at this scale, where different sources contribute: shell reorganization electrons from radon  $\alpha$ -decays, secondary electrons from ionizing collisions of keV-range electrons from tritium  $\beta$ -decay and radon  $\alpha$ -decay, as well as secondary electrons from  $\mu$ -induced interactions in the vessel wall. Additionally, these measurements are essential in order to verify and optimize the removal procedures and to determine the required dipole strength and magnetic field reduction.



## Conclusion

The observation of neutrino oscillations has given unequivocal evidence for massive neutrinos and motivated a series of experiments to search for the absolute neutrino mass scale. The Karlsruhe Tritium Neutrino experiment KATRIN is a next-generation neutrino mass experiment, which will use high-precision  $\beta$ -spectroscopy as a tool to reach a sensitivity of  $200 \text{ meV}/c^2$ , corresponding to an improvement of one order of magnitude compared to predecessor experiments. In terms of the experimental observable  $m_{\nu_e}^2$ , this is equivalent to an improvement by two orders of magnitude, imposing stringent requirements on key experimental parameters.

The focus of this thesis has been on the development of tools and methods to study background and transmission properties in the electrostatic spectrometers of the KATRIN experiment, both by experiment as well as by large-scale simulations. The large main spectrometer is the key component for a successful electron energy determination. The low signal count rate of  $10^{-2}$  electrons/s requires a background rate on the same level or even less. At the same time, the transport of signal electrons through the experimental setup, as quantified by the *transmission function*, has to be understood at a level of 1% or better.

In a first step, a program package was developed which automatically optimizes the magnetic transport characteristics of the main spectrometer. The work allows to adjust and fine-tune the operating parameters of a large volume air coil system, providing high flexibility and versatility of the magnetic guiding field in the central region of the spectrometer. On the one hand, the setup of the magnetic field has to be optimized with regard to the intrinsic magnetic shielding properties against muon-induced secondary electrons from the inner vessel surface (*magnetic field strength*). On the other hand, by fine-tuning the air coil currents (*magnetic field shape*), optimal transmission properties (*transmission condition*) for the signal electrons have to be implemented. To fulfill both requirements, a set of optimized magnetic field setups was provided, featuring different magnetic field strengths and shapes.

These magnetic field setups were then used to study in detail the transmission properties of the main spectrometer. The main focus here was on the disentanglement of

---

the source (electrons from an angular-selective electron gun) and spectrometer properties, which can have similar signatures in the transmission function. To do so, extensive Monte-Carlo simulations were performed with the KATRIN simulation software KASSIOPEIA. This technique was employed to generate data sets of the transmission function for various source and spectrometer potentials, taking into account the specific source angular distributions, central magnetic field strengths, as well as pinch magnetic field strengths. On this basis, appropriate measurement and analysis strategies were worked out and tested by making use of the generated data samples. As a result, a complementary sequence of measurements was found which will allow to fully characterize the main spectrometer as a high-pass MAC-E filter for high-precision  $\beta$ -spectroscopy of tritium  $\beta$ -decay electrons close to the  $\beta$ -endpoint.

The second part of this thesis was devoted to a detailed investigation of possible background sources and on assessing their impact on the KATRIN neutrino mass sensitivity. In this context, both cosmic muon- as well as radon-induced background components were studied.

As the KATRIN experiment is operated at sea level, a large number of cosmic muons ( $10^5/s$ ) will pass through the spectrometer, thereby creating an equivalently large number of secondary electrons on the inner surface. Again, detailed simulations with KASSIOPEIA were performed to identify the electromagnetic conditions where a secondary electron will penetrate into the sensitive volume of the main spectrometer, thus producing irreducible background. These investigations will be of major importance to select field configurations which minimize these effects. Second, an external muon detector system was commissioned to identify and tag muon-induced background events. By combining simulations with dedicated measurements, and following an appropriate strategy outlined in this work, a thorough understanding of the muon-induced background component will be obtained which is an essential pre-requisite to suppress it below the design limit of  $10^{-2}$  cps.

The second major background contribution in electrostatic spectrometers originates from electrons stored in the magnetic bottle configuration inherent to a MAC-E filter. Previous test measurements with the pre-spectrometer have identified the  $\alpha$ -decays of the isotopes  $^{219}\text{Rn}$  and  $^{220}\text{Rn}$  as a major source for low-energy (eV-scale) as well as high-energy (multi-keV) stored electrons. Within this work, a detailed model to describe the complex electron emission processes accompanying the initial radon  $\alpha$ -decay was developed and validated in a series of test measurements with the pre-spectrometer. The excellent agreement for different vacuum conditions has allowed to gain profound insight to the relevant background processes. In particular, it was possible to model electron cooling processes by ionization and synchrotron emission in detail. It is the distinct non-Poissonian nature of these additional background events (Radon-spike) that severely reduces the neutrino mass sensitivity of KATRIN if no countermeasures are applied.

Consequently, final works of this thesis were targeted to study two promising methods to actively remove stored electrons from the sensitive main spectrometer volume: the *electric dipole method* and the *magnetic pulse method*. It could be shown that the electric dipole is highly efficient at removing low-energy ( $E < 1$  keV) electrons, while the

magnetic pulse is best suited to remove the high-energy part ( $E > 1$  keV) of the stored electron spectra. Hence, a complete clearing of the main spectrometer volume from stored electrons can be achieved by a combination of both methods. However, dedicated large-scale Monte-Carlo simulations showed that the low-energy electrons in particular are of major concern for KATRIN, as these electrons feature very short storage times. Consequently, in order to limit the frequencies of application for the active background reduction pulses to an acceptable level, an excellent vacuum of  $\mathcal{O}(10^{-11})$  mbar or better is required.

The models and methods, which have been developed in this thesis, will be of major importance for the upcoming commissioning measurements at the main spectrometer. In return, these measurements will be vital to validate the investigations of this work for the large main spectrometer, to further study and disentangle the different background components investigated here, as well as to optimize the active background reduction techniques. It is only by this close interplay of experiment and large-scale Monte-Carlo simulations with KASSIOPEIA that the KATRIN experiment will achieve its full physics potential in measuring the absolute neutrino mass scale and searching for New Physics.

---

# Appendix

## .1 Implications of the short-circuited wire electrodes

The quasi-massless inner electrode system of the KATRIN main spectrometer covers the whole inner surface for the following reasons [315]:

- Background suppression of secondary electrons from the vessel surface: An incident muon or gamma can knock-on an electron from an atom close to the inner surface of the main spectrometer vessel wall. When entering the sensitive volume of the spectrometer (flux tube), an electron can produce background, either directly by hitting a detector pixel or indirectly via tertiary processes such as ionization. Since most of these electrons are expected to be of low energies, they can be screened electrostatically from the volume by application of a retarding potential (see section 6.2).
- Removal of background electrons by an electric dipole: The inner electrode system was designed to allow for the application of different potentials on the two half shells of the electrode system (with a maximum potential difference of 1 kV). This static dipole leads to an  $\vec{E} \times \vec{B}$  drift for stored electrons, so that they are removed from the sensitive spectrometer volume (see section 8.2).
- Transmission: The inner electrode system allows a fine-tuning of the electric potential and field inside the main spectrometer to fulfill the transmission condition (see section 4.2 and 5).
- Screening of electronic noise on the spectrometer vessel: Electric consumers and devices, such as turbo-molecular pumps, which are attached to the spectrometer vessel, can induce significant electronic noise. In this case, the retarding potential would fluctuate, which would directly induce a systematic error to the electron energy analysis. In the presence of the inner electrode system, this noise contribution can be suppressed greatly, if the voltage on the inner electrode can be kept sufficiently stable [154].
- Field shaping to avoid Penning traps: In the region close to the entrance and exit of the spectrometer, the steep magnetic and electric field gradients can create deep Penning traps, which are known to be a significant source of background.

This can be avoided by adapting a specific shape of the ground and anti-Penning electrodes [183].

The first three objectives have been investigated in detail in the course of this thesis. During the bake-out procedure of the main spectrometer in January 2013, electrical shorts developed between some rings and between the layers of specific rings. In the following, a brief overview of the implications of this configuration are given:

- Background suppression from the vessel surface: In the current situation, the whole central region and the source side conical region can be operated in a single layer configuration only. As pointed out in [315], the background suppression concept is only efficient if the inner electrode is nearly massless, otherwise it will itself be a source of background electrons. In the current situation, the inner layer will neither shield the outer layer nor the support structure, which reduces the background reduction efficiency by about a factor of 10 [276].
- Removal of background electrons by an electric dipole: The voltage difference has to be applied between the half shells of the electrode system. Since there are no electrical shorts between any of the half shells, the inner electrode can still be operated in a dipole mode.
- Electric shielding of spectrometer vessel potential: A single layer configuration modifies the electric shielding of the spectrometer vessel potential from the inner vessel volume, e.g. in the presence of potential fluctuations. It was shown in [276] that there are only marginal influences concerning the electronic noise penetration (*temporal inhomogeneities*) into the spectrometer volume. Spatial fluctuations, however, caused by imprecisions in the geometrical shape of the vessel, can produce potential inhomogeneities if the wire layers are significantly more negative than the vessel ( $\Delta U > 100$  V).
- Field shaping to avoid Penning traps: Penning traps, if at all, will occur in the entrance and exit regions only. Since no electric shorts developed beyond the flat cones, no additional Penning traps due to the electric shorts are expected.
- Transmission: The short circuits at the central modules mainly affect the transmission condition, and hence the spectrometer transmission properties, for outer radii, which will be discussed in the following.

For the following investigations, it was crucial to treat the spectrometer in its full 3-dimensional geometry [191]. So far, for most investigations, it was sufficient to approximate the spectrometer as a discrete rotationally symmetric system, neglecting details of the inner electrode system (C-profiles and pump ports). Such an approximation is, however, not valid anymore in the present situation [276].

The short-circuited wire electrode system significantly influences the transmission properties of the spectrometer. The transmission condition was investigated in section 4.2. There, the situation without electric shorts was discussed. In the following, it

will be shown that in the standard magnetic setups with electric shorts the transmission condition is violated on outer field lines (section .1.1). Hence, an alternative setup, which fulfills the transmission condition is suggested (section .1.2).

### .1.1 Transmission condition with electric shorts

The electric shorts of the inner electrode mainly influence the potential on outer field lines ( $r > 3.5$  m). Therefore, we expect a large influence on the transmission properties for this region. In the following, the simulation results using the magnetic field setups of section 4.5.1, but now with a short-circuited inner electrode system, will be shown. Evidently, the magnetic field lines, as shown in figure 1 (a), are not influenced by the potential. It is the electric potential along the field lines that is modified as shown in figure 1 (b). For outer (red) field lines, the potential maximum is no longer located at the  $z=0$  plane, but moves towards  $|z| = 1$  m, resulting in a two maxima configuration. On the inner field lines, where the potential is rather homogeneous, the transmission condition can still be fulfilled by a careful selection of the magnetic field configuration. On outer field lines, however, the electric potential shows a larger axial inhomogeneity. If the magnetic field is chosen to be very homogeneous in axial direction, then the potential defines the analyzing point, independently of the starting polar angle, and the weak transmission condition can be fulfilled. Figure 2 shows the longitudinal energy along the magnetic field lines. In can clearly be seen that for outer field lines, the position of the minimal longitudinal energy follows the position of the potential minimum.

Looking in more detail at the analyzing points in fig. 3, it can be seen that for inner field lines ( $r < 3.5$  m), the mathematical optimization yields good results with analyzing point positions very close to the  $z = 0$  plane without any radial dependence. For outer field lines, however, the analyzing points are shifted away from  $z = 0$  and a dependence on the initial polar angle starts to develop. In this case, an evaluation

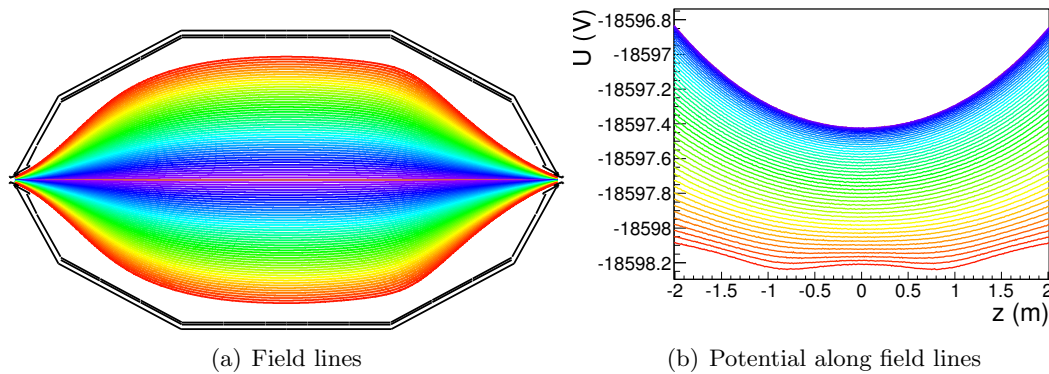


**Figure 1:** (a) Field lines for the 3.5 G setup featuring a global magnetic field minimum. (b) Potential along the field lines of (a). Due to the electric short circuits, on outer field lines the potential maxima are shifted away from the analyzing plane.

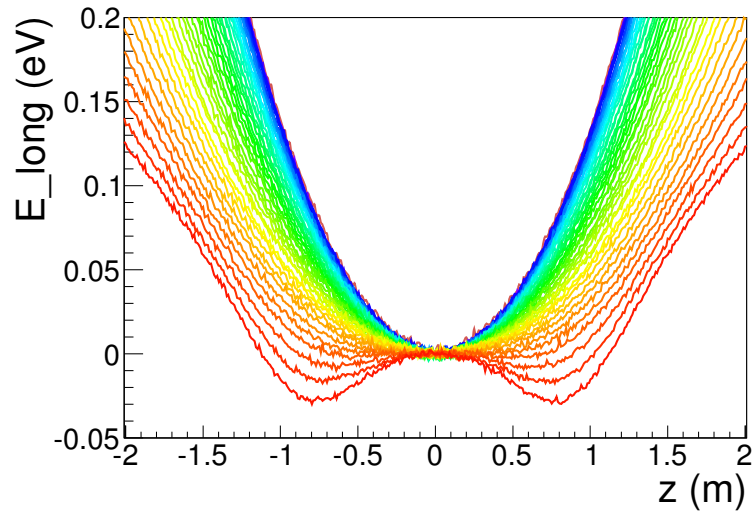


**Figure 2:** Longitudinal kinetic energy along field lines of figure 1, for the maximal starting angle ( $60^\circ$  in the pre-spectrometer magnet PS2).

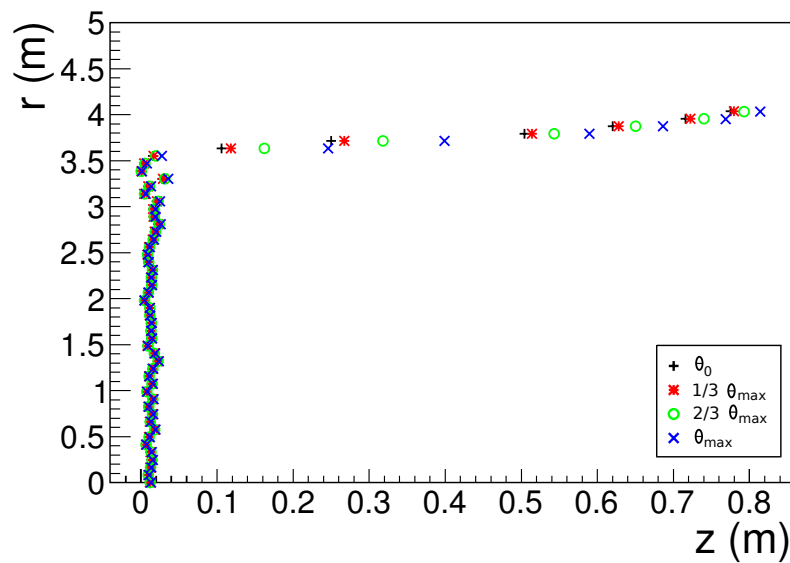


**Figure 3:** Analyzing points for the different field lines of figure 1. Displayed are four exemplary starting polar angles between  $\theta_0 = 0^\circ$  and  $\theta_{\max} = 60^\circ$ .

of the transmission properties of the main spectrometer requires a rather complicated procedure for the outer field lines, which is not desirable.

### .1.2 Fulfilling the transmission condition with electric shorts

In the previous section, the electric shorts were shown to mainly influence the outer field lines with  $r > 3.5$  m. A straightforward solution to prevent this interference of the shorted electrodes is to constrain the flux tube to radii  $r < 3.5$  m. This can be achieved by increasing the magnetic field strength to about 0.5 mT. The resulting field lines and the electric potential along these field lines are shown in figure 4. It is clearly visible that the inhomogeneity of the axial potential does not penetrate as deeply into the flux tube. Consequently, the longitudinal kinetic energy minimum, as displayed in figure 5, is located very close to the  $z = 0$  plane. Figure 6 shows that with this setup, the strong transmission condition is fulfilled (the analyzing point spread is of the order of a few mm only).

From the above investigations, it can be concluded that the influence of the electric shorts at the inner electrode system on the transmission condition is limited to the outer field lines only. This effect entails that the analysis of the transmission properties of the main spectrometer would be much more complicated for outer pixels. The situation can be improved by choosing appropriate magnetic field setups.

Additional details on this topic can be found in [276].

## .2 Background measurements at low retarding voltages

During the initial commissioning measurements of the main spectrometer the vessel will stay on ground potential for safety reasons. The inner electrodes, however, can be operated at retarding voltages of up to -1 kV. Although the electromagnetic layout will thus be different from standard neutrino mass measurement conditions, these initial measurements allow for a first investigation of the main spectrometer background components, such as *trapped particles* and *secondary electron emission*. So far, only rough

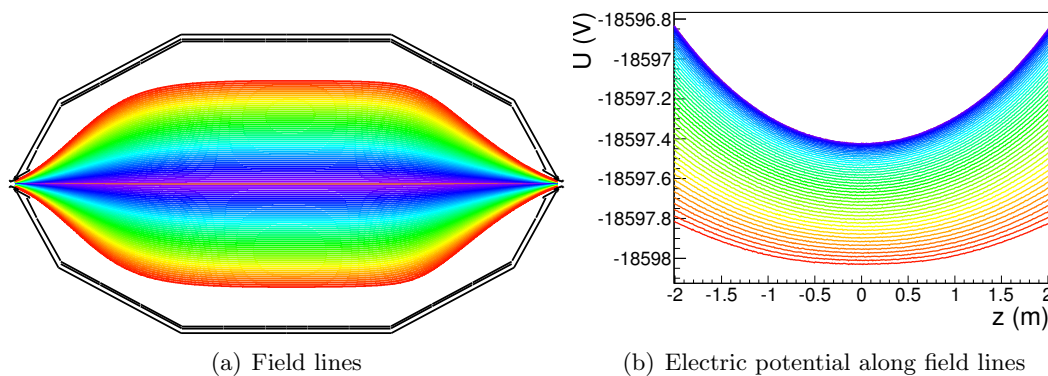


**Figure 4:** (a) Field lines for the 0.5 mT setup featuring a local magnetic field maximum. (b) Potential along the field lines of (a). The influence of the electrical shorts is negligible due to the increased distance to the inner electrode system.

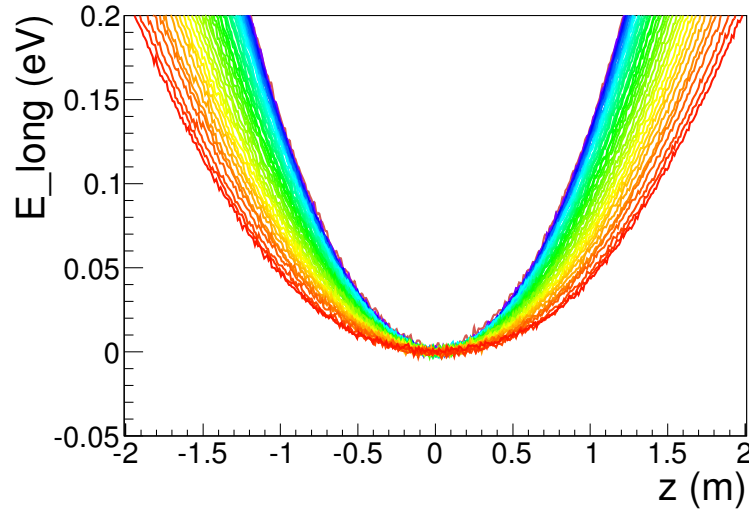


**Figure 5:** Longitudinal kinetic energy along field lines of figure 4, for the maximal starting angle ( $60^\circ$  in the pre-spectrometer magnet PS2).

estimates for these values exist and an early measurement would yield important information that can be included in simulations for the preparation of measurements of the actual SDS<sup>1</sup> commissioning phase, as well as offering the possibility to compare measurements and corresponding simulations to validate the simulation software. In addition, the knowledge of the expected background level will help to make better estimates for the measurement time required for the SDS measurements. Depending on the outcome, there might also be a change of the measurement priorities.

### .2.1 Measurement objectives

The measurement objectives can be sub-divided into *investigations on trapped particles* and *investigations on secondary electron emission*.

#### Investigations on trapped particles

These measurement are ideally performed using the nominal magnetic field setup of the neutrino mass measurements (4.5 T at PS side, 6.0/3.6 T at FPD side). In this phase, radon decays in the main spectrometer volume are expected to be the dominant source for trapped electrons. The goal here is to determine the rate of this background component and to investigate its characteristics.

- Of prime interest is the efficiency of the baffle system as a passive radon cold-trap by increasing the cold-trap area provided by the LN<sub>2</sub>-cooled baffles.

---

<sup>1</sup>Spectrometer and Detector System

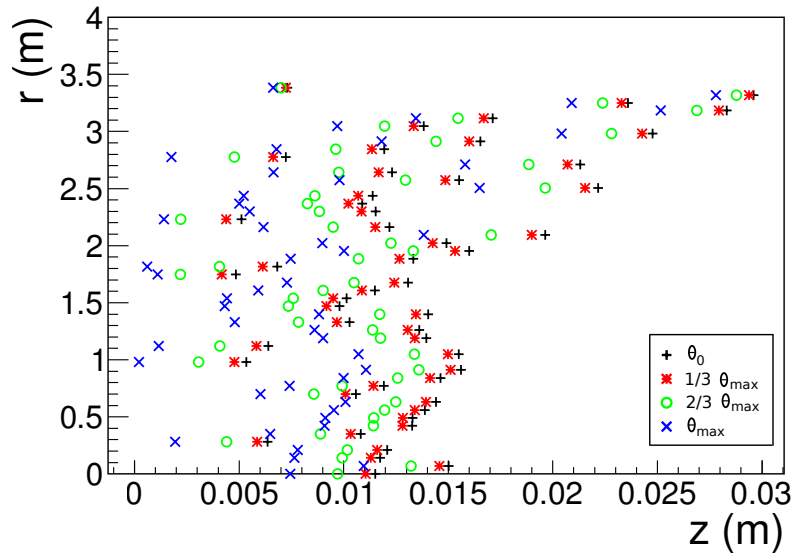


**Figure 6:** Analyzing points for the different field lines of figure 4. Displayed are four exemplary starting polar angles between  $\theta_0 = 0^\circ$  and  $\theta_{\max} = 60^\circ$ .

- The topology of Rn-induced background can be studied by its radial dependence: Assuming that radon decays are isotropically distributed in the main spectrometer volume, a linear increase of the background rate as a function of the radius is expected. Such a behavior was previously observed at the pre-spectrometer (see figure 7.12).
- Investigation of the pressure dependence of the background: The residual pressure and gas composition can be adjusted by the number of active PMTs and baffles.
- Identification of individual nuclear decays. This could be achieved by applying a moderate potential ( $|\Delta U| \leq 1$  kV) to the inner wire electrode system.
- Background dependence on absolute magnetic field strength: A decrease of the stored electron background component is expected when ramping down the magnetic field to smaller values. A decrease of the secondary electron background component is expected when ramping up the magnetic field to higher values.
- Test of magnetic pulsing as an active method to reduce stored electron background.
- Test of an electric dipole as an active method to reduce stored electron background (potential difference of 50-100 V between dipole halves).

### Investigations on secondary electron emission

This measurement should be performed with an asymmetric magnetic field setup, such that the secondary electrons will be guided directly from the spectrometer wall to the

detector. The goal is then to determine the electron emission rate from the spectrometer wall and to test the electric shielding efficiency. The following investigations are of interest:

- Check for coincidences between secondary electrons and cosmic muons with the help of the external muon detector (section 6).
- Determine the shielding efficiency of the wire electrode against low-energy secondaries by applying a retarding potential of up to -100 V. This effect can be checked for a symmetric and an asymmetric magnetic field setup.
- Test the dependence of the background rate on the pinch and detector solenoid field strength (magnetic mirror effect).
- In contrast to the stored electron background component, the secondary electron background is expected to decrease with increasing magnetic field strength within the symmetric magnetic field setup. Data taken to investigate the trapped electron background can be scrutinized for such an effect, which would yield information on the magnetic shielding efficiency.

Monte-Carlo simulations have been performed to estimate the expected background rate and characteristics for the individual measurements, which will be discussed in the next sections. Furthermore, the magnetic field configurations for these measurements have been determined.

## .2.2 Background due to stored electrons

In the standard KATRIN setup ( $B_{\min} = 3.5 \cdot 10^{-4}$  T,  $B_{\max} = 6$  T,  $U_{\text{ret}} = -18.6$  keV), all electrons starting at the analyzing plane with a transversal energy exceeding

$$E_{\perp}^{\max} = qU_{\text{ret}} \cdot \frac{B_{\min}}{B_{\max}} \approx 1 \text{ eV}, \quad (1)$$

will be stored in the volume. This fact does not hold anymore in case of a with reduced or vanishing electrostatic potential as in this case only the magnetic bottle effect will be responsible for the storage of electrons. Therefore, all electrons with a polar angle above

$$\theta_{\max} = \arcsin \sqrt{\frac{B_{\text{start}}}{B_{\max}}} \quad (2)$$

are stored in the volume. Assuming an average magnetic field of  $5 \cdot 10^{-4}$  T, the average maximal polar angle is about  $\theta_{\max} \approx 0.5^{\circ}$ . It is important to notice that this value is independent of the kinetic energy of the stored electron. As a result, the electron loss mechanism is of stochastic nature as electrons have to undergo a specific number of scattering interactions (elastic scattering in the low-energy regime) in order to change their polar angle  $\theta$  (for details see section 8.4.1).

An analytic calculation of the average storage time of a 5 eV electron at a pressure of  $p = 10^{-11}$  mbar can be performed analogously to section 8.4.1. The average time between two scattering events can be read from figure 8.14 to be  $t_{\text{scat}} \approx 20$  s. Assuming that the angular change is isotropic after a scattering process (this assumption is valid for low kinetic energies as shown in figure 8.19), the number of scattering events required to escape the magnetic mirror can be calculated to

$$N_{\text{scat}} = 1 - \cos(\theta_{\text{max}}) \approx 3 \cdot 10^4. \quad (3)$$

Consequently, an average rather long storage time of  $t_{\text{sto}} \approx 6 \cdot 10^5$  s is found. This is about 3 orders of magnitude larger than in the case of standard electrostatic potential. Consequently, no correlation between primary nuclear decay events and succeeding secondary electron detector hits can be established, most likely rendering an identification of individual radon  $\alpha$ -decays impossible. However, the average background rate will not be affected by these changes in the storage times.

The storage times can be greatly reduced by applying a retarding voltage as low as -200 V to the inner electrodes. The corresponding potential at the analyzing plane then is -183 V, which results in a maximal transversal electron energy of 9 meV in order not to be stored. At kinetic energies  $\mathcal{O}(\text{meV})$ , electrons start to gain energy when scattering off molecules with a thermal velocity distribution around 25 meV. Therefore, the average kinetic electron energy is 25 meV, but statistically, the energies can go down below 9 meV. Corresponding Monte-Carlo simulations were performed by starting electrons with a kinetic energy of 5 eV which are distributed homogeneously in the main spectrometer. Figure 7 compares the resulting storage times for a setup without (left) and with reduced (right) electrostatic potential. In the configuration with vanishing potential, the average storage time of  $8 \cdot 10^5$  s is in agreement with the analytical value above. The storage time is reduced by 3 orders of magnitude in the case of a small electrostatic potential applied, down to an average of 500 s. Because the cooling time of radon-induced primary electrons down to 5 eV is of the same order of magnitude or larger than the escape time of 5 eV electrons, this configuration would indeed allow for an identification of individual decay events, if the decay rate is in the low mBq region. Calculations performed in [146] point to an expected radon decay rate of about 200 mBq without baffle, and 6 mBq with baffle. Therefore, at least with active baffle, events should not overlap significantly. The investigations clearly show the advantage of applying a potential to the inner wire electrodes within the risk assessment restrictions.

In [146], the background rates obtained in the pre-spectrometer were extrapolated to the main spectrometer. Without active baffles, a background rate of about 1 cps is expected. This value will be reduced by about a factor of 10 in the case of 3 active baffles. Therefore, we expect radon-induced background rates between 0.1 cps and 1 cps using the standard magnetic field setup ( $B_{\text{min}} = 3.5 \cdot 10^{-4}$  T,  $B_{\text{max}} = 6$  T). This high background rate clearly calls for active background reduction methods.

An electric dipole can remove stored electrons via the  $\vec{E} \times \vec{B}$  drift, as detailed in section 8.2. Figure 8 shows the removal times for electrons starting with 5 eV, which are exposed to a 5 V/m electric dipole field. The maximal removal time is in the order of

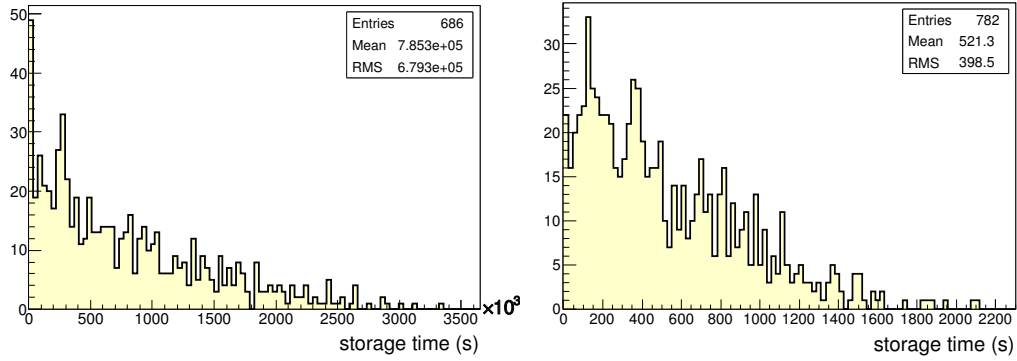


**Figure 7:** Storage time of 5 eV electrons without (left) and with (right) electrostatic potential applied. Electrons were started equally distributed in the main spectrometer volume with a start time  $t = 0$  s.

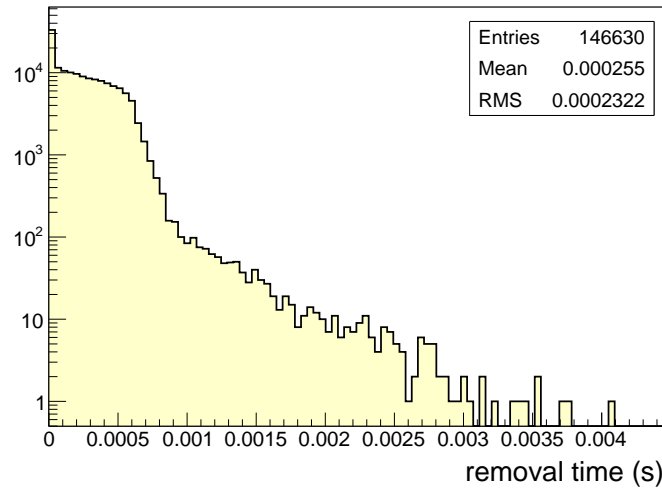


**Figure 8:** Removal time of 5 eV electrons, which are exposed to a 5 V/m electric dipole field. Electrons were started equally distributed in the main spectrometer volume with a start time  $t = 0$  s.

ms, which is well below the shortest possible application time of a dipole pulse of about 100 ms. In this period of time, about 99 % of all electrons with energies  $< 5$  eV can be removed.

### .2.3 Background due to secondary electron emission

The underlying mechanism to create muon-induced secondary electrons was discussed in section 6. In case of a symmetric magnetic field setup, the special case of short-circuited wire electrodes was considered in section 6.4, revealing that radial electron motion is strongly suppressed for this electromagnetic field configuration. Consequently, all measurement results with symmetric magnetic fields but vanishing potential cannot

easily be extrapolated to measurements at nominal potentials. Nevertheless, they can be useful to improve the understanding of electron transportation mechanisms from the inner surface of the spectrometer to the detector. Furthermore, when going to lower central magnetic field strengths, the influence of non-axially symmetric field components will be enhanced, which could allow for an investigation of this subject even without electric potential applied.

The investigation of muon-induced background is easier in the case of an asymmetric magnetic field setup, with field lines directly connecting the spectrometer wall and the detector. Considering the expected high electron production rate of  $10^5$ /s at the surface, a rather large count rate at the detector would be expected. However, the count rate is significantly suppressed by the magnetic mirror effect, similar to the case of stored electrons, as discussed in Appendix .2.3. In a configuration with pre-spectrometer solenoids turned off, pinch magnet on 6 T and the detector surveying 4 % of the spectrometer surface, a count rate of about  $4 \cdot 10^{-2}$  cps is expected. Increasing the surveyed area to 33 % of the spectrometer surface increases the background rate to about 0.35 cps. In addition to varying the observed surface area, the background rate can be influenced by varying the field strength at the starting position and/or at the pinch magnet. Reducing the pinch field to 1.5 T, while keeping the field at the starting position approximately constant, would further increase the count rate to about 1 cps.

It has to be noted that all simulations were performed for electrons with a starting kinetic energy of 5 eV. Without electric potential, the storage probability is generally independent of the starting kinetic energy. However, electrons with energies above about 20 eV will suffer from non-adiabatic effects, which strongly influences their escape probability. This effect is visualized in figure 9. The results of a simulation are shown, where electrons were started from the inner surface of the inner electrode system with energies equally distributed between 1 eV and 100 eV and a polar angle  $\theta = 0^\circ$ . In case of a fully adiabatic motion, all of these electrons are expected to reach the detector, which evidently is not the case for  $E_{\text{kin}} > 20$  eV. This important effect has to be taken into account when extrapolating the measurement results to the muon-induced secondary electron rate.

### .3 Main spectrometer electromagnetic field setups

In the course of this thesis, a variety of magnetic as well as electric field configurations have been utilized for different investigations. The individual settings are listed here.

#### Magnetic field settings:

- Table 1: standard central magnetic field strength ( $3.5 \cdot 10^{-4}$  T) featuring a global magnetic field minimum or a local magnetic field maximum.
- Table 2: increased central magnetic field of  $6 \cdot 10^{-4}$  T and  $10 \cdot 10^{-4}$  T respectively. Both setups feature a local magnetic field maximum.

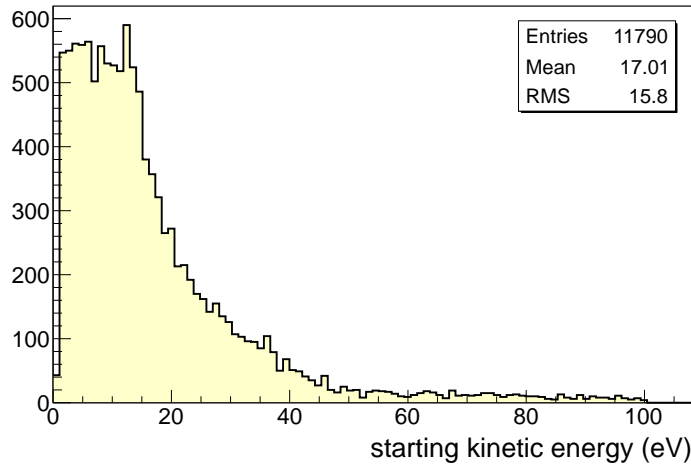


**Figure 9:** Simulation results for electrons starting at the main spectrometer vessel surface parallel to the magnetic field lines ( $\theta = 0^\circ$ ) with energies between 1 and 100 eV in an asymmetric magnetic field setup. Shown is the number of electrons, which reaches the detector. Electrons with higher energies have a smaller probability to reach the detector due to non-adiabatic effects.

- Table 3: symmetric setup with field lines touching certain parts of the vessel surface to investigate muon-induced secondary electron background.

**Electric potential settings:**

- Table 4: standard electrostatic potential setup with an analyzing potential of about -18.6 kV.
- Table 5: setup with a by a factor of 10 reduced potential, as used for transmission investigations.
- Table 6: setup with vessel and anti-penning electrode on ground potential as required for the initial commissioning measurements. Inner electrode system in short-circuit mode, operated at low retarding voltages.

## .4 Adiabatic behavior of electron motion

The adiabatic transport of signal electrons through the main spectrometer is a prerequisite for a successful neutrino mass determination. Therefore, the main spectrometer was designed to have excellent adiabatic conditions for moderate surplus energies  $E_{\text{surp}} < 100$  eV. Stored electrons, however, which significantly contribute to the spectrometer-related background rate, feature kinetic energies of up to  $\mathcal{O}(100)$  keV and thus surplus energies well above the adiabatic design limit. A potential non-adiabatic behavior of these electrons can significantly reduce the expected background rate, as discussed in section 8.4. In the following, the degree of adiabatic behavior of stored electrons will be reviewed in an approach to answer the following questions:

**Table 1:** LFCS setup for the standard central magnetic field strength of  $3.5 \cdot 10^{-4}$  T.

coil index	$I$ (A) [1 minimum]	$I$ (A) [2 minima]
1	-11.2	-0.5
2	-15.3	0.0
3	-7.9	-4.8
4	-13.4	-7.1
5	-12.2	-6.6
6	-24.2	-19.4
7	-17.1	-57.2
8	-20.3	-51.2
9	-18.5	-22.7
10	-23.1	-12.5
11	-21.9	-7.7
12	-18.1	-16.8
13	-13.3	-15.9
14	27.3	42.1

1. What is adiabaticity?
2. How is adiabaticity related to chaos?
3. How large is the effect at the KATRIN spectrometers?

#### .4.1 What is adiabaticity?

An adiabatic electron motion is achieved if electrons follow a well-defined, regular trajectory, where the starting conditions fully determine the solution of the equation of motion. In the case of charged particle motion in a magnetic mirror, the following three quantities have to be conserved:

- energy: kinetic and potential energy
- axial angular momentum: According to Noether's theorem, a symmetry always implies a conservation law. Here, axial symmetry implies the conservation of the axial angular momentum  $\vec{L}$ .
- orbital magnetic moment: the first adiabatic invariant  $\mu = E_{\perp}/B$ .

The focus here will be on the third quantity, the orbital magnetic moment. In general, an adiabatic invariant is a property of a physical system that stays constant when changes occur slowly. Applying this principle to the KATRIN experiment, this means that  $\mu$  will remain constant if changes of the magnetic field  $B$  occur slowly. Trajectory calculations with KASSIOPEIA allow to investigate  $\mu$  as a function of the electron position. If the orbital magnetic moment is conserved, the electron should retain the same value of  $\mu$

**Table 2:** LFCS setup for an increased magnetic field strength. Setup 1:  $6 \cdot 10^{-4}$  T, Setup 2:  $1 \cdot 10^{-3}$  T.

coil index	$I$ (A) [Setup 1]	$I$ (A) [Setup 2]
1	-99.2	-90.3
2	-4.0	-81.6
3	-18.3	-90.5
4	-40.3	-87.8
5	-5.4	-92.5
6	-92.1	-92.7
7	-46.0	-90.4
8	-86.4	-93
9	-57.0	-93
10	-17.5	-91.7
11	-30.4	-81.5
12	-69.6	-89.8
13	-1.0	-89.2
14	8.5	5.7

**Table 3:** Magnet setup for symmetric setups used to investigate the  $\mu$ -induced background component. The PS1 magnet is found at  $z = -15.5$  m, which is the position used for the e-gun measurements. All coils, which are not shown in the table, are assumed to carry no current.

coil	$I$ (A) [Setup 1]	$I$ (A) [Setup 2]
PS1	-157	-157
PS2	-157	-157
LFCS1	-80	-80
LFCS2	-40	-40
LFCS13	0	5
LFCS14	0	80
Pinch	-87	-87
Det	-56	-56

**Table 4:** Standard electrostatic potential input parameters for the simulations.

module	$U$ (V)
vessel	-18400
anti-penning electrode	-18400
outer cylindrical wire	-18500
inner cylindrical wire	-18600
outer conical wire	-18500
inner conical wire	-18600
steep cone wire 1	-18560
steep cone wire 2	-18420

**Table 5:** Electrostatic potential input parameters for transmission function measurements at high energy resolution.

module	$U$ (V)
vessel	-184.0
anti-penning electrode	-184.0
outer cylindrical wire	-185.0
inner cylindrical wire	-186.0
outer conical wire	-185.0
inner conical wire	-186.0
steep cone wire 1	-185.6
steep cone wire 2	-184.2

**Table 6:** Electrostatic potential input parameters for zero vessel potential commissioning measurements.

module	$U$ (V)
vessel	0
anti-penning electrode	0
outer cylindrical wire	-200
inner cylindrical wire	-200
outer conical wire	-200
inner conical wire	-200
steep cone wire 1	-199
steep cone wire 2	-198

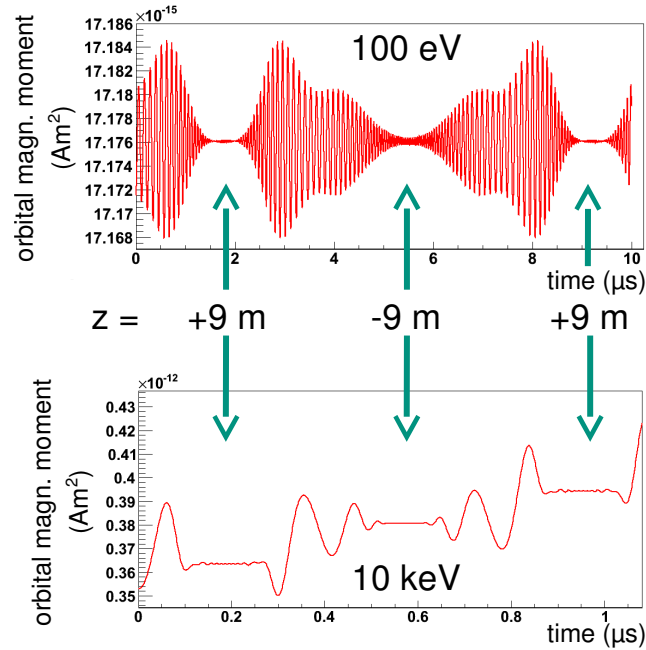


**Figure 10:** Magnetic moment  $\mu$  for initial turns of a stored 100 eV electron (top) and 10 keV electron (bottom). An adiabatic motion entails a constant value of  $\mu$  at the turning points of the trajectory at  $z = \pm 9$  m.

when moving in the same magnetic field. Figure 10 shows  $\mu$  as a function of the flight time of a trapped electron for starting kinetic energies of 100 eV and 10 keV respectively. As the 100 eV electron travels back and forth between the magnetic mirror reflection points at  $z = \pm 9$  m, it passes regions of low magnetic field, with large variations of  $\mu$ , and high magnetic field, where  $\mu$  is approximately constant. The oscillation period of  $\mu$  corresponds to the gyration period of the electron. The apparently large variations of  $\mu$  in the spectrometer center result from the fact that the real adiabatic invariant is a superposition of three adiabatic invariants: the magnetic moment  $\mu$ , the longitudinal invariant  $J = \int p_{\parallel} ds$ , where the momentum integral is between the two reflection points, and the third adiabatic invariant  $\Phi$ , the total magnetic flux enclosed by the drift surface, caused by the magnetron motion. Consequently,  $\mu$  alone does not necessarily have to be perfectly conserved in low magnetic field regions. In high magnetic field regions, however, the 100 eV electron retains the same value of  $\mu$  when returning to the same axial position, while this is not the case for the 10 keV electron. This effect is caused by an uncontrolled change of the polar angle  $\theta$  of the electron, which changes  $E_{\perp}$  and hence  $\mu$ .

This effect is also illustrated in figure 11, where two high-energy electron trajectories are shown. In both cases, the z-position of the reflection points changes, caused by the change of  $\theta$ . The higher the electron kinetic energy, the more chaotic the trajectory will become.

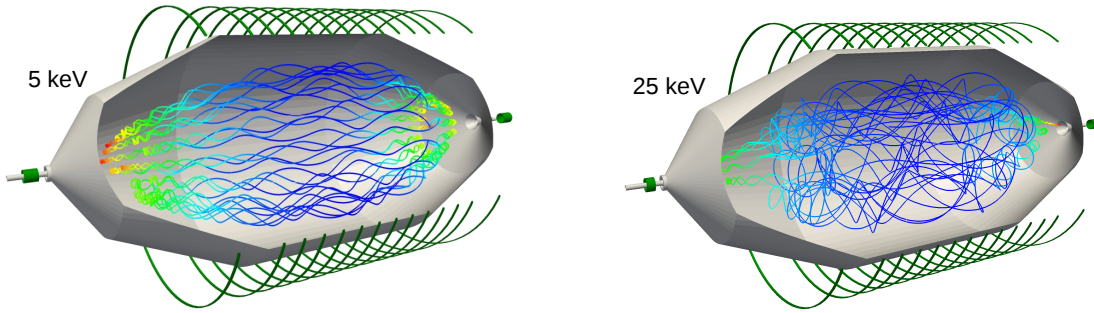


**Figure 11:** Trajectories of stored electrons with kinetic energies of (a) 5 keV and (b) 25 keV. Both trajectories show already some degree of non-adiabaticity. In both cases, the  $z$ -position of the reflection points changes. The higher the electron kinetic energy, the more chaotic the trajectory becomes.

#### .4.2 How is adiabaticity related to chaos?

Figure 11 visualizes that electron trajectories tend to display some degree of chaotic behavior when the electron kinetic energies are increased. According to chaos theory, a dynamical system is chaotic if it shows a sensitive dependence on the initial conditions [316]. This statement can be tested by calculating two electron trajectories with identical starting parameters except for a change in the starting position by  $10^{-14}$  m. In case of an adiabatic behavior, the distance between the two calculated trajectories should remain approximately constant. Figure 12 shows the corresponding simulation results for a 100 eV electron and a 15 keV electron. The low-energy electron, which performs a regular motion, shows only a small dependence on the starting conditions. A linear increase of the distance is observed, which is caused by the numerical errors accumulated in the calculation. The high-energy electron, however, shows an exponential divergence, as typical for a chaotic system.

Another approach to chaotic systems is found in the literature related to the motion of charged particles in the magnetosphere of the Earth [317, 318]. There, the transition between the regular (adiabatic) and chaotic (non-adiabatic) regime is investigated by means of a Poincaré surface of section plot. Within such a plot, only the crossing points of a trajectory with an appropriate surface in the phase space is recorded, as illustrated in figure 13. Such a representation can be used to further investigate the behavior of  $\theta$ . In figure 14, the values of  $\theta$  were recorded whenever the electron crossed the analyzing plane at  $z = 0$  (surface of section). The two separated regions are caused by the fact that the electron moves back ( $\theta > 90^\circ$ ) and forth ( $\theta < 90^\circ$ ). In case of perfect adiabatic conditions, the crossing points are expected to be ordered along lines, as observed for the 5 keV electron, while the chaotic system, the solutions are irregularly scattered over the surface of section, as is the case for the 25 keV electron. For a particular magnetic field strength, the degree of adiabaticity depends on the parameters kinetic energy and starting polar angle. Generally, electron motion in weaker magnetic fields shows a higher degree of non-adiabaticity.

#### 4. Adiabatic behavior of electron motion

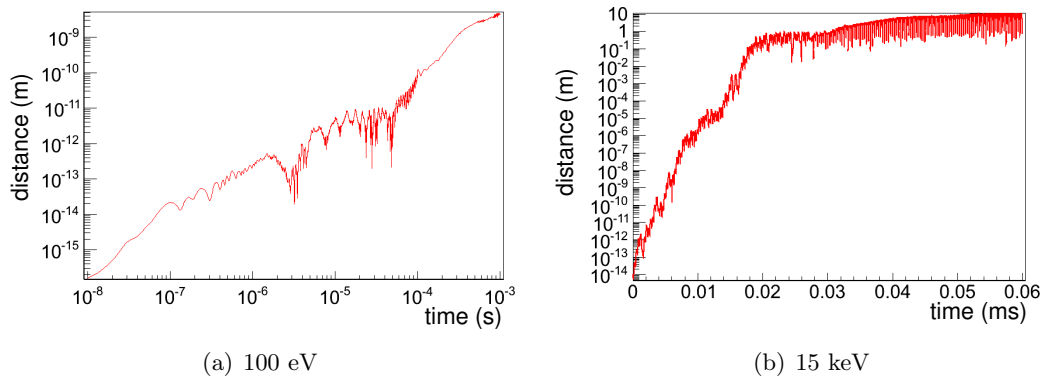


**Figure 12:** Test of non-adiabaticity by an investigation of the starting condition dependence of two electron trajectories. Shown is the distance between two trajectories when varying the starting position by  $10^{-14}$  m. (a) Linear dependence of the adiabatic motion of a 100 eV electron. (b) Exponential dependence of a non-adiabatic (chaotic) motion of a 15 keV electron.

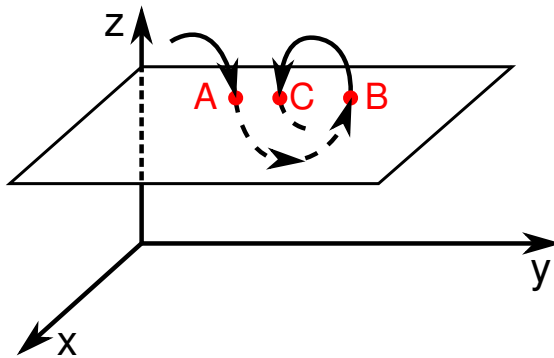


**Figure 13:** Poincaré surface of section: when recording only the crossing points of a trajectory with an appropriate surface in the phase space, the transition between the regular (adiabatic) and chaotic (non-adiabatic) regime can be investigated.

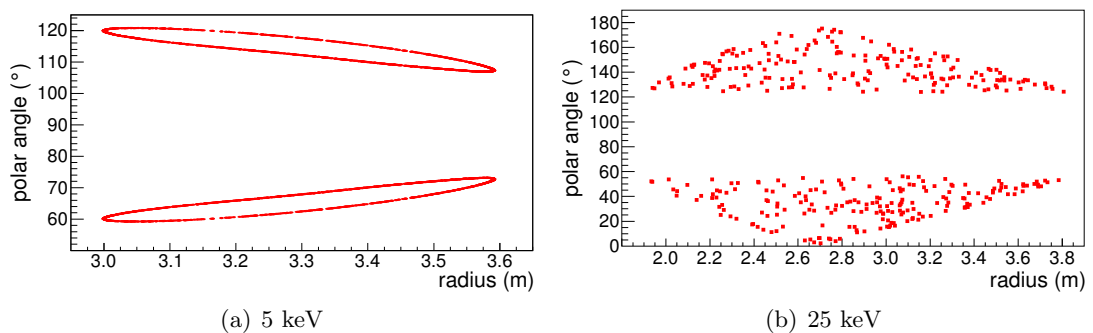


**Figure 14:** Poincaré surface of section plots applied to electron trajectories within the KATRIN spectrometers. Behavior of the polar angle when crossing the analyzing plane at  $z = 0$  m for the (a) 5 keV (regular) and (b) 25 keV (chaotic) electron of figure 11.

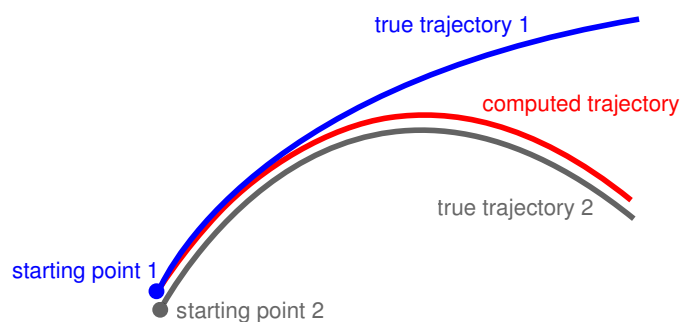


**Figure 15:** Shadowing theorem: Although a numerical (computed, red) trajectory diverges exponentially from the true trajectory (1, blue) with the same initial conditions, there exists a true (errorless) trajectory (2, grey) with a slightly different initial condition that stays near the numerical one.

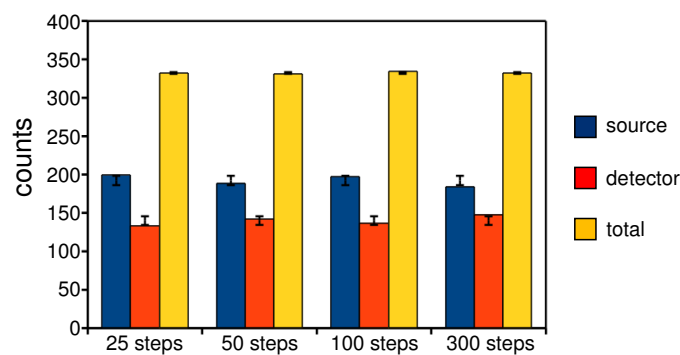


**Figure 16:** Numerical effects on chaotic behavior. If numerical instabilities would cause the observed non-adiabatic behavior, a dependence on the step size ( $\hat{=}$  number of steps per gyration) is expected. The simulation results, however, are independent of the chosen number of steps per gyration.

The last important point is to question whether or not chaos could be a computer-generated artifact caused by the large number of iterations required to calculate electron trajectories within the KATRIN experimental setup. In this context, the so called shadowing theorem, illustrated in figure 15, applies: Although a numerical trajectory diverges exponentially from the true trajectory with the same initial conditions, there exists a true (errorless) trajectory with a slightly different initial condition that stays near the numerical one [319]. The shadowing theorem can be tested when computing a large number of electron trajectories using different step sizes. If numerical errors would generate the observed chaotic behavior, the results would depend on the chosen step size. Figure 16 shows the simulation results for an ensemble of about 1000 electrons, started with a kinetic energy of 15 keV and homogeneously distributed within the main spectrometer. The figure displays the number of electrons, which have escaped towards the detector side and towards the source side separately, and the combination of both (the remaining electrons hit the spectrometer vessel). No dependence on the chosen number

of steps is observed, underlining the independence of the observed chaotic behavior on the numerical stability.

### .4.3 How large is the effect at the KATRIN spectrometers?

The effect of non-adiabatic electron motion can be directly tested with dedicated measurements with the KATRIN spectrometers.

#### Monitor spectrometer

The monitor spectrometer is utilized to measure the line position of the krypton conversion line K-32 at  $\sim 17.8$  keV [160], utilizing a solid krypton source and a MAC-E filter with a central analyzing field strength of about  $3 \cdot 10^{-4}$  T. The krypton spectrum features a large additional number of conversion and Auger lines. Figure 17 shows the krypton energy spectrum for two measurements at different analyzing magnetic field strengths as a function of the electrostatic retarding potential  $U_0$ , which was varied between  $-6$  kV and  $-32$  kV. When decreasing  $U_0$ , more and more lines are expected to be transmitted, resulting in a step-wise increase of the count rate, as approximately observed in the case of large central magnetic field strength in figure 17 (b). The continuous increase of the count rate (as opposed to the expected step-function) is caused by the loss electrons, which deposit a part of their kinetic energy within the source. The measurement at low magnetic field strength shows a decrease of the rate when further decreasing the potential after a certain line has been transmitted. This rate drop-off is caused by the non-adiabatic motion of the krypton decay electrons, which consequently hit the spectrometer wall instead of being transmitted to the detector.

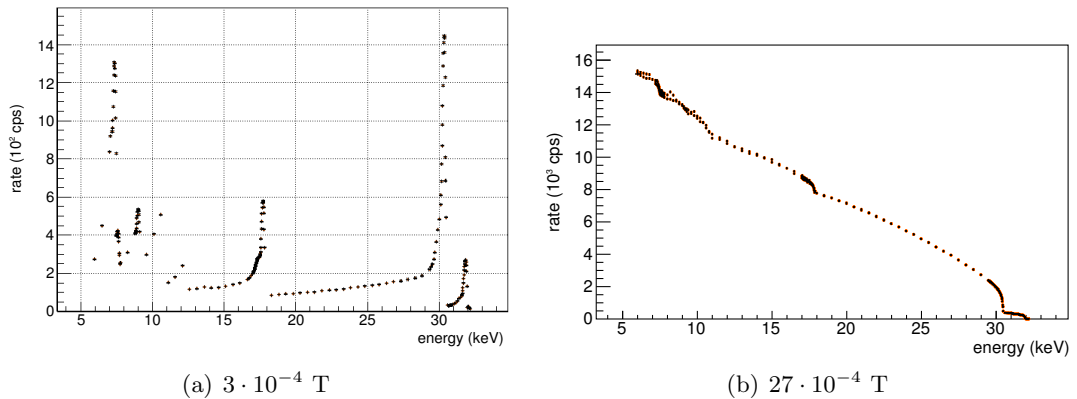


**Figure 17:** Measurement of the conversion line spectra of krypton with the monitor spectrometer. (a) For an analyzing magnetic field strength of  $3 \cdot 10^{-4}$  T, non-adiabaticity causes the rate to quickly drop off after a certain line was passed by decreasing the retarding potential. (b) When increasing the analyzing magnetic field strength to  $27 \cdot 10^{-4}$  T, the count rate increases throughout the whole spectrum, as expected in case of an adiabatic electron motion.

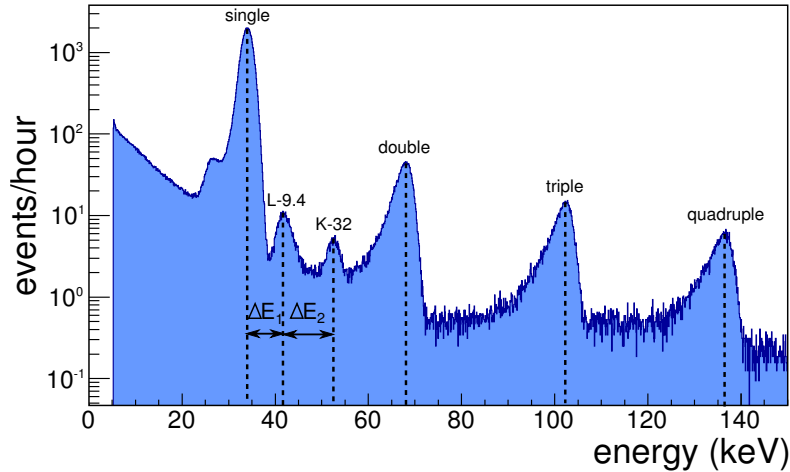


**Figure 18:** Monitor spectrometer background measurement with krypton being emitted into the spectrometer volume. When decaying there, high-energy stored electrons are produced which generate background via ionization of residual gas. In addition to the resulting peak at the spectrometer potential (and multiples thereof), two peaks are observed, which are found to correspond to the L-9.4 line with  $\Delta E_1 \approx 7.4$  keV and the K-32 line with  $\Delta E_1 + \Delta E_2 \approx 17.8$  keV. A part of these electrons can leave the spectrometer non-adiabatically before undergoing any scattering events.

Non-adiabaticity is also observed when elevating the spectrometer to a potential of -35 kV. In this case, the electrons from the source cannot reach the detector. An external krypton source was attached to one of the pump ports, releasing single krypton atoms into the spectrometer volume where they can decay and produce high-energy stored electrons. Figure 18 shows the measurement results. The expected peak at an energy corresponding to the spectrometer retarding potential is observed (and multiples thereof due to multiple hits within the shaping time of the detector), which is caused by the low-energy secondary electrons, created via ionization of the residual gas. Additionally, two smaller peaks are visible with a spacing of  $\Delta E_1 \approx 7$  keV and  $\Delta E_2 \approx 11$  keV, which can be identified as the L-9.4 line ( $\Delta E_1$ ) and the K-32 line ( $\Delta E_1 + \Delta E_2$ ), respectively. These electrons left the spectrometer due to non-adiabatic electron motion, without undergoing a significant number of scattering events (no energy losses observed).

### Pre-spectrometer

A similar measurement was performed at the pre-spectrometer [146]. There, the krypton decay electrons were used to test the efficiency of electron cyclotron resonance as an active background reduction method. Prior to this test, background measurements were performed for different central magnetic field strengths, as shown in figure 19. Corresponding simulations, performed in the framework of this thesis, were able to reproduce the measurement results. As expected, the background rate decreases with decreasing central magnetic field strength, as stored high-energy electrons leave the spectrom-

ter due to non-adiabatic effects before converting their full kinetic energy to secondary electrons and hence background rate.

The maximal background rate is observed at a central field strength of about  $10^{-2}$  T, where all electrons perform a fully adiabatic motion. The decrease of the background rate for even higher field strengths is caused by the fact that the spectrometer volume, which is observed by the detector, decreases with increasing field strength (the flux tube radius decreases). Assuming a homogeneous distribution of the krypton decays in the volume, a corresponding decrease in count rate is expected.

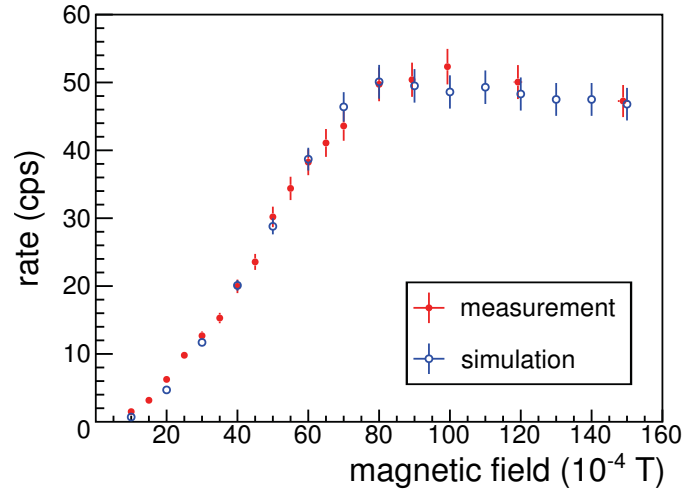


**Figure 19:** Pre-spectrometer background measurement with krypton atoms decaying in the volume. The measurement was performed in [146]. The corresponding simulations, performed in the course of this work, are in very good agreement with the measurements. The rate decrease towards lower central field strengths is attributed to the increasingly non-adiabatic motion of the stored electrons.

# List of Figures

1.1	Energy spectrum of radium $\beta$ -decay . . . . .	2
1.2	Solar neutrino flux . . . . .	6
1.3	Illustration of 2-neutrino oscillation . . . . .	9
1.4	Neutrino mass hierarchy . . . . .	13
1.5	Contribution of neutrinos to total density in the Universe . . . . .	18
1.6	Evolution of the density contributions in the Universe . . . . .	19
1.7	Matter power spectrum and influence of neutrinos . . . . .	20
1.8	Mass parabola . . . . .	21
1.9	Double $\beta$ -decay Feynman graph and energy spectrum . . . . .	22
1.10	Single $\beta$ -decay Feynman graph and energy spectrum . . . . .	24
2.1	KATRIN experimental setup. . . . .	28
2.2	Tritium source WGTS . . . . .	28
2.3	Rear section . . . . .	30
2.4	Differential pumping section . . . . .	31
2.5	Cryogenic pumping section . . . . .	32
2.6	Pre-spectrometer setup . . . . .	33
2.7	Photograph of the main spectrometer . . . . .	35
2.8	Photograph of the monitor spectrometer . . . . .	35
2.9	Focal plane detector system . . . . .	36
2.10	MAC-E filter principle . . . . .	38
2.11	Normalized main spectrometer transmission function . . . . .	40
2.12	KATRIN response function . . . . .	41
2.13	Penning traps and magnetic mirror traps . . . . .	46
3.1	Exact and adiabatic electron motion . . . . .	55
3.2	Electron-hydrogen scattering cross section . . . . .	59
3.3	Parameterization of a coil . . . . .	61
3.4	Legendre polynomial expansion . . . . .	63

4.1	191 Tcm <sup>2</sup> flux tube without air coil system . . . . .	72
4.2	Transmission energy dependence . . . . .	75
4.3	Transmission condition with a global magnetic field minimum . . . . .	79
4.4	Transmission condition with a local magnetic field maximum . . . . .	79
4.5	191 Tcm <sup>2</sup> flux tube with EMCS . . . . .	81
4.6	191 Tcm <sup>2</sup> flux tube with complete air coil system . . . . .	82
4.7	Main spectrometer surrounded by the large volume air coil system . . . . .	83
4.8	Magnetic field asymmetry in the main spectrometer . . . . .	89
4.9	Magnetic field lines in the main spectrometer: $3.5 \cdot 10^{-4}$ T . . . . .	90
4.10	Magnetic field strength along field lines: $3.5 \cdot 10^{-4}$ T . . . . .	91
4.11	Electrostatic potential in the main spectrometer and interplay with mag- netic field . . . . .	92
4.12	Longitudinal energy along field lines: $3.5 \cdot 10^{-4}$ T . . . . .	93
4.13	Spatial coordinates of the analyzing points: $3.5 \cdot 10^{-4}$ T . . . . .	94
4.14	Radial magnetic field inhomogeneity: $3.5 \cdot 10^{-4}$ T . . . . .	95
4.15	Field lines: $6 \cdot 10^{-4}$ T . . . . .	97
4.16	Magnetic field along field lines: $6 \cdot 10^{-4}$ T . . . . .	97
4.17	Longitudinal energy along field lines: $6 \cdot 10^{-4}$ T . . . . .	98
5.1	Transmission function for an ideal angular selective, mono-energetic source and an isotropic source . . . . .	103
5.2	Transmission function influenced by a magnetic field and an electrostatic potential . . . . .	104
5.3	Illustration of the e-gun principle . . . . .	106
5.4	Transmission function influenced by source energy or angular distribution	108
5.5	Transmission function influenced by source angular and energy distribution	109
5.6	Source energy distribution with variable spectrometer potential . . . . .	112
5.7	Source energy distribution at variable e-gun potential. . . . .	113
5.8	Simulated transmission function with source energy distribution. . . . .	114
5.9	Transmission function and numerical differentiation . . . . .	115
5.10	Source energy distribution determined by numerical differentiation. . . . .	116
5.11	Analytical TF $T(\epsilon)$ . . . . .	118
5.12	Analytical TF $T(U_{\text{egun}})$ . . . . .	118
5.13	Deviation of Monte-Carlo and analytical results. . . . .	119
5.14	Transmission function depending on pinch magnetic field . . . . .	121
5.15	Transmission function depending on pinch magnetic field strength . . . . .	123
5.16	Angular distribution determined from pinch magnetic field measurement . . . . .	123
5.17	Analytical transmission function determined from source angular distri- bution . . . . .	124
5.18	Transmission function depending on source angular distribution . . . . .	125
5.19	TF depending on source angular distribution as determined with MC . . . . .	127
5.20	Source angular distribution determined by differentiation ( $B_{\text{Pa}} = 1 \cdot 10^{-3}$ T)	128
5.21	Calculated analytical TF for $B_{\text{Pa}} = 1 \cdot 10^{-3}$ T . . . . .	129

5.22	Comparison of MC and analytical TF: $1 \cdot 10^{-3}$ T . . . . .	130
5.23	TF MC for $B_{P_a} = 3.5 \cdot 10^{-4}$ T . . . . .	131
5.24	Analytical TF for $B_{P_a} \sim 3.5 \cdot 10^{-4}$ T . . . . .	131
5.25	Illustration of TF with fully considered source effects . . . . .	132
5.26	Monte-Carlo simulation taking into account full source effects . . . . .	134
5.27	Angular distribution as determined from MC data for energy and angular source distribution . . . . .	135
5.28	Comparison of MC and analytical TF with full source effects . . . . .	135
6.1	Magnetron drift in axially symmetric fields . . . . .	142
6.2	Magnetron drift in non-axially symmetric fields . . . . .	142
6.3	Principle of electrostatic shielding . . . . .	144
6.4	Schematic drawing of a muon detector module . . . . .	146
6.5	Emission spectrum of BICRON BC-412 . . . . .	146
6.6	Break-down of detection efficiency in magnetic fields . . . . .	148
6.7	Layout of the rate-sensitive detector design . . . . .	150
6.8	Layout of the position-sensitive detector design . . . . .	151
6.9	Landau spectra of all modules . . . . .	153
6.10	Detection efficiency in magnetic fields after installation of mu-metal shield- ing . . . . .	153
6.11	Fluctuations of detected muon rate . . . . .	154
6.12	Drift velocity and critical energy for standard setup, global minimum . . .	155
6.13	Potential penetration . . . . .	156
6.14	Drift velocity and critical energy for standard setup, local maximum . . .	157
6.15	Drift velocity and radial electric field for single layer mode . . . . .	158
6.16	Drift velocity and critical energy for low potential setup . . . . .	159
6.17	Field lines for symmetric field setups . . . . .	161
6.18	Field lines for asymmetric field setup . . . . .	162
6.19	Magnetic field and electrostatic potential for asymmetric field setup . . .	163
6.20	Electron trajectories for setup without magnetic field . . . . .	165
6.21	Neutrino mass sensitivity . . . . .	166
7.1	Electron storage within a MAC-E filter . . . . .	168
7.2	Illustration of the radon decay process . . . . .	170
7.3	Sketch of the relaxation process . . . . .	174
7.4	Flowchart of the radon event generator . . . . .	177
7.5	Energy spectrum as obtained with the radon generator . . . . .	179
7.6	Charge states of Po-daughters . . . . .	181
7.7	Detector hits per radon decay event . . . . .	182
7.8	Pre-spectrometer background measurement . . . . .	183
7.9	Number of secondary electrons as function of primary energy . . . . .	185
7.10	Simulated trajectory of a trapped electron . . . . .	189
7.11	Detector signature of typical radon-induced background events . . . . .	189
7.12	Ring radius distribution . . . . .	191

7.13	Time structure of a period of elevated rate . . . . .	191
7.14	Time structure of a period of elevated rate with increased rate at the beginning . . . . .	192
7.15	Time difference between successive detector hits . . . . .	193
7.16	Number of detector hits as a function of the event duration . . . . .	198
7.17	Calculated radon activity within the pre-spectrometer . . . . .	200
7.18	Event rates per class and measurement . . . . .	202
7.19	Background rate per class . . . . .	202
7.20	Storage probability in the spectrometers . . . . .	205
7.21	Tritium storage in the spectrometers . . . . .	206
7.22	Radon storage in the spectrometers . . . . .	207
7.23	Neutrino mass sensitivity as function of the background rate . . . . .	208
8.1	3-dimensional view of a trapped electron in the main spectrometer. . . . .	212
8.2	Trapping probability for electrons in the main spectrometer . . . . .	213
8.3	Visualization of the dipole principle . . . . .	214
8.4	Illustration of the effect of different dipole strengths . . . . .	215
8.5	3-dimensional illustration of the motion of a stored electron influenced by an electric dipole field. . . . .	217
8.6	Removal efficiency of the electric dipole method . . . . .	218
8.7	Possible background production by an electric dipole. . . . .	219
8.8	Effect of magnetic field reduction within magnetic pulse. . . . .	221
8.9	Effect of an induced electric field on the electron motion. . . . .	221
8.10	Magnetic pulse principle. . . . .	222
8.11	Magnetic pulse principle. . . . .	222
8.12	3-dimensional illustration of the motion of a stored electron influenced by a magnetic pulse. . . . .	223
8.13	Removal efficiency of a magnetic pulse . . . . .	225
8.14	Time between two successive scattering events. . . . .	228
8.15	Scattering cross sections. . . . .	228
8.16	Trapping and escape probability. . . . .	229
8.17	Energy loss due to scattering events. . . . .	230
8.18	Number of scatterings to break storage condition. . . . .	231
8.19	Change of polar angle by scattering. . . . .	231
8.20	Analytically determined electron storage times. . . . .	233
8.21	Storage times of tritium electrons. . . . .	233
8.22	Storage times of radon-induced electrons. . . . .	234
8.23	Secondary electron energies following tritium and radon primary electron storage . . . . .	235
8.24	Background reduction for tritium and radon . . . . .	237
1	Field lines and potential at standard field strength with electrical shorts . . . . .	247
2	Longitudinal kinetic energy at standard field strength with electrical shorts	248
3	Analyzing points at standard field strength with electrical shorts . . . . .	248

4	Field lines and potential at increased field strength with electrical shorts .	249
5	Longitudinal kinetic energy at increased field strength with electrical shorts	250
6	Analyzing points at increased field strength with electrical shorts . . . . .	251
7	Storage time of 5 eV electrons with and without electrostatic potential applied . . . . .	254
8	Removal time of 5 eV electrons for a 5 V/m electric dipole field . . . . .	254
9	Non-adiabatic behavior of $\mu$ -induced electrons in an asymmetric field setup	256
10	Magnetic moment of electron trajectories . . . . .	260
11	Trajectories of high-energy electrons . . . . .	261
12	Starting condition dependence . . . . .	262
13	Poincaré surface of section . . . . .	262
14	Behavior of polar angle for non-adiabatic electrons . . . . .	262
15	Shadowing theorem . . . . .	263
16	Shadowing theorem applied to KATRIN . . . . .	263
17	Non-adiabaticity for monitor spectrometer line spectra measurements . .	264
18	Monitor spectrometer krypton measurement . . . . .	265
19	Pre-spectrometer krypton measurement . . . . .	266



# List of Tables

1.1	Leptons in the Standard Model . . . . .	4
4.1	Overview of LFCS parameters . . . . .	82
4.2	Overview of magnetic field producing components . . . . .	87
4.3	Overview of optimized LFCS current settings . . . . .	89
5.1	Influence of spectrometer and source properties on transmission characteristics . . . . .	109
5.2	Influence of input parameters on angular distribution. . . . .	128
7.1	Internal conversion emission probabilities . . . . .	172
7.2	Shake-off emission probabilities . . . . .	173
7.3	Electron emission probabilities per decay and process . . . . .	180
7.4	Pumping speeds and decay probabilities in the pre-spectrometer . . . . .	187
7.5	Overview of pre-spectrometer measurement conditions and results . . . . .	187
7.6	Time difference parameters . . . . .	194
7.7	Overview of Monte-Carlo results . . . . .	200
7.8	Radon emanation rates per unit volume . . . . .	201
7.9	Background rate due to C0 events . . . . .	203
8.1	Path length and duration of an electron trajectory within a full magnetron turn . . . . .	218
8.2	Average storage times of secondary electrons . . . . .	234
8.3	Background rates due to tritium and radon decay . . . . .	238
1	LFCS setup for standard central magnetic field strength . . . . .	257
2	LFCS setup for increased magnetic field strength . . . . .	258
3	Magnet setup for symmetric setup for muon investigations . . . . .	258
4	Standard electrostatic potential input parameters for the simulations. . . . .	259
5	Electrostatic potential input parameters for transmission function measurements at high energy resolution. . . . .	259

6	Electrostatic potential input parameters for zero vessel potential commissioning measurements. . . . .	259
---	--	-----

# Bibliography

- [1] C. Kraus *et al.*, “Final results from phase II of the Mainz neutrino mass search in tritium,” *Eur. Phys. J. C*, vol. 40, pp. 447–468, 2005.
- [2] V. V. Aseev *et al.*, “Upper limit on the electron antineutrino mass from the troitsk experiment,” *Phys. Rev. D*, vol. 84, no. 112003, 2011.
- [3] J. Chadwick, “Intensitätsverteilung im magnetischen Spektrum von  $\beta$ -Strahlen von Radium B+C,” *Verh. d. Deutsch. Phys. Ges.*, vol. 15, p. 383, 1914.
- [4] F. A. Scott, “Energy Spectrum of the  $\beta$ -Rays of Radium E,” *Phys. Rev.*, vol. 48, pp. 391–395, 1935.
- [5] W. Pauli, “Letter to Gauvereinstagung in Tübingen: ”Sehr geehrte radioaktive Damen und Herren”, ” published in *R.Kronig and V. Weisskopf (Eds.), Wolfgang Pauli, Collected scientific Papers, Vol.2, Interscience, New York (1964)*, 1930.
- [6] J. Chadwick, “Possible Existence of a Neutron,” *Nature*, vol. 312, p. 312, 1932.
- [7] E. Fermi, “Versuch einer Theorie der  $\beta$ -Strahlen,” *Zeitschrift für Physik A*, vol. 88, pp. 161–177, 1934. 10.1007/BF01351864.
- [8] H. Bethe and R. Peierls, “The ”Neutrino”, ” *Nature*, vol. 133, p. 532, 1934.
- [9] C. L. Cowan, F. Reines, F. B. Harrison, H. W. Kruse, and A. D. McGuire, “Detection of the Free Neutrino: a Confirmation,” *Science*, vol. 124, no. 3212, pp. 103–104, 1956.
- [10] F. Reines, C. L. Cowan, F. B. Harrison, A. D. McGuire, and H. W. Kruse, “Detection of the Free Antineutrino,” *Phys. Rev.*, vol. 117, pp. 159–173, Jan 1960.
- [11] J.-M. Gaillard, K. Goulianos, L. M. Lederman, N. Mistry, M. Schwartz, J. Steinberger, and G. Danby, “Observation of High-Energy Neutrino Reactions and the Existence of Two Kinds of Neutrinos,” *Phys. Rev. Lett.*, vol. 9, pp. 36–44, 1962.

- [12] K. Kodama *et al.*, “Observation of tau neutrino interactions,” *Phys. Lett. B*, vol. 504, no. 3, pp. 218–224, 2001.
- [13] D. Decamp *et al.*, “A precise determination of the number of families with light neutrinos and of the Z boson partial widths,” *Phys. Lett. B*, vol. 235, no. 3-4, pp. 399–411, 1990.
- [14] D. Decamp *et al.*, “Determination of the number of light neutrino species,” *Phys. Lett. B*, vol. 231, no. 4, pp. 519–529, 1989.
- [15] ALEPH Collaboration, DELPHI Collaboration, L3 Collaboration, OPAL Collaboration, SLD Collaboration, LEP Electroweak Working Group, SLD Electroweak and Heavy Flavour Groups, “Precision electroweak measurements on the Z resonance,” *Phys. Rep.*, vol. 427, no. 5-6, pp. 257–454, 2006.
- [16] S. Groh. PhD thesis, KIT, 2014. in preparation.
- [17] S. L. Glashow, “Partial-symmetries of weak interactions,” *Nucl. Phys.*, vol. 22, no. 4, pp. 579–588, 1961.
- [18] S. Weinberg, “A Model of Leptons,” *Phys. Rev. Lett.*, vol. 19, pp. 1264–1266, 1967.
- [19] A. Salam *Proc. of the 8th Nobel Symposium*, 1968.
- [20] F. Englert and R. Brout, “Broken Symmetry and the Mass of Gauge Vector Mesons,” *Phys. Rev. Lett.*, vol. 13, no. 9, pp. 321–323, 1964.
- [21] P. W. Higgs, “Broken Symmetries and the Masses of Gauge Bosons,” *Phys. Rev. Lett.*, vol. 13, no. 16, pp. 508–509, 1964.
- [22] G. Aad and others (ATLAS Collaboration), “Observation of a New Particle in the Search for the Standard Model Higgs Boson with the ATLAS Detector at the LHC,” *Phys. Lett. B*, vol. 716, no. 1, pp. 1–29, 2012.
- [23] “Combined results of searches for the standard model Higgs boson in pp collisions at  $\sqrt{s} = 7$  TeV,” *Phys. Lett. B*, vol. 710, no. 1, pp. 26–48, 2012.
- [24] M. Goldhaber, L. Grodzins, and A. W. Sunyar, “Helicity of neutrinos,” *Phys. Rev.*, vol. 109, no. 3, pp. 1015–1017, 1958.
- [25] J. N. Bahcall, A. M. Serenelli, and S. Basu, “New Solar Opacities, Abundances, Helioseismology, and Neutrino Fluxes,” *Astrophys. J.*, vol. 621, no. 1, pp. 85–88, 2005.
- [26] B. T. Cleveland *et al.*, “Measurement of the solar neutrino flux with the Homestake chlorine detector,” *Astrophys. J.*, vol. 496, no. 1, pp. 505–526, 1998.
- [27] R. Davis, “A review of the Homestake solar neutrino experiment,” *Prog. Part. Nucl. Phys.*, vol. 32, pp. 13–32, 1994.

- 
- [28] “Homepage of J. Bahcall.” <http://www.sns.ias.edu/jnb/> [last update: 2005].
- [29] GALLEX Collaboration, “GALLEX solar neutrino observations: results for GALLEX IV,” *Phys. Lett. B*, vol. 447, no. 1-2, pp. 127–133, 1999.
- [30] GNO Collaboration, “Complete results for five years of GNO solar neutrino observations,” *Phys. Lett. B*, vol. 616, no. 3-4, pp. 174–190, 2005.
- [31] SAGE Collaboration, “Solar neutrino flux measurements by the Sovjet-American gallium experiment (SAGE) for half the 22-year solar cycle,” *J. Exp. Theo. Phys.*, vol. 95, pp. 181–193, 2002.
- [32] Kamiokande Collaboration, “Solar Neutrino Data Covering Solar Cycle 22,” *Phys. Rev. Lett.*, vol. 77, pp. 1683–1686, 1996.
- [33] B. Aharmim and others (SNO Collaboration), “Determination of the  $\nu_e$  and total  $B8$  solar neutrino fluxes using the Sudbury Neutrino Observatory Phase I data set,” *Phys. Rev. C*, vol. 75, no. 4, p. 045502, 2007.
- [34] V. Gribov and B. Pontecorvo, “Neutrino astronomy and lepton charge,” *Phys. Lett. B*, vol. 28, no. 7, pp. 493–496, 1969.
- [35] Q. R. Ahmad (SNO Collaboration), “Direct Evidence for Neutrino Flavor Transformation from Neutral-Current Interactions in the Sudbury Neutrino Observatory,” *Phys. Rev. Lett.*, vol. 89, no. 011301, 2002.
- [36] Q. R. Ahmad (SNO Collaboration), “Measurement of the Rate of  $\nu_e + d \rightarrow p + p + e^-$  Interactions Produced by  $B8$  Solar Neutrinos at the Sudbury Neutrino Observatory,” *Phys. Rev. Lett.*, vol. 87, no. 7, p. 071301, 2001.
- [37] J. N. Bahcall, “Solving the mystery of the missing neutrinos,” 2004. arXiv:physics/0406040 [pop-ph].
- [38] Z. Maki, M. Nakagawa, and S. Sakata, “Remarks on the unified model of elementary particles,” *Prog. Theor. Phys.*, vol. 28, no. 5, pp. 870–880, 1962.
- [39] B. Pontecorvo *Zh. Eksp. Teor. Fiz.*, vol. 34, p. 247, 1957.
- [40] Particle Data Group, “Review of particle physics,” *Phys. Rev. D*, vol. 86, no. 010001, 2012.
- [41] C. Giunti and C. W. Kim, *Neutrino Physics and Astrophysics*. Oxford University Press, 2007.
- [42] “Homepage of the T2K experiment.” <http://www.lppp.lancs.ac.uk/neutrinos/theory.html>.
- [43] L. Wolfenstein, “Neutrino oscillations in matter,” *Phys. Rev. D*, vol. 17, no. 9, pp. 2369–2374, 1978.

- [44] S. P. Mikheev and A. Y. Smirnov, “Resonance amplification of oscillations in matter and spectroscopy of solar neutrinos,” *Sov. J. Nucl. Phys.*, vol. 42, pp. 913–917, 1985.
- [45] SNO Collaboration, “Independent Measurement of the Total Active  $^8\text{B}$  Solar Neutrino Flux Using an Array of  $^3\text{He}$  proportional counters at the Sudbury Neutrino Observatory,” *Phys. Rev. Lett.*, vol. 101, no. 111301, 2008.
- [46] Y. Fukuda and others (Super-Kamiokande Collaboration), “Evidence for Oscillation of Atmospheric Neutrinos,” *Phys. Rev. Lett.*, vol. 81, pp. 1562–1567, Aug 1998.
- [47] R. Wendell and others (Super-Kamiokande Collaboration), “Atmospheric neutrino oscillation analysis with subleading effects in Super-Kamiokande I, II and III,” *Phys. Rev. D*, vol. 81, 2010.
- [48] M. H. Ahn and others (K2K Collaboration), “Measurement of neutrino oscillation by the K2K experiment,” *Phys. Rev. D*, vol. 74, 2006.
- [49] K. Abe and others (T2K Collaboration), “Indication of Electron Neutrino Appearance from an Accelerator-Produced Off-Axis Muon Neutrino Beam,” *Phys. Rev. Lett.*, vol. 107, p. 041801, 2011.
- [50] M. Apollonio and others (CHOOZ Collaboration), “Limits on neutrino oscillation from the CHOOZ experiment,” *Phys. Lett. B*, vol. 466, 1999.
- [51] P. Adamson and others (MINOS Collaboration), “Improved Search for Muon-Neutrino to Electron-Neutrino Oscillations in MINOS,” *Phys. Rev. Lett.*, vol. 107, 2011.
- [52] Y. Abe and others (Double Chooz Collaboration), “Indication for the disappearance of reactor electron antineutrinos in the Double Chooz experiment,” *Phys. Rev. Lett.*, vol. 108, 2012.
- [53] F. P. An and others (DAYA-BAY Collaboration), “Observation of electron-antineutrino disappearance at Daya Bay,” *Phys. Rev. Lett.*, vol. 108, 2012.
- [54] J. K. Ahn and others (RENO Collaboration), “Observation of reactor electron antineutrino disappearance in the RENO experiment,” *Phys. Rev. Lett.*, vol. 108, 2012.
- [55] Y. Abe and others (Double Chooz Collaboration), “Reactor electron antineutrino disappearance in the Double Chooz experiment,” *Phys. Rev. D*, vol. 86, 2012.
- [56] S. F. King and C. Luhn, “Neutrino mass and mixing with discrete symmetry,” *Rep. Prog. Phys.*, vol. 76, no. 056201, 2013.
- [57] R. N. Mohapatra, “Theory of neutrinos: a white paper,” *Rep. Prog. Phys.*, vol. 70, no. 11, p. 1757, 2007.

- 
- [58] W. R. Hamilton, “On a General Method in Dynamics,” *Philosophical Transaction of the Royal Society Part I & Part II*, 1834/1835. Papers edited by David R. Wilkins, School of Mathematics, Trinity College, Dublin 2, Ireland (2000).
- [59] S. Weinberg, *The Quantum Theory of Fields Vol. I*. Cambridge University Press, 2005.
- [60] K. Zuber, *Neutrino Physics, Second Edition (Series in High Energy Physics, Cosmology and Gravitation)*. Taylor & Francis, 2011.
- [61] T. W. B. Kibble, “Symmetry Breaking in Non-Abelian Gauge Theories,” *Phys. Rev.*, vol. 155, no. 5, pp. 1554–1561, 1967.
- [62] R. N. Mohapatra and P. B. Pal, *Massive Neutrinos in Physics and Astrophysics (Third Edition)*. World Scientific, 2004. World Scientific Lecture Notes in Physics Vol. 72.
- [63] E. Majorana, “Teoria simmetrica dell elettrone e del positrone,” *Il Nuovo Cimento (1924-1942)*, vol. 14, pp. 171–184, 1937.
- [64] M. Gell-Mann, P. Ramond, and R. Slansky, “Complex spinors and unified theories,” *Conf. Proc. Supergravity Workshop, Stony Brook, New York*.
- [65] R. N. Mohapatra and G. Senjanović, “Neutrino mass and spontaneous parity non-conservation,” *Phys. Rev. Lett.*, vol. 44, no. 14, pp. 912–915, 1980.
- [66] R. N. Mohapatra and G. Senjanović, “Neutrino masses and mixings in gauge models with spontaneous parity violation,” *Phys. Rev. D*, vol. 23, pp. 165–180, Jan 1981.
- [67] G. Lazarides, Q. Shafi, and C. Wetterich, “Proton lifetime and fermion masses in an SO(10) model,” *Nucl. Phys. B*, vol. 181, no. 2, pp. 287–300, 1981.
- [68] E. Ma, “Verifiable radiative seesaw mechanism of neutrino mass and dark matter,” *Phys. Rev. D*, vol. 73, no. 7, p. 077301, 2006.
- [69] S. Antusch, M. Drees, J. Kersten, M. Lindner, and M. Ratz, “Neutrino mass operator renormalization in two Higgs doublet models and the MSSM,” *Phys. Lett. B*, vol. 525, no. 1-2, pp. 130–134, 2002.
- [70] J. Schechter and J. W. F. Valle, “Neutrino masses in SU(2)⊗U(1) theories,” *Phys. Rev. D*, vol. 22, no. 9, pp. 2227–2235, 1980.
- [71] J. A. Casas, J. R. Espinosa, A. Ibarra, and I. Navarro, “Nearly degenerate neutrinos, supersymmetry and radiative corrections,” *Nucl. Phys. B*, vol. 569, no. 1-3, pp. 82–106, 2000.
- [72] R. N. Mohapatra, S. Nasri, and H.-B. Yu, “Grand unification of symmetry,” *Phys. Lett. B*, vol. 636, no. 2, pp. 114–118, 2006.

- [73] N. Arkani-Hamed, S. Dimopoulos, G. Dvali, and J. March-Russell, “Neutrino masses from large extra dimensions,” *Phys. Rev. D*, vol. 65, no. 2, p. 024032, 2001.
- [74] L. Bergström and A. Goobar, *Cosmology and Particle Astrophysics*. Springer, 2006.
- [75] A. A. Penzias and R. W. Wilson, “A Measurement of Excess Antenna Temperature at 4080 Mc/s,” *Astrophys. J.*, vol. 142, no. 1, pp. 419–421, 1965.
- [76] J. C. Mather *et al.*, “A preliminary measurement of the cosmic microwave background spectrum by the cosmic background explorer (COBE) satellite,” *Astrophys. J.*, vol. 354, pp. 37–40, 1990.
- [77] J. Lesgourgues and S. Pastor, “Neutrino Mass from Cosmology,” *Adv. in High Energy Phys.*, vol. 2012, no. 608515, 2012.
- [78] S. Dodelson, *Modern Cosmology*. Academic Press, New York, USA, 2003.
- [79] A. Friedmann, “Über die Krümmung des Raumes,” *Zeitschrift für Physik*, vol. 10, pp. 377–387, 1922.
- [80] A. Einstein, “Die Grundlagen der allgemeinen Relativitätstheorie,” *Annalen der Physik*, vol. 354, no. 7, pp. 769–822, 1916.
- [81] Planck Collaboration, “Planck 2013 results. XVI. Cosmological parameters,” 2013. Submitted to *Astron. Astrophys.*
- [82] J. Angrik *et al.*, “KATRIN Design Report (FZKA Report 7090).” 2004.
- [83] H. Aihara and others (SDSS Collaboration), “The Eighth Data Release of the Sloan Digital Sky Survey: First Data from SDSS-III,” *Astrophys. J. Suppl. S.*, vol. 193, no. 2, p. 29, 2011.
- [84] M. Tegmark, “Cosmological Neutrino Bounds for Non-Cosmologists,” *Physica Scripta*, vol. 2005, no. T121, p. 153, 2005.
- [85] S. Bird, M. Viel, and M. G. Haehnelt, “Massive neutrinos and the non-linear matter power spectrum,” *Mon. Not. R. Astron. Soc.*, vol. 420, no. 3, pp. 2551–2561, 2012.
- [86] S. Agarwal and H. A. Feldman, “The effect of massive neutrinos on the matter power spectrum,” *Mon. Not. R. Astron. Soc.*, vol. 410, no. 3, pp. 1647–1654, 2011.
- [87] S. Hannestad, “Neutrino physics from precision cosmology,” *Prog. Part. Nucl. Phys.*, vol. 65, no. 2, pp. 185–208, 2010.
- [88] A. Giuliani and A. Poves, “Neutrinoless Double-Beta Decay,” *Adv. in High Energy Phys.*, vol. 2012, no. 857016, 2012.

- 
- [89] M. Goeppert-Mayer, “Double beta-disintegration,” *Phys. Rev.*, vol. 48, no. 6, pp. 512–516, 1935.
- [90] S. R. Elliot, A. A. Hahn, and M. K. Moe, “Direct evidence for two-neutrino double-beta decay in  $^{82}\text{Se}$ ,” *Phys. Rev. Lett.*, vol. 59, no. 18, pp. 2020–2023, 1987.
- [91] G. Racah, “Sulla simmetria tra particelle e antiparticelle,” *Il Nuovo Cimento (1924-1942)*, vol. 14, pp. 322–328, 1937.
- [92] W. H. Furry, “On transition probabilities in double beta-disintegration,” *Phys. Rev.*, vol. 56, no. 12, pp. 1184–1193, 1939.
- [93] F. Deppisch and H. Päs, “Pinning down the mechanism of neutrinoless double beta decay with measurements in different nuclei,” *Phys. Rev. Lett.*, vol. 98, no. 23, p. 232501, 2007.
- [94] T. D. Lee and C. N. Yang, “Question of Parity Conservation in Weak Interactions,” *Phys. Rev.*, vol. 104, no. 1, pp. 254–258, 1956.
- [95] C. S. Wu *et al.*, “Experimental Test of Parity Conservation in Beta Decay,” *Phys. Rev.*, vol. 105, no. 4, pp. 1413–1415, 1957.
- [96] A. Faessler, *Grand unified theories and the double beta-decay*. Springer Berlin/Heidelberg, 1987. Lecture Notes in Physics Vol. 279.
- [97] M. Doi *et al.*, “Neutrino masses and the double  $\beta$  decay,” *Phys. Lett. B*, vol. 103, no. 3, pp. 219–224, 1981.
- [98] H. V. Klapdor-Kleingrothaus, A. Dietz, H. L. Harney, and I. V. Krivosheina, “Evidence for Neutrinoless Double Beta Decay,” *Mod. Phys. Lett. A*, vol. 16, pp. 2409–2420, 2001.
- [99] C. E. Aalseth *et al.*, “Comment on ‘Evidence for Neutrinoless Double Beta Decay’,” *Mod. Phys. Lett. A*, vol. 17, no. 22, pp. 1475–1478, 2002.
- [100] S. Schönert *et al.*, “Status of the GERmanium Detector Array (GERDA) for the search of neutrinoless  $\beta\beta$  decays of  $^{76}\text{Ge}$  at LNGS,” *Prog. Part. Nucl. Phys.*, vol. 57, no. 1, pp. 241–250, 2006.
- [101] “Gerda homepage.” <http://www.mpi-hd.mpg.de/gerda/>.
- [102] C. Arnaboldi *et al.*, “CUORE: a cryogenic underground observatory for rare events,” *Nucl. Inst. Meth. A*, vol. 518, no. 3, pp. 775 – 798, 2004.
- [103] M. Sisti *et al.*, “From Cuoricino to CUORE: Investigating neutrino properties with double beta decay,” *Journal of Physics: Conference Series*, vol. 203, no. 1, p. 012069, 2010.
- [104] “Cuore homepage.” <http://crio.mib.infn.it/wig/Cuorepage/CUORE.php>.

- [105] M. Auger *et al.*, “Search for Neutrinoless Double-Beta Decay in  $^{136}\text{Xe}$  with EXO-200,” *Phys. Rev. Lett.*, vol. 109, no. 032505, 2012.
- [106] “Exo-200 homepage.” <http://www-project.slac.stanford.edu/exo/> [12-Sep-2011].
- [107] G. Drexlin, V. Hannen, S. Mertens, and C. Weinheimer, “Current Direct Neutrino Mass Experiments,” *Adv. in High Energy Phys.*, vol. 2013, no. 293986, 2013.
- [108] M. Schlösser, *Accurate calibration of the Raman system for the Karlsruhe Tritium Neutrino Experiment*. PhD thesis, KIT, 2013.
- [109] E. Otten, “Searching the absolute  $\nu$  mass in tritium  $\beta$ -decay: interplay between nuclear, atomic and molecular physics,” *Hyperfine Interactions*, vol. 196, pp. 3–23, 2010.
- [110] G. Altarelli and K. Winter, *Neutrino Mass*. Springer Tracts in Modern Physics, Springer, 2003.
- [111] F. Gatti, “Microcalorimeter measurements,” *Nucl. Phys. B - Proc. Sup.*, vol. 91, no. 1-3, pp. 293–296, 2001.
- [112] R. B. Firestone, S. Y. F. Chu, and C. M. Baglin, “Table of Isotopes, 8th Edition,” 1999.
- [113] M. Sisti *et al.*, “New limits from the Milano neutrino mass experiment with thermal microcalorimeters,” *Nucl. Instr. Meth. Phys. A*, vol. 520, pp. 125–131, 2004.
- [114] A. Nucciotti, “The MARE Project,” *J. Low Temp. Phys.*, vol. 151, pp. 597–602, 2008.
- [115] “MARE homepage.” <http://mare.dfm.uninsubria.it/frontend/exec.php> [last update: 18-Mar-2011].
- [116] MARE Collaboration, “MARE-1 in Milan: Status and Perspectives,” *J. Low Temp. Phys.*, vol. 167, pp. 1035–1040, 2012.
- [117] M. Galeazzi *et al.*, “The Electron Capture Decay of  $^{163}\text{Ho}$  to Measure the Electron Neutrino Mass with sub-eV Accuracy,” 2012. arXiv:1202.4763v3 [physics.ins-det].
- [118] J.-P. Porst *et al.*, “Low temperature magnetic calorimeters for high precision measurements of  $^{163}\text{Ho}$  and  $^{187}\text{Re}$  spectra,” *Nucl. Phys. B (Proc. Suppl.)*, vol. 446, pp. 229–232, 2012.
- [119] P. C.-O. Ranitzsch *et al.*, “Development of Metallic Magnetic Calorimeters for High Precision Measurements of Calorimetric  $^{187}\text{Re}$  and  $^{163}\text{Ho}$  Spectra,” *J. Low Temp. Phys.*, vol. 167, no. 5-6, pp. 1004–1014, 2012.
- [120] E. Otten and C. Weinheimer, “Neutrino mass limit from tritium beta decay,” *Rep. Prog. Phys.*, vol. 71, p. 36 pp., 2008.

- 
- [121] J. Bonn *et al.*, “The mainz neutrino mass experiment,” *Nucl. Phys. B Proc. Suppl.*, vol. 91, no. 1-3, pp. 273–279, 2001. Neutrino 2000.
- [122] V. M. Lobashev *et al.*, “Direct search for mass of neutrino and anomaly in the tritium beta-spectrum,” *Phys. Lett. B*, vol. 460, no. 1-2, pp. 227–235, 1999.
- [123] V. M. Lobashev *et al.*, “Direct search for neutrino mass and anomaly in the tritium beta-spectrum: Status of troitsk neutrino mass experiment,” *Nucl. Phys. B Proc. Suppl.*, vol. 91, no. 1-3, pp. 280–286, 2001. Neutrino 2000.
- [124] M. Babutzka *et al.*, “Monitoring of the operating parameters of the KATRIN Windowless Gaseous Tritium Source,” *New J. Phys.*, vol. 14, no. 103046, 2012.
- [125] M. Sturm, *Aufbau und Test des Inner-Loop-Systems der Tritiumquelle von KATRIN*. PhD thesis, KIT, 2010.
- [126] T. Bode, “Optimierung des 2-Phasen-Kühlkonzepts für den WGTS-Demonstrator von KATRIN,” Master’s thesis, KIT, 2011.
- [127] S. Grohmann *et al.*, “Precise temperature measurement at 30 K in the KATRIN source cryostat,” *Cryogenics*, vol. 51, no. 8, pp. 438 – 445, 2011.
- [128] M. Hötzel, “Berechnung von KATRIN Messspektren unter Einbeziehung der Eigenschaften der fensterlosen gasförmigen Tritiumquelle,” Master’s thesis, KIT, 2009.
- [129] M. Hötzel, *Simulation and analysis of source-related effects for KATRIN*. PhD thesis, KIT, 2012.
- [130] M. Babutzka, “Status of the rear section.” KATRIN Collaboration meeting, March 2013, <http://fuzzy.fzk.de/bscw/bscw.cgi/774000/95-TRP-5401-S1-MBabutzka.pptx>.
- [131] M. Röllig, “Studien zu einem Röntgendetektorsystem zur Bestimmung der Aktivität in der KATRIN Tritiumquelle,” Master’s thesis, KIT, 2011.
- [132] S. Mertens *et al.*, “Background due to stored electrons following nuclear decays at the KATRIN experiment,” *Astropart. Phys.*, vol. 41, pp. 52–62, 2013.
- [133] A. Kosmider, *Tritium Retention Techniques in the KATRIN Transport Section and Commissioning of its DPS2-F Cryostat*. PhD thesis, KIT, 2012.
- [134] X. Luo *et al.*, “Monte-Carlo simulation of gas flow through the KATRIN DPS2-F differential pumping system,” *Vacuum*, vol. 80, no. 864, 2006.
- [135] S. Lukic *et al.*, “Measurement of the gas-flow reduction factor of the KATRIN DPS2-F differential pumping section,” *Vacuum*, vol. 86, no. 1126, 2012.

- [136] M. Ubieto-Díaz, *Off-line commissioning of a non-destructive FT-ICR system for monitoring the ion concentration in the KATRIN beamline*. PhD thesis, Ruprecht-Karls-Universität Heidelberg, MPIK, 2011.
- [137] M. Ubieto-Díaz *et al.*, “A broad-band FT-ICR Penning trap system for KATRIN,” *Int. J. Mass Spectrom.*, vol. 288, no. 1-3, pp. 1–5, 2009.
- [138] A. Windberger, “Berechnungen und Simulationen zum Verhalten von Ionen in der differentiellen Pumpstrecke des KATRIN-Experiments,” Master’s thesis, KIT, 2010.
- [139] F. Glück, “Electrons and ions in KATRIN STS.” KATRIN Collaboration meeting, October 2010, <http://fuzzy.fzk.de/bscw/bscw.cgi/662596/95-TRP-4936-C2-FG1ck.ppt>.
- [140] S. Reimer, “Ein elektrostatisches Dipolsystem zur Eliminierung von Ionen in der DPS2-F des KATRIN Experiments,” Master’s thesis, KIT, 2009.
- [141] W. Gil *et al.*, “The cryogenic pumping section of the KATRIN experiment,” *IEEE Trans. Appl. Supercond.*, vol. 20, no. 316, 2010.
- [142] X. Luo and C. Day, “Test particle Monte Carlo study of the cryogenic pumping system of the Karlsruhe tritium neutrino experiment,” *J. Vac. Sci. Technol. A*, vol. 26, no. 5, pp. 1319–1325, 2008.
- [143] M. Prall *et al.*, “The KATRIN pre-spectrometer at reduced filter energy,” *New J. Phys.*, vol. 14, no. 073054, 2012.
- [144] F. Habermehl, *Electromagnetic measurements with the KATRIN pre-spectrometer*. PhD thesis, KIT, 2009.
- [145] F. M. Fränkle, *Background Investigations of the KATRIN Pre-Spectrometer*. PhD thesis, KIT, 2010.
- [146] S. Mertens, *Study of Background Processes in the Electrostatic Spectrometers of the KATRIN Experiment*. PhD thesis, KIT, 2012.
- [147] F. M. Fränkle, “Erste Messungen der elektromagnetischen Eigenschaften des KATRIN Vorspektrometers,” Master’s thesis, KIT, 2006.
- [148] M. Lammers, “Untersuchung der Untergrundrate des KATRIN Vorspektrometers im Bereich hoher Feldstärken,” Master’s thesis, KIT, 2009.
- [149] S. Görhardt, “Reduktion der durch Radon induzierten Untergrundprozesse in den KATRIN Spektrometern,” Master’s thesis, KIT, 2010.
- [150] J. Reich *et al.*, “Technical design and commissioning of the KATRIN large volume air coil system,” 2013. in preparation.

- 
- [151] F. Glück *et al.*, “Electromagnetic design of the KATRIN large-volume air coil system,” 2013. subm. to *New J. Phys.*
- [152] K. Bokeloh (nee Hugenberg), “Design of the electrode system of the KATRIN main spectrometer,” Master’s thesis, University of Münster, 2008.
- [153] M. Zacher, “Electromagnetic design and field emission studies for the inner electrode system of the KATRIN main spectrometer,” Master’s thesis, University of Münster, 2009.
- [154] K. Valerius, *Spectrometer-related background processes and their suppression in the KATRIN experiment*. PhD thesis, University of Münster, 2009.
- [155] K. Valerius, “Electromagnetic design and inner electrode for the KATRIN main spectrometer,” *Prog. Part. Nucl. Phys.*, vol. 57, no. 1, pp. 58–60, 2006.
- [156] K. Valerius, “The wire electrode system for the KATRIN main spectrometer,” *Prog. Part. Nucl. Phys.*, vol. 64, no. 2, pp. 291–293, 2010.
- [157] J. Wolf, “Size matters: The vacuum system of the Katrin neutrino experiment,” *Journal of the Vacuum Society of Japan*, vol. 52, pp. 278–284, 2009.
- [158] C. Day *et al.*, “Determination of the sticking probability of a Zr–V–Fe non-evaporable getter strip,” *Journal of Vacuum Science and Technology A: Vacuum, Surfaces, and Films*, vol. 25, no. 4, pp. 824–830, 2007.
- [159] X. Luo, L. Bornschein, C. Day, and J. Wolf, “KATRIN NEG pumping concept investigation,” *Vacuum*, vol. 81, no. 6, pp. 777–781, 2007. Proceedings of the European Vacuum Conference (EVC-9).
- [160] M. Zboril, *Solid electron sources for the energy scale monitoring in the KATRIN experiment*. PhD thesis, University of Münster, 2011.
- [161] M. Slezak, “The source of monoenergetic electrons for the monitoring of spectrometer in the KATRIN neutrino experiment,” Master’s thesis, Charles University Prague, NPI Rez, 2011.
- [162] M. Erhard, “Untersuchung der Langzeitstabilität des nuklearen Standards für die Energieskala des KATRIN-Experiments,” Master’s thesis, KIT, 2012.
- [163] J. Goullon, “Installation and commissioning of the monitor spectrometer,” Master’s thesis, KIT, 2010.
- [164] M. Schupp, “Inbetriebnahme des Monitorspektrometers und erste Messungen,” Master’s thesis, KIT, 2011.
- [165] F. Harms, “Assembly and First Results of the KATRIN Focal-Plane Detector System at KIT,” Master’s thesis, KIT, 2012.

- [166] J. Beamson *et al.*, “The collimating and magnifying properties of a superconducting field photoelectron spectrometer,” *J. Phys. E*, vol. 13, no. 64, 1980.
- [167] V. M. Lobashev and P. E. Spivak, “A method for measuring the electron antineutrino rest mass,” *Nucl. Instrum. Methods Phys. Res., Sect. A*, vol. 240, no. 2, pp. 305–310, 1985.
- [168] A. Picard *et al.*, “A solenoid retarding spectrometer with high resolution and transmission for keV electrons,” *Nucl. Instrum. Methods Phys. Res., Sect. B*, vol. 63, no. 3, pp. 345–358, 1992.
- [169] H. Higaki *et al.*, “Electrons Confined with an Axially Symmetric Magnetic Mirror Field,” *AIP Conference Proceedings*, vol. 1037, no. 1, pp. 106–114, 2008.
- [170] C. Kranz, “Optimierung der Methoden und Messprozeduren zur Entfaltung der Energieverlustfunktion beim KATRIN-Experiment,” Master’s thesis, University of Münster, 2011.
- [171] S. Ziegler, “Die Extraktion der Energieverlustfunktion beim KATRIN Experiment,” Master’s thesis, KIT, 2013.
- [172] N. Doss *et al.*, “Molecular effects in investigations of tritium molecule  $\beta$ -decay endpoint experiments,” *Phys. Rev. C*, vol. 73, no. 025502, 2006.
- [173] N. Doss and J. Tennyson, “Excitations to the electronic continuum of  ${}^3\text{He}^+$  in investigations of the  $t_2$  beta-decay experiments,” *J. Phys. B*, vol. 41, no. 125701, 2008.
- [174] W. Käfer, *Investigation of the KATRIN sensitivity*. PhD thesis, KIT, 2012.
- [175] K. N. Abazajian *et al.*, “Light Sterile Neutrinos: A White Paper,” 2012. arXiv:1204.5379 [hep-ph].
- [176] J. Bonn *et al.*, “The KATRIN sensitivity to the neutrino mass and to right-handed currents in beta decay,” *Phys. Lett. B*, vol. 703, no. 3, pp. 310–312, 2011.
- [177] A. E. Bernardini and O. Bertolami, “Lorentz violating extension of the standard model and the  $\beta$ -decay endpoint,” *Phys. Rev. D*, vol. 77, no. 8, 2008.
- [178] J. S. Diaz, V. A. Kostelecky, and R. Lehnert, “Relativity violations and beta decay,” 2013. arXiv:1305.4636 [hep-ph].
- [179] S. Groh, “Untersuchung von UV-Laser induziertem Untergrund am KATRIN Vorspektrometer,” Master’s thesis, KIT, 2010.
- [180] B. Hillen, *Untersuchung von Methoden zur Unterdrückung des Spektrometeruntergrunds am KATRIN Experiment*. PhD thesis, University of Münster, 2011.

- 
- [181] M. Prall, *Transmission properties of the pre-spectrometer at high surplus energies*. PhD thesis, University of Münster, 2011.
- [182] J. Reich, *Magnetic Field Inhomogeneities and Their Influence on Transmission and Background at the KATRIN Main Spectrometer*. PhD thesis, KIT, 2013.
- [183] M. Zacher. PhD thesis, University of Münster, 2013. in preparation.
- [184] B. Leiber. PhD thesis, KIT, 2013. in preparation.
- [185] M. Beck *et al.*, “Effect of a sweeping conductive wire on electrons stored in a Penning-like trap between the KATRIN spectrometers,” *EPJ A*, vol. 44, pp. 499–511, 2010.
- [186] E. Otten, “Removing stored electrons by a magnetic pulse.” Internal KATRIN report, 2010.
- [187] D. Furse *et al.*, “Kassiopeia - the simulation package for the KATRIN experiment,” in preparation.
- [188] D. Furse. PhD thesis, MIT, 2013. in preparation.
- [189] M. Haag. PhD thesis, KIT, 2014. in preparation.
- [190] T. J. Corona, “Tools for Electromagnetic Field Simulation in the KATRIN Experiment,” Master’s thesis, MIT, 2009.
- [191] T. J. Corona. PhD thesis, UNC, 2013. in preparation.
- [192] F. Glück, “Runge-Kutta method for numerical solution of differential equation system.” <http://fuzzy.fzk.de/bscw/bscw.cgi/d479152/rungekutta.pdf>.
- [193] P. W. Sharp, “Numerical comparisons of some explicit Runge-Kutta pairs of orders 4 through 8,” *ACM Trans. Math. Softw.*, vol. 17, pp. 387–409, September 1991.
- [194] S. Filippi and J. Gräf, “New Runge Kutta Nystroem formula-pairs of order 8(7), 9(8), 10(9) and 11(10) for differential equations of the form  $y'' = f(x, y)$ ,” *Journal of Computational and Applied Mathematics*, vol. 14, no. 3, pp. 361 – 370, 1986.
- [195] J. Barrett, “Embedded Runge-Kutta Steppers for KMath.” <http://fuzzy.fzk.de/bscw/bscw.cgi/216568/EmbeddedRungeKutta-JBarrett.pdf>.
- [196] J. C. Butcher, *Numerical Methods for Ordinary Differential Equations*. John Wiley and Sons, Ltd, 2005.
- [197] J. Faust, “Predictor Corrector Methods.” Internal KATRIN report, <http://fuzzy.fzk.de/bscw/bscw.cgi/216568/PredictorCorrectorMethods.doc>, 2012.

- [198] B. Jung, “Simulation des Myon-induzierten Untergrundes und dessen Speicherwahrscheinlichkeit am KATRIN Hauptspektrometer,” Master’s thesis, KIT, 2011.
- [199] H. Tawara *et al.*, “Cross sections and related data for electron collisions with hydrogen molecules and molecular ions,” *J. Phys. Chem. Ref. Data*, vol. 19, no. 3, pp. 617–636, 1990.
- [200] J. Liu and S. Hagstrom, “Dissociative cross section of  $H_2$  by electron impact,” *Phys. Rev. A*, vol. 50, no. 4, 1994.
- [201] S. Trajmar, D. F. Register, and A. Chutjian, “Electron scattering by molecules II. Experimental methods and data,” *Phys. Rep.*, vol. 97, pp. 219–356, 1983.
- [202] Y.-K. Kim and M. E. Rudd, “Binary-encounter-dipole model for electron impact ionization,” *Phys. Rev. A*, vol. 50, no. 5, 1994.
- [203] W. Hwang, Y.-K. Kim, and M. E. Rudd, “New model for electron-impact ionization cross section of molecules,” *J. Chem. Phys.*, vol. 104, no. 8, 1996.
- [204] G. Arrighini, F. Biondi, and C. Guidotti, “A study of the inelastic scattering of fast electrons from molecular hydrogen,” *Mol. Phys.*, vol. 41, no. 6, pp. 1501–1514, 1994.
- [205] Z. Chen and A. Z. Msezane, “Calculation of the excitation cross sections for the  $^1\Sigma_u^+$  and  $C^1\Pi_u^+$  states in  $e - H_2$  scattering at 60 eV,” *Phys. Rev. A*, vol. 51, no. 5, pp. 3745–3750, 1995.
- [206] E. Gargioni and B. Grosswendt, “Electron-Impact Cross Sections for Ionization and Excitation,” <http://physics.nist.gov/PhysRefData/Ionization/molTable.html>.
- [207] E. Gargioni and B. Grosswendt, “Electron scattering from argon: Data evaluation and consistency,” *Rev. Mod. Phys.*, vol. 80, pp. 451–480, 2008.
- [208] B. Leiber, “Non-axially symmetric field and trajectory calculations for the KATRIN-experiment,” Master’s thesis, KIT, 2009.
- [209] W. H. Press *et al.*, *Numerical Recipes 3rd Edition: The Art of Scientific Computing*. New York, NY, USA: Cambridge University Press, 3 ed., 2007.
- [210] F. Glück, “Axisymmetric magnetic field calculation with zonal harmonic expansion,” *Progress In Electromagnetics Research B*, vol. 32, pp. 351–388, 2011.
- [211] F. Glück, “Axisymmetric electric and magnetic field calculations with zonal harmonic expansion,” *PIER Proceedings, Kuala Lumpur*, pp. 1698–1702, 2012.
- [212] F. Glück, “Collection of codes to calculate magnetic fields, including documentation.” Internal KATRIN reports, <http://fuzzy.fzk.de/bscw/bscw.cgi/216558>, 2006.

- 
- [213] R. J. LeVeque, *Finite Difference Methods for Ordinary and Partial Differential Equations: Steady-State and Time-Dependent Problems*. SIAM, 2007.
- [214] S. C. Brenner and L. R. Scott, *The mathematical theory of finite element methods*. Springer Texts in Applied Mathematics, Springer, 2008.
- [215] W. C. Gibson, *The Method of Moments in Electromagnetics*. Springer Texts in Applied Mathematics, Chapman & Hall/CRC, 2008.
- [216] F. Glück *et al.*, “Students’ Workshop on KATRIN EMD 04-05-2006.” Internal KATRIN documents, <http://fuzzy.fzk.de/bscw/bscw.cgi/213805>, 2006.
- [217] J. Formaggio *et al.*, “Solving for micro- and macro-scale electrostatic configurations using the Robin Hood algorithm,” *Progress in Electromagnetics Research B*, vol. 39, no. 1, 2012.
- [218] W. J. Cody, “Chebyshev approximations for the complete elliptic integrals K and E,” *Math. of Comp.*, vol. 19, no. 105, 1965.
- [219] F. Glück, “Axisymmetric electric field calculation with zonal harmonic expansion,” *Progress In Electromagnetics Research B*, vol. 32, pp. 319–350, 2011.
- [220] T. Corona, “Fully Three-Dimensional Electrostatic Simulations of the Main Spectrometer.” KATRIN Collaboration meeting, March 2013, <http://fuzzy.fzk.de/bscw/bscw.cgi/774166/95-TRP-5453-S5-TJCorona.pdf>.
- [221] F. Glück, “Collection of codes to calculate electric fields, including documentation.” Internal KATRIN reports, <http://fuzzy.fzk.de/bscw/bscw.cgi/216563>, 2006.
- [222] F. Glück, “LFCS air coil current set computations by mathematical optimization.” KATRIN Collaboration meeting, October 2012, <http://fuzzy.fzk.de/bscw/bscw.cgi/751346/95-TRP-5357-E2-FGlueck.pptx>.
- [223] N. Stallkamp, “LFCS optimization for the main spectrometer.” KATRIN Collaboration meeting, March 2013, <http://fuzzy.fzk.de/bscw/bscw.cgi/774161/95-TRP-5449-D2-NStallkamp.pdf>.
- [224] N. Stallkamp Master’s thesis, KIT, 2013. in preparation.
- [225] F. James, “MINUIT - Function Minimization and Error Analysis,” *Reference Manual*, 2000.
- [226] S. Schams, “Data analysis and sterile neutrino sensitivity of the KATRIN experiment,” Master’s thesis, KIT, 2013.
- [227] J. Nelder and R. Mead, “A Simplex Method for Function Minimization,” *The Computer Journal*, vol. 7, no. 308, 1965.

- [228] N. Wandkowsky, “Design and Background Simulations for the KATRIN Main Spectrometer and Air Coil System,” Master’s thesis, KIT, 2009.
- [229] F. Glück *et al.*, “Air coil system and magnetic field sensor system.” Internal KATRIN report, <http://fuzzy.fzk.de/bscw/bscw.cgi/d530439/Air%20Coil%20System%20and%20Magnetic%20Field%20Sensor%20System.pdf>, 2009.
- [230] D. Goldmann, “Untersuchung systematischer Störeffekte auf das  $\beta$ -Spektrum im Mainzer Neutrinoruhemassenexperiment,” Master’s thesis, University of Mainz, 1995.
- [231] B. Müller, “Umbau des Mainzer Neutrinomassenexperiments und Untergrunduntersuchungen im Hinblick auf KATRIN,” Master’s thesis, University of Mainz, 2002.
- [232] S. Macmillan and S. Maus, “International Geomagnetic Reference Field - the tenth generation,” *Earth Planets Space*, vol. 57, pp. 1135–1140, 2005.
- [233] “On-line calculators to estimate current and past values of the magnetic field.” [www.ngdc.noaa.gov/geomag/magfield.shtml](http://www.ngdc.noaa.gov/geomag/magfield.shtml).
- [234] J. Reich, “Magnetfeldmessungen und Designarbeiten für das EMCS Luftspulensystem am KATRIN Hauptspektrometer,” Master’s thesis, KIT, 2009.
- [235] M. Fujita, “The coil design of the superconducting MRI magnet,” *IEEE Trans. Magn.*, vol. 24, no. 6, pp. 2907–2909, 1988.
- [236] J. L. Kirschvink, “Uniform Magnetic Fields and Double-Wrapped Coil Systems: Improved Techniques for the Design of Bioelectromagnetic Experiments,” *Bioelectromagnetics*, vol. 13, no. 5, pp. 401–411, 1992.
- [237] I. Sasada and Y. Nakashima, “Planar coil systems consisting of three coil pairs for producing a uniform magnetic field,” *J. Appl. Phys.*, vol. 99, no. 08D904, 2006.
- [238] J. W. Clark, “A New Method for Obtaining a Uniform Magnetic Field,” *Rev. Sci. Instrum.*, vol. 9, no. 10, pp. 320–322, 1938.
- [239] J. E. Everett and J. E. Osemeikhian, “Spherical coils for uniform magnetic fields,” *J. Sci. Instrum.*, vol. 43, no. 7, pp. 470–474, 1966.
- [240] F. Glück, “Earth-field compensation with cylindrical or ellipsoidal coils.” KATRIN EMD meeting, April 2004, [http://fuzzy.fzk.de/bscw/bscw.cgi/d99726/FG\\_compcoil.pdf](http://fuzzy.fzk.de/bscw/bscw.cgi/d99726/FG_compcoil.pdf).
- [241] A. Osipowicz, “Compensation and manipulation of the magnetic field at the main spectrometer.” Internal KATRIN report, <https://fuzzy.fzk.de/bscw/bscw.cgi/d159319/earth%20magnetic%20field%20compensation.pdf>, 2005.

- 
- [242] F. Glück and A. Osipowicz, “Air coil design at the main spectrometer.” KATRIN Collaboration meeting, April 2008, <http://fuzzy.fzk.de/bscw/bscw.cgi/d443733/95-TRP-4440-D1-FGlueck-A0sipowicz.ppt>.
- [243] J. Nocedal and S. J. Wright, *Numerical Optimization*. Springer, 2006.
- [244] J. M. A. Bhatti, *Practical Optimization methods*. Springer, New York, 2000.
- [245] J. A. Snyman, *Practical Mathematical Optimization*. Springer, New York, 2005.
- [246] H. Hein, “Angular defined photo-electron sources for the KATRIN experiment,” Master’s thesis, University of Münster, 2010.
- [247] N. Steinbrink. PhD thesis, University of Münster, 2015. in preparation.
- [248] M. Dropmann, “Elektrostatisches Design der Pumpports des KATRIN Hauptspektrometers,” Master’s thesis, University of Münster, 2011.
- [249] V. Hannen *et al.*, “E-gun update and installation at the main spectrometer.” KATRIN Collaboration meeting, March 2013, <http://fuzzy.fzk.de/bscw/bscw.cgi/774130/95-TRP-5418-A1-VHannen.pdf>.
- [250] G. Cowan, *Statistical Data Analysis*. Oxford Science Publications, 1998.
- [251] G. M. Phillips and P. J. Taylor, *Theory and Applications of Numerical Analysis*. Acad. Press, 1973.
- [252] D. Bourgin, “Transmission function simulation for the KATRIN main spectrometer.” Internal KATRIN report, 2012.
- [253] private communication with F. Glück, 2013.
- [254] A. D. Polyanin and A. V. Manzhirov, *Handbook of Integral Equations*. CRC Press, 1998.
- [255] S. Groh, “Investigation of high rate transmission measurements including detector electronics.” KATRIN Collaboration meeting, March 2013, <http://fuzzy.fzk.de/bscw/bscw.cgi/774151/95-TRP-5440-C1-SGroh.pdf>.
- [256] J. P. Schall, “Untersuchung zu Untergrundprozessen am Mainzer Neutrinomassenexperiment,” Master’s thesis, Mainz, 2001.
- [257] B. Flatt, *Voruntersuchungen zu den Spektrometern des KATRIN-Experiments*. PhD thesis, University of Mainz, 2004.
- [258] F. Glück, “Background theory: radial motion of electrons from spectrometer electrodes into the fluxtube.” Internal KATRIN report, [http://fuzzy.fzk.de/bscw/bscw.cgi/d174403/background\\_theory\\_Glueck.pdf](http://fuzzy.fzk.de/bscw/bscw.cgi/d174403/background_theory_Glueck.pdf), 2005.

- [259] F. Glück, “Steel in the KATRIN buildings and the magnetic field in the main spectrometer.” Internal KATRIN report, [http://fuzzy.fzk.de/bscw/bscw.cgi/d176563/steel\\_buildings\\_Glueck.pdf](http://fuzzy.fzk.de/bscw/bscw.cgi/d176563/steel_buildings_Glueck.pdf), 2005.
- [260] S. Agostinelli and J. Allison, “Geant4a simulation toolkit,” *Nucl. Instrum. Meth. A*, vol. 506, no. 3, pp. 250–303, 2003.
- [261] J. Allison *et al.*, “Geant4 developments and applications,” *IEEE Transactions on Nuclear Science*, vol. 53, pp. 270–278, feb. 2006.
- [262] F. Glück, “Secondary electron emission in the pre-spectrometer and in the Mainz spectrometer.” KATRIN Collaboration meeting, March 2009, <http://fuzzy.fzk.de/bscw/bscw.cgi/540728/95-TRP-4652-A5-FGlueck.ppt>.
- [263] S. Miereis, “Investigation of muon induced Background in the KATRIN Experiment,” Master’s thesis, KIT, 2012.
- [264] P. Rovedo Master’s thesis, KIT, 2013. in preparation.
- [265] J. Reichenbacher, *Final KARMEN-Results on Neutrino-Oscillations and Neutrino-Nucleus-Interactions in the Energy-Regime of Supernovae*. PhD thesis, KIT, 2004.
- [266] B. Armbruster *et al.*, “Improved limits on  $\bar{\nu}_e$  emission from  $\mu^+$  decay,” *Phys. Rev. Lett.*, vol. 90, no. 181804, 2003.
- [267] J. Reichenbacher, “Untersuchung der optischen Eigenschaften großflächiger Plastikzintillatoren für den KARMEN-Upgrade,” Master’s thesis, Forschungszentrum Karlsruhe, 1998.
- [268] H. Arlinghaus, “Investigation of the muon-induced secondary electron background in the KATRIN Experiment,” Master’s thesis, University of Münster, 2009.
- [269] “CAEN SY127 - Technical Information Manual.” [http://www.tunl.duke.edu/documents/public/electronics/CAEN/caen\\_sy127.pdf](http://www.tunl.duke.edu/documents/public/electronics/CAEN/caen_sy127.pdf).
- [270] M. Leber, *Monte Carlo Calculations of the Intrinsic Detector Backgrounds for the Karlsruhe Tritium Neutrino Experiment*. PhD thesis, University of Washington, 2010.
- [271] M. Howe, “ORCA - Object-oriented Real-time Control and Acquisition.” [http://orca.physics.unc.edu/~markhowe/Orca\\_Help/About\\_Orca.html](http://orca.physics.unc.edu/~markhowe/Orca_Help/About_Orca.html).
- [272] M. Howe *et al.*, “Sudbury neutrino observatory neutral current detector acquisition software overview,” *IEEE Transactions on Nuclear Science*, vol. 51, no. 3, pp. 878–883, 2004.
- [273] E. Aguayo *et al.*, “The MAJORANA Experiment,” *AIP Conf. Proc.*, vol. 1417, pp. 95–99, 2011.

- 
- [274] R. Brun and F. Rademakers, “ROOT - An object oriented data analysis framework,” *Nucl. Instrum. Meth. A*, vol. 389, pp. 81–86, 1997.
- [275] P. Rovedo, “Status of the muon detection system.” KATRIN Collaboration meeting, March 2013, <http://fuzzy.fzk.de/bscw/bscw.cgi/d774809/95-TRP-5447-D2-PRovedo.pdf>.
- [276] F. Glück *et al.*, “EMD consequences of electrical shorts at the inner electrode system.” Internal KATRIN report, <http://fuzzy.fzk.de/bscw/bscw.cgi/775422>, 2013.
- [277] F. Glück, “EMD properties of the main spectrometer with short circuited wire electrode system.” <http://fuzzy.fzk.de/bscw/bscw.cgi/774010/95-TRP-5411-S3-FGlueck.pptx>.
- [278] E. Otten, “The Mainz neutrino mass experiment,” *Prog. Part. Nucl. Phys.*, vol. 32, pp. 153–171, 1994.
- [279] F. M. Fränkle *et al.*, “Radon induced background processes in the KATRIN pre-spectrometer,” *Astropart. Phys.*, vol. 35, no. 3, pp. 128–134, 2011.
- [280] N. Wandkowsky *et al.*, “Modeling of electron emission processes accompanying Radon- $\alpha$ -decays within electrostatic spectrometers,” *subm. to New J. Phys.*, 2013. arXiv:1304.1375.
- [281] N. Wandkowsky *et al.*, “Validation of a model for Radon-induced background processes in electrostatic spectrometers,” *J. Phys. G*, 2013. in press, arXiv:1304.1379.
- [282] S. Mertens *et al.*, “Stochastic Heating by ECR as a Novel Means of Background Reduction in the KATRIN spectrometers,” *JINST*, vol. 7, no. P08025, 2012.
- [283] A. Sonzogni, “Interactive Chart of Nuclide.” National Nuclear Data Center: Brookhaven National Laboratory, <http://www.nndc.bnl.gov/chart/>.
- [284] K. Siegbahn, *Alpha-, beta- and gamma-ray spectroscopy*, vol. 2. North Holland Pub. Co. Amsterdam, 1968.
- [285] A. L.-M. Ch. Theisen and C. Bonnelle, “Internal conversion and summing effects in heavy-nuclei spectroscopy,” *Nucl. Instrum. Meth. A*, vol. 589, pp. 230–242, 2008.
- [286] E. Browne, “Nuclear Data Sheets for  $A = 215, 219, 223, 227, 231$ ,” *Nuclear Data Sheets*, vol. 93, no. 4, pp. 763–1061, 2001.
- [287] S.-C. and Wu, “Nuclear Data Sheets for  $A = 216$ ,” *Nuclear Data Sheets*, vol. 108, no. 5, pp. 1057 – 1092, 2007.
- [288] M. S. Freedman, “Ionization by Nuclear Transitions,” *Conference: Summer course in atomic physics, Carry-le-Rouet, France*, Jan 1975.

- [289] J. S. Hansen, "Internal ionization during alpha decay: A new theoretical approach," *Phys. Rev. A*, vol. 9, pp. 40–43, Jan 1974.
- [290] M. S. Freedman, "Atomic structure effects in nuclear events," *Annu. Rev. Nucl. Sci.*, vol. 24, pp. 209–248, 1974.
- [291] J. Bang and J. M. Hansteen, "Coulomb deflection effects on ionization and pair-production phenomena," *K. Dan. Vidensk. Selsk. Mat. - Fys. Medd.*, vol. 31, no. 13, pp. 1–43, 1959.
- [292] M. S. Rapaport, F. Asaro, and I. Perlman, "K-shell electron shake-off accompanying alpha decay," *Phys. Rev. C*, vol. 11, pp. 1740–1745, May 1975.
- [293] M. S. Rapaport, F. Asaro, and I. Perlman, "M- and L-shell electron shake-off accompanying alpha decay," *Phys. Rev. C*, vol. 11, pp. 1746–1754, May 1975.
- [294] S. Szucs and J. M. Delfosse, "Charge Spectrum of Recoiling  $^{216}\text{Po}$  in the  $\alpha$ -Decay of  $^{220}\text{Rn}$ ," *Phys. Rev. Lett.*, vol. 15, pp. 163–165, Jul 1965.
- [295] A. Migdal, "Ionization of atoms accompanying  $\alpha$ - and  $\beta$ -deca," *J. Phys. (USSR)*, vol. 4, p. 449, 1970.
- [296] E. H. S. Burhop, *The Auger effect and other radiationless transitions*. University Press Cambridge, 1952.
- [297] F. P. Larkins, "Semiempirical Auger-electron energies for elements  $10 \leq Z \leq 100$ ," *At. Data Nucl. Data Tables*, vol. 20, no. 4.
- [298] E. Pomplun, "Auger Electron Spectra - The Basic Data for Understanding the Auger Effect," *Acta Oncologica*, vol. 39, no. 6.
- [299] C. C. Lu *et al.*, "Relativistic Hartree-Fock-Slater eigenvalues, radial expectation values, and potentials for atoms,  $2 \leq Z \leq 126$ ," *Atomic Data*, vol. 3, pp. 1–131, 1971.
- [300] M. Mathsumoto and T. Nishimura, "Mersenne Twistor: A 623-dimensional equidistributed uniform pseudorandom number generator," *ACM T. Model. Comput. S.*, vol. 8, pp. 3–30, 1998.
- [301] C. Robert and G. Casella, *Monte Carlo Statistical Methods*. Springer Texts in Statistic, 2004.
- [302] J. B. E. Pomplun and D. E. Charlton, "A Monte Carlo Simulation of Auger Cascades," *Radiation Research*, vol. 111, pp. 533–552, 1987.
- [303] M. H. Chen, B. Crasemann, and H. Mark, "Relativistic radiationless transition probabilities for atomic K- and L-shells," *At. Data Nucl. Data Tables*, vol. 24, no. 1, pp. 13–37, 1979.

- 
- [304] E. J. McGuire, “Atomic M-Shell Coster-Kronig, Auger, and Radiative Rates and Fluorescence Yields for Ca-Th,” *Phys. Rev. A*, vol. 5, no. 3, pp. 1043–1047, 1972.
- [305] E. J. McGuire, “Atomic N-Shell Coster-Kronig, Auger, and radiative rates and fluorescence Yields for  $38 < Z < 103$ ,” *Phys. Rev. A*, vol. 9, no. 5, pp. 1840–1851, 1974.
- [306] M. Drescher *et al.*, “Time-resolved atomic inner-shell spectroscopy,” *Nature*, vol. 4198, pp. 803–807, 2002.
- [307] P. K. D.W. McCamant and R. Mathies, “Femtosecond Time-Resolved Stimulated Raman Spectroscopy: Application to the Ultrafast Internal Conversion in  $\beta$ -Carotene,” *J. Phys. Chem. A*, vol. 107, no. 40, pp. 8208–8214, 2003.
- [308] W. Maneschg *et al.*, “Measurement of extremely low radioactivity levels in stainless steel for GERDA,” *Nucl. Inst. Meth. A*, vol. 593, pp. 448–453, 2008.
- [309] S. P. Khare, “Ionizing Collisions of Electrons with Atoms and Molecules,” *Radiation Research*, vol. 64, no. 1, pp. 106–118, 1975.
- [310] G. Zuzel and H. Simgen, “High sensitivity radon emanation measurements,” *Appl. Rad. Isot.*, vol. 67, no. 5, pp. 889–893, 2009.
- [311] H. Simgen, “Radon Background in Low Level Experiment.” KATRIN Collaboration meeting, October 2010, <http://fuzzy.fzk.de/bscw/bscw.cgi/662565/95-TRP-4920-S4-HSimgen.pptx>.
- [312] R. L. Martin and J. S. Cohen, “Excitation and ionization accompanying the beta decay of  $T_2$ ,” *Physics Letters A*, vol. 110, no. 2, pp. 95–98, 1985.
- [313] D. Furse, “Magnetic pulse at the monitor spectrometer.” KATRIN Collaboration meeting, March 2012, <http://fuzzy.fzk.de/bscw/bscw.cgi/734881/95-TRP-5238-D1-DFurse.pdf>.
- [314] T. Thümmeler, “Entwicklung von Methoden zur Untergrundreduzierung am Mainzer Tritium  $\beta$ -Spektrometer,” Master’s thesis, Johannes Gutenberg Universität Mainz, 2002.
- [315] K. Valerius, “Elektromagnetisches Design für das Hauptspektrometer des KATRIN Experiments,” Master’s thesis, Universität Bonn, 2004.
- [316] E. Glasner and B. Weiss, “Sensitive dependence on initial conditions,” *Nonlinearity*, vol. 6, pp. 1067–1075, 1993.
- [317] J. Büchner and L. M. Zelenyi, “Regular and chaotic particle motion in sheared magnetic field reversals,” *Adv. Space Res.*, vol. 11, no. 9, pp. 9177–9182, 1991.

- 
- [318] H. V. Malova and M. I. Sitnov, “Nonlinear structure, stochasticity and intermittency in the dynamics of charged particles near a magnetic field reversal,” *Phys. Lett. A*, vol. 140, no. 3, pp. 136–140, 1989.
- [319] B. A. Coomes, H. Kocak, and K. J. Palmer, “A Shadowing Theorem for ordinary differential equations,” *Z. angew. Math. Phys.*, vol. 46, pp. 85–106, 1995.

# Acknowledgement

An dieser Stelle möchte ich allen danken, die mich während meiner Doktorarbeit unterstützt haben. Ganz besonderer Dank gebührt hierbei folgenden Personen:

- ◇ PROF. DR. G. DREXLIN für die Möglichkeit nach meiner Diplomarbeit auch meine Doktorarbeit bei KATRIN durchführen zu können und ganz besonders für seine Unterstützung und sein Engagement, mit dem er zum Gelingen dieser Arbeit beigetragen hat,
- ◇ PROF. DR. W. DE BOER, der sich freundlicherweise als Korreferent für diese Arbeit zur Verfügung gestellt hat,
- ◇ DR. F. GLÜCK für die unglaublich hilfreichen Diskussionen und die stete Geduld, mit der er einem jegliche Fragen beantwortet,
- ◇ DR. S. MERTENS für ihre stete Unterstützung und die tolle Zusammenarbeit beim Kampf gegen den Untergrund,
- ◇ DIPL.-PHYS. S. GROH für die großartige Unterstützung bei allen programmiertechnischen Problemen und für die stete moralische Unterstützung,
- ◇ B. BENDER, H. WEINGARDT, B. FRETZ, M. HELLMANN, S. MIEREIS, P. ROVEDO und DR. F. FRÄNKLE für die unschätzbare Unterstützung beim Aufbau des Myon-Detektor Systems,
- ◇ DR. F. GLÜCK, D. BOURGIN, T. PLATON und N. STALLKAMP für ihre Beiträge zur LFCS Optimierung,
- ◇ DR. K. SCHLÖSSER für die tolle Unterstützung und Geduld bei den Messungen am Monitorspektrometer,
- ◇ DR. J. REICH und N. TROST (und allen vor ihm) für die gute Atmosphäre im Büro,
- ◇ DIPL.-PHYS. S. GROH und DR. F. GLÜCK für das emsige Korrekturlesen meiner Arbeit, und

- 
- ◇ allen MITARBEITERN DER INSTITUTE FÜR KERNPHYSIK UND TECHNISCHE PHYSIK am Campus Nord für die sehr angenehme Arbeitsatmosphäre, die immer spaßigen Dienstreisen und die stets vorhandene Hilfsbereitschaft, sowie jedem, der nicht namentlich erwähnt ist.

Außerdem möchte ich Nico Trost danken, dem für mich wichtigsten Menschen, der mich während der gesamten Zeit unterstützt hat.